Lecture Notes in Networks and Systems 41

Utpal Biswas
Amit Banerjee
Sukhomay Pal
Arindam Biswas
Debashis Sarkar
Sandip Haldar *Editors*

Advances in Computer, Communication and Control

Proceedings of ETES 2018

Springer

Lecture Notes in Networks and Systems

Volume 41

The series "Lecture Notes in Networks and Systems" publishes the latest developments in Networks and Systems—quickly, informally and with high quality. Original research reported in proceedings and post-proceedings represents the core of LNNS.

Volumes published in LNNS embrace all aspects and subfields of, as well as new challenges in, Networks and Systems.

The series contains proceedings and edited volumes in systems and networks, spanning the areas of Cyber-Physical Systems, Autonomous Systems, Sensor Networks, Control Systems, Energy Systems, Automotive Systems, Biological Systems, Vehicular Networking and Connected Vehicles, Aerospace Systems, Automation, Manufacturing, Smart Grids, Nonlinear Systems, Power Systems, Robotics, Social Systems, Economic Systems and other. Of particular value to both the contributors and the readership are the short publication timeframe and the world-wide distribution and exposure which enable both a wide and rapid dissemination of research output.

The series covers the theory, applications, and perspectives on the state of the art and future developments relevant to systems and networks, decision making, control, complex processes and related areas, as embedded in the fields of interdisciplinary and applied sciences, engineering, computer science, physics, economics, social, and life sciences, as well as the paradigms and methodologies behind them.

More information about this series at http://www.springer.com/series/15179

Utpal Biswas · Amit Banerjee
Sukhomay Pal · Arindam Biswas
Debashis Sarkar · Sandip Haldar
Editors

Advances in Computer, Communication and Control

Proceedings of ETES 2018

Springer

Editors
Utpal Biswas
Department of Computer Science
and Engineering
University of Kalyani
Kalyani, West Bengal, India

Amit Banerjee
Department of Electrical
and Computer Engineering
National University of Singapore
Singapore, Singapore

Sukhomay Pal
Department of Mechanical Engineering
Indian Institute of Technology Guwahati
Guwahati, Assam, India

Arindam Biswas
Department of Electronics
and Communication Engineering
Asansol Engineering College
Asansol, West Bengal, India

Debashis Sarkar
Department of Mechanical Engineering
Asansol Engineering College
Asansol, West Bengal, India

Sandip Haldar
Department of Physics
Asansol Engineering College
Asansol, West Bengal, India

ISSN 2367-3370 ISSN 2367-3389 (electronic)
Lecture Notes in Networks and Systems
ISBN 978-981-13-3121-3 ISBN 978-981-13-3122-0 (eBook)
https://doi.org/10.1007/978-981-13-3122-0

Library of Congress Control Number: 2018963046

This Springer imprint is published by the registered company Springer Nature Singapore Pte Ltd.
The registered company address is: 152 Beach Road, #21-01/04 Gateway East, Singapore 189721, Singapore

Preface

A revolutionary change has been observed in the field of computer, communications, control and systems during the last two decades. Keeping this in mind, Asansol Engineering College, Asansol, West Bengal (WB), India, organised the first international conference on Emerging Trends in Engineering and Science (ETES 2018) held on 23 and 24 March 2018. ETES 2018 focuses on the integration of intelligent communication systems, control systems and devices related to all aspects of engineering and sciences. ETES 2018 aims to provide a forum and vibrant platform for researchers, academicians, scientists and industrial practitioner to share their original research work, findings and practical development experiences. The proceedings will be published in the Lecture Notes in Networks and Systems book series of Springer. This book contains high-quality research papers divided into 56 chapters which are completely relevant to this lecture note series.

The general aim of the conference is to promote international collaboration in education and research in all fields and disciplines of engineering. More than 225 researchers and delegates attended the conference. ETES 2018 is an international forum for those who presented their research findings. It also provides the opportunity to presenters to discuss the main aspects and the latest results in the field of education and research.

The organising committee is extremely grateful to the authors who had shown a tremendous response to the call for papers. Over 135 papers were submitted from the researchers, academicians and students on a wide area of three parallel tracks in intelligent communication systems, control systems and devices, along with a poster presentation session. A total of 56 papers are accepted for publication with Springer.

We are obliged to Prof. S. K. Dey, honourable Pro-Vice Chancellor, Maulana Abul Kalam Azad University of Technology, West Bengal (MAKAUT, WB), India; Prof. S. P. Mukherjee, Centenary Professor, Calcutta University, Kolkata, WB, India; Prof. N. R. Das, Calcutta University, Kolkata, WB, India; Prof. N. Ganguly, IIT Kharagpur, WB, India, for their confidence they have invested on us for organizing this international conference.

Asansol, India — Sandip Haldar

Contents

Editors and Contributors

About the Editors

Utpal Biswas received his B.E., M.E. and Ph.D. in Computer Science and Engineering from Jadavpur University, India, in 1993, 2001 and 2008, respectively. He served as Faculty Member in the Department of Computer Science and Engineering, National Institute of Technology (NIT) Durgapur, India, from 1994 to 2001. Currently, he is working as Professor and Dean in the Department of Computer Science and Engineering, University of Kalyani, West Bengal, India. He is co-author of 65 research articles in a number of journals, chapters and conferences. His research interests include optical communication, ad hoc and mobile communication, semantic web services and e-governance.

Amit Banerjee is Scientist ER in the Department of Electrical and Computer Engineering at the National University of Singapore. Previously, he was Scientific Researcher at the Advanced Device Research Division, Shizuoka University, Japan. He was also Research Associate at Energy Research Unit, Indian Association for the Cultivation of Science, Jadavpur, and has worked as Engineer at Farris Engineering, Gurgaon. He completed his Ph.D. in synthesis and optimisation of nano-materials in 2016 at Jadavpur University and his Master's in physics from JNU, New Delhi. His areas of interest include microelectronics, semiconductor and solid-state devices, optoelectronics–photonics, solar cells and thin films. He is an active reviewer, editor and advisory committee member of several international conferences. He has published in numerous high-impact journals and has filed two patents. He is currently involved in the development of instrumentation.

Sukhomay Pal is Associate Professor at the Indian Institute of Technology Guwahati. He was Postdoc Fellow at University of Pretoria, South Africa, and was also a Co-chief Adviser and Maintenance Engineer for Pal & Das Ceramic, Asansol, West Bengal. He completed his Ph.D. in the development and validation of soft computing-based models for pulsed gas metal arc welding processes at the

Department of Mechanical Engineering, IIT Kharagpur. He received his Master's from Bengal Engineering and Science University, West Bengal, and Bachelor's from Jadavpur University. His research interests include welding process monitoring and control, tool condition monitoring, non-conventional machining process, application of artificial neural network and genetic algorithms. He actively publishes in these areas and is also a reviewer for several journals and conferences.

Arindam Biswas is Associate Professor in the Department of Electronics and Communication Engineering, Asansol Engineering College. He received his Ph.D. in the effect of electric field in ferroelectronics and discrete breathers in optical communication from the National Institute of Technology Durgapur; his M.Tech. from Calcutta University; and his B.Tech. from West Bengal University. He completed his postdoc in optical material at Pusan National University, South Korea. His research interests include electron devices and circuits, IMPATT THz source and electrical engineering. He has published numerous papers in high-impact journals and conferences. He also has one patent and is a reviewer and editor of a number of journals and conferences.

Debashis Sarkar is Associate Professor in the Department of Mechanical Engineering, Asansol Engineering College. He completed his Ph.D. in mechanical engineering at Jadavpur University. His area of research interest is maintenance and maintenance modelling. He has more than 10 years of teaching experience in areas such as engineering mechanics, graphics, primary and advanced manufacturing process and industrial engineering. He has actively published in these areas.

Sandip Haldar is Associate Professor in Asansol Engineering College. He completed his Ph.D. in solid-state physics at Jadavpur University, and at present, he is working on nano-materials. He received his M.Sc. in physics from Calcutta University. He has published papers in numerous journals as well as conference proceedings. He has been an investigator in various research projects funded by DST and UGC.

Contributors

Arunabha Adhikari Department of Physics, West Bengal State University, Barasat, India

Aman Agarwal Asansol Engineering College, Asansol, India

Md. Aref Billaha Department of Applied Electronics & Instrumentation Engineering, Asansol Engineering College, Asansol, India

Arun Atta Department of Electronics and Communication Engineering, Jalpaiguri Government Engineering College, Jalpaiguri, India

Amit Bakshi School of Electronics Engineering, Kalinga Institute of Industrial Technology (KIIT) Deemed to be University, Bhubaneswar, Odisha, India

Abhik Banerjee Department of Electrical Engineering, National Institute of Technology, Yupia, Arunachal Pradesh, India

Khushi Banerjee Department of Electronics and Communication Engineering, Asansol Engineering College, Asansol, India

Tushar Kanti Banerjee Department of Electrical Engineering, Jalpaiguri Government Engineering College, Jalpaiguri, West Bengal, India

Subhendu Barat Department of Computer Science and Engineering, NSHM Knowledge Campus, Durgapur, India

Banani Basu Department of ECE, National Institute of Technology, Silchar, Silchar, Assam, India

Shayari Basu Department of Physics, Indian Institute of Engineering Science and Technology, Shibpur, Howrah, India

Santi Kumari Behera Department of Computer Science and Engineering, VSSUT, Burla, Odisha, India; Department of Computer Science and Engineering, VSSUT, Sambalpur, Odisha, India

Anup K. Bhattacharjee Department of Electronics and Communication Engineering, National Institute of Technology, Durgapur, Durgapur, WB, India

Ankan Bhattacharya Department of Electronics and Communication Engineering, National Institute of Technology, Durgapur, Durgapur, WB, India; Department of Electronics and Communication Engineering, Mallabhum Institute of Technology, Bishnupur, India

Lumbini Bhaumik Department of Computer Science and Engineering, Asansol Engineering College, Asansol, West Bengal, India

Biplab Bhowmick Department of Electronics and Communication Engineering, Asansol Engineering College, Asansol, India

Bubu Bhuyan Department of Information Technology, North Eastern Hill University, Shillong, Meghalaya, India

Arindam Biswas Department of Electronics and Communication Engineering, Asansol Engineering College, Asansol, India

Ashim Kumar Biswas Department of ECE, National Institute of Technology, Silchar, Silchar, Assam, India

Shreerupa Biswas Institute of Radio Physics and Electronics, University of Calcutta, Kolkata, West Bengal, India

Syed Nisar Bukhari National Institute of Electronics & Information Technology (NIELIT) Srinagar, Srinagar, J&K, India

Sudipta Chakrabarty Department of Physics, Indian Institute of Engineering Science and Technology, Shibpur, Howrah, India

Ankit Chakraborty Department of Electrical Engineering, Jalpaiguri Government Engineering College, Jalpaiguri, West Bengal, India

Saswata Chakraborty Department of Electronics and Communication Engineering, Asansol Engineering College, Asansol, West Bengal, India

Ujjal Chakraborty Department of ECE, National Institute of Technology, Silchar, Silchar, Assam, India

Arup Kumar Chandra Department of Electronics & Instrumentation Engineering, Asansol Engineering College, Asansol, West Bengal, India

Avinash Chandra School of Electronics Engineering, Vellore Institute of Technology, Vellore, India

Apurba Chatterjee Department of Electrical Engineering, Asansol Engineering College, Asansol, India

D. Chaudhuri Department of Electronics & Communication Engineering, Modern Institute of Engineering & Technology, Hooghly, West Bengal, India

Santosh Kumar Choudhary Department of Electronics and Communication Engineering, VNR Vignana Jyothi Institute of Engineering and Technology, Hyderabad, India

Binayak S. Choudhury Department of Mathematics, Indian Institute of Engineering Science and Technology, Shibpur, Howrah, West Bengal, India

Muneer Ahmad Dar National Institute of Electronics & Information Technology (NIELIT) Srinagar, Srinagar, J&K, India

Ashmi Chakraborty Das Department of Electronics Engineering, Indian Institute of Technology (Indian School of Mines), Dhanbad, Dhanbad, India

Nikhil R. Das Institute of Radio Physics and Electronics, University of Calcutta, Kolkata, West Bengal, India

Rupam Das Department of Electronics and Communication Engineering, Asansol Engineering College, Asansol, India

Santanu Das Department of Electrical Engineering, Jalpaiguri Government Engineering College, Jalpaiguri, West Bengal, India

Subir Kumar Das Department of Production Engineering, Jadavpur University, Kolkata, West Bengal, India; Department of Computer Application, Asansol Engineering College, Asansol, West Bengal, India

Sumanta Das Department of Electronics and Telecommunication Engineering, Dr. B. C. Roy Polytechnic, Durgapur, India

Sushrut Das Department of Electronics Engineering, Indian Institute of Technology (Indian School of Mines) Dhanbad, Dhanbad, Jharkhand, India

Arkabrata Dattaroy Department of Electrical Engineering, Jalpaiguri Government Engineering College, Jalpaiguri, West Bengal, India

Arnab De Department of Electronics and Communication Engineering, National Institute of Technology, Durgapur, Durgapur, WB, India

Tanmay De Department of Computer Science and Engineering, National Institute of Technology, Durgapur, Durgapur, India

Somen Debnath Department of Information Technology, Mizoram University, Aizawl, India

Subir Kumar Debnath Department of Production Engineering, Jadavpur University, Kolkata, West Bengal, India

M. Dey Department of Mathematics, Asansol Engineering College, Asansol, West Bengal, India

P. S. Dhara Department of Mathematics, Indian Institute of Engineering Science and Technology, Shibpur, Howrah, West Bengal, India

Divyansh School of Computer Science Engineering, KIIT, Bhubaneswar, India

Santosh Dora Department of Computer Science and Engineering, National Institute of Technology, Durgapur, Durgapur, India

Ajoy Kumar Dutta Department of Production Engineering, Jadavpur University, Kolkata, West Bengal, India

Santanu Dwari Department of Electronics Engineering, Indian Institute of Technology (Indian School of Mines), Dhanbad, Dhanbad, India

Ayandeep Ganguly Electrical Engineering Department, HIT, Haldia, India

Ujjwal Ghanta School of Materials Science and Engineering, Indian Institute of Engineering Science and Technology, Shibpur, Howrah, India

Aniruddha Ghosal Institute of Radio Physics and Electronics, University of Calcutta, Kolkata, India

Abhijyoti Ghosh Department of ECE, Mizoram University, Aizawl, Mizoram, India

Pratik Ghosh Department of Electronics & Communication Engineering, Murshidabad College of Engineering and Technology, Murshidabad, West Bengal, India

Chiranjib Goswami Department of Electronics & Instrumentation Engineering, Asansol Engineering College, Asansol, West Bengal, India; Department of AEIE, Asansol Engineering College, Asansol, West Bengal, India

Kuheli Goswami Electrical Engineering Department, BGI, Kolkata, India

Pabitra Kumar Guchhait Department of Electrical Engineering, National Institute of Technology, Yupia, Arunachal Pradesh, India

Shampa Guin Institute of Radio Physics and Electronics, University of Calcutta, Kolkata, West Bengal, India

Aggraj Gupta Department of Electronics Engineering, Indian Institute of Technology (Indian School of Mines) Dhanbad, Dhanbad, Jharkhand, India

Naimul Hasan Department of Electronics & Communication Engineering, Sanaka Educational Trust's Group of Institution, Durgapur, West Bengal, India

Syed Minhaz Hossain Department of Physics, Indian Institute of Engineering Science and Technology, Shibpur, Howrah, India

Intekhab Hussain AEIE Department, Asansol Engineering College, Asansol, West Bengal, India

Muzaffar Imam SAP Research Laboratory, Department of Electronics Engineering, IIT (ISM), Dhanbad, India

Md. Kamiul Hoque Purulia Government Engineering College, Puruliya, West Bengal, India

Souvik Kar Department of Electrical Engineering, Jalpaiguri Government Engineering College, Jalpaiguri, West Bengal, India

Anup Karak Department of Physics, Vidyasagar University, Midnapore, India

Debashree Patra Karmakar Department of ECE, Mallabhum Institute of Technology, Bishnupur, West Bengal, India

Sumanta Karmakar Department of Electronics and Communication Engineering, Asansol Engineering College, Asansol, India

Basuki Nath Keshri Department of Computer Science and Engineering, NSHM Knowledge Campus, Durgapur, India

Mohammad Imroz Khan Department of Electronics and Communication Engineering, Vignan's Foundation for Science, Technology and Research, Guntur, India

Ummer Iqbal Khan National Institute of Electronics & Information Technology (NIELIT) Srinagar, Srinagar, J&K, India

Kundan Kumar Asansol Engineering College, Asansol, West Bengal, India

Manoj Kumar SAP Research Laboratory, Department of Electronics Engineering, IIT (ISM), Dhanbad, India

Praveen Kumar Department of Electronics Engineering, Indian Institute of Technology (Indian School of Mines) Dhanbad, Dhanbad, Jharkhand, India

S. Kumar Department of Power Engineering, Jadavpur University, Kolkata, India

Vikash Kumar Department of Electronics Engineering, Indian Institute of Technology (Indian School of Mines) Dhanbad, Dhanbad, India

Aparna Kundu Department of ECE, National Institute of Technology, Durgapur, Durgapur, WB, India

Krishanu Kundu Department of Electronics and Communication Engineering, Dronacharya College of Engineering, Gurgaon, India

Heranmoy Maity NSHM Knowledge Campus Durgapur, Durgapur, India

Nishanta Majumdar Department of Electronics and Communication Engineering, Jalpaiguri Government Engineering College, Jalpaiguri, India

Pratyaya Majumdar Department of Electrical Engineering, Jalpaiguri Government Engineering College, Jalpaiguri, West Bengal, India

Lipika Mandal Department of Applied Electronics & Instrumentation Engineering, Asansol Engineering College, Asansol, India

Sambit S. Mandal Asansol Engineering College, Asansol, India

Swarnendu Mandal Department of Electrical Engineering, Jalpaiguri Government Engineering College, Jalpaiguri, West Bengal, India

Kaushik Mazumdar Department of Electronics Engineering, Indian Institute of Technology (Indian School of Mines) Dhanbad, Dhanbad, Jharkhand, India

M. Mishra Institute of Radio Physics and Electronics, University of Calcutta, Kolkata, West Bengal, India

Partha Mishra Department of Electrical Engineering, CEMK, Kolaghat, West Bengal, India

Bikas Mondal Department of Applied Electronics & Instrumentation Engineering, Asansol Engineering College, Asansol, India

S. Mondal Department of Mechanical, Jadavpur University, Kolkata, India

Sourav Mondal Department of Electronics and Communication Engineering, Jalpaiguri Government Engineering College, Jalpaiguri, India

F. Morichetti Department of Electronics Information and Bioengineering, Politecnico di Milano, Milan, Italy

Arpita Mukherjee Electrical Engineering Department, Camellia Group of Institutions, Kolkata, India

P. P. Mukherjee Department of Electronics & Communication Engineering, Academy of Technology, Adisaptagram, Hooghly, India

Piyali Mukherjee Institute of Radio Physics and Electronics, University of Calcutta, Kolkata, West Bengal, India

Sabyasachi Mukherjee Department of Computer Science and Engineering, Asansol Engineering College, Asansol, West Bengal, India

Soumen Mukherjee Department of Computer Application, RCC Institute of Information Technology, Kolkata, India

V. Mukherjee Department of Electrical Engineering, IIT (Indian School of Mines) Dhanbad, Dhanbad, Jharkhand, India

A. Nag Department of Physics, Modern Institute of Engineering & Technology, Hooghly, West Bengal, India

Deepa Naik Department of Computer Science and Engineering, National Institute of Technology, Durgapur, Durgapur, India

Nikita Department of Computer Science and Engineering, National Institute of Technology, Durgapur, Durgapur, India

Morrel V. L. Nunsanga Department of Information Technology, Mizoram University, Aizawl, India

Tuhin Pahari Department of Electronics and Communication Engineering, Jalpaiguri Government Engineering College, Jalpaiguri, India

Pintu Pal Department of Computer Application, Asansol Engineering College, Asansol, West Bengal, India

Sarit Pal Department of Electronics and Communication Engineering, Dr. B. C. Roy Engineering College, Durgapur, India

Manjusha Pandey School of Computer Science Engineering, KIIT, Bhubaneswar, India

Narendra Nath Pathak Department of Electronics and Communication Engineering, Dr. B. C. Roy Engineering College, Durgapur, India

S. N. Patra Department of Instrumentation Science, Jadavpur University, Kolkata, India

Udayabhaskar Pattapu Department of Electronics Engineering, Indian Institute of Technology (Indian School of Mines) Dhanbad, Dhanbad, Jharkhand, India

Prajit Paul Department of Electronics and Communication Engineering, Asansol Engineering College, Asansol, India

Shruti Pradhan School of Computer Science Engineering, KIIT, Bhubaneswar, India

Sanchita Pramanik Department of Electronics, Vidyasagar University, Midnapore, India

Dharmbir Prasad Asansol Engineering College, Asansol, West Bengal, India

Achyut Raj Asansol Engineering College, Asansol, West Bengal, India

Amit Rai Asansol Engineering College, Asansol, India

Pooja Raj School of Electronics Engineering, Kalinga Institute of Industrial Technology (KIIT) Deemed to be University, Bhubaneswar, Odisha, India

Somnath Rakshit Department of Computer Science and Engineering, Jalpaiguri Government Engineering College, Jalpaiguri, West Bengal, India

Sourav Rakshit Department of Applied Electronics & Instrumentation Engineering, Asansol Engineering College, Asansol, India

Amiya Kumar Rath Department of Computer Science and Engineering, VSSUT, Burla, Odisha, India

Siddharth S. Rautaray School of Computer Science Engineering, KIIT, Bhubaneswar, India

Bijayalaxmi Routray Department of Computer Science and Engineering, VSSUT, Sambalpur, Odisha, India

Aakash Kumar Roy Asansol Engineering College, Asansol, West Bengal, India

Bappadittya Roy Department of Electronics and Communication Engineering, National Institute of Technology, Durgapur, Durgapur, WB, India; Department of Electronics and Communication Engineering, Madanapalle Institute of Technology and Science, Madanapalle, India

Bhaskar Roy Department of Applied Electronics & Instrumentation Engineering, Asansol Engineering College, Asansol, India

Jibendu Sekhar Roy School of Electronics Engineering, Kalinga Institute of Industrial Technology (KIIT) Deemed to be University, Bhubaneswar, Odisha, India

Kousik Roy Department of Electronics and Communication Engineering, Asansol Engineering College, Asansol, West Bengal, India

Madhusudan Roy Surface Physics and Material Science Division, Saha Institute of Nuclear Physics, Kolkata, India

S. Sadique Anwer Askari SAP Research Laboratory, Department of Electronics Engineering, IIT (ISM), Dhanbad, India

Mamoni Saha Department of Electronics and Communication Engineering, National Institute of Technology, Durgapur, Durgapur, WB, India

P. Saha Department of Mathematics, Indian Institute of Engineering Science and Technology, Shibpur, Howrah, West Bengal, India

Laxminarayan Sahoo Department of Mathematics, Raniganj Girls' College, Raniganj, India

Shrabani Sangita Department of Computer Science and Engineering, VSSUT, Burla, Odisha, India

Debashis Sarkar Department of Mechanical Engineering, Asansol Engineering College, Asansol, India

Rajan Sarkar Department of Electrical Engineering, Asansol Engineering College, Asansol, India

Santu Sarkar Institute of Radio Physics and Electronics, University of Calcutta, Kolkata, West Bengal, India

Shubham Sarkar Department of Electronics and Communication Engineering, Jalpaiguri Government Engineering College, Jalpaiguri, India

Shubhasish Sarkar Department of Electrical Engineering, Jalpaiguri Government Engineering College, Jalpaiguri, West Bengal, India

Sujan Sarkar Department of Electronics and Communication Engineering, Jalpaiguri Government Engineering College, Jalpaiguri, India

S. Sau Department of Mechanical, Jadavpur University, Kolkata, India

Anupama Senapati School of Electronics Engineering, Kalinga Institute of Industrial Technology (KIIT) Deemed to be University, Bhubaneswar, Odisha, India

Prabira Kumar Sethy Department of Electronics, Sambalpur University, Sambalpur, Odisha, India

Ritika Sharma School of Electronics Engineering, Kalinga Institute of Industrial Technology (KIIT) Deemed to be University, Bhubaneswar, Odisha, India

Koushik Shit National Power Training Institute, Faridabad, India

Arindam Kumar Sil Electrical Engineering Department, Jadavpur University, Kolkata, India

Braj Kishore Singh Asansol Engineering College, Asansol, West Bengal, India

Rudra Pratap Singh Asansol Engineering College, Asansol, West Bengal, India

A. K. Sinha Kalyani Government Engineering College, Kaylani, West Bengal, India

Md. Tasinul Hoque Kalyani Government Engineering College, Kaylani, West Bengal, India

M. G. Tiary ECE Department, Asansol Engineering College, Asansol, West Bengal, India

Anushka Tiwari Department of Electronics Engineering, Indian Institute of Technology (Indian School of Mines) Dhanbad, Dhanbad, Jharkhand, India

A. Upadhyay Department of Mathematics, Asansol Engineering College, Asansol, West Bengal, India

Kumari Arti Yadav Department of Applied Electronics & Instrumentation Engineering, Asansol Engineering College, Asansol, India

Ruchi Yadav School of Electronics Engineering, Kalinga Institute of Industrial Technology (KIIT) Deemed to be University, Bhubaneswar, Odisha, India

Transient Voltage Analysis of a Hybrid Power System Model by Using Novel Symbiosis Organism Search Algorithm

Abhik Banerjee, Pabitra Kumar Guchhait, Apurba Chatterjee and V. Mukherjee

Abstract Symbiosis organism search (SOS) algorithm is a novel meta-heuristic search algorithm based on the interactions of organisms in the environment. In SOS, the behaviour of the organisms in the nature is taken into consideration for the purpose of optimization. In this paper, the effectiveness of this SOS algorithm is being tested for the compensation of reactive power of the isolated hybrid power system. In the tested isolated power system, this paper has been considered as a wind engine based induction generator and a diesel engine based synchronous generator. Under the running condition, minimizing the gap between the demand and supply of reactive power has been provided by a static synchronous compensator (STATCOM). In the studied model, a PID controller is also carried out to track the degree of reactive power compensation under small input perturbation.

1 Introduction

Now, the renewable energy sources are more important than the conventional energy sources due to its various advantages. But renewable energy sources have the major disadvantage is that it is intermittent in nature. So now, the hybrid energy system is often much acceptable than any other energy system. Usually, the hybrid energy sys-

A. Banerjee (✉) · P. K. Guchhait
Department of Electrical Engineering, National Institute of Technology, Yupia, Arunachal Pradesh, India
e-mail: abhik_banerjee@rediffmail.com

P. K. Guchhait
e-mail: pabitraguchhait@gmail.com

A. Chatterjee
Department of Electrical Engineering, Asansol Engineering College, Asansol, India
e-mail: apurbanirsha@gmail.com

V. Mukherjee
Department of Electrical Engineering, IIT (Indian School of Mines), Dhanbad, Jharkhand, India
e-mail: vivek_agamani@yahoo.com

U. Biswas et al. (eds.), *Advances in Computer, Communication and Control*, Lecture Notes in Networks and Systems 41, https://doi.org/10.1007/978-981-13-3122-0_1

tem consists of synchronous generator (SG) and induction generator (IG). The hybrid energy system may consist a diesel engine based synchronous generator (SG) and a wind engine based induction generator (IG). For running the hybrid energy system, the synchronous generator provides active as well as reactive power to the system but the induction generator only provides active power to the system. Induction generator required reactive power for its operation under the running of a constant slip (s). Most of the loads are reactive in nature so to drive a specified load their always required active as well reactive power. So, in the hybrid system, there is a mismatch in reactive power occurred. The deficit or excess in reactive power of a hybrid power system may cause various problems like abruptly voltage fluctuations, steady state as well as transient stability. So, reactive power compensation is required for the healthy operation of the system. The requirement of desirable reactive power may provide by the various flexible ac transmission systems (FACTs) devices [1]. A shunt or series reactor may provide adequate amount of reactive power [2]. In the paper [3], condenser provides the deficit of reactive power but it may not be suitable for the hybrid system because it has no capability to maintain the stability when abruptly voltage fluctuations have occurred in the system. So, for healthy operation of the isolated hybrid power system, the FACTs devices like SVC, STATCOM, TCSC, etc., are used. There are various papers [4–9] where SVC-, TCSC- and STATCOM-based FACTs controller is used to maintain the reactive power of the system. Static synchronous compensator (STATCOM) has various advantages than the SVC controller [10]. STATCOM has the tremendous capability to perform the system as a stable one when the system senses large disturbances [11]. In the research paper [11], STATCOM-based PI controller is described to maintain the reactive power of the isolated diesel-wind hybrid power system. The STATCOM-PI controller parameters are optimized using algorithms GA, ANN and ANFIS.

Symbiosis organism search (SOS) algorithm is a new meta-heuristic search algorithm developed by Cheng and Prayogo [12] in 2014 inspired from the behaviours of various living organisms in nature. SOS algorithm has been developed with the three simple basic steps that include: (a) mutualism phase where the two organisms in nature interact with each other and both of them are benefitted (e.g. Oxpecker and Zebra). (b) commensalism phase where the two organisms interact with each other and in this case, one is benefitted but another may or may not be benefitted (e.g. Tree and Spider). (c) Parasitism phase where the one becomes beneficial from the interaction and it is the fittest in the system and fully destroyed the other (e.g. Plasmodium parasite and human body). The SOS algorithm is better than the other algorithms because of its no specific parameters that should be optimized and it has the quick convergent rates than the others.

In the present work, the objectives are (a) to develop a isolated hybrid wind-diesel power system model (b) use STATCOM-PID controller to tune of the parameters and to maintain the system stability under small voltage fluctuations and (c) a novel heuristic algorithm SOS is used to optimize the parameters of the isolated hybrid system and compare the results with ALO-based algorithm results for its efficacy.

2 Mathematical Modelling of Isolated Hybrid Power System

The single line diagram of the depicted hybrid power system model and the Simulink model of this design model are given in Figs. 1 and 2.

From Fig. 1, it has been shown that the under normal operating condition, the real and reactive power balance equations are written as

$$\Delta P_{SG} + \Delta P_{IG} - P_{load} = 0 \tag{1}$$

$$\Delta Q_{SG} + \Delta Q_{STATCOM} - \Delta Q_{IG} - Q_{load} = 0 \tag{2}$$

When any sort of disturbances occurs in the system, the reactive power demanded by the load as well as IG is increased therefore a reactive power mismatch happens in the system. But the grid has a permissible limit to control the certain tolerance. Therefore the surplus of reactive power may cause effect the voltage profile. So, reactive power control is more necessary to maintain the terminal voltage profile (Table 1).

The Simulink model of the isolated hybrid wind-diesel model in s-domain has been focused in Fig. 2. The principal transfer function of the studied hybrid model is given in s-domain as

$$\Delta V(s) = \frac{K_V}{(1 + sT_V)}[\Delta Q_{SG} + \Delta Q_{STATCOM} - \Delta Q_{IG} - Q_{load}] \tag{3}$$

For any sort of disturbances, the incremental change of reactive power in SG, IG and STATCOM is written as

$$\Delta Q_{SG} = K_1 \Delta E_q(s) + K_2 \Delta V(s) \tag{4}$$

$$\Delta Q_{IG}(s) = K_5 \Delta V(s) \tag{5}$$

$$\Delta Q_{STATCOM}(s) = K_j \Delta \alpha(s) + K_k \Delta V(s) \tag{6}$$

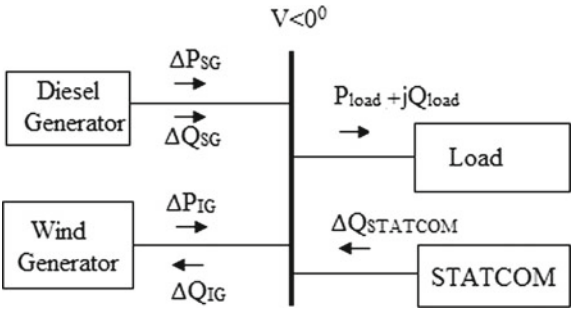

Fig. 1 Single line block diagram of the studied model

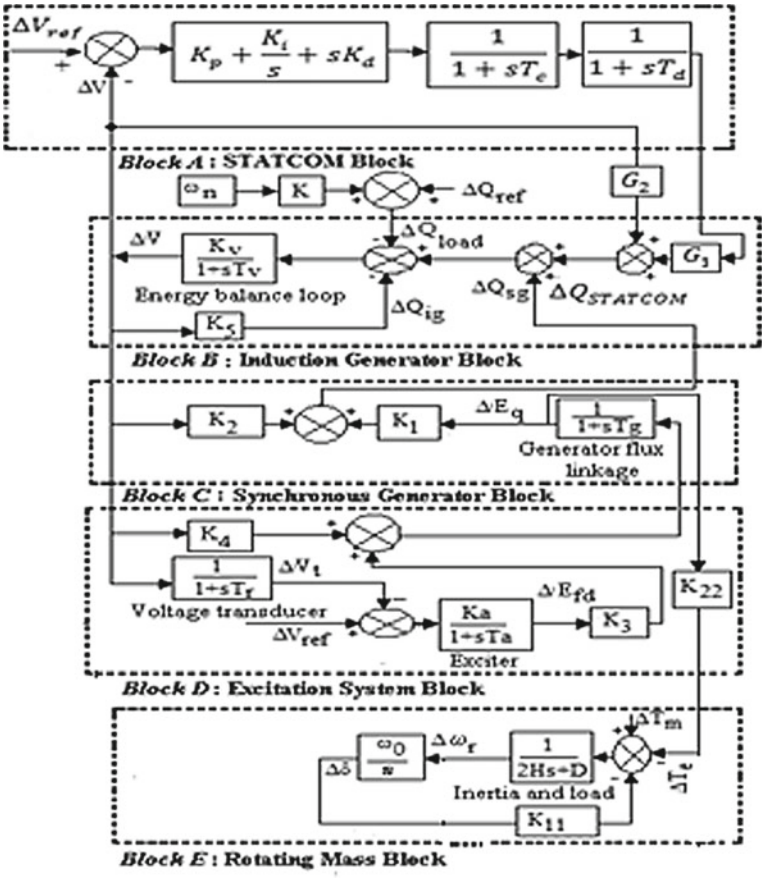

Fig. 2 Transfer function model of the studied hybrid system with STATCOM

The various parameter values of the studied model are given in appendix Tables 2 and 3.

3 Objective Function Formulation of the Present Problem

The objectives of the present work may be worked out by doing the mathematical analyses of the system eigenvalues. Eigenvalue analysis approach is done to tune the parameters of the isolated hybrid power system model and to achieve some degree of relative stability as well as the damping of the electrical modes of oscillations [1, 13]. An objective function based on eigenvalue analysis is structured as [13]

Table 1 Optimal parameters values and the best fitness value for different algorithms under different input conditions

Model + STATCOM	V and Xeq in p.u.	Optimal parameters value	Best fitness value	Elapsed time
SOS	1.03; 1.0	−31.8058, 6.0802, 0.0010, 0.7466, 0.0010	23.8103	4.331280
ALO		1.0004, 10.0000, 31.2518, 0.5655, 0.2613	26.4590	8.404380
SOS	1.01; 1.0	−19.8890, 8.3208, 2.0852, 0.7410, 0.1268	23.8103	4.445983
ALO		1.0001, 10.0000, 30.2851, 0.5916, 0.2245	26.2601	8.154146
SOS	1.0; 1.08	−25.8571, 10.0000, 0.0010, 0.7708, 0.0807	23.8103	4.149989
ALO		1.0037, 10.0000, 25.8699, 0.4227, 0.5074	26.1604	8.156278
SOS	1.0; 0.93	−21.8773, 6.0716, 0.0010, 0.7422, 0.1749	23.8103	4.387885
ALO		1.0044, 10.0000, 26.2550, 0.3906, 0.5284	26.1619	8.108451
SOS	1.0; 0.4752	−23.0773, 7.8866, 0.0010, 0.7672, 0.0398	23.8103	3.975375
ALO		1.0000, 10.0000, 29.8870, 0.6032, 0.2054	26.1650	7.963798
SOS	0.99; 1.08	−21.6163, 9.8857, 0.0010, 0.1492, 0.7547	23.8103	4.162304
ALO		1.0000, 10.0000, 34.2157, 0.0100, 0.6459	26.0735	8.059489
SOS	0.97; 1.08	−23.1996, 8.0000, 0.0010, 0.7485, 0.0513	23.8103	4.473538
ALO		1.0002, 10.0000, 22.7910, 0.5080, 0.4621	25.8705	8.127750
SOS	0.97; 0.93	−32.5864, 10.0000, 0.0010, 0.0010, 0.8577	23.8103	4.015157
ALO		1.0000, 10.0000, 23.3619, 0.5489, 0.4034	25.8703	8.178638
SOS	0.97; 0.4752	−15.7685, 9.2936, 0.0010, 0.7458, 0.2418	23.8103	4.552873
ALO		1.0000, 10.0000, 22.7246, 0.4939, 0.4783	25.8693	8.157957
SOS	1.01; 1.08	−26.3569, 9.5277, 0.0010, 0.0010, 0.7772	23.8103	4.011459
ALO		1.0000, 10.0000, 26.6509, 0.4561, 0.4688	26.2596	8.066174
SOS	1.01; 0.93	−28.5989, 9.6884, 0.0010, 0.0010, 0.8176	23.8103	4.132353
ALO		1.0004, 10.0000, 27.1707, 0.5234, 0.3856	26.2592	8.242917
SOS	1.01; 0.4752	−19.0985, 8.5236, 3.4818, 0.1115, 0.7412	23.8103	4.166023
SOS		1.0002, 10.0000, 26.6894, 0.4514, 0.4725	26.2567	8.066964

$$J = 10 \times J_1 + 10 \times J_2 + 0.01 J_3 + J_4 \tag{7}$$

During the optimization process, the various weighting factors of the given equation J_1, J_2, J_3 and J_4 are chosen properly and make them mutually competitive. The objective function J is made to be minimum as much as possible in the optimizing process such that the closed-loop poles of the system consistently pushed further left of the *jw-axis* that is why the relative stability of the system enhanced and the damping ratio ε_0 be increased. As much as, the minimization of objective function J then the relative stability of the system can be enhanced in greater extension.

Table 2 Data used for the proposed hybrid model

Synchronous generator	Induction generator	Load	STATCOM
P_{SG} = 0.4 p. u. kW	P_{IG} = 0.6 p. u. kW	P_{load} = 1.0 p. u. kW	Q = 0.841 p.u. kVAR
Q_{SG} = 0.2 p. u. kVAR	Q_{IG} = 0.291 p. u. kVAR	Q_{load} = 0.75 p. u. kVAR	$\alpha = 138.8°$
E_q = 1.12418 p. u.	P_{in} = 0.667 p. u. kW	Power factor = 0.8	
$\delta = 17.2483^0$	$\eta = 90\%$		
$E_q^{'}$ = 0.9804 p. u.	Power factor = 0.9		
U = 1.0 p. u.	$r_1 = r_2^{'}$ = 0.19 p. u.		
X_d = 1.0 p. u.	$x_1 = x_2^{'}$ = 0.56 p. u.		
$X_d^{'}$ = 0.15 p. u.	$S = -3.5\%$		
$T_{do}^{'}$ = 5.0 s	–		

Table 3 Consists of the various parameters of STATCOM with their range of values

Name of the controller	Controller parameters	Minimum value	Maximum value
STATCOM	T_c	0.001	1.67
	T_d	0.001	1.67

4 Brief Discussion on the Proposed Algorithm

4.1 Symbiosis Organism Search Algorithm

SOS [12] algorithm is much better than any other algorithm due to its less complexity and no permanent optimization parameters. SOS algorithm developed in three basic steps.

4.1.1 Mutualism Phase

In mutualism phase, consider two organisms randomly from the ecosystem X_i and X_j where $(X_i \neq X_j)$ are mutually interact with each other and in this interactions both the organism are benefitted and update their fitness to the better one. The new organisms are updated as

$$X_{inew} = X_i + rand(0, 1) * (X_{best} - Mutual\_vector * BF_1)$$

$$X_{jnew} = X_j + rand(0, 1) * (X_{best} - Mutual\_vector * BF_2)$$

$$Mutual\_vector = \frac{X_i + X_j}{2}$$

where $rand(0, 1)$ is the random variable range from 0 to 1 and BF_1 and BF_2 are the benefitted factor usually chosen either 1 or 2. $Mutual\_vector$ represents the relationship between the organisms X_i and X_j and the benefitted factors represent the level of benefit which they got benefit from the mutual interactions, i.e. either it will be fully or partially benefitted. The equations represent the increase of degree of adaptation in the ecosystem where X_{best} is the highest degree of adaptation to the ecosystem. The new solution accepted when the fitness function is better than the previous one.

4.1.2 Commensalism Phase

In commensalism phase of SOS algorithm, consider the *i*th and *j*th organisms X_i and X_j where $(X_i \neq X_j)$ from the ecosystem randomly thereafter they are allowed to interact with each other and in this phase X_i tries to get benefitted without hampering X_j. Therefore, the new solution of X_i will be as $X_{inew} = X_i + rand(-1, 1) * (X_{best} - X_j)$ Where the benefit result for adaptation of X_i is provided by X_j from $(X_{best} - X_j)$.

4.1.3 Parasitism Phase

In this phase, an organism X_i is selected from the ecosystem which is like Anopheles mosquitoes. First, anopheles mosquitoes create artificial parasite name as Parasite_vector and this Parasite_vector is produced similar X_i randomly with all its possible dimensions and thereafter choose an organism from the ecosystem X_j that is host (human body). If the fitness value of X_j is better than Parasite_vector, then host builds immunity in the ecosystem and parasites no longer exist and vice versa effect also happened and then parasites kill the organism X_j. The flowchart of SOS algorithm is presented in Fig. 3.

5 Simulation Result Analysis

The simulations of the present work are carried out on the isolated hybrid power system model using STATCOM-PID controller and the observations are presented below.

The various state differential components of the given model are depicted below:

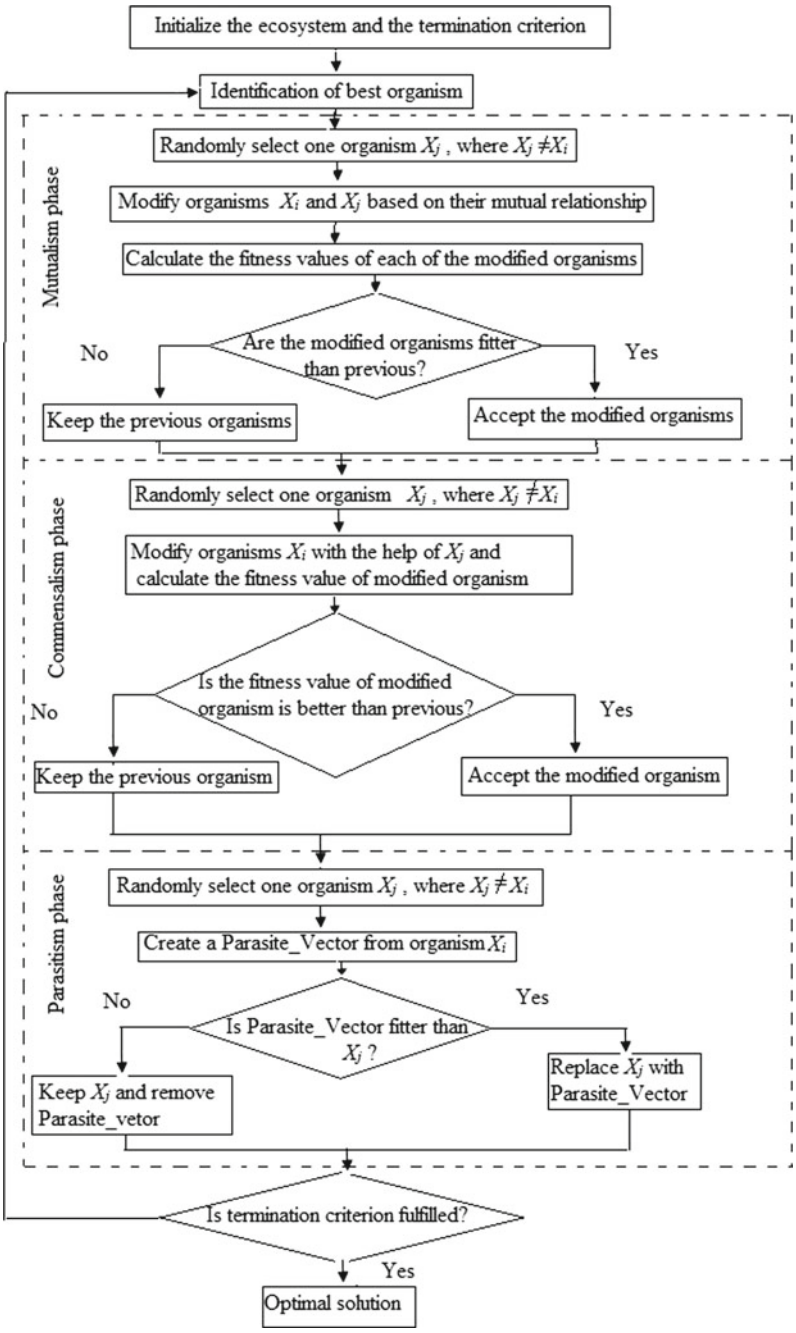

Fig. 3 Flowchart of SOS algorithm

$$\Delta \underline{X} = \left[\Delta w_r \ \Delta\delta \ \Delta E_{fd} \ \Delta E_q \ \Delta V_t \ \Delta V \ T_c \ T_d\right]^T$$

$$\Delta \underline{U} = \left[\Delta V_{ref} \ \Delta T_m\right]^T$$

$$\Delta \underline{P} = \left[\Delta Q_{ref}\right]$$

The SOS algorithm is used to control the reactive power of the isolated hybrid power system and the ALO algorithm is taken into here for the sake of comparison. The simulation is performed in MATLAB considering the same population size and run time for both of the algorithm.

6 Discussion on Results

The simulation is carried out under the small perturbation 0.01 p.u. which is applied to either incremental change in reference voltage or the incremental change in mechanical torque or simultaneously both of them. The major observations of the present work are discussed below.

6.1 Eigenvalue-Based Analysis

The different optimal parameters values of the studied model for a given set of input operating condition are presented in Table 1. This table concludes that the fitness value for SOS algorithm is lesser than the ALO algorithm that means the proposed SOS algorithm technique is better than the ALO-based algorithm technique.

6.2 Analysis of Transient Voltage Response

The time-domain transient voltage response ΔV_t (p.u.) is depicted in figure for the studied test case under the 1% simultaneous change in reference voltage and load. In this figure, it is shown that the SOS algorithm gives the better voltage response profile than the ALO algorithm for the same nominal input condition. It is also seen from Fig. 4 that the SOS-based controller gives the quick optimal response.

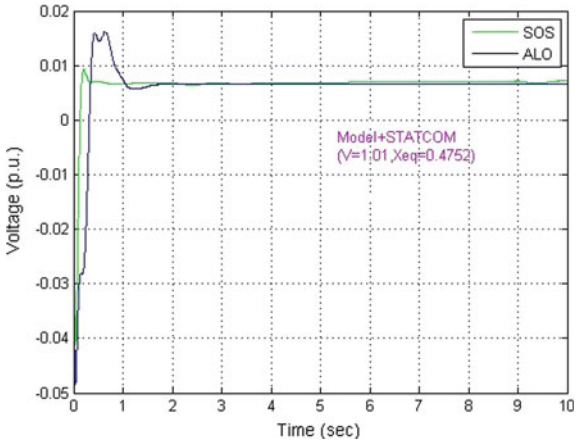

Fig. 4 Transient voltage response profile of the studied model under different algorithms taking input condition (V = 1.01, X_{eq} = 0.4752 in p. u.)

6.3 *Comparison of Convergence Profile Under Different Algorithms*

The convergence profiles of the studied hybrid model for different algorithms are given in Fig. 5 under the input conditions (V = 1.0 p.u. X_{eq} = 1.08 p.u.) and it is shown that the convergence profiles for the proposed SOS-based algorithm are faster than the ALO-based algorithm for any test cases. So, SOS-based approach is more reliable than ALO-based approach.

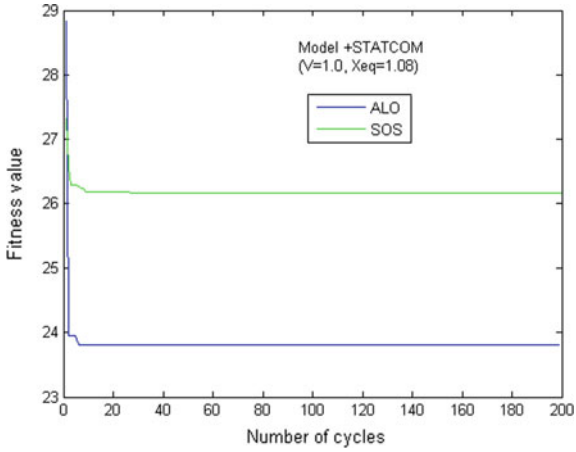

Fig. 5 Comparison of fitness value for input condition (V = 1.0, X_{eq} = 1.08) under SOS and ALO algorithms

7 Conclusion

In this paper, it is shown that the usefulness of the SOS algorithm is a better approach for the studied model, i.e. STATCOM-PID based wind-diesel isolated hybrid model. This paper also said that the parameter values of the studied model are more optimized in case of SOS algorithm than ALO algorithm. The fitness value and the transient voltage response are better converged for SOS algorithm. Better convergence profiles imply system is more stable.

Appendix

See Tables 2 and 3.

References

1. Kundur, P.: Power System Stability and Control. Tata-McGraw-Hill, India (2006)
2. Mathur, R.M., Varma, R.K.: Thyristor Based FACTs Controllers for Electrical Transmission Systems. IEEE Press, New York (2002)
3. Bansal, R.C., Bhatti, T.S.: Small Signal Analysis of Isolated Hybrid Power Systems. Narosa Publishing House, India (2008)
4. Banerjee, A., Mukherjee, V., Ghoshal, S.P.: Modeling and seeker optimization based simulation for intelligent reactive power control of an isolated hybrid power system. Swarm Evol. Comput. **13**, 85–100 (2013)
5. Banerjee, A., Mukherjee, V., Ghoshal, S.P.: Intelligent fuzzy-based reactive power compensation of an isolated hybrid power system. Int. J. Elec. Power Energy Syst. **57**, 164–177 (2014)
6. Eslami, M., Shareef, H., Mohamed, A., Khajehzadeh, M.: PSS and TCSC damping controller coordinated design using GSA. Energy Proc. **14**, 763–769 (2012)
7. Morsali, J., Zare, K., Hagh, M.T.: Applying fractional order PID to design TCSC-based damping controller in coordination with automatic generation control of interconnected multi-source power system. Eng. Sci. Technol. Int. J. **20**(1), 1–17 (2017)
8. Yu, Q., Li, P., Liu, W., Xie, X.: Overview of STATCOM technologies. In: Proceeding of the IEEE International Conference on Electric Utility Deregulation, Restructuring and Power Technologies, pp. 647–652 (2004)
9. Sharma, P., Saxena, N.K., Ramakrishna, K.S.S., Bhatti, T.S. Reactive power compensation of isolated wind-diesel hybrid power systems with STATCOM and SVC. Int. J. Electr. Eng. Inform. 192–203 (2010)
10. Hingorani, N.G., Gyugyi, L.: Understanding FACTs: Concepts and Technology of Flexible AC Transmission Systems. IEEE Power Eng. Soc., New York (2000)
11. Saxena, N.K., Kumar, A.: Reactive power control in decentralized hybrid power system with statcom using GA, ANN and ANFIS method. Int J. Elec. Power Energy Syst. **83**, 175–187 (2016)
12. Cheng, M.Y., Prayogo, D.: Symbiotic organisms search: a new metaheuristic optimization algorithm. Comput. Struct. **139**, 98–112 (2014)
13. Shaw, B., Banerjee, A., Ghoshal, S.P., Mukherjee, V.: Comparative seeker and bio-inspired fuzzy logic controllers for power system stabilizers. Int. J. Electr. Power Energy Syst. **33**, 1728–1738 (2011)

Rectangular Microstrip Antenna with Defected Patch Surface for Miniaturization and Improved Polarization Purity

Abhijyoti Ghosh and Banani Basu

Abstract A simple single element rectangular microstrip patch antenna with a semi-circular defect on patch surface is proposed to eliminate the electric fields due to first higher order orthogonal mode (TM_{02}) consequently to improve the co-polarized (CP) to cross-polarized (XP) radiation mainly in the broadside direction in H-plane without affecting its co-polarized radiation characteristics. Around 25 dB polarization purity (co-polarized to cross-polarized ratio) is obtained from the proposed structure. The optimum shape of the defect has been chosen with theoretical justification and verified through simulation. Along with the improvement of polarization purity, the proposed structure also reveals moderate gain and miniaturization.

Keywords Rectangular microstrip patch antenna · Defected patch structure (DPS) Miniaturization · Gain · Polarization purity

1 Introduction

The features like lightweight, tininess, easy fabrication process, etc. make rectangular microstrip patch antenna (RMPA) popular and effective candidate as a microwave radiator in the field of wireless communications. However, RMPA has some limitations like narrow bandwidth, low gain, and low polarization purity [1, 2]. Rectangular microstrip patch antenna radiates co-polarized radiation in the broadside direction in its dominant (TM_{10}) mode. At the same time, it also radiates some orthogonal radiation called cross-polarized radiation (XP) which limits its polarization purity. As found in open literature, the effect of XP radiation is more significant in H-plane rather that E-plane and the primary source of the XP radiation are mainly the radiation from the non-radiating edges of RMPA [3]. Cross-polarized radiation is more prominent in probe feed design of microstrip antenna [4]. Thus,

A. Ghosh (✉)
Department of ECE, Mizoram University, Aizawl 796004, Mizoram, India
e-mail: abhijyoti_engineer@yahoo.co.in

B. Basu
Department of ECE, National Institute of Technology, Silchar, Silchar 788010, Assam, India

U. Biswas et al. (eds.), *Advances in Computer, Communication and Control*, Lecture Notes in Networks and Systems 41, https://doi.org/10.1007/978-981-13-3122-0_2

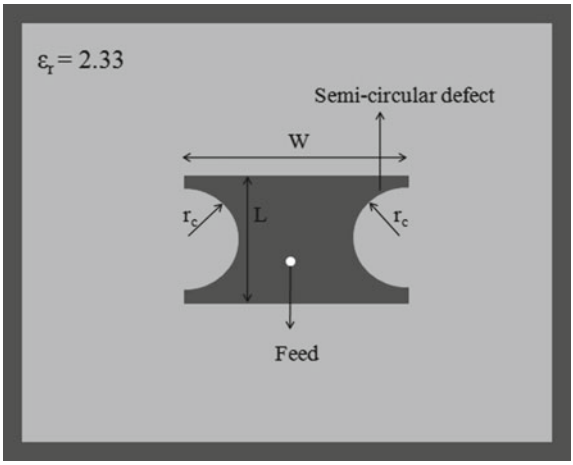

Fig. 1 Schematic representation of top view of proposed rectangular microstrip patch antenna with semicircular defected patch surface

XP radiation is a limitation for various wireless applications where polarization purity is the primary focus.

Researchers have tried different methods to suppress the cross-polarized radiation like a modification of feed structure [5, 6], stack patch structure [7], and stack patch with "mirror pair" feeding [8]. In all these reported, article CP-XP isolation of 15 dB is reported. However, those structures are quite complex, bulky and hence suffer from the complexity of the manufacturing process. Defected ground structure (DGS) is an established technique to reduce the XP radiation and has been reported in [9–11]. Polarization purity maximum 12–18 dB is achieved through all these structures. Nevertheless, the DGS structure produces a noticeable amount of back radiation which affects the gain of the antenna significantly. Shorted comb-shaped patch has been studied for the improvement of XP radiation in [12]. Nevertheless, the structure reported in [12] suffers from a major drawback of increased size and hence not suitable for the miniaturized device.

The defected patch surface (DPS) is relatively new and simple technique to limit the radiation from the non-radiating edges of the patch which are key contributors of XP radiations without affecting the back radiation performances. In the present investigation, the XP radiation is suppressed by incorporating a semicircular defect on the patch rather than in ground plane as shown in Fig. 1. The pair of the semicircular defect is placed near the non-radiating edges of the patch in such a way that it hampers only the electric fields in that region which are mainly responsible for cross-polarized radiation without hampering the co-polarized radiation. The final structure of the defect has been obtained through complete theoretical study and validated through simulated study. The final proposed structure provides a polarization purity of 23 dB along with a moderate gain of 7.41 dBi. Nevertheless, the proposed structure exhibits miniaturization in relation to resonant frequency. Around 70% miniaturization is achieved with the present structure.

2 Theory, Parametric Studies, and Proposed Structure

2.1 Theory

According to the theory of cavity model based open resonator, the top and bottom metallic sheets (i.e., patch and ground plane) of a rectangular microstrip patch antenna form electric walls while four open sides form magnetic walls. Any defect on the patch surface alters the electromagnetic fields which alter the field profile under the patch. The changes in field profile under the patch also affect the radiation characteristics of the RMPA. Few recently reported articles clearly show that the electric fields associated with first higher order orthogonal mode (TM_{02}) are mainly responsible for XP radiation which are situated near the non-radiating edges of the patch. So, to rearrange those electric fields, a semicircular defect on the patch has been introduced.

As obtained in open literature, the electric fields below the patch corresponding to the TM_{02} mode is

$$E_x = C\cos\frac{2\pi}{W}z \tag{1}$$

$$H_y = C\sin\frac{2\pi}{W}z \tag{2}$$

From Eq. (1), it is clear that at z = 0 and at z = W/2; E_x is equal to C and its value is maximum. Hence, between these two limits null occurs,

$$E_x = C\cos\frac{2\pi}{W}z = 0 \text{ for } 0 \lhd z \lhd W\big/2 \tag{3}$$

Therefore, for null to occur,

$$\frac{2\pi}{W}z_1 = \frac{m\pi}{2} \text{ where } m = 1,\ 3,\ 5,\ldots \tag{4}$$

$$z_1 = \frac{mW}{4} = \frac{W}{4};$$

with $W = 18$ mm; $z_1 = 4.5$ mm.

Therefore to perturb the fields responsible for XP radiation, i.e., fields corresponding to TM_{02} mode the defect should be incorporated in the region between $z_1 = W/2 = 9$ mm and $z_2 = 4.5$ mm.

Corresponding to TM_{02} mode, the electric surface current ($\bar{J}_s$) on the patch surface can be written as

$$\bar{J}_s = \hat{n} \times \bar{H} = \hat{a}_x \times \left|H_y\right|\hat{a}_y \tag{5}$$

Therefore,

$$\bar{J}_s = \left| C \sin 2\pi / W \right| \hat{a}_z \tag{6}$$

Thus, corresponding to TM_{02} mode, the surface current flows along an orthogonal direction which produces strong XP radiation along ±50° around broadside direction in H-plane. This $\bar{J}_s$ becomes maximum at 4.5 mm for the present structure.

So the semicircular defect has been introduced on the patch surface on both side near non-radiating edges as shown in Fig. 1. The defects within the limit of z consequently interact much with the patch surface current $\bar{J}_s$. As a result, the defect will efficiently perturb the fields of TM_{02} mode which considerably improve the XP radiation in H-plane and in turn improve polarization purity.

2.2 *Proposed Structure*

An RMPA has been designed using a thin copper strip of height 0.5 mm over an RT-duroid material as substrate of size 70×70 mm^2 with thickness 1.575 mm and dielectric constant ($\varepsilon_r = 2.33$). The patch with length L = 12 mm and width W = 18 mm is operating at 7.28 GHz. A pair of semicircular defects centered on the middle of the non-radiating edges with radius r_c are cut near the non-radiating edges from the patch (Fig. 1). The optimum value of radius of the defect is finalized through the thorough parametric studies to provide good matching and good polarization purity.

2.3 *Parametric Studies*

The parametric studies are done using the commercially available software package (High-Frequency Structure Simulator, HFSS v. 14) [13]. The variation of gain with the radius of the defect is shown in Fig. 2. It is clear from Fig. 2 that the gain is almost constant with the variation of defect size. It means that the defect on the patch does not hamper the co-polarized radiation or the dominant mode radiation.

Figure 3 shows that the minimum CP-XP isolation with the variation of the defect size. As the size of the defect increases, CP-XP isolation is also increases up to defect size (r_c) 4.5 mm. After this optimum value, the CP-XP isolation tends to decreases. If we increase the defect size more then it may hamper the co-polarized radiation of the proposed antenna. Therefore, we refrain from increasing defect size more than $r_c = 4.5$ mm.

The variation of resonance frequency with respect to defect size is presented in Fig. 4. As we increase the defect size, the resonance frequency of the proposed antenna decreases very rapidly. This shows clear miniaturization of the proposed antenna. At optimum defect size ($r_c = 4.5$ mm), the resonance frequency is 5.7 GHz

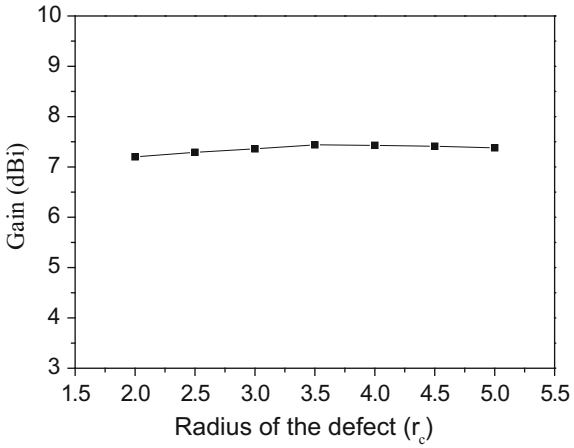

Fig. 2 Variation of co-polarized gain of the proposed RMPA as a function of radius of the defect (r_c)

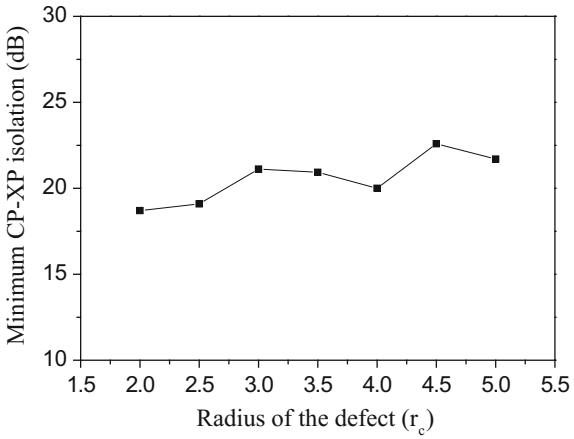

Fig. 3 Variation of minimum CP-XP isolation of the proposed RMPA as a function of radius of the defect (r_c)

which clearly shows that almost 70% miniaturization of antenna size compared to conventional RMPA.

The normalized H-plane XP radiation pattern is shown in Fig. 5. It appears that as r_c increases, the XP radiation compared to peak co-polarized gain in H-plane improves over a wide elevation angle in the broadside direction. As a result, polarization purity of the proposed structure improves simultaneously. Around 23 dB CP-XP isolation is confirmed from the proposed antenna geometry which is only 15 dB with conventional rectangular microstrip patch antenna with the same size.

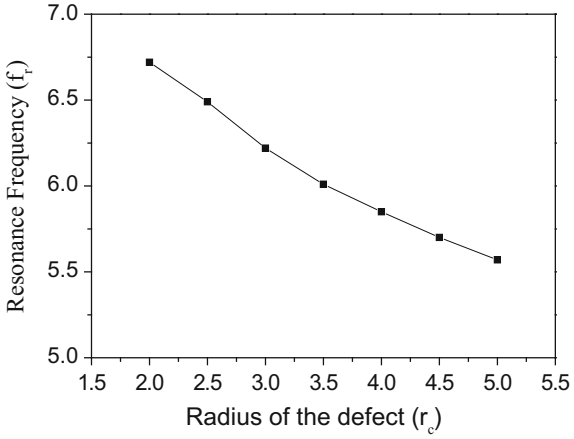

Fig. 4 Variation of the resonance frequency of the proposed RMPA as a function of the radius of the defect (r_c)

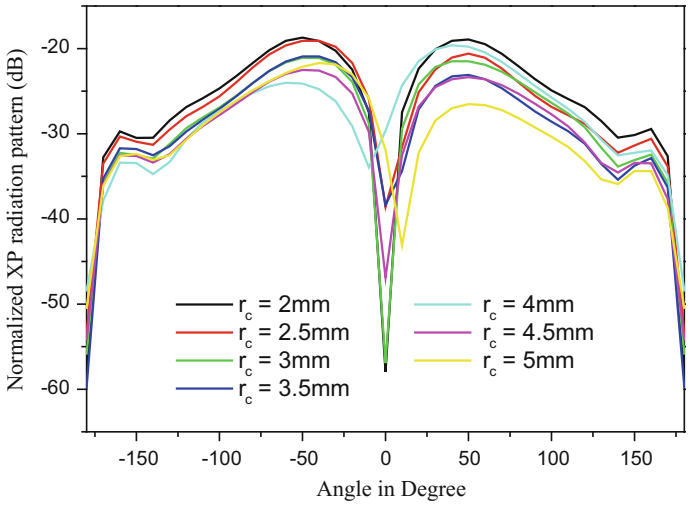

Fig. 5 Simulated normalized H-plane XP radiation pattern of the proposed RMPA as a function of the radius of the defect (r_c)

3 Results and Discussions

The reflection coefficient profile with and without defect is shown in Fig. 6. The proposed antenna resonates at 5.70 GHz whereas the same antenna resonates at 7.28 GHz without placing the defect on the patch. This clearly depicts the miniaturization of antenna size. The complete radiation pattern of the proposed antenna and the convention patch antenna is shown in Fig. 7. Both in E-plane and H-plane there is no

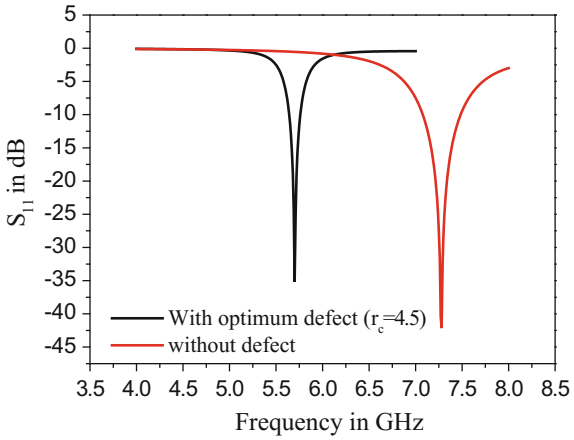

Fig. 6 Reflection coefficient profile of conventional and proposed rectangular microstrip patch antenna with semicircular defected patch surface

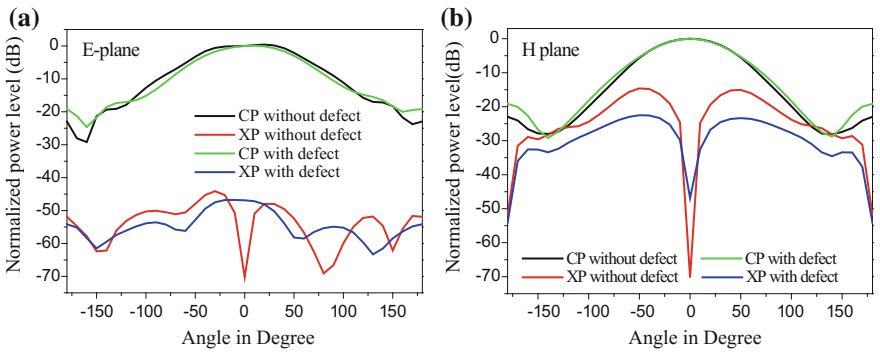

Fig. 7 Normalized radiation pattern of conventional and proposed RMPA at corresponding center frequency **a** E-plane, **b** H-plane

change in co-polarized radiation patterns. That means that the proposed antenna does not hamper the dominant mode radiation characteristics. E-plane cross-polarization radiation does not have any significance as its value is always below −50 dB. This is true with the proposed antenna. The H-plane radiation pattern is shown in Fig. 7b. For conventional patch antenna, the XP level is −15 dB whereas for the proposed antenna, it is −23 dB. The XP level in H-plane for the proposed antenna is very much low (almost 9 dB) than the conventional patch antenna. Hence, this improvement is very much significant for the proposed antenna.

4 Conclusion

A new semicircular shape defected patch surface integrated rectangular microstrip patch antenna is proposed for considerable improvement of polarization purity as compared to conventional patch antenna without affecting the dominant mode radiation characteristics. Around 23 dB polarization, purity is obtained from the proposed structure. The proposed structure also confirms almost 70% miniaturization. The proposed structure is very simple and can be utilized for the applications where polarization purity is the primary requirement.

References

1. Garg, R., Bhartia, P., Bahl, I., Ittipiboon, A.: Microstrip Antenna Design Handbook. Artech House, Norwood (2001)
2. Guha, D., Antar, Y.M.M. (eds.): Microstrip and Printed Antennas—New Trends, Techniques and Applications, Wiley, U.K. (2011)
3. Huynh, T., Lee, K.F., Lee, R.Q.: Cross-polarization characteristics of rectangular patch antennas. Electron. Lett. **24**(8), 463–464 (1988)
4. Petosa, A., Ittipiboon, A., Gagnon, N.: Suppression of unwanted probe radiation in wideband probe-fed microstrip patches. Electron. Lett. **35**(5), 355–357(1999)
5. Li, P., Lai, H.W., Luk, K.M., Lau, K.L.: A wideband patch antenna with cross-polarization suppression. IEEE Antennas Wireless Propag. Lett. **3**, 211–214 (2004)
6. Chen, Z.N., Chia, M.Y.W.: Broad-band suspended probe-fed plate antenna with low cross-polarization level. IEEE Trans. Antennas Propag. **51**, 345–346 (2003)
7. Loffler, D., Wiesbeck, W.: Low-cost X-polarised broadband PCS antenna with low cross-polarisation. Electron. Lett. **35**(20), 1689–1691 (1999)
8. Granholm, J., Woelders, K.: Dual polarization stacked microstrip patch antenna array with very low cross-polarization. IEEE Trans. Antennas Propag. **49**, 1393–1402 (2001)
9. Ghosh, A., Ghosh, D., Chattopadhyay, S., Singh, L.L.K.: Rectangular microstrip antenna on slot type defected ground for reduced cross polarized radiation. IEEE Antennas Wirel. Propag. Lett. **14**, 324–328 (2015)
10. Ghosh, A., Chakraborty, S., Chattopadhyay, S., Basu, B.: Rectangular microstrip antenna with the dumbbell-shaped defected ground structure for improved cross polarised radiation in wide elevation angle and its theoretical analysis. IET Microw. Antennas Propag. **10**, 68–78 (2016)
11. Chakraborty, S., Chattopadhyay, S.: Substrate fields modulation with defected ground structure: a key to realize high gain, wideband microstrip antenna with improved polarization purity in principal and diagonal planes. Int. J. RF Microw. Comput. Aided Eng. **26**, 174–181 (2016)
12. Pawar, U.A., Chakraborty, S., Chattopadhyay, S.: A compact and grounded comb-shaped microstrip antenna: a key to realize enhanced radiation performance, Int. J. RF Microw. Comput. Aided Eng. 1–11 (2017). https://doi.org/10.1002/mmce.21101
13. HFSS, High-frequency structure simulator, Ver. 14, Ansoft Corp. USA

Numerical Analysis of a Wideband Rectangular to Square Waveguide Transition for X-Band Orthomode Transducer Applications

Ashmi Chakraborty Das and Santanu Dwari

Abstract MoM-based numerical analysis of a wideband rectangular to square waveguide transition has been presented in this paper for X-band orthomode transducer applications. Four cavities and two waveguide sections have been used to model the network. Derived frequency response has been compared with CST Microwave Studio simulated data to verify the analysis. Input and output aperture field distributions have been obtained to analyze the effect of higher order modes on aperture field distribution (for port 1 excitation).

Keywords Square waveguide · Waveguide transition · Method of moments Cavity modeling technique

1 Introduction

Rectangular-to-square waveguide transitions find wide applications in microwave circuitry, especially in orthomode transducers (OMT) and dual-polarized antenna feed systems. These are physically two-port matching networks but can be represented as three-port electrical networks due to the presence of two-orthogonal polarizations (or modes) at the square waveguide.

In the proposed work, a wideband rectangular to square waveguide transition has been designed by cascading multiple stepped waveguide junctions and analyzed using method of moments (MoM). To apply the MoM, the input and output sections have been assumed as waveguides whereas the stepped sections have been assumed as cavities. Previously multiple stepped waveguide junctions were analyzed using modal analysis [1], variational method [2], Schwarz procedure [3], quasi-optical

A. C. Das (✉) · S. Dwari
Department of Electronics Engineering, Indian Institute of Technology (Indian School of Mines), Dhanbad, Dhanbad, India
e-mail: ashmi.chakraborty@gmail.com

S. Dwari
e-mail: santanu_dwari@rediffmail.com

U. Biswas et al. (eds.), *Advances in Computer, Communication and Control*, Lecture Notes in Networks and Systems 41, https://doi.org/10.1007/978-981-13-3122-0_3

theory [4], moment method [5], principle of conservation of complex power [6], and ray theory [7]. However, they were not focused on rectangular to square waveguide transition and also do not involve propagating orthogonal modes at the output port.

2 Analysis

Schematic diagram and cavity model of a stepped rectangular to square waveguide transition are shown in Fig. 1a and Fig. 1b, respectively. The network has been modeled using two waveguide regions (W1–W2) and four cavity regions (C1–C4). Equivalence principle has been applied to represent the unknown electric fields on the apertures (A1–A5) in terms of unknown magnetic current densities. This converts the magnetic walls between into electric walls and enables the steps to be represented as cavities.

In the proposed work, the unknown magnetic current densities M1–M5 have been assumed as weighted 2D triangular basis function. The weights of the basis function are unknown and have been derived from the boundary conditions using MoM.

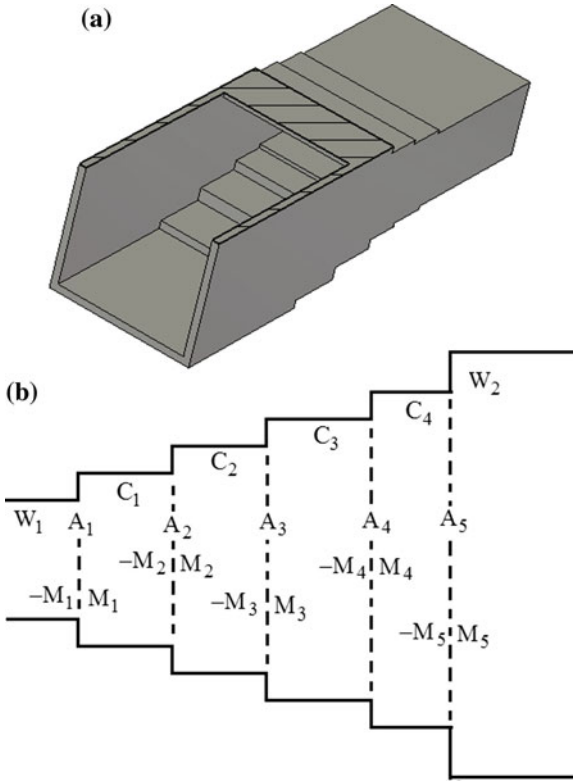

Fig. 1 Rectangular to square waveguide transition **a** Schematic view, **b** Cavity modeling

The boundary conditions are obtained by equating the tangential magnetic fields in the surrounding regions. The scattered magnetic fields in the waveguide and cavity regions have been derived using modal expansion method [8] and Greens function approach [9], respectively. The excitation field is the dominant TE_{10} mode.

3 Result and Discussion

The frequency responses of the |S11| and |S21| of the transition have been found using the proposed technique and then compared with |S11| and |S21| obtained using CST Microwave Studio simulation. The comparisons are shown in Fig. 2. The figure reveals wide bandwidth covering the complete X-band. The field distributions at the port 1 and port 2, are shown in Fig. 3, which reveals the presence of higher order modes.

4 Conclusion

This paper presents a MoM-based analysis of an X-band rectangular to square waveguide transition for orthomodal transducer applications. To verify the analysis, the theoretical |S11| and |S21| data have been compared with CST Microwave Studio simulated data. Aperture electric field distributions at port 1 and port 2 have been plotted, which reveals the presence of significant amount of higher order modes.

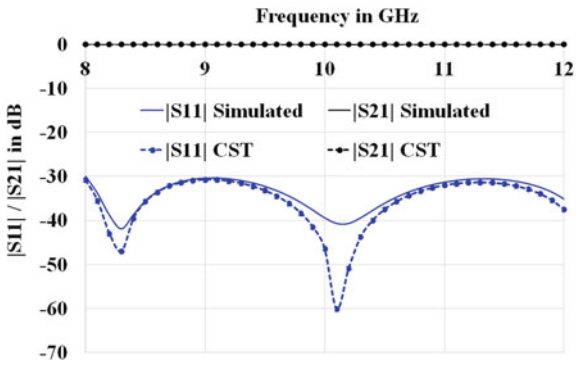

Fig. 2 $|S_{11}|$ and $|S_{21}|$ response of the rectangular to square waveguide transition

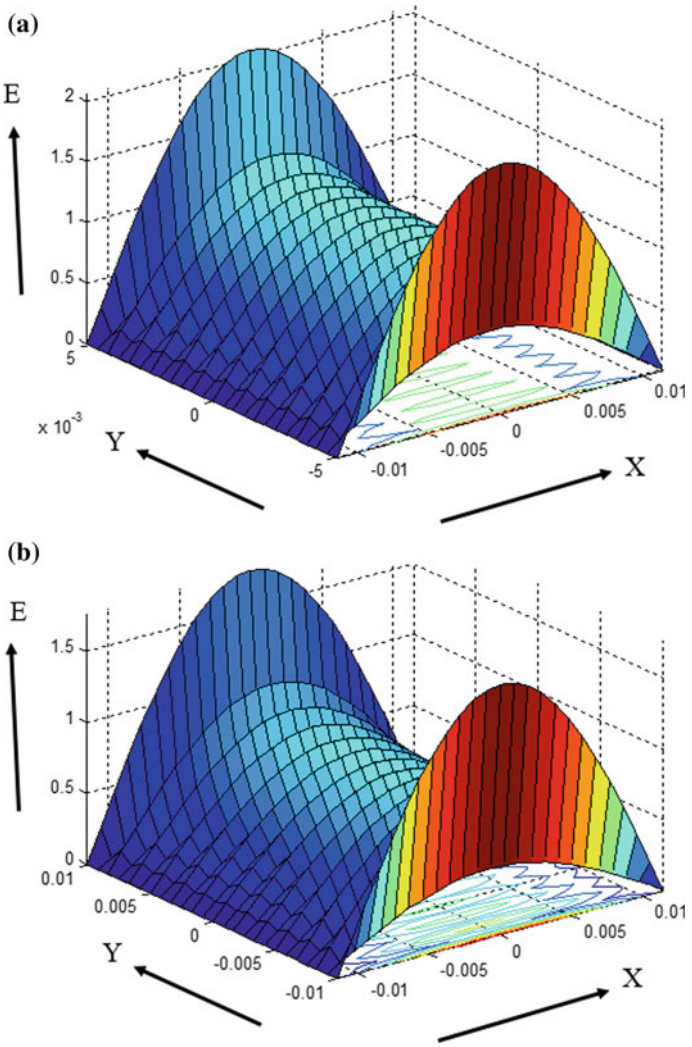

Fig. 3 Field distribution at port **a** 1, and **b** 2 when excited through port 1

References

1. Gesell, G.A., Ciric I.R.: A novel modal analysis formulation for multiple waveguide discontinuities. In: 1992 Symposium on Antenna Technology and Applied Electromagnetics, pp. 277–282 (1992)
2. Rozzi, T.E., MeckJenbrauker, W.F.G.: Wide-band network modeling of interacting inductive irises and steps. IEEE Trans. Microw. Theor. Tech. **MTT-23**(2), 235–245 (1975)
3. Goyal, K.G.: Analysis of the field structure in comers and tees in rectangular waveguides. In: M. Sc. Thesis, Department of Electrical Engineering, University of Toronto (1966)

4. Kao, K.C.: Approximate solution of the H-plane right-angled comer in overmoded rectangular waveguide operating in the H 10 mode. Proc. lEE **3**(4), 624–628 (1964)
5. Sinha, S.: Analysis of multiple-strip discontinuity in a rectangular waveguide. IEEE Trans. Microw. Theor. Tech. **MTT-34**(6), 696–700 (1986)
6. Safavi-Naina, R., MacPhie, R.H.: On solving waveguide junction scattering problems by conservation of complex power technique. IEEE Trans. Microw. Theor. Tech. **MTT-29**(4), 337–343 (1981)
7. Kashyap, S.C., Harnid M.: Diffraction by a slit in a thick conducting screen. IEEE Trans. Antennas Propag. **AP-19**(4) (1971)
8. Harrington, R.F.: Time-Harmonic Electromagnetic Fields. Mc Graw-Hill Book Company, New York (1961)
9. Vengadarajan, A.: Multiple Cavity Modeling Technique For Solving Aperture Coupled Waveguide Junctions. In: Ph.D. Dissertation, Department of Electronics & Electrical Communication Engineering, Indian Institute of Technology, Kharagpur, India 1999

A 2.45 GHz Harmonic Suppression Filtenna for Rectenna Application

Udayabhaskar Pattapu, Aggraj Gupta and Sushrut Das

Abstract This paper proposes a novel single frequency harmonic suppression antenna operating at 2.45 GHz for wireless energy transfer applications. The harmonic suppression antenna consists of antenna integrated with a low-pass filter that is called as filtenna. The filter helps to suppress the higher order harmonics. This single-frequency harmonic suppression antenna is useful for high RF to dc conversion efficiency.

Keywords Filtenna · Low-pass filter · Rectifying antenna (rectenna)
Wireless power transmission

1 Introduction

For wireless power transmission system, from the space, the RF power is received by the antenna and convert into DC power [1]. The rectifying antenna (rectenna) device is one of the most important components. This rectenna should be more compact and more efficient. To increase the RF to DC efficiency, harmonic suppression antenna is needed. A conventional rectenna system consists of a receiving antenna, filter, matching circuit, rectifying circuit, post rectification filter, and resistive load [2]. The filtenna is useful for high conversion RF to DC efficiency.

To suppress the harmonics, different techniques have been proposed. Designing a harmonic suppressed antenna (HSA) for the elimination of the integrated separate filter becomes a better choice, especially when the size of the device is strictly limited. Many techniques and structure have been used to design various HSAs, such as defected ground structure (DGS) [3, 4], compact microstrip resonant cell (CMRC) [5], right angle embedded slits [6], slot antenna [7], defected microstrip feed and stub [8] etc., all these techniques can effectively block the harmonics.

U. Pattapu (✉) · A. Gupta · S. Das
Department of Electronics Engineering, Indian Institute of Technology (Indian School of Mines) Dhanbad, Dhanbad 826004, Jharkhand, India
e-mail: uday.pattapu@hotmail.com

U. Biswas et al. (eds.), *Advances in Computer, Communication and Control*, Lecture Notes in Networks and Systems 41, https://doi.org/10.1007/978-981-13-3122-0_4

Suppression of harmonics can be implemented through different techniques, and some techniques have been introducing filter in the RF front ends due to these techniques for the suppression of harmonics, and size is increased also insertion loss. The other techniques are harmonics suppresses antenna itself.

2 Antenna Configuration

The antenna is printed on 28 mm × 35 mm size FR4 substrate of thickness (h) 1.6 mm, the relative permittivity (ε_r) of 4.4, and loss tangent tan (δ) =0.02 has been considered as dielectric material. The planar antenna has been considered in the proposed work as the receiving element of the rectenna circuit. Design and optimization of the antenna have been carried out using CST Microwave Studio (Version 14.0) (Fig. 1).

3 Simulation Results and Discussion

3.1 Antenna Without Filter

The return loss of the proposed antenna is shown in Fig. 2. There are two resonant frequencies including 2.45 and 7.2 GHz. The harmonics of the first, second, and third order of 2.45 GHz, those are 4.9, 7.35, and 9.8 GHz. Here to suppress the higher frequencies filter should be used to block other frequencies.

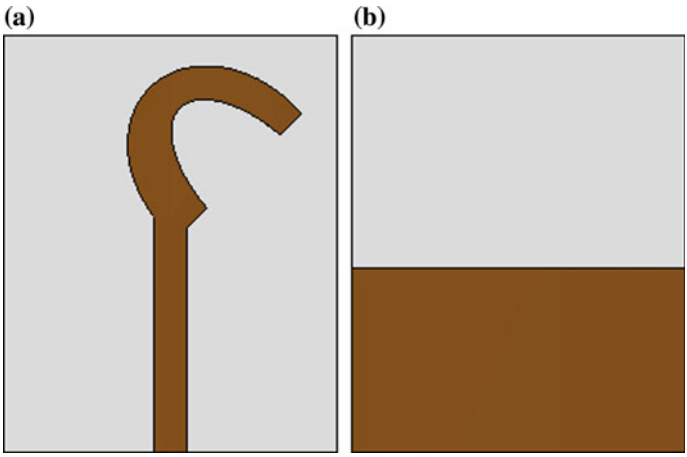

Fig. 1 Planar antenna **a** Top view **b** bottom view

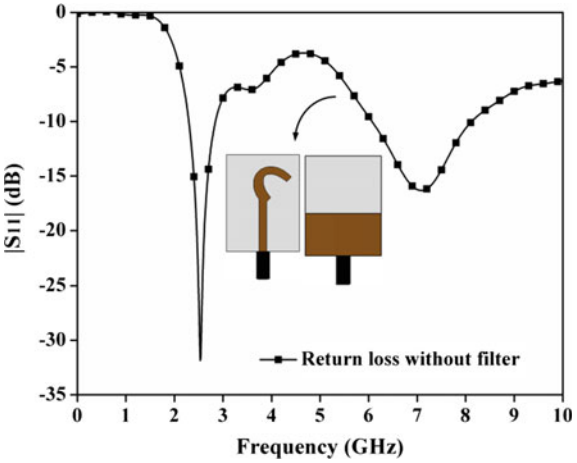

Fig. 2 Simulated frequency response of the proposed antenna

3.2 Filter Characteristics

The filter design and dimensions parameters are shown in Fig. 3a the frequency characteristics of the S-parameters are shown in Fig. 3b this filter allow the lower frequencies, i.e., below 2.45 GHz and rejects the higher frequencies. This filter characteristic is a low-pass filter. The filter helps suppress the second-order, third-order, and fourth-order harmonic frequencies.

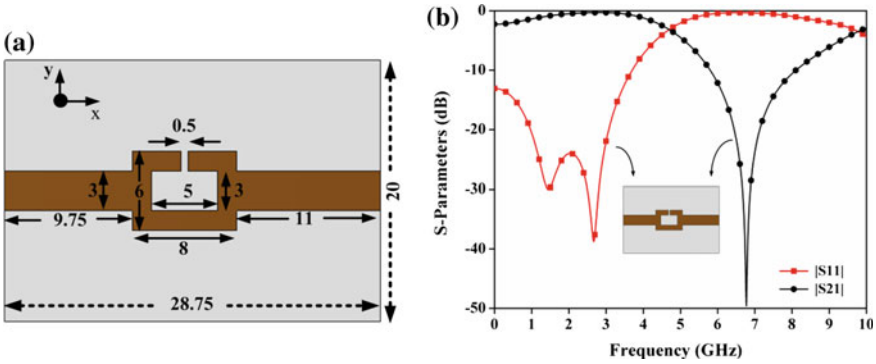

Fig. 3 **a** Low-pass filter **b** Simulated frequency response of the low-pass filter

3.3 Antenna Design with Filter

The antenna integrated with filter, which is filtenna. This is a compact harmonic suppression antenna. This paper presents a filer loaded harmonic rejection antenna for 2.45 GHz wireless power transfer applications. The antenna has been developed on FR4 substrate with height 1.6 mm and dielectric constant of 4.4, and the filtenna dimensions are given L = 35 mm, W = 28 mm, d = 8 mm, a = 8.25 mm, H = 19.75 mm, x = 7.5 mm, y = 9.5 mm, c = (4.4 mm, 9 mm), b = 15.4 mm.

Harmonic suppression antenna is needed to get high conversion efficiency of the rectifying antenna (Rectenna) A high-efficient 2.45 GHz harmonic rejection low-pass filter (LPF). And high-order harmonic rejection low-pass filter (LPF). The use of the harmonic suppression antenna in the rectenna design results in high conversion efficiency (Fig. 4).

The frequency response characteristics of the filtenna are shown in Fig. 5a. The harmonics have been suppressed by using low-pass filter. Figure 5b shows the real and imaginary parts of the impedances, for better impedance matching shift towards 50 and 0 ohms at operating frequency the impedance is 49 – j10 ohm, the real and imaginary parts of the different frequencies are at second harmonic frequency (4.9 GHz) is 259 + j304 ohm, third harmonic frequency (7.35 GHz) is 6.37 + j12.59 ohm, and fourth harmonic frequency (9.8 GHz) is 92.79 − j113 ohm. Very good impedance matching at operating frequency only, rest of the frequencies are either high a value of impedance either capacitance or inductance. The antenna is capable of harmonic rejection up to fourth harmonics due to these impedance mismatches.

The surface current distributions on the radiating patch and on the ground plane of the proposed antenna at fundamental and up to fourth harmonics are shown in Fig. 6. Figure 6 gives the return loss behavior of the surface current distribution of the proposed antenna, and the current distribution can be better as understood as

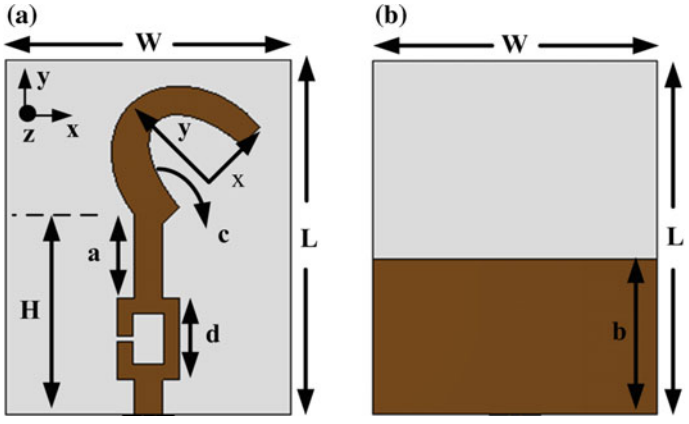

Fig. 4 **a** Front view of the antenna integrated with filter **b** back view

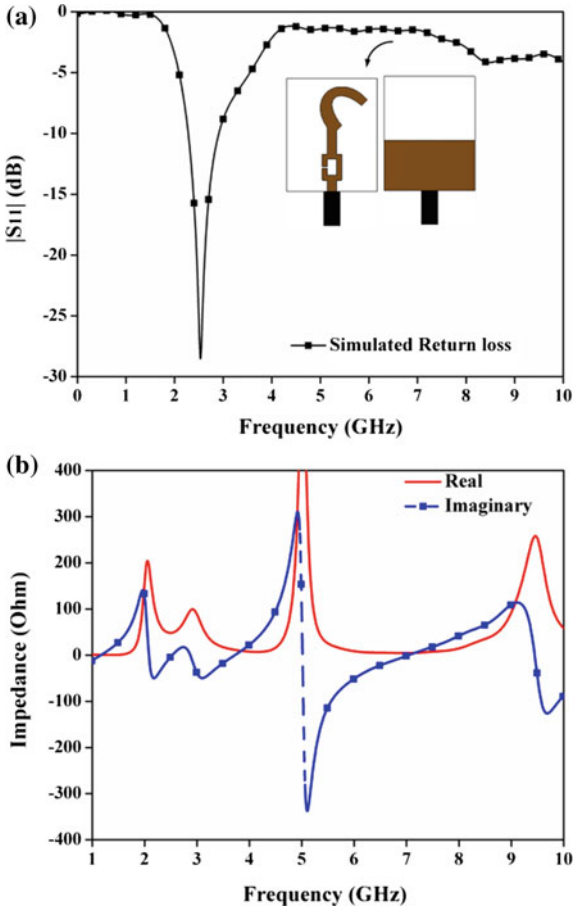

Fig. 5 **a** Frequency response of the filtenna **b** Impedance characteristics of the filtenna

the return loss behavior. The surface current distribution of the proposed antenna without a filter and with a filter can be seen from Fig. 6a–h at different frequencies of harmonics. The current distribution at 2.45 GHz shows maxima along the patch and it can be shown in Fig. 6a, e. So it can be concluded that the resonance is maximum at 2.45 GHz. By using low-pass filter, the harmonics have been suppressed, and the surface current distribution is maximum concentrated at the filter.

The simulated co and cross-polarized radiation patterns of the proposed antenna at both orthogonal planes (yz and xz) are shown in Fig. 7. It reveals that the 3-dB beamwidth of the proposed antenna is 84.4° in the yz-plane (Phi = 90° and theta = all) and omnidirectional in the xz-plane (Phi = 0° and theta = all). The cross-polarization levels in both the planes in the broadside direction are 19 dB.

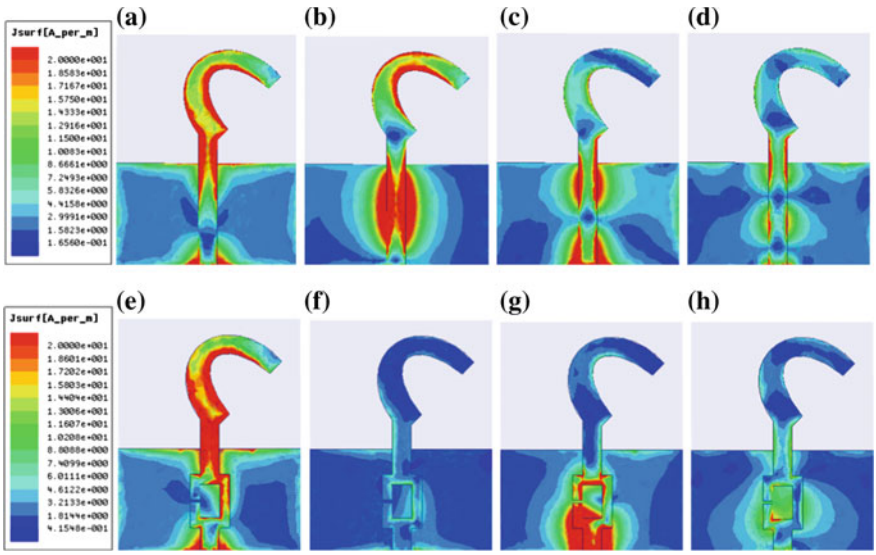

Fig. 6 Simulated surface current distributions on the radiating patches and ground planes of the antenna, without filter and with filter, at **a**, **e** fundamental (2.45 GHz). **b**, **f** second harmonic (4.9 GHz). **c**, **g** third harmonic (7.35 GHz) and **d**, **h** fourth harmonic (9.8 GHz) frequencies

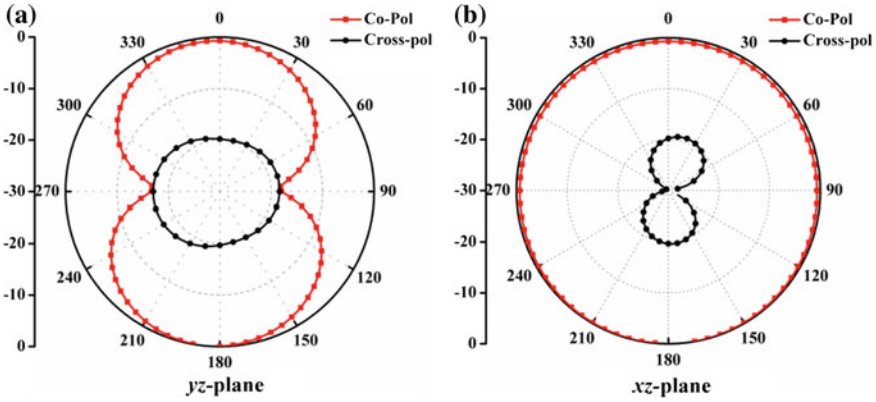

Fig. 7 Simulated normalized co- and cross-polarized radiation pattern on **a** *yz*-plane (Phi = 90° and theta = all) **a** *xz*-plane (Phi = 0° and theta = all)

The simulated gain and radiation efficiency of the proposed antenna have been plotted with frequency in Fig. 8. It reveals that in the entire 10 dB return loss bandwidth, the gain of the antenna remains almost constant. The proposed antenna has gained is 2.2 dB and 94% radiation efficiency is at the resonating frequency of 2.45 GHz.

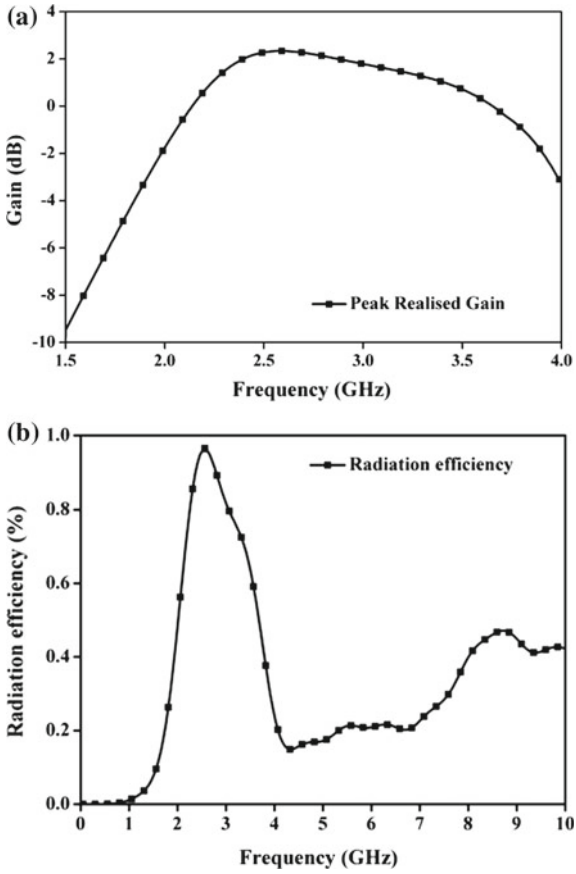

Fig. 8 Simulated results of the antenna **a** gain response of the antenna **b** radiation efficiency of the antenna

4 Conclusion

This filtenna can be used for reducing the loss. The proposed filtenna circuit is compact size. The percentage bandwidth is more than 20%. The radiation efficiency is more than 90%, Co and cross-polarization levels of both the planes at the broadside are more than 15 dB. The proposed antenna is well suited for designing of rectenna.

References

1. Brown, W.C.: The history of power transmission by radio waves. IEEE Trans. Microw. Theor. Techniques **9** (1984)
2. Ladan, S., Ghassemi, N., Ghitto, A., Wu, K.: High efficient compact rectenna for wireless energy harvesting application. IEEE Microw. Magazine 117–122 (2013)

3. Udayabhaskar, P., Sonika Priyadarsini, B., Sushrut Das: A 2.45 GHz DGS based harmonic rejection antenna for rectenna application. USNC-URSI Radio Science AP-S Symposium, 2017, pp. 123–124, San Diego, USA (2017)
4. Sung, Y., Kim, M., Kim, Y.: Harmonics reduction with defected ground structure for a microstrip patch antenna. IEEE Antennas Wireless Propag. Lett. **2**, 111–113 (2003)
5. Zhongkun, M., Guy, A.E., Vandenbosch: Wideband harmonic rejection filtenna for wireless power transfer. IEEE Trans. Antenna Propag. **62**(1) (2014)
6. Huang, F.J., Yo, T.C., Lee, C.M. Luo, C.H.: Design of circular polarization antenna with harmonic suppression for rectenna application. IEEE Antennas Wireless Propag. Lett. **11** (2012)
7. Xu, Y., Gong, S. and Hong, T.: Circularly polarized slot microstrip antenna for harmonic suppression. IEEE Antennas Wireless Propag. Lett. **12** (2013)
8. Kumar, A., Pattapu, U., Chakraborty Das, A., Das, S: A 2.45 GHz harmonic rejection antenna for wireless power transfer applications. In: IEEE-APS Topical Conference, 2017, pp. 81–84, Verona, Italy (2017)

Current Differencing Transconductance Amplifier (CDTA) Based Current Mode Quadrature Oscillator

Rupam Das, Biplab Bhowmick, Prajit Paul, Sumanta Karmakar and Khushi Banerjee

Abstract This paper presents a current mode quadrature oscillator using current differencing transconductance amplifier (CDTA). The proposed circuit uses a single CDTA, one resistor, and two capacitors. The designed circuit enjoys the advantages of independent control of condition of oscillation (CO) and frequency of oscillation (FO). The performance of the proposed circuit is examined using PSPICE with model parameters of TSMC 0.18 μm.

Keywords Quadrature oscillator · CDTA · Current mode signal processing

1 Introduction

In electrical engineering, one of the important basic building blocks is an oscillator which has many applications. For example in communication system, it can be used as a carrier in a modulator, generating signal in instrumentation and measurement systems in sender application, etc. There are various oscillators present in VLSI

R. Das (✉) · B. Bhowmick · P. Paul · S. Karmakar · K. Banerjee
Department of Electronics & Communication Engineering, Asansol Engineering College, Asansol, India
e-mail: das_rupam@rediffmail.com

B. Bhowmick
e-mail: dipdur@yahoo.co.in

P. Paul
e-mail: jeetnics@rediffmail.com

S. Karmakar
e-mail: sumanta.karmakar@gmail.com

K. Banerjee
e-mail: khushi_banerjee@rediffmail.com

U. Biswas et al. (eds.), *Advances in Computer, Communication and Control*, Lecture Notes in Networks and Systems 41, https://doi.org/10.1007/978-981-13-3122-0_5

industry among them an oscillator which provides two sinusoids with 90° phase difference is called quadrature oscillator (QO). It is important in various applications such as in single sideband generators, in telecommunications for quadrature mixer, in measurement purpose, in selective voltmeters in vector generators. In 2003, D. Biolek first found the new active building block CDTA [1]. This is a versatile component for realizing analog signal processing circuit especially in analog frequency filters [2]. Both input and output signals of CDTA block are current and output current can be electronically adjusted.

From our survey [3–17], it was found that several oscillators build by CDTA have been reported but these circuits suffer from following weakness: use of more number of CDTAs, large number of passive elements which is not suitable for IC fabrication and when observing these circuits in transistor level, then these circuits become more complicated.

In this paper, quadrature oscillator circuits using CDTA are proposed. The proposed circuit uses one CDTA, one resistor, and two capacitors. In this circuit, the oscillation condition and frequency of oscillation can be electronically controlled and oscillation condition is independently adjusted.

The paper is organized as follows: the CDTA fundamentals and proposed design are presented in Sects. 2 and 3 respectively. Nonideal analysis is included in Sect. 4. Finally, PSPICE simulation results and conclusions are given in Sects. 5 and 6 respectively.

2 CDTA Fundamentals

CDTA circuit symbol, its equivalent circuit, and its internal structure are shown in Fig. 1a, Fig. 1b and Fig. 2, respectively.

The port relationship of the CDTA can be characterized by the following matrix:

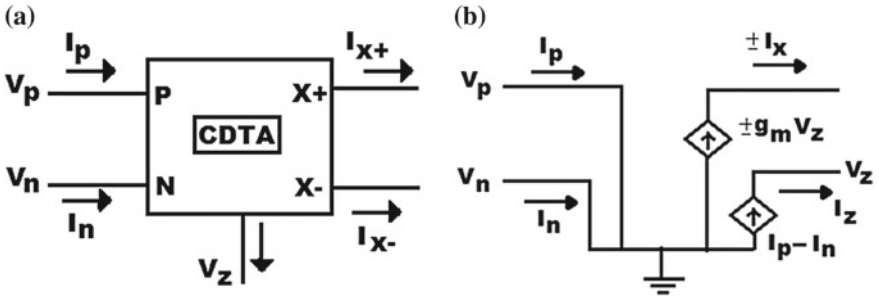

Fig. 1 CDTA **a** Symbol, **b** Equivalent circuit

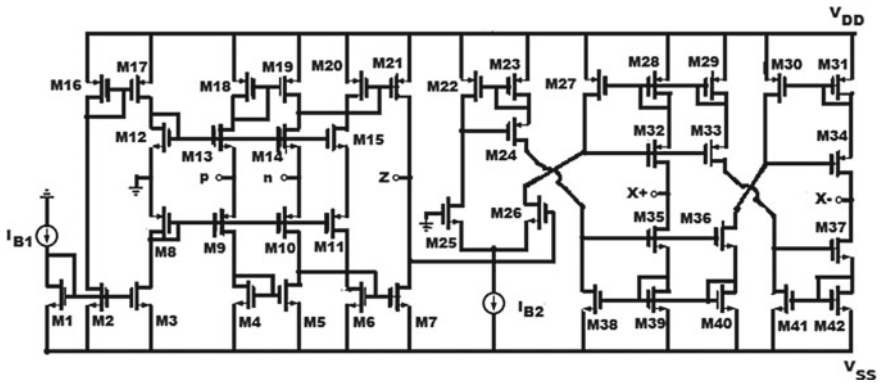

Fig. 2 Internal structure of CDTA

$$\begin{bmatrix} V_p \\ V_n \\ I_z \\ I_x \end{bmatrix} = \begin{bmatrix} 0 & 0 & 0 & 0 \\ 0 & 0 & 0 & 0 \\ 1 & -1 & 0 & 0 \\ 0 & 0 & 0 & g_m \end{bmatrix} \begin{bmatrix} I_p \\ I_n \\ V_x \\ V_z \end{bmatrix} \tag{1}$$

An extra terminal is added in Fig. 2 to copy the current through terminal z. Transconductance gain (g_m) can be expressed as

$$g_m = \sqrt{\mu C_{ox}\left(\frac{W}{L}\right) I_b}$$

where μ and C_{ox} are the mobility and gate oxide capacitance per unit area, W is effective width, and L is the effective channel length. By adjusting the bias current I_b, the transconductance gain can be electronically controlled.

3 Proposed Current Mode Quadrature Oscillator

In analog signal processing, all-pass filters (AP) are very important circuit. Many all-pass filters are available in the literature but very few of them are suitable for quadrature oscillator, such types of all-pass filter [6] used for quadrature oscillator are shown in Fig. 3.

The proposed current mode quadrature oscillator is designed by cascading a first-order all-pass filter and a non-inverting lossless integrator shown in Fig. 4. Depending on this block diagram, a quadrature oscillator using a CDTA is shown in Fig. 5.

The characteristics equation of the proposed oscillator in Fig. 5 can be expressed as follows:

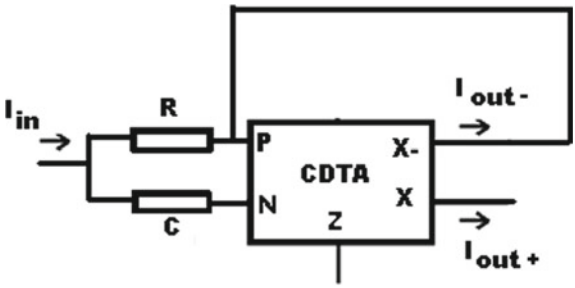

Fig. 3 CDTA based current mode AP filter

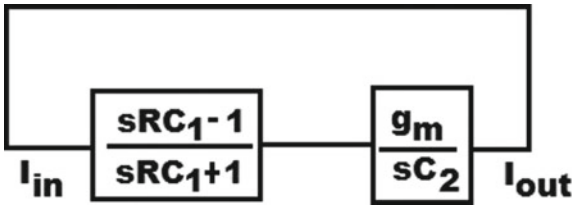

Fig. 4 Block diagram of quadrature oscillator

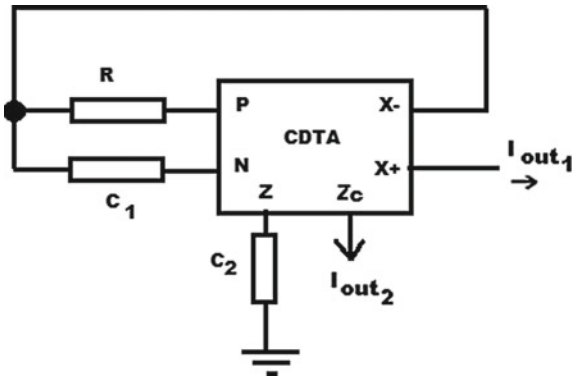

Fig. 5 Proposed current mode quadrature oscillator

$$s^2 C_1 C_2 R + s(C_2 - C_1 g_m R) + g_m = 0 \tag{2}$$

a sinusoidal signal is produced if the oscillation condition is fulfilled:

$$g_m R = \frac{C_2}{C_1} \tag{3}$$

Equation (3) is called condition of oscillation and it can be achieved by setting

$$C_2 = C_1 \tag{4}$$

And

$$g_m = \frac{1}{R} \tag{5}$$

So the characteristic equation of the circuit becomes

$$s^2 C_1 C_2 R + g_m = 0 \tag{6}$$

From Eq. (6), the frequency of oscillation of the circuit can be obtained

$$\omega_{osc} = \sqrt{\frac{g_m}{RC_1C_2}} = \frac{1}{RC} \tag{7}$$

The quadratic current output relationship is

$$\frac{I_{02}(s)}{I_{01}(s)} = \frac{g_m}{sC_2} \tag{8}$$

Under sinusoidal steady-state Eq. (8) becomes

$$\frac{I_{02}(j\omega)}{I_{01}(j\omega)} = \frac{g_m}{\omega C_2} e^{-j90^\circ} \tag{9}$$

The phase difference φ between output currents I_{01} and I_{02} is

$$\varphi = -90^0 \tag{10}$$

This ensures that output currents I_{01} and I_{02} are in quadrature form. All the passive and active sensitivities of the oscillator are low and it is shown in Eqs. (11) and (12)

$$S_{C_1}^{\omega_{0SC}} = S_{C_2}^{\omega_{0SC}} = S_R^{\omega_{0SC}} = -\frac{1}{2} \tag{11}$$

$$S_{g_m}^{\omega_{0SC}} = \frac{1}{2} \tag{12}$$

4 Effect of Nonideality

Considering the nonideality current–voltage relationship of CDTA, the port relationship can be rewritten as

$$I_z = \alpha_p I_p - \alpha_n I_n \tag{13}$$

$$I_x = \beta g_m V_z \tag{14}$$

where α_p is the current transfer error from p to z terminal, α_n is the current transfer error from n to z terminal, and β is the transconductance inaccuracy factor from z to x terminal. Using the no ideal case, the proposed oscillator circuit in Fig. 5 yields the modified characteristics equation as follows:

$$s^2 C_1 C_2 R + s[C_2 - b g_m a_n C_1 R] + a_p b g_m = 0 \tag{15}$$

$$\text{CO: } \frac{C_2}{C_1} = \alpha_n \beta g_m \tag{16}$$

$$\text{FO: } \omega_{osc} = \sqrt{\frac{\alpha_p \beta g_m}{R C_1 C_2}} \tag{17}$$

Sensitivity analysis of the proposed oscillator in nonideal case is expressed as

$$S_{C_1}^{\omega_{OSC}} = S_{C_2}^{\omega_{OSC}} = S_R^{\omega_{OSC}} = -\frac{1}{2} \tag{18}$$

$$S_{\alpha_p}^{\omega_{OSC}} = S_\beta^{\omega_{OSC}} = S_{g_m}^{\omega_{OSC}} = \frac{1}{2} \tag{19}$$

5 Simulation Results

The CDTA based all-pass filter has been simulated in PSPICE using CMOS-based CDTA shown in Fig. 3. The model parameter of TSMC 0.18 μm CMOS process and supply voltage ±2.5 V is used. The aspect ratio of various transistors is shown in Table 1. Simulation is performed with passive component values selected as C = 1.21 nf, R = 1.1 KΩ and I_{b1} = 200 μA and I_{b2} = 150 μA. The gain and phase response of the all-pass filter is shown in Fig. 6. The time response of the input and output signals for an input sinusoidal signal of 500 mA, 5 kHz is shown in Fig. 7. The Fourier spectrum of the output signal at I_{out} showing at a high selectivity for the applied signal frequency 5 kHz is shown in Fig. 8. Simulation result of oscillator output from the initial state is shown in Fig. 9 and for this, we are using R = 1.1 kΩ and C1 = C_2 = 1.21 nf. The quadrature output is also shown in Fig. 10. The Fourier spectrum of the output signals at I_{out1} and I_{out2} is shown in Fig. 11 and Fig. 12 respectively. Theoretical frequency of oscillation value calculated from Eq. (7) is 119.6 kHz while simulated value is 110.4 kHz. Lissagous fig is shown in Fig. 13 which verifies the quadrature relationship between output waveforms. Comparison with the previously published work is shown in Table 2.

Table 1 Aspect ratio of various transistors

Transistor	W (μm)	L (μm)
M1–M21, M24, M27–M42	20	1
M22–M23	45	1
M25–M26	35	0.7

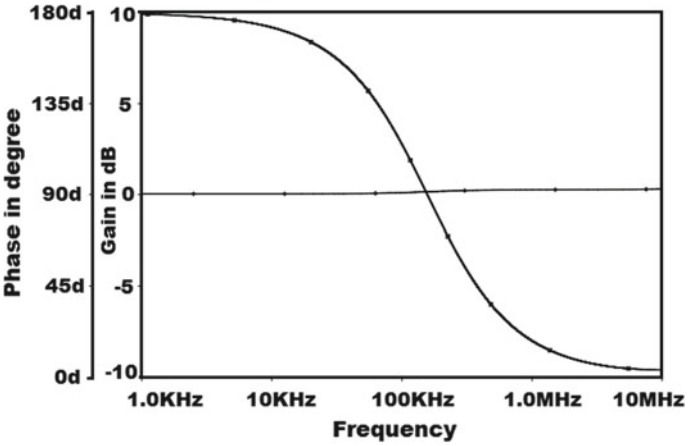

Fig. 6 Gain and phase response of the all-pass filter at I_{out} of Fig. 3

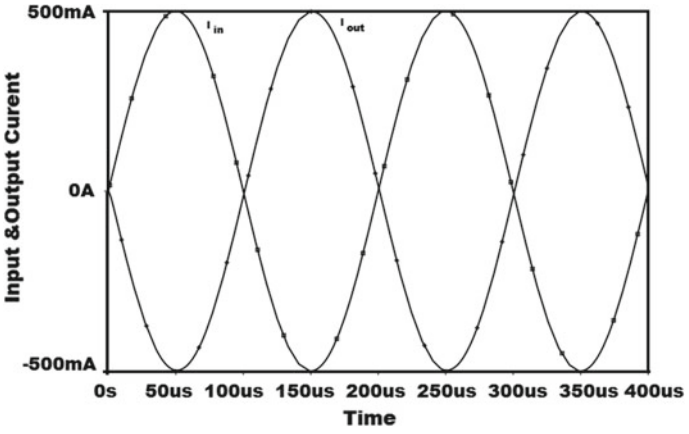

Fig. 7 Simulated sinusoidal input and output waveform of Fig. 3

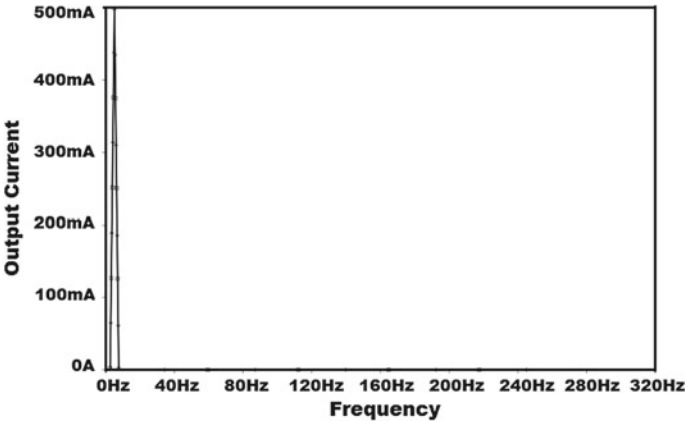

Fig. 8 The simulated frequency spectrum I_{out} of Fig. 3

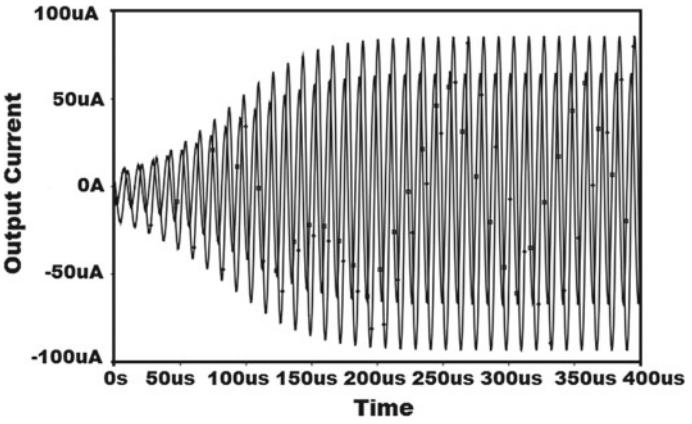

Fig. 9 The simulated result of output waveforms from the initial state of Fig. 5

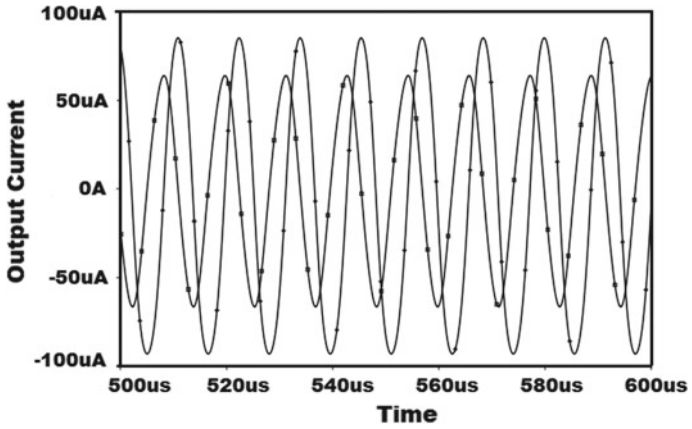

Fig. 10 The simulated result of quadrature outputs of Fig. 5

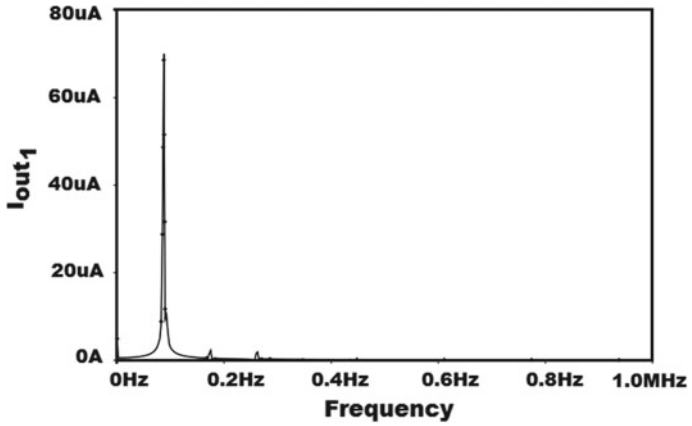

Fig. 11 The simulated result of output spectrum at I_{out1} of Fig. 5

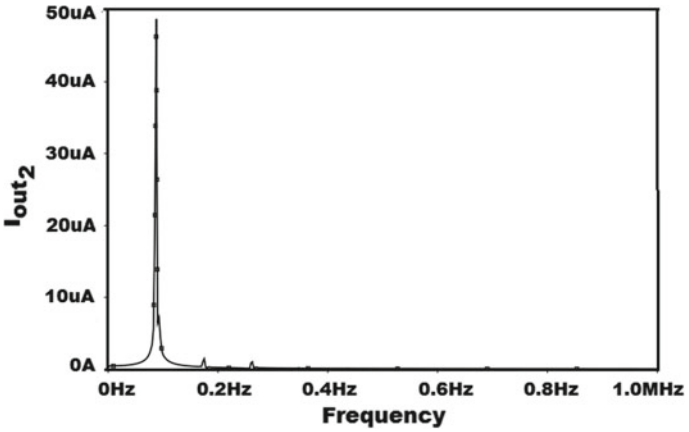

Fig. 12 The simulated result of output spectrum at I_{out2} of Fig. 5

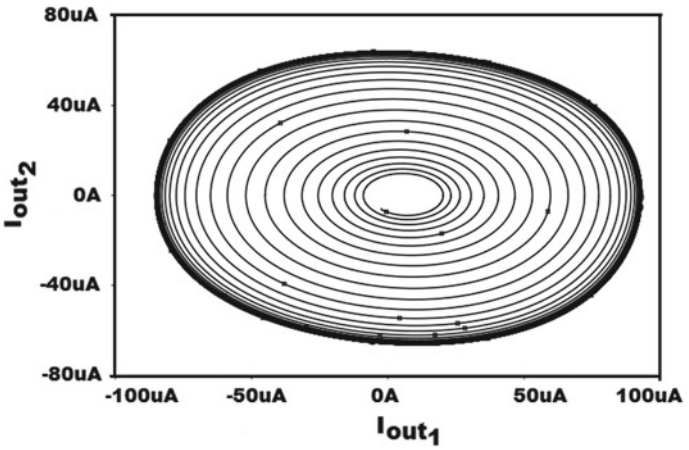

Fig. 13 Lissagous figure of the proposed oscillator

Table 2 Comparison with the previously published work

References	ABB	No of ABB	Technology used	Supply voltage (V)	MOS/ BJT based	Electronically control of CO & FO	Grounded C	No of R + C	Current mode QO output
[3]	CDTA	3	0.5 μm TSMC	±2.5	MOS	YES	YES	1 + 2	YES
[4]	CDTA	3	NR-100 N/PR-100 N	±3	BJT	YES	YES	0 + 2	YES
[5]	CDTA	3	NR-100 N/PR-100 N	±2	BJT	YES	YES	0 + 2	YES
[6]	CDTA	2	0.5 μm MIETEC	±2.5	MOS	NO	NO	4 + 2	YES
[7]	CDTA	2	0.35 μm AMIS	±0.75	MOS	NO	NO	4 + 2	YES
[8]	CDTA	2	0.5 μm MIETEC	±2.5	MOS	YES	YES	1 + 2	YES
[9]	CDTA	2	0.35 μm TSMC	±1.8	MOS	YES	YES	0 + 2	YES
[10]	CDTA	2	0.35 μm TSMC	±1.8	MOS	YES	NO	2 + 2	YES
[11]	CDTA	2	0.35 μm TSMC	±1.5	MOS	YES	YES	0 + 2	YES
[12]	CDTA	2	0.35 μm TSMC	±1.6	MOS	YES	YES	0 + 2	YES
[13]	CDTA	2	0.5 μm MIETEC	±2.5	MOS	YES	YES	1 + 2	YES
[14]	CDTA	2	0.18 μm CMOS	±2.5	MOS	YES	YES	1 + 2	YES
[15]	CDTA	2	0.18 μm CMOS	±1.5	MOS	YES	YES	0 + 2	YES
[16]	CDTA	1	AD844+ LM3080	±6	–	NO	NO	2 + 2	NO
[17]	CDTA	3	NR-100 N/PR-100 N	±3	BJT	YES	YES	0 + 2	YES
Our work	CDTA	1	0.18 μm TSMC	±2.5	MOS	YES	NO	1 + 2	YES

6 Conclusion

A new CDTA-based QO has been presented here. The proposed circuit uses a single CDTA block, one resistor, and two capacitors. The frequency of oscillation and condition of oscillation of this QO circuit can be independently adjusted and the oscillation condition can be tuned electronically. Theoretical results agree well with PSPICE simulation results.

References

1. Biolek, D.: CDTA—building block for current mode analog signal processing. In: Proceedings of the European Conference on Circuit Theory and Design, Krakow, Poland, pp. 397–400 (2003)
2. Biolek, D., Biokova, V.: Universal biquard using CDTA elements for cascading filter design. In: Proceedings of the 13th International Multiconference on Circuits, Systems, Communications and Computers(CSCC-2003), Greece, pp. 8–12 (2003)
3. Jin, J., Wang, C.: Current-mode four-phase quadrature oscillator using current differencing transconductance amplifier based first-order allpass filter. Rev. Roum. Sci. Techn. Électrotechn. et Énerg. **57**, 291–300 (2012)
4. Tangsrirat, W., Tanjareon, W.: Current-mode sinusoidal quadrature oscillator with independent control of oscillation frequency and condition using CDTAs. Indian J. Pure Appl. Phys. **48**, 363–366 (2010)
5. Tanjaroen, W., Tangsrirat, W.: Resistorless current-mode quadrature sinusoidal oscillator using CDTAs. In: Proceedings of the Asia-Pacific Signal and Information Processing Association Annual Summit and Conference, pp. 307–310 (2009)
6. Keskin, A.U., Biolek, D.: Current mode quadrature oscillator using current differencing transconductance amplifiers (CDTA). IEE Proc.Circuits Devices Syst. **153**, 214–218 (2006)
7. Uygur, A., Kuntman, H.: CDTA-based quadrature oscillator design. In: Proceedings of the 14th European Signal Processing Conference (2006)
8. Lahiri, A.: New current-mode quadrature oscillator using CDTA. IEICE Electron. Express **6**, 135–140 (2009)
9. Pandey, N., Paul, S.K.: Single CDTA based current mode all pass filter and its applications. J. Electr. Comput. Eng. ID:897631 (2011)
10. Hasan, Md., Paul, S.K.: A noval current mode quadrature oscillator using current differencing transconductance amplifier. J. VLSI Des. Tools & Technol. **4**(1), 39–42 (2014)
11. Kaçar, F., Kuntman, H.: Design Of Quadrature Oscillator Using Current Differencing (CDTA). Transconductance Amplifier 399–403
12. Summart, S., Saetiaw, C., Thosdeekoraphat, T., Thongsopa, C.: First order filter based current-mode sinusoidal oscillators using current differencing transconductance amplifiers (CDTAs) world academy of science, engineering and technology. Int. J. Electr. Robot. Electron. Commun. Eng. **8**(7), (2014)
13. Kumngern, M., Dejhan, K.: Electronically Tunable Current-Mode Quadrature Oscillator Using Current Differencing Transconductance Amplifiers. 978-1-4244-4547-9/09/2009 IEEE, TENCON (2009)
14. Jin, J., Wang, C.: CDTA-based electronically tunable current-mode quadrature oscillator. Int. J. Electron. (2013)
15. Jin, J., Wang, C.: Current-mode universal filter and quadrature oscillator using CDTAs. Turk. J. Electr. Eng. & Comput. Sci. **22,** 276–286 (2014)

16. Prasad, D., Bhaskar, D.R., Singh, A.K.: Realisation of single-resistance-controlled sinusoidal oscillator: a new application of the CDTA. WSEAS Trans. Electron. **5**, 257–259 (2008)
17. Tanjaroen, W., Pukkalanun, T., Surakampontorn, W.: Resistorless realization of current mode first order allpass filter using current differencing transconductance amplifier. Microelectron. J. **41**, 178–183 (2010)

Metamaterial Substrate and Superstrate Based Circular Microstrip Antenna

Debashree Patra Karmakar and Chiranjib Goswami

Abstract A circular microstrip patch antenna partially loaded with homogeneous substrate and superstrate consisting of double-negative (DNG), epsilon negative (ENG), and mu negative (MNG) is investigated to observe the changes in resonance. It is observed that embedded double-negative substrate placed under the patch displays dual band resonance characteristics with moderate realized peak gain bandwidth and superstated disc increases the gain as high as 10 dBi. Embedded ε-negative substrate provides moderate peak gain with bandwidth as high as 500 MHz and superstate metamaterial depicting dual resonance phenomena with similar gain in both bands. In either case of embedded substrate and superstate, μ- negative material exhibits dual band characteristic with poor impedance matching. The DNG or ENG metamaterial embedded substrate antenna exhibits broadside null in its elevation plane radiation pattern but that is not observed for the case of metamaterial superstate disc loading on patch.

Keywords Metamaterial (MTM) · Dispersive media · Circular microstrip antenna

1 Introduction

For wireless communication, compact antennas with high gain and wide bandwidth are required. As the microstrip patch antenna has most useful features like low cost, low weight, and low profile, so they are widely used. Though compact antennas have been neglected because of low gain. Certain techniques to miniaturised planar antenna size are reported like slots on the surface of the patch [1], use of shorting pins [2] and use of high dielectric materials as well as thick substrates. Though radiation

D. P. Karmakar
Department of ECE, Mallabhum Institute of Technology, Bishnupur, West Bengal, India
e-mail: dpatrakarmakar@gmail.com

C. Goswami (✉)
Department of AEIE, Asansol Engineering College, Asansol 713305, West Bengal, India
e-mail: avi.chiranjib@gmail.com

U. Biswas et al. (eds.), *Advances in Computer, Communication and Control*, Lecture Notes in Networks and Systems 41, https://doi.org/10.1007/978-981-13-3122-0_6

efficiency and cross polarization level may degrade with addition of these features. Using metamaterials improves the antenna efficiency, impedance matching, bandwidth [3], and miniaturize antenna size. These materials can be classified into those with negative real part of their permittivity (ε–negative or ENG), negative real part of their permeability (μ–negative or MNG) and both these quantity being negative (double-negative or DNG) in specific frequency range [4]. Ziolkowski has proposed that the DNG metamaterials can enhance the power radiation from electrically small antenna [5]. MTM was also used to miniature the physical size of the patch antennas [6, 7]. The modified TM mode of patch antenna loaded with DPS-MNG or DNG for dual band application is reported in [9]. The effect of resonance and radiation characteristics for inclusion of metamaterial substrate and superstate of rectangular microstrip antenna is also reported in [10]. In this work, we investigate the effect on resonance and radiation characteristics of microstrip antenna on partial inclusions of DNG and MNG superstrate or substrate for circular microstrip antenna. The advents of new miniaturized SRR have motivated the work in the view that the substrate height may be further reduce unlike those reported in [11]. All simulations in this paper are performed using CST Microwave Studio which is based on finite integration technique [12]. The rest of paper is organized as follows. Section 2 describes the modeling of MTM homogeneous media. Section 3 discusses the effects on antenna characteristics (resonance and radiation) with inclusion of MTM materials as substrate or superstrate for circular microstrip antenna. Finally, concluding remarks are given in Sect. 4.

2 Homogeneous Modeling of Microwave MTM Media

Traditionally, MTM is realized with array of sub-wavelength split ring resonators (MNG) and thin wires (ENG). For observing the benefits of MTM in the circuit, the split ring resonators and thin wires are incorporated with the actual design and the resultant circuit is analyzed numerically. A problem is that to design homogeneous MTM sample, a large array of these sub-wavelength structures needs to be considered. For proper numerical computation, the meshing of the structures should be fine enough. This inherently increases the solution time. Moreover, if solution time is reduced by considering a less dense array, then a continuous MTM sample may not be modeled properly. In this work, we modeled the MTM homogeneous block defined by using Drude/Lorentz model. According to Drude/ Lorentz model, the effective permittivity (ε_{eff}) and effective permeability (μ_{eff}) are defined by respectively.

$$\varepsilon_{eff}(\omega) = \varepsilon_{\infty} - \frac{\omega_p^2}{\omega(\omega - i\nu_c)} \tag{1}$$

$$\mu_{eff}(\omega) = \mu_{\infty} + \frac{(\mu_s - \mu_{\infty})\omega_0^2}{\omega_0^2 + i\omega\delta - \omega^2} \tag{2}$$

Table 1 Optimized value of parameters for Drude/Lorentz model

Parameter	Optimized value
ε_∞	1.26
ω_p	2 π 14.63 GHz
ν_c	30.69 MHz
μ_s	1.26
μ_∞	1.12
ω_0	2 π . 9.67 GHz
δ	1.24 GHz

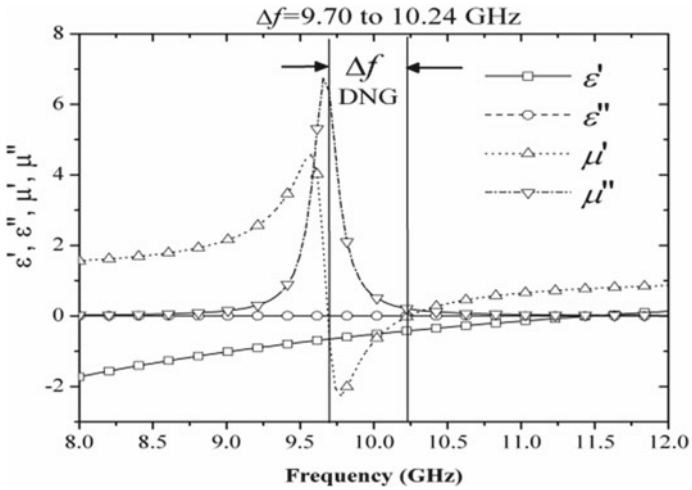

Fig. 1 Effective material characteristics plotted against frequency

ε_∞ is the relative electric permittivity at the high frequency limit of the model, ω_p is the radial frequency of the electric plasma, ν_c is the collision frequency and μ_s is the static permeability, μ_∞ is the relative magnetic permeability at the high frequency limit of the model, ω_0 is the radial resonant frequency, and δ is the damping frequency.

The optimized values of the Drude and Lorentz parameters are in following Table 1 [13]. Though the conventional SRRs are sub-wavelength being about $\lambda_g/8$, so these can be actually analyzed with EM simulator. It may also be noted that unlike [8] where substrate based on MTM was taken as 5 mm, here the analysis consider 0.8 mm substrate to realize the antenna. To the best of our knowledge, such investigations have not been carried out. The motivation of using these MTM slabs was the realizeability of highly miniaturized SRR as reported in [11]. In the frequency range 9.70–10.24 GHz, the MTM block behave as DNG materials as seen in Fig. 1. For MNG, the block is defined by Lorentz model.

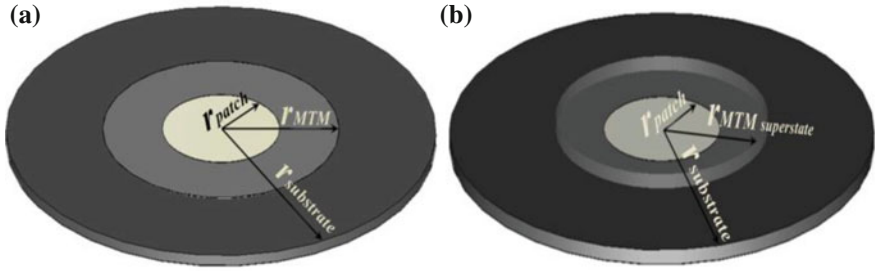

Fig. 2 Proposed antenna geometry **a** Metamaterial (MTM) embedded substrate **b** Metamaterial (MTM) loaded superstrate and double positive substrate (DPS)

3 Effect on Resonance and Radiation Characteristics of Antenna

The circular microstrip antenna designed at 10 GHz for which the radial dimension (r_{patch}) is computed as 5.50 mm. The antenna is excited with a probe feed where the probe is inserted at 2.2 mm towards the edge of the patch from the center. The double positive substrate (DPS) chosen for realizing the antenna has $\varepsilon_r = 2.2$, $\tan\delta = 0.00022$ and substrate height of 0.795 mm. For analyzing the effect of including MTM, the study is divided into two broad cases (a) metamaterials embedded on the antenna substrate and rest of part is DPS and (b) metamaterials loaded on the patch as superstrate covering the entire patch and antenna substrate is DPS. The proposed antennas' geometries are shown in Fig. 2. The embedded metamaterial redial dimension denoted by r_{MTM} and substrate dimension of $r_{substrate}$ is depicted in Fig. 2a. In case of superstate loading the superstate metamaterial dimension is $r_{MTM\ superstate}$ as observed in Fig. 2b. For all simulation, the DPS substrate radial dimension is fixed at 20 mm.

3.1 MTM Embedded in Substrate

In this subsection, the effect of resonance and radiation characteristics of circular microstrip antenna embedded with metamaterial (DNG) is investigated. The parametric variation of filling ratio ($r_{MTM}/r_{substrate}$) is discussed here for different MTM cases. When the antenna substrate embedded with DNG metamaterial, due to the mode splitting, the dual band phenomenon is observed which is shown in Fig. 3. The narrow lower band is tuned around 10 GHz which is the resonance frequency of unloaded resonance of circular antenna and comparatively wider higher band is around 11 GHz. It is also observed that for lower value of filling ratio, the impedance matching is improved in lower band and same phenomena is also observe for higher filling ratio in higher band. When filling ratio increases, small right shift is also

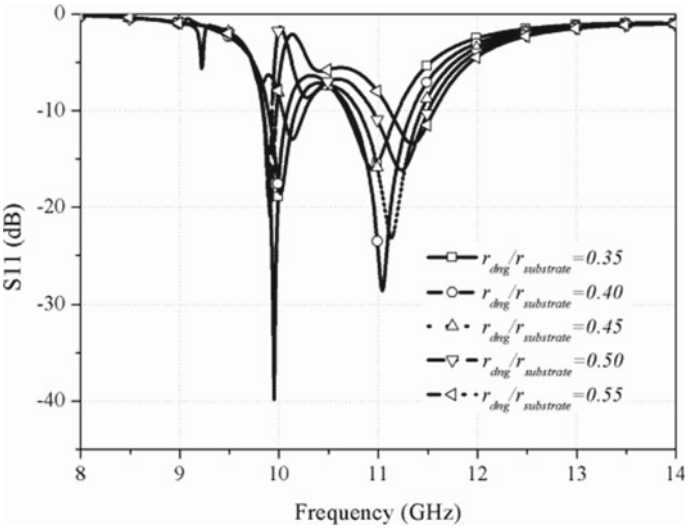

Fig. 3 Parametric study of effect on resonance characteristics of DNG embedded antenna by varying filling ratio as shown in Fig. 2a

Table 2 Peak realized gain at different resonant frequencies for the DNG embedded substrates, as indicated in Fig. 3

$r_{dng}/r_{substrate}$	Lower resonance frequency (GHz), bandwidth (MHz)	Higher resonance frequency (GHz), bandwidth (MHz	Peak realized gain (dBi) G_{RL},G^{a}_{RH}
0.35	9.9543,257	10.938,546	1.5,3.9
0.40	10,298	11.043,660	1.85,5.1
0.45	10.154,235	11.127,635	2.03,5.28
0.50	9.8969,90	11.242,560	1.12,6.39
0.55	9.9167,134	11.34,536	1.05,6.6

[a] G_{RL}, G_{RH} are the peak realized gain corresponding to lower and higher resonant frequency, respectively

observed with respect to 10 GHz. The lower and higher band gain and bandwidth are tabulated in Table 2 for different filling ratios. Comparatively higher gain and wider bandwidth performances are exhibited for 0.45 filling ratio.

The principal plane radiation pattern is shown in Fig. 4 for $r_{dng}/r_{substrate}$ is 0.45. Similar radiation pattern is observed in both frequency bands. Broad side null is observed in elevation plane radiation pattern of every frequency bands. Here, broad side null is observed in elevation plane pattern which is also observed in case of DNG embedded antennas. However, the azimuthal plane pattern is omnidirectional in both cases.

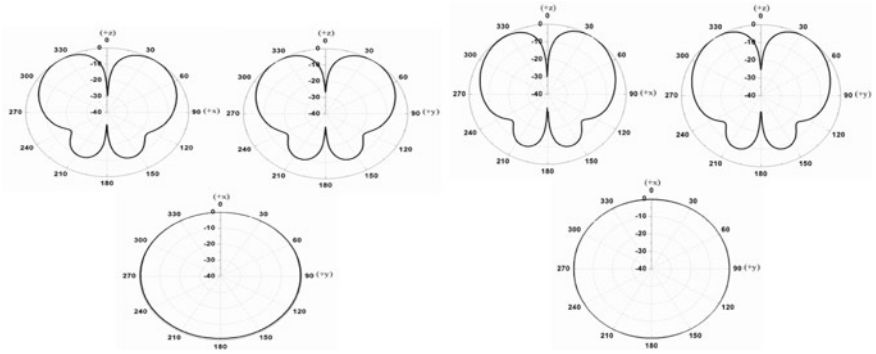

Fig. 4 Parametric study of effect on resonance characteristics of DNG superstated antenna by varying filling ratio $r_{dng\ superstate}/r_{substrate}$ as shown in Fig. 2b

3.2 Superstrate MTM Disc Covering the Patch

In this section, the effect of resonance and radiation characteristics for superstate MTM disc loading on the circular patch is discussed. The redial dimension of superstate metamaterial disc is denoted with $r_{MTM\ superstate}$ and other notations related with antennas and position of feed points are unaltered as shown in Fig. 2b. The height of metamaterial disc is keeping fixed to 0.80 mm for all simulations. The parametric study of the effect of resonance characteristics for DNG superstate antenna with different filling ratio is demonstrated in Fig. 5. The resonance frequencies are gathered around 11 GHz though the filling ratios are change from 0.30 to 0.50. It can be observed that the resonance frequencies are shifted towards 10 GHz with step of around 30 MHz and bandwidth is initially increases for lower value of filling ratio but for higher values it gets gradually decrease and impedance is being improved. Comparatively higher bandwidth is obtained for filling ratio of 0.40. The resonance, bandwidth information, and realized peak gain are tabulated in Table 3.

One can observe from the table that the DNG superstated antenna exhibits height gain of 10.26 dBi at 10.987 GHz and lowest bandwidth of 181 MHz for filling ratio of 0.50.

The principal plane radiation pattern is displayed in Fig. 6 for DNG superstate loading at 10.987 GHz for filling ratio $r_{dng\ superstate}/r_{substrate}$ of 0.50. No broadside null is observed in elevation plane radiation pattern.

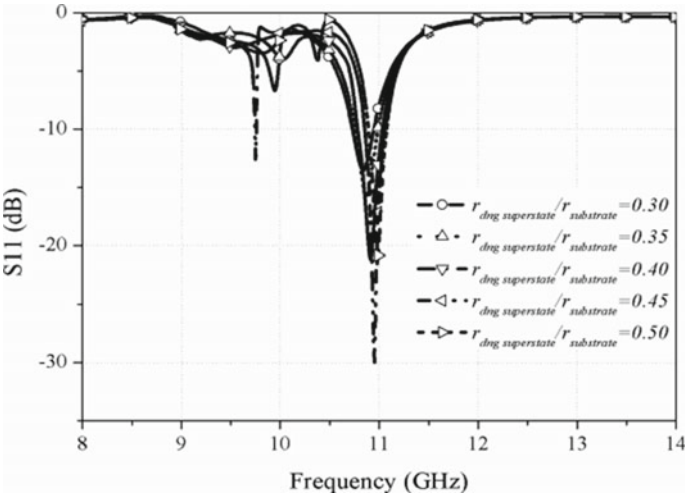

Fig. 5 Parametric study of effect on resonance characteristics of DNG superstated antenna by varying filling ratio $r_{dng\ superstate}/r_{substrate}$ as shown in Fig. 2b

Table 3 Peak realized gain at different resonant frequencies for the DNG superstate, as indicated in Fig. 4

$r_{dng\ superstate}/r_{substrate}$	Resonance frequency (GHz)	Bandwidth (MHz)	Peak realized gain (dBi)
0.30	10.833	215	6.2
0.35	10.86	233	6.9
0.40	10.922	258	8.2
0.45	10.974	217	9.3
0.50	10.987	181	10.3

4 Conclusion

The effects on resonance and radiation characteristics for embedded metamaterial substrate and metamaterial superstate loaded circular patch are investigated. One can conclude from above discussion that embedded DNG substrate has capability to operate the antenna in dual band with moderate gain allowable bandwidth. On the other hand DNG superstated antenna exhibits realized peak gain as high as 10.26 dBi and considerable amount of bandwidth which is much greater then unloaded antenna. One common thing to observe is that MTM embedded substrate antenna exhibiting broadside null in its elevation plane radiation pattern.

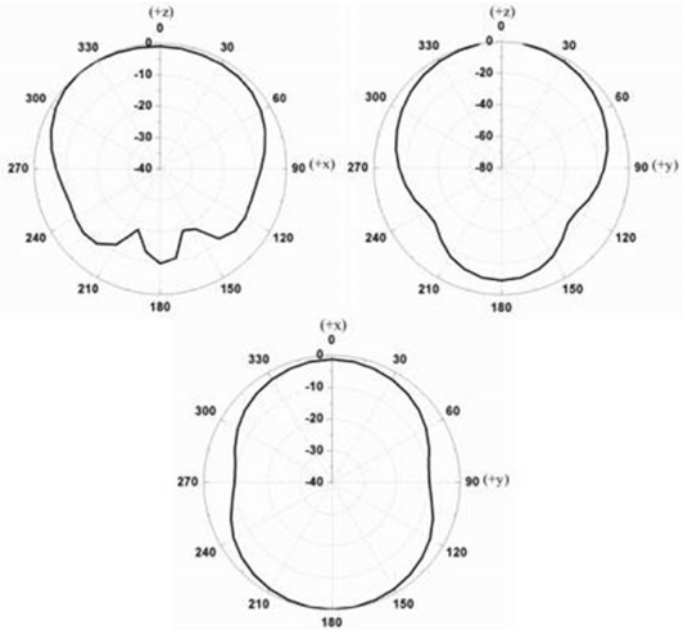

Fig. 6 Principal plane radiation patterns of the proposed antenna at 10.987 GHz for filling ratio $r_{dng\ superstate}/r_{substrate}$ of 0.50

References

1. Maci, S., Biffi Gentili, G., Piazzesi, P., Salvador, C.: Dual-band slot-loaded patch antenna. Proc. Inst. Elect. Eng. Microw. Antennas Propag. **142**(3), 225–232 (1995)
2. Porath, R.: Theory of miniaturized shorting-post microstrip antennas. IEEE Trans. Antennas Propag. **48**(1), 41–47 (2000)
3. Itoh, T. et al.: Composite right/left-handed transmission line metamaterials. IEEE Microw. Magazine 34–50 (2004)
4. Engheta, N., Ziolkowski, R.W.: Metamaterials, pp. 6–7. Wiley, New York (2006)
5. Ziolkowski, R.W., Kipple, A.: Application of double negative metamaterials to increase the power radiated by electrically small antennas. IEEE Trans. Antennas Propagation **51**(10), 2626–2640 (2003)
6. Mahmoud, S.F.: A new miniaturizes annular ring patch antenna resonator partially loaded by metamaterials ring with negative permeability and permittivity. IEEE Antennas Wireless Propag. Lett. **3**, 19–22 (2004)
7. Alu, A., Bilotti, F., Engheta, N., Vegni, L.: Subwavelength, compact, resonant patch antennas loaded with metamaterials. IEEE Trans. Antennas Propag. **55**(1), 13–25 (2007)
8. Bilotti, F., Alu, A., Vegni, L.: Design of miniaturized metamaterials patch antennas with μ-negative loading. IEEE Trans. Antennas Propag. **56**(6), 1640–1647 (2008)
9. Xiong, J., Li, H., Jin, Y., He, S.: Modified TM_{020} mode of a rectangular patch antenna partially loaded with metamaterial for dual-band applications. IEEE Antennas Wireless Propag. Lett. **8** 1006–1009 (2009)
10. Ghatak, R., Chiranjib, G., Poddar, D.R.: Investigation on resonance and radiation properties of rectangular microstrip antennas with partially filled metamaterial substrates and superstrates.

Int. J. RF Microw. Comput. Aided Eng. Special Issue on "Metamaterial: RF and Microwave Applications", **22**(4), 558–568 (2012)
11. Yousefi, Leila, Ramahi, Omar M.: Artificial magnetic materials using fractal hilbert curves. IEEE Trans. Antennas Propag. **58**(8), 2614–2622 (2010)
12. Computer Simulation Technology (CST). http://www.cst.com
13. Lubkowski, G., Schuhmann, R., Weiland, T.: Extraction of effective metamaterial parameters by parameter fitting of dispersive model. Microw. Opt. Technol. Lett. **29**(2) (2007)

Smart Coordination Approach for Power Management with Modern PEV Technology

Md. Tasinul Hoque, Md. Kamiul Hoque and A. K. Sinha

Abstract This paper presents a smart method for charging an electrical vehicle to meet up the energy crisis as a cost-effective solution of the energy market and commercial success. Electric vehicles are meant to charge during off-peak hours of the day to overcome the abnormal voltage variation of the distribution network, power loss, and bad power quality. This method effectively decreases the peak demand of the system and improves power quality of the electricity to fulfill the demand shortage. The generation unit runs with full capacity to meet up the demand to accomplish the maximum efficiency and robust reliability. The backup storage system of the electric vehicles improves the demand response curves with a quickest smart charging station during the off-peak hour load of the power system by virtue of which battery storage system hurls to manage power demand during the peak hour load of the power grid. The consumers exchange their demand by charging and discharging their storage systems to sell excess electricity and buy power as per the requirements of the open market policy of the electricity.

Keywords Plugged in electric vehicle (PEV)
Smart grid technology, demand response · Peak demand management
Simulation and result

Md. Tasinul Hoque (✉) · A. K. Sinha
Kalyani Government Engineering College, Kaylani, West Bengal, India
e-mail: tasinul.kgec92@gmail.com; mdtasimul@gmail.com

A. K. Sinha
e-mail: abhi.hmhs2@gmail.com

Md. Kamiul Hoque
Purulia Government Engineering College, Puruliya, West Bengal, India
e-mail: kamiul.pgec@gmail.com

U. Biswas et al. (eds.), *Advances in Computer, Communication and Control*, Lecture Notes in Networks and Systems 41, https://doi.org/10.1007/978-981-13-3122-0_7

1 Introduction

According to the survey of branch of energy shipping is the prime emitter of carbon dioxide in the whole world, clerical for more or less one-third of the total CO_2 production [1]. So, the time has come to think for alternative energy as well as other eco-friendly means of the transportation system. One of the substitutes for transportation is PEVs/PHEVs (Plug-in electric vehicles/Plug-in hybrid electric vehicles) [2]. Naturally, electric motors are more efficient as compared to gasoline engines. Such type vehicles are eco-friendly as to not release any type of greenhouse gas. There are many challenges to the adoption of EVs which include high cost of PEVs, long charging times of batteries, high costs of charging infrastructure, high costs of upfront infrastructure, peak load impacts of uncontrolled charging, and local distribution system impacts from clustering of PEVs [3, 4]. One solution to the problem of overloading of transformer and lines is smart grid. Smart grid provides power in both directions as to give-and-take and also provide communicating date for a particular variation of time. For this reason, it is very helpful for the customer to charge their electric vehicle [5]. As a result, utilities can watchfully manage when and how EV charging occurs, collect EV specific meter data, apply specific rates for EV charging, implement Demand Response (DR) programs [6, 7], engage consumers with information on EV charging status and bill impacts, and collect data for greenhouse gas credits. The plug-in electric vehicles represent an ideal off-peak load that means these batteries can be charged during late night hours and in early morning hours and can be made to discharge during peak hours of the day when the cost of electricity is maximum [8]. By doing so, the peak demand will be reduced; as a result, the problem of line congestion and overloading of the distribution network will also get solved. The consumer can play an active role in determining the price of electricity. Due to the reduction of peak demand, the price of electricity will get reduced. The consumers exchange their demand by charging and discharging their storage systems to sell excess electricity and buy power as per requirements of the open market policy of electricity. The demand for the electricity in demand response is considered as varying prices of the power market just as share markets. The prices of the electricity during peak time discourage customer to use electricity due to higher price of electricity in the market. In this approach, the consumers may reduce their demand in self-controlled techniques or sell excess electricity to power grid to earn a financial benefit.

2 Plug-in Electric Vehicle Technology

The growing use of electricity increases grid loading, power losses, and the risk of jamming. However, employing electricity for heating and shipping also introduces a significant level of elasticity to the traditional consumption pattern. Over the past 5 years, the transportation sector has been revolutionized due to the advent of plug-

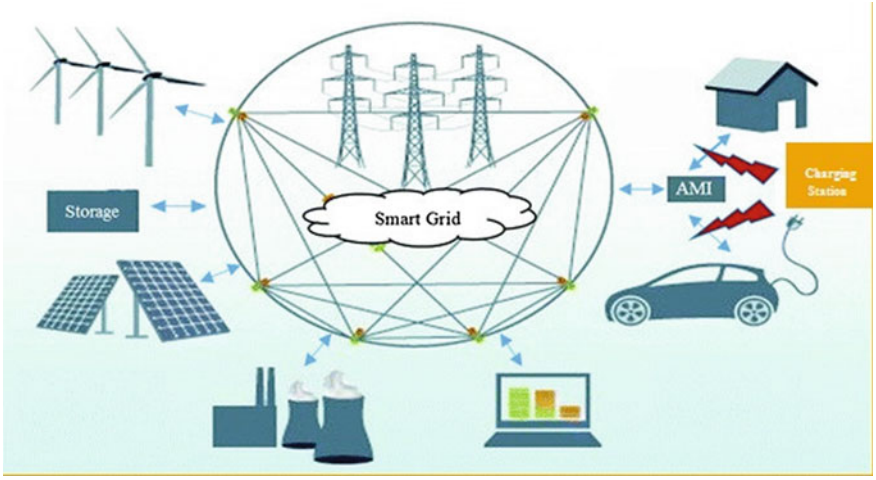

Fig. 1 Generation of charging process

in electric vehicles. The growing common awareness of ecological issues as well as continuing concerns about reducing belief on foreign oil or petroleum has made the concept of PEV very popular during the past few plug-in hybrid electric vehicles (PHEVs) that are becoming more popular as we move toward a greener future. PHEVs are equipped with rechargeable batteries, which can be charged by connecting it to an electric power source. Several studies have shown that PHEVs produce less CO_2 and other pollutants over their entire fuel cycle, compared to conventional vehicles (Fig. 1).

To drive a PEV as plainly as feasible, it needs to be charged in the off-peak hours of the sunrise, when power demand is at its lowest and when wind power is typically at its peak. Smart grid technologies will help to congregate this goal by interacting with the PEV to charge it at the most optimal time. And you will still be able to demand an instantaneous recharge when you need it.

3 Smart Grid Technology

The smart grid is also used to transmit power in both directions as give-and-take way. It is associated with communication system to communicate with the electricity rate for a particular time delay. It also works in a two-way power flow way. It also organizes the power announcement system (Fig. 2).

Functions of a smart grid are as follows:

- More capable communication of electricity.
- Faster reinstallation of electricity after power fighting.

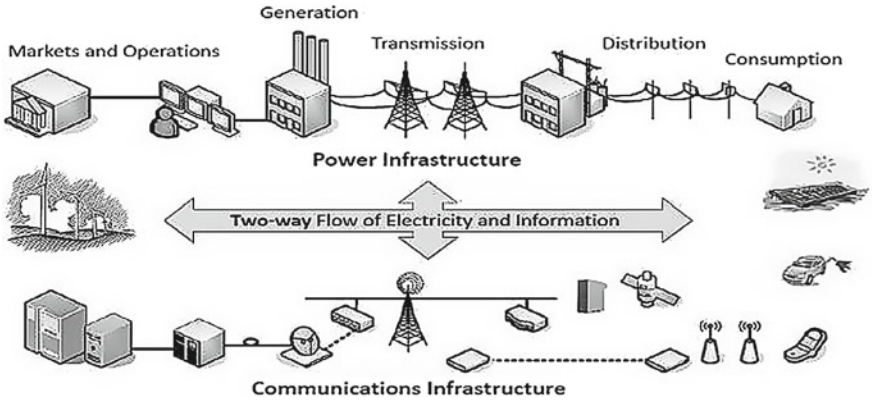

Fig. 2 Smart grid

- Improve the operations and management costs for utilities and ultimately lower tariff for consumers.
- Compact peak demand, which will also help lower electricity cost.
- Amplified integration of large-scale renewable energy systems.
- Better integration of customer–owner power generation systems, including renewable energy systems.
- Enhanced security.

4 Price Responsive Model of PEV

Gasoline mode of PEVs.
Let the mileage of gasoline operated PEV car = M_1 km/L and cost of gasoline = "Q" Rs/L.

To drive M Km, it takes "Q" rupees. For 1 km drive, it takes Q/M_1 Rupees.

Battery mode of PEVs.
Let the mileage of gasoline operated PEV car = M_2 km/L and cost of gasoline = "P" Rs/L.

To drive M_2 km, it takes "P" rupees. For 1 km drive, it takes P/M_2 Rupees.

For optimum price for charging,

$$\frac{Q}{M_1} = PM_2$$

i.e.

$$P = P_{opt} = \frac{Q \times M_2}{M_1}$$

5 Simulation

The IEEE 30 bus system under normal load has the following parameters; bus data and line data used in IEEE 30 bus system are as given below:
Base MVA = 100.
The bus coding is follows:

Slack Bus = 1.
Generator Bus (PV) = 2.
Load Bus (PQ) = 0.

V	Voltage magnitude of bus.
<δ	Voltage angle of bus.
P_g	Generated active power in MW.
Q_g	Generated reactive power in MVar.
P_d	Active power demand in MW.
Q_d	Reactive power demand in MVar.
Q_{min}	Minimum limit of reactive power of generator bus.
Q_{max}	Maximum limit of reactive power of generator bus.

Bus data:

Bus no	Bus code	V In p.u	<δ radian	P_a MW	Q_d MVar	P_g MW	Q_g MVar	Q_{min} MVar	Q_{max} MVar	Q MVar	Remarks
1	1	1 06	0.0	0.0	0 0	0.0	0.0	0	0	0	SLACK BUS
2	2	1.043	0.0	21.70	12.7	40.0	0.0	–40	50	0	LIG PV BUS
3	0	1.0	0.0	2.4	1.2	0.0	0 0	0	0	0	LIG
4	0	1.06	0.0	7.6	1.6	0.0	0.0	0	0	0	LIG
5	2	1.01	0.0	94.2	19.0	0.0	0.0	–40	40	0	PV BUS
6	0	1.0	0.0	0.0	0.0	0.0	0.0	0.0	0.0	0	LIG
7	0	1.0	0.0	22.8	10.9	0.0	0.0	0	0	0	MIG
8	2	1.01	0.0	30.0	30.0	0.0	0.0	–10	60	0	MIG
9	0	1.0	0.0	0.0	0.0	0.0	0.0	0.0	0.0	0.0	LIG
10	0	1.0	0.0	5.8	2.0	0.0	0.0	–6	24	19	LIG
11	2	1.082	0.0	0.0	0.0	0.0	0.0	0.0	0.0	0.0	HIG
12	0	1.00	0	11.2	7.5	0	0	0	0	0	MIG
13	2	1.071	0	0	0	0	0	–6	24	0	HIG
14	0	1	0	6.2	1.6	0	0	0	0	0	HIG
15	0	1	0	8.2	2.5	0	0	0	0	0	MIG
16	0	1	0	3.5	1.8	0	0	0	0	0	HIG
17	0	1	0	9.0	5.8	0	0	0	0	0	MIG

(continued)

(continued)

Bus data:											
Bus no	Bus code	V In p.u	<δ radian	P_a MW	Q_d MVar	P_g MW	Q_g MVar	Q_{min} MVar	Q_{max} MVar	Q MVar	Remarks
18	0	1	0	3.2	0.9	0	0	0	0	0	MIG
19	0	1	0	9.5	3.4	0	0	0	0	0	MIG
20	0	1	0	2.2	0.7	0	0	0	0	0	MIG
21	0	1	0	17.5	11.2	0	0	0	0	0	LIG
22	0	1	0	0	0	0	0	0	0	0	LIG
23	0	1	0	3.2	1.6	0	0	0	0	0	HIG
24	0	1	0	8.7	6.7	0	0	0	0	4.3	HIG
25	0	1	0	0	0	0	0	0	0	0	HIG
26	0	1	0	3.5	2.3	0	0	0	0	0	HIG
27	0	1	0	0	0	0	0	0	0	0	HIG
28	0	1	0	0	0	0	0	0	0	0	MIG
29	0	1	0	2.4	0.9	0	0	0	0	0	HIG
30	0	1	0	10.6	1.9	0	0	0	0	0	HIG

Line date:					
Bus no	Bus no	Resistance (R.-in p.u)	Reactance (X-in p.u)	Line charging admittance $\left(\frac{1}{2}B\right)$	Transformer tapping
1	2	0.0192	0.0575	0.0264	1
1	3	0.0452	0.1852	0.0204	1
2	4	0.0570	0.1737	0.0l84	1
3	4	0.0132	0.0379	0.0042	1
2	5	0.0472	0.1983	0.0209	1
2	6	0.0581	0.1763	0.0187	1
4	6	0.0119	0.0414	0.0045	1
5	7	0.0460	0.1160	0.0102	1
6	7	0.0267	0.0820	0.0085	1
6	8	0.0120	0.0420	0.0045	1
6	9	0.0	0.2080	0	0.987
6	10	0.0	0.5560	0	0.969
9	11	0.0	0.2080	0	1
9	10	0.0	0.1100	0	1
4	12	0.0	0.2560	0	0.932
12	13	0.0	0.1400	0	1
12	14	0.1231	0.2559	0	1

(continued)

(continued)

Line date:					
Bus no	Bus no	Resistance (R.-in p.u)	Reactance (X-in p.u)	Line charging admittance $\left(\frac{1}{2}B\right)$	Transformer tapping
12	15	0.0662	0.1304	0	1
12	16	0.0945	0.1987	0	1
14	15	0.2210	0.1997	0	1
16	17	0.0824	0.1923	0	1
15	18	0.1073	0.2185	0	1
18	19	0.0639	0.1292	0	1
19	20	0.0340	0.0680	0	1
10	20	0.0936	0.2090	0	1
10	17	0.0324	0.0845	0	1
10	21	0.0348	0.0749	0	1
10	22	0.0727	0.1499	0	1
21	22	0.0116	0.0236	0	1
15	23	0.1000	0.2020	0	1
22	24	0.1150	0.1790	0	1
23	24	0.1320	0.2700	0	1
24	25	0.1885	0.3292	0	1
25	26	0.2544	0.3800	0	1
25	27	0.1093	0.2087	0	1
28	27	0	0.3960	0	0.968
26	29	0.2198	0.4153	0	1
27	30	0.3202	0.6027	0	1
29	30	0.2399	0.4533	0	1
8	28	0.0636	0.2000	0.0214	1
6	28	0.0169	0.0599	0.065	1

The limit of generation for each voltage-controlled (PV) bus with bus no code is given below:

$$\begin{bmatrix} Bus\ code & P_{min} & P_{max} \\ 1 & 50 & 200 \\ 2 & 20 & 80 \\ 5 & 15 & 50 \\ 8 & 10 & 35 \\ 11 & 10 & 30 \\ 13 & 12 & 40 \end{bmatrix}$$

The alpha, beta and gamma values of all PV buses are also provided below:

$$\begin{bmatrix} Bus\,No & \alpha & \beta & \gamma \\ 1 & 0.00375 & 2 & 10 \\ 2 & 0.0075 & 1.75 & 10 \\ 5 & 0.0025 & 1 & 10 \\ 8 & 0.0083 & 2 & 10 \\ 11 & 0.065 & 3 & 15 \\ 13 & 0.075 & 3 & 20 \end{bmatrix}$$

The total cost of generation for load of 283.4 MW = **724.5546 Rs/h.**

The generation of each PV bus is given below:

$$\begin{bmatrix} Bus\,No & MW(P) \\ 1 & 111.2941 \\ 2 & 70.5819 \\ 5 & 50 \\ 8 & 35 \\ 11 & 10 \\ 13 & 12 \end{bmatrix}$$

The voltage profile of each load dispatch center is as follows:

VV = [1.0600 1.0430 1.0260 1.0178 1.0100 1.0150 1.0050 1.0100 1.0531 1.0470 1.0820 1.0600 1.0710 1.0451 1.04041.0473 1.0418 1.0306 1.0279 1.0319 1.0347 1.0353 1.0298 1.0240 1.0209 1.0033 1.0275 1.0130 1.0078 0.9963]

The total transmission loss is 5.6481 MW.

From the result of this program, it is clear that all the voltages at different load dispatch centers (LDCs) are within the permissible limit of $\pm 5\%$. Hence, the voltage stability of the system is maintained.

CASE 1: When the PEVs are connected at zone 1 at different load dispatch centers.

Average load of 1 PEV = 6.6 KW

In order to charge 10,000 PEVs

$$\begin{aligned} \text{The increased load} &= 10,000 \times 6.6\,\text{KW} \\ &= 66,000\,\text{KW} \\ &= 66\,\text{MW}. \end{aligned}$$

First of all, we put this 66 MW of load on zone 1 of HIG group at different load dispatch centers.

We have distributed 66 MW of load equally among 11 HIG LDC.

The increased load is shown by bold letters in the following table:

Bus data											
Bus no	Bus code	V In p.u	<δ radian	P_a MW	Q_d MVar	P_g MW	Q_g MVar	Q_{min} MVar	Q_{max} MVar	Q MVar	Remarks
1	1	1.06	0.0	0.0	0.0	0.0	0.0	0	0	0	SLACK BUS
2	2	1.043	0.0	21.70	12.7	40.0	0.0	–40	50	0	LIG PV BUS
3	0	1.0	0.0	2.4	1.2	0.0	0.0	0	0	0	LIG
4	0	1.06	0.0	7.6	1.6	0.0	0.0	0	0	0	LIG
5	2	1.01	0.0	94.2	19.0	0.0	0.0	–40	40	0	PV BUS
6	0	1.0	0.0	0.0	0.0	0.0	0.0	0.0	0.0	0	LIG
7	0	1.0	0.0	31.8	10.9	0.0	0.0	0	0	0	MIG
8	2	1.01	0.0	31.8	10.9	0.0	0.0	0	0	0	MIG
9	0	1.0	0.0	0.0	0.0	0.0	0.0	0.0	0.0	0.0	LIG
10	0	1.0	0.0	5.8	2.0	0.0	0.0	–6	24	19	LIG
11	2	1.082	0.0	0.0	0.0	0.0	0.0	0.0	0.0	0.0	HIG
12	o	1.00	0	20.2	7.5	0	0	0	0	0	MIG
13	2	1.071	0	0	0	0	0	–6	24	0	HIG
14	0	1	0	6.2	1.6	0	0	0	0	o	HIG
15	0	1	0	17.2	2.5	0	0	0	0	0	MIG
16	0	1	0	3.5	1.8	0	0	0	0	0	HIG
17	0	1	0	18.0	5.8	0	0	0	0	0	MIG
18	0	1	0	12.2	0.9	0	0	0	0	0	MIG
19	0	1	0	18.5	3.4	0	0	0	0	0	MIG
20	0	1	0	11.2	0.7	0	0	0	0	0	MIG
21	0	1	0	17.5	11.2	0	0	0	0	0	LIG
22	0	1	0	0	0	0	0	0	0	0	LIG
23	0	1	0	3.2	1.6	0	0	0	0	0	HIG
24	0	1	0	8.7	6.7	0	0	0	0	4.3	HIG
25	0	1	0	0	0	0	0	0	0	0	HIG
26	0	1	0	3.5	2.3	0	0	0	0	0	HIG
27	0	1	0	0	0	0	0	0	0	0	HIG
28	0	1	0	10	0	0	0	0	0	0	MIG
29	0	1	0	2.4	0.9	0	0	0	0	0	HIG
30	0	1	0	10.6	1.9	0	0	0	0	0	HIG

The total cost of generation as per the program is found to be **1023.5 Rs/Hr.**
The generation of each PV bus is given below:

$$\begin{bmatrix} Bus\ No & MW(P) \\ 1 & 200.00 \\ 2 & 66.9569 \\ 5 & 36.8241 \\ 8 & 26.3301 \\ 11 & 12.8894 \\ 13 & 21.5326 \end{bmatrix}$$

The voltage profile of each load dispatch center is as follows:
Columns 1 through 15
[1.0600 1.0430 1.0192 1.0100 1.0100 1.0092 0.9998 1.0100 1.0461 1.0370 1.0820 1.0537 1.0710 1.0351 1.0234 1.0380 1.0299 1.0017 0.9980 1.0047 1.0245 1.0250 1.0153 1.0129 1.0133 0.9955 1.0221 1.0067 1.0022 0.9907]
Transmission loss (TL) = **15.1331 MW**
In this case, also the voltages at different load dispatch centers (LDCs) are within permissible limit of $\pm 5\%$. Hence, the voltage stability of the system is maintained.

6 Result Analysis

The total cost of generation for a load of 283.4 MW = **724.5546 Rs/h.**

Total demand load (MW)	Zone/group	Cost of generation (Rs/Hr)
283.4 + 66 = 349.4	ZONE 1 (HIGH INCOME GROUP)	1048.20
Total demand load (MW)	Zone/group	Cost of generation (Rs/Hr)
283.4 + 66 = 349.4	ZONE 1 (HIGH INCOME GROUP)	1048.20
349.4	Zone 2 (MEDIUM INCOME GROUP)	1023.5
349.4	Zone 3 (LOW INCOME GROUP)	983.11

Result analysis 1
If the PEVs of high income group people charge on zone 1, then the cost will be 1048.20 Rs/Hr. but if these PEVs are charged on zone 3, then the cost will be 983.1156 Rs/Hr only. This means there is a considerable saving in money.
Per hour saving = (1048.20 – 983.11) = 65.09 Rs.

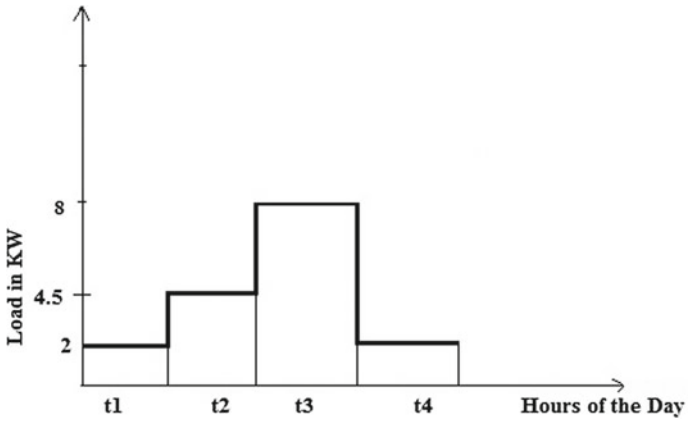

Fig. 3 Load distribution of HIG without PEV

Let the battery of plug-in electric vehicles (PEVs) charged in 12 h a day.

Per day saving = 12 × 65.09 = 781.08 Rs.

And **annual saving = 365 × 781.08 = 285094.20 Rs.**

Result analysis 2

In a similar way, if the PEVs are meant to charge at Zone 2 instead of Zone 1.

Per hour saving = (1048.20–1023.50) = 24.70 Rs.

Per day saving = 12 × 24.70 = 296.40 Rs.

And, **annual saving = 296.40 × 365 = 108,186 RS.**

The demand for the PEV charging station depends on the price of gasoline rather than the price of electricity. When the price of electricity is less than the price of gasoline for a particular amount of power, PEV charging station has to cater the demand whatever may be the price of electricity. Thus, this type of PEV avails continuous charging for any price less than the present market price of fossil fuel.

To determine the optimum price of charging, Independent System Operator (ISO) may use the following calculations:

The load distribution of HIG group for different hours of day is given in Figs. 3, 4.

From the diagram, it can be seen that the peak demand of HIG group is 8 KW when there is no PEV connected. But when the PEV is connected, the peak demand increases to 14.6 KW. The price of electricity will be more in peak hours than during off-peak hours of the day. So, the consumer will have to pay much more money to charge their PEVs.

Not only this, due to the increased load, the distribution network will be overloaded resulting in line congestion and the continuity of the supply will be hampered. There will be a common problem of voltage drop amongst the various feeders due to overloading.

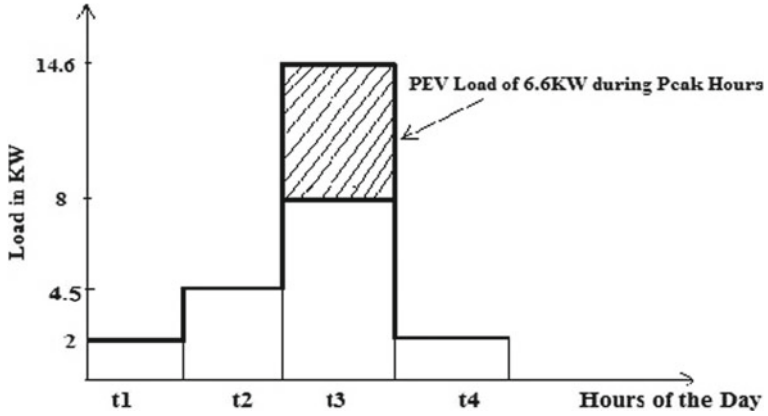

Fig. 4 Load distribution of HIG with PEV

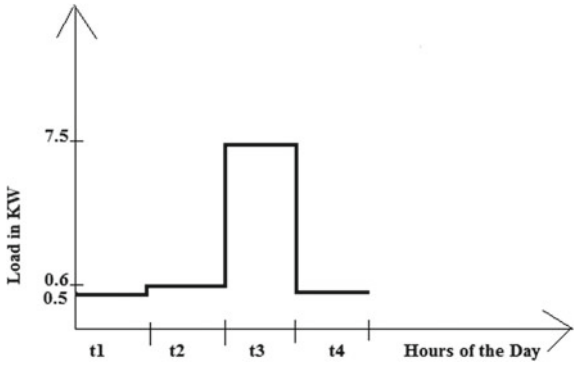

Fig. 5 Load distribution of LIG without PEV

It can be seen from Fig. 5 that the off-peak demand of a LIG group is very much less as compared to their peak demand. Also, the cost of electricity per unit is lower than any other group. So, the idea is if the PEVs are made to charge during off-peak hours of the LIG group, the problem of overloading and overcrowding of the distribution and transmission lines and other equipments such as transformers can be easily managed. The consumers have to pay less price for the charging.

6.1 Effects of the PEVs Charging on the Demand Response

Electricity price per unit consumption is to be considered as lower price during the off-peak hours of the power grid when the power demand is short particularly during night and early morning of a day, and it is also top requirements of the electric power

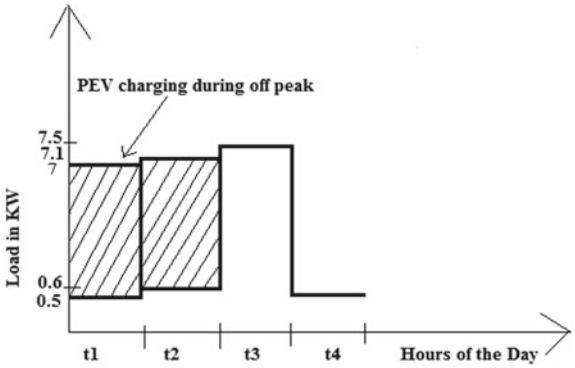

Fig. 6 Load distribution of LIG with PEV

during peak hours of a day. In the present scenario of the power market, the power demand may be controlled through the smart chargers of the electric vehicles. The consumer harvests electricity using storage systems of the electric vehicles as per requirements. The consumers exchange their demand by charging and discharging their storage systems to sell excess electricity and buy power as per the requirements of the open market policy of the electricity. The demand for the electricity in demand response is considered as varying prices of the power market just as share markets. A consumer may ask for whether the users are willing to purchase electricity at higher price during the peak hour of the load. The prices of the electricity during this time discourage the customer to use electricity due to higher price of electricity in the market.

In this approach, the consumers may reduce their demand in self-controlled techniques or sell excess electricity to power grid to earn financial benefit. As a result, the peak demand of the system decreases using a series storage system of electric vehicles. These types of the system may reduce peak demand of electrical power and saving the peak demand as shown in Fig. 6 as wider clarification. If a series of the electric vehicle is charged during off-peak hours of a day, then the price of charging will be lower as open market policy of the power market and a series of the storage of the electric vehicle (EV) systems are used to charge battery which may be used to supply the domestic load during peak hours as shown in Fig. 7 as the distributed generators. If EVs are charged during peak hours, it will invite ruthless networks of the grid, volatile system of the peak demand, and abnormal voltage variation of distribution inviting sizeable increase of power loss and bad power quality. So charging of the EV systems during off-peak hours not only decreases the peak demand of the system but also improves power quality of the electricity to fulfill the demand shortage so that the generation units run with full capacity to meet up demand to accomplish the maximum efficiency and robust reliability. Another big advantage of PEVs is demand.

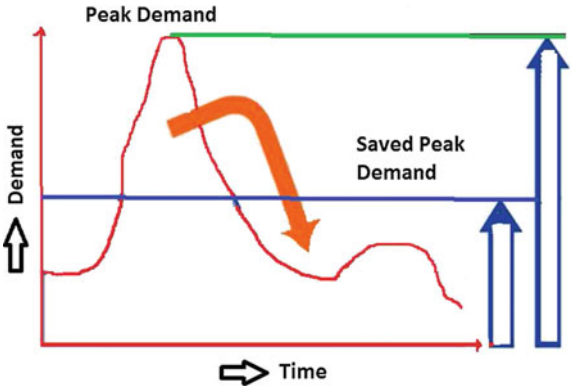

Fig. 7 Demand response curve of the power system

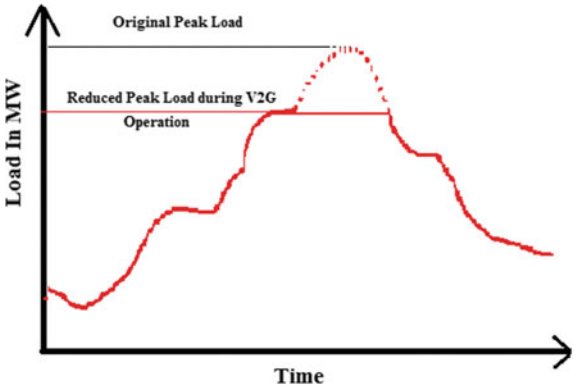

Fig. 8 Load demand curve showing V2G operation

Vehicle to Grid:

When we are charging our vehicle during the off-peak hour, then we get price benefit and during peak hour of the day, we disconnect our power system supply by connecting it to our vehicle battery or also deliver the storage power in battery to grid because peak demand also will decrease as shown in Fig. 8. As a result, the price of electricity will get reduced and the consumer will get power at a lower price. Due to the decrease in peak demand line, congestion will reduce and power quality will improve.

7 Conclusions

- Plug-in electric vehicles are clean source of transportation.
- It is cost-effective when the PEVs are charged at Zone 2 or Zone 3 instead of Zone 1.
- There is reduction in peak demand of HIG.
- Electricity cost will be lower.
- Overloading of transformers during peak hours is also eliminated.
- Due to the decrease in peak demand, line congestion will reduce and power quality will improve.
- Consumer can get financial benefits by selling the excess electricity to grid by discharging their PEVs during peak hours using vehicle-to-grid (V2G) mode.
- Plug-in electric vehicles are ideal off-peak load because of surplus power available during night and early morning hours at a lower cost.

References

1. Hanke, C., Hülsmann, M., Fornahl, D.: Socio-Economic Aspects of Electric Vehicles: A Literature Review. Springer, Berlin Heidelberg (2014)
2. Electric Power Research Institute.: Environmental assessment of plug-in hybrid electric vehicles. In: Volume 1: Nationwide Greenhouse Gas Emissions 1015325. EPRI, Palo Alto, CA (2007)
3. Fernandez, L., Roman, T., Cossent, R., Domingo, C., Frias, P.: Assessment of the impact of plug-in electric vehicles on distribution networks. IEEE Trans. Power Syst. **26**(1), 206–213 (2011)
4. Lopes, J., Soares, F., Almeida, P.: Integration of electric vehicles in the electric power system. Proc. IEEE **99**(1), 168–183 (2011)
5. Ramachandran, B., Geng, A.: Abstract Smart Coordination Approach for Power Management and Loss Minimization in Distribution Networks with PEV Penetration Based on Real Time Pricing. Springer Science + Business Media Singapore (2015)
6. Rahimi, F., Ipakchi, A.: Demand response as a market resource under the smart grid paradigm. IEEE Trans. Smart Grid **1**(1), 82–88 (2010)
7. Dam, Q.B., Mohagheghi, S., Stoupis, J.: Intelligent demand response scheme for customer side load management. In: Proceedings of IEEE Energy 2030 Conference, pp. 1–7 (2008)
8. Sinha, A.K., Hoque, T., Sau, D., Halder, T.: A smart & green charging station using the CMOS Devices for Electrical Vehicle (EV) IEEE Kolkata EDS student chapter at KGEC (2016)

A Cost Function Based Multi-objective Multicast Communication over WDM Optical Fiber Mesh Network

Subhendu Barat, Basuki Nath Keshri and Tanmay De

Abstract Multicast optical fiber communication is basically a typical multi-objective optimization problem where usage of resources like wavelength channels, splitters, converters, transceivers, and QoS parameters like delay, fault tolerance, etc. need to be optimized. In this paper, we have used a novel cost function based heuristic approach to optimize delay, splitting, wavelength usage, simultaneously. Here, we have proposed a routing algorithm which effectively minimizes splitting and splitterrequirement keeping delay in communication in consideration. The routing algorithm when combined with standard first-fit wavelength assignment provides a set of wavelength optimized light-trees for a given set of static multicast traffic. We have analyzed its efficiency through simulation over standard physical networks like NSFNET.

Keywords Multicast routing and wavelength assignment (MRWA) Wavelength division multiplexing (WDM) · Multi-objective optimization Heuristic

1 Introduction

Modern society is experiencing a drastic change in its business process, social life, and in governance. Things are getting automated and connected through the Internet. Thus, business and governance procedures are converting into online applications which is increasing the need of faster and safer data transmission worldwide. Optical fiber communication is attracting most of the focus of today's communication

S. Barat (✉) · B. N. Keshri
Department of Computer Science and Engineering, NSHM Knowledge Campus, Durgapur, India
e-mail: barat.subhendu@gmail.com

T. De
Department of Computer Science and Engineering, National Institute of Technology, Durgapur, Durgapur, India

U. Biswas et al. (eds.), *Advances in Computer, Communication and Control*, Lecture Notes in Networks and Systems 41, https://doi.org/10.1007/978-981-13-3122-0_8

researchers due to its huge bandwidth and negligible attenuation of power while transmission of signal over nations. As data is transmitted via LASER ray using the principle of total internal refraction through very thin optical fibers, the communication is very fast, secure, and communicating circuitry is very compact. Although latest switching and doping technologies in optical fiber increased the capacity of optical fiber communication, the traffic in the Internet is increasing at much faster rate than the technological growth. Especially the growth of multimedia and networking applications in e-commerce, video conference, e-learning, etc. are creating requirement of huge bandwidth.

Wavelength division multiplexing (WDM) technology enhanced the capacity of optical fiber communication further by allowing multiple messages (assigned with different wavelength) to be multiplexed in a single optical fiber cable slotted into multiple wavelength channels. A *light-path* is a path in optical layer which connects a source with another node which is the destination for a message to be communicated and it may span multiple optical fiber links in a WDM network. Without wavelength conversion capability at the optical switches, a light-path must use the same wavelength on all the fiber links through which it traverses; this property is known as the wavelength-continuity constraint [16]. Multiple recipients of a single message originated from a common sender is becoming a common phenomena in today's e-commerce and e-learning trend. In fiber optics communication, this problem is studied as Multicast Routing and Wavelength Assignment (MRWA) problem. The general approach to deal with this MRWA problem is to divide it into two subproblems: (i) Routing, i.e. constructing a multicast tree routed at the source node and connecting all the destination nodes; and (ii) Wavelength Assignment problem, which is to assign a wavelength on each link in the multicast tree to generate a *light-tree*. A light-tree may need a signal to split into multiple signals at some internal nodes. These branch nodes, called multicast capable (MC) nodes [1, 8] are more expensive due to active/passive amplification to regenerate strength of outgoing split signal, than those without, which are called as multicast incapable (MI) nodes. In this work, we have proposed a cost function based routing algorithms using some static aspect of the network and dynamic aspects of a run time multicast session establishment request to provide an efficient light-tree solution of the MRWA problem.

2 Previous Works

The latest researches on the field of Multicast Routing and Wavelength Assignment (MRWA) are based on establishing *light-tree* [12, 16] for each multicast session requests. Unicast RWA problems are encountered in [4, 6, 14] using light-path concept. Several RWA schemes have been proposed in [3, 12] which differ in the assumptions on the traffic pattern, availability of the wavelength converters, and desired objectives. The MRWA problem is an NP-Complete problem [10]. Due to this NP-completeness nature several heuristics, meta-heuristics, stochastic, and randomized approximate algorithms are proposed in literature to deal with the MRWA problem. Among the meta-heuristic algorithms Genetic Algorithm has drawn the maximum

attention. A multicast routing genetic algorithm is proposed in [13]. Although the algorithm was proposed to minimize the usage of splitters, the proposed algorithm used Dijkstra algorithm to determine the shortest path for every pair of the source and destination. Hence the entire process was not genetic. Some of the researchers have applied other techniques like: Memetic Algorithm [9], Simulated Annealing [2] and many other techniques also. A Tabu search technique is used in [15]. A chaotic optimization adaptive GA is proposed in [11]. The chaotic optimization technique adopted in this work prevents searching process stuck at local minima. A variety of research is performed on wavelength converters [5], an opto-electronics device which can convert an incoming laser ray into an outgoing ray of different wavelength. Using wavelength convertors throughput of the network can be improved a lot with increase in network cost, as the converters are very costly. A new multicast routing structure, named as *light-hierarchy*, was proposed for all multicast routing in [18], which permits the cycle introduced by *Cross Pair Switching* (CPS) capability of *Multicast Incapable* (MI) nodes. In practice, an all-optical WDM network is equipped with a limited number of MC nodes or splitters. Hence, in wavelength assignment for WDM multicast, we need to consider the splitting constraint [14]. Splitter placement problem in wavelength-routed network (SP-WRN) is studied in [2]. In a sparse splitting network multicasting requires the provision to use multiple wavelengths to be used to establish a single connection due to lack of MC nodes, which generates a set of light-trees, named as *light-forest* [17]. Two genetic algorithms to generate light forest are proposed in [7]. A new cost model employing wavelength usage and communication cost is defined there to optimize the cost of light forest.

3 Problem Formulation

In this section, we present the problem in a formal mathematical way. Here, we model a WDM optical fiber network as a graph $G = (V, E)$, where $V = (v_1, v_2, \ldots, v_N)$ is a set of nodes represented as a set of vertices and $E = (e_{ij} \mid \forall v_i, v_j \in V)$ is a set of physical links between nodes represented as a set of edges. G is a bidirectional graph such that $e_{ij} = e_{ji}$. $|V| = N$, and $|E| = \eta$.

A multicast session is defined as $r_k = (s_k, D_k)$ and the solution multicast tree can be defined as $t_k = (V_k, E_k)$ where s_k is the source and D_k is the set of destination nodes for the session r_k. $D_k = (d_k^1, d_k^2, ., d_k^n)$, where $|D_k| = n$ and $V_k \subseteq V$ is the set of vertices t_k consists of. $E_k \subseteq E$, is the set of branches constituting t_k.

3.1 Assumptions

In this paper, we have assumed the following:

- A light-tree is generated for each session.
- There is no wavelength converter hosted at any node in the network.

- All the nodes have full splitting capability and splitting at a node is independent of the splitting done for other sessions.
- There is a single optical fiber in each link and the links are bidirectional.
- No node or link failure occurs in the network.

3.2 Objectives

In this work, we have considered multiple objectives together.

The major objective of this work is to maximize the throughput, i.e., the ratio of the number of requests successfully established, say *EST* with total number of session requests appeared in a static traffic, say *REQ*. Hence, we can express our objective as:

$$Maximize \quad Throughput = \frac{|EST| \times 100\%}{|REQ|} \tag{1}$$

One of the objectives of this work is to minimize the splitting requirement to establish a multicast session. The problem can be formulated as:

$$Minimize \quad \sum_{i=1}^{N} Z_i C_i \tag{2}$$

Here, Z_i is a binary variable and C_i is another variable which stores the out-degree of node $v_i \in V$, in the multicast tree t_k, also referred as splitting capacity of the node.

$$Z_i = 1, \quad v_i \in V_k \tag{3}$$

$$Z_i = 0, \quad otherwise \tag{4}$$

Another objective of our work is to minimize the delay associated with the multicast tree t_k, represented as Δ_k. Let $P^d_{t_k}$ is the component light-path of t_k, i.e., set of edges connecting destination node $d \in D_k$ from source node s_k. The delay associated with the component light-path $P^u_{t_k}$ is represented by $\Delta(P^d_{t_k})$ and can be formulated as:

$$\Delta(P^d_{t_k}) = \sum_{e_{ij} \in P^d_{t_k}} dist(e_{ij}) \tag{5}$$

Here, $dist(e_{ij})$ represents the delay associated with the link $e_{ij} \in P^d_{t_k} \subseteq E_k$. If we assume $dist(e_{ij}) = 1, \forall e_{ij} \in E$, the delay functions represents the hop count between source–destination pair. Hence the delay associated with the establishment of the multicast session is defined as the maximum among the distance between all source–destination pair, which can be represented mathematically as follows:

$$\Delta_k = \max(\Delta(P^d_{t_k})), \forall d \in D_k \tag{6}$$

Hence, our second objective is formulated as:

$$Minimize \quad \Delta_k \tag{7}$$

3.3 Constraints

- There must be atleast one node in destination set D_k.

$$|D_k| \geq 1 \tag{8}$$

- All the destinations belonging to the destination set D_k of a request r_k have to be included in the resulting multicast tree t_k exactly once.

$$D_k \subseteq V_k \subseteq V \tag{9}$$

- multicast tree t_k must be free from loop and redundant edges.

$$\nexists e_{ac}, e_{bc} \in E_k \mid v_a, v_b, v_c \in V_k \forall a, b, c \tag{10}$$

$$\nexists e_{as_k} \in E_k \mid v_a \in V_k \tag{11}$$

- No node is repeated in the multicast tree t_k.

$$\sum_{i=1}^{N} Z_i = |V_k| \tag{12}$$

4 Proposed Approach

Throughput is one of the major parameters in establishing communication over any network. The more the throughput greater is the success ratio to establish a connection. In WDM optical fiber communication, one of the major physical constraint is the number of wavelength channels available in every optical fiber cable. Hence, it imposes a restriction over number of message signals which can transmit through a optical fiber cable. Due to distinct wavelength constraint, two different signals cannot be transmitted with the same wavelength channel in a single optical fiber simultaneously. This makes a major performance issue in MRWA. Here, we tried to reduce number of distinct wavelength channels required within an optical fiber to establish session for all multicast requests generated at a time. If the wavelength channel

requirement for each session can be reduced then on an average more multicast session requests can be established successfully. This, in turn, will reduce blocking due to unavailability of wavelength channels in any optical fiber cable in the network. This way we can optimize throughput for a given set of static requests.

Throughput can further be degraded because of request blocking due to violation of splitting constraint at any internal node of the solution multicast tree. As we know, MC nodes are very costly, all the nodes in the network may not be MC node, and even all the MC nodes may not split an incoming request into infinite number of outgoing signals, i.e., there is a finite splitting capacity in all MC nodes in a WDM optical fiber network. If an internal node in the solution routing tree tries to split an incoming signal into x number of outgoing signals, where the splitting capacity of the branch node is, say y, and $x > y$, then the signal cannot be split into desired amount, and some of the destinations in the request cannot be connected with the common source. As we assumed that all the destination nodes need to be connected with the common source, in this case, request blocking will occur due to splitting capacity constraint. In this paper, we try to minimize branching of any internal node in the routing phase, so as probability to violation of splitting capacity constraint can be minimized.

As lesser branching off imposes skewness in tree, it, in turn, increases the delay in communication. We have tried to optimize the delay as well as the splitting requirement for establishing a multicast session where delay is treated as a major QoS parameter in digital communication and optical splitters and wavelength channels are taken as major cost parameter. A minimum splitting is attained when no internal nodes are split into multiple branches, i.e., all the destinations are in a chain starting from the source node. This type of skewed tree increases the depth of the traversal as well as the overall delay associated with the multicast tree, hence delay starts increasing. So a trade-off must be attained. Here, we have proposed one technique to solve this multi-objective problem in efficient manner. Here we have devised a new cost function for each link in the networks which takes the length of the link as well as the proximity of destination nodes from the incidents nodes, which restricts the branching from an internal node as well as exploration of links are tunneled towards destination nodes only. The mathematical formulation of our cost function is as below.

$$Cost(v_i, v_j) = (k1 * Dist(v_i, v_j) + k2 * Prox(v_j))/(isDest(v_j) + 1) \tag{13}$$

Here, $Cost(v_i, v_j)$ is computed as the cost to explore node v_j from node v_i through the link e_{ij}. A link will be traversed only when the algorithm decides the cost associated with that edge is increasing the total cost of exploration by the minimum amount, i.e., we want to find a solution tree t_k for a multicast session r_k, if t_k connects all destination nodes $d \in D_k$, and $COST^{t_k}$ is minimum.

$$Cost^{t_k} = \sum_{e_{ij} \in E_k} (Cost(v_i, v_j)) \tag{14}$$

$Dist(v_i, v_j)$ is the actual distance from node v_i to v_j in the WDM optical fiber mesh network . Thus, longer distance will make a node costlier to be explored.

$$Prox(v_j) = \frac{Number\_of\_Neighbour(v_j)}{Number\_of\_Destination\_Neighbour(v_j) + 1} \tag{15}$$

$Prox(v_j)$ measures the proximity of v_j from destination node(s). Lower value of $Prox(v_j)$ estimates higher possibility of exploring destination nodes. Thus it affects on the size of the multicast tree, and reduces hop count.

The value of $isDest(v_j)$ will be 1 if v_j is a destination node itself and the value is 0 otherwise. Due to this the cost to explore a destination node will be less than to explore a non-destination node. Thus, it reduces wavelength channel requirement. $k1$, $k2$ is are positive constants which can tune the impact of the controlling parameters as per the application requirement.

Hence, Eq. 13 generates a cost of exploration for each link in the network. As all the controlling parameters return a positive value, cost of exploration for every link in the network is also positive. As we need to minimize the total exploration cost, here we have applied modified Dijkstra's Algorithm to find out the solution routing tree. Unlike original Dijkstra's Algorithm we are not trying to find out shortest path for all nodes in the network from the common source, rather we are exploring the nodes until all the destination nodes are explored. The detailed pseudocode of the proposed "*Cost-Based Multicast Routing*" *(CBMR)* is explained in Algorithm 1.

As shown in Algorithm 1, at first the cost matrix is generated for the given multicast session request r_k. Then, we initialize *MinCost* vector as the computed minimum cost to reach every node from the source node. As distance of source node with itself is 0, its *MinCost* is always 0. Then, in each iteration, we will find the closest node to be explored and will freeze its *MinCost*, if its computed cost is least among the costs of all unexplored nodes. If a new node is explored cost of its adjacent nodes may be updated, if better path is explored. The iteration continues until all the destination nodes are explored. After this, the multicast tree is extracted by backtracing every explored destination nodes upto the common source node.

5 Result Analysis

To analyze the performance of our proposed CBMR algorithm, we have simulated the algorithm over various physical WDM optical fiber mesh networks, and compared its performance with standard Dijkstra's Algorithm. As the distance between two nodes in a physical network is always positive, Dijkstra's Algorithm always guarantees minimum delay to reach any node in the network. Hence it provides the lower bound of delay in multicast communication, which is one of the major QoS parameter in all types of communication. Thus, Dijkstra's Algorithm becomes a good choice to compare the performance of our proposed algorithm in this multi-objective optimization scenario. Here, we have simulated our proposed algorithm over the graphical model

Algorithm 1: Cost-Based Multicast Routing (CBMR)

Input : A Multicast Session Request r_k
Output: A multicast tree t_k

```
for i = 1 to N do
    for j = 1 to N do
        Cost_ij is set as per Eq. 13
Set Unexplored = D_k
for i = 1 to N do
    Set MinCost_i = ∞
    Set Reached_i = 0
Set MinCost_{s_k} = 0
while Unexplored ≠ φ do
    Set v = findClosest()
    Set Reached_v = 1
    if v ∈ Unexplored then
        Remove v from Unexplored
    Set NEI = findNeighbours(v)
    while NEI ≠ φ do
        Pick and remove u from NEI
        if MinCost_u < (MinCost_v + Cost_vu) then
            Set MinCost_u = (MinCost_v + Cost_vu)
            Set Parent_u = v
Construct t_k by backtracing paths upto source s_k
```

of NSFNET presented in Sect. 4 of this paper with a set of 500 random multicast requests. We have varied the maximum session size of each such random request from 2 (unicast) to 14 (broadcast), and compared the performance with Dijkstra's algorithm. The multicast session size is increased by one node for each simulation point from unicast test case to broadcast test case, for all possible simulation points for the network. We have taken following parameters for comparison purpose: total splitting requirement per session, splitters requirement per session, number of optical channels required per session, average delay in communication, average hop count, and total number of wavelength channels required to establish all 500 randomly generated static requests.

In Fig. 1, it is found that our proposed CBMR algorithm is reducing the tree size of the multicast tree more than the standard Dijkstra's Algorithm. Due to this reason, lesser number of optical channels are required in CBMR algorithm.

As lesser number of optical links are required for each multicast session request using CBMR algorithm, there will be lesser requirement of wavelength channel capacity in optical cables of the network to establish sessions for entire static set of requests. This is justified in Fig. 2, where First-Fit wavelength assignment is performed on the multicast trees generated by CBMR and Dijkstra's algorithm. This is the vital achievement of our proposed algorithm. As wavelength channel capacity of an optical fiber cable is a cost-sensitive physical constraint in optical fiber network,

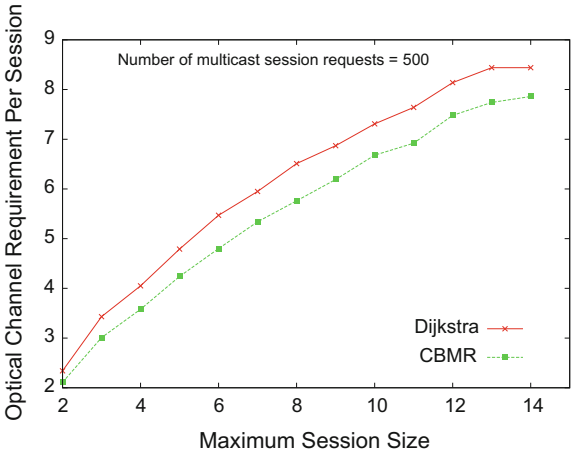

Fig. 1 Comparison on optical channel requirement per session

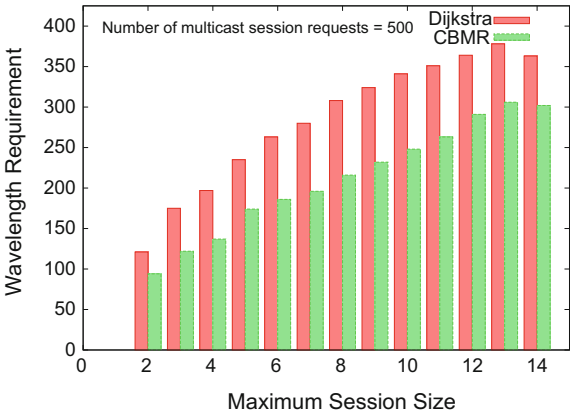

Fig. 2 Comparison on wavelength requirement

lesser requirement of wavelengths makes the algorithm robust even for low-cost, low-capacity WDM networks also. Thus, it guarantees better throughput.

Table 1 shows that our proposed CBMR algorithm requires lesser number of splitters, and splitting. It also reduces hop delay and increases the distance to be traversed by a moderate fraction than Dijkstra's algorithm, which traverses optimum distance to establish the multicast sessions.

Table 1 Comparison on splitting and delay

Session size	Dijkstra				CBMR			
	No. of splitter	Total splitting	Hop delay	Max distance traversed	No. of splitter	Total splitting	Hop delay	Max distance traversed
2	0	0	2.34	2278	0	0	2.11	2428
3	0.44	0.44	2.74	2628.8	0.39	0.39	2.43	2885
4	0.69	0.75	2.85	2776.8	0.65	0.69	2.52	3033.2
5	0.92	1.04	3.09	2984.8	0.85	0.97	2.7	3271.2
6	1.11	1.34	3.21	3132.6	1.04	1.22	2.82	3519
7	1.28	1.57	3.29	3202	1.23	1.5	2.85	3567.8
8	1.48	1.82	3.38	3313.4	1.37	1.69	2.98	3701.6
9	1.63	2.04	3.46	3314.2	1.52	1.91	2.99	3719.4
10	1.83	2.28	3.55	3342.6	1.7	2.19	3.02	3834.2
11	1.96	2.45	3.57	3483.4	1.81	2.3	3.06	3892
12	2.18	2.75	3.61	3499.4	2.04	2.65	3.09	3910.2
13	2.24	2.87	3.71	3645.4	2.11	2.78	3.12	4026.8
14	2.3	2.95	3.62	3546.2	2.17	2.88	3.04	3913

6 Conclusion

As traditional business is transforming in e-commerce and academics is shifting toward e-learning, communication is becoming bandwidth sensitive, which is making optical fiber networks as the choice of transmission media. One-to-many communication in optical fiber communication requires more research to optimize costly resources like splitters, wavelength channels and also to improve quality of service by minimizing delay in communication. In this paper, we have formulated one such multi-objective MRWA problem for WDM mesh network and proposed a cost function based multicast routing algorithm which reduces splitting requirement and wavelength channel requirement simultaneously keeping delay in communication bounded in a low limit. We have shown the efficiency of our proposed algorithm with simulation results and proved that our proposal works economically in WDM mesh networks.

References

1. Ali, M., Deogun, J.S.: Power-efficient design of multicast wavelength-routed networks. IEEE J. Sel. Areas Commun. **18**(10), 1852–1862 (2000)
2. Ali, M., Deogun, J.: Allocation of splitting nodes in alloptical wavelength-routed networks. Photonic Netw. Commun. **2**(3), 247–265 (2000)

3. Banerjee, D., Mukherjee, B.: A practical approach for routing and wavelength assignment in large wavelength-routed optical networks. IEEE J. Sel. Areas Commun. **14**(5), 903–908 (1995)
4. Bermond, J.C., Gargano, L., Perennes, S., Rescigno, A.A., Vaccaro, U.: Efficient collective communication in optical networks. Theor. Comput. Sci. **233**(1–2), 165–189 (2000)
5. Chatterjee, M., Barat, S., Majumder, D., Bhattacharya, U.: New strategies for static routing and wavelength assignment in de Bruijn WDM networks. In: COMSNETS, pp. 1–4 (2011)
6. Chen, B., Wang, J.: Efficient routing and wavelength assignment for multicast in wdm networks. IEEE J. Sel. Areas Commun. **20**(1), 97–109 (2002)
7. Din, D.R.: Genetic algorithm for finding minimal cost light-forest of multicast routing on WDM networks. Artif. Intell. Rev. **29**(3–4), 195–222 (2008)
8. Ding, A., Poo, G.S.: A survey of optical multicast over WDM networks. Comput. Commun. **26**(2), 193–200 (2003)
9. Donoso, Y., Perez, A., Fabregat, C.: Optimizing multiple objectives on multicast networks using memetic algorithms. GESTS Int. Trans. Comput. Sci. Eng. **20**(1), 192–204 (2005)
10. Hadas, R.L., Melhem, R.G.: Multicast routing and wavelength assignment in multihop optical networks. IEEE/ACM Trans. Netw. **10**(5), 621–629 (2002)
11. Li, C., Wang, Y., Du, M., Yue, C.: Multicast routing scheme based on chaotic optimization adaptive genetic algorithm. In: Proceedings of the 2007 IEEE International Conference on Granular Computing. pp. 471–476. GRC '07, IEEE Computer Society (2007)
12. Ozdaglar, A.E., Bertsekas, D.P.: Routing and wavelength assignment in optical networks. IEEE/ACM Trans. Netw. **11**(2), 259–272 (2003)
13. Siregar, J.H., Zhang, Y., Takagi, H.: Optimal multicast routing using genetic algorithm for WDM optical networks. IEICE Trans. Commun. **88**(1), 219–226 (2005)
14. Wang, J., Qi, X., Chen, B.: Wavelength assignment for multicast in all-optical WDM networks with splitting constraints. IEEE/ACM Trans. Netw. **14**(1), 169–182 (2006)
15. Yan, S., Deogun, J.S., Ali, M.: Routing in sparse splitting optical networks with multicast traffic. Comput. Netw. **41**(1), 89–113 (2003)
16. Yang, D.N., Liao, W.: Design of light-tree based logical topologies for multicast streams in wavelength routed optical networks. INFOCOM **1**, 32–41 (2003)
17. Zhang, X., Wei, J., Qiao, C.: Constrained multicast routing in wdm networks with sparse light splitting. INFOCOM **3**, 1781–1790 (2000)
18. Zhou, F., Molnár, M., Cousin, B.: Light-hierarchy: the optimal structure for multicast routing in WDM mesh networks. CoRR abs/1012.0017 (2010)

Detection and Counting of Marigold Flower Using Image Processing Technique

Prabira Kumar Sethy, Bijayalaxmi Routray and Santi Kumari Behera

Abstract Analytically, in view of nation's unavoidable pecuniary development and its input toward farming like floriculture is essentially an extensive area and a catalyst in the structural socioeconomic building of India. As it is the age of computerization, in the field of harvest, estimation which stimulates an idea of an automated approach using precision agriculture having the degree of ability to count acres of flowers in a specific field which indeed saves time and money in contrast to manual counting. So, the marigold harvest and its production estimation can be done through image processing which may help largely in the planning of good marketing and its management easily. In this paper, we have proposed a methodology which can detect and count marigold flower successfully by using HSV color transform and circular Hough transform (CHT) methodologies. The proposed methodology is applied to marigold flower which is captured in an open field with an average error of 5%.

Keywords Circular hough transform · HSV color transform · Marigold flower Image processing

1 Introduction

There are about 250,000 named flower species in the world; on a daily basis, we can see many blooming flowers in the roadside, garden, park, mountain path, wild field, greenhouses, etc. [1]. Floriculture is a discipline of horticulture concerned with the cultivation of flowers and ornamentals plants for floral industry and for

P. K. Sethy (✉)
Department of Electronics, Sambalpur University, Sambalpur, Odisha, India
e-mail: prabirasethy@suniv.ac.in

B. Routray · S. K. Behera
Department of Computer Science and Engineering, VSSUT, Sambalpur, Odisha, India
e-mail: bijaylaxmiroutray7@gmail.com

S. K. Behera
e-mail: b.santibehera@gmail.com

U. Biswas et al. (eds.), *Advances in Computer, Communication and Control*, Lecture Notes in Networks and Systems 41, https://doi.org/10.1007/978-981-13-3122-0_9

the garden. Floriculture crops include houseplants, bedding plants, pot plants, and cut flowers. The cut flower is used in business in which flower is usually sold in bunches or as bouquets with foliage. Cut flowers are used in drink, decoration, for making medicine, cosmetics, etc. Currently, everyday the utilization of technology within the field of agriculture is increasing day by day for reducing the workforce and increasing the assembly capability. Produced flowers sold in the market by the farmers in the form of the bunch. But in the market, these flowers sold in the form of units; hence the profit gain by the agent is more than the farmer because a farmer does not know how many (in units) flowers are there in his garden. Bairwa [2] addressed issues in flower counting. Fifteen Gerbera flower images are processed and applied image processing techniques to achieve 95.01% of accuracy over manual counting. Nandyal and Jagadeesha [3] conferred a crop growth prediction system using machine vision in which the fruit region is found using edge detection and circular fitting algorithm. Wijethunga et al. [4] developed machine-controlled enumeration approach with application to kiwifruit enumeration system. Three easy enumeration strategies followed by a minimum distance classifier-based segmentation technique in L * a * b * color space is discussed. The recognition accuracy is above 90%. Sarkate et al. [5] counted Gerbera flowers using Hue Saturation Value (HSV) color space and histogram analysis. The proposed algorithm is given less accurate result due to overlapped flowers. Dorz et al. [6] estimated tangerine yield by counting of the tangerine flower using machine vision. Flowers are counted with the help of Gaussian filter and RGB color detection method. Salvo et al. [7] predicated blueberry based on the counting of a number of flowers buds. Bud counting relates the number of enough of fruit for the harvest and also relates weather variable. Sural et al. [8] have studied the important properties of HSV color space and developed and framework for extracting features which is used for both segmentation and histogram generation in their approach. They used the saturation value of a pixel to extract the object. Cauchie et al. [9] Presented improved Hough transform which applied to search of a common center of circular or partial circular object present in an image. The designed algorithm is applied for analysis of x-ray diffraction. Dorj et al. [10] developed color detection and counting algorithm, and the tangerine flower, under natural lighting condition, it used Gaussian filter to reduce noise and illumination adjustment for better clarity. The algorithm is capable of detecting and counting partially and semipartially occluded tangerine flowers with the error of 10%.

2 Proposed Methodology

Marigold flower images are captured by the digital camera. The distance between the camera and the flower is less than one meter. In the experiment, images were processed using Dual Core processor with 2 GHz frequency and 2 GB RAM. The experiment was carried out on MATLAB R2016a. Flower counting is used to yield approximation or estimation of a particular crop in floriculture field. The manual counting is costly and time-consuming. In this work, to develop an algorithm for

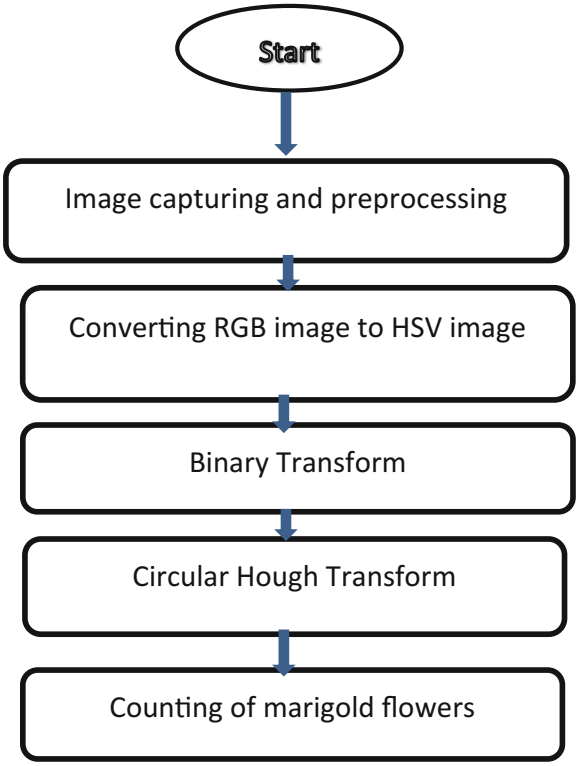

Fig. 1 Flowchart of marigold flower detection and counting

computer vision-based automated system for fast and precise counting of flowers. The flowchart Fig. 1 shows the stepwise process of marigold flower detection and counting.

2.1 Collection of Sample

The steps intend to capture an image through the camera. The quality of the image depends on camera parameters such as lighting condition, size of objects, and distance from the image. For better results, cameras with higher resolution are preferred. Figure 2 shows the two variety of marigold flower.

Fig. 2 Sample images of marigold flower

2.2 HSV Color Transform

For flower recognition in counting algorithm, three different types of method are possible using shape, color, and texture. HSV color space is used for flower color extraction. Figure 3 shows the original image, HSV transformed image, scaling of HSV and Binary image.

2.3 Circular Hough Transform

The circular Hough transform is a feature extraction technique to detect circles. This is a special type of Hough transform which can detect multiple numbers of circles with unknown radius. The CHT iterate through possible radii. First, it is required to produce accumulator metrics by dividing parameter space into the bucket as per grid. The component in the accumulator metrics denotes the numbers of circles within the parameter area that passes through the corresponding grid cell. Initially, every element in the metrics zeroes and for each edge point in the original space form a circle and increase the amount of grid cell which the circle passing through. This method is known as voting. After voting, we are able to find neighborhood maxima in the accumulator metrics. The location of the local maxima in the corresponding to the circle center. The voting process is as follows:

Step 1: For each pixel (x, y) find the possible radius between 10 and 60.
Step 2: For each pixel (x, y) find the possible theta between 0 and 360.
Step 3: Update the polar coordinate for center using equation

$$a = x - r * \cos(t * PI/180);$$
$$b = y - r * \sin(t * PI/180);$$

Step 4: Update voting by A[a, b, r]+ = 1 (Fig. 4).

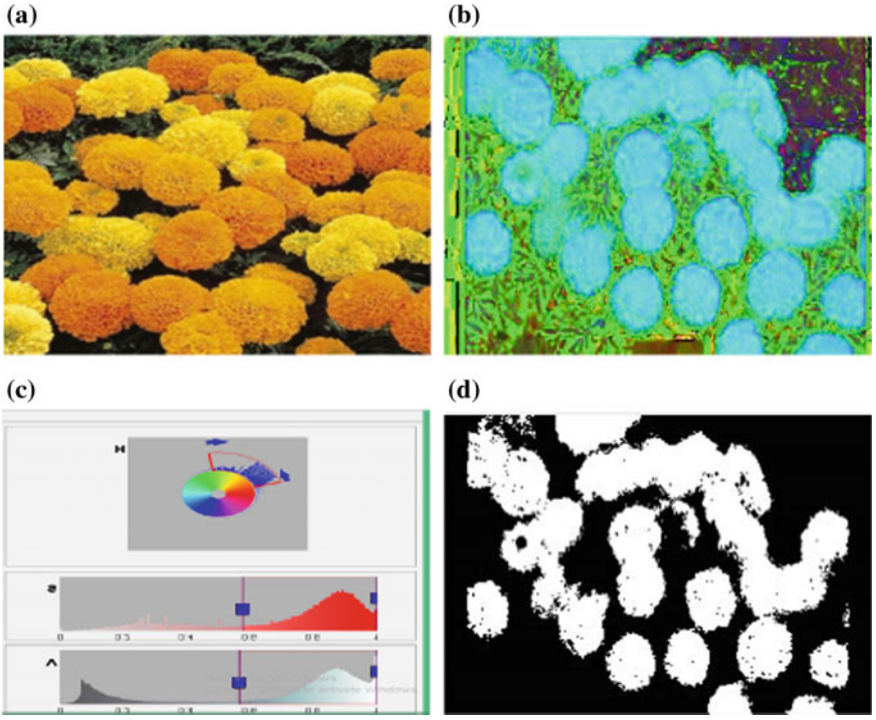

Fig. 3 **a** Original image **b** HSV transformed image **c** Scaling of HSV **d** Binary image

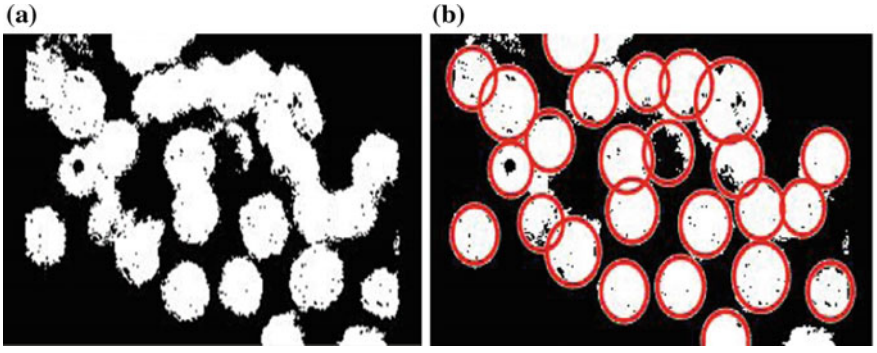

Fig. 4 **a** Binary image, **b** Circle fitting image

3 Experimental Results

In the developed algorithm, HSV color space transformation of RGB image provides a better segmentation. After color segmentation, circle fitting algorithms are applied and then counting can be done according to a number of the center present. Here, we

Table 1 Performance evaluation of manual count and algorithmic count with false counting

Sl. no.	MC	AC	False counting	Sl. no.	MC	AC	False counting
1	33	30	3	11	15	15	0
2	40	38	2	12	14	12	2
3	42	40	2	13	18	17	1
4	23	24	1	14	6	6	0
5	22	21	1	15	5	4	1
6	23	20	3	16	2	2	0
7	30	29	1	17	4	3	0
8	31	30	1	18	12	12	0
9	28	26	2	19	12	13	1
10	18	18	0	20	8	9	1

Average error = 5.5%. * *AC* Algorithmic Count, *MC* Manual Count

Table 2 Comparison between manual and algorithmic count with false counting

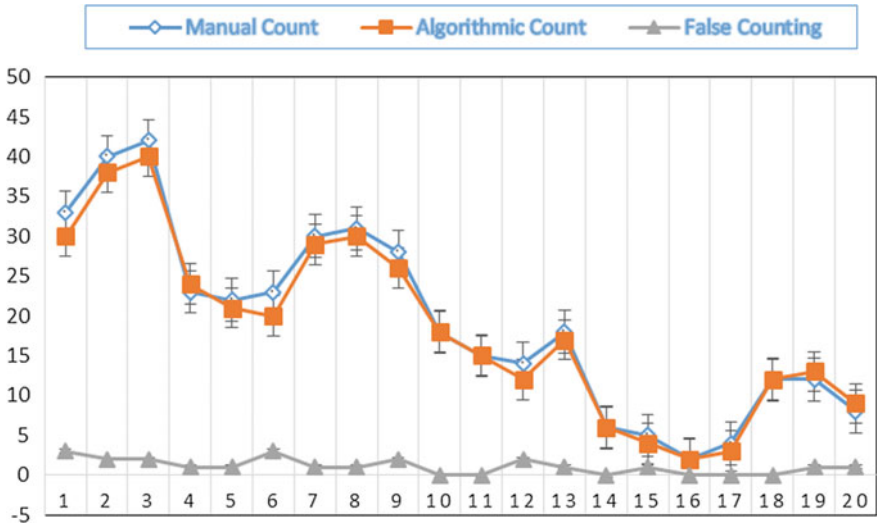

use circular Hough transform for circle fitting, which is more robust and solves the problem of overlapping of flowers. The advantage of this algorithm is that it is capable of detecting and counting marigold flower even if in occluded and/or overlapping condition (Tables 1 and 2).

The performance of the developed algorithm is measured by a number of false detections with respect to manual count which is illustrated below.

$$\text{Error in } \% = \frac{\text{Number of False Counts}}{\text{Number of Manual Counts}} \times 100.$$

4 Conclusion

In the developed algorithm, HSV color space transformation of RGB image provides a better segmentation. After color segmentation-based image, circle fitting algorithms are applied and then counting can be done. Here, we use circular Hough transform for circle fitting algorithm which is more robust and is capable of counting the occluded as well as overlap flower. The developed algorithm successfully detects and counts the marigold flower of an open field with an error of 5%. The perspective algorithm will facilitate to design an automatic counting system of marigold flower and will be capable of providing information to farmers about flower production.

References

1. Hsu, T.H., Lee, C.H., Chen, L.H.: An interactive flower image recognition system, Springer Science + Business Media, 53, 53–73 (2010)
2. Bairwa, N.: Counting of flowers using image processing, (IJERT), vol. 3 Issue 9, September 2014. ISSN 2278-0181
3. Nandyal, S., Jagadeesha, M.: Crop growth prediction based on fruit recognition using machine vision. Int. J. Comput. Trends Technol. (IJCTT) **4**(9) 3132–3138 (2013)
4. Wijethunga, P., Samarasinghe, S., Kulasiri, D., Woodhead, I.: Digital image analysis based automated kiwifruit counting techniques. In: International Conference on Image and Vision Computing, New Zealand (2008)
5. Sarkate, R.S., Kalyankar, N.V., Khanate, P.B.: Application of Computer vision and color image segmentation of yield prediction precision. In: IEEE International Conference on Information Systems and Computer Networks (ISCON), pp. 9–13 (2013)
6. Dorj, U.O., Lee, M., Senthilkumar, S.: A novel technique for tangerine yield estimation via flower detection. In: 2nd International Conference on Information Science and Technology, vol. 7, pp. 405–412 (2013)
7. Salvo, S., Munoz, C., Avila, J., Bustos, J., Ramirez-Valdivia, M., Silva, C., Vivallo, G.: An estimative of potential blueberry yield using regression models that relate the number of fruits to the number of buds and to climate variables. Sciatica Horticulture **133**, 56–63 (2012)
8. Sural, S., Qian, G., Pramanik, S.: Segmentation and histogram generation using the HSV color space for image retrieval. In: International Conference on Image Processing, pp. II-589–II-592 (2002)
9. Cauchie, J., Fiolet, V., Villers, D.: Optimization of a hough transform algorithm for the search of a center. J. Pattern Recogn. **41**, 567–574 (2008)
10. Dorj, U.O., Lee, M., Senthilkumar, S.: A Novel technique for tangerine yield estimation via flower detection. 2nd International Conference on Information Science and Technology **7**, 405–412 (2013)

A Dual Band, Dual Polarized Slot Antenna Using Coplanar Waveguide

Mohammad Imroz Khan, Avinash Chandra and Sushrut Das

Abstract This letter presents a multiband antenna exhibiting dual polarization characteristics. The antenna consists of a circular-shaped slot etched in the ground plane. A rectangular patch is inserted in the slot energized by CPW feed. Three conducting strips are attached to the radiating patch on either side of the feed line along with a circular slot notched on the patch for introducing asymmetric excitation. Further, a number of rectangular slits are embedded in the ground plane protruding into the circular slot for achieving dual polarization characteristics. Asymmetric excitation results in generation of circular polarized radiations for the lower band while the upper band remains linearly polarized. Overlapping lower band i.e. $S_{11} < -10$ dB and Axial ratio <3 dB extends from 2.33 to 3.90 GHz while the linear polarized upper band extends from 5.4 to 6.3 GHz thereby proposed antenna covering Bluetooth and WLAN usable bands by dual resonating bands.

Keywords Coplanar waveguide · Dual polarized · Slot antenna · Circular slot Dual band

M. I. Khan (✉)
Department of Electronics and Communication Engineering, Vignan's Foundation for Science, Technology and Research, Guntur, India
e-mail: iitdhanbad.imroz@gmail.com

A. Chandra
School of Electronics Engineering, Vellore Institute of Technology, Vellore, India
e-mail: avinashchandra888@gmail.com

S. Das
Department of Electronics Engineering, Indian Institute of Technology (Indian School of Mines) Dhanbad, Dhanbad 826004, Jharkhand, India
e-mail: sushrut_das@yahoo.com

U. Biswas et al. (eds.), *Advances in Computer, Communication and Control*, Lecture Notes in Networks and Systems 41, https://doi.org/10.1007/978-981-13-3122-0_10

1 Introduction

With the age of growing wireless communication system, multiband antennas are highly entertained these days by researchers. In [1] a dual band antenna, operating in GSM band and WLAN band has been proposed with dual polarizations, i.e., lower band circular polarized and upper band linear polarized. In [2], another dual band antenna is proposed with both bands circular polarized. Multiband antenna with multiple polarization characteristics have become prominent [3, 5] and various techniques are used to enable the same antenna to radiate both circular polarized and linear polarized radiations. In [3], stacked-patch triple band antenna exhibiting dual polarization has been presented. In [4], a dipole-like structure has been studied with tapered arms and an open-ended slot resulting in dual band antenna with lower band circular polarized and upper band linear polarized. Similarly, in [5], a sector-shaped coaxial fed antenna with truncated corners is introduced to integrate both linear polarized and circular polarized characteristics in the same antenna, thereby the same antenna radiates both linear polarized and circular polarized radiations.

2 Antenna Configuration

Schematic view of the antenna along with its geometrical dimensions is presented in Fig. 1. Antenna presented is a 35 mm $\times$ 35 mm structure designed on FR4 substrate of height 1.6 mm, dielectric constant 4.4 and loss tangent 0.02. The antenna is fed by a 50 Ω feed line of width 3.2 mm placed at 0.4 mm from ground. The signal strip is attached to the stair-shaped patch energizing the antenna. A circular-shaped ground is used with a circular notch created in the patch to improve dual band nature. A key feature of the proposed antenna lies in use of circular ground which along with asymmetric patch results in very easy generation of circular polarization and dual band characteristics. The antenna is modeled on CST Microwave Studio and its key antenna parameters are optimized for acceptable values. Couple of rectangular stubs attached to the radiating patch is responsible for generation of two orthogonal electric field components in phase quadrature which generates circular polarized radiations. Nonuniform perturbation of conducting slits into the circular slots helps in tuning the axial ratio bandwidth (Table 1).

3 Parametric Study and Antenna Evolution

Antenna prototypes shown in Fig. 2 illustrate the steps involved for antenna improvement. It is evident that the proposed antenna starts resonating when primary stub was introduced in the slot but it was not working as a circular polarized antenna due to high value of axial ratio. After the introduction of rectangular stubs on the diagonally

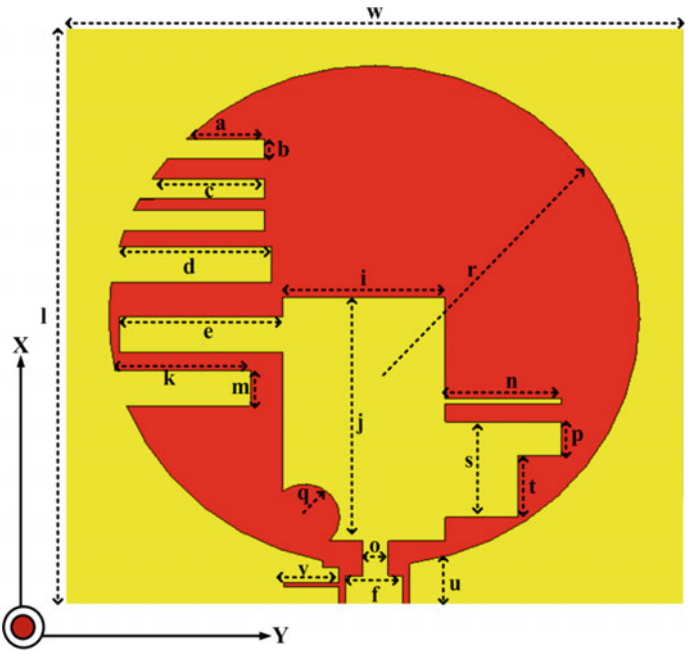

Fig. 1 Schematic view of antenna

Table 1 Antennal dimensions (mm)

a	b	c	d	e	f	h	i	j	k
4.4	1.2	6.4	8.7	9.2	3.2	1.6	9.2	14.6	7.6
l	m	n	o	p	q	r	s	t	u
35	2.1	6.6	1.43	2	2	15	5.7	3.7	2.7
v	w								
3.1	35								

opposite ends of the primary stub, the proposed antenna starts resonating for a wide range of frequencies and axial ratio suddenly drops below but still remains greater than 3 dB which indicates that the necessary condition of exciting orthogonal components of same amplitude but 90° out of phase in time is fulfilled. Now, number of rectangular metallic stubs embedded in the ground are introduced into the circular slot with stubs remaining in the close vicinity of the radiating patch which reduces the axial ratio below 3 dB. Dual polarization characteristics are introduced in the structure by incorporating a circular notch in the radiating patch. From the distribution of surface current for various time instants, it can be observed that current vectors on the patch and ground plane follows an anticlockwise rotation which adds to the RHCP nature of antenna.

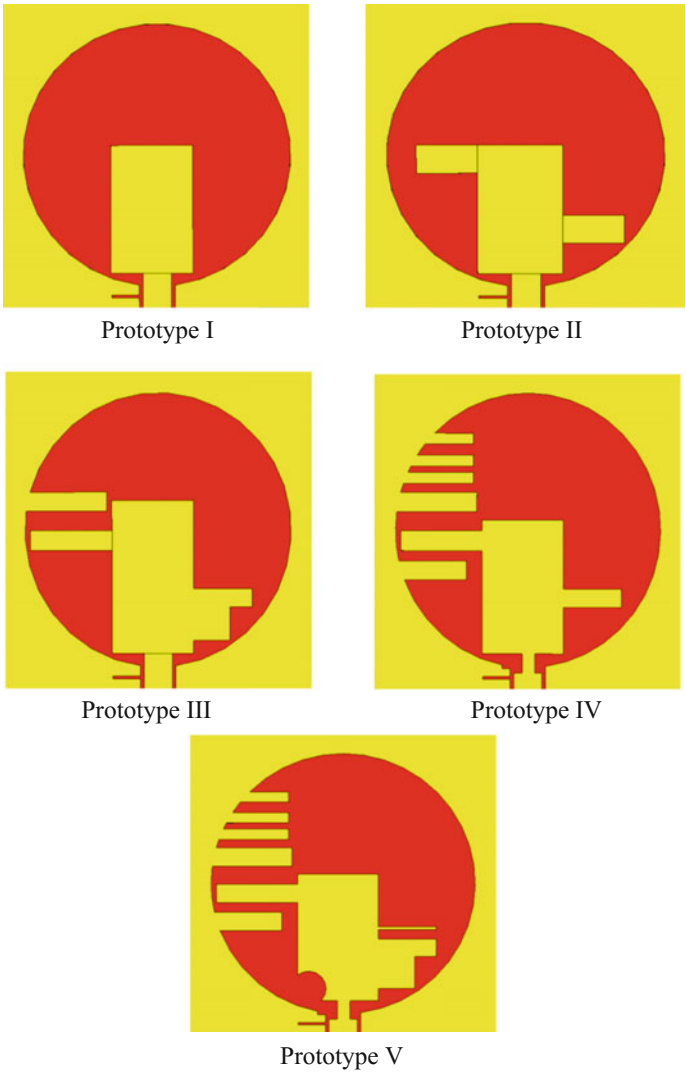

Fig. 2 Steps for improvement of antenna

So it can be inferred that the crucial parameter for circular polarized behavior of the proposed antenna is the circular smooth ground and proper placement of rectangular stubs into the slot leading to asymmetric excitation. Figures 3, 4 show S_{11} (dB) and axial ratio (dB), respectively, for all the antenna prototypes which show the step by step improvement of antenna. From Fig. 4, it is evident that asymmetric excitation in Prototype IV results in obtaining dual polarization characteristics of the proposed antenna.

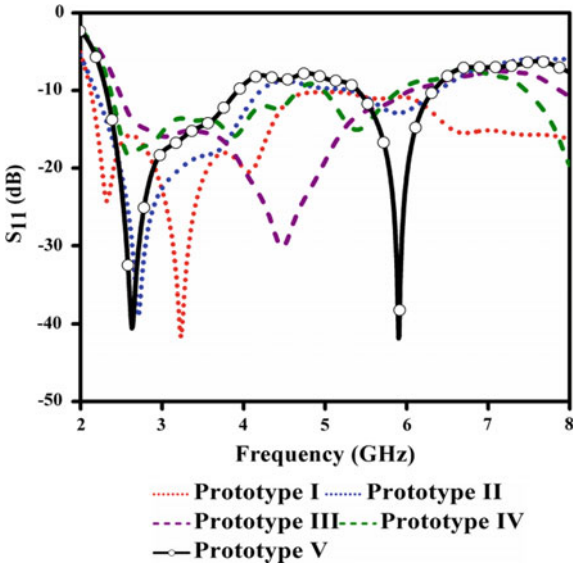

Fig. 3 S-parameter of antenna prototypes

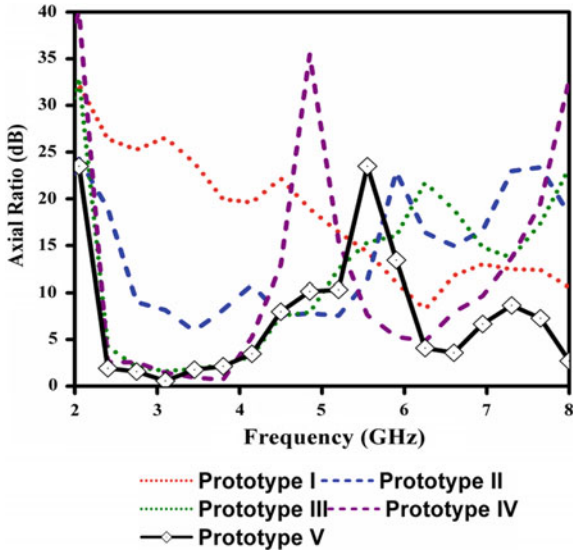

Fig. 4 Axial ratio of antenna prototypes

3.1 CP Analysis

Study of surface current distribution with advancing time also helps in analyzing circular polarized behavior of the antenna. For a circular polarized antenna, current vector follows a circular path as it rotates either in clockwise or in anticlockwise direction. At t = 0, t = T/4, t = T/2 and t = 3T/4 current distribution is studied along

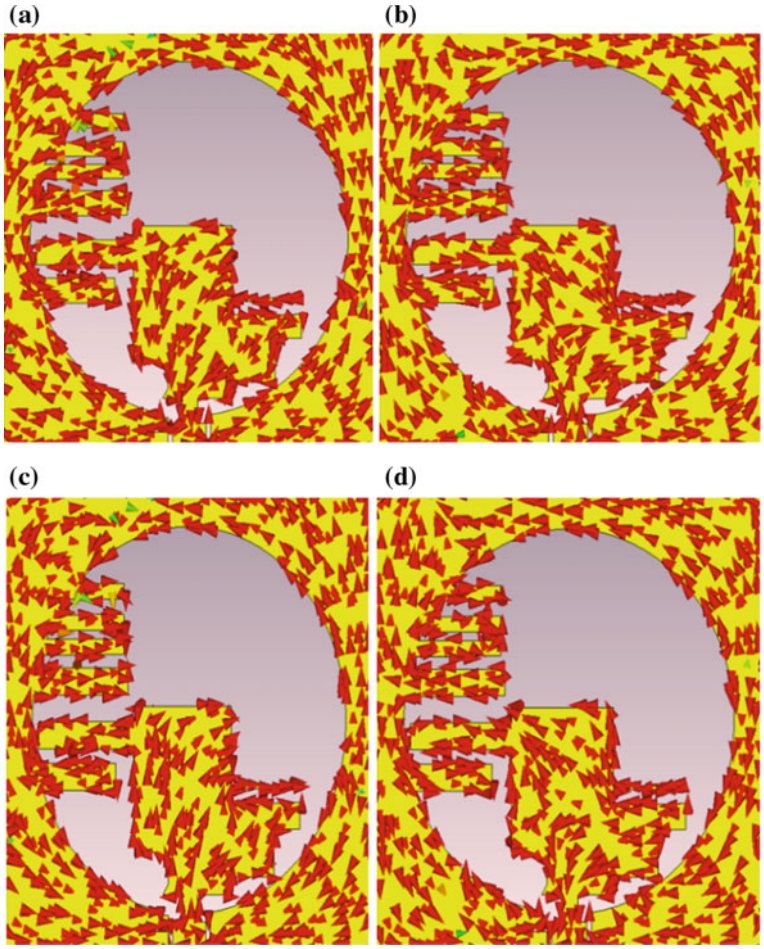

Fig. 5 Surface current density distribution at 3.1 GHz **a** t = 0, **b** t = T/4, **c** t = T/2, **d** t = 3T/4

with their sense of rotation in the azimuthal plane with +z axis being considered as the direction of propogation. A clockwise rotation shows LHCP nature while anti-clockwise rotation depicting RHCP nature. From the plotted current distribution at various time instants in Fig. 5, we observe that current vector follows anti-clockwise rotation with +z axis being considered as the direction of propagation which results in RHCP nature of polarization. So the direction of rotation of current vector along with axial ratio less than 3 dB confirms circular polarized behavior of antenna for a frequency range 2.33–3.90 GHz. Axial ratio in the upper band is quite high and also the current vector just oscillates about its position between 0 and 180° thereby confirming the linear polarized behavior in the upper band.

4 Result and Discussion

The proposed antenna is designed and simulated on CST Microwave Studio. The simulated farfield parameters of the proposed antenna are optimized for acceptable values. Figure 6 shows the simulated S_{11} (dB) of the proposed antenna which remains below −10 dB for a frequency range extending from 2.3 to 3.90 GHz and 5.4–6.3 GHz.

The overlapping frequency for lower resonating band resides between 2.33 and 3.90 GHz, i.e., $S_{11} < -10$ dB and axial ratio less than 3 dB. Hence, the circular polarized nature of the proposed antenna is observed for this overlapping frequency band (Fig. 7).

Maximum achievable gain of the proposed antenna is 4.27 dBi and is depicted in Fig. 8. Normalized LHCP and RHCP radiation pattern of the proposed antenna at

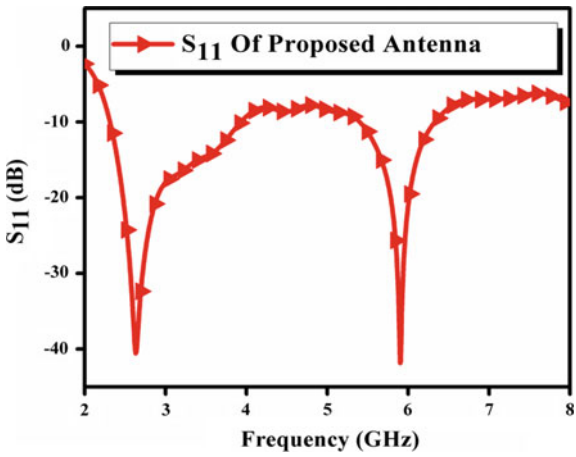

Fig. 6 Simulated S-parameter of proposed antenna

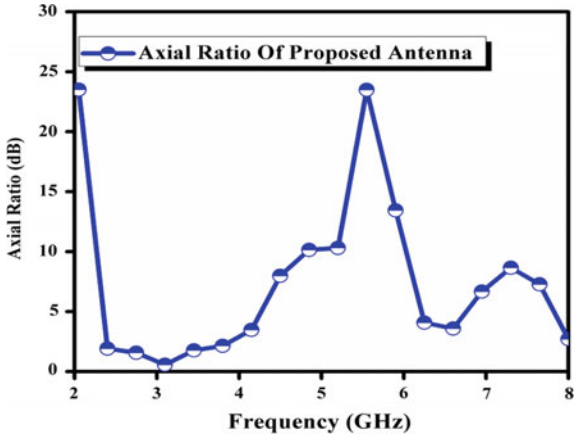

Fig. 7 Simulated axial ratio of proposed antenna

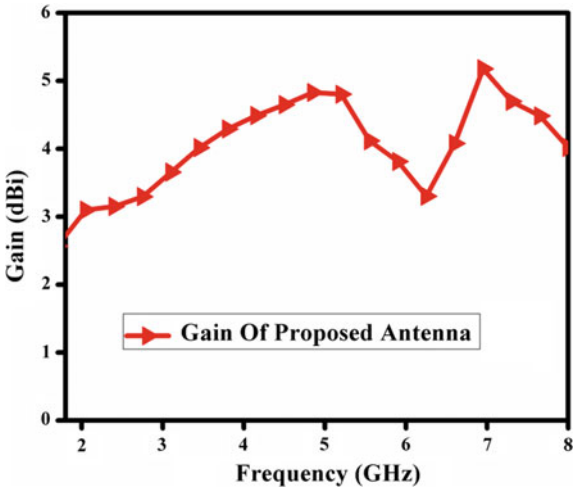

Fig. 8 Gain of proposed antenna

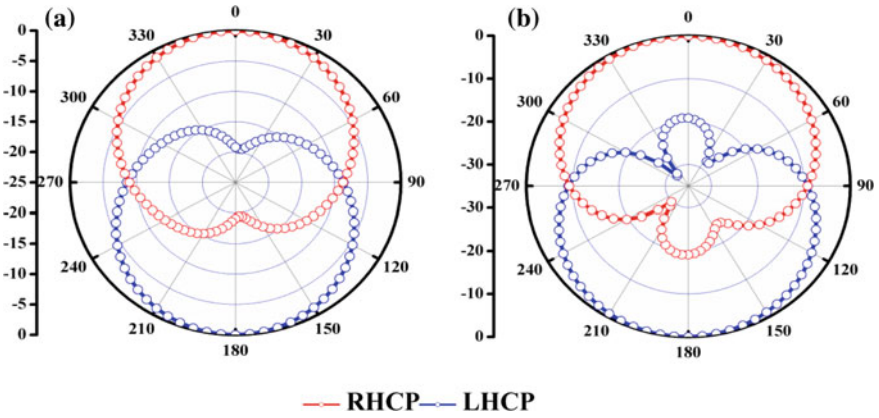

Fig. 9 Normalized LHCP and RHCP radiation patterns of proposed antenna **a** at 3.1 GHz at *xz*-plane, **b** at 3.1 GHz at *yz*-plane

3.1 GHz in both XZ and YZ plane with considering +z direction as the boresight of antenna is shown in Fig. 9 which confirms the RHCP nature of the antenna. The lower resonating band is circularly polarized while the upper band is linearly polarized with both bands resonating at two different frequency. The basic challenge in designing of the proposed antenna was that the impedance bandwidth must entirely enclose the axial ratio bandwidth which means axial ratio must be less than 3 dB for resonant frequencies for which S_{11} is less than −10 dB which is called as overlap bandwidth.

5 Conclusion

A dual band dual polarized planar slot antenna is presented in this paper using coplanar waveguide feed technique. The proposed antenna consists of circular slot in the ground plane and an asymmetric radiating patch directly connected to the feed acting as a primary radiator. Numbers of rectangular conducting slits are embedded in the ground plane and are perturbed into the circular slot to achieve circular polarized characteristics. A circular notch is created in the radiating patch to introduce dual polarization characteristics. The proposed antenna has a quite simplified geometry with same antenna exhibiting both linear polarized and circular polarized characteristics for different resonating bands and it covers Bluetooth and WLAN band. The proposed antenna is a dual band antenna with lower band is right-handed circularly polarized and the upper band is linear polarized.

References

1. Moghadasi, M., Sadeghzadeh, R., Asadpor, L., et al.: A small dual-band CPW-fed monopole antenna for GSM and WLAN applications. IEEE Antennas Wirel. Propag. Lett. **12**, 508–511 (2013)
2. Liu, Q., Shen, J., Liu, H., et al.: Dual-band circularly-polarized unidirectional patch antenna for RFID reader applications. IEEE Trans. Antennas Propag. **62**(12), 6428–6434 (2014)
3. Falade, P., Gao, Y., Chen, X., et al.: Stacked-patch dual-polarized antenna for triple-band handheld terminals. IEEE Antennas Wirel. Propag. Lett. **12**, 202–205 (2013)
4. Bao, X.L., Ammann, M.J.: Wideband dual-frequency dual-polarized dipole like antenna. IEEE Antennas Wirel. Propag. Lett. **10**, 831–834 (2011)
5. Mathew, S., Anitha, R., Deepak, U., et al.: A compact tri-band dual-polarized corner-truncated sectoral patch antenna. IEEE Trans. Antennas Propag. **63**(12), 5842–5845 (2015)
6. Pourahmadazar, J., Ghobadi, C., Nourinia, J., Felegari, N., Shirzad, H.: Broadband CPW-fed circularly polarized square slot antenna with inverted-L strips for UWB applications. Antennas Wirel. Propag. Lett. IEEE. **10**, 369–372 (2011)
7. Sim, C.Y.D., Chen, H.D., Zuo, L., Chen, T.A.: CPW-fed sqaure ring slot antenna with circular polarization radiation for WiMAX/WLAN applications. Microw. Opt. Technol. Lett. **57**, 886–891
8. Edwards, T.C., Steer, M.B.: Foundation of Interconnect and Microstrip Design, 3rd edn. Wiley, New York (2000)
9. Zhang, L., Jiao, Y., Chen, B., Weng, Z.: CPW-fed broadband circularly polarized monopole antenna with improved ground-plane structure. IEEE Trans. Antennas Propag. **61**(9), 4824–4828 (2013)

Broadband Circularly Polarized Planar Slot Antenna for Bluetooth/WiMAX Application

Vikash Kumar, Mohammad Imroz Khan, Avinash Chandra and Sushrut Das

Abstract A wideband circular polarized slot antenna using coplanar waveguide feed (CPW) technique is presented in this work. A rectangular slot is created in the ground plane and an asymmetric patch residing in the rectangular slot is fed by central signal strip. The rectangular slot is perturbed by a conducting stub embedded in the ground. Ground is further modified by etching a few rectangular slots in it aiming at broadband circular polarized behavior. A grounded metallic arm of L-shape is incorporated in the structure which improves the axial ratio bandwidth of the proposed antenna. The proposed antenna provides an overlap band, i.e., S_{11} <−10 dB and axial ratio<3 dB from 1.83 to 3.37 GHz which provides a large axial ratio bandwidth of greater than 1.5 GHz for which antenna exhibits circularly polarized behavior thereby covering Bluetooth and WiMAX usable bands.

Keywords Coplanar waveguide · Wideband · Circular polarized

V. Kumar (✉) · S. Das
Department of Electronics Engineering, Indian Institute of Technology (Indian School of Mines) Dhanbad, Dhanbad, India
e-mail: Vikash988@gmail.com

S. Das
e-mail: sushrut_das@yahoo.com

M. I. Khan
Department of Electronics and Communication Engineering, Vignan's Foundation for Science, Technology and Research, Guntur, India
e-mail: iitdhanbad.imroz@gmail.com

A. Chandra
School of Electronics Engineering, Vellore Institute of Technology, Vellore, India
e-mail: avinashchandra888@gmail.com

U. Biswas et al. (eds.), *Advances in Computer, Communication and Control*, Lecture Notes in Networks and Systems 41, https://doi.org/10.1007/978-981-13-3122-0_11

1 Introduction

The increasing demand for wireless and high-speed communication has triggered the requirement of wideband circular polarized planar antennas with low profile, easy integration with microwave-integrated circuits and reduced losses. Circular polarized antennas are less affected by polarization mismatch loss, multipath fading, adverse weather conditions, Faraday rotation, and reflections. In [1], circular polarized behavior is studied by introducing multiple feeds, in [2] circular polarization is achieved by using notch slots and ground feed, in [3] rectangular slot contains a parasitic element which is energized by an L-shaped feed line in order to produce wideband circular polarization. In [4], instead of a wide rectangular slot, step-shaped slot has been used for obtaining wideband circular polarization by controlling the impedance of slot. In [5] rectangular slot with grounded metallic ring is implemented to increase the 3 dB axial ratio bandwidth. Lightning-shaped feed line proposes a new option for gradual variation in slot impedance, resulting in wide impedance bandwidth.

2 Antenna Configuration

Figure 1 shows the top view of proposed coplanar waveguide antenna along with its geometrical dimensions (mm) illustrated in Table 1. An asymmetric slot is incorporated in the ground plane in place of conventional rectangular slot and is energized by a 50 Ω feed line having width of 3.2 mm and a distance of 0.4 mm from the ground plane. FR4 epoxy is used as a substrate of height = 1.6 mm, $\varepsilon_r = 4.4$, having loss tangent = 0.02 is used to model the antenna. Grounded stubs are protruded into the slot for obtaining broadband circular polarization performance.

Table 1 Antennal dimensions (mm)

a	b	c	d	e	f	h	i	j	k
4.4	1.2	6.4	8.7	9.2	3.2	1.6	9.2	14.6	7.6
l	m	n	o	p	q	r	s	t	u
35	2.1	6.6	1.43	2	2	15	5.7	3.7	2.7
v	w								
3.1	35								

Fig. 1 Schematic view of antenna

3 CP Mechanism

Magnetic current vector distribution for circular polarized frequency band at 3.3 GHz is depicted in Fig. 5. Path of rotation traced by current vector in azimuthal plane with advancing time is studied. Considering +z axis as direction of propagation, the dominant current vector follows anti-clockwise sense of rotation. Hence conforming right-handed circular polarized behavior. Sense of rotation followed by dominant current vector along with axial ratio less than 3 dB confirms the circular polarized nature of antenna. Surface current density is illustrated in Fig. 6 depicting the regions responsible for dominant CP radiation. So direction of rotation of current vector along with axial ratio less than 3 dB confirms circular polarized behavior of antenna for a frequency range of 1.83–3.37 GHz (Fig. 2).

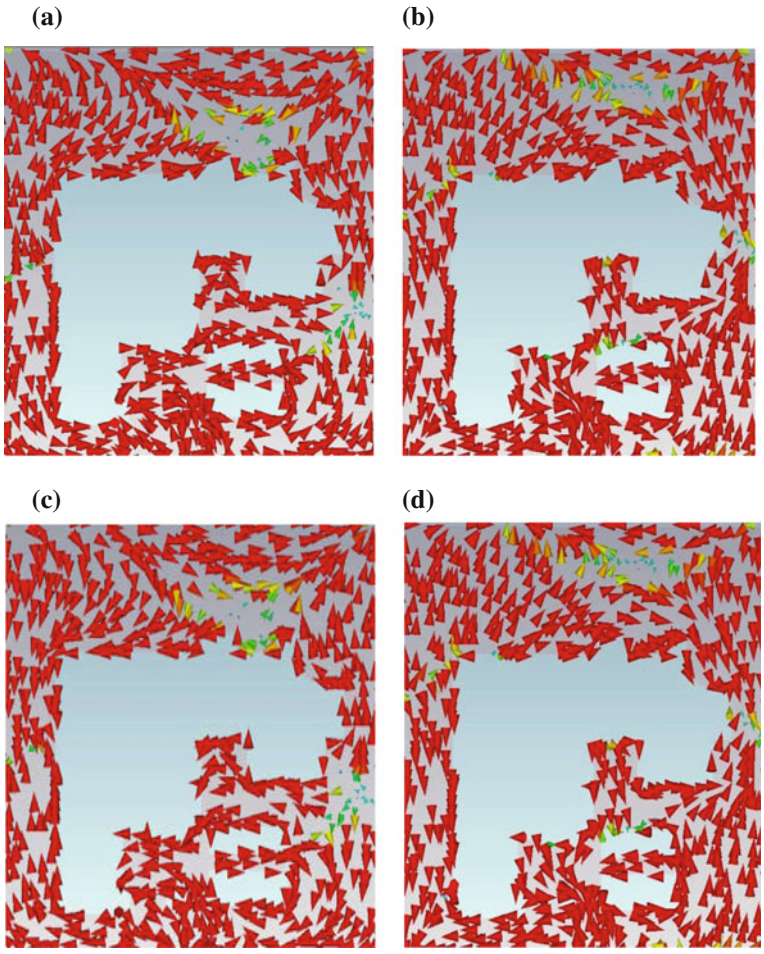

Fig. 2 Magnetic current vector distribution at 3.1 GHz **a** t = 0 **b** t = T/4 **c** t = T/2 **d** t = 3T/4

4 Result and Discussion

S_{11} for the antenna is depicted in Fig. 3 which confirms that the antenna resonates for a frequency range extending from 1.70 to 4.46 GHz. A positive gain is observed for the resonating band as Fig. 4 illustrates an average gain of 3 dBi for the antenna. Circular polarization (CP) performance for the antenna is depicted in Fig. 5 by axial ratio. Figure 5 confirms the wideband circular polarized nature as the axial ratio is less than 3 dB along with return loss less than −10 dB for frequency range extending from 1.83 to 3.37 GHz. Normalized radiation pattern is plotted in Fig. 6 which confirms RHCP nature of antenna.

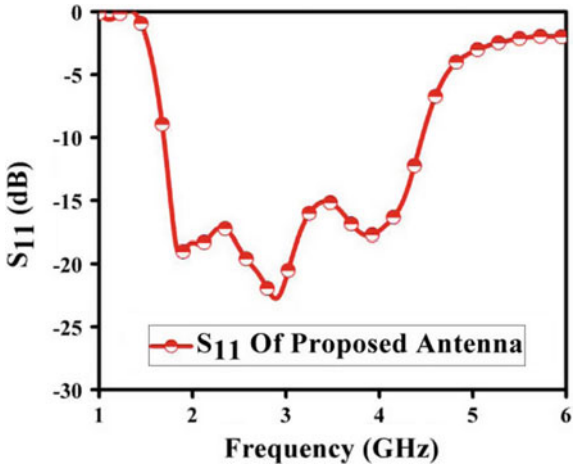

Fig. 3 Return loss for antenna

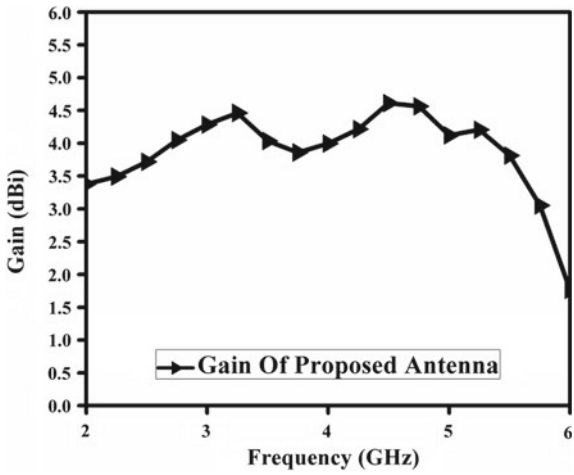

Fig. 4 Gain for antenna

5 Conclusion

A broadband band circular polarized coplanar waveguide antenna has been presented in this letter. Use of asymmetric patch and grounded L-shaped arm for generation of circular polarization is studied in this work. Antenna miniaturization is achieved by incorporating asymmetric slot which replaces the conventional rectangular slot. CP performance for the antenna is precisely controlled by grounded arm which is protruded into the slot. Circular polarization is achieved for a wide range of frequency and the antenna can be applied for Bluetooth and WiMAX applications.

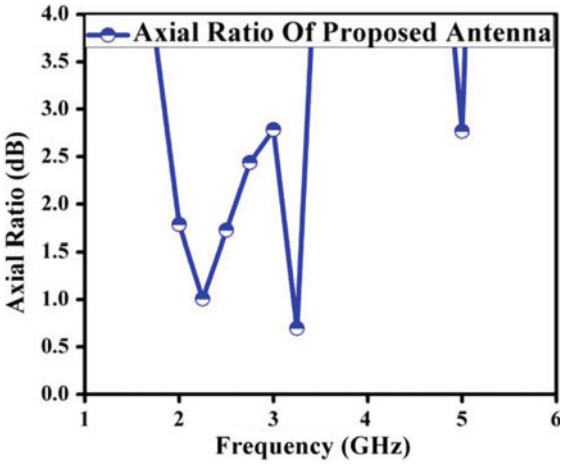

Fig. 5 CP performance for antenna

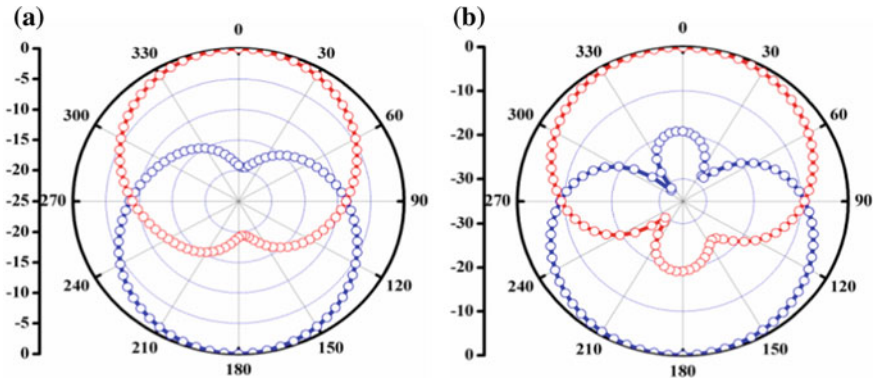

Fig. 6 Normalized radiation pattern at 3.1 GHz at *xz*-plane and *yz*-plane

References

1. Hu, Y.-J., Ding, W.-P., Ni, W.-M., Cao, W.-Q.: Broadband circularly polarized cavity-backed slot antenna array with four linearly polarized disks located in a single circular slot. IEEE Antennas Wirel. Propag. Lett. **11**, 496–499 (2012)
2. Ren, H., Yu, Y., Shen, Z.: Broadband circularly-polarized antenna consisting of four notch slot radiators. Electron. Lett. **48**(23), 1447–1449 (2012)
3. Saini, R.K., Dwari, S.: CPW-fed broadband circularly polarized rectangular slot antenna with L-shaped feed line and parasitic elements. Microw. Opt. Technol. Lett. **57**, 1788–1794 (2015). https://doi.org/10.1002/mop.29188

4. Jiang, L., Gong, S., Hong, T., Jiang, W.: Broadband CPW-FED slot antenna with circular polarization. Microw. Opt. Technol. Lett. **52**, 2111–2114. https://doi.org/10.1002/mop.25363
5. Sze, J.-Y., Hsu, C.-I.G., Chen, Z.-W., Chang, C.-C.: Broadband CPW-fed circularly polarized square slot antenna with lightening-shaped feedline and inverted-L grounded strips. IEEE Trans. Antennas Propag. **58**(3), 973–977
6. Jan, J.-Y., Pan, C.-Y., Chiu, K.-Y., Chen, H.-M.: Broadband CPW-fed circularly polarized slot antenna with an open slot. IEEE Trans. Antennas Propag. **61**(3), 1418–1422

Study and Scope of Signcryption for Cloud Data Access Control

Somen Debnath, Morrel V. L. Nunsanga and Bubu Bhuyan

Abstract As cloud storage service provides convenience, high computation and a capable service from local to remote server through the internet; it attracts the user to outsource data from remote cloud server. Storing and outsourcing of sensitive data directly to multi-tenant cloud is unsafe and it also raises the privacy and security issues. Ciphertext Policy-Attribute Based Encryption (CP-ABE) with attribute based signature (ABS) provides confidentiality and anonymous authentication for such environment and called Attribute Based Syncryption(ABSC). This technique can acquire security and privacy together, which might be more suitable for cloud data outsourcing. This paper delivers a widespread survey on attribute-based signcryption schemes to finding out the suitability and requirements for access control of outsourced cloud data and identify the research gap. Moreover, we compare the existing scheme's functionality and characteristic to analyses efficiency and performance of recent attribute-based signcryption to fulfill outsourcing properties.

Keywords Access control · Data outsourcing · Security · Privacy
Attribute-based signcryption

1 Introduction

Data outsourcing is important feature of cloud computing, where we can store our data including sensitive (like, health, social, financial etc.) to reduce the burden of maintenance and local storage in reliable way. This is economically attractive process of cloud environment, which reduce complexity and cost of long-term as well as large-scale data storage but does not provide assurance on data security and

S. Debnath (✉) · M. V. L. Nunsanga
Department of Information Technology, Mizoram University, Aizawl 796004, India
e-mail: somen@mzu.edu.in

B. Bhuyan
Department of Information Technology, North Eastrn Hill University, Shillong, Meghalaya, India

U. Biswas et al. (eds.), *Advances in Computer, Communication and Control*, Lecture Notes in Networks and Systems 41, https://doi.org/10.1007/978-981-13-3122-0_12

privacy [2]. The privacy of data is also most considerable issue because of sensitive data must be protected from unauthorized access. The user need to authenticate them self before starting any transaction and also need to ensure that the cloud server does not modify any data which is outsourcing. The user identity needs to hide from cloud server and also from un-authorized users.

Recently, a lot of researches are going to explore the possibility of data access control to protect the stored data in cloud [11, 14]. The primarily focus of researchers are empowering of data owner by securely handle of data among users. To overcome these problems, it is very important to have an efficient cryptographic mechanism, which can provide fine-grained data access control including authenticity,confidentiality and user privacy at the same time. A promising and feasible solution might be possible by using Attribute-Based Signcryption (ABSC) [3, 4, 9, 13], which is a logical combination of Attribute-Based Signature (ABS) [8] and Attribute-Based Encryption (ABE) [6]. ABE has been planned as a cryptographic technique on encrypted data with the provision of fine-grained access control. ABS has been developed as a privilege way, where the signing of message can be done without disclosing the signers identity. In another words, Signer privacy by ABS does not leak any information about the signers credentials except that the user whose satisfies the access structure created at the time of signature. However, a signcryption mechanism has public verifiability system, which allows to check without knowing of the underlying secret keys of encrypted data and also the plaintext.

The concept of signcryption introduced around three decade ago by Zheng [15] but the idea is extended by the context of attribute based encryption in 2010 by [4]. Gagne et al. [4] initiated first a formal study of attribute based signcryption scheme with threshold policies. They used Fuzzy identity based encryption for encryption and threshold ABS for signature scheme and also shown secure under selective predicate model. Later Emura et al. [3] explained a dynamic attribute based signcryption with monotone access structure policy for sender and AND-gate wildcard for receiver and secured under selective model. Both the model ware not supports signer privacy and unforgeability. Wang et al. [12] discuss an scheme in signcryption-policy form by using monotone access tree. The functionality of confidentiality and unforgeability were proven in adaptive-predicates models for this scheme. The unforgeability was proven by random oracle model and confidentiality was proven by generic group model where unsigncrypt mechanism is inaccessible to the adversary.

A combined public-key scheme(signing and encryption) with attribute based setup proposed by Chen et al. [1] followed by the scheme of Water's [6] CP-ABE scheme and maji's [8] ABS scheme to construct identical public parameters and key distribution. Chen et al. [1] used selectively security model (against attack) in their combined scheme. Security assumption for this scheme is monotone span program for both signer and receiver policy. In this scheme, the authors proved public verifiability and signer privacy as well as confidentiality and unforgeability under selective-predicate models. Wei et al. [13] proposed traceable attribute-based signcryption. They assume as security parameters decisional BDHE and computational DHE. It is provides confidentiality, unforgeability and non-flammability under selectively predicate models. Signer privacy was not maintained by the scheme. In 2014, Rao et al. [10] shown a

attributed based signcryption based on key policy based and it is also maintain the constant cipher text encryption. The policy used here monotone spam programs for both sender and receiver policy structure. This scheme maintained signer privacy, confidentiality and also unforgeability which were proven by selective-predicate models. Pandit et al. [9] construct an attribute based signcryption which is support confidentiality, signer privacy, strong unforgeability and it is selectively secured in adaptive predicate model.

Recently, Liu et al. [7] constructed a CP-ABSC scheme, which was based on Water's [6] CP-ABE scheme and Maji's [8] ABS scheme. They had claimed their method satisfy the confidentiality properties against indistinguishability of ciphertexts under adaptive chosen ciphertext attack and selective encryption predicate. This construction has not follows the standard signcryption methods such as Sign-then-Encrypt (StE), Encrypt-then-Sign(EtS) and logical mixture of signing and encryption techniques. It is not supported public verifiability.

In Table 1, we have shown the comparison of various ABSC scheme based on functionality and characteristics. The characteristics of the schemes, we consider here are security assumption or the hard problem based on which the schemes implemented, encryption policy structure, signing policy structure, policy type like key based policy(KP), ciphertext policy(CP), signcryption-policy etc., signer privacy, public verifiability, security proof like confidentiality, Unforgeability.

Our contributions in this paper are:

- We survey various attributed based signcryption(ABSC) based on functionality and characteristics for third party un-trusted cloud and distributed environment.
- We analyze the scope and significance of attributed based signcryption with its detail variations for access control of cloud outsourced data.
- We present here the performance of existing attribute based signcryption based on the size of signing key, encryption key, cipher text and also signcrypt and unsigncrypt on basis of computation cost.
- We find here the challenges and open issues of ABSC based access control for outsourced cloud data and to provide future direction. According to our knowledge, this is the first effort that discusses about ABSC for access control of outsourced cloud data.

The remaining part of this paper is structured as follows. We explained Preliminaries and signcryption schemes in Sect. 2 and Sect. 3 respectively. Sections 4 and 5 presented about the detail of Performance analysis and open issues respectively. Last section gives conclusion.

Table 1 Comparison of functionality of different ABSC schemes

Functionality	Gagne et al. [4]	Emura et al. [3]	Chen et al. [1]	Wei et al. [13]	Pandit et al. [9]	Liu et al. [7]	Rao et al. [10]
Security assumptions	d(Hm)BDHE	dBDHE, c(h)DHE	n-BDHE, cDHE	dBDHE, cDHE	Decisional SubGroup	dBDHE Generic group	dBDHE, cDHE
Policy type	KP	CP	SCP	KP	SCP	CP	CP
Encryption	Threshold policy	AND-gate policy	MSP	Threshold policy	MSP	MSP	MSP
Signing	Threshold policy	Monotone tree	MSP	Threshold policy	MSP	MSP	MSP
Anonymous authentication	Yes	No	Yes	No	Yes	Yes	Yes
Public verifiability	No	Yes	Yes	No	Yes	No	Yes
Confidentiality	IND-CCA	IND-CCA	IND-CPA	IND-CPA	IND-CCA	IND-CPA	IND-CCA
Unforgeability	EUF-CPA	sEUF-CPA	EUF-CPA	EUF-CPA	sUF-CPA	EUF-CPA	EUF-CPA

The abbreviations d(Hm)BDHE = decisional (hashed modified) bilinear Diffie-Hellman Exponent, c(m)DHE = computational (modified) Diffie-Hellman Exponent, MSP = monotone spam program, (s)EUF-CPA = (strongly) existential un-forgeability under chosen plaintext attack, SCP = signcryption-policy, IND-CC(P)A = indistinguishability of ciphertexts under chosen ciphertext (plaintext) attack. All schemes are selectively secure in this table

2 Background

2.1 Notations

Let [n] be the set $\{1, 2, \ldots, n\}$ of positive integer $n \in \mathbb{N}$, $\{X_i\}_{i\in[n]}$ be the sequence of elements $X_1, X_2, \ldots, X_n$. ($x \xleftarrow{R} X$) defined as a variable x which picked uniformly at random from X, and $\mathcal{U}$ denoted as attribute universe. $\mathbb{Z}_p^{l\times n}$ denoted as set of matrices of $l \times n$ size with elements in $\mathbb{Z}_p$ and $\mathbf{M}_i$ indicates ith row of the LSSS matrix $\mathbf{M}$.

2.2 Bilinear Pairings

Definition 1 Let $\mathbb{G}$ and $\mathbb{G}_T$ are multiplicative cyclic groups and their prime order is q. A bilinear pairing $e : \mathbb{G} \times \mathbb{G} \to \mathbb{G}_T$ fulfills the following properties:

1. $e(u^m, v^n) = e(u, v)^{mn}$; $u, v \in \mathbb{G}$ and $m, n \in \mathbb{Z}_q, \mathbb{Z}_q = \{0, 1, 2, \ldots, q-1\}$;
2. Non-degenerate: $e(g_1, g_2) \neq 1$, g_1 and g_2 are generator of $\mathbb{G}$;
3. Computable: Efficient procedure to compute $e(g_1, g_2), \forall(g_1, g_2) \in \mathbb{G} \times \mathbb{G}$.

We represent the bilinear parameter shortly as $\Sigma := (q, \mathbb{G}, \mathbb{G}_T, e)$ for friendly handling inside this paper.

2.3 Complexity Assumptions

We define here Bilinear Diffie-Hellman Exponent(BDHE) problem with variation.

Definition 2 (Computational BDHE Assumption [10]): If we consider bilinear pairing parameters as $\Sigma := (p, \mathbb{G}, \mathbb{G}_T, e)$ and $(g, g^x, g^{x^2}, g^y) \in \mathbb{G}$ as inputs, then the cBDHE problem is to compute g^{xy},where $x, y \in \mathbb{Z}_q^*$. We can say that the cBDHE problem in $\mathbb{G}$ is (t, ϵ)-hard, if for all probabilistic polynomial-time (PPT) algorithm at most time t, an advantage, ϵ where $Pr[\mathcal{B}(\Sigma, g, g^x, g^{x^2}, g^y) = g^{xy}] \geq \epsilon$ is negligible.

Definition 3 (Decisional BDHE Assumption [4]): Denoting the bilinear pairing parameters as $\Sigma := (p, \mathbb{G}, \mathbb{G}_T, e)$ and considering the distributions $(g, g^x, g^y, g^z, S) \in \mathbb{G}^4 \times \mathbb{G}_T$ as inputs, then the dBDHE problem is to decide $Z = e(g, g)^{xyz}$ or not, where $x, y, z \in_R \mathbb{Z}_q^*$. We can say that the dBDHE problem in $\mathbb{G}$ is (t, ϵ)-hard, if for all PPT algorithm at most time t, an advantage, ϵ where $Adv_{DBDH}(\mathcal{B})$: $Pr[\mathcal{B}(\Sigma, g, g^x, g^y, g^z, e(g, g)^{xyz}) = 0] - Pr[\mathcal{B}(\Sigma, g, g^x, g^y, g^z, e(g, g)^S) = 0] \geq \epsilon$ and $e(g, g)^S \in \mathbb{G}_T \setminus \{e(g, g)^{xyz}\}$, is negligible.

Definition 4 (Decisional SubGroup Assumptions [9]): Consider composite order bilinear pairing parameter $\Sigma' := (N = p_1p_2p_3, \mathbb{G}, \mathbb{G}_T, e)$. Decisional SubGroup Assumptions(DSG)

DSG1: Let $g \xleftarrow{R} \mathbb{G}_{p_1}$; $Z_3 \xleftarrow{R} \mathbb{G}_{p_3}$; $T_0 \xleftarrow{R} \mathbb{G}_{p_1}$; $T_1 \xleftarrow{R} \mathbb{G}_{p_1 p_2}$. Define $D := (\Sigma', g, Z_3)$.
DSG2: Let $g, Z_1 \xleftarrow{R} \mathbb{G}_{p_1}$; $Z_2, W_2 \xleftarrow{R} \mathbb{G}_{p_2}$; $W_3, Z_3 \xleftarrow{R} \mathbb{G}_{p_3}$; $T_0 \xleftarrow{R} \mathbb{G}_{p_1 p_3}$; $T_1 \xleftarrow{R} \mathbb{G}$. Define $D := (\Sigma', g, Z_1 Z_2, W_2, W_3, Z_3)$.

In breaking DSGi, for $i = 1, 2$, advantage of an algorithm $\mathcal{B}$ is defined by

$$Adv_{DSGi}(\epsilon) = Pr[\mathcal{B}(D, T_0) = 1] - Pr[\mathcal{B}(D, T_1) = 1].$$

We say that the DSGi problem in Σ' is ϵ-hard, if for every PPT algorithm $\mathcal{B}$, the advantage $Adv_{DSGi}(\epsilon)$ is negligible.

2.4 Access Structures

Definition 5 (Access Structures [4]): Let $\mathcal{U}$ be the universe of attribute. A collection $\mathbb{M}$ of non-empty sets of attributes, i.e. $\mathbb{M} \subseteq 2^{\mathcal{U}} \setminus \{\}$ define as an access structure on $\mathcal{U}$. The sets in $\mathbb{M}$ are called the authorized sets and the sets not in $\mathbb{M}$ are called the unauthorized sets.
Additionally, an access structure $\mathbb{M}$, if $\forall X, Y \in \mathbb{M}$: if $X \in \mathbb{M}$ and $X \subseteq Y$, then $Y \in \mathbb{M}$ is called monotone access structure.

2.5 Linear Secret-Sharing Scheme [5]

Definition 6 Let $\mathcal{U}$ be the universe of attribute. For the access structure $\mathbb{M}$, a secret-sharing scheme $\Pi_{\mathbb{M}}$ over $\mathcal{U}$ is called linear (in $\mathbb{Z}_p$) if $\Pi_{\mathbb{M}}$ fulfills the following two polynomial time algorithms, where A, a share-generating matrix for $\Pi_{\mathbb{M}}$ of size $l \times n$ and row labeling function,$\rho : [l] \to I_{\mathcal{U}}$ maps each row of the matrix A to an attribute in $\mathbb{M}$, and also $I_{\mathcal{U}}$ is the index set of $\mathcal{U}$.
Distribute(M, ρ, ϕ). It takes as input, a secret $\phi \in \mathbb{Z}_p$ which is to be shared, row labeling function ρ and the share-generating matrix A. It selects $s_2, s_3, \ldots, s_n \in_R \mathbb{Z}_p$ and sets $\mathbf{v} = (\phi, s_2, s_3, \ldots, s_k) \in \mathbb{Z}_p^n$. It generate a set $\{\mathbf{A}_i \cdot \mathbf{v} : i \in [l]\}$ of l shares, where $\{\mathbf{M}_i \in \mathbb{Z}_p^n\}$ is the ith row of the matrix A. The share $\lambda_{\rho(i)} = \mathbf{A}_i \cdot \mathbf{v}$ belongs to an attribute $\rho(i)$.
Reconstruct$(A, \rho, Attr)$). It takes as input (A, ρ) and a set of attributes $Attr \in \mathbb{M}$. Let $I = i \in [l] : \rho(i) \in I_{Attr}$, where I_{Attr} denotes the index set of the attribute set $Attr$. It returns a set $\omega_i : i \in I$ of secret reconstruction constants such that $\Sigma_{i \in I} \omega_i \lambda_{\rho(i)} = \phi$, if $\{\lambda_{\rho(i)} : i \in I\}$ is a valid set of shares of the secret ϕ as per $\Pi_{\mathbb{M}}$.

The objective vector $(1, 0, ..., 0)$, which is categorized the access structures i.e., a set $Attr \in \mathbb{M}$ are indexed by each row of A where vector $(1, 0, \ldots, 0)$ is the linear span of matrix A.

2.6 Algorithms

Attribute-based signcryption scheme has following algorithm: Setup, sExtract, dExtract, Signcrypt and Designcrypt. An Attribute-Based Signcryption (ABSC) scheme, $\prod_{ABSC}$ briefly as

$$\prod_{ABSC} := \begin{bmatrix} (\mathcal{PP}, \mathcal{MK}) & \leftarrow Setup(1^k) \\ SK_{A_s} & \leftarrow sExtract(\mathcal{PP}, \mathcal{MK}, A_d), \\ SK_{A_d} & \leftarrow dExtract(\mathcal{PP}, \mathcal{MK}, A_s) \\ CT_{\Upsilon_e} & \leftarrow Signcryption(\mathcal{PP}, m, SK_{A_s}, \Upsilon_s, \Upsilon_e), \\ m \text{ or } \perp & = Designcryption(\mathcal{PP}, CT_{\Upsilon_e}, \Upsilon_s, SK_{A_d}) \end{bmatrix}$$

Definition 7 We can say that the $\prod_{ABSC}$ (ABSC scheme) is correct if for all attribute sets A_s and A_d, all claim-predicates Υ_s and Υ_e and all $m \in M$, such that $\Upsilon_e(A_d) = 1 = \Upsilon_s(A_s)$, all $(\mathcal{PP}, \mathcal{MK}) \leftarrow Setup(1)$, all decryption keys $SK_{A_d} \leftarrow dExtract(\mathcal{PP}, \mathcal{MK}, A_d)$, all signing keys $SK_{A_s} \leftarrow sExtract(\mathcal{PP}, \mathcal{MK}, A_s)$, all signcryptions $CT_{\Upsilon_e} \leftarrow Signcryption(\mathcal{PP}, m, SK_{A_s}, \Upsilon_s, \Upsilon_e)$, it is always true that Designcryption $(\mathcal{PP}, CT_{\Upsilon_e}, \Upsilon_s, SK_{A_d}) = m$.

3 Signcryption Schemes

3.1 Threshold Attribute-Based Signcryption [4]

Assumption: hashed modified d(Hm)BDHE problem

Setup: The master secret $\mathcal{MK}$ is $s \overset{R}{\leftarrow} \mathbb{Z}_p^*$. The public parameter

$$\mathcal{PP} = (g, h, g_1, t_1, \ldots, t_{n+1}, u_1, \ldots, u_{n_m}, \acute{u}, MAC, H, H_1, H_2, Y)$$

where n is the size of attribute set and n_m denoted the message size and g, h, $g_1, t_1, \ldots, t_{n+1}$, $Y = \hat{e}(g, g_1)^s$, $u', u_1, \ldots, u_{n_m} \in_R \mathbb{G}$, $H_1 : \{0,1\}^* \rightarrow \mathbb{Z}_p^*$ $H_2 : \{0,1\}^{2n_m} \rightarrow \{0,1\}^{n_m}$, $H : \mathbb{G}_T \rightarrow \{0,1\}^{n_m} \times Z_q^*$.

sExtract: (ω_s, d): The secret key with the set of signature attributes ω_s is

$$SK_{A_s} = \{D_{s,1_i} = g_1^{f(i)} \cdot T(i)^{r_i}, D_{s,2_i} = g^{r_i}\}_{i \in \omega_s}$$

where $r_i \in_R \mathbb{Z}_q^*$ and $f(0) = s$ and threshold d.

dExtract: (ω_d, d): The secret key with the set of encryption attributes ω_d is

$$SK_{A_d} = \{D_{d,1_i} = g_1^{f(i)} \cdot T(i)^{r_i}, D_{d,2_i} = g^{r_i}, D_{d,3_i} = g^{r_i}\}_{i \in \omega_d}$$

where $r_i \in_R \mathbb{Z}_q^*$ and $f(0) = s$, and threshold, d

Signcryption: $(\mathcal{PP}, M, \omega_d, \omega_s, SK_{A_s}, |\omega_s|)$: Here, $\omega_d(\omega_s)$ is a set of encryption (signature) attributes, and SK_{A_s} is Signature Key. Choosing $r, r' \in_R \mathbb{Z}_q^*$ and considered $t = H_1(g^r)$ then compute $(h_1, h_2, h_3) = H(Y^r)$ and

$$Z = g^{h_2} \cdot W(H_2(M||h_1)^{r'} \cdot \prod_{i \in \omega_s} (D_{d,1_i})^{\nabla_{i,\omega_s}(0)}.$$

where$\nabla_{i,N}(x) = \prod_{j \neq i, i \in N} \frac{x-j}{i-j}$ is the Lagrange coefficient and then
The signcryption of M is:

$$CT = (\omega_d, \omega_s, g_r, \{(T(i)h^t)^r\}_{i \in \omega_d}, M \oplus h_1, Z, \{(D_{s,2_i})^{\nabla_{i,\omega_s}(0)}\}_{i \in \omega_s}, g^{r'}, tag),$$

where tag is the MAC of all preceding elements in the ciphertext under key h_3

Designcryption: $(\mathcal{PP}, CT, SK_{A_d})$: Here $SK_{u,\omega_m u,d}$ is unsigncryption Key. It choose a subset $S \subset (\omega_\mu \cap \omega_d)$ containing d subset, and compute the following: $t = H_1(g_r)$., $Y' = \prod_{i \in S} (\frac{e((D_{1_i} D_{3_i}^t), g_r)}{e(D_{2_i}, \{(T(i)h^t)^r\}_{i \in \omega_d})})$, $(h_1, h_2, h_3) = H(Y')$ and $Z' = Z \cdot g^{-h-2}$. After that, it test

$$e(g, Z') = Y \cdot e(g^{r'}, W(H_2((M \oplus h_1 \oplus h_1)||h_1)) \cdot \prod_{i \in \omega_s} e(\{(D_{s,2_i})^{\nabla_{i,\omega_s}(0)}\}_{i \in \omega_s}, T(i)).$$

If it holds, and tag is equal to the MAC of all preceding elements in the ciphertext under key h_3, output $M \oplus h_1$, otherwise, output $\perp$.

3.2 Combined Public-Key Scheme(ABE&ABS)[1]

Assumption: n-BDHE, cDHE problem

Setup: It generate master key and public parameters as

$$\mathcal{PP} := (g, g^a, e(g, g)^\alpha, u, h, \{h_x\}_{x \in U}, v_0, v_1, \ldots, v_k), MSK := (\alpha).$$

where k :security parameter, U: Attribute Universe, collision-resistant hash functions $H_1 : \{0, 1\}^* \to \{0, 1\}^k$, $H_2 : \{0, 1\}^* \to \mathbb{Z}_p$. It choose randomly $g, \{h_x\}_{x \in U}$, $u, h, v_0, v_1, \ldots, v_k \in \mathbb{G}$ and $\alpha, a \in \mathbb{Z}p$.

KeyGen: $(\mathcal{PP}, MK, S)$ It picks $t \in_R \mathbb{Z}p$ and compute

$$SK_S := (D := g^{\alpha+at)}, L := g^t, \{Dx := h_x^t\}_{x \in S}).$$

where $S \in U$ is attribute set

Encryption: $(\mathcal{PP}, \mathbb{M}, m)$. Here $\mathbb{M}$ is access structure of $\mathbb{M} = (A_{(l\times n)}, \rho)$. It picks vector $v := (s, y_2, \ldots, y_n) \in_R \mathbb{Z}_n$ and set $\lambda_i := \langle v, A_i\rangle_{i=1,2\ldots,l}$, and it compute $K := e(g, g)^{\alpha s}$ and $\delta := H_2(C_0, C_1, \ldots, C_l, \mathbb{M})$.

$$CT := (C := E_K(m), C_0 := g^s, \{C_i := g^{a\lambda_i} h_{\rho(i)}^{-s}\}_{i=1,\ldots,l}, C' := (PH_2(\delta))^s).$$

Decryption: $(\mathcal{PP}, CT, SK_S)$ Calculate an index set $I := i : \rho(i) \in S$ and $\alpha_i i \in I$ such that $\Sigma_{i\in I}\alpha_i \cdot A_i = (1, 0, \ldots, 0)$.

$$CT := \frac{e(C_0, D \cdot PH_2(\delta))}{e(C', g) \cdot \prod_{i\in I}(e(C_i, L) \cdot e(C_0, D_{\rho(i)}))^{\alpha_i}}$$

Output $m := D_K(CT)$.

Sign: $(\mathcal{PP}, m, \mathbb{M} = (A_{(l\times n)}, \rho), SK_S)$

- Calculate $\{\alpha_i\}_{i\in I}$ and an index set $I = i : \rho(i) \in S$ such that $\sum_{i\in I}\alpha_i \cdot A_i = (1, 0, \ldots, 0)$.
- Choose random $\beta_{i\,i=1,\ldots,l}$ satisfying $\Sigma_{i=1}^{l}\beta_i \cdot A_i = (0, 0, \ldots, 0)$.
- Choose $t' \in_R \mathbb{Z}_p$

$$D' := g^{\alpha+a(t+t')}, L' := g^{(t+t')}, \forall x \in SD'_x := h_x^{(t+t')}.$$

- Choose randomly $z, r \in \mathbb{Z}_p$ and calculate $\omega := H_1(\mathbb{M}, m)$ and the signature will be

$$\sigma := \begin{pmatrix} \sigma_0 := D' \cdot (PH_1(\omega))^r, \sigma'_0 := g^r, \\ \{\sigma_{0,i} := (L')^{\alpha_i}(g^z)^{\beta_i}, \sigma_{1,i} := (D'_{\rho(i)})^{\alpha_i}(h_{\rho(i)}^z)^{\beta_i}\}_{i=1,\ldots,l} \end{pmatrix}$$

- Output the signature $\sigma := (\sigma_0, \sigma'_0, \{(\sigma_{0,i}, \sigma_{1,i})\}_{i=1,\ldots,l}, \mathbb{M})$.

Verify: $(\mathcal{PP}, \sigma, m)$

- Choose a vector $v := (s, y_2, \ldots, y_n) \in_R \mathbb{Z}_p^n$ and calculate the shares $\lambda_i := \langle v, M_i\rangle$ for $i = 1, \ldots, l$.
- Calculate $\omega := H_1(\mathbb{M}, m)$ and

$$\nabla := \frac{e(g^s, \sigma_0)}{e(PH_1(\omega)^s, \sigma'_0) \cdot \prod_{i=1,\ldots,l} e(g^{a\lambda_i} h_{\rho(i)}^{-s}, \sigma_{0,i}) \cdot e(g^s, \sigma_{1,i})}.$$

- Accept if the signature σ as correct,the output will be 1 if $e(g, g)^{\alpha s} = \nabla$. Otherwise, output will be 0.

3.3 Ciphertext-Policy Attribute-Based Signcryption [10]

Assumption: dBDHE and cDHE problem

Setup(1^k): It takes security parameter $k \in \mathbb{N}$ as input. It generate public parameter $\mathcal{PP}$

$$\mathcal{PP} := [\Sigma, \nabla, \vartheta, \gamma_1, \gamma_2, y_0, y_i i \in [l], \{h_x\}_{x \in U}, H_2, H_3, H_4, \Pi_{SE}, KDF, \mathcal{M}, U],$$

and master key $MK := g^{\alpha}$
where $\prod_{SE} := (SE_{Encrypt}, SE_{Decrypt})$ denote one-time symmetric-key cryptosystem, Message space $M := \{0, 1\}^*$, Key space $K := \{0, 1\}^{\tau}$, U = Attribute Universe, bilinear pairing parameters $\Sigma := (p, \mathbb{G}, \mathbb{G}_T, e)$, $g \in_R \mathbb{G}$ and cryptographic collision resistant hash functions $H_2 : \{0, 1\}^* \to \{0, 1\}^l$, $H_3 : \mathbb{G} \to \mathbb{Z}_p^*$ and $H_4 : \{0, 1\}^* \to \mathbb{Z}_p^*$. It picks randomly $\alpha \in_R \mathbb{Z}_p^*$ and consider sets $\nabla := e(g, g)^{\alpha}$, for each of attribute $x \in U$, it randomly samples $h_x \in_R \mathbb{G}$ and $\vartheta, \gamma_1, \gamma_2, y_0, y_1, \ldots, y_l \in_R \mathbb{G}$.

sExtract $(\mathcal{PP}, MK, A_s)$:

- It samples randomly $r \in_R \mathbb{Z}_p^*$ and consider sets $K_s := g^{\alpha} \vartheta^r$, $K_s' := g^r$, $K_{s,x} := h_x^r, \forall x \in A_s$.
- The signing key for A_s is $SK_{A_s} := [A_s, K_s, K_s', \{K_{s,x}\}_{x \in A_s}]$.

dExtract $(\mathcal{PP}, MK, A_d)$:

- It chooses $\tilde{r} \in_R \mathbb{Z}_p^*$ and consider sets $K_d := g^{\alpha} \vartheta^{\tilde{r}}$, $K_d' := g^{\tilde{r}}$, $K_{s,x} := h^{\tilde{r}_x}, \forall x \in A_s$.
- The decryption key for A_d is $SK_{A_d} := [A_s, K_d, K_d', \{K_{d,x}\}_{x \in A_s}]$.

Signcryption :$(\mathcal{PP}, m, SK_{A_s}, \Upsilon_s, \Upsilon_e)$ Here, $\Upsilon_s := (M_s, \rho_s)$ and $\Upsilon_e := (M_e, \rho_e)$, where M_s (resp. M_e) is an $l_s \times n_s$ (resp. $l_e \times n_e$) matrix with row labeling function $\rho_s : [l_s] \to U$ (resp. $\rho_e : [l_e] \to U$). Let $\mathbf{M}_s^{(i)}$ (resp.$\mathbf{M}_s^{(i)}$) be the i^{th} row of the matrix M_s (resp. M_e).

- Since $\Upsilon_s(A_s) = 1$, this algorithm computes a vactor $\mathbf{a} := (a_1, a_2, \ldots, a_{l_s}) \in \mathbb{Z}_p^{ls}$ such that $a.M_s = 1_{n_s}$, that is,$\sum_{i \in [l_s]} a_i.\mathbf{M}_s^{(i)} = \mathbf{1}_{n_s}$, and $a_i = 0$ for all i where $\rho_s(i) \notin A_s$.
- It considers a vector $\mathbf{b} := (b_1, b_2, \ldots, b_{l_s}) \overset{R}{\leftarrow} \mathbb{Z}_p^{ls}$ such that $\sum_{i \in [l_s]} b_i.\mathbf{M}_s^{(i)} = \mathbf{1}_{n_s}$.
- It re-randomizes the signing key SK_{A_s} as follows: choose $r' \in_R \mathbb{Z}_P^*$ and consider set $\breve{K}_s := K_s \cdot \vartheta^{r'}$, $\breve{K}_s' := K_s' \cdot g^{r'}$ and $\breve{K}_{s,x} := K_{s,x} \cdot h_x^{r'}, \forall x \in A_s$.
- It randomly chooses $\xi, \theta \in_R \mathbb{Z}_p^*$ and $\boldsymbol{\lambda} := (\xi, \varsigma_2, \ldots, \varsigma_{n_e})$, here $(\varsigma_2, \ldots, \varsigma_{n_e}) \in_R \mathbb{Z}_p^*$.
- After that it calculate the followings:

- $E_1 := g^{\xi}$, $S_1 := g^{\xi \cdot \theta}$, $E_2 := SE_{Encrypt}(KDF(\nabla^{\xi}||S_1||tt), m)$, where tt is the current time,
- $E_3 := \{E_3^{(i)} := \vartheta^{\lambda \cdot \mathbf{M}_e^{(i)}} h_{\rho e(i)}^{\xi}\}_{i \in [l_e]}$,
- $\mu := H_3(E_1)$, $E_4 := (\gamma_1 \gamma_2^{\mu})^{\xi}$,
- $S_2 := \{S_2^{(i)} := g^{b_i} (\breve{K}_s')^{a_i}\}_{i \in [ls]}$,
- $H_2(S_2, tt, \Upsilon_s, \Upsilon_e) = (j_1, \ldots, j_l) \in \{0,1\}^l$, $H_4(S_1, E_2, E_3, E_4, \Upsilon_s, \Upsilon_e) = \beta$,

$$S_3 := \breve{K}_s(\prod_{i \in [l_s]} (\breve{K}_{s,\rho s(i)})^{a_i} \cdot h_{\rho s(i)}^{b_i})(y_0 \prod_{i \in [l]} y_i^{ji})^{\xi} E_4^{\beta \cdot \theta}$$

- The ciphertext is $CT_{\Upsilon_e} := [\Upsilon_e, E_1, E_2, E_3, E_4, S_1, S_2, S_3, tt]$.

Designcryption $(PK, CT_{\Upsilon_e}, \Upsilon_s, SK_{A_d})$.

- It samples $\varrho_2, \ldots, \varrho_{n_s} \xleftarrow{R} \mathbb{Z}_p^*$ and computes $\varpi_i := (1, \varrho_2, \ldots, \varrho_{n_s}) \cdot M_s^{(i)}, \forall i \in [l_s]$.
- It next computes $H_3(E_1) = \mu$, $H_2(S_2, tt, \Upsilon_s, \Upsilon_e) = (j_1, \ldots, j_l) \in \{0,1\}^l$, $H_4(S_1, E_2, E_3, E_4, \Upsilon_s, \Upsilon_e) = \beta$.
- Now validity of the ciphertext CT_{Υ_e} checked using

$$\nabla \stackrel{?}{=} \frac{e(S_3, g)}{(\prod_{i \in [l_s]} e(\vartheta^{\varpi_i} \cdot h_{\rho_s(i)}, S_2^{(i)})), e(y_0 \prod_{i \in [l]} y_i^{ji}, E_1) \cdot e((\gamma_1 \gamma_2^{\mu})\beta, S_1}$$

  if it is invalid, return $\perp$, otherwise, proceed as follows
- Because $\Upsilon_e(A_d) = 1$, compute a vector $a' := (a_1', a_2', \ldots, a_{l_e}') \in \mathbb{Z}_p^{l_e}$ such that $\mathbf{a'} \cdot M_e = \mathbf{1}_{n_e}$, that is, $\sum_{i \in [le]} a_i' M_e^{(i)} = \mathbf{1}_{n_e}$, and $a_i' = 0$ for all i where $\rho_{e(i)} \notin A_d$.
- Recover ∇^{ξ} from

$$\nabla^{\xi} = \frac{e(K_d \cdot \prod_{i \in [l_e]} K_{d,\rho_{e(i)}}^{a_i'}, E_1)}{e(K_d', \prod_{i \in [l_e]} (E_3^{(i)})^{a_i'})}$$

- Atlast, retrieve the correct message $m = SE_{Decrypt}(KDF(\nabla^{\xi}||S_1||tt), E_2)$.

4 Performance Analysis

There are a number of schemes already existing for attribute based signcryption. Transmission and communication cost need to be measure for each of the schemes for identifying efficiency of scheme. The consideration of ABSC scheme for outsourced cloud data access control required to satisfy some functionality which might not hold all the existing schemes, that can be possible to ensure form characteristic analysis and performance analysis. In this section, we analyze various parameters to find out the performance of different attribute based signcryption(ABSC) schemes.

Table 2 Comparison of different ABSC Scheme

Scheme	Size of signing key	Size of decryption key	Size of ciphertext
Gagne et al. [4]	$2\|N_s\|B_G$	$3\|N_d\|B_G$	$(l_s + l_e + 3)B_G + msg$
Emura et al. [3]	$2\|N_s\|B_G$	$(2\|N_d\| + 2v_k + 1)B_G$	$(u_e + l_s + v_k + 2)B_G + s_{ot} + v_k + msg$
Chen et al. [1]	$(\|N_s\| + 2)B_G$	$(\|N_d\| + 2)B_G$	$(2l_s + l_e + 4)B_G + msg$
Wei et al. [13]	$(\|N_s\| + d)^2 B_G$	$2\|N_d\|B_G$	$(id + l_e+)B_G + msg$
Pandit et al. [9]	$(\|N_s\| + 2)B_G$	$(\|N_d\| + 2)B_G$	$(2l_s + 2l_e + 4)B_G + msg$
Liu et al. [7]	$(\|N_s\| + 2)B_G$	$(\|N_d\| + 2)B_G$	$(l_s + w_s + l_e + 3)B_G + msg$
Rao et al. [10]	$(\|N_s\| + 2)B_G$	$(\|N_d\| + 2)B_G$	$(l_s + l_e + 4)B_G + B_{tt} + msg$

v_k verification key's bit length; $|N_s|$: nos. of signing key attributes, $|N_d|$: nos. decryption key attributes, l_s: nos. attributes in a signing predicate; $\phi_e(\phi_s)$: nos. of signing (encryption) attributes required in decryption process. ω_s: nos. of column in signing MSP matrix. l_e: nos. of attributes in an encryption predicate; u_e: Size of attribute universe; $B_G(B_Z)$: length of an element of group $G(Z_p)$; msg: length of a message; B_{tt}: bit length of time stamp; S_{ot}: length of the signature scheme; id = length of user's identity, l_s:

Table 3 Comparison of different ABSC Scheme

Scheme	Signcryption cost		Designcryption cost	
	Exponential	Pair	Exponential	Pair
Gagne et al. [4]	$(l_s + l_e)$	–	ϕ_e	$\phi_e + \phi_s$
Emura et al. [3]	$l_s w_s + w_s + 2\phi_e + 4$	–	–	$u_e + l_s + v_k + 3$
Chen et al. [1]	$4l_s + 2l_e + 5$	1	$2l_s + \phi_e + 3$	$2l_s + 2\phi_e + 4$
Wei et al. [13]	$id + l_e$	–	ϕ_e	$id + \phi_e$
Pandit et al. [9]	$4l_s + 4l_e + 7$	2	$2l_s + 2\phi_e + 5$	$2l_s + 2\phi_e + 6$
Liu et al. [7]	$2l_s w_s + 3l_s + 2l_e + 3$	–	$2l_s w_s + w_s + \phi_e$	$l_s w_s + w_s + 2\phi_e + 4$
Rao et al. [10]	$4l_s + 2l_e + 6$	–	$l_s + 2\phi_e + 2$	$l_s + 5$

$\phi_e(\phi_s)$ nos. of signing and encryption attributes used in decryption process. id = length of user's identity, l_s: nos. of attributes used in signing predicate; l_e: nos. of attributes used in encryption predicate; u_e: Size of universal attributes; v_k: verification key's bit length; ω_s: nos. of column in signing MSP matrix.

In Table 2. we have compare the size of Signing key, Decryption Key and Cipher text of different ABSC Schemes which can effect computation as well as transmission cost.

In Table 3. we explain about computation cost of signcryption and designcryption algorithms for existing ABSC schemes based on number of required pairing and exponential operation.

5 Open Issues

Data outsourcing and its access control is very important issue because it is multitenant environment and also maintain by un-trusted third party. In this section, we highlight some of issue are arise in deployment and utilizing of attribute based signcryption in distributed and cloud environment. Comparing of functionality and characteristic with drawback of existing ABSC scheme, we have shown some of the open issues based on the above discussion are as follows:

Lightweight data signing and encryption: Recently, many customers of business and enterprises have outsourced their data from remote cloud server through light weight device like mobile. So, it is significant to develop the data access control providing security and privacy of outsourced cloud data without further limitation and requirement. Lightweight data access control with considerable security measure minimize the computation cost and transmission cost.

Revocation: ABSC scheme with user revocation is another challenging task. Unless proper and dynamic revocation process access control of outsourced cloud data using ABSC will not possible. Attribute revocation in ABSC allows the data owner to revoke a group of user whose are hold that particular attribute.

Backward and Forward security: Backward and forward security issue in ABSC have not been addressed yet among the existing ABSC scheme. Backward security under ABSC based access control means the newly joined user should not able to decrypt the previous data for the period of the data before joining. Similarly, Forword security under access control of outsourced cloud data means the revoked user must not have access right the data after revocation.

Distributed ABSC: Existing ABSC approaches are centralized in architectural view which has some limitations in distributed environment. All users under centralized approach need to trust as member of single authority.

ABSC based Access Control: As ABSC scheme provides good services like confidentiality, public verifiability, signer privacy together in one schemes, so with this methodology developing data access control basically in cloud and IoT environment will be more beneficial.

6 Conclusion

Cloud data outsourcing of sensitive data require not only the concern of confidentiality but it is also essential anonymous authentication. After analysis of functionality and characteristics of ABSC, we have seen this technique can provide efficiently authentication and confidentiality together compare to the technique of sign and encrypt (S&E). Here, we thoroughly discuss various attribute based signcryption schemes for access control mechanisms, which are efficient and applicable for cloud and distributed environment. We also arise here some requirements with current technologies, which need to resolve for proper access control of cloud data outsourcing.

References

1. Chen, C., Chen, J., Lim, H.W., Zhang, Z., Feng, D.: Combined public-key schemes: the case of ABE and ABS. In: International Conference on Provable Security, pp. 53–69. Springer (2012)
2. Chen, D.: Data security and privacy protection issues in cloud computing (973), 647–651 (2012)
3. Emura, K., Miyaji, A., Rahman, M.S.: Dynamic attribute-based signcryption without random oracles. Int. J. Appl. Cryptogr. **2**(3), 199–211 (2012)
4. Gagné, M., Narayan, S., Safavi-Naini, R.: Threshold attribute-based signcryption. In: International Conference on Security and Cryptography for Networks, pp. 154–171. Springer (2010)
5. Hong, H., Sun, Z.: An efficient and secure attribute based signcryption scheme with lsss access structure. SpringerPlus **5**(1), 644 (2016)
6. Lewko, A., Waters, B.: Decentralizing attribute-based encryption. In: Annual International Conference on the Theory and Applications of Cryptographic Techniques, pp. 568–588. Springer (2011)
7. Liu, J., Huang, X., Liu, J.K.: Secure sharing of personal health records in cloud computing: ciphertext-policy attribute-based signcryption. Future Gener. Comput. Syst. **52**, 67–76 (2015)
8. Maji, H.K., Prabhakaran, M., Rosulek, M.: Attribute-Based Signatures. Springer, Berlin, Heidelberg, 6558 LNCS:376–392 (2011)
9. Pandit, T., Pandey, S.K., Barua, R.: Attribute-based signcryption: Signer privacy, strong unforgeability and ind-cca2 security in adaptive-predicates attack. In: International Conference on Provable Security, pp. 274–290. Springer (2014)
10. Rao, Y.S.: A secure and efficient ciphertext-policy attribute-based signcryption for personal health records sharing in cloud computing. Future Gener. Comput. Syst. **67**, 133–151 (2017)
11. Ruj, S., Stojmenovic, M.: Decentralized access control with anonymous authentication of data stored in clouds. IEEE Trans Parallel Distrib. Syst. **25**(2), 384–394 (2014)
12. Wang, C., Huang, J.: Attribute-based signcryption with ciphertext-policy and claim-predicate mechanism. In: 2011 Seventh International Conference on Computational Intelligence and Security (CIS), pp. 905–909. IEEE (2011)
13. Wei, J., Xuexian, H., Liu, W.: Traceable attribute-based signcryption. Secur. Commun. Netw. **7**(12), 2302–2317 (2014)
14. Yang, K., Jia, X.: Expressive, efficient, and revocable data access control for multi-authority cloud storage. IEEE Trans. Parallel Distrib. Syst. **25**(7), 1735–1744 (2014)
15. Zheng, Y.: Digital signcryption or how to achieve cost (signature & encryption) cost (signature) + cost (encryption). In: Annual International Cryptology Conference, pp. 165–179. Springer (1997)

Comparative Analysis of Current for Specific Scattering in GaN MOSFET

Kaushik Mazumdar, Praveen Kumar and Aniruddha Ghosal

Abstract The behavior of gallium nitride transistor under the electric–optical phonon scattering is studied and the variation of current density with the concentration charge density is explained. Due to polarization in GaN, two-dimensional electron gas causes the electrons drift velocity to change when some voltage applied to device. The mobility of GaN MOSFET is been studied and plotted with respect to the temperature. The current density which is related to the drift velocity and carrier concentration is analyzed and plotted.

Keywords High electron mobility transistors (HEMTs)
Two-dimensional electron gas (2DEG) · Carrier charge concentration
Phonon saturation · Optical phonon scattering · Polarization
Effective electron velocity
Metal oxide semiconductor field effect transistor (MOSFET)

1 Introduction

The III–V semiconductor has made a great impact in the field of Nano devices in the past few years. In the III–V group semiconductor, the most popular one is GaN which has attracted many researchers. The selection of GaN is because of its chemical and thermal properties, high mobility, and large direct bandgap and is widely used in various applications. Nowadays, GaN material is mostly used for transistors. The

K. Mazumdar (✉) · P. Kumar (✉)
Department of Electronics Engineering, Indian Institute
of Technology (Indian School of Mines) Dhanbad, Dhanbad 826004, Jharkhand, India
e-mail: kaushik_edu@yahoo.co.in

P. Kumar
e-mail: pk.16mt001112@ece.ism.ac.in

A. Ghosal
Institute of Radio Physics and Electronics,
University of Calcutta, 92, A.P.C. Road, Kolkata 700009, India

U. Biswas et al. (eds.), *Advances in Computer, Communication and Control*, Lecture Notes in Networks and Systems 41, https://doi.org/10.1007/978-981-13-3122-0_13

reason for their use in the transistor is due to its lower loss in power and potential to drastically cut the energy consumption. Also, it offers much higher energy efficiency and faster switching frequency. The devices (MOSFETs) which were earlier based on the silicon and germanium are now the base materials over which the other layers are grown. The various layer deposition processes can be used but the most likely ones are Metal Oxide Chemical Vapor Deposition (MOCVD) and MBE. GaN-based high electron mobility transistors (HEMTs) have numerous features, which is still a mystery to be solved, polarization is one that exhibits great importance [1].

In this research, due to polarization in GaN MOSFET channel two-D electron gas (2DEG) induces sheet charge densities. Maximum saturation velocity found by researchers are around 1.1×10^7 cm/s [2] and 1.32×10^7 cm/s [3]. The projected lower saturation velocity is all because of the sum of the various combination of self-heating [4], parallel conducting paths [2, 5], nonuniform electric fields and contacts [6], and optical phonon scattering [5, 7]. Sheet charge density value changes in the range of $c_{ec} = 1\text{–}4 \times 10^{13}$ cm^{-2}. If an effective electron velocity is assumed to be about v_c—10^7 cm/s, the drain current per unit device width (W) has the value of about—5 A/mm for c_{ec}—3×10^{13} cm^{-2}. The saturation current that has been calculated experimentally were far smaller than what was expected. This could be due to the low electron velocity at the source of the MOSFET that is may be lower than 10^7 cm/s for higher values of V_{gs}. Thus, our first priority is to understand the current carrying capabilities of 2DEG in GaN HEMT.

Section 2, focuses on the device model and specification of MOSFET and Sect. 3 will give a broad explanation of the drain current with electron charge concentration. Section 4 is the result of the experiment performed using the model. Section 5 concludes the experiment.

2 Device Specifications

The AlGaN/GaN HEMT made up of a single cell "pi" structure with L_g = 50 nm "T" gate. The device structure chosen for phonon saturation model is an $Al_{0.35}Ga_{0.65}N$/GaN HEMT with a $t_{bar} = 5$ nm barrier as shown in Fig. 1. The structure is three-layered with the Si substrate at the bottom, then the GaN and then above it is AlGaN. The AlGaN/GaN is grown on the silicon substrate using the process MOCVD. The AlGaN is doped which will help the 2DEG channel to form as it will supply charge.

The features that are mentioned in Sect. 1 can be examined to resolve using the electron–optical phonon scattering process. Also, due to the light mass of the nitrogen atom (the lightest in all III–V semiconductors), the polar optical phonon energy is high. Combining with nitrogen, which is highly electronegative, thus results in a very high scattering rate.

Figure 1 shows the band diagram of a typical GaN transistor. The study about electron distribution at the "source injection point" helped to understand short-gate-length device characteristics [8, 9]. The energy and the **k**-space distribution of 2DEG

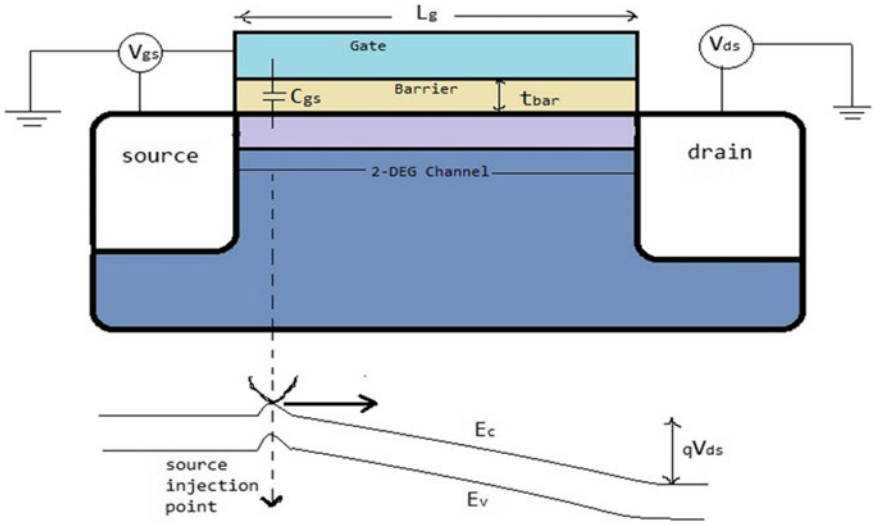

Fig. 1 The GaN transistor with the cross-sectional view and energy band diagram with source injection point

electrons at this point are depicted for various carrier densities dictated by the gate voltage and the gate-to-source injection plane capacitance.

3 Analysis and Discussion

As the charge concentration which is the main reason of the polarization and causes the electrons to move with the velocity called as effective electron velocity, v_c by which the current through the MOSFET changes when some voltage supply is given to it. The relation between the current flowing per unit width in the device and the electron charge concentration is derived in the below equations.

$$I = \sigma \in \tag{1}$$

$$v_c = \mu \in \tag{2}$$

$$\sigma = q\mu_n c_{ec} \tag{3}$$

From (2) and (3), we have got another equation for the current which is given as (4)

$$\frac{I_d}{W} = c_{ec}\, q v_c \tag{4}$$

The terms used are σ which is conductivity and W is the width of the device (gate of MOSFET). As the charge concentration, c_{ec} is directly proportional to the current

I_d, flowing through the device MOSFET, so the variation of the current will be linear from (1). As from (2), the current is proportional to the mobility and as the mobility changes the current also varies. The mobility which is the function of relaxation rate, $1/\tau_{po}$ of the electron caused due to polar optical phonon scattering is given as (5) where m_{eff} the electron effective mass of GaN is 0.67 m_0.

$$\mu = \frac{e\tau_{po}}{m_{eff}} \tag{5}$$

The relaxation time due to optical phonon scattering which is a function of the relaxation time of electron t_0.

$$\tau_{po} = \frac{t_0}{3N}\sqrt{\frac{\hbar\omega_0}{W_0}} \tag{6}$$

The reduced value of Planck constant $\hbar$ is 6.582×10^{-16} eVs/rad, N is density state given as, $e^{-\hbar/kT}$. As the mobility changes from the (2) and (4) current value also vary accordingly. The term W_0 is a function which related to the gate length L_g which is given as

$$W_0 = \frac{(\hbar\pi)^2}{2m_{eff}L^2} \tag{7}$$

From (6) and (7), the relaxation rate can be said that it is a function of gate length also.

4 Result

The polarization makes the electron to align along a path and thus mobility comes into the picture. The mobility varies with temperature. This mobility decreases with the increase in temperature as can be seen in Fig. 2. At 300 K, the mobility of MOSFET is 4.465×10^4 m^2/Vs which is the lowest value derived. For our model, with minimum velocity of $v_c = 0.1 \times 10^7$ cm/s, current flowing is very low as can be seen in Fig. 3. As the effective electron velocity changes, we can see that the current also increases sufficiently fast with it. Thus, for maximum velocity $v_c = 3 \times 10^7$ cm/s, the maximum current of 5 A/mm flows through the device with the lesser amount of the concentration, c_{ec} of about 1×10^{13} cm^{-2} as shown in Fig. 3. The different currents for different drift velocities given in below I, shown as four different colored linear graph in Fig. 3 (Table 1).

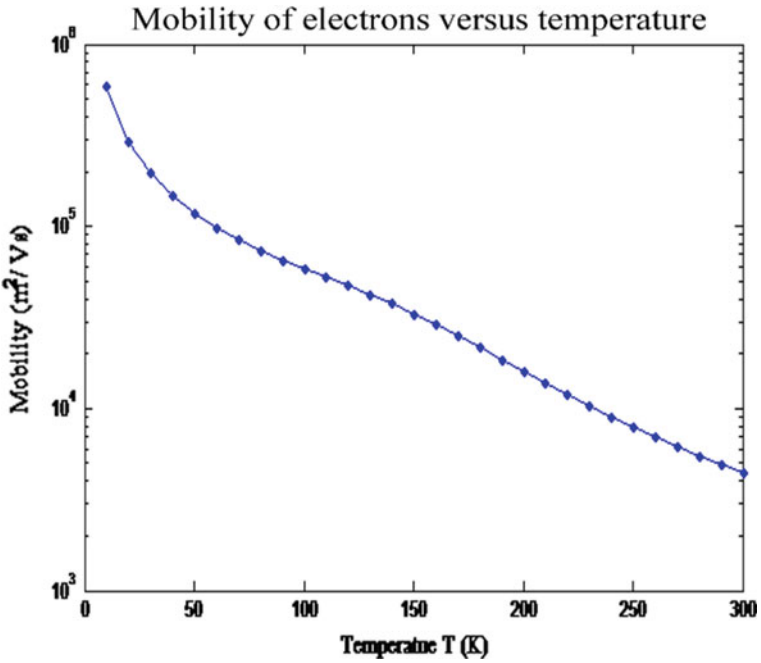

Fig. 2 Variation of mobility with the temperature in GaN

Table 1 Current values for different drift velocities at charge concentration of 1×10^{13} per sq. cm

Color	Drift velocity ($\times 10^7$) (cm/s)	Current density (A/mm)
Pink	0.1	0.1602
Red	1	1.602
Blue	2	3.204
Green	3	4.806

5 Conclusion

The current driving capacity of GaN MOSFET is mainly focused on our model. As the mobility changes with the temperature showing a decreasing curve. The value of mobility obtained from the curve is 4.465×10^4 m^2/Vs. The variation of current with concentration shows a linear nature. We have assumed that our model is based on the k-space distribution of two-DEG that makes it a ballistic transistor and makes it useful for analytical design tool. Since we have seen that velocity and electron charge density is a strong function of the current density. With the low electron charge concentration of about 1×10^{13} cm^{-2}, we can achieve the maximum current needed for the MOSFET to break the two-DEG channel with maximum electron

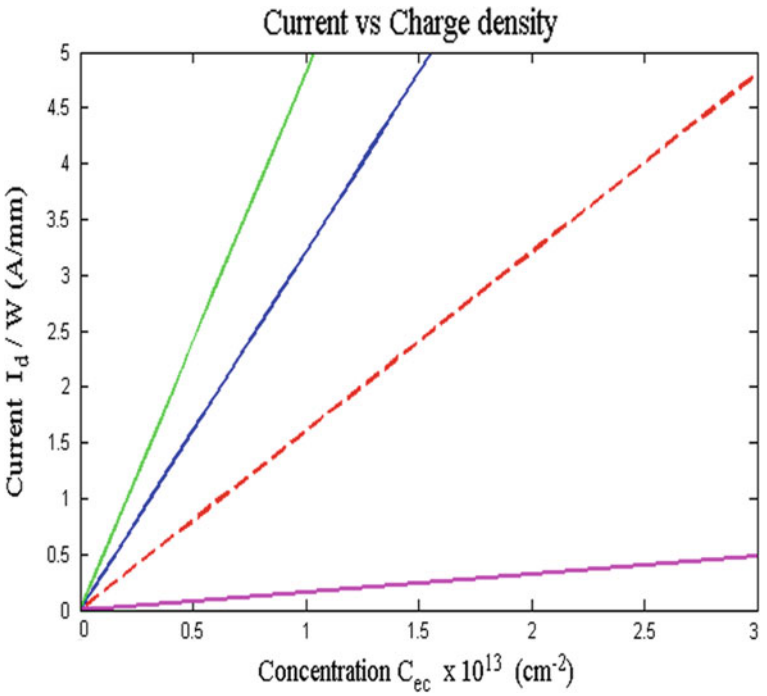

Fig. 3 Plot showing the current density (I_d/W) in A/mm versus the electron charge density (C_{ec}) in per sq. cm

velocity of 3×10^7 cm/s. Thus we can say that the speed of the MOSFET is much greater than that was achieved previously [10].

Acknowledgements This research work was done with the support of my colleagues in the Department of Electronics Engineering, IIT(ISM), Dhanbad India and for their support and allowing me to work in this field.

References

1. White, B.D., Bataiev, M., Goss, S.H., Hu, X., Karmarkar, A., Fleetwood, D.M., Schrimpf, R.D., Schaff, W.J., Brillson, L.J.: Electrical, spectral, and chemical properties of 1.8 MeV proton irradiated AlGaN/GaN HEMT structures as a function of proton fluence. IEEE Trans. Nucl. Sci. **50**(6), 1934–1941 (2003)
2. Oxley, C.H., Uren, M.J.: Measurement of unity gain cutoff frequency and saturation velocity of a GaN HEMT transistor. IEEE Trans. Electron. Devices **52**(2), 165–170 (2005)
3. Eastman, L.F., Tilak, V., Smart, J., Green, B.M., Chumbes, E.M., Dimitrov, R., Kim, H., Ambacher, O.S., Weiman, N., Prunty, T., Murphy, M., Schaff, W.J., Shealy, J.R.: Undoped AlGaN/GaN HEMTs for microwave power amplification. IEEE Trans. Electron. Devices **48**(3), 479–485 (2001)

4. Ardaravicius, L., Liberis, J., Matulionis, A., Eastman, L.F., Shealy, J.R., Vertiatchikh, V.: Self-heating and microwave noise in AlGaN/GaN. Phys. Status Solidi (a) **201**(2), 203–206 (2004)
5. Ardaravicius, L., Matulionis, A., Liberis, J., Kiprijanovic, O., Ramonas, M., Eastman, L.F., Shealy, J.R., Vertiatchikh, A.: Electron drift velocity in AlGaN/GaN channel at high electric fields. Appl. Phys. J. **83**(19), 4038–4040 (2003)
6. Barker, J.M., Ferry, D.K., Goodnick, S.M., Koleski, D.D., Allerman, A., Shur, R.J.: High-field transport in GaN/AlGaN heterostructures. J. Vac. Sci. Technol. B Microelectron. Process. Phenom. **22**(4), 2045–2050 (2004)
7. Ridley, B.K., Schaff, W.J., Eastman, L.F.: Hot-phonon induced velocity saturation in GaN. J. Appl. Phys. **96**(3), 1499–1502 (2004)
8. Natori, K.: Ballistic metal–oxide–semiconductor field effect transistor. J. Appl. Phys. **76**(8), 4879 (1994)
9. Lundstrom, M.: Elementary scattering theory of the Si MOSFET. IEEE Electron. Device Lett. **18**(7), 361–363 (1997)
10. Matulionis, A., Liberis, J., Matulioniene, I., Ramonas, M., Eastman, L.F., Shealy, J.R., Tilak, V., Vertiatchikh, A.: Hot-phonon temperature and lifetime in a biased $Al_xGa_{1-x}N$/GaN channel estimated from noise analysis. Phys. Rev. B Condens. Matter Mater. Phys. **68**(3), 335–338 (2003)

Adaptive Smart Antenna of Aperiodic Array

Pooja Raj, Anupama Senapati and Jibendu Sekhar Roy

Abstract In this paper, aperiodic antenna array, where inter-element spacing between antenna elements is non-uniform, is used for beamforming of smart antenna. Here, least mean square (LMS) algorithm is used for adaptive beamforming of smart antenna. Side lobe level (SLL) of antenna radiation beam causes interference for other users and should be reduced in mobile network. Aperiodic array produces lower side lobe level compared to uniform array. The aim of this research work is to investigate nature of adaptive beamforming at different angles using aperiodic array with reduced side lobe level while producing main beam and null towards the desired directions.

Keywords Smart antenna · Aperiodic array · LMS algorithm · Side lobe level

1 Introduction

International Telecommunication Union (ITU) has declared smart antenna technology as one of the major technologies for mobile communication in 4G and beyond. A smart antenna system can provide high security by forming radiation beam only towards the desired user and generating null towards the interferer [1, 2]. Efficient spectral utilization and huge power saving in mobile network are possible by using smart antenna technology. After estimating the direction of arrival (DOA) of the user signal, smart antenna generates the desired beam towards the user using adaptive signal processing algorithm [1, 3]. In literature, research works are available

P. Raj · A. Senapati · J. S. Roy (✉)
School of Electronics Engineering, Kalinga Institute of Industrial Technology (KIIT) Deemed to be University, Bhubaneswar 751024, Odisha, India
e-mail: drjsroy@rediffmail.com

P. Raj
e-mail: rajpooja444556@gmail.com

A. Senapati
e-mail: senapati.anupama@gmail.com

U. Biswas et al. (eds.), *Advances in Computer, Communication and Control*, Lecture Notes in Networks and Systems 41, https://doi.org/10.1007/978-981-13-3122-0_14

for beamforming of smart antenna using various types of adaptive signal processing algorithms and popular method of adaptive beamforming is the use of least mean square (LMS) algorithm [4, 5]. Most of these works are devoted to beamforming using periodic or uniform antenna arrays. In a uniform antenna array, inter-element spacing between the antennas is constant.

In an aperiodic array, inter-element spacing in the array is non-uniform. Reports on array antennas using aperiodic array are available [6–8], where aperiodic arrays are used for side lobe reduction and grating lobe reduction during beam tilting in phased array. Research work on smart antenna of aperiodic arrays is very rare. In this paper, performance of smart antenna using aperiodic array is presented. Adaptive beams are formed for aperiodic arrays at different user directions using LMS algorithm and the results are compared with those of periodic arrays. Lower side lobe levels (SLL) are achieved for aperiodic array than periodic array.

2 Least Mean Square Algorithm

For beamforming of adaptive smart antenna, least mean square (LMS) algorithm is used. Adaptive algorithm LMS incorporates an iterative procedure which makes successive corrections to the weight vector in the direction of the negative of the gradient vector which eventually minimizes mean square error. Error e(n) between desired signal d(n) and array output y(n), is [4, 5]

$$\mathrm{e(n)} = \mathrm{d(n)} - \mathrm{y(n)}. \tag{1}$$

Weight vectors in LMS algorithm are updated according to the equation

$$\mathrm{w(n+1)} = \mathrm{w(n)} + \mu \mathrm{x(n)e^{*}(n)}. \tag{2}$$

Here, μ is the step size parameter and e*(n) is the complex conjugate of e(n) and $x(n)=[x_1(n), x_2(n) - x_N(n)]$ is the signal received by the multiple antenna elements.

3 Beamforming of Adaptive Smart Antenna of Aperiodic Array

In a uniform linear antenna array, the antenna elements are arranged in a line with equal inter-element spacing (d) which is shown in Fig. 1. The antennas are fed by current having progressive phase shift of 'α'.

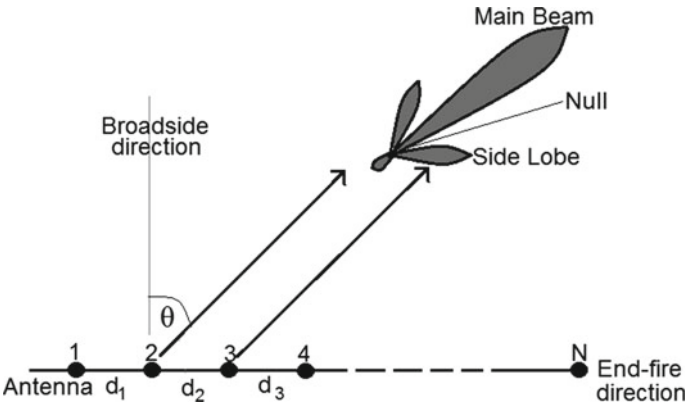

Fig. 1 Linear antenna array

Aperiodic array produces lower side lobe level compared to uniform array. The aim of this research work is to investigate nature of adaptive beamforming at different angles using aperiodic array with reduced side lobe level while producing main beam and null towards the desired directions. The array factor (AF) of an aperiodic array of N number of isotropic elements is given by [9]

$$AF = \sum_{n=1}^{N} A_n e^{j(n-1)\beta d_{n-1} sin\theta}. \tag{3}$$

Here, inter-element spacing d_{n-1} is the aperiodicity of the array. For a periodic array, d_{n-1} is constant. LMS algorithm is used for beamforming of adaptive smart antenna of periodic and aperiodic arrays at different angles. Simulated results for periodic and aperiodic arrays for 10 element antenna arrays for beam direction (BD) at 0° and null direction (ND) at −10° are shown in Fig. 2 and Fig. 3, respectively.

The corresponding error plots for periodic and aperiodic arrays are shown in Fig. 4a, b.

Simulated results for periodic and aperiodic arrays for 10 element arrays for beam direction (BD) at −5° and null direction (ND) at +5° are shown in Figs. 5 and 6.

The corresponding error plots for periodic and aperiodic arrays are shown in Fig. 7a, b.

Simulated results for smart antenna of periodic and aperiodic arrays are compared in Table 1.

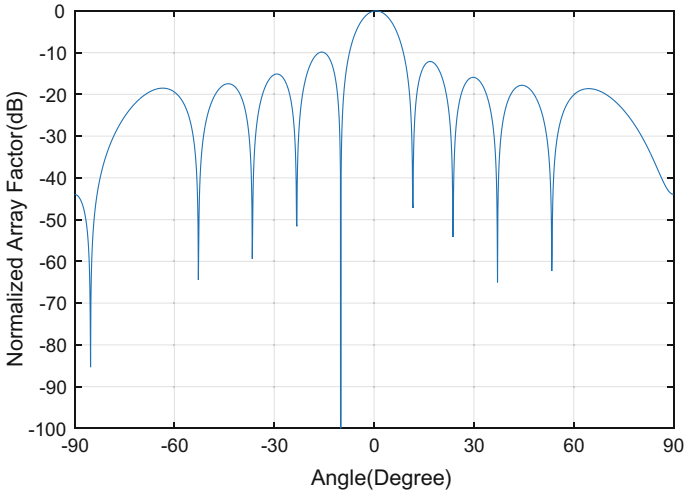

Fig. 2 Smart antenna of periodic array (d = 0.5λ)

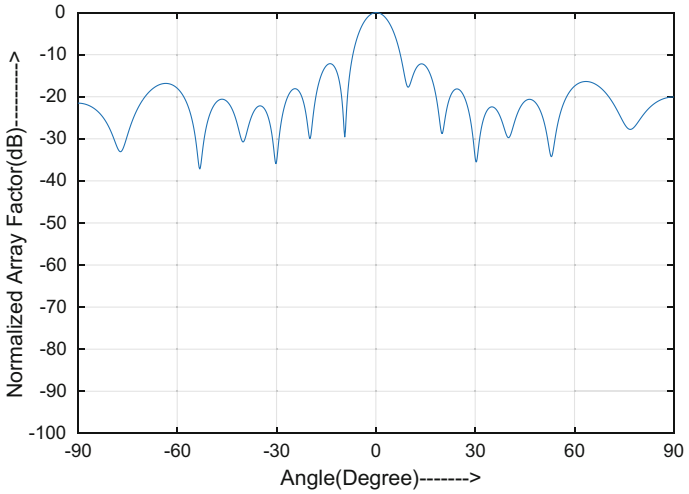

Fig. 3 Smart antenna of aperiodic array (d = 0.3λ, 0.33λ, 0.36λ, …, 0.54λ)

In Table 1, in both the cases, more than 2 dB lower SLLs are achieved using aperiodic array in smart antenna than periodic array. Half power beamwidths (HPBW) in both the cases are narrower than HPBWs obtained using periodic array which means that the directivity of smart antenna of aperiodic array is more than that of periodic

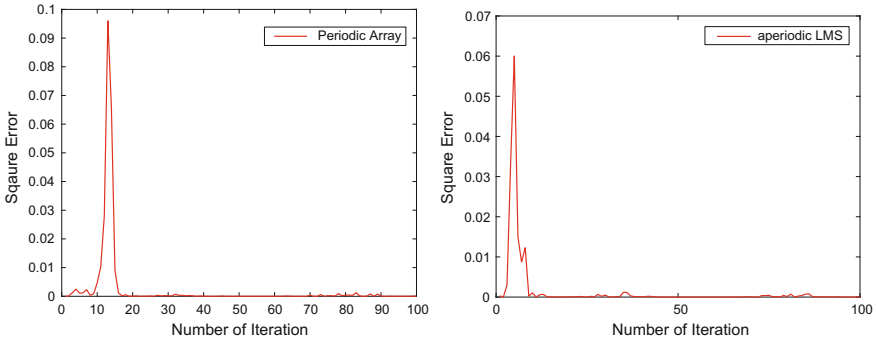

(a) Periodic array (b) Aperiodic array

Fig. 4 Error plot for periodic and aperiodic arrays

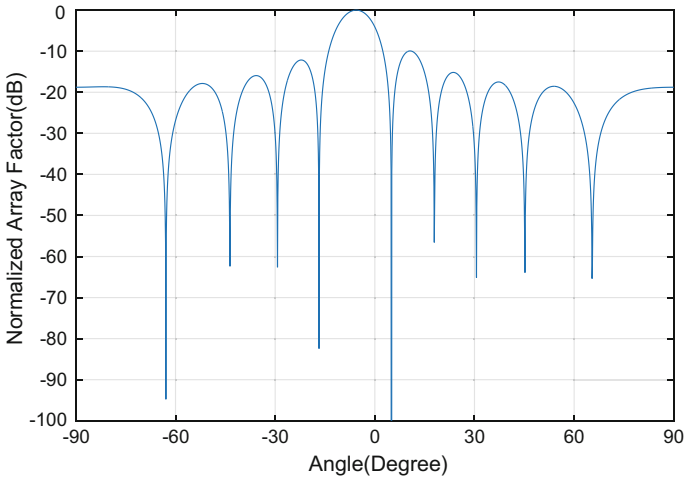

Fig. 5 Smart antenna of periodic array (d = 0.5λ)

array. In an aperiodic array, appearance of grating lobes is less [7] but proper spacing between the elements should be maintained otherwise grating lobes may appear. Figure 8 shows the appearance of grating lobes for N = 10 with aperiodic element spacing, d = 0.7λ, 1.4λ, 2.1λ, …, 6.3λ.

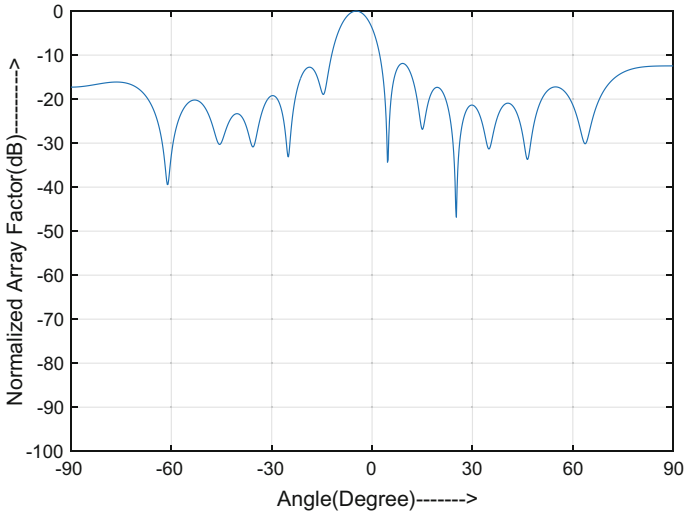

Fig. 6 Smart antenna of aperiodic array (d = 0.3λ, 0.33λ, 0.36λ, …, 0.54λ)

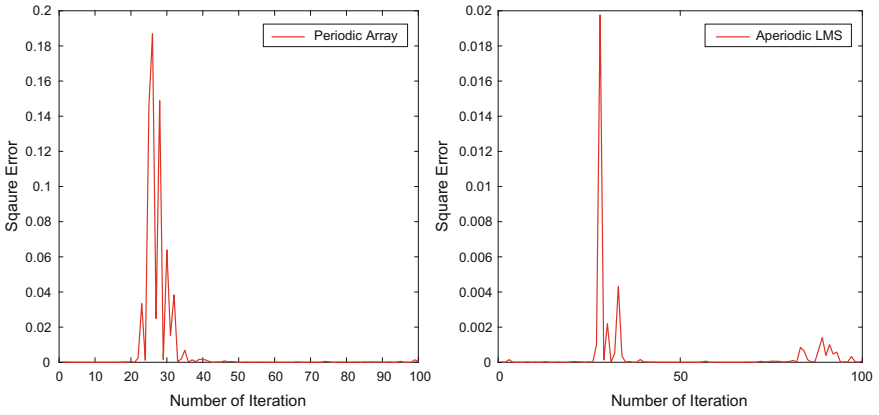

(a) Periodic array (b) Aperiodic array

Fig. 7 Error plot for periodic and aperiodic arrays

4 Conclusions

Beamforming of smart antenna using aperiodic arrays are presented here. MATLAB simulated results for aperiodic arrays are compared with the results for smart antenna of periodic array. Number of iteration in all the cases is 100. Directivity of aperiodic array is found to be more than the smart antenna of periodic array. Lower side lobe

Table 1 Comparison between smart antennas of periodic and aperiodic arrays

Specifications	Type of array	BD	ND	HPBW	$SLL_{max\ (dB)}$
N = 10 Desired BD = 0° and ND = −10°	Periodic μ = 0.022	0.6°	−10.1°	9.7°	−9.88
	Aperiodic μ = 0.0189	0.2°	−9.4°	8.5°	−12.2
N = 10 Desired BD = −5° and ND = +5°	Periodic μ = 0.022	−5.6°	5.1°	9.9°	−9.96
	Aperiodic μ = 0.0189	−4.8°	4.8°	8.6°	−12

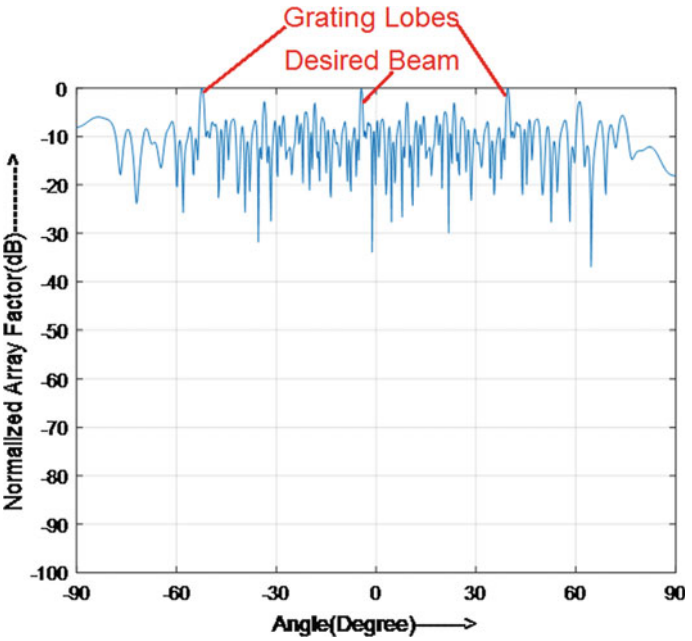

Fig. 8 Appearance of grating lobes in smart antenna of aperiodic array (BD = −5°, ND = +5°)

level is achieved for smart antenna of aperiodic array which is desired in mobile network for interference suppression. Performances of adaptive smart antenna of aperiodic arrays with different types of non-uniform spacing may be the direction of future work.

References

1. Godara, L.C.: Application of antenna arrays to mobile communications. Part II: Beam-forming and direction-of-arrival considerations. Proc. IEEE **85**(8), 119–1245 (1997)
2. Balanis, C.A., Bellofiore, S.: Smart antenna system for mobile communication network. Part-1: Overview and antenna design. IEEE Antennas Propag. Mag. **44**(3), 145–154 (2002)
3. Sarkar, T.K., Wicks, M.C., Salazar-Palma, M.: Smart Antenna. Wiley-IEEE Press (2003)
4. Ali, W.A.E., Mohamed, D.A.E., Hassan, A.H.G.: Performance analysis of least mean square and sample matrix inversion algorithms for smart antenna system. In: Loughborough Antennas & Propagation Conference IEEE Xplore, pp. 624–629 (2013)
5. Senapati, A., Roy, J.S.: Adaptive beamforming in smart antenna using Tchebyscheff distribution and variants of least mean square algorithm. J. Eng. Sci. Technol. (JESTEC) **12**(3), 716–724 (2017)
6. Andreasen, M.G.: Linear arrays with variable interelement spacings. IRE Trans. Antennas Propag. **10**(2), 137–143 (1962)
7. Krivosheev, Y.V., Shishlov, A.V., Denisenko, V.V.: Grating lobe suppression in aperiodic phased array antennas composed of periodic subarrays with large element spacing. IEEE Antennas Propag. Mag. **57**(1), 76–85 (2015)
8. Gabrielli, A.H., Fernandez-Figueroa, H.E.: Aperiodic antenna array for secondary lobe suppression. IEEE Photonics Technol. Lett. **28**(2), 209–212 (2016)
9. Ishimaru, A.: Theory of unequally-spaced arrays. IRE Trans. Antennas Propag. **8**(11), 691–702 (1962)

Design of Smart Antenna Using Normalized Leaky LMS and Sign Leaky LMS Algorithms—A Comparative Study

Ritika Sharma, Anupama Senapati and Jibendu Sekhar Roy

Abstract The main component used in the present day cellular network is an adaptive smart antenna, which with the help of a cell site transmit signal in a specific direction reduces undesired interference. In this paper, a sign leaky least mean square (SLLMS) algorithm and normalized leaky least mean square (NLLMS) algorithm is introduced for beam forming in smart antenna. A comparative study is done based on ability to generate main beam towards desire user, to generate null toward interferer, maximum side lobe level (SLL_{max}) and convergence by varying the signal-to-noise ratio (SNR).

Keywords Smart antenna · Beam forming · Least mean square algorithm
Side love level

1 Introduction

The advent and popularity of wireless technology has demanded for a greater bandwidth in order to increase its user base by using a smart antenna [1]. In smart antenna, multiple antennas in array form are used to enhance the orientation of the main beam towards the desired user. The null is aligned towards the interferer and the side lobe level is lowered. Multiple antennas and smart signal processing algorithm permit the smart antenna to carry out the desired actions mentioned above. The smart signal processing algorithm in a smart antenna performs several functions which includes sizing up the spatial signal signature to get the direction of arrival of signal, rectifying

R. Sharma · A. Senapati · J. S. Roy (✉)
School of Electronics Engineering, Kalinga Institute of Industrial Technology (KIIT) Deemed to be University, Bhubaneswar 751024, Odisha, India
e-mail: drjsroy@rediffmail.com

R. Sharma
e-mail: ritika.s0110@gmail.com

A. Senapati
e-mail: senapati.anupama@gmail.com

U. Biswas et al. (eds.), *Advances in Computer, Communication and Control*, Lecture Notes in Networks and Systems 41, https://doi.org/10.1007/978-981-13-3122-0_15

the beam forming vectors which helps in tracking and locating the main beam of the antenna array towards the mobile target [2].

Many beam forming algorithms are available in literature with their advantages and disadvantages. With many schemes of direction of arrival estimations, various methods applicable to adaptive beam forming have been described in [3]. For multilobe pattern and adaptive nulling, a sequential quadratic programming based algorithm is used in [4]. Hybridization of soft computing methods used for beam forming is reported in [5]. Beam forming of polarization-sensitive electromagnetic vector-sensor is done using a complex quaternion LMS algorithm [6]. A comparative study on beam formation using least mean square (LMS) algorithm and recursive least square algorithm (RLS) is reported in [7]. A constrained LMS algorithm is used for adaptive beam forming using perturbation sequences [8]. Report on beam formation in adaptive smart antenna using LLMS algorithm is relatively less.

In this paper, beam forming for smart antenna using sign leaky LMS algorithm and normalized leaky LMS is done. Analysis of beam forming is done based on main beam direction, null direction, maximum side lobe level, and convergence by varying the signal to noise ratio for different numbers of antenna elements in the array.

2 Variants of Leaky Least Mean Square Algorithm

One of the most commonly used variant of least mean square (LMS) algorithm is leaky least mean square (LLMS) algorithm. In leaky least mean square algorithm, a leak factor is introduced to overcome the slow convergence of LMS algorithm in case of high value eigen spread [9]. The leak factor (ψ) has been mentioned in the weight update equation to solve the drifting problem which occurs in LMS algorithm by bounding the parameter estimate [9]. The leak factor also improves the capability, convergence and stability of LMS algorithm [10].

In Fig. 1, the LLMS adaptive algorithm is used to minimize the error e(n) between desired signal d(n) and array output y(n), [9]

$$e(n) = d(n) - y(n). \tag{1}$$

Weight updating equation using LLMS algorithm at 'n'th iteration is given by [9]

$$w(n+1) = (1 - 2\mu\psi) * w(n) + \mu * e(n) * x(n). \tag{2}$$

where μ is the step size parameter, is the leak factor, w(n) is the filter coefficients vector, and x(n) is received signal. When = 0, the leaky LMS algorithm will be equal to standard LMS algorithm.

In signed leaky LMS, the polarity of the error or data or both is used for error updation. Also a leak factor (ψ) is present to minimize the cost function. Referring to weight updating equation for sign LMS in [11], the weight update equation for signed leaky LMS algorithm is

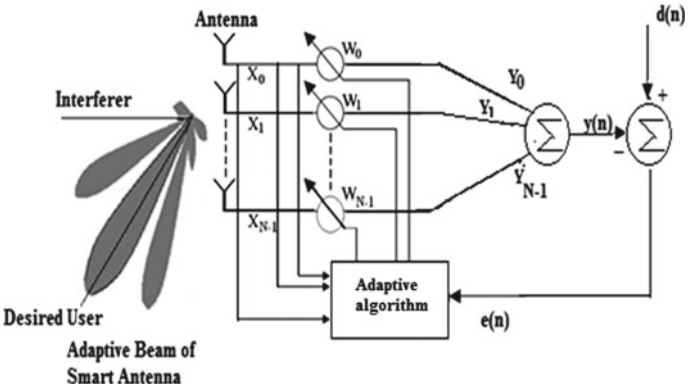

Fig. 1 Adaptive beam forming system with N antenna elements

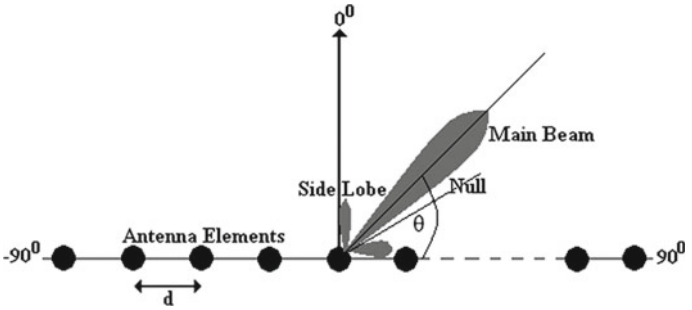

Fig. 2 Uniform linear array (ULA) configuration of isotropic elements

$$w(n+1) = (1 - 2\mu\psi) * w(n) + \mu * e(n) * \mathrm{sgn}(x) \tag{3}$$

where μ is the step size parameter, is the leak factor, w(n) is the filter coefficients vector, and x(n) is the received signal.

In normalized leaky LMS algorithm, the step size is divided by the norm of the input signal to avoid gradient noise amplification due to x(n). Referring to weight updating equation for normalized LMS in [10], the weight update equation for normalized leaky LMS algorithm is

$$w(n+1) = (1 - 2\mu\psi) * w(n) + \frac{\mu * e(n) * x(n)}{x(n) * x(n)}. \tag{4}$$

where μ is the step size, ψ is the leak factor, e(n) is the error signal and, w(n) is the filter coefficients vector, and x(n) is filter input vector (Fig. 2).

Array factor (AF) of N elements uniform linear antenna array is expressed as [8]

$$AF = \sum_{n=0}^{N-1} A_n e^{(jn(\frac{2\pi d}{\lambda} \sin\theta + \alpha))} \tag{5}$$

where to generate the main beam at wavelength λ toward the desired beam direction from the broadside direction, the progressive phase shift is

$$\alpha = -\frac{2\pi d}{\lambda} \sin\theta_0 \tag{6}$$

Normalized array factor is

$$AF_{norm} = \frac{AF}{AF\max} \tag{7}$$

3 Simulation Results

Simulations are done using MATLAB for ULA with inter-element spacing of 0.5λ for 10 and 40 antenna elements with varying SNR. Programs are run for 100 iterations with step size of 0.02 and leak factor of 0.001. Desired user is at 20° and interferer is at 30°. Figures 3, 4, 5, and 6 show normalized array factor plot with varying SNR value using SLLMS and NLLMS algorithm for 10 and 40 number of antenna elements respectively.

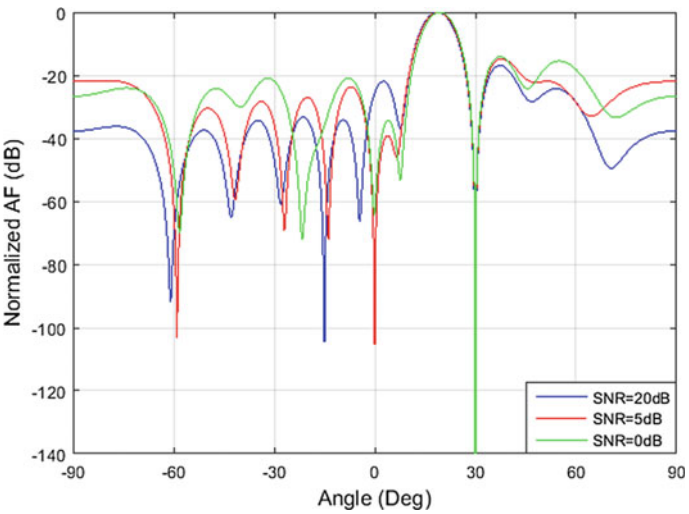

Fig. 3 Normalized array factor plot using SLLMS algorithm with N = 10

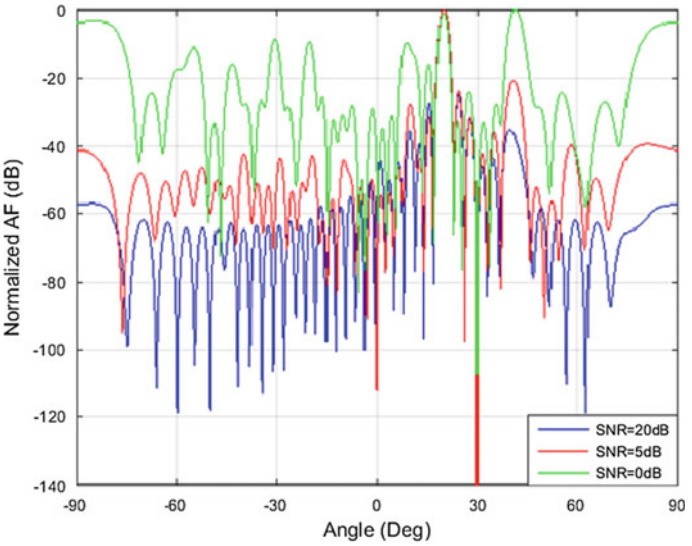

Fig. 4 Normalized array factor plot using SLLMS algorithm with N = 40

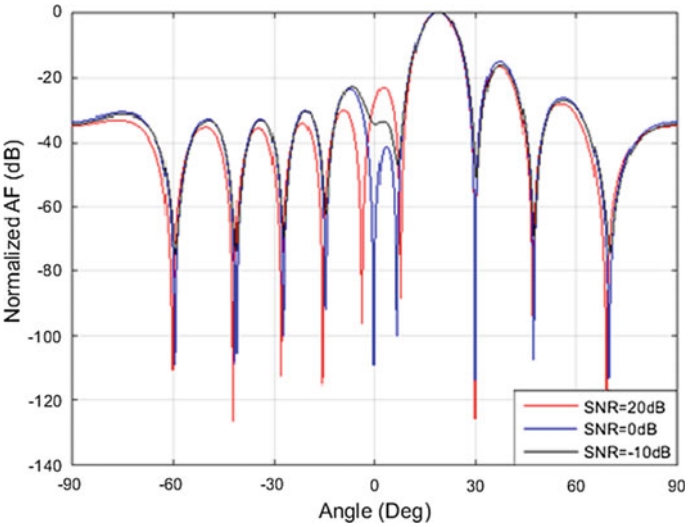

Fig. 5 Normalized AF plot using NLLMS algorithm with N = 10

For SNR, 0 dB grating lobe appears and desired beam forming is not achieved for SNR below 0 dB using SLLMS algorithm. But better beam forming is achieved using NLLMS for SNR below 0 dB. NLLMS algorithm cannot be used for beam forming for SNR below −10 dB.

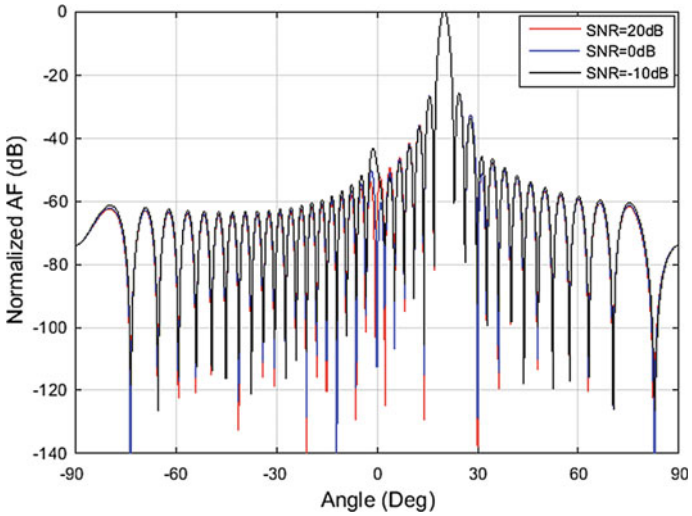

Fig. 6 Normalized array factor plot using NLLMS algorithm with N = 40

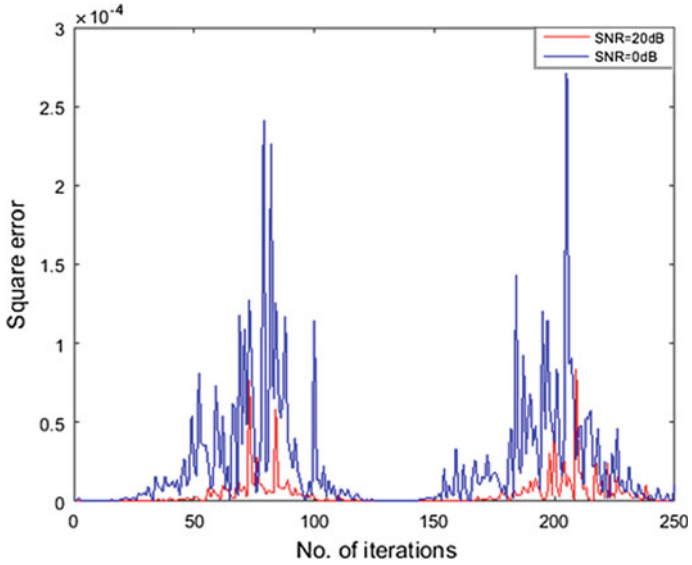

Fig. 7 Square error plot using SLLMS algorithm with N = 10 for SNR = 20 dB, 0 dB

Figures 7, 8, 9 and 10 show square error plot with varying SNR value using SLLMS and NLLMS algorithm for 10 and 40 number of antenna elements respectively.

Square error decreases with increase in SNR value. Figures 11 and 12 shows SNR versus SLL_{max} plot using SLLMS and NLLMS algorithm.

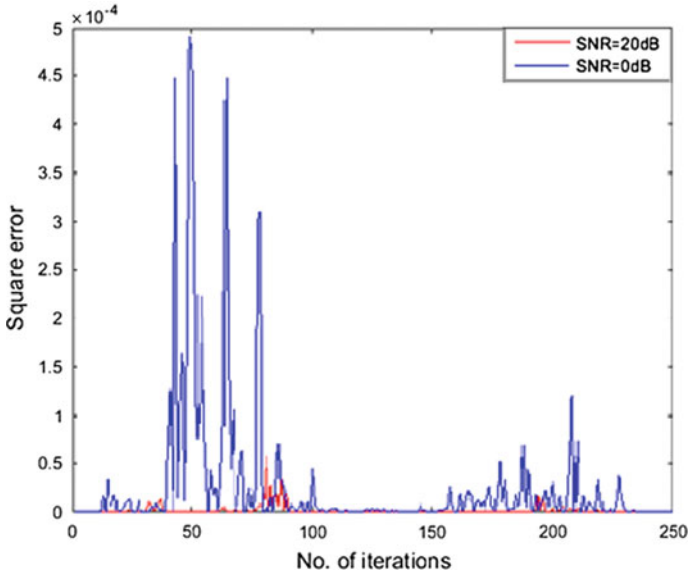

Fig. 8 Square error plot using SLLMS algorithm with N = 40 for SNR = 20 dB, 0 dB

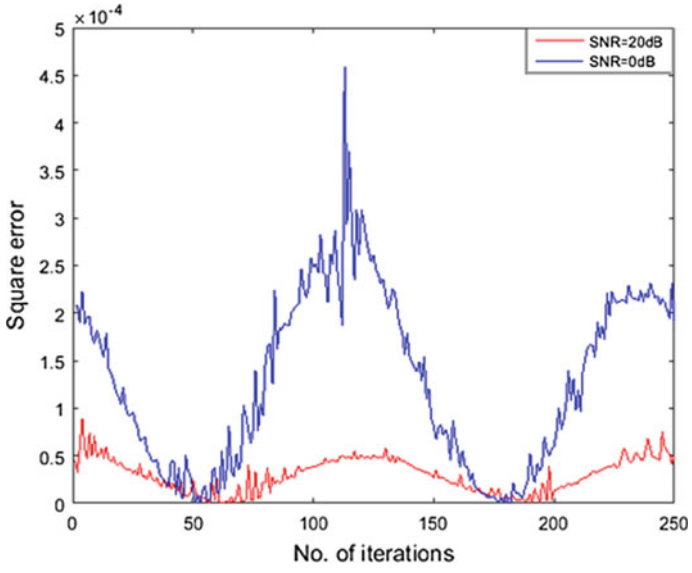

Fig. 9 Square error plot using NLLMS algorithm with N = 10 for SNR = 20 dB, 0 dB

Side lobe level decreases with increased antenna elements. Simulated results are compared in Tables 1 and 2.

Table 1 Comparison of SLLMS and NLLMS algorithm for different SNR (N = 10)

Algorithm	SNR (dB)	Main beam (degree)	Null (degree)	SLL_{max} (dB)	FNBW (degree)
SLLMS	20	18.6	30	−16.9	22.4
	15	18.8	30	−15.52	22
	10	18.8	30	−14.59	22.2
	5	19	30	−14.8	23.4
	0	19.4	30	−14.25	22.2
	−3	Not working	Not working	Not working	Not working
	−8	Not working	Not working	Not working	Not working
	−10	Not working	Not working	Not working	Not working
NLLMS	20	18.8	30	−16.93	22.2
	10	19	30	−16.28	22.6
	5	19	30	−15.45	23.4
	0	19	30	−15.35	23.4
	−3	19	30	−15.53	23.4
	−8	19.2	30	−16.84	23
	−10	19.8	30	−16.42	22

Table 2 Comparison of SLLMS and NLLMS algorithm for different SNR (N = 40)

Algorithm	SNR (dB)	Main beam (degree)	Null (degree)	SLL_{max} (dB)	FNBW (degree)
SLLMS	20	20	30	−25.31	6
	15	20	30	−25.02	6
	10	20	30	−25.63	6
	5	20	30	−21.07	6
	0	Not working	Not working	Not working	Not working
	−3	Not working	Not working	Not working	Not working
	−8	Not working	Not working	Not working	Not working
	−10	Not working	Not working	Not working	Not working
NLLMS	20	20	30	−26.05	6
	10	20	30	−26.05	6
	5	20	30	−26.05	6
	0	20	30	−26.05	6
	−3	20	30	−26.05	6
	−8	20	30	−26.05	6
	−10	20	30	−26.05	6

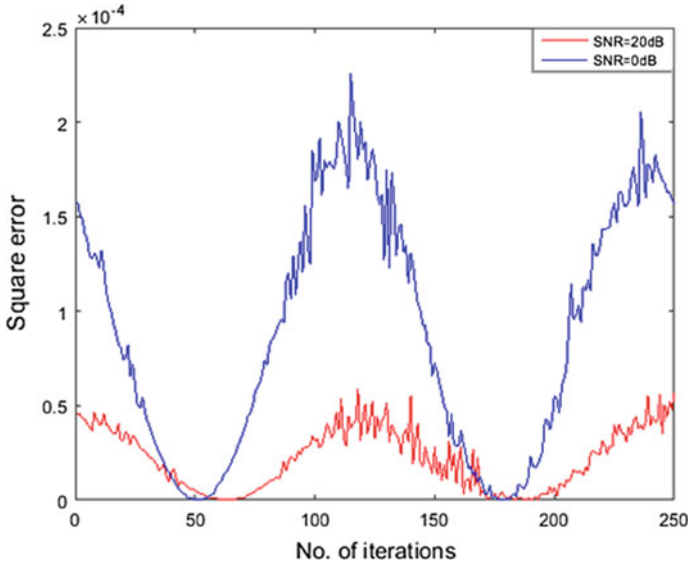

Fig. 10 Square error plot using NLLMS algorithm with N = 40

Fig. 11 SNR v/s SLL_{max} plot using SLLMS algorithm

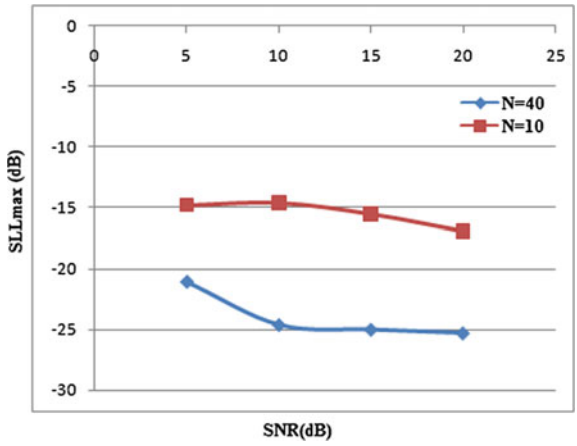

4 Conclusion

In this paper, a comparative analysis, based on adaptive beam forming, is done between two variants of leaky LMS algorithm, sign leaky LMS and normalized leaky LMS algorithm. Analysis is done by varying the SNR value and number of antenna elements used. The accuracy of the main beam increased for more number of antenna elements with the reduction of SLL_{max}. NLLMS is working for low SNR, i.e., 0 dB and less whereas SLLMS ceased to work for SNR values less than 0 dB.

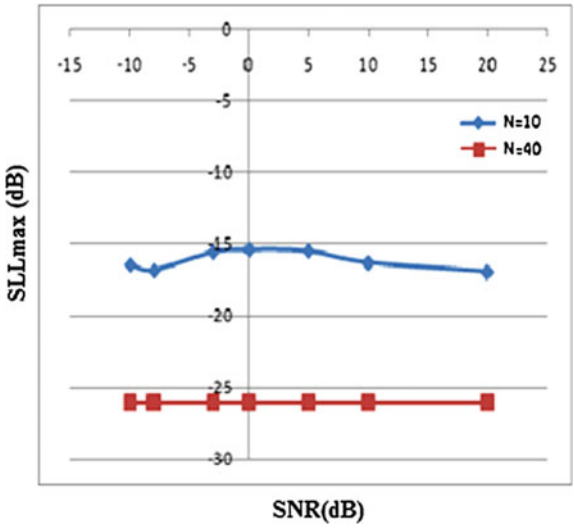

Fig. 12 SNR v/s SLL_{max} plot using NLLMS algorithm

With the reduction in SNR value, there is a subsequent increase in square error. The SLLMS algorithm converges better with more number of antenna elements and also its convergence is better than NLLMS. SLL_{max} for NLLMS is less with respect to SLLMS algorithm.

References

1. Herscovici, N., Chirstodoulou, C., Chryssomallis, M.: Smart antennas. IEEE Antennas Propag. Mag. **42**(3), 129–136 (2000)
2. Gross, F.: Smart Antenna for Wireless Communication. McGraw-Hill (2005)
3. Godara, L.C.: Application of antenna arrays to mobile communications. Part II: Beam-forming and direction-of-arrival considerations. Proc. IEEE **85**(8), 1195–1245 (1997)
4. Rao, A.P., Sarma, N.V.S.N.: Adaptive beamforming algorithms for smart antenna systems. WSEAS Trans. Commun. **13**, 44–50 (2014)
5. Basha, T.S.G., Sridevi, P.V., GiriPrasad, M.N.: Beam forming in smart antenna with precise direction of arrival estimation using MUSIC algorithm. Wirel. Pers. Commun. **71**(2), 1353–1364 (2013)
6. Tao, J.W., Chang, W.X.: Adaptive beamforming based on complex quaternion processes. Math. Probl. Eng. Hindawi **2014**, 1–10 (2014)
7. Sarkar, T.K., Wicks, M.C., Palma, S., Bonneau, R.J.,: Smart Antennas. Wiley-IEEE Press (2003)
8. Wang, H., Zhang, Z., Li, Y., Feng, Z.: Improved main-beam nulling through single switchable displaced element for small scale adaptive array. IEEE Trans. Antenna Propag. **62**(5), 2522–2530 (2014)
9. Kamenetsky, M., Widrow, B.: A variable leaky LMS adaptive algorithm. In: Thirty-Eighth Asilomar Conference on Signals, Systems and Computers, pp. 125–128 (2004)

10. Senapati, A., Ghatak, K., Roy, J.S.: A Comparative study of adaptive beamforming techniques in smart antenna using LMS algorithm and its variants. In: International Conference on Computational Intelligence and Networks, pp. 58–62 (2015)
11. Wang, W., Zhao, H.: Diffusion signed LMS algorithms and their performance analysis for cyclostationary white Gaussian inputs. IEEE Access **5**, 18876–18894 (2017)
12. Sowjanva, M., Sahoo, A.K., Kumar, S.: Distributed incremental Leaky LMS. In: International Conference on Communications and Signal Processing, pp. 1753–1757 (2015)
13. Bellofiore, S., Balanis, C.A., Foutz, J., Spanias, A.S.: Smart-antenna systems for mobile communication network. Part I: Overview and antenna design. IEEE Antennas Propag. Mag. **44**(3), 145–154 (2002)

Low-Power Subthreshold Adiabatic Logic for Combinational and Sequential Circuits

Ruchi Yadav and Amit Bakshi

Abstract The foremost idea dominating the ongoing trends in VLSI circuits is to offer large-scale integration coupled with extensive power reduction solutions. This significant increase in the gate switching energy has resulted in higher power decadence and a costly replacement of heat sinks. At such places to limit the dissolution of power, elective arrangements at various levels of contemplation are suggested. This power dissipation is significantly minimized by the adiabatic logic structure at the cost of circuit complexity to accomplish minimal power dissipation. A brief approach of the aforementioned is included in this paper introducing the adiabatic logic family SAL. The implementation of the 4-bit CLA and 2×1 multiplexer combinational circuit and the sequential circuit of D flip-flop using NAND gates validates the credibility of the logic. A graph has been plotted to show the effect of temperature on subthreshold adiabatic logic-based 4-bit CLA. It aims at comparing the effectiveness of adiabatic logic with respect to power dissipation and delay. The setup and hold time graphs for sequential circuits have been plotted, respectively. The simulation results obtained from the virtuoso environment of cadence tool suggest commendable threefold power reduction in the SAL topology as compared to the conventional adiabatic topology.

Keywords Adiabatic logic · SAL · Low power · Energy restoration · NAND Power dissipation

R. Yadav (✉) · A. Bakshi
School of Electronics Engineering, Kalinga Institute of Industrial Technology (KIIT) Deemed to be University, Bhubaneswar, Odisha 751024, India
e-mail: ruchiyadav616@gmail.com

A. Bakshi
e-mail: abakshi.ece@gmail.com

U. Biswas et al. (eds.), *Advances in Computer, Communication and Control*, Lecture Notes in Networks and Systems 41, https://doi.org/10.1007/978-981-13-3122-0_16

1 Introduction

The CMOS technology prominence can mainly be accredited to naturally low-power dissipation and comparatively higher level of integration. Nonetheless, the researchers are curious and are searching for techniques to reprocess the energy from circuits because of the recent inclination toward ultralow power domain. Nearly, the beginning researchers used to generally focus on prospect of processing physical machines that almost consumed zero energy in the computation process and the lower bound of the energy consumed was tried to estimate [1]. The voltage swing at every switching occasion causes an energy exchange starting from the power supply to the present node at the output or else from the output node to ground. Amid for a 0 to VDD change of the output, the aggregate output charge $Q = C_{load}$. V_{dd} is drawn at a steady voltage from the power supply provided. Subsequently, during this change, $E_{supply} = 1/2\ CV_{dd}^2$ is drawn from the supply [2]. Now when the output node capacitance is charged to the voltage level $-V_{dd}$ the V_{dd} n it indicates toward the finish of the charge and the measure of the stored energy in the output node Estored = $1/2\ CV_{dd}^2$. The energy that has been injected from the power supply is distributed in two halves: one half is sent to the output node, while the other half is conveyed to the PMOS. To diminish the power dissipation, the switching events can be limited by the circuit designer; the node capacitance can in the long run be decreased, voltage swing can be lessened to a specific level, and blend of these techniques can be connected [3]. So far, in each one of these cases, the energy that has been received from the supplied power has been utilized just once (Fig. 1).

Now different steps can be presented for reusing the energy drawn from the supply that would help to build energy-effective logic circuits [4]. Adiabatic logic is an alternate class of logic circuits which presents the likelihood of lessening the dissipation of energy amid the switching events, and the likelihood of reprocessing, a portion of the energy that is received from the respective supply. To achieve the mentioned objective, the topology of circuit and the standards of working must be changed a bit, or now and then profoundly [5]. The measure of energy reusing is additionally conceivable by utilizing techniques of adiabatic logic and also dogged by the technology of fabrication, switching speed, and the voltage swing.

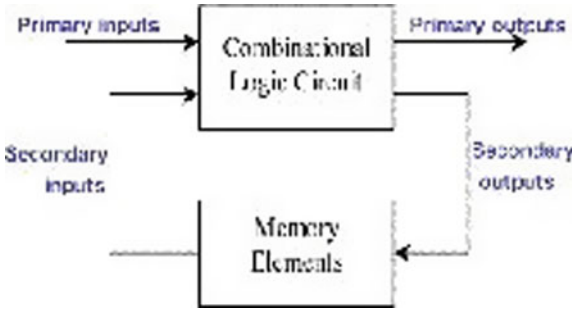

Fig. 1 Block diagram of logic circuit design

2 Related Work

Adiabatic logic is essentially an elective way to deal with low-power operation circuits which proposes the reliance of adiabatic logic circuits on the control or power clock and a few other parameters. This logic can be utilized for the execution of some complicated circuits that dissipate less energy when contrasted with regular CMOS circuits. SAL shows significant upgrades as far as factors like switching characteristics and energy saving are concerned. The demerit that subthreshold adiabatic logic has is that it requires higher supply voltage and speed of operation is low. Several papers have analyzed the power clock generation and energy performance of adiabatic logic families. This logic can be used for execution of some moderately vast, complicated sequential circuits and flip-flops that have been proposed in several papers. It also uses lesser number of transistors when compared to other adiabatic logic. Power clock of single phase is used, which is operated at low supply voltage, and hence it scatters less energy when compared to the conventional CMOS circuits.

3 Logic Design and Implementation

3.1 Implementation of Sequential Circuit Using Adiabatic Logic

The study and design of D flip-flop using SAL logic is presented here to spot out the expediency and consequently the practicability of the suggested logic [6]. While checking the logical practicality, cell library associated with SAL has been resolved that has the basic digital NAND gate; here, 2-input or 3-input NAND gates are used for the implementation of D flip-flop [3]. The logic structures in SAL are implemented by either the pull-up or pull-down network of the conventional CMOS logic. The number of transistors in SAL logic is reduced by a factor of 2 when compared to CMOS logic [7–10]. For designing D flip-flop using SAL logic, profound information regarding parameters like leakage current, power gain, voltage swing variations, etc. are required [3] (Fig. 2).

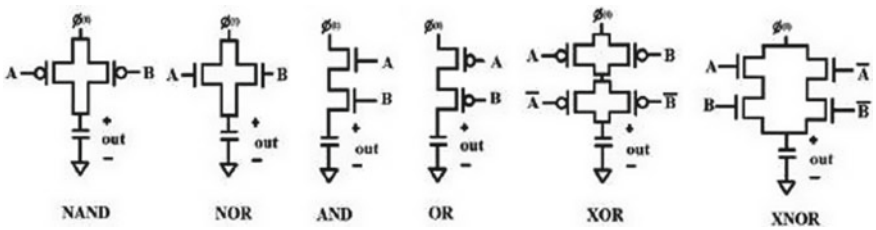

Fig. 2 Basic logic gate design by SAL

MOSFET current in subthreshold regime is modeled by

$$I_0 = 2\eta_p \mu_p C_{ox}(W/L)V_T \tag{1}$$

where η_p is the slope factor of subthreshold,
μ_p is the PMOS device's mobility,
V_T (kT/q) is the thermal voltage.

$$V_{TH}^{[\delta]} = V_{TO} - \gamma V_{SB} - \eta V_{SD}. \tag{2}$$

$\eta = 1/2\cos h(C_{eff}/2l_t)$ which is DIBL coefficient where $l_t = (\in_{si} T_{ox} X_{dep} \beta_{ox})^{1/2}$ (Figs. 3 and 4).

3.2 SAL Full Adder Design

The *i*th sum and i + 1th carry can be given as (Figs. 5 and 6)

$$Si^{[6]} = Ai \oplus Bi \oplus Ci \tag{3}$$

$$Ci + 1^{[6]} = AiBi + (Ai \oplus Bi)Ci \tag{4}$$

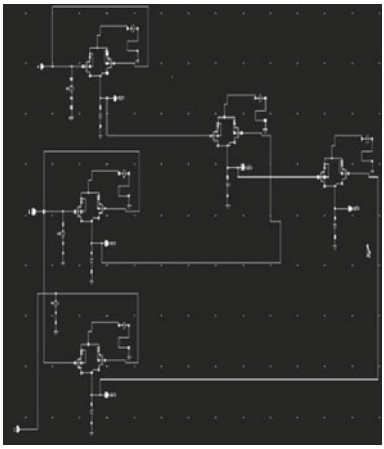

Fig. 3 D flip-flop schematic by SAL using NAND 3 gates

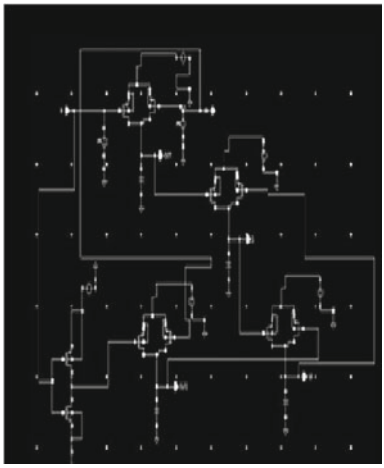

Fig. 4 D flip-flop design by SAL using NAND 2 gates

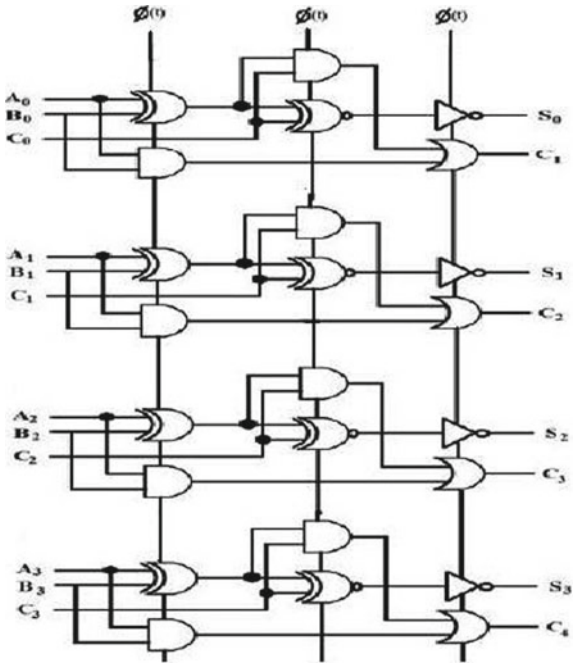

Fig. 5 4 bit CLA by SAL

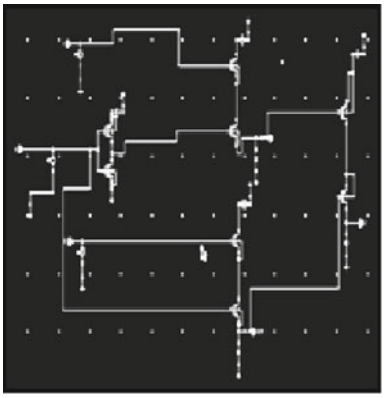

Fig. 6 Logic design of 2 × 1 MUX using SAL

4 Analysis and Evaluation

NAND logic with two input gates has been utilized to plan a D flip-flop which has two data sources D and a clock pulse and the respective outputs are named as Q and Qbar. Presently, NAND logic with three sources of input has been utilized to plan a D flip-flop which has contributions as Preset, Clear, D, and clock pulse individually. Combinational circuits and flip-flops are utilized for the outline of a few sequential circuits. The aggregate number of transistors utilized is nearly less and the power expended can be named as the summation of the power consumed by sequential circuits, the power that has been used up in clock circulation and the power consumed by flip-flops.

Further, the parametric examination for setup time from 0.05 to 0.5 ns has been done and the parametric investigation for hold time from 0.25 to 0.5 ns has additionally been performed. For acquiring full yield swing, the cross-coupled transistors are utilized as a part of the recuperation and pre-charge period of exchanging process [2]. The amount of energy loss can be given as $E = C|V_{tp}|^2/2$ (Figs. 7, 8, and 9).

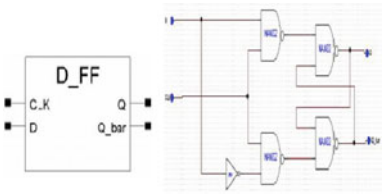

Fig. 7 Logic design and schematic using NAND 2

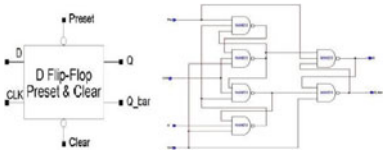

Fig. 8 Logic design and schematic using NAND 3

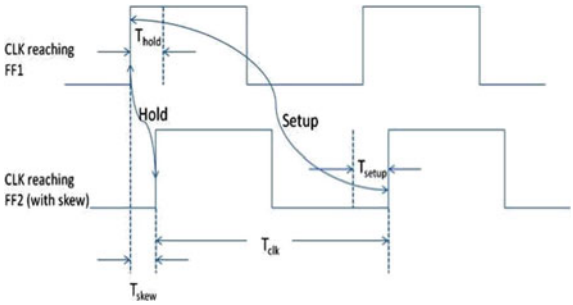

Fig. 9 Setup and hold timing diagram

5 Simulation Results

The above plot demonstrates that there is a close direct increment in power dissipation as the temperature is shifted from 20 to 80 °C. A 50 °C temperature variation brings about a five times increment in power dissipation with the power dispersal at 0 °C as standard reference. The SAL–CLA is not abundantly influenced by voltage corruption when the temperature is shifted from −20 to 80 °C run. Impact of temperature variation in subthreshold logic essentially goes for bringing down the power utilization. If there should be an occurrence of temperature varieties, subthreshold current will fluctuate because of its exponential connection with temperature (Figs. 10, 11, 12, 13, 14, 15, 16, and 17).

The above plot demonstrates the parametric examination for setup time from 0.05 to 0.5 ns and for hold time from −0.25 to 0.5 ns, the progression measure being 20. Flip-flop has a locking circuit that goes about as a consecutive inverter. If logic low is 0 V and logic high is 1.8 V, then if some other value other than the correct estimations of low logic or high logic is given, it might play out some latch cycles and after that it gives a totally inverted output (Tables 1, 2 and 3; Figs. 18, 19 and 20).

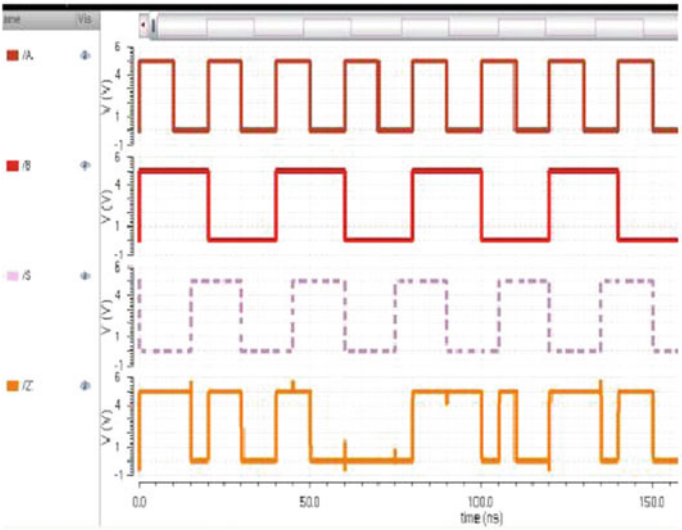

Fig. 10 Result of 2:1 MUX using SAL logic bit

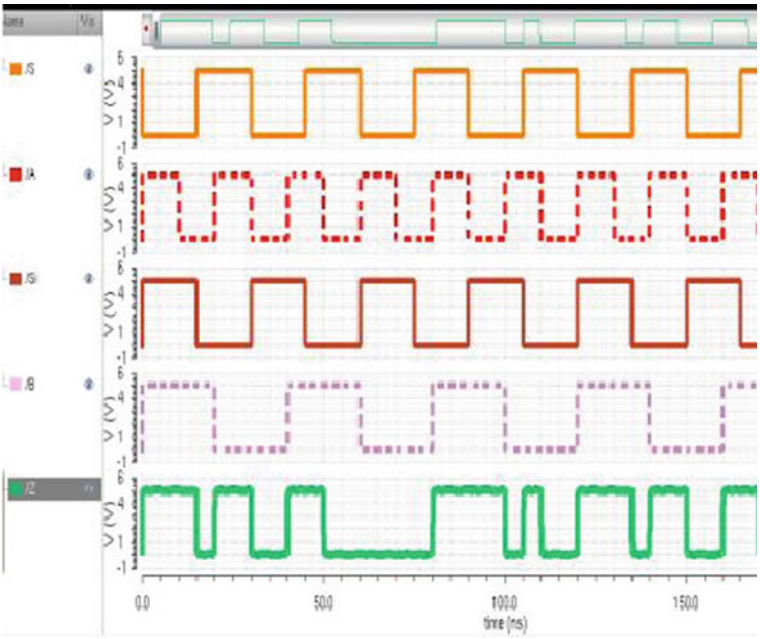

Fig. 11 Simulation result of 4 CLA using SAL

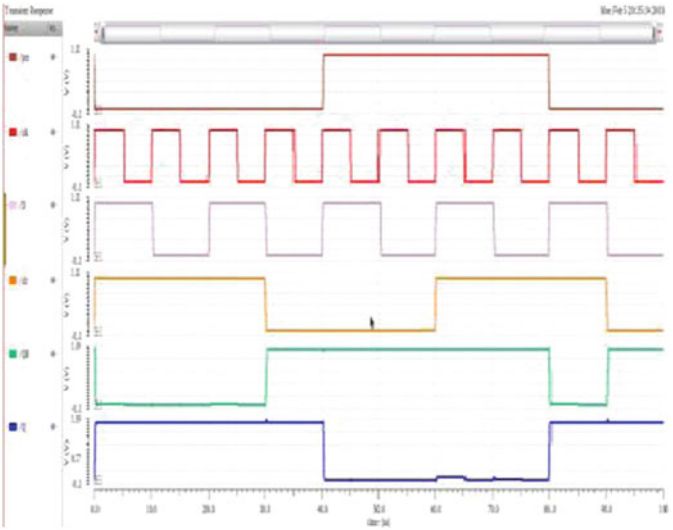

Fig. 12 Simulation result of delay flip-flop using conventional adiabatic logic

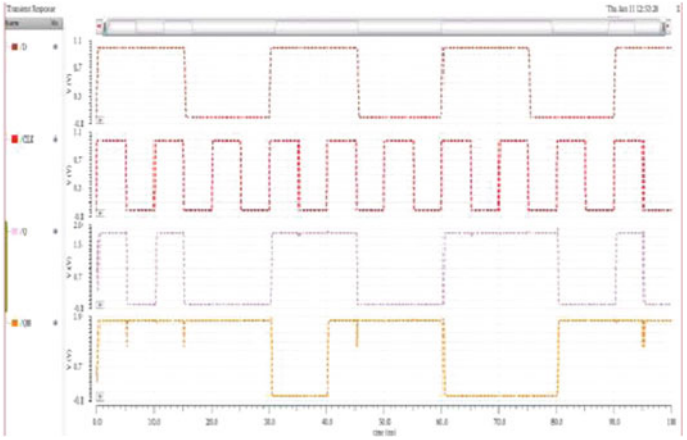

Fig. 13 Simulation result of delay flip-flop using SAL (NAND 2)

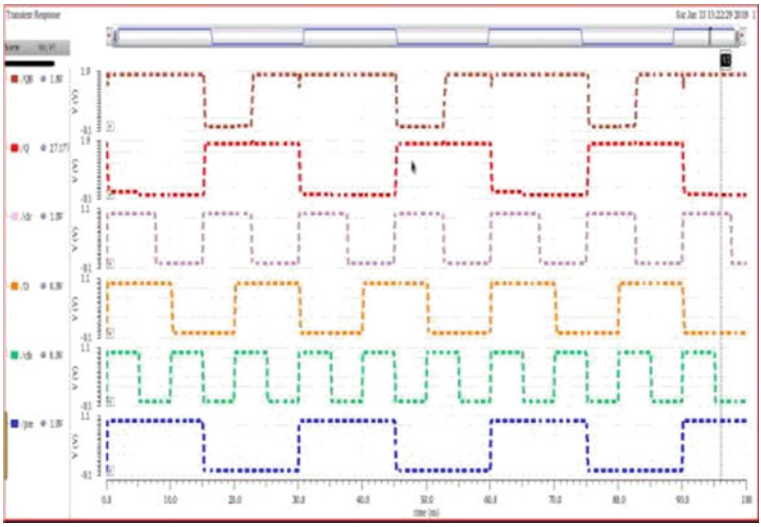

Fig. 14 Simulation result of delay flip-flop using SAL (NAND 3)

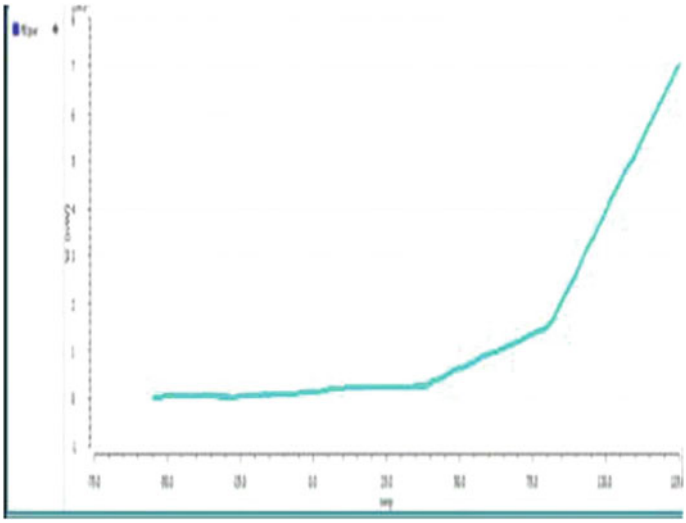

Fig. 15 Temperature versus power dissipation plot for 4-bit CLA

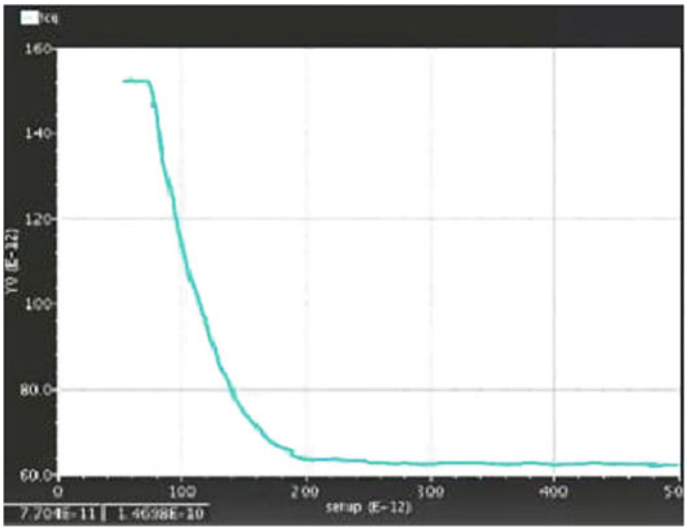

Fig. 16 Setup time graph

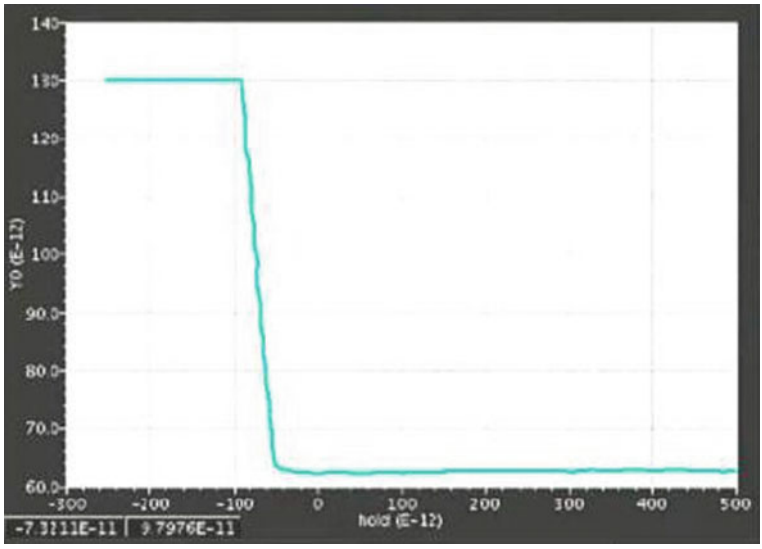

Fig. 17 Hold time graph

Table 1 Design specifications

Specifications	Values
Technology	180 nm
PMOS transistor width	800 nm
NMOS transistor width	400 nm
PMOS transistor length	180 nm
NMOS transistor length	180 nm
Power supply	1.8 V

Table 2 Comparison of power dissipation among various logic styles

Logic cell	DFF (conv. AL)	DFF using NAND 2 (SAL)	DFF using NAND 3 (SAL)	2 × 1 MUX (SAL)	4-bit CLA (SAL)
Transistor count	20	10	18	8	24
Rise time (ps)	10	10	10	10	10
Fall time (ps)	10	10	10	10	10
Delay (ns)	18.68	5.74	6.06	7.98	10.03
P_{total} (μW)	11.89	2.72	5.63	2.75	6.19
$P_{dynamic}$ (μW)	4.23	1.75	2.67	2.61	4.72
P_{static} (μW)	1.27	0.37	1.35	3.27	5.8

Table 3 Simulated results are compared with other published results

Logic cell	Technology used	Frequency (MHz)	Power dissipation (μW)
Ref. [11]. (D flip-flop-CMOS)	90 nm at 1 V	100	11.19761
Presented method (SAL DFF)	180 nm at 1.8 V	100	2.72
Ref. [12]. (full adder)	180 nm at 1.8 V	100	8.30
SAL (4-bit CLA)	180 nm at 1.8 V	100	6.19
Ref. [12]. (2 × 1 MUX)	180 nm at 1.8 V	100	4.66
SAL (2 × 1 MUX)	180 nm at 1.8 V	100	2.75

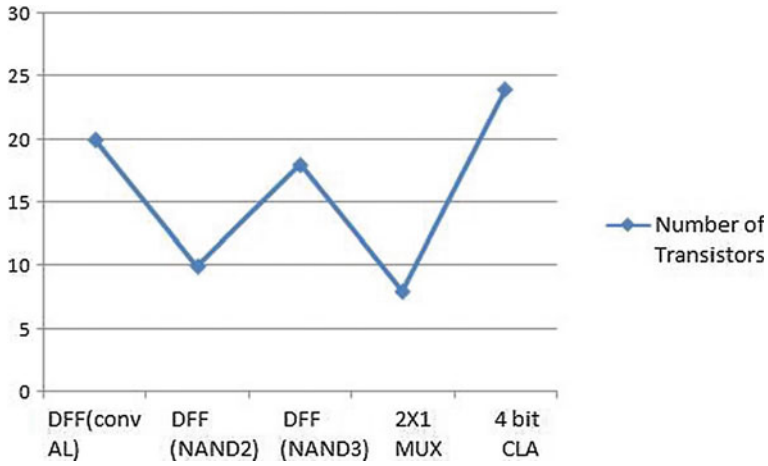

Fig. 18 Plot representing the number of transistors used in different logic designs

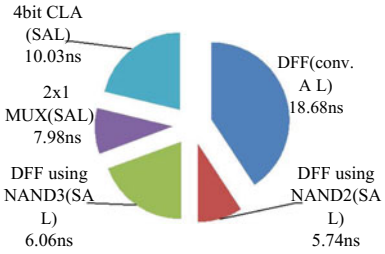

Fig. 19 Chart representing delay in various logic designs

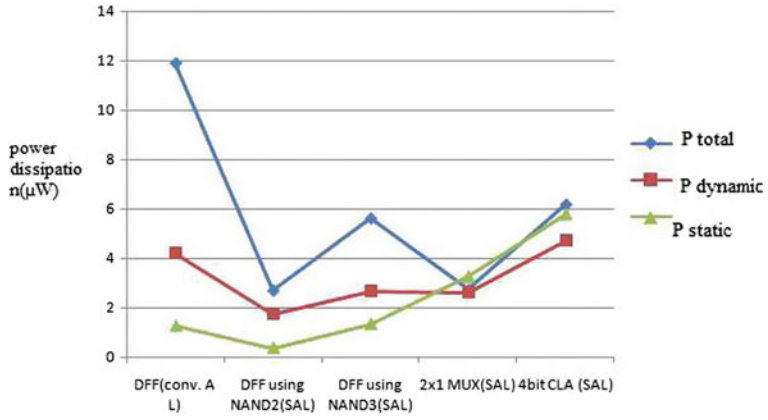

Fig. 20 Power comparison of various logic designs

6 Conclusion

In this paper, an analysis on subthreshold adiabatic logic has been done and the mentioned adiabatic logic has been implemented in combinational and sequential circuits. In accordance with the simulation results, SAL dissipates 60% less power when compared with the conventional logic style and the number of transistors used is comparatively less. The temperature Vs power dissipation graph that has been plotted for 4-bit CLA designed using SAL logic shows that in case of temperature variations, subthreshold current will vary due to its exponential relation with temperature. The setup and hold time graphs are plotted with their values when calculated are 174 ps and 97 ps respectively. The delay time and power dissipation values have been analyzed and evaluated for each logic design.

References

1. Maurya, A.K., Kumar, G.: Adiabatic logic: energy efficient technique for VLSI applications. In: International Conference on Computer and Communication Technology (ICCCT), pp. 234–238. IEEE (2011)
2. Kalyani, P., Kumar, P.S., Chandrashekhar, P.: Energy efficient logic gates using subthreshold adiabatic logic. In: IEEE International Conference on Electronics and Communication Systems (2015)
3. Chanda, M., Jain, S., Sarkar, C.K.: Implementation of subthreshold adiabatic logic for ultralow-power application. IEEE **23**(12) (2015)
4. Athas, W.C., Svensson, L.J.: Low power digital system based on adiabatic-switching principles. IEEE Trans. VLSI Syst. **2**(4), 398–407 (1994)
5. Mishra, A., Singh, N.: Low power design using positive feedback adiabatic logic (PFAL). Int. J. Sci. Res. **3**(6) (2014)
6. Kanungo, J., Dasgupta, S.: Performance analysis of a complete adiabatic logic system driven by the proposed power clock generator. IOPscience **35**(9) (2014)
7. Soeleman, H., Roy, K., Paul, B.C.: Robust subthreshold logic for ultra-low power operation. IEEE Trans. Very Large Scale Integr. (VLSI) Syst. **9**(1), 90–99 (2001)
8. Wang, A., Calhoun, B.H., Chandrakasan, A.P.: Sub-Threshold Design for Ultra Low-Power Systems. Springer, New York, NY, USA (2006)
9. Calhoun, B.H., Chandrakasan, A.P.: Static noise margin variation for sub-threshold SRAM in 65-nm CMOS. IEEE J. Solid-State Circuits **41**(7), 1673–1679 (2006)
10. Narendra, S.G., Chandrakasan, A.: Leakage in Nanometer CMOS Technologies. Springer, New York, NY, USA (2006)
11. Ojha, P., Rana, C.: Design of low power sequential circuit by using adiabatic techniques. Int. J. Intell. Syst. Appl. **08**, 45–50 (2015). https://doi.org/10.5815/ijisa.2015.08.06
12. Bhati, P., Rizvi, N.Z.: Adiabatic logic: an alternative approach to low power application circuits. In: International Conference on Electrical, Electronics, and Optimization Techniques (ICEEOT) (2016)
13. Kumar, C.P., Tripathy, S.K., Tripathi, R.: High performance sequential circuits with adiabatic complementary pass-transistor logic (ACPL). In: TENCON, pp. 1–4. IEEE (2009)

A Survey Report on the Electrical Installations Adopted by the Traditional Tea Factories in North Bengal

Arkabrata Dattaroy, Ankit Chakraborty, Swarnendu Mandal and Santanu Das

Abstract Tea industry, the Queen of North Bengal has accelerated downhill lately, owing to inefficient machineries. This survey pivots over Chronological Conditional Load Monitoring of the electrical machineries under CTC (Cutting, Tearing & Curling) texture, considering widely varying conditions, namely three types of tea leaves: Hard, Medium and Soft, as well as seasonal variation between Summer (July) and Monsoon (September). The entire load distribution of surveyed factory has been monitored, noted and analyzed. Developed Power Layout Diagram and associated survey data with extensive analyses have also been reported here. Based on the conducted survey reports and analyses, possible scopes of improvement of energy consumption and subsequent implementation schemes have been proposed in this report.

Keywords Energy efficiency · Loading percentage · Power factor
Reactive power

1 Introduction

Tea has been "The Beverage of the Masses" in India since time immemorial. Tea industry is the backbone of earning FOR-EX (Foreign Exchange) on behalf of North Bengal, especially in the Darjeeling Hills and the Dooars [1]. However, the major

A. Dattaroy (✉) · A. Chakraborty · S. Mandal · S. Das
Department of Electrical Engineering, Jalpaiguri Government Engineering College, Jalpaiguri 735102, West Bengal, India
e-mail: arkabratadattaroy@gmail.com

A. Chakraborty
e-mail: ankitskyblue@gmail.com

S. Mandal
e-mail: swarnendu146@gmail.com

S. Das
e-mail: santanu.ddas@gmail.com

U. Biswas et al. (eds.), *Advances in Computer, Communication and Control*, Lecture Notes in Networks and Systems 41, https://doi.org/10.1007/978-981-13-3122-0_17

technical issues (electrical) that lie beyond the unfortunate rapid shutdowns lately and deteriorations in the profitability of these tea factories, mainly the load monitoring and efficiency issues, are addressed in this project.

The major technical reasons leading to the downfall of late can be initially ascertained to be the inefficient and poor power factor operation of the electrical machineries, and their relative effects are quantified and referenced in this project.

2 Objectives of the Survey

- Detailed survey and Load monitoring of the tea factory:
  - (a) Graphical approach with respect to time.
  - (b) Comparison of calculated and measured values.
  - (c) Determining optimal size and capability of the machines.
- Power Flow analysis
  - (a) Traditional installations.
  - (b) Active and reactive power calculations.
- Loading percentage calculations
  - (a) Present loading percentage for the CTC Motors.
  - (b) Attempts at improvement of loading percentage and their effects on power flow, without hampering productivity and employment.

3 Survey Details

The survey details as obtained on cumulative data collection have been depicted below with the help of a sample tea factory reference.

3.1 Sample Tea Factory Courtesy

Name and Address of the factory: Bikram Tea Factory,
CTC Units,
Assam More,
Jalpaiguri,
West Bengal, India.

3.2 Machineries and Outline of Operation

The electrical supply of the tea factory is catered to with the help of an incoming WBSEDCL (West Bengal State Electricity Distribution Corporation Ltd.) 11 kV feeder via HT (High Tension) valley, switchgear, a 500 KVA step down 11 kV/440 V, Star-Delta transformer and a charging Diesel Generator set of capacity 250 KVA. The connections to the panel room are via underground cables. The panel room consists of three panels-CTC *(Cutting, Tearing & Curling)* Main Panel, Change-Over Panel and Auxiliary Panels. The Main Panel has capacitor banks installed in delta to have Power Factor Correction (PFC).

Induction motors play the pivotal role in the CTC section of the industry. There are 3 sections of CTC Rows in the factory, out of which only 2 rows can be active at a time. The raw tea leaves start their journey via the path-Trough (where they are collected and dried via fans), Monorails and thereafter into the Rotor vane of each of the 3 rows of CTC, with the help of which they are dried and cut preliminarily. Thereafter, they continue their journey via the CTC rows for CTC Operation, with each row having 4 *Cuts*-1st Cut, 2nd Cut, 3rd Cut and the 4th Cut motors, all ending at revolving drums named Googies. There is an extra set of Googie and 1st Cut motor, in case there are bits and pieces of tea leaves yet to curl and fine tune. Thereafter, they traverse through the CFM (Continuous Fermenting Machine) section via Conveyors, where they are fermented and cooled via CFM fans and they ultimately derive their texture. Next they are dried and roasted well in the Groover and Vibrator section. The heat for the combustion is derived from burning of coal, which is oxidized via air intake with the help of Hot Blower and Cold Blower motors. Heating is done with the help of Hot Heater and Cold Heater. The fumes are released through a chimney and ash is collected and disposed off. Next comes the Sorting and Grading Section, where the tea leaves are separated with respect to their quality with the help of a Sieving Technique and then packed for sale. The total lighting load is of the LED (Light Emitting Diode) type, estimated at 2 kW.

The panels have the following functions:

The CTC Main Panel accounts for the voltage and current absorbed by the CTC sections combined. It also possesses the capacitor banks, which indicate the corrected power factor at any instant of time. The Change-Over Panel accounts for the voltages and currents absorbed by the CFM, Groover, Vibrator, Grading and Sorting sections. The Auxiliary panel takes care of the transformer charging power, the lighting loads and other unaccounted power supplied.

For the purpose of this project, the meter readings are focused only on the part consuming variable reactive power with variation in loading, that is, the CTC section. The loading percentage of the CTC Cut motors is observed and the corresponding CTC panel readings help to find out energy efficiency estimates and the power factor, both in the operating and improved case, with the help of capacitor bank estimates.

3.3 Load Distribution

The load distribution along with the rated load is enlisted as follows:

A. HT Valley & Gear.
B. Transformer: 500 KVA, 11 kV/440 Volts, Star-Delta.
C. Diesel Generator Set: 250 KVA.
D. Trough Fans: 11 Troughs × 2 Fans × 3 HP = 66 HP.
E. Monorails: 2 HP.
F. Rotor vane: 3 × 20 HP = 60 HP.
G. CTC Cutting: (Cut 1–25 HP, Cut 2–20 HP, Cut 3–20 HP, Cut 4–20 HP, Blower-2 HP, 3 HP) × 3 sets + extra 1st cut-25 HP, all 415 Volts, all rated at 0.75 power factor lagging = 295 HP.
H. Googie: 4 × 3 HP = 12 HP.
I. CTC Conveyors: 6 × 1.5 HP = 9 HP.
J. CFM (Continuous Fermenting Machine) Conveyor: 1.5 HP.
K. CFM Motors: 1 × 5 HP, 1 × 3 HP, Brush Motors: 2 HP = 10 HP.
L. CFM Fans: 7.5 HP, Small fans: 4 × 1 HP, Water Sprayer: 0.5 HP = 12 HP.
M. Groover Motors: 1 × 7.5 HP, 1 × 5 HP, 1 × 2 HP = 14.5 HP.
N. Groover Conveyor: 1 × 2 HP = 2 HP.
O. Vibrator: 1 × 5 HP = 5 HP.
P. Cold Blower: 1 × 3 HP = 3 HP.
Q. Hot Blower: 1 × 2.5 HP = 2.5 HP.
R. Cold Heater DC Motor: 1 × 1 HP = 1 HP.
S. Hot Heater: 1 × 2 HP = 2 HP.
T. Chimney: 1 × 5 HP = 5 HP.
U. Sorting: 2 × 3 HP = 6 HP.
V. Sorting Conveyor: 4 × 2 HP = 8 HP.
W. LED (Light Emitting Diode) Lighting Load: 2 KW.
X. CTC Main Panel with capacitor bank connected in delta.
Y. Change-Over Panel.
Z. Auxiliary Panel.

3.4 Power Layout Diagram of the Factory

The power layout diagram of the factory has been depicted here (Fig. 1).

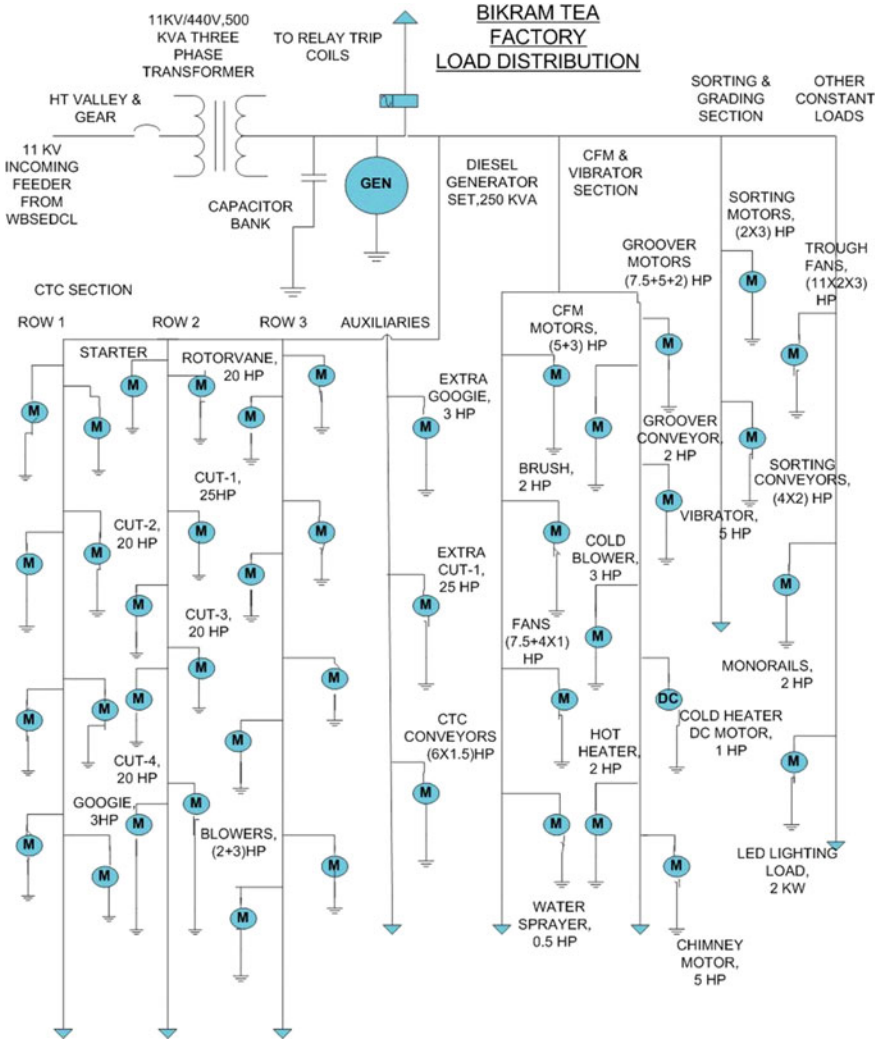

Fig. 1 This figure depicts the extensive power layout diagram of the factory under survey. It also categorizes the distribution into various sections and reveals the associated *ratings* of the machineries therewith

4 Survey Data Collection and Analysis

4.1 Rated Loading Calculations

For Cut 1 Motor: 25 HP, 415 V, 0.75 lag power factor

$$\text{I(full load)} = (25 \times 746)/(1.732 \times 415 \times 0.75) = 34.6 \text{ Amperes} \quad (1)$$

For Cut 2, 3 & 4 Motors: 20 HP, 415 V, 0.75 lag power factor

$$\text{I(full load)} = (20 \times 746)/(1.732 \times 415 \times 0.75) = 27.68 \text{ Amperes} \quad (2)$$

4.2 Loading Observed Under Varying Conditions

Analysis of the loading observed

For the 4 Cut motors under variable conditions, the loading as observed under Tables 1, 2 and 3 are quite as expected. The Cut motors are rated at 0.75 lagging power factor and this data is used for determining the loading percentages of the individual motors (Fig. 2, 3 and 4).

As the raw tea leaf changes from Soft to Hard via Medium under different weather conditions, seasons and days, the average loading percentage of each individual motor

Table 1 Data collected on 24. 07. 2017, Type of leaf: Soft

Time (pm)	Cut 1 Current (A)	Cut 2 current (A)	Cut 3 current (A)	Cut 4 Current (A)
12.30	20	13	10	11
12.40	19	12	8	9
12.50	18	14	10	11
1.00	20	15	13	12
1.10	20	13	9	10
1.20	18	15	12	13
1.30	23	19	15	15

Table 2 Data collected on 07. 09. 2017, Type of leaf: Medium

Time (pm)	Cut 1 current (A)	Cut 2 current (A)	Cut 3 current (A)	Cut 4 current (A)
3.00	20	13	10	11
3.15	19	12	8	9
3.30	18	14	10	11
3.45	20	15	13	12
4.00	20	13	9	10

Table 3 Data collected on 29. 07. 2017, Type of leaf: Hard

Time (pm)	Cut 1 current (A)	Cut 2 current (A)	Cut 3 current (A)	Cut 4 current (A)
12.45	28	17	14	15
12.55	22	15	12	13
1.05	40	24	17	16
1.15	26	15	13	11
1.25	22	15	11	12
1.35	26	16	13	11
1.45	28	18	15	13

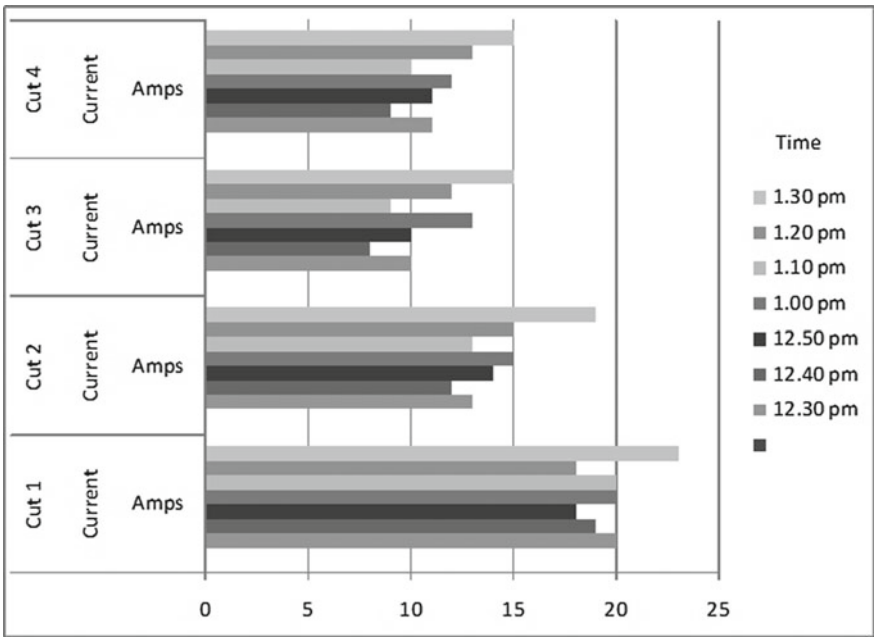

Fig. 2 Bar graph representation of loading on 24.07.17 (*Soft leaf*)

also increases, since amount of current drawn is *directly proportional* to the hardness of the raw leaf, as it requires more power for crushing it. It is found that the loading percentage gradually decreases from 1st to 4th Cut, which is obvious since the 1st Cut gets the hardest raw leaf.

The loading observed reveals the following information:

(i) *Soft Leaf*: The Cut 1 motor loading percentage varies from 52.04 to 66.49%; the Cut 2 motor loading percentage varies from 43.35 to 68.64%; the Cut 3 motor loading percentage varies from 28.9 to 54.19% and the Cut 4 motor loading percentage varies from 32.51 to 54.19%.

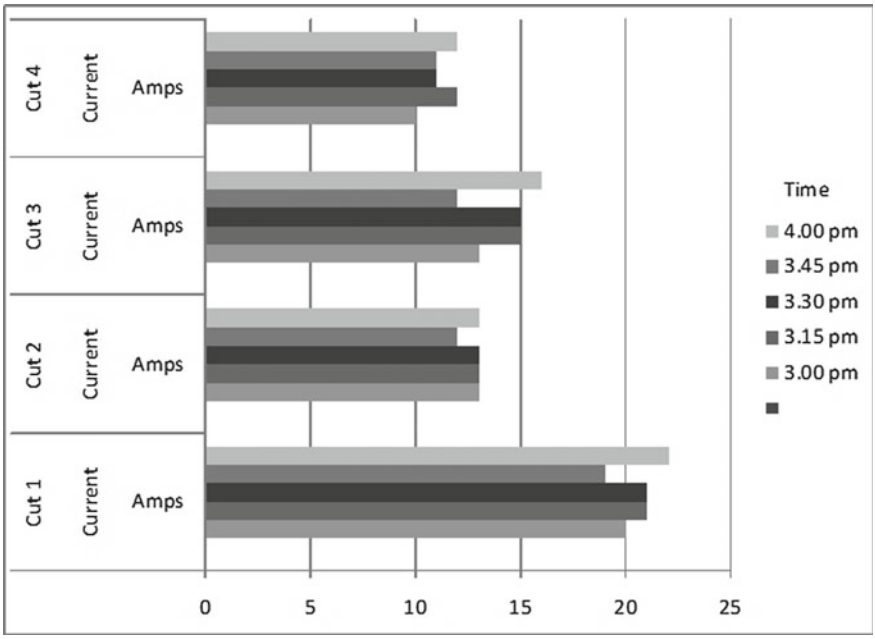

Fig. 3 Bar graph representation of loading on 07.09.2017 (*Medium leaf)*

(ii) *Medium Leaf:* The Cut 1 motor loading percentage varies from 57.82 to 63.6%; the Cut 2 motor loading percentage varies from 43.37 to 46.98%; the Cut 3 motor loading percentage varies from 43.37 to 57.82% and the Cut 4 motor loading percentage varies from 36.14 to 43.37%.

(iii) *Hard Leaf:* The Cut 1 motor loading percentage varies from 63.6% to an occasional 115.64%; the Cut 2 motor loading percentage varies from 54.19to 86.71%; the Cut 3 motor loading percentage varies from 39.74 to 61.42% and the Cut 4 motor loading percentage varies from 39.74 to 57.8%.

It is observed that there is no appreciable change in the loading of the 3rd and 4th cut motors under any condition, they are always poor. More the loading percentage, less is the reactive power consumed by the motor, and higher is the efficiency and power factor of the plant. If power factor improves by itself, there would be a lower tariff slab for the owners, ensuring profitability and providing further impetus to the industry. So, the loading percentage of 3rd & 4th cut motors are hypothetically assumed next to be 75% each and having an improved power factor of 0.75 and then analyzed.

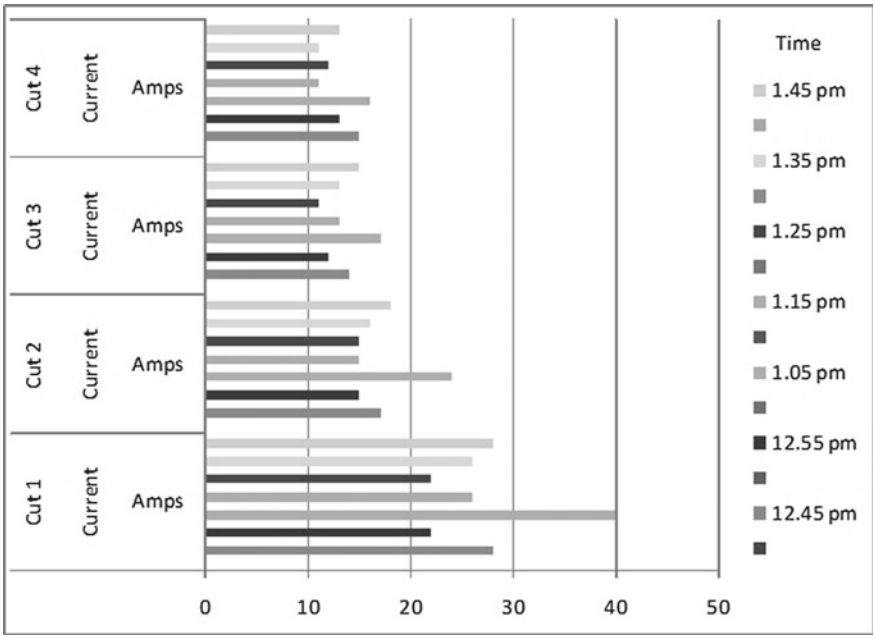

Fig. 4 Bar graph representation of loading on 29.07.2017 *(Hard leaf)*

5 Reactive Power Calculations and Comparative Analysis of Normal Loading with Theoretically Improved Loading Percentage and Improved Power Factor of the 3rd and 4th Cut Motors with Same Rating

For the comparative analysis, we take the case of 29.07.2017 with Hard Loading.

5.1 Normal Loading

Here, we take the power factor of the motors as 0.7 lagging instead of rated 0.75 lagging, owing to ageing and de-rating of the age-old motors (Table 4, 5).

Table 4 Reactive power calculation with normal loading and power factor of all motors at 0.7 lagging

Time (pm)	CTC Panel Voltage (V)	CTC Panel Current (A)	Total reactive power drawn by 4 motors (KVAR)	Primary panel voltage (V)	Primary panel current (A)	Power factor (lag)	Reactive power supplied from Source (KVAR)	Reactive power drawn by the 2 CTC rows (KVAR)	Reactive Power supplied by the capacitor Banks (KVAR)
12.45	385	100	35.23	365	225	0.98	28.3	70.46	42.16
12.55	390	85	29.88	360	238	0.98	29.53	59.76	30.23
1.05	390	120	46.78	365	237	0.96	41.95	93.56	51.61
1.15	390	85	31.35	360	275	0.98	34.12	62.7	28.58
1.25	385	75	28.56	360	281	0.98	34.87	57.12	22.25
1.35	380	85	31.04	360	245	0.98	30.4	62.08	31.68
1.45	380	100	34.78	360	229	0.98	28.42	69.56	41.14

Table 5 Reactive power calculations with Cut 3 & 4 motors at 75% loading, all at 0.7 lag power factor

Time (pm)	CTC Panel Voltage (V)	CTC Panel Current (A)	Total reactive power drawn by 4 motors (KVAR)	Primary Panel Voltage (V)	Primary Panel Current (A)	Power factor (lag)	Reactive power supplied from Source (KVAR)	Reactive power drawn by the 2 CTC rows (KVAR)	Reactive Power supplied by the capacitor Banks (KVAR)
12.45	385	100	41.21	365	225	0.98	28.3	82.42	54.12
12.55	390	85	37.88	360	238	0.98	29.53	75.76	46.23
1.05	390	120	50.89	365	237	0.96	41.95	101.78	59.83
1.15	390	85	39.8	360	275	0.98	34.12	79.6	45.48
1.25	385	75	37.4	360	281	0.98	34.87	74.8	39.93
1.35	380	85	39.27	360	245	0.98	30.4	78.54	48.14
1.45	380	100	41.13	360	229	0.98	28.42	82.26	53.84

5.2 Theoretically Improved Loading of 3rd and 4th Cut Motors Fixed at 75%, All Operating at 0.7 Power Factor Lag

Here, hypothetically 3rd and 4th cut motors are considered to have a high 75% fixed loading, and all motors operating at 0.7 power factor lagging, reactive power calculations are performed (Table 5).

5.3 Theoretically Improved Loading Percentage of 3rd and 4th Cut Motors Fixed at 75% with Higher Power Factor of 0.75 Lagging

Here, the loading percentage of 3rd and 4th Cut motors is fixed at 75% and higher power factor of 0.75 lagging (for the 3rd & 4th Cut motors) and reactive power calculations are performed (Table 6).

5.4 Analysis of Reactive Power Calculations

Reactive power calculations are performed under three conditions taking hard leaf as a sample:

(i) *Normal loading, all 0.7 lag power factor*:

First of all, we consider the normal loading percentages with power factor taken as 0.7 lag power factor instead of rated 0.75 for the motors, owing to the ageing and depreciated quality of the long-used motors and the reactive power consumed by each CTC row is calculated, and thereby for 2 CTC rows in total, working in tandem. The Primary Main Panel readings and improved power factor after rectification by the capacitor bank are calculated. The reactive power supplied from the source after Power Factor Correction (PFC) is calculated. The difference between the reactive power consumed by the 2 CTC rows and that supplied from source results in the reactive power supplied by the capacitor bank. So, the capacity of the capacitor bank installed can be estimated.

(ii) *3*rd *& 4*th *Cut Motors at 75%, all operate at 0.7 lag power factor:*

Next the hypothetical case where the 3rd & 4th Cut motors are operating at higher loading of 75% and operating at the same 0.7 lag power factor is considered. Here, an increased reactive power consumption by the motors due to increase in the currents drawn is observed, since reactive power drawn = (1.732*Line Voltage*Line Current*power factor). Also, the reactive power supplied by the capacitor bank increases, thus indicating the need for a higher rated capacitor bank.

Table 6 Reactive power calculations with Cut 3 & 4 Motors at 75% loading and 3rd & 4th Cut Motors operating at 0.75 lag power factor

Time (pm)	CTC panel voltage (V)	CTC panel current (A)	Total reactive power drawn by 4 motors (KVAR)	Primary panel voltage (V)	Primary panel current (A)	Power factor (lag)	Reactive power supplied from Source (KVAR)	Reactive power drawn by the 2 CTC rows (KVAR)	Reactive power supplied by the capacitor banks (kvar)
12.45	385	100	39.71	365	225	0.98	28.3	79.42	51.12
12.55	390	85	36.38	360	238	0.98	29.53	72.76	43.23
1.05	390	120	49.39	365	237	0.96	41.95	98.78	56.83
1.15	390	85	38.3	360	275	0.98	34.12	76.6	42.48
1.25	385	75	35.9	360	281	0.98	34.87	71.8	36.93
1.35	380	85	37.79	360	245	0.98	30.4	75.58	45.18
1.45	380	100	39.65	360	229	0.98	28.42	79.3	50.88

(iii) *3*rd *&* *4*th *Cut Motors at 75% and 0.75 lag power factor, other 2 Cut Motors at 0.7 lag power factor:*

Next, the hypothetical case where the 3rd & 4th Cut motors operate at 75% loading and at an improved power factor of 0.75 lag is considered, the 1st and 2nd Cut still essentially operating at the same 0.7 lag power factor. It is found by calculations, the reactive power drawn by the motors and the reactive power supplied by the capacitor bank has decreased from its value as in case (ii). This ensures the fact that, with an increase of power factor of the motors and loading percentage towards full load, lower capacity capacitor bank suffices, which is lower in cost and volume if installed in place of the present one. Also, an increase in loading ensures higher efficiency, due to increase in utilization factor of the machines. Also, a lower capacity motor can be substituted in place of the present one, to ensure higher loading near full load. Also, problems on loss can be addressed with a lower size motor.

6 Results

Chronological data monitoring has been performed under wide variety of raw leaf and weather conditions. Loading percentage and reactive power calculations are performed and ultimately, it is observed that an increase in loading percentage and power factor lead to better performance of the factory, ensuring profitability.

With an estimated increase in power factor of the motors and loading percentage towards full load, lower capacity capacitor bank can serve the purpose and be installed. Also, an increase in loading of 3rd and 4th Cut CTC motors along with improved power factor ensures higher efficiency, and lower reactive power consumption, as is calculated and observed graphically. Entire load distribution of surveyed factory, power layout diagram and associated survey data with extensive analyses is presented in this survey. The graphical comparison of reactive power consumed under the three different cases is depicted below.

There are two major scopes of improvement of the situation which are discussed below (Fig. 5 and 6).

(i) *Usage of energy efficient motors of smaller adequate rating.*

Energy efficiency is the prime concern while installing any machinery in an industry. However, if the running cost for such a machine exceeds the installation cost in the long run, with efficiency having decreased, it might well be non-profitable to the industry. So, it is important to re-install newer energy efficient motors with lower operation costs, after detailed cost-benefit analysis. Also, due to smaller air gap in the IE classes of motors, reactive power requirement is lesser, hence more efficient.

There are energy efficient classes of motor, which can substitute the age-old induction motors hereby in operation. The energy efficiency classes of these motors are classified as follows in terms of IE (International Efficiency):

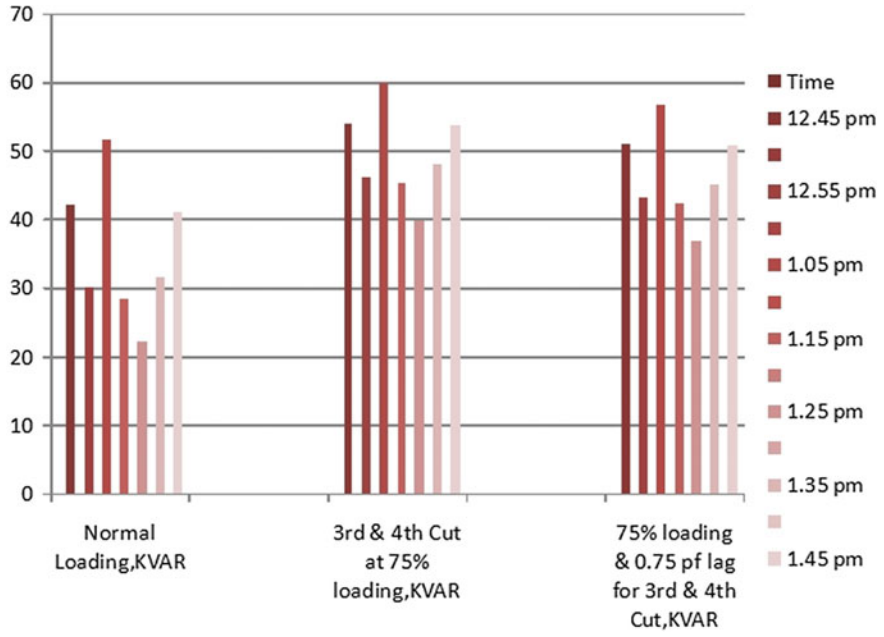

Fig. 5 Comparison of Reactive Power supplied by the Capacitor Bank during normal loading, increased loading percentage and both increased loading percentage and power factor (Left to Right respectively)

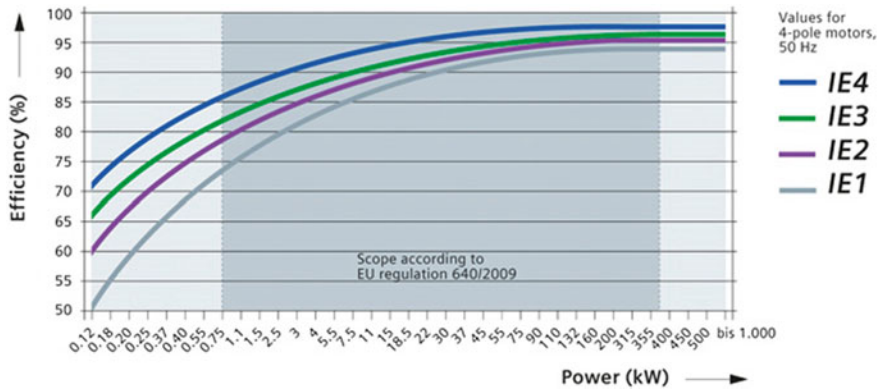

Fig. 6 Energy Efficiency Classes of motors and their range of percentage efficiency [2]

(a) IE1 (Standard Efficiency).
(b) IE2 (High Efficiency).
(c) IE3 (Premium Efficiency).
(d) IE4 (Super Premium Efficiency).

From these energy efficient motors, IE2 or IE3 motor with rating near 20 HP or 15KW (approximately) can be appropriately installed in place of the 3rd and 4th Cut motors in the CTC rows for healthier operation.

(ii) *Installing Power Factor Correction equipments, specifically FACTS (Flexible AC Transmission System) devices.*

FACTS devices are connected in series or parallel with an electrical catering, consists of power electronic switching devices in order to regulate reactive power flow and improve power factor of operation.

"APFC (Automatic Power Factor Correction) devices are the ideal choice. APFC essentially employs a current control loop, which is fed by input sinusoidal supply. A bridge rectifier is used to convert it into DC (Direct Current). There is a second outer voltage control loop, which employs appropriate scaling factor by analog multiplier. APFC is a sine magnitude controlled loop employing current control [3]".

These devices can be operated along with the tea factory machineries in operation to improve the power factor of the industry.

7 Conclusion

It is observed that an increase in loading percentage and power factor leads to better performance of the factory, ensuring profitability. A highly efficient alternate solution to this problem lies in installing energy efficient IE2/IE3 Class motors with smaller ratings. Also, Specific Energy Consumption (SEC) decreases with IE Class Motors.

Acknowledgements The authors owe their gratitude to all the employees and technicians of the Bikram Tea Factory. This survey would not have been possible without their incessant help and support.

References

1. Indian Brand Equity Foundation, http://www.ibef.org: Tea Statistics of India, India (2016)
2. Siemens, http://w3.siemens.com/drives/global/en/motor/low-voltage-motor/efficiency-standards/pages/line-motors.aspx
3. Tiwari, S., Rana, B., Santoki, A., Limbachiya, H., Choubey, S.: Power Factor Improvement By Using APFC Panel. Int. J. Eng. Sci. Comput. Bengaluru (Feb 2017)

Analysis and Dispersion Engineering for Generation of Ultra-flattened Dispersion in Photonic Crystal Fibers

Anup Karak and Sanchita Pramanik

Abstract We study the variation of group velocity dispersion with wavelength in photonic crystal fibers having triangular lattice air holes. The first ring of air holes of the fiber is considered to be infiltrated with water-glycerin solution as it is one of the most efficient liquid for photonic crystal fiber infiltration. Concentration of the solution, pitch and diameter of air holes are the parameters we seek to optimize to get flattest dispersion. In our investigation, almost flat and near zero dispersion characteristics is observed when glycerine concentration = 20%, the pitch = 2.3 μm and air hole diameter = 1.9 μm. Our finding will exhibit huge potential advantage in supercontinuum generation and various sensing applications.

Keywords Photonic crystal fiber · Group velocity dispersion
Full vectorial finite difference method

1 Introduction

Since last few decades, much attention is being received in the field of photonic crystal fibers (PCF) [1–13]. By tailoring the shape, pitch, diameter of air hole and arrangement of air holes in the PCF structure one can achieve endlessly single moded operation, highly tailorable mode field diameters and flat group velocity dispersion (GVD), high nonlinearity etc. [1–3]. These unique characteristics have huge applications in various optical fiber communications, supercontinuum generations, sensing and others [14–16].

PCF has shown unprecedented light guiding mechanism which is not present in normal conventional fibers. Due to the high index difference, structural complexity and the absence of rotational symmetry in PCF, the theoretical or analytical analysis

A. Karak (✉)
Department of Physics, Vidyasagar University, Midnapore 721102, India
e-mail: anupkarak@hotmail.com

S. Pramanik
Department of Electronics, Vidyasagar University, Midnapore 721102, India

U. Biswas et al. (eds.), *Advances in Computer, Communication and Control*, Lecture Notes in Networks and Systems 41, https://doi.org/10.1007/978-981-13-3122-0_18

of such special type of fibers is very complicated. Various numerical methods such as, finite-element method, effective index method, finite-difference method (FDM), multipole method, step index fiber approximation etc. have been developed for analyzing the propagation dynamics of PCF [4–11]. We have chosen the FDM due to its simplicity in formulation and execution. We have used full-vectorial finite difference method (FVFDM) since high index difference and lack of symmetry in PCF demands it, instead of scalar or semi-vectorial method as found in literature so far.

Nowadays, liquid filled PCF has acquired huge attention in the field of photonics because the infiltration of liquids of various refractive indices provides an additional degree of freedom in controlling its various propagation dynamics [15, 17]. Due to the advent in technology of sealing and filling of liquid in PCF, a new era is opened in the field of photonics [18, 19]. These liquid filled fibers have many applications in gas sensing, coupling, waveguiding mechanism etc. Recently, such analyses have started to draw worldwide attention to achieve ultra high dispersion characteristics and supercontinuum generation. Reports are also being proliferated on liquid filled nonlinear soft glass based PCF [15]. Though various liquids such as toluene, chloroform, benzene, methanol, water, castor oil etc. are infiltrated in PCF, only few works are available where flat, near zero dispersion characteristics is obtained. Using glycerin-water solution, we have found more flattened and near zero dispersion characteristics over large range of wavelengths.

In this paper, the PCF having its first ring infiltrated with 20% glycerin-water solution is investigated to achieve ultra flat, near zero dispersion using FVFDM. Various pitches and air hole diameters are considered in our analysis. In our study, almost flat and near zero dispersion characteristics is observed when the pitch = 2.3 μm and air hole diameter = 1.9 μm.

2 Theory and Method

This section is divided into three subsections, in the first sub-section the structural geometry of our taken PCF is discussed, in the second section the finite difference methodology and the solution of Helmholtz equation using our full-vectorial method is elucidated and in the third i.e., last sub-section the formulation of GVD is explained. The subsections are elaborated as below.

2.1 Structure of the PCF

The PCF is a cylindrical or tubular structure made up of pure silica. It is filled with tubular air holes having a triangular lattice structure. The lattice constant (pitch) is Λ and d is the diameter of air holes in host material silica. In this periodic structure, a central defect is created, by eliminating the central hole. The hole-matrix having hole-pitch Λ acts as the cladding of the PCF. This structure remains invariant along

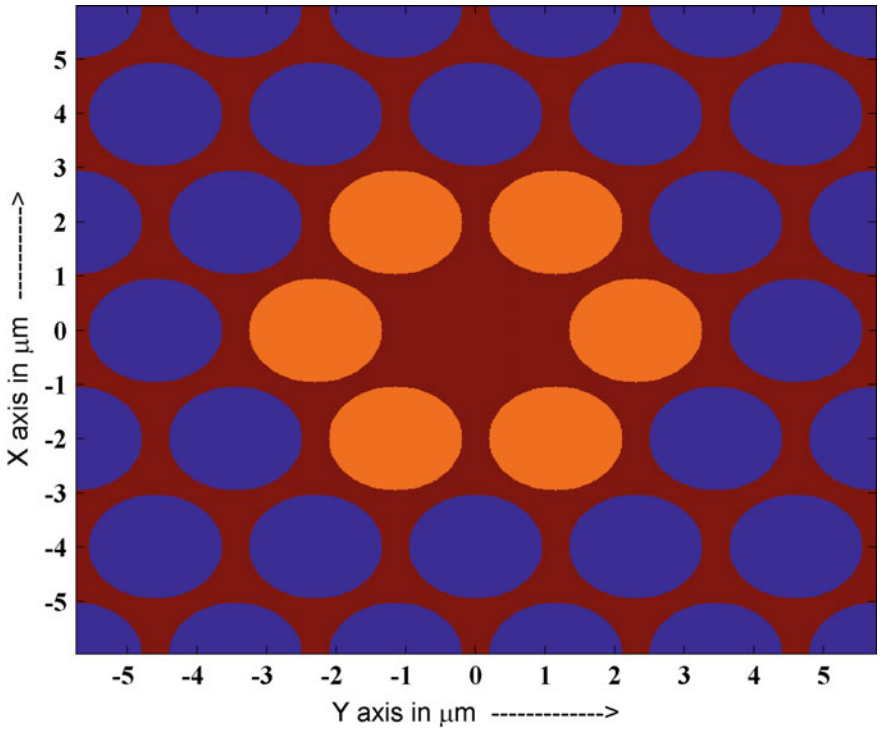

Fig. 1 Photonic crystal fiber structure infiltrated with liquid at its first ring

the longitudinal direction. We consider a PCF whose first ring is filled with liquid, the cross-sectional view is shown in Fig. 1. Here, we chose 20% glycerin-water solution for the PCF infiltration since this solution provides better flat dispersion characteristics.

2.2 Full Vectorial Finite Difference Inverse Iteration Method

Helmholtz equation involving different dielectric medium is

$$\nabla^2\vec{E} + \vec{\nabla}\left(\frac{\vec{E}}{n^2}.\vec{\nabla}n^2\right) = k_0^2 n^2 \vec{E} \tag{1}$$

In a waveguide, the electric field propagates in the z-direction. Transverse components $\overrightarrow{E}_t (E_x$ and $E_y)$ of $\overrightarrow{E}$ are coupled through the second term. Helmholtz Eq. (1) reduces to

$$\nabla_t^2 \vec{E}_t + \vec{\nabla}_t \left(\frac{\vec{E}_t}{n^2} . \vec{\nabla}_t n^2 \right) + \left\{ k_0^2 n^2(x, y) - \beta^2 \right\} \vec{E}_t = 0 \tag{2}$$

where β is the propagation constant and n is the refractive index. There will be two modes or two sets of E_t—(1) quasi-TE mode in which E_y is the major component with a minor component E_x—(2) quasi-TM mode: major E_x, minor E_y. Two modes will have different β.

Component wise, the above equation is split into two equations:

$$\frac{\partial}{\partial x}\left[\frac{1}{n^2}\frac{\partial}{\partial x}(n^2 E_x)\right] + \frac{\partial^2 E_x}{\partial y^2} + \frac{\partial}{\partial x}\left[\frac{E_y}{n^2}\frac{\partial n^2}{\partial y}\right] + k_0^2 n^2 E_x = \beta^2 E_x \tag{3}$$

$$\frac{\partial}{\partial y}\left[\frac{1}{n^2}\frac{\partial}{\partial y}(n^2 E_y)\right] + \frac{\partial^2 E_y}{\partial x^2} + \frac{\partial}{\partial y}\left[\frac{E_x}{n^2}\frac{\partial n^2}{\partial x}\right] + k_0^2 n^2 E_y = \beta^2 E_y \tag{4}$$

The above equations can be expressed as

$$P_{xx} E_x + P_{xy} E_y = \beta^2 E_x \tag{5}$$

$$P_{yy} E_y + P_{yx} E_x = \beta^2 E_y \tag{6}$$

These two equations can be put in a compact form as

$$P E_t = \beta^2 E_t \tag{7}$$

where $P = \begin{bmatrix} P_{xx} & P_{xy} \\ P_{yx} & P_{yy} \end{bmatrix}$ and $E_t = \begin{bmatrix} E_x \\ E_y \end{bmatrix}$

The above matrix equation can be solved with FDM. The cross-sectional window shown in Fig. 1 is discretized into M × N cells. In each cell E_x, E_y, n, has a discrete value. E_t is a column matrix of 2MN dimensions; P is a matrix of dimension 2MN × 2MN. Equation (7) is an eigenvalue equation. The eigenvalue β can be found efficiently with Inverse Iteration Method (IIM). In this method, one starts with a trial field for $E_t = E_{t0}$ and a trial value of $\beta = \beta_0$. Modified E_{t1} is obtained from the relation.

$$\left(P - \beta_0^2\right) E_{t1} = E_{t0} \tag{8}$$

Modified β_{t1} is obtained from this improved E_{t1}.

$$\beta_{t1}^2 = \frac{\langle E_{t1} | P | E_{t1} \rangle}{\langle E_{t1} | E_{t1} \rangle} \tag{9}$$

In the next step, E_{t0} is replaced by E_{t1} and β_0 by β_{t1}. With a few iterations, the improved values of E_t and β converge to the actual value.

2.3 Group Velocity Dispersion

It is very important to acquire knowledge about the dispersion properties of PCF for various practical applications like optical telecommunications, supercontinuum generation and others. The structural and wavelength dependency of GVD is evaluated for the PCF using FVFDM. The GVD is calculated using the formula as given below:

$$\beta_2(\omega) = \frac{d^2\beta(\omega)}{d\omega^2} = \frac{\lambda^3}{2\pi c^2}\frac{d^2 n_e(\lambda)}{d\lambda^2} \tag{10}$$

where, n_e is the effective refractive index and λ is the operating wavelength

3 Results and Discussion

We calculate the effective refractive index of the fundamental mode and finally the corresponding GVD for the liquid infiltrated PCF using our accurate FVFDM. Our full vectorial method is very efficient and take very little time to compute the various propagation dynamics of practical interest such as effective refractive index, GVD, modal field etc. In case of PCF, since the structure does not have rotational symmetry and also it has a large index variation in its structure, and hence, a full vectorial method is preferable while considering PCF and other complex structures. The fundamental modal field calculated using our FVFDM is shown in the Fig. 2a, b, respectively. Here, the quasi TE mode is considered, where, the major field component E_y and minor field component is E_x. Also, for the quasi TM mode the field distribution pattern will be quite similar only except that the major field component is E_x and minor field component is E_y. Here we have shown the quasi TE mode field distribution only.

Since, the PCF has large scale of design flexibility and liquid infiltrated PCF has another degree of freedom in choosing various liquids of different refractive indices, we further divide our findings of GVD results with variation of wavelength into four sections. In the first sub-section we compute the GVD with wavelength for change in refractive indices in the infiltrated liquid of the PCF first ring. In second and third sub-section we compute the GVD with variation of wavelength for change in hole-diameter and pitch respectively. Finally our best observation for the chosen fiber parameter and infiltrated liquid of available nearest refractive index is computed and compared with available literature. For all the study the infiltration of the PCF is done at its first ring.

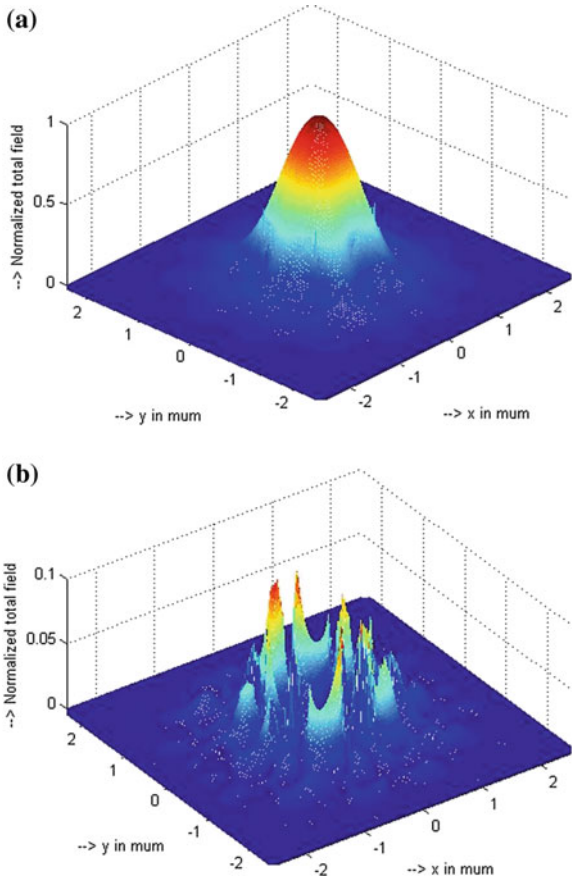

Fig. 2 **a** The plot of major field component E_y for Quasi-TE mode. **b** The plot of minor field component E_x for Quasi-TE mode

3.1 GVD Calculation for PCF Infiltrated with Liquid Having Various Refractive Indices

In this section, we choose a PCF of equal hole-diameter 1.9 μm and pitch 2.3 μm. Infiltration of liquid having various refractive indices is considered in the first ring of the PCF. The GVD of the PCF with change in wavelength considering infiltrated liquid of various refractive indices is calculated with our FVFDM and the results are shown in the Fig. 3. It is evident from the figure that, the GVD is almost flat and near zero within the wavelength range 1.0–2.0 μm. The best result is found when the infiltration is considered with liquid of refractive index 1.354.

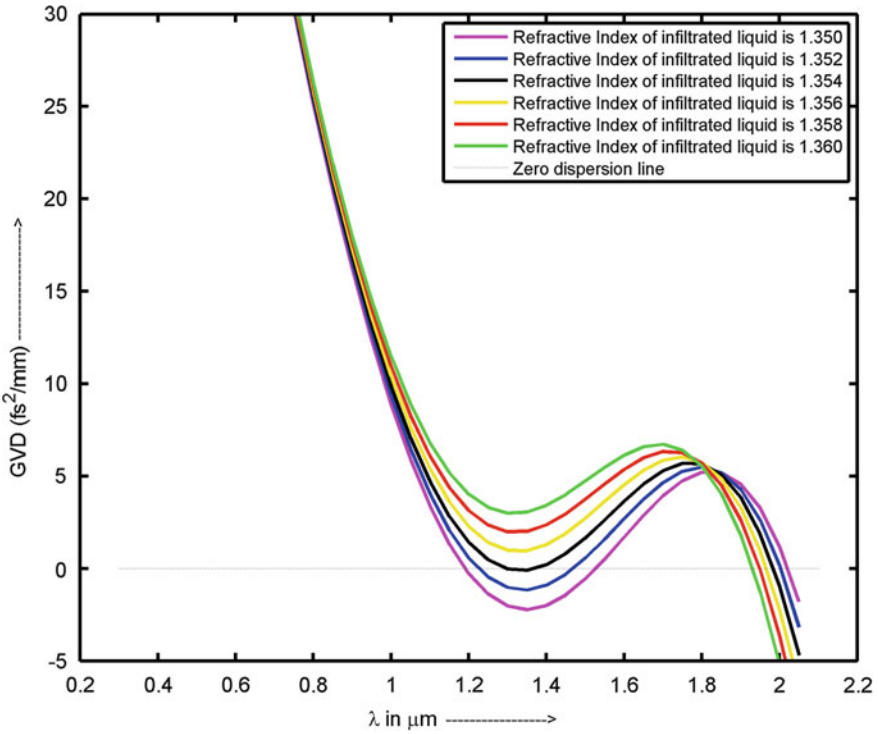

Fig. 3 GVD versus wavelength for PCF infiltrated with liquids of various refractive indices at its first ring with pitch = 2.3 μm and hole-diameter = 1.9 μm

3.2 GVD Calculation for PCF Infiltrated with Liquid Having Various Hole-Diameters at a Fixed Pitch

Further, for various hole-diameters, the GVD of the PCF with change in wavelength at a fixed pitch equal to 2.3 μm is calculated using our FVFDM. Here also, we consider the liquid infiltrated PCF. The liquid is filled at its first ring. Since the liquid with refractive index 1.354 is yielding more flat and near zero dispersion, we take an experimentally available 20% glycerin-water solution whose refractive index is 1.35749 which is close to our required value [20]. With this refractive index parameter we continue our entire investigation and the results are shown in the Fig. 4. It is seen that the result is very attractive at hole-diameter = 1.9 μm which provide a flat and near zero GVD within the wavelength range 1.0–2.0 μm.

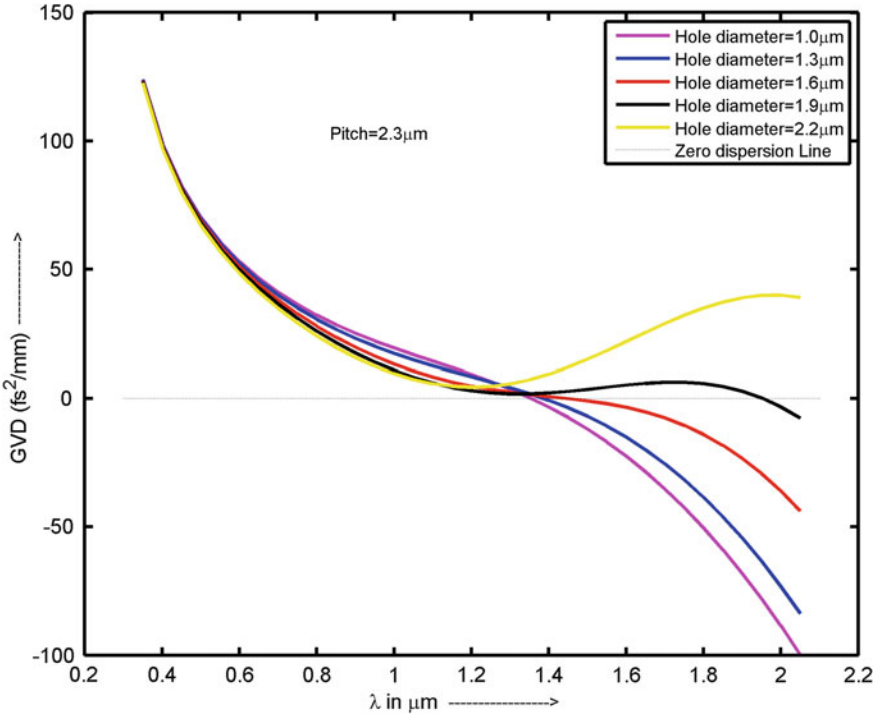

Fig. 4 GVD versus wavelength for liquids infiltrated PCF at its first ring with various hole-diameter with fixed pitch = 2.3 μm

3.3 GVD Calculation for PCF Infiltrated with Liquid Having Various Pitches at a Fixed Hole-Diameter

Now, for various pitches, the GVD of the PCF with change in wavelength at a fixed hole-diameter equal to 1.9 μm is estimated with our accurate FVFDM. In this case, we further take the liquid infiltrated PCF whose first ring is filled with 20% glycerin-water solution of refractive index 1.35749 [20]. The variation of GVD with wavelength for the above mentioned parameters are shown in the Fig. 5. It is clearly seen from the Fig. 5 that, a very flat and near zero GVD within the wavelength range 1.0–2.0 μm is observed when the pitch equal to 2.3 μm.

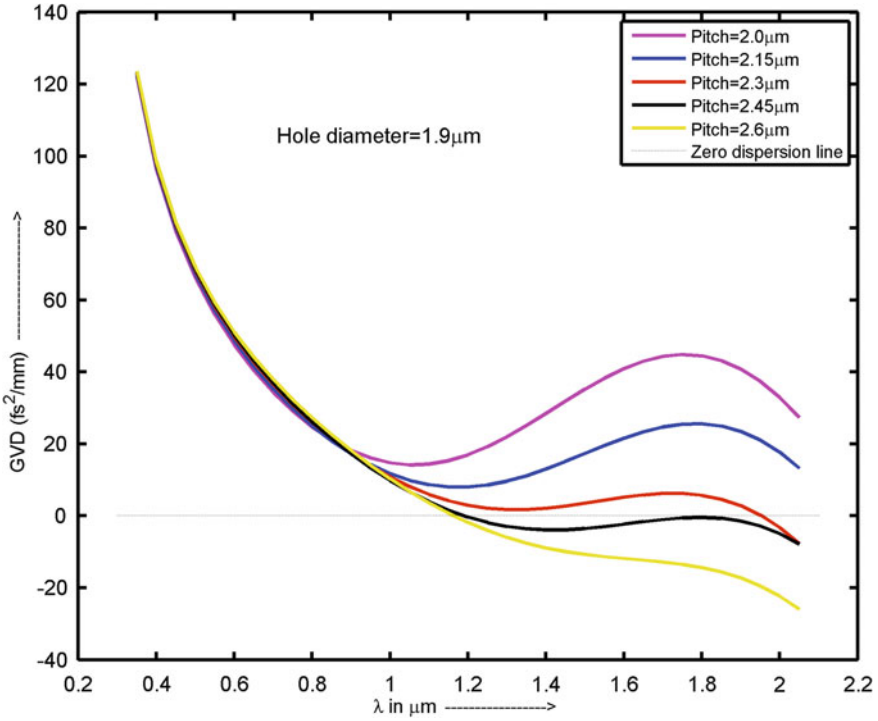

Fig. 5 GVD versus wavelength for liquids infiltrated PCF at its first ring with various pitch with fixed hole-diameter = 1.9 μm

3.4 Comparative Study of GVD Calculation for Liquid Infiltrated PCF

A comparative study is carried out to show the improvement in flatness of GVD over a range of wavelengths with our chosen parameters. The comparison is shown in Fig. 6. We obtain the best result when the first ring of the PCF is filled with 20% glycerin-water solution whose refractive index is 1.35749 [20], where the pitch and hole-diameter of the PCF is taken as 2.3 μm and 1.9 μm respectively. It is evident from Fig. 6 that, the calculated GVD using our chosen parameters is showing better flatness compared to results available in literature for GVD calculation [17].

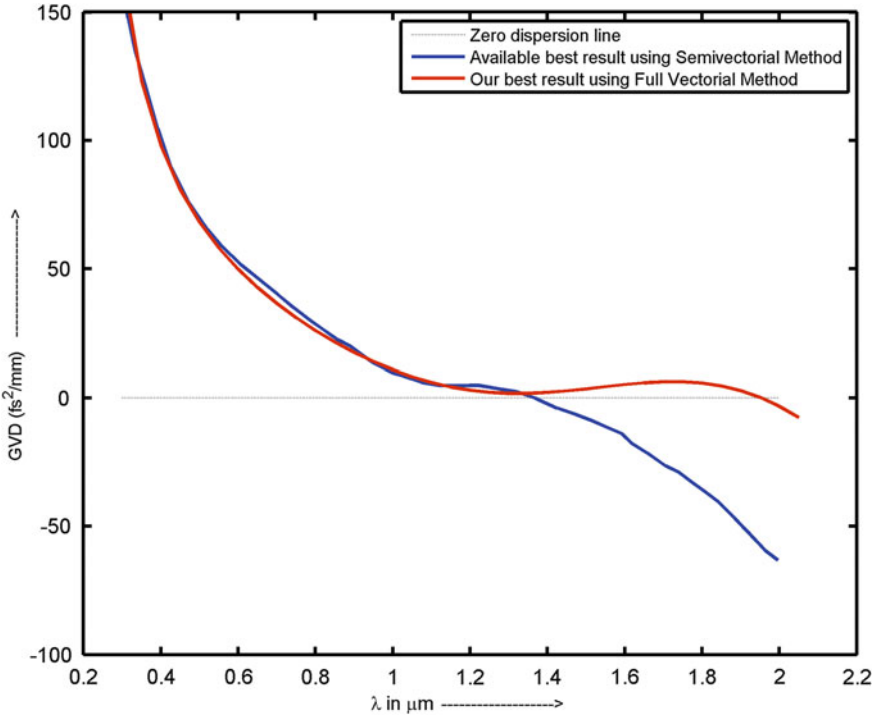

Fig. 6 Comparative study of GVD versus wavelength for liquids infiltrated PCF at its first ring

4 Conclusion

The PCF having its first ring filled with the 20% glycerin-water solution is investigated using our full vectorial finite difference method for various PCF parameters like pitches, air hole diameters. We achieve an ultra flat, near zero group velocity dispersion throughout the wavelength region from 1.0 μm to 2.0 μm when the pitch and hole-diameter are kept at 2.3 μm and 1.9 μm respectively. Our finding will exhibit huge potential advantage in supercontinuum generation and various sensing applications.

Acknowledgements The authors are grateful to Prof. (Dr.) Somenath Sarkar, former UGC Emeritus Fellow, Department of Electronic Science, University of Calcutta for introducing us to such a fascinating field of photonics. We are also grateful to Dr. Dharmadas Kumbhakar, Professor at the Department of Electronics and Communication Engineering, Asansol Engineering College for continuous support and encouragement in various crucial stages during development of the finite difference method and other important discussions. The financial support under UGC Innovative Research Scheme of Vidyasagar University, Midnapore, West Bengal, India, is gratefully acknowledged by the second author.

References

1. Russell, P.S.J.: Photonic-crystal fibers. J. Lightwave. Tech. **24**(12), 4729–4749 (2006)
2. Birks, T.A., Knight, J.C., Russell, P.S.J.: Endlessly single-mode Photonic crystal Fiber. Opt. Lett. **22**(13), 961–963 (1997)
3. Knight, J.C.: Photonic crystal fibres. Nature **424**(6950), 847 (2003)
4. Park, K.N., Lee, K.S.: Improved effective-index method for analysis of photonic crystal fibers. Opt. Lett. **30**(9), 958–960 (2005)
5. He, Y.J., Shi, F.G.: Finite-difference imaginary-distance beam propagation method for modeling of the fundamental mode of photonic crystal fibers. Opt. Commun. **225**, 151–156 (2003)
6. Brechet, F., et al.: Complete analysis of the characteristics of propagation into photonic crystal fibers by the Finite Element Method. Opt. Fiber Technol. **6**(2), 181–191 (2000)
7. White, T.P., et al.: Calculations of air-guided modes in photonic crystal fibers using the multipole method. Opt. Express **9**(13), 721–732 (2001)
8. Karak, A., Kundu, D., Sarkar, S.N.: Simplified loss estimation of splice to photonic crystal fiber using new model. J. Opt. Commun. **37**(2), 169–175 (2015)
9. Koshiba, M., Saitoh, K.: Applicability of classical optical fiber theories to holy fibers. Opt. Lett. **29**(15), 1739–1741 (2004)
10. Xu, Z., et al.: Numerical analyses of splice losses of photonic crystal fibers. Optics Communications **282**(23), 4527–4531 (2009)
11. Díaz-Soriano, A., Ortiz-Mora, A., Dengra, A.: Comparative Study of Numerical Methods Used in Modeling of Photonic Crystal Fibers. Microwave and Optical Technology Letters **55**, 1049–1053 (2013)
12. Karak, A., Kundu, D., Mukhopadhyay, S., Sarkar, S.N.: Investigation of coupling of a laser diode to photonic crystal fiber via hyperbolic microlens on the fiber tip by ABCD matrix formalism. Opt. Eng. **54**(8), 086102 (2015)
13. Karak, A., Kundu, D., Sarkar S. N.: Optimum launch optics involving laser excited photonic crystal fibers via hyperbolic microlens on its tip in presence of transverse and angular misalignments. In: 6th International Conference on Computers and Devices for Communication (CODEC) (2015)
14. Dudley, J.M., Genty, G., Coen, S.: Supercontinuum generation in photonic crystal fiber. Rev. Mod. Phys. **78**(4), 1135 (2006)
15. Pniewski, J., et al.: Dispersion engineering in nonlinear soft glass photonic crystal fibers infiltrated with liquids. Appl. Opt. **55**(19), 5033–5040 (2016)
16. Van, L.C., Anuszkiewicz, A., Ramaniuk, A., Kasztelanic, R., Xuan, K.D., Trippenbach, M., Buczyński, R.: Supercontinuum generation in photonic crystal fibres with core filled with toluene. J. Opt. **19**(12), 125604 (2017)
17. Ghosh, P., Sarkar, S.N.: Versatile dispersion characteristics of water solution of glycerine in selective filling of holes in photonic crystal fibers. App. optics **56**(10), 2927–2936 (2017)
18. Huang, Y., Yong, X., Yariv, A.: Fabrication of functional microstructured optical fibers through a selective filling technique. Appl. Phys. Lett. **85**, 5182–5184 (2004)
19. Wang, Y., Liao, C.R., Wang, D.N.: Femtosecond laser assisted selective infiltration of microstructured optical fibers. Opt. Express **18**, 18056–18060 (2010)
20. Hoyt, L.F.: New table of the refractive index of pure glycerol at 20 C. Ind. Eng. Chem. **26**(3), 329–332 (1934)

Optimal Choice of Location for Establishing Production Units by Application of Fuzzy Logic

P. Saha, A. Upadhyay, P. S. Dhara, M. Dey and Binayak S. Choudhury

Abstract In the present work we propose an economic decision making protocol by use of fuzzy logic. The problem here is the decision making problem of a multinational company which wants to establish a production unit to minimize its cost of production while the information available are fuzzy quantities. The main tool of fuzzy logic used here is the rank determination of fuzzy numbers. We apply the properties of fuzziness with any recourse to a defuzzification procedure.

1 Introduction

Fuzzy concepts were introduced by L. A. Zadeh in 1965 [1] which created a new approach in problems of applied mathematics where there are uncertainties which are different in nature from those coming under the treatment through probability theory. Generic examples of these uncertainties were given in the introductory work and in subsequent works by Zadeh himself and others. Today fuzzy approaches are recognised to have revolutionary effects in problems like those in the fields of pattern recognition, data mining, decision making, etc. For that purpose fuzzy logic has developed in different directions. It has modalities very different from the conventional logic. In this paper we concentrate on an economic decision making

P. Saha · P. S. Dhara (✉) · B. S. Choudhury
Department of Mathematics, Indian Institute of Engineering Science and Technology, Shibpur, Botanic Garden, Shibpur, Howrah 711103, West Bengal, India
e-mail: parus850@gmail.com

P. S. Dhara
e-mail: partha.besu2013@gmail.com

B. S. Choudhury
e-mail: binayak12@yahoo.co.in

A. Upadhyay (✉) · M. Dey
Department of Mathematics, Asansol Engineering College, Asansol 713305, West Bengal, India
e-mail: aupadhyay2004@rediffmail.com

U. Biswas et al. (eds.), *Advances in Computer, Communication and Control*, Lecture Notes in Networks and Systems 41, https://doi.org/10.1007/978-981-13-3122-0_19

problem which is the problem of choice of a country for a multinational company in order to establish a production unit for certain commodities. The description of the situation is made practically oriented by assuming that there are uncertainties in the information supplied by the surveys. These uncertainties are modeled with the help of fuzzy arithmetic. The ordering of the fuzzy numbers which is obtained by use of fuzzy logic [2–5] is applied for the fuzzy decision making [6–8]. In fact we put forward a fuzzy protocol in which we apply fuzzy reasoning to accomplish the goal of arriving at a decision. We discuss a hypothetical example to illustrate our protocol. A special feature of the protocol is that there is no defuzzification in the whole process. We note some similar works in [9, 10].

2 Technical Preliminaries

Below we briefly give some basic notions and important definitions which are required in our present discussion.

Definition 1 A fuzzy number $\tilde{F} = (\alpha, \beta, \gamma, \eta; \xi)$ is a fuzzy subset of the real line $\Re$ with the membership function $f_{\tilde{F}} : \Re \rightarrow [0, \xi]$ which satisfies the following properties:

(i) $f_{\tilde{F}}$ is upper semicontinuous.
(ii) $f_{\tilde{F}} = 0$, for all $x \notin [\alpha, \eta]$
(iii) $f_{\tilde{F}}$ is strictly increasing in $[\alpha, \beta]$
(iv) $f_{\tilde{F}} = \xi$, for $\beta \leqq x \leqq \gamma$, where ξ is a constant and $0 \leqq \xi \leqq 1$
(v) $f_{\tilde{F}}$ is strictly decreasing in $[\gamma, \eta]$, where $\alpha, \beta, \gamma, \eta$ are real numbers.

In the above definition, if $\xi = 1$, then the fuzzy number is called a normal fuzzy number, otherwise a non-normal fuzzy number.

Therefore the above membership function can be expressed in a compact form as in below:

$$\begin{aligned} f_{\tilde{F}}(x) &= f_{\tilde{F}}^{L}(x), \quad \alpha \leq x \leq \beta, \\ &= 1, \qquad \beta \leq x \leq \gamma, \\ &= f_{\tilde{F}}^{R}(x), \quad \gamma \leq x \leq \eta, \\ &= 0, \qquad \text{otherwise.} \end{aligned} \tag{1}$$

where

(i) $f_{\tilde{F}}^{L}(x) : [\alpha, \beta] \rightarrow [0, \xi]$ is strictly increasing and continuous.
(ii) $f_{\tilde{F}}^{R}(x) : [\gamma, \eta] \rightarrow [0, \xi]$ is strictly decreasing and continuous and
(iii) $0 \leq \xi \leq 1$.

The functions $f_{\tilde{F}}^{L}$ and $f_{\tilde{F}}^{R}$ are called left and right reference functions of the fuzzy number $\tilde{F}$ respectively. The set of all fuzzy numbers as defined above is denoted by G.

Now since $f_{\tilde{F}}^{L}$ and $f_{\tilde{F}}^{R}$ are continuous and strictly monotonic, so their inverse functions also exists and let us denote them by $h_{\tilde{F}}^{L}$ and $h_{\tilde{F}}^{R}$ respectively. Clearly $h_{\tilde{F}}^{L} : [0, \xi] \to [\alpha, \beta]$ and $h_{\tilde{F}}^{R} : [0, \xi] \to [\gamma, \eta]$ both are continuous on $[0, \xi]$, so $\int h_{\tilde{F}}^{L}(y)dy$ and $\int h_{\tilde{F}}^{R}(y)dy$ both exists.

Definition 2 A generalised trapezoidal fuzzy number $\tilde{F} = (\alpha, \beta, \gamma, \eta; \xi)$ is defined as any fuzzy subset of the real line $\Re$ with the membership function given by,

$$\begin{aligned} f_{\tilde{F}}(x) &= \xi \frac{(x-\alpha)}{\beta-\alpha}, \quad \alpha \le x \le \beta, \\ &= \xi, \qquad \beta \le x \le \gamma, \\ &= \xi \frac{(\eta - x)}{\eta - \gamma}, \quad \gamma \le x \le \eta, \\ &= 0, otherwise, \qquad\qquad where \ 0 \le \xi \le 1 \end{aligned} \tag{2}$$

In the above definition if $\xi = 1$, then the trapezoidal fuzzy number is called normal.

Remark 1 In the above definition if $\beta = \gamma$, then the fuzzy number is called a normal triangular fuzzy number $\tilde{F} = (\alpha, \beta, \eta)$. Moreover if $\alpha = \beta = \gamma = \eta$, then $\tilde{F}$ becomes a crisp real number.

For the fuzzy number $\tilde{F}$, the inverse function of $f_{\tilde{F}}^{L}(x)$ and $f_{\tilde{F}}^{R}(x)$ are given by $h_{\tilde{F}}^{L}(y) = \alpha + y\frac{\beta-\alpha}{\xi}$ and $h_{\tilde{F}}^{R}(y) = \eta - y\frac{\eta-\gamma}{\xi}$ respectively.

Definition 3 The image or opposite of a fuzzy number $\tilde{F} = (\alpha, \beta, \gamma, \eta; \xi)$ is also a fuzzy number given by $-\tilde{F} = (-\eta, -\gamma, -\beta, -\alpha; \xi)$.

Definition 4 For any fuzzy number on the real line $\Re$, the support of $\tilde{F}$ is defined as $\text{supp}(\tilde{F}) = x \in \Re : f_{\tilde{F}}(x) > 0$.

Definition 5 The required arithmetic operations between two generalised trapezoidal fuzzy numbers $\tilde{F}_1 = (\alpha_1, \beta_1, \gamma_1, \eta_1; \xi_1)$ and $\tilde{F}_2 = (\alpha_2, \beta_2, \gamma_2, \eta_2; \xi_2)$ are given as follows:

(i) $\tilde{F}_1 \oplus \tilde{F}_2 = (\alpha_1 + \alpha_2, \beta_1 + \beta_2, \gamma_1 + \gamma_2, \eta_1 + \eta_2; min(\xi_1, \xi_2))$
(ii) $\tilde{F}_1 \ominus \tilde{F}_2 = (\alpha_1 - \eta_2, \beta_1 - \gamma_2, \gamma_1 - \beta_2, \eta_1 - \alpha_2; min(\xi_1, \xi_2))$
(iii) $\tilde{F}_1 \otimes \tilde{F}_2 = (\alpha_1 \times \alpha_2, \beta_1 \times \beta_2, \gamma_1 \times \gamma_2, \eta_1 \times \eta_2; min(\xi_1, \xi_2))$
(iv) $\tilde{F}_1 \oslash \tilde{F}_2 = (\alpha_1 \div \eta_2, \beta_1 \div \gamma_2, \gamma_1 \div \beta_2, \eta_1 \div \alpha_2; min(\xi_1, \xi_2))$.

Definition 6 [11] Let $\tilde{F}$ be an arbitrary fuzzy number having height $\xi = 1$ with the inverse functions $h_{\tilde{F}}^{L} : [0, \xi] \to [\alpha, \beta]$ and $h_{\tilde{F}}^{R} : [0, \xi] \to [\gamma, \eta]$ and let $g : [0, 1] \to [0, 1]$ be a reducing function. Then the value of $\tilde{F}$ with respect to g is given by,

$$V(\tilde{F}) = \int_0^{\xi} g(y)[h_{\tilde{F}}^{L}(y) + h_{\tilde{F}}^{R}(y)]dy \tag{3}$$

Definition 7 [12] The angle between left and right reference functions of a trapezoidal fuzzy number $\tilde{F} = (\alpha, \beta, \gamma, \eta; \xi)$ is called Angle of Fuzzy sets (AFS) which is denoted as $L\tilde{F}R$ and defined as,

$$cos(L^{\tilde{F}}R) = \frac{v_1.v_2}{|v_1||v_2|} = \frac{\xi^2 - (\beta - \alpha)(\eta - \gamma)}{\sqrt{1 + (\beta - \alpha)^2}\sqrt{1 + (\eta - \gamma)^2}} \tag{4}$$

where "." is the scalar product of direction vectors v_1 and v_2 and $|v_1|$, $|v_2|$ are the magnitude of the vectors v_1 and v_2.

Definition 8 [13] Let $\phi :\rightarrow -1, 1$ be a function defined as follows:
for all $\tilde{F} \in G$:

$$\begin{aligned} \phi(\tilde{F}) &= 1, if sign(\int_0^1 [h_{\tilde{F}}^{L}(y) + h_{\tilde{F}}^{R}(y)]dy) \geq 0 \\ &= -1, if sign(\int_0^1 [h_{\tilde{F}}^{L}(y) + h_{\tilde{F}}^{R}(y)]dy) \geq 0 \end{aligned} \tag{5}$$

3 Procedure to Evaluate the Ranking Index $R(\tilde{F}_i)$ for the fuzzy number $\tilde{F}_i$

In the following we describe the ranking index of fuzzy numbers. It is determined as following by the method described in [14].

Let $\tilde{F}_i = (\alpha_i, \beta_i, \gamma_i, \eta_i; \xi_i), i = 1, 2, \ldots, n$ be a set of fuzzy numbers, where $0 \leq \xi_i \leq 1$ with membership function of each fuzzy number defined as in Eq. 1.

Step 1. Let $\alpha_{min} = min(\alpha_1, \alpha_2, \ldots, \alpha_n)$ and $\eta_{max} = min(\eta_1, \eta_2, \ldots, \eta_n)$. The left area $\delta_{\tilde{F}}^{L}$ from α_{min} to the left reference function $f_{\tilde{F}_i}^{L}$ and the right area $\delta_{\tilde{F}}^{R}$ from η_{max} to the right reference function $f_{\tilde{F}_i}^{R}$ of the fuzzy number $\tilde{F}_i$ are defined as follows:

$$\begin{aligned} \delta_{\tilde{F}}^{L} &= \xi_i(\beta_i - \alpha_{min}) - \int_0^{\xi_i} [h_{\tilde{F}_i}^{L}(y)]dy \\ \text{and } \delta_{\tilde{F}}^{R} &= \xi_i(\eta_{max} - \gamma_i) - \int_0^{\xi_i} [h_{\tilde{F}_i}^{R}(y)]dy \end{aligned} \tag{6}$$

Step 2. Consider ϵ_1, a very small positive number, $U_{min} = min(U_{\tilde{F}_1}, U_{\tilde{F}_2}, \ldots, U_{\tilde{F}_n})$ and $U_{max} = max(U_{\tilde{F}_1}, U_{\tilde{F}_2}, \ldots, U_{\tilde{F}_n})$, then the $\epsilon-$ transfer coefficient for the fuzzy number $\tilde{F}_i$ is given as,

$$\tau_{\tilde{F}_i} = \frac{U_{\tilde{F}_i} - U_{min} + \frac{\epsilon_1}{2}}{U_{max} - U_{min} + \epsilon_1}, \tag{7}$$

where $U_{\tilde{F}_i}$ is the value and angle contribution expression for which is,

$$U_{\tilde{F}_i} = \int_0^{\xi_i} g(y)[h^L_{\tilde{F}_i}(y) + h^R_{\tilde{F}_i}(y) + \phi(\tilde{F}_i)cos(L^{\tilde{F}}R)]dy, \tag{8}$$

where $g(y) = y$ and $\phi(\tilde{F}_i)$ is defined as previously.

Step 3. Now the required ranking index is given as follows,

$$R(\tilde{F}_i) = \left[\frac{\epsilon_2 + \delta^L_{\tilde{F}_i}.\tau_{\tilde{F}_i}}{\epsilon_2 + \delta^R_{\tilde{F}_i}.(1 - \tau_{\tilde{F}_i})}\right]^{\mu} \tag{9}$$

where ϵ_2 is very very small quantity and $\mu > 0$.

For any two fuzzy numbers $\tilde{F}_1$ and $\tilde{F}_2$ we have the following,

$$\begin{aligned} &(i) \text{ if } R(\tilde{F}_1) > R(\tilde{F}_2), \text{ then } \tilde{F}_1 > \tilde{F}_2 \\ &(ii) \text{ if } R(\tilde{F}_1) < R(\tilde{F}_2), \text{ then } \tilde{F}_1 < \tilde{F}_2 \\ &(iii) \text{ if } R(\tilde{F}_1) = R(\tilde{F}_2), \text{ then } \tilde{F}_1 \sim \tilde{F}_2 \end{aligned} \tag{10}$$

4 Selection of Country for Establishing Production unit

With the machinery developed in the last two sections, we are now in a position to obtain our main objectives in this paper, that is, an economic decision making protocol for selection of a country for establishing of a unit of production of certain commodity under fuzzy decision environment. A multi-national company has several options to choose a country among n countries $C_1, C_2, \ldots, C_n$. Before establishing any production unit in any one of the place his main concern will be revenue (per unit quantity), production cost and the taxation system in that place. So first of all he wants to estimate the expected revenue, production cost and possible taxes in that place. Moreover the company assumes that all the raw materials required to establish the unit are available locally. Clearly the possible revenues, the production cost and the taxes varies from country to country, as a result all the above said quantities contain uncertainties. So at the time of making decisions during the selection process the company prefers to take the above quantities as fuzzy numbers $\tilde{r_i}$,$\tilde{c_i}$ and $\tilde{t_i}$ respectively for the countries $C_1, C_2, \ldots, C_n$. Particularly the company prefers to represents the quantities as trapezoidal fuzzy numbers. Consequently the quantities now become fuzzy variables taking values in the set of trapezoidal fuzzy numbers.

The company then tries to make the following protocol using the mathematical process which is briefly discussed in the previous section and is encapsulated in the following steps:

Step 1. The revenue per unit quantity in the country C_i is estimated and represented by a trapezoidal fuzzy number $\tilde{r_i}, i = 1, 2, \ldots, n$.
Step 2. The production cost per unit quantity in the country C_i is estimated and represented by a trapezoidal fuzzy number $\tilde{c_i}, i = 1, 2, \ldots, n$.
Step 3. The taxes per unit quantity in the country C_i is estimated and represented by a trapezoidal fuzzy number $\tilde{t_i}, i = 1, 2, \ldots, n$.
Step 4. The profit per unit quantity in the country C_i is estimated and represented by a trapezoidal fuzzy number $\tilde{p_i} = \tilde{r_i} - (\tilde{c_i} + \tilde{t_i}), i = 1, 2, \ldots, n$.
Step 5. The indices $\delta_{\tilde{p}_1}, \delta_{\tilde{p}_2}, \ldots, \delta_{\tilde{p}_n}$ are calculated.

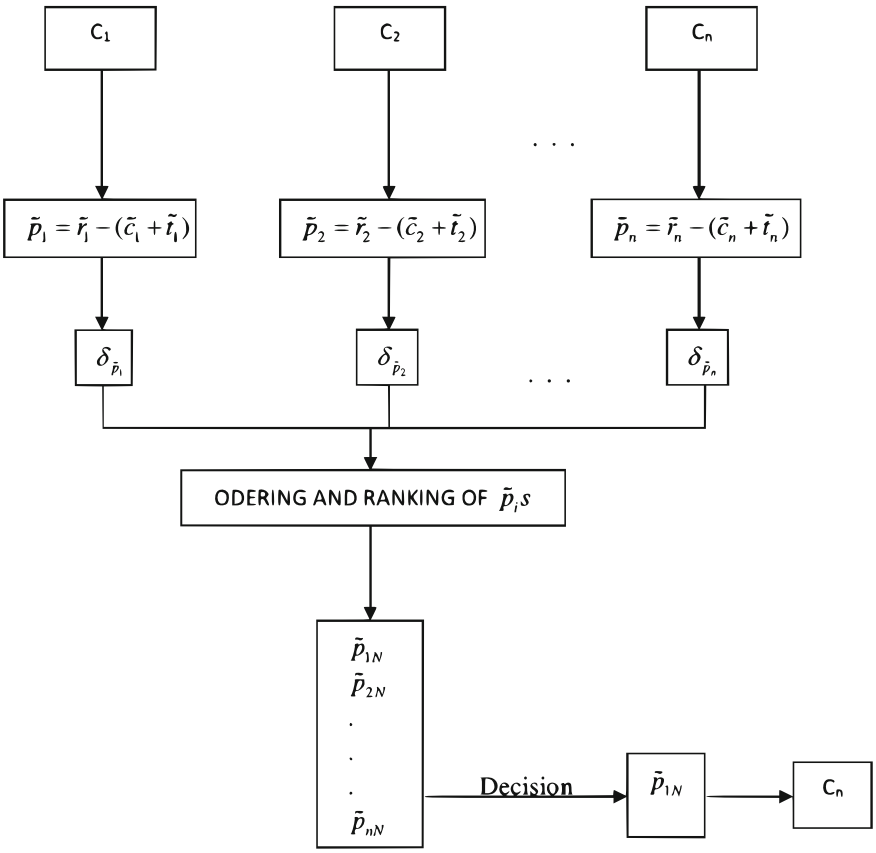

Fig. 1 C_is are countries, $\tilde{r_i}$s are possible revenues, $\tilde{c_i}$s are possible costs, $\tilde{t_i}$s are possible taxes, $\tilde{p_i}$s are profits and $\delta_{\tilde{p_i}}$s are indices

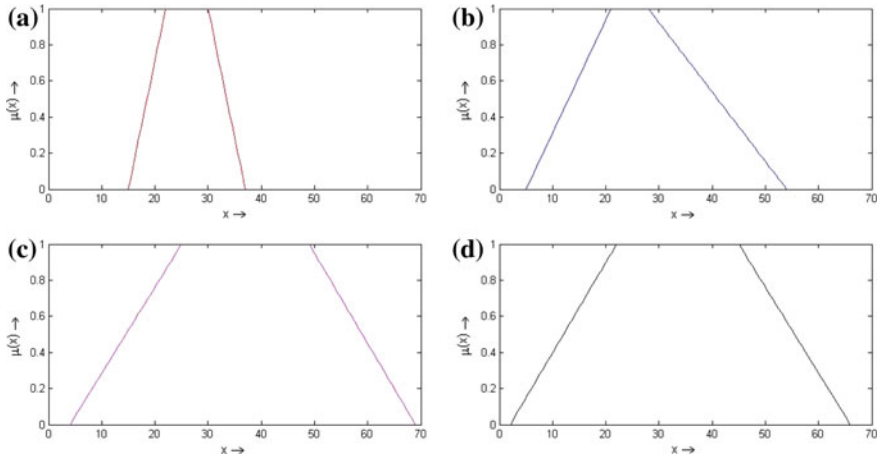

Fig. 2 **a** Trapezoidal fuzzy number $\tilde{p}_1$; **b** Trapezoidal fuzzy number $\tilde{p}_2$; **c** Trapezoidal fuzzy number $\tilde{p}_3$ and **d** Trapezoidal fuzzy number $\tilde{p}_4$

Step 6. The calculated indices in the previous step are arranged in descending order according to their values $\delta_{\tilde{p}_{1N}}, \delta_{\tilde{p}_{2N}}, \ldots, \delta_{\tilde{p}_{nN}}$.

Step 7. The fuzzy profits are then arranged in the same order as in Step 5, that is, $\tilde{p}_{1N}, \tilde{p}_{2N}, \ldots, \tilde{p}_{nN}$.

Step 8. The company chooses the number having highest rank among the numbers $\delta_{\tilde{p}_{1N}}, \delta_{\tilde{p}_{2N}}, \ldots, \delta_{\tilde{p}_{nN}}$, that is, the chosen number is $\tilde{p}_{1N}$.

Step 9. The decision is made, that is, the country C_{1N} is chosen.

Step 10. If there are more than one country having the same calculated profit $\tilde{p}_i s$, then arbitrarily one number having highest rank is chosen among the numbers having the same rank and again execute Step 8.

The above protocol can be represented by Figs. 1 and 2.

5 Illustration

In this section, we give a numerical example in support of the above protocol described in Sect. 4.

Let there be four countries C_1, C_2, C_3 and C_4.

Let the revenues $\tilde{r}_i$s, costs $\tilde{c}_i$s and taxes $\tilde{t}_i$s, $i = 1, 2, 3, 4$ at these countries be described respectively by the following trapezoidal fuzzy numbers;

$$\tilde{r}_1 = (25, 30, 35, 40),\ \tilde{r}_2 = (35, 45, 55, 65)$$

$$\tilde{r}_3 = (40, 55, 70, 85),\ \tilde{r}_4 = (44, 58, 72, 86)$$

$$\tilde{c}_1 = (2, 3, 5, 6), \quad \tilde{c}_2 = (7, 10, 15, 18)$$

$$\tilde{c}_3 = (11, 13, 17, 20), \quad \tilde{c}_4 = (12, 17, 21, 25)$$

and

$$\tilde{t}_1 = (1, 2, 3, 4), \quad \tilde{t}_2 = (4, 7, 9, 12)$$

$$\tilde{t}_3 = (5, 8, 13, 16), \quad \tilde{t}_4 = (8, 10, 15, 17)$$

Then by the formula of the previous section $\tilde{p}_i = \tilde{r}_i - (\tilde{c}_i + \tilde{t}_i)$ we have,

$$\tilde{p}_1 = (15, 22, 30, 37), \quad \tilde{p}_2 = (5, 21, 28, 54)$$

$$\tilde{p}_3 = (4, 25, 49, 69) \; and \; \tilde{p}_4 = (2, 22, 45, 66)$$

Now, $g^L_{\tilde{p}_1} = 7y + 15$, $g^R_{\tilde{p}_1} = 37 - 7y$;
$g^L_{\tilde{p}_2} = 16y + 5$, $g^R_{\tilde{p}_2} = 54 - 16y$;
$g^L_{\tilde{p}_3} = 21y + 4$, $g^R_{\tilde{p}_3} = 69 - 20y$;
and
$g^L_{\tilde{p}_4} = 20y + 2$, $g^R_{\tilde{p}_4} = 66 - 21y$;
$\alpha_{min} = min(15, 5, 4, 2) = 2$, and $\eta_{max} = max(37, 54, 69, 66) = 69$.
Now,

$$\delta^L_{\tilde{p}_1} = 1.5, \; \delta^R_{\tilde{p}_1} = 5.5, \qquad \text{by (6)}$$

$$\delta^L_{\tilde{p}_2} = 5, \quad \delta^R_{\tilde{p}_2} = 15, \qquad \text{by (6)}$$

$$\delta^L_{\tilde{p}_3} = 8.5, \; \delta^R_{\tilde{p}_3} = 39, \qquad \text{by (6)}$$

$$\delta^L_{\tilde{p}_4} = 8, \quad \delta^R_{\tilde{p}_4} = 31.5, \qquad \text{by (6)}$$

$\phi(\tilde{p}_1) = 1 = \phi(\tilde{p}_2) = \phi(\tilde{p}_3) = \phi(\tilde{p}_4)$ by (5)

Also $cos(L^{\tilde{p}_1} R) = -0.96$, $cos(L^{\tilde{p}_2} R) = -0.9953$, by (4)

$cos(L^{\tilde{p}_3} R) = -0.9957$ and $cos(L^{\tilde{p}_4} R) = -0.9952$, by (4)

Now, $U_{\tilde{p}_1} = 25.52$, $U_{\tilde{p}_2} = 29.0023$, by (8)

$U_{\tilde{p}_3} = 36.3355$ and $U_{\tilde{p}_4} = 33.1691$, by (8)

$U_{max} = max(25.52, 29.0023, 36.3355, 33.1691) = 36.3355$ and

$U_{min} = min(25.52, 29.0023, 36.3355, 33.1691) = 25.52$

$\tau_{\tilde{p}_1} = 0.0004618724$, $\tau_{\tilde{p}_2} = 0.32213755$, by (7)

$\tau_{\tilde{p}_3} = 0.99953813$, and $\tau_{\tilde{p}_4} = 0.70704355$, by (7)

Now we have the ranking indices for the four fuzzy numbers $\tilde{p}_1$, $\tilde{p}_2$,

$\tilde{p}_3$ and $\tilde{p}_4$ as follows,

$R_{\tilde{p}_1} = 0.001941$, $R_{\tilde{p}_2} = 0.15923539$, by (9)

$R_{\tilde{p}_3} = 303.64814$ and $R_{\tilde{p}_4} = 0.61336542$, by (9)

As $R_{\tilde{p}_3}$ is the highest among $R_{\tilde{p}_1}$, $R_{\tilde{p}_2}$, $R_{\tilde{p}_3}$ and $R_{\tilde{p}_4}$, hence according to the protocol discussed previously, the producer decides to select the country C_3 for establishing the production unit.

6 Conclusion

In this paper we have solved the decision making problem for the choice of country where production unit can be established by an application of fuzzy logic where the environment is uncertain. The protocol can be suitably modified and applied to other similar situations as well. The most remarkable feature of the protocol is that there is no defuzzification process in the protocol. The fuzzy logic is used in its original form where comparisons are made between fuzzy objects.

References

1. Zadeh, L.A.: Fuzzy sets. Inf. Control 338–353 (1965)
2. Bede B.: Mathematics of Fuzzy Sets and Fuzzy Logic. Springer (2012)
3. Harris J.: An Introduction To Fuzzy Logic Applications: microprocessor-based and intelligent systems engineering. Kluwer Academic Publishers (2000)
4. Niimura T., Tanaka K.: An Introduction to Fuzzy Logic for Practical Applications (1997)
5. Ross J.T.: Fuzzy Logic with Engineering Applications. Wiley(1995)
6. Bellman, R.E., Zadeh, L.A.: Decision-Making in a Fuzzy Environment. Manag. Sci. **17**(4), B141–B164 (1970)
7. Kahraman C., Onar C. S., Oztaysi B.: Fuzzy Decision Making: Its Pioneers and Supportive Environment. In: Studies in Fuzziness and Soft Computing, 341. Springer International Publishing Switzerland (2016). https://doi.org/10.1007/978-3-319-31093-0-2

8. Wierzchon, T.S.: Applications of fuzzy decision-making theory to coping with ill-defined problems. **7**(1), 1–18 (1982)
9. Hajjari, T., Abbasbandy, S.: A note on "The revised method of ranking LR fuzzy number based on deviation degree.", Expert Syst. Appl. **38**, 13491–13492 (2011)
10. Yu, V.F., Chi, H.T.X., Shen, C.W.: Ranking fuzzy numbers based on epsilon-deviation degree. Appl. Soft Comput. **13**, 3621–3627 (2013)
11. Delgado, M., Vila, M.A., Voxman, W.: On a canonical representation of fuzzy numbers. Fuzzy Sets Syst. **93**(1), 125–135 (1998)
12. Nasseri, S.H., Zadeh, M.M., Kardoost, M., Behmanesh, E.: Ranking of fuzzy quantities based on the angle of the reference functions. Appl. Math. Model. **37**, 9230–9241 (2013)
13. Abbasbandy, S., Asady, B.: Ranking of fuzzy numbers by sign distance. Inf. Sci. **176**(16), 2405–2416 (2006)
14. Chutia, R.: Ranking of fuzzy numbers by using value and angle in the epsilon-deviation degree method. Appl. Soft Comput. **60**, 706–721 (2017)

Application of Particle Swarm Optimization in Design of a Low-Profile Fractal Patch Antenna

Ankan Bhattacharya, Arnab De, Arindam Biswas, Bappadittya Roy and Anup K. Bhattacharjee

Abstract In this paper, a novel approach in Microstrip Patch Antenna analysis and design has been introduced. Here, a low-profile fractal microstrip antenna has been presented. 'Sierpinski Triangular' fractal geometry has been applied in the designing the antenna. Evolutionary Particle Swarm Optimization technique has been utilized for optimizing the design parameters. Triangular slots have been etched in the ground plane, repeated in the subsequent iterative stages. An inverted triangular patch has been placed on top of almost 1.00 mm thick Roger 4350 substrate having an electrical permittivity of 3.48 and loss tangent of 0.004. The antenna resonating frequency is 3.5 GHz with an impedance bandwidth of 700 MHz. The antenna finds its application in 3.5 GHz WiMAX band with a maximum gain of 3.34 dBi and return loss factor of 24 dB at the resonant frequency, which is reasonably better than conventional microstrip patches.

Keywords Compact microstrip patch antenna · Fractal geometry
Particle swarm optimization

A. Bhattacharya (✉) · A. De · B. Roy · A. K. Bhattacharjee
Department of Electronics and Communication Engineering, National Institute of Technology, Durgapur, Durgapur, India
e-mail: bhattacharya.ankan@ieee.org; bhattacharya.ankan1987@gmail.com

A. K. Bhattacharjee
e-mail: akbece12@yahoo.com

A. Bhattacharya
Department of Electronics and Communication Engineering, Mallabhum Institute of Technology, Bishnupur, India

A. Biswas
Department of Electronics and Communication Engineering, Asansol Engineering College, Asansol, India
e-mail: mailarindambiswas@yhaoo.co.in

B. Roy
Department of Electronics and Communication Engineering, Madanapalle Institute of Technology and Science, Madanapalle, India

U. Biswas et al. (eds.), *Advances in Computer, Communication and Control*, Lecture Notes in Networks and Systems 41, https://doi.org/10.1007/978-981-13-3122-0_20

1 Introduction

The need for compact-sized antenna is increasing day by day. Modern communication world is fully dependent on Microstrip Patches embedded in mobile devices. A major disadvantage of Conventional Patch Antennas is low bandwidth and high return loss factor. In recent times, Fractal Shapes are being introduced in Patches for bandwidth improvement and minimizing the return loss factor. The advantages of Fractal Shapes have been studied from the available literature [1, 2]. In this paper, a novel approach in Microstrip Patch Antenna analysis and design has been introduced. Here, a low-profile fractal microstrip antenna has been presented. 'Sierpinski Triangular' fractal geometry has been applied in the designing the antenna. Evolutionary Particle Swarm Optimization technique has been utilized for optimizing the design parameters. Triangular slots have been etched in the ground plane, repeated in the subsequent iterative stages. An inverted triangular patch has been placed on top of almost 1.00 mm thick Roger 4350 substrate having an electrical permittivity of 3.48 and loss tangent of 0.004. The antenna resonating frequency is 3.5 GHz with an impedance bandwidth of 700 MHz. The antenna finds its application in 3.5 GHz WiMAX band with a maximum gain of 3.34 dBi and return loss factor of 24 dB at the resonant frequency, which is reasonably better than conventional microstrip patches. The shape and size of the antenna is kept compact so that it can easily be incorporated in wireless devices.

2 Antenna Design

The antenna has been designed in IE3D Software (MoM based) environment. The front and rear views of the proposed structure have been shown in Fig. 1. The small compact rectangular-shaped patch has a dimension of $W \times L = 31.25 \times 37.75$ mm. The antenna consists of an inverted triangular-shaped patch. The altitude of the triangle has been specified as *l3*. The feed length and feed width have been specified as *l1* and *l2*, respectively. The ground plane consists of four Sierpinski triangular slots. There is a triangular slot in the centre of the ground plane. The centre triangular slot is surrounded by three other triangular slots at each side of the centre triangle. The dimensions of the triangular slots are specified by *S1* and *S2*, which are related as

$$S1 = 2.7 \times S2. \tag{1}$$

and *l1* and *l2*, the patch dimensions are related as

$$l1 = 6 \times l2. \tag{2}$$

The parameter dimensions of the antenna are specified in Table 1. The feed line width should be carefully chosen in order to match the impedance and transfer of

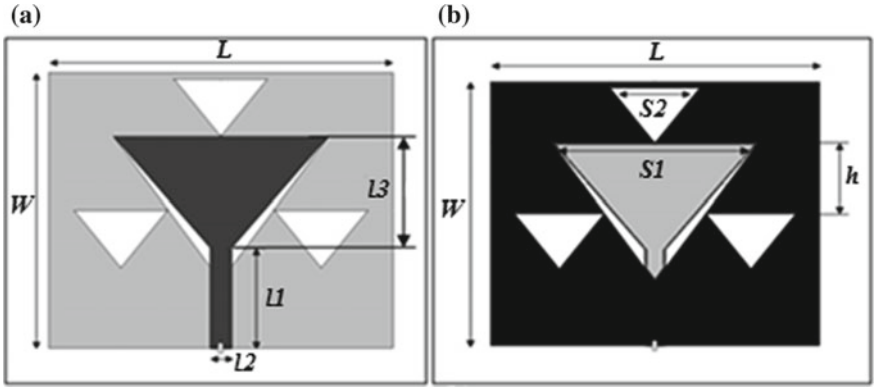

Fig. 1 Proposed fractal microstrip patch antenna: **a** Front view **b** Rear view

Table 1 Parameter dimensions in mm

Parameters	Basic dimension	Opt. dimension
L	38.00	37.75
W	31.00	31.25
l1	15.00	14.75
l2	02.50	02.50
l3	16.00	15.85
S1	23.00	22.75
S2	08.50	08.55
h	11.00	11.15
L	38.00	37.75

maximum power from the transmission line section to the radiating structure. An optimized feed width (*l2*) of 2.50 mm has been chosen for impedance matching and transmission of maximum power to the patch and minimization of return loss factor. The optimization process has been discussed in the following section.

3 PSO and Its Application in Antenna Design

Particle Swarm Optimization or in short PSO is a very popular and efficient optimization algorithm. The concept was originated from a very common event observed in nature. Feather flopping of birds is a very common event observed daily. The idea was to represent it in a graphical pattern. Later, an algorithm was formulated using a satisfactory solution which can be obtained for real-time complex computational problems. The solutions, here, are termed as 'Particles'. The best or the fittest value of the solution is regarded as the *pbest*. The overall best value, tracked by the global version of swarm and whose location is known, is called as the *gbest*. The moto is to

obtain these *pbest* and *gbest* values of the solutions and drive the problem towards an optimum direction.

The following stages explain the implementation process of PSO:

1. First, an initial population is selected for particles with random position and velocities.
2. The Fitness Function for each particle is computed next.
3. The *pbest* (δ_{id}) value is compared with the obtained fitness value. If the latter is better, it is selected as the current value for the particular particle.
4. Next, *gbest* (δ_{gd}) value is compared with evaluated best fitness value, and the better result is set equal to the current value.
5. The position (ψm) and velocity (ζm) for each particle are given as

$$\psi m = \psi m + \alpha 1 * rand() * (\delta id - \zeta m) + \alpha 2 * rand() * (\delta gd - \psi m). \quad (3)$$

$$\psi m = \psi m + \zeta m. \quad (4)$$

   where $\alpha 1$ and $\alpha 2$ are the acceleration constants.
6. The process is recycled till desired optimized values are obtained [3–5].

The basic antenna parameters, as specified in Table 1, have been optimized using the PSO technique to minimize the return loss factor at the frequency point of interest, i.e. 3.5 GHz.

The proposed Compact Microstrip Patch Antenna (CMPA) has been designed and simulated using few commonly available substrates in the market. The basic objective of the work is to improve the return loss factor $|S_{11}|$ at the resonant frequency, i.e. 3.5 GHz (WiMAX Networks). Selection of a proper substrate material is an important aspect of antenna design. Each and every substrate is characterized by its unique property of electrical permittivity and loss tangent factor. As observed from Fig. 2, FR-4 substrate with an electrical permittivity (εr) of 4.3 shows low return loss factor, but there is a frequency deviation at the frequency of interest, i.e. 3.5 GHz. Duroid with an electrical permittivity (εr) of 2.2 shows a poor response as observed from Fig. 2. On the other hand, Foam with an electrical permittivity (εr) of 1.05 gives an unsatisfactory result. The return loss, $|S_{11}|$ has been improved and the bandwidth has been enhanced using Roger 4350 substrate, having an electrical permittivity of 3.48 and loss tangent of 0.004. The antenna resonating frequency is exactly at 3.5 GHz with almost 700 MHz of impedance bandwidth.

In the following sections, the antenna responses before and after optimization by PSO algorithm has been discussed sequentially along with comparison plots.

There has been an improvement in return loss level by 2 dB (Fig. 3), with the new optimized dimensions. It may be noted that the obtained bandwidth has been kept constant in this regard. The resonant frequency has been kept constant at 3.5 GHz. The minimum return loss factor level $|S_{11}|$ for Roger Substrate, as observed from Fig. 3 is 22 dB. Whereas, after optimization, the return loss has changed to 24 dB. Figures 4 and 5 reflect the improvement in antenna VSWR and realized gain respectively. As observed from Fig. 5, there has been a significant increase in antenna gain.

The Elevation Pattern Gain display for $\varphi = 0°$ and $\varphi = 90°$ have been displayed in Fig. 6. The antenna gain has also been reflected from the 'Elevation Pattern Gain

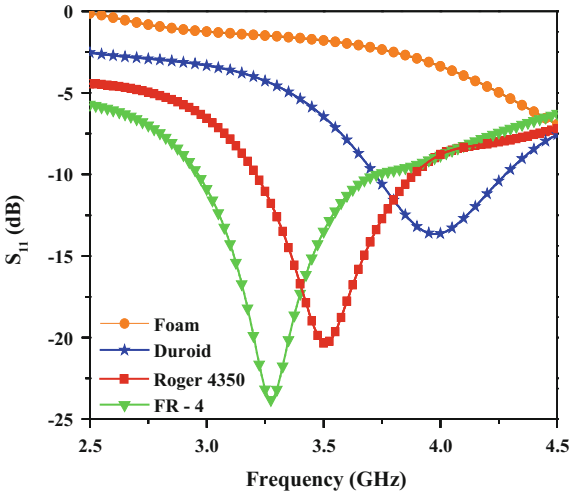

Fig. 2 Plot of S_{11} versus frequency for different substrates

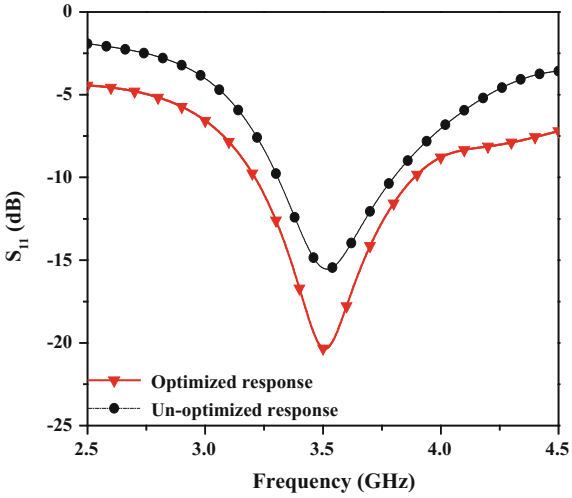

Fig. 3 Return loss factor (optimized vs. Un-optimized)

Display'. An idea of the radiation pattern of the antenna can also be obtained from Fig. 6. The min. and max. gain limits are 1.75 and 3.75 dBi as observed from Fig. 6a and Fig. 6b, respectively. The gain is equal to 3.5 dBi at the resonant frequency point, i.e. at 3.5 GHz. Figure 7 shows the antenna surface current distribution pattern at 3.5 GHz. It has been observed that there has been an accumulation of surface current near the slots which is the driving factor for improvements in antenna gain, return loss and VSWR.

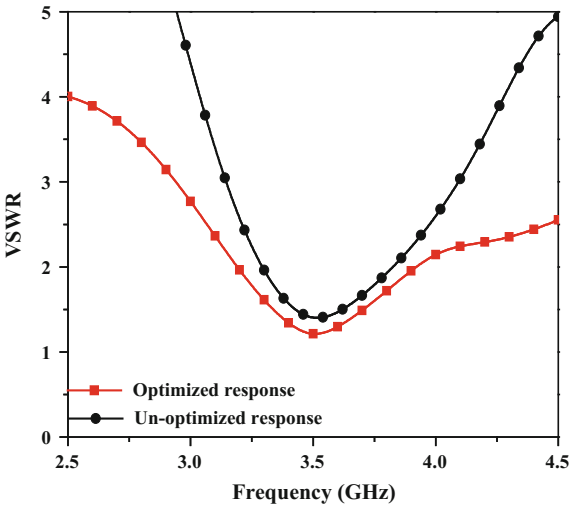

Fig. 4 VSWR (Optimized vs. Un-Optimized)

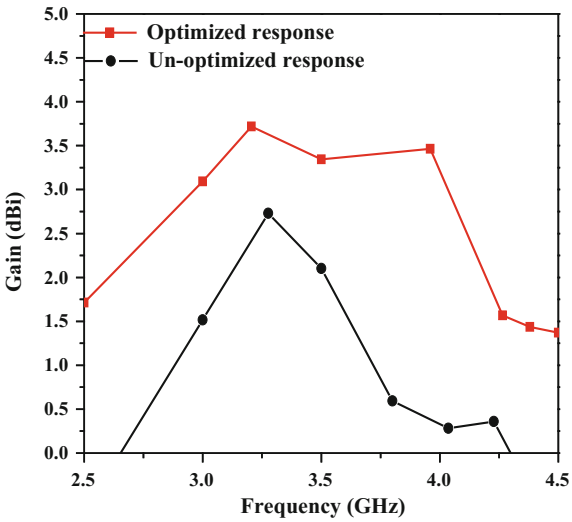

Fig. 5 Antenna gain (Optimized vs. Un-Optimized)

4 Conclusion

The above studies reveal that Particle Swarm Optimization has been extremely useful in optimization of the return loss factor at the resonating frequency point. The designed antenna shows quite good and accurate results which justifies its practical applicability. The proposed antenna finds its applicability in 3.5 GHz WiMAX band with a maximum realized gain of 3.5 dBi at the resonant frequency. Also, the compactness and simplicity of the proposed design make it quite suitable to be incorporated in mobile devices supporting wireless communications.

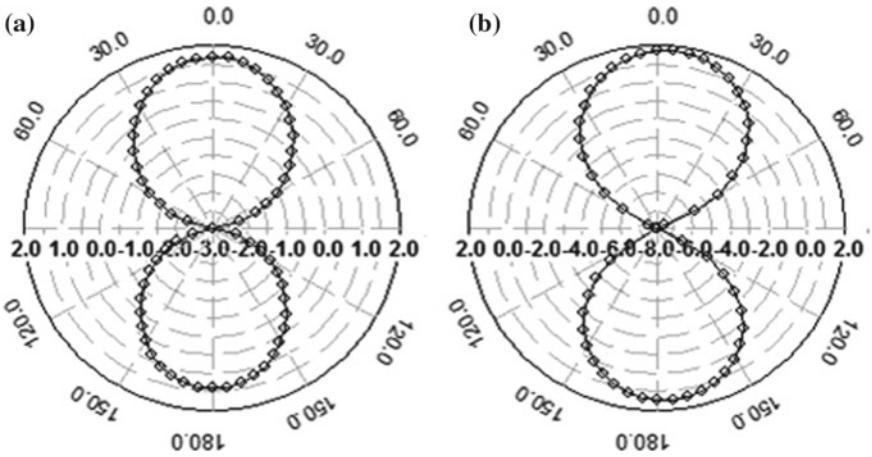

Fig. 6 Elevation pattern gain display **a** $\varphi = 0°$ **b** $\varphi = 90°$

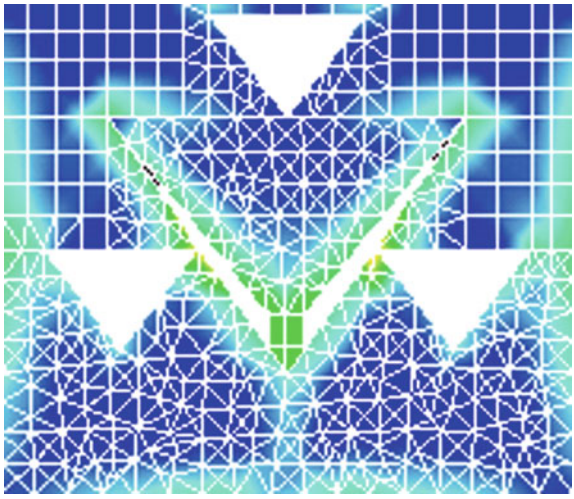

Fig. 7 Antenna surface current distribution at 3.5 GHz

Acknowledgements The authors express their sincere gratitude to Dr. S. K. Chowdhury, Retired Professor of ETCE Dept., Jadavpur University, Kolkata, India for his constructive comments and suggestions for this work.

References

1. Gianvittorio, J.: Fractal Antennas: Design, characterization and applications. Ph.D. Dissertation. Department of Electrical Engineering, University of California at Los Angeles, Los Angeles (2007)
2. Bhattacharya, A., Roy, B., Chowdhury, S.K., Bhattacharjee, A.K.: Design and analysis of a Koch snowflake fractal monopole antenna for wideband communication. Appl. Computat. Electromag. Soc. J. (ACES) **32**(6), 548–554 (2017)
3. Robinson, J., Rahmat, Samii Y.: Particle swarm optimization in electromagnetics. IEEE Trans. Antennas Propag. **52**(2), 397–407 (2004)
4. Shi, Y., Eberhart R.: Experimental study of particle swarm optimization. In: Proceedings of SCI2000, Conference, Orlando, FL (2000)
5. Kennedy, J.: Stereotyping; improving particle swarm performance with cluster analysis. Proceedings of the 2000 Congress on Evolutionary Computation, La Jolla, CA, vol. 2, pp. 1507–1512 (2000)

Coaxial Probe-Fed Slotted Antenna with Defected Ground Structure for Multi-band Applications

Arnab De, Mamoni Saha, Ankan Bhattacharya, Arindam Biswas, Bappadittya Roy and Anup K. Bhattacharjee

Abstract This paper describes a coaxial probe-fed slotted antenna with Defected Ground Structures (DGS) which can be tuned to resonate at our desired frequency bands by changing the position of DGS and width of the slots in the ground plane. The proposed antenna can be made to work in the WLAN (2.4/5.2/5.8 GHz) band and WiMAX applications. In this paper, we have tried to reflect a detailed study of the slots in the ground plane and its effect on the antenna parameters such as gain, polarization, return loss, radiation pattern, etc. The proposed antenna produced a multi-band application providing return loss of 11.81 dB at 1.69 GHz, 18.81 dB at 2.5 GHz, 19.59 dB at 2.89 GHz, 22.98 dB at 4.81 GHz, 19.80 dB at 5.80 GHz and 12.70 dB at 6.17 GHz by using FR-4 Epoxy substrate with dielectric constant (ε_r) of 4.4 and a substrate height (h) of 1.60 mm.

Keywords Slot antennas · DGS · WLAN

A. De (✉) · M. Saha · A. Bhattacharya · B. Roy · A. K. Bhattacharjee
Department of Electronics and Communication Engineering, National Institute of Technology, Durgapur, Durgapur, WB, India
e-mail: ade.ece1990@gmail.com

A. Bhattacharya
e-mail: bhattacharya.ankan@ieee.org

A. K. Bhattacharjee
e-mail: akbece12@yahoo.com

A. Bhattacharya
Department of Electronics and Communication Engineering, Mallabhum Institute of Technology, Bishnupur, India

A. Biswas
Department of Electronics and Communication Engineering, Asansol Engineering College, Asansol 713305 , India
e-mail: mailarindambiswas@yhaoo.co.in

B. Roy
Department of Electronics and Communication Engineering, Madanapalle Institute of Technology and Science, Madanapalle, India

U. Biswas et al. (eds.), *Advances in Computer, Communication and Control*, Lecture Notes in Networks and Systems 41, https://doi.org/10.1007/978-981-13-3122-0_21

1 Introduction

In recent years, there has been a trend in the miniaturization of the sizes of electronic devices. As antenna plays an important role in the overall package volume, the reduction in antenna size has become very important [1]. The DGS is extensively used for bandwidth enhancement, producing band notches and disturb inductance and capacitance of the slotted regions [2]. The antenna is slotted at two places using tree-shaped structure to reduce the size of the antenna and giving good bandwidth. The 2.4 GHz band is used mainly in cell phones, radios, microwave ovens, etc. while the 5.5 GHz band is used mainly for wireless communications providing a wireless alternative to cable and Digital Subscriber Line (DSL) for last mile broadband access [3, 4]. The slots are given various shapes such as L, I, etc. and optimizing the feed points, the results are shown step by step with precision. By tuning the slots, the antenna can be made operational at the desirable frequencies giving an advantage of multi-band frequency operations [5, 6]. The antenna is simulated in IE3D software and the results are analyzed. The antenna design has been carried out by a set of Method of Moments (MoM) simulations [7].

2 Antenna Design

The reference antenna is shown in Fig. 1 which constitute of a radiating patch and a ground plane fed by a coaxial probe of impedance 50 Ω.

The patch dimensions are 36.49×27.76 mm^2 and the ground plane dimensions are 40×40 mm^2 (Table 1). In the next step, two symmetric slots are cut from the radiating patch and the ground plane is held as it is. The resulting figure is shown in Fig. 2. Then, adding open-ended L-shaped slots on the ground plane, we get the proposed figure as shown in Fig. 3.

Table 1 Antenna dimensions in mm

Parameters	Values (mm)
W	27.76
L	36.49
W_x	40.00
L_x	40.00
P_x	17.00
P_y	2.50
Q_y	1.50

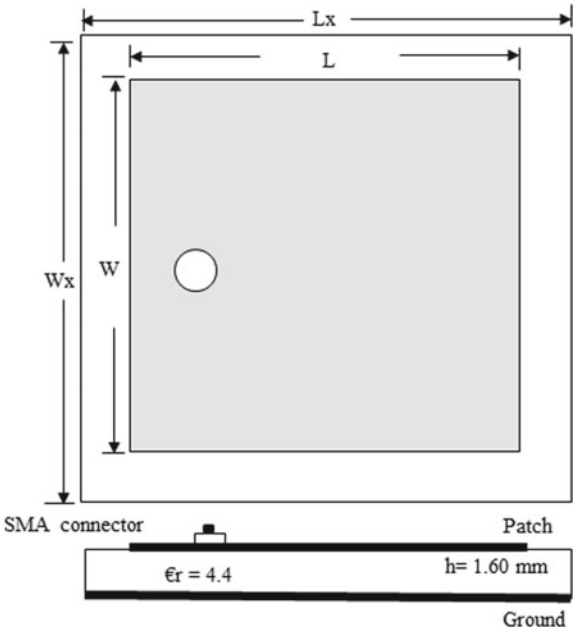

Fig. 1 Reference antenna with an optimized feed point

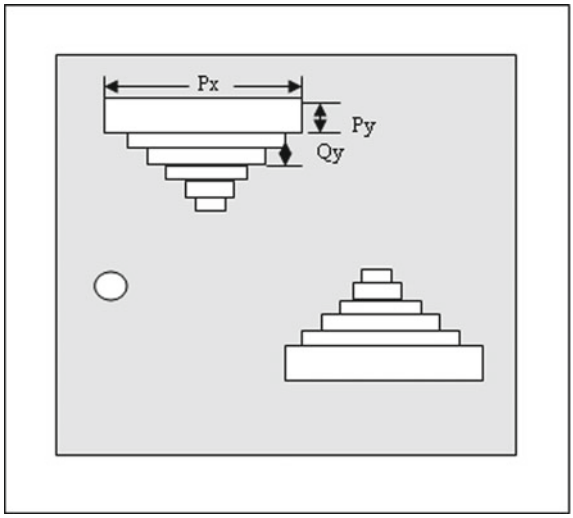

Fig. 2 Slotted antenna without DGS

We denote the reference antenna as Antenna 1, while the slotted antenna (without DGS) as Antenna 2 and the slotted antenna (with DGS) as Antenna 3.

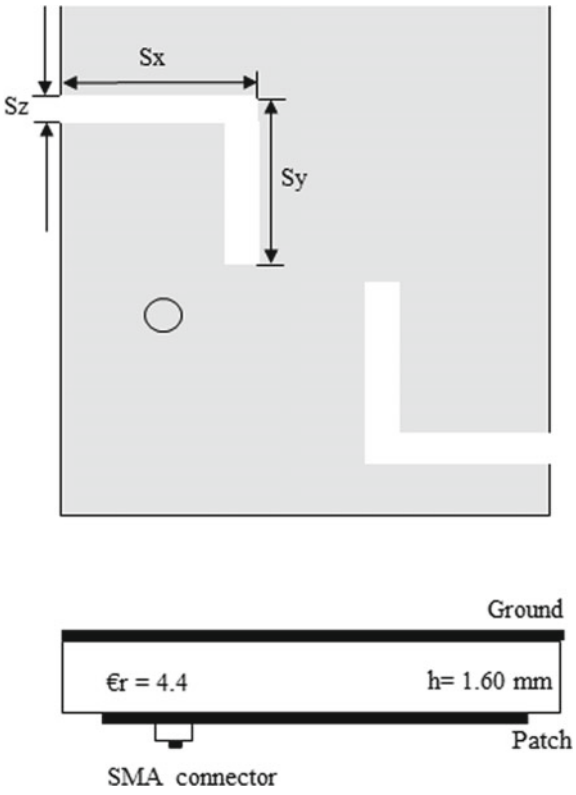

Fig. 3 Slotted antenna with DGS (back view where front view contain same antenna dimensions as in Fig. 2)

3 Results and Discussion

Now, we will compare the performance of the antennas, namely Antenna 1, Antenna 2 and Antenna 3. Antenna 2 resonates at different frequencies. Whereas, maximum return loss of 20.43 dB at 5.8 GHz is shown in Fig. 4. With the help of the slots, we can overcome the drawback of simple microstrip antenna which provides narrow bandwidth and low gain of 2 dBi. The Current Distribution Pattern and Gain versus Frequency Plot is shown in Figs. 5 and 6, respectively.

The gain is found to be 4.05 dBi which is much greater than a simple microstrip line-fed patch antenna giving us an idea about the utility of slotted antennas. In the next step, we show the results of Antenna 3 where ground slots are added to make the antenna resonate at multiple frequencies. In Antenna 3 (slotted antenna with DGS), we can see that with the help of Defected Ground Structure made by open-ended L-shaped slots, we can see that the antenna can be made to resonate at 2.5 GHz applicable for WLAN band and as well as 5.8 GHz applicable for WiMAX applications. The return loss plot is shown below in Fig. 7 for our proposed antenna.

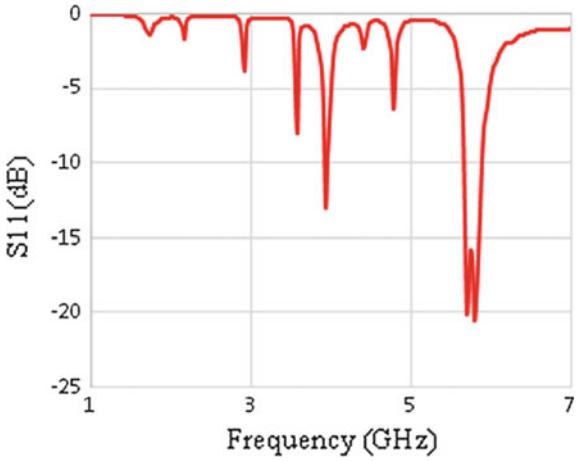

Fig. 4 S_{11} versus frequency plot of Antenna 2

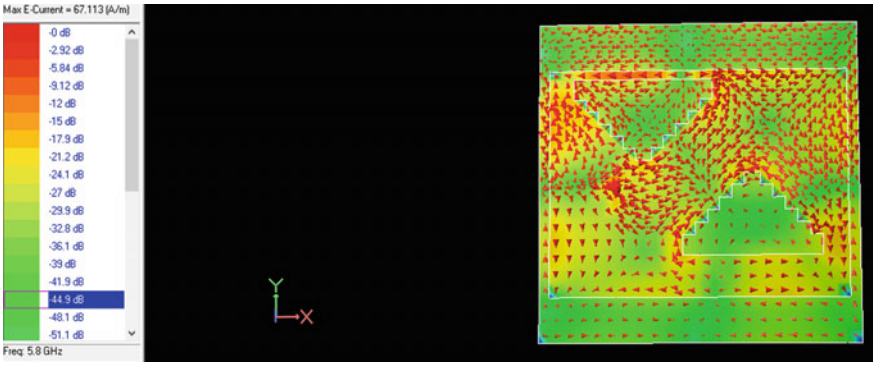

Fig. 5 Current distribution pattern at 5.8 GHZ of Antenna 2

We can see that the antenna can be made to work at different ISM bands by tuning the shape of the slots or its dimensions. The antenna provides a return loss of 18.81 dB at 2.5 GHz and 19.80 dB at 5.80 GHz. The Current Distribution Pattern plot is shown below in Fig. 8 at 5.8 GHz. It also provides low profile, cost-effective, and can be easily integrated with other circuits.

The combined result of three antennas is shown in Fig. 9. The antenna radiation pattern at 2.5, 5.5 and 5.8 GHz is shown in Fig. 10.

In this paper, the proposed antenna is fabricated and the measured results are compared with the simulated one. The prototype of the antenna as depicted previously is shown in Fig. 11.

In Fig. 12, measured and simulated comparison plot of S-parameters of Antenna 3, i.e. our proposed antenna are shown where the discrepancy between the measured

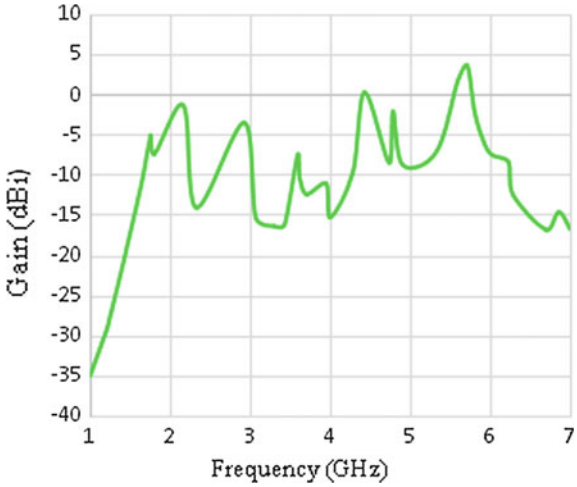

Fig. 6 Gain versus frequency plot of Antenna 2

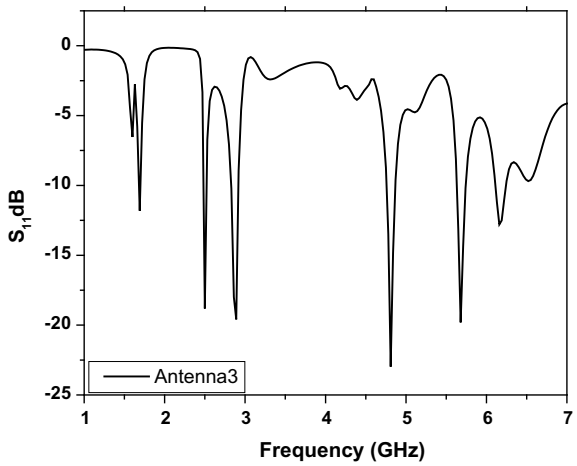

Fig. 7 S_{11} versus frequency plot (Antenna 3)

and simulated S-parameters is very small mainly due to the effect of the soldering and fabrication tolerance.

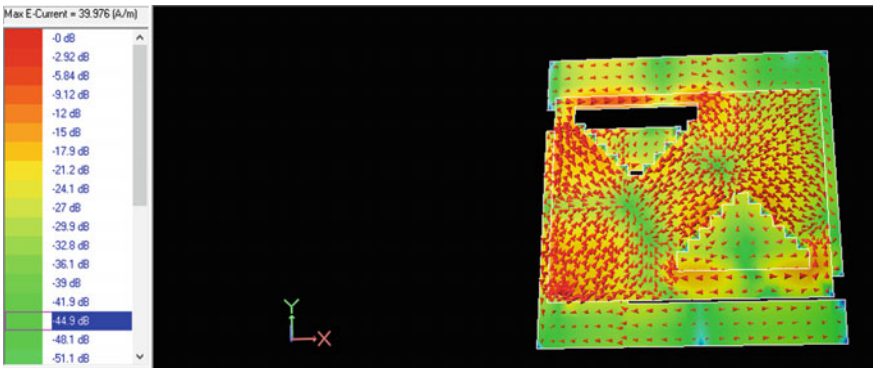

Fig. 8 Current distribution of Antenna 3 at 5.8 GHz

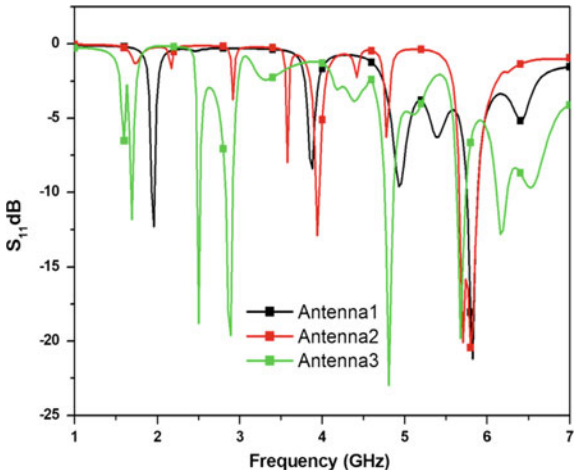

Fig. 9 Comparative S_{11} graph of Antenna 1, 2 and 3

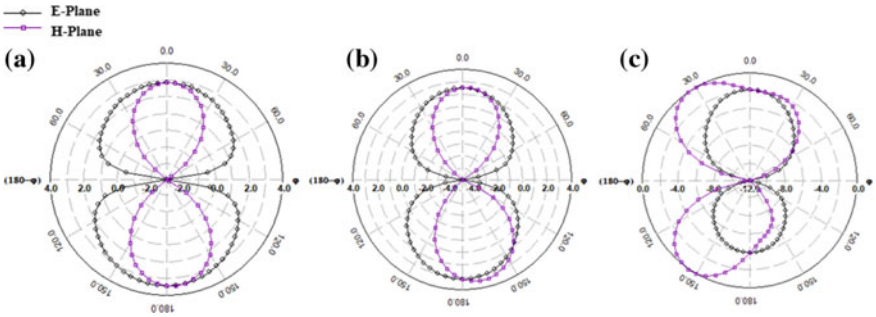

Fig. 10 Antenna radiation pattern at **a** 2.5 GHz, **b** 5.5 GHz and **c** 5.8 GHz

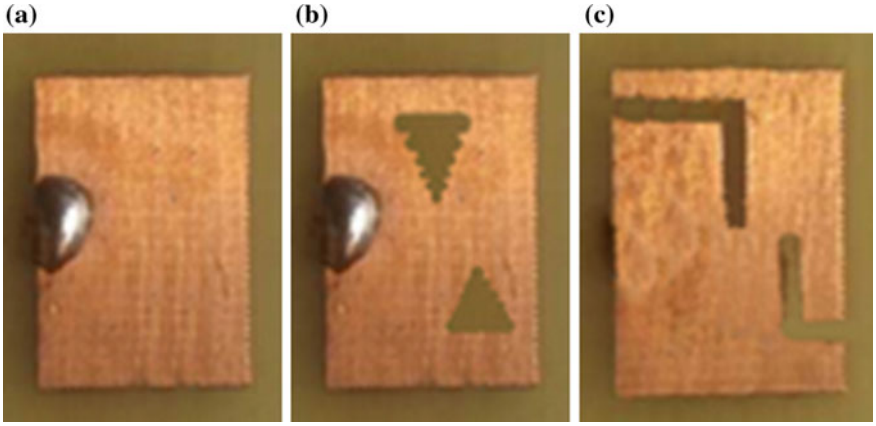

Fig. 11 Fabricated prototype **a** Antenna 1 (reference antenna) **b** Antenna 2 (front view) **c** Antenna 3 (back view where front view is same as Antenna 2)

Fig. 12 Frequency response of Antenna 3 (Sim. vs. Mea.)

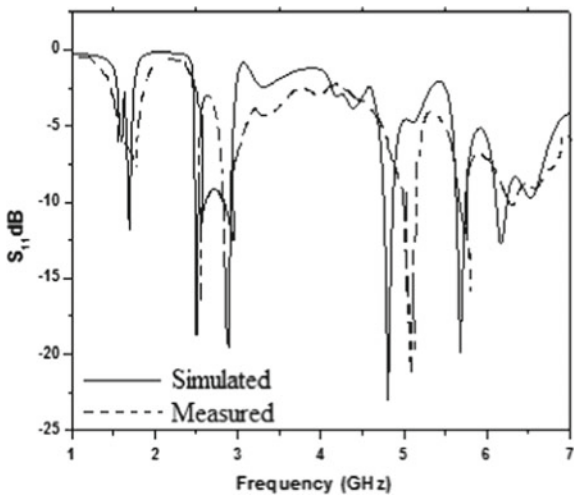

4 Conclusion

Rectangular coaxial probe-fed slotted antenna created an operating bandwidth of wireless communications. The performance of the proposed antenna has been investigated. Simulated results of the proposed antenna show high gain, return loss and efficiency, etc. The slots tend to reduce the size of the microstrip antenna and change the direction of the current. The current has to travel extra patch as compared to the antenna without slots. The antenna is applicable for various wireless bands which cover WLAN and WiMAX frequencies.

References

1. Wang, K.: Compact and Broadband Microstrip Antenna. A Wiley Interscience Publication
2. Balanis, C.A.: Antenna Theory, Analysis and Design. Wiley, New York (1997)
3. Liu, W.C., Wu, C.M., Dai, Y.: Design of triple—frequency micro strip-fed monopole antenna using defected ground structure. IEEE Trans. Antennas Propag. **59**(7) (2011)
4. Kundu, A., Roy, B., Batabyal, S., Chakraborty, U., Bhattacharjee, A.K.: Coaxial fed compact rectangular microstrip antenna with multi-layer configuration for WLAN 2.4/S.2/S.8 GHZ band applications. In: ICIIS 2014, pp. I-4, lS-17. IEEE (2014)
5. Roy, B., Bhattacharya, A., Bhattacharjee, A.K., Chowdbury, S.K.: Effect of different slots in a design of microstrip antennas. In: ICECS 201S, pp. 386–390, 26–27. IEEE (2015)
6. Pozar, D.M.: A reciprocity method of analysis for printed slot and slot-coupled microstrip antennas. IEEE Trans. Antennas Propag. **AP-34**, 1439–1446 (1986)
7. IE3D User's Manual, Release 9, Zeland Software, Inc

State-Space Model Based Induction Motor Stator Winding Inter-turn Fault Detection Technique

Pratyaya Majumdar, Partha Mishra, Shubhasish Sarkar and Santanu Das

Abstract Detection of fault at its inception point is extremely important to avoid catastrophic failure in the industrial process. In three-phase induction motor, stator winding inter-turn faults involving a small number of turns is not easily discernible and the motor under such fault condition may continue to operate for a certain time until the initiated fault is enhanced and propagated to a major fault resulting in an irreparable motor failure. In this paper, a state-space model has been proposed to detect stator winding inter-turn faults in three-phase induction motor using System Identification Toolbox of MATLAB®. The proposed model is validated and subsequently used for determining the step response, which will carry significant information which is capable to detect stator winding inter-turn faults.

Keywords Stator winding inter-turn fault · Three-phase induction motor
State-space analysis · System identification toolbox

1 Introduction

Induction Motors (IMs) are widely used in the industrial system due to their efficient and cost-effective performance. An induction motor fault results in severe damage not only to the motor itself, but also to the motor-related equipment devices in an industry resulting in unscheduled machine downtime, which can cause heavy financial losses. Therefore, motor condition monitoring is of great importance to detect a fault at its inception points to avoid catastrophic failure in the industrial system.

P. Majumdar · S. Sarkar · S. Das (✉)
Department of Electrical Engineering, Jalpaiguri Government Engineering College, Jalpaiguri 735102, West Bengal, India
e-mail: santanu.das@ee.jgec.ac.in; santanu.ddas@gmail.com

P. Mishra
Department of Electrical Engineering, CEMK, Kolaghat, West Bengal, India

U. Biswas et al. (eds.), *Advances in Computer, Communication and Control*, Lecture Notes in Networks and Systems 41, https://doi.org/10.1007/978-981-13-3122-0_22

The major faults of electrical machines can broadly be classified as the following [1, 2]:

(a) stator faults resulting in the opening or shorting of one or more of a stator phase winding.
(b) abnormal connection of the stator windings.
(c) broken rotor bar or cracked rotor end-rings.
(d) static and/or dynamic air-gap irregularities.
(e) bent shaft (akin to dynamic eccentricity).
(f) shorted rotor field winding.
(g) bearing and gearbox failures.

Of the above type of faults, stator winding inter-turn short-circuit is one of the most common faults that prevails and covers approximately 30–40% of the overall fault conditions in IMs [3, 4]. Therefore, detection of faults at an early stage of evolution is extremely important to avoid the catastrophic failure in the industrial process [5]. During the past two decades, several techniques to detect stator inter-turn fault have been proposed. Each and every approach for detection of faults requires a model suited for fault detection. In this paper, a simple and fast yet efficient technique has been proposed by introducing a state-space model using system identification toolbox of MATLAB®. The model is validated and subsequently used to determine step responses, which carries significant information capable to detect stator winding's inter-turn short-circuit fault of varying severity.

1.1 Stator Winding Inter-turn Fault

Induction motors are subjected to various undesirable stresses [6, 7] resulting in deterioration of stator winding insulation. Inter-turn fault incepts an insulation failure between two windings in the stator winding phase.

As the name suggests, in an inter-turn fault number of turns in a stator coil gets short-circuited as shown in Fig. 1. The current in the shorted turns is of the order of twice the full load current, which causes several localized hot-spots. Stator winding inter-turn fault involving a smaller number of turns are not easily detected and the motor under such condition may continue to operate until the initiated fault is enhanced and propagates to larger section of the windings, which results in a coil-to-coil short-circuit or a phase-to-phase short-circuit [8]. These faults again can develop phase-to-ground faults, which can cause significant damage to the motor [9].

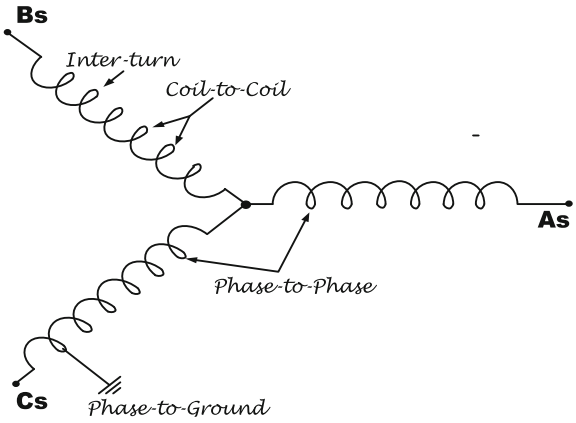

Fig. 1 Schematic representation of stator possible failure modes

The stator winding inter-turn fault can create following problems [1, 5]:

(a) Unbalanced air-gap voltages and line currents;
(b) Increased torque pulsations;
(c) Decreased average torque;
(d) Noise and vibration;
(e) Increased losses and reduction in efficiency;
(f) Excessive heating [8].

Hence, detecting an inter-turn fault at an early stage of evolution would eliminate above damages caused to the motor, reduce downtime and thus save operational costs [10] (Fig. 2).

1.2 System Identification and MATLAB Toolbox

During the past two decades, several techniques have been proposed to detect stator inter-turn fault. Each and every approach to detection requires a model. First principle modeling method is one of the most popular methods of modeling. This method is sometimes referred to as white-box modeling because it depends on the dynamical structure of the system under study. Thus, the structure of the system must be known [11].

On the contrary, system identification is a method for obtaining dynamical models from observations of the system under study. System identification is sometimes referred to as black-box modeling. The models are constructed under the assumption that the system structure is unknown.

System Identification Toolbox provides MATLAB® functions, Simulink® blocks, and an app for creating linear and nonlinear dynamic system models from measured input–output data [12]. Time-domain or frequency-domain input–output data

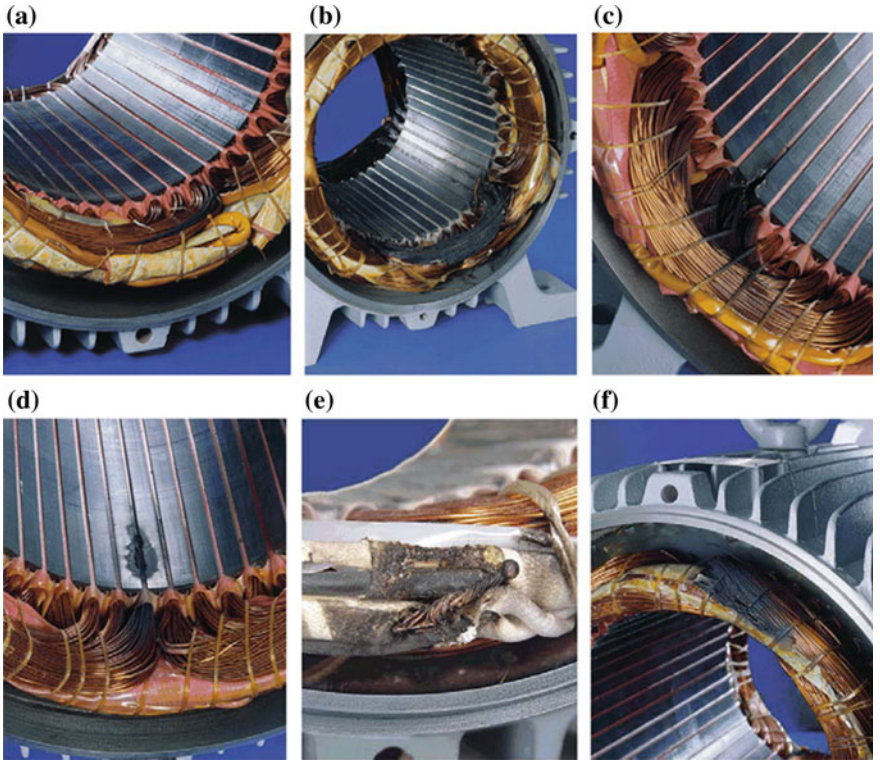

Fig. 2 Insulation damage leading to inter-turn short-circuit of the stator windings in three-phase induction motors. **a** Inter-turn short-circuits between turns of the same phase. **b** Winding short-circuited. **c** Short-circuits between winding and stator core at the end of the stator slot. **d** Short-circuits between winding and stator core in the middle of the stator slot. **e** Short-circuit at the leads. **f** A short-circuit between phases [7]

to determine transfer functions, state-space models of the concerned system. The toolbox also provides algorithms for online parameter estimation. The toolbox can be obtained in MATLAB by using 'ident' command in command window of MATLAB (Fig. 3).

2 IM Modeling

The dynamic mathematical model of an induction motor is usually represented in the stationary *a*bc reference frame in terms of voltage, current, and flux linkage.

In order to describe the stator winding short-circuit fault, an additional shorted winding is added in a three-phase axis of an induction motor. Figure 4 shows a stator winding short-circuit fault in Phase *a*.

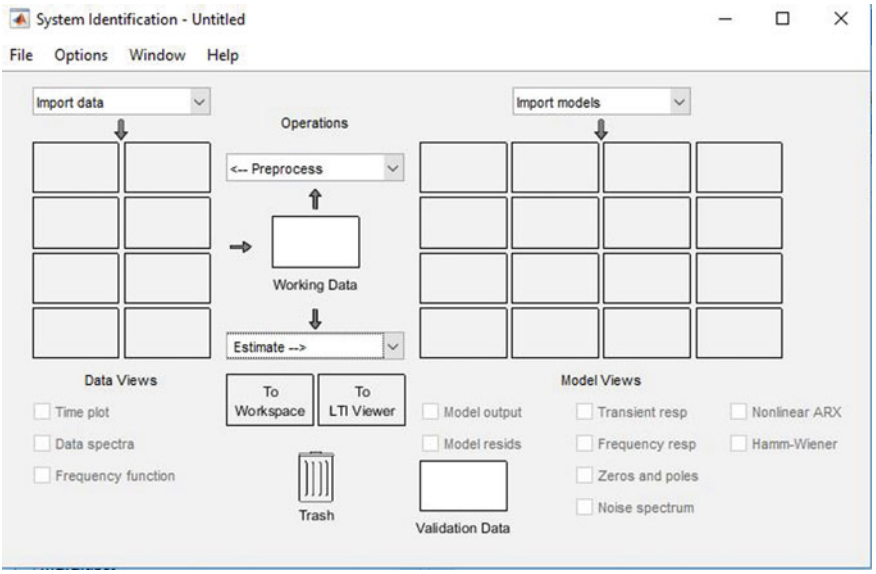

Fig. 3 Graphical user interface of system identification toolbox of MATLAB®

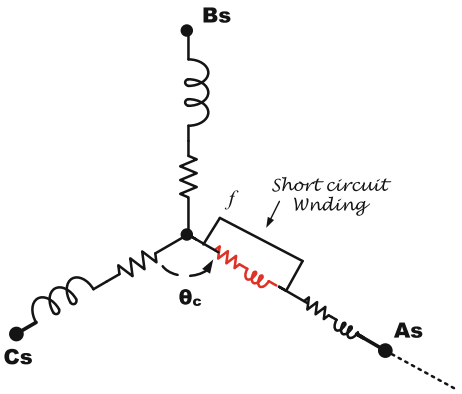

Fig. 4 Stator winding short-circuit fault at phase A

Two characteristic parameters, location parameter θ_c and fault level f, are utilized to describe stator short-circuit fault in a three-phase induction motor.

In our study, $\theta_c = 2\pi/3 \times n$, where $n = \{0, 1, 2\}$ represents for stator short-circuit fault in phase a, b, and c, respectively.

The induction motor mathematical model with stator short-circuit fault can be expressed by the following equations:

$$\begin{bmatrix} vas \\ vbs \\ vcs \end{bmatrix} = \mathrm{Rs} \begin{bmatrix} ias \\ ibs \\ ics \end{bmatrix} + \frac{d}{dt} \begin{bmatrix} \lambda as \\ \lambda bs \\ \lambda cs \end{bmatrix}, \tag{1}$$

$$0 = \mathrm{Rr}\begin{bmatrix} iar \\ ibr \\ icr \end{bmatrix} + \frac{d}{dt}\begin{bmatrix} \lambda ar \\ \lambda br \\ \lambda cr \end{bmatrix}, \tag{2}$$

$$0 = \mathrm{R_f}\,\mathrm{i_f} + \frac{d}{dt}\lambda_\mathrm{f} \tag{3}$$

$$\begin{bmatrix} \lambda as \\ \lambda bs \\ \lambda cs \end{bmatrix} = \mathrm{Lsr}\begin{bmatrix} iar \\ ibr \\ icr \end{bmatrix} + \mathrm{Lss}\begin{bmatrix} ias \\ ibs \\ ics \end{bmatrix} + \mathrm{Lsf}(\mathrm{i_f}) \tag{4}$$

$$\begin{bmatrix} \lambda ar \\ \lambda br \\ \lambda cr \end{bmatrix} = \mathrm{Lrr}\begin{bmatrix} iar \\ ibr \\ icr \end{bmatrix} + \mathrm{Lrs}\begin{bmatrix} ias \\ ibs \\ ics \end{bmatrix} + \mathrm{Lrf}(\mathrm{i_f}) \tag{5}$$

$$\lambda_\mathrm{f} = \mathrm{Lsf}\begin{bmatrix} ias \\ ibs \\ ics \end{bmatrix} + \mathrm{Lrf}\begin{bmatrix} iar \\ ibr \\ icr \end{bmatrix} + \mathrm{Lf}(\mathrm{i_f}) \tag{6}$$

where $\mathrm{Rf} = \mathrm{f} * \mathrm{Rs}$ is short-circuit resistance; $\mathrm{i_f}$ and λ_f are short-circuit current and flux, respectively; $\mathrm{Lf} = \mathrm{f}^2(\mathrm{Lls} + \mathrm{Ls})$ is short-circuit inductance. The mutual inductances between stator, rotor and short-circuited windings are dependent on the rotor angle.

The mathematical model is also transferred from abc to αβ coordinates to simplify the computation. The transformation matrices of stator short-circuit fault-related variables ($\mathrm{i_f}$, λ_f) are defined as

$$\begin{bmatrix} i\alpha\mathrm{f} \\ i\beta\mathrm{f} \end{bmatrix} = \begin{bmatrix} \cos\theta_c \\ \sin\theta_c \end{bmatrix} * \mathrm{i_f} \tag{7}$$

$$\begin{bmatrix} \lambda\alpha\mathrm{r} \\ \lambda\beta\mathrm{r} \end{bmatrix} = \begin{bmatrix} \cos\theta_c \\ \sin\theta_c \end{bmatrix} * \lambda_\mathrm{f} \tag{8}$$

Applying transformation matrices to the induction motor model, the motor model in αβ coordinates can be expressed as

$$\begin{bmatrix} v\alpha\mathrm{s} \\ v\beta\mathrm{s} \end{bmatrix} = \mathrm{Rs}\begin{bmatrix} i\alpha\mathrm{s} \\ i\beta\mathrm{s} \end{bmatrix} + \frac{d}{dt}\begin{bmatrix} \lambda\alpha\mathrm{s} \\ \lambda\beta\mathrm{s} \end{bmatrix}, \tag{9}$$

$$0 = \mathrm{Rr}\begin{bmatrix} i\alpha\mathrm{r} \\ i\beta\mathrm{r} \end{bmatrix} + \frac{d}{dt}\begin{bmatrix} \lambda\alpha\mathrm{r} \\ \lambda\beta\mathrm{r} \end{bmatrix} - \mathrm{w_r}\,\mathrm{T_r}(\pi/2)\begin{bmatrix} \lambda\alpha\mathrm{r} \\ \lambda\beta\mathrm{r} \end{bmatrix}, \tag{10}$$

$$\begin{bmatrix} \lambda\alpha\mathrm{s} \\ \lambda\beta\mathrm{s} \end{bmatrix} = \mathrm{L_{ls}}\begin{bmatrix} i\alpha\mathrm{s} \\ i\beta\mathrm{s} \end{bmatrix} + \mathrm{L_m}\left(\begin{bmatrix} i\alpha\mathrm{s} \\ i\beta\mathrm{s} \end{bmatrix} + \begin{bmatrix} i\alpha\mathrm{r} \\ i\beta\mathrm{r} \end{bmatrix} + \sqrt{\frac{2}{3}} * f * \begin{bmatrix} i\alpha\mathrm{f} \\ i\beta\mathrm{f} \end{bmatrix}\right), \tag{11}$$

$$\begin{bmatrix} \lambda\alpha\mathrm{r} \\ \lambda\beta\mathrm{r} \end{bmatrix} = \mathrm{L_{lr}}\begin{bmatrix} i\alpha\mathrm{r} \\ i\beta\mathrm{r} \end{bmatrix} + \mathrm{L_m}\left(\begin{bmatrix} i\alpha\mathrm{s} \\ i\beta\mathrm{s} \end{bmatrix} + \begin{bmatrix} i\alpha\mathrm{r} \\ i\beta\mathrm{r} \end{bmatrix} + \sqrt{\frac{2}{3}} * f * \begin{bmatrix} i\alpha\mathrm{f} \\ i\beta\mathrm{f} \end{bmatrix}\right), \tag{12}$$

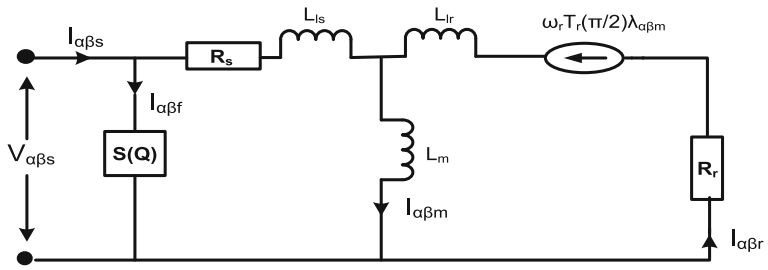

Fig. 5 Equivalent circuit of an induction motor with stator short-circuit inter-turn fault in $\alpha\beta$ reference frame

$$\begin{bmatrix} \lambda\alpha f \\ \lambda\beta f \end{bmatrix} = \sqrt{\frac{2}{3}} * f * L_m * S(Q)\left(\begin{bmatrix} i\alpha s \\ i\beta s \end{bmatrix} + \begin{bmatrix} i\alpha r \\ i\beta r \end{bmatrix}\right) + f^2(L_{ls} + 2/3 * L_m) * S(Q) * \begin{bmatrix} i\alpha f \\ i\beta f \end{bmatrix} \quad (13)$$

where

$$S(Q) = \begin{bmatrix} \cos\theta_c * \cos\theta_c & \sin\theta_c * \cos\theta_c \\ \sin\theta_c * \cos\theta_c & \sin\theta_c * \sin\theta_c \end{bmatrix}$$

$$0 = f * Rs\begin{bmatrix} i\alpha f \\ i\beta f \end{bmatrix} + \begin{bmatrix} i\alpha f \\ i\beta f \end{bmatrix} \quad (14)$$

The above mathematical model can be represented in the state-space equation as

$$\begin{cases} \dot{x}(t) = A * x(t) + B * u(t) \\ y(t) = C * x(t) + D * u(t) \end{cases}$$

where $x = \left[i_{\alpha s}\ i_{\beta s}\ \lambda_{\alpha s}\ \lambda_{\beta s}\right]^T$ is the state-space vector.

$u = \begin{bmatrix} v_{\alpha s} \\ v_{\beta s} \end{bmatrix}$, $y = \begin{bmatrix} i_{\alpha s} \\ i_{\beta s} \end{bmatrix}$ are the system input–outputs (Fig. 5).

3 Experimental Analysis

In a model-based approach of detection, a dynamic model of the concerned system is first built using measured input and output data. A **3-Φ, 2.5 Hp, 400 V, 4 pole** induction motor with isolated neutral has been used for the purpose of detection of a fault. A series of experiments are being carried out on three-phase induction motor under different loaded conditions in healthy and faulty conditions. Under each experimental condition, 10 cycles of steady-state three-phase current and voltage signals of the motor were captured as time series with 20 kHz as a sampling frequency for analysis (Fig. 6).

Fig. 6 Experimental setup

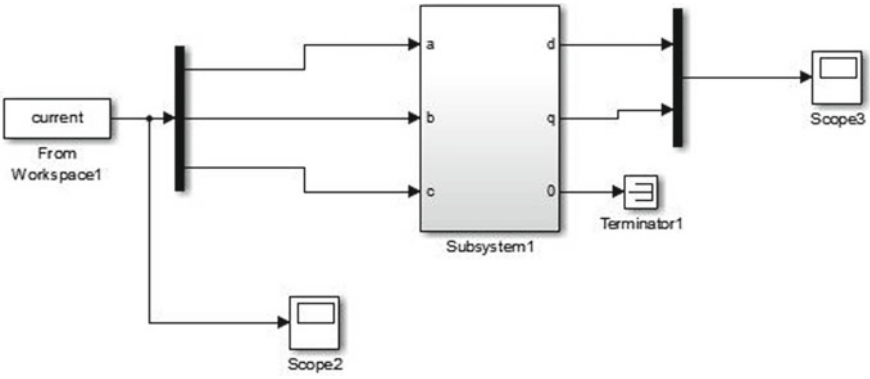

Fig. 7 Simulink block diagram for conversion of abc-αβ coordinate

The measured input (three-phase stator voltage) and output (three-phase stator current) datasets are imported to MATLAB. The signals which are actually in abc coordinate are first transformed into αβ coordinate before being used to simplify the experimental process (Figs. 7 and 8).

The transformed signals of healthy and faulty condition under different loading conditions are being imported in system identification toolbox of MATLAB as input (stator voltage) and output (stator current) with a sampling period of 0.00005 s (Fig. 9).

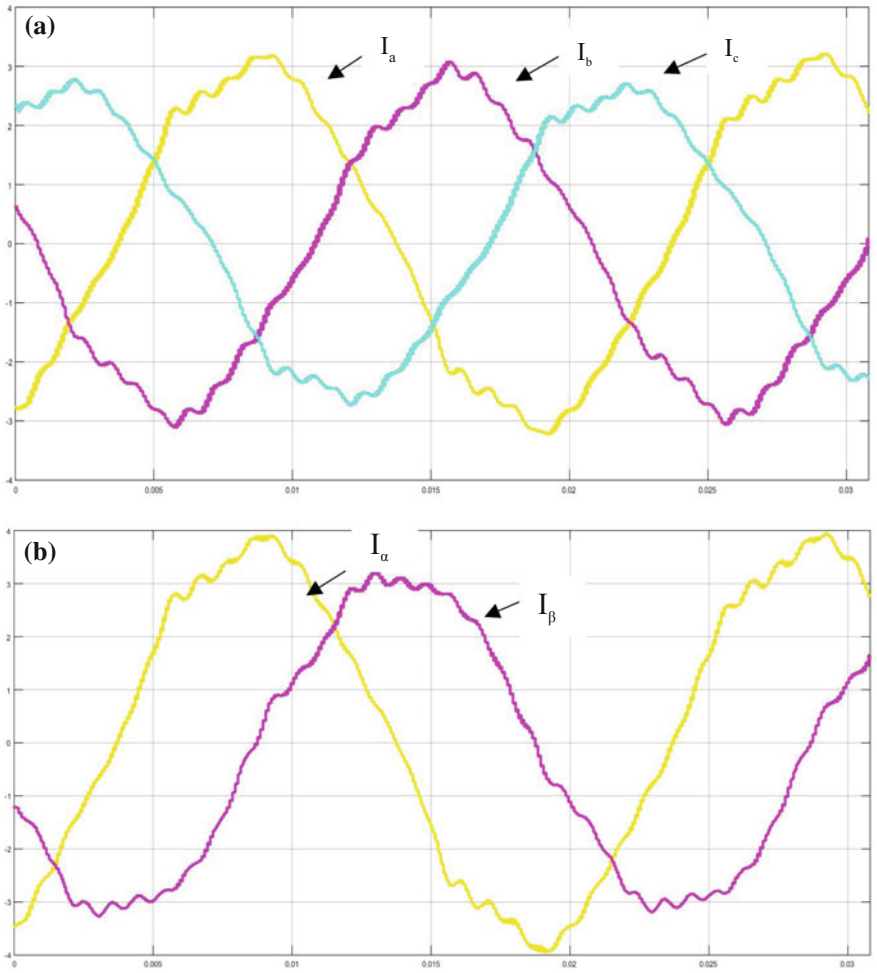

Fig. 8 **a** Stator current response(I_a, I_b, I_c) in abc coordinate. **b** Transformed current response (I_α, I_β) in αβ reference frame under full load in faulty condition

The imported signals are used to estimate a state-space model using system identification toolbox. The model order was chosen by cross validation, i.e., checking the fit to validation data. The model was validated and subsequently used for determining transient response of the system to a step input.

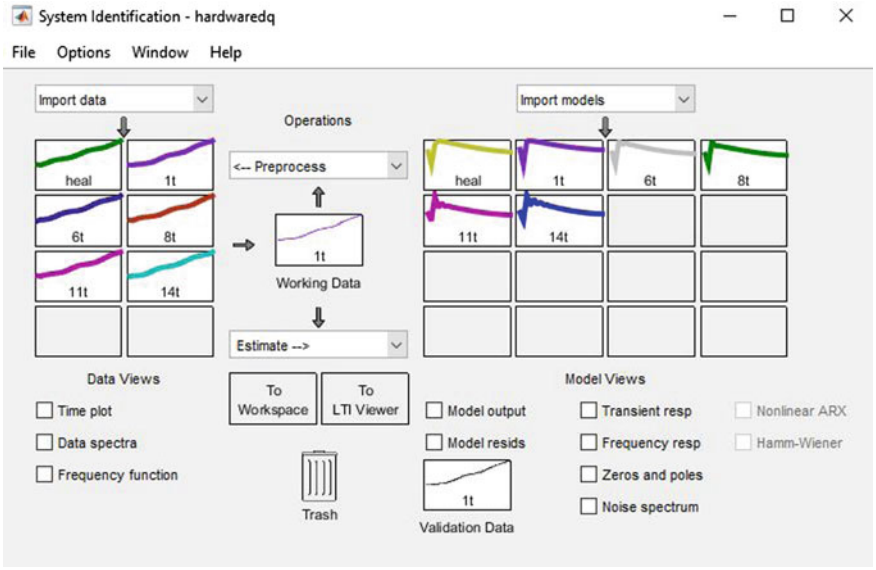

Fig. 9 GUI of system identification toolbox of MATLAB®

4 Results

The state-space model is validated and subsequently used for determining the transient response for a step input.

It is clearly visible from Fig. 10 that there is a variation in step responses of the proposed state-space model under healthy and faulty conditions It has been observed from the above responses that as the fault severity increases, peak overshoot as well as steady-state value increases, which gives sufficient information for detection of stator inter-turn fault.

5 Conclusion

Detection of stator winding inter-turn fault at an incipient stage is extremely important in the industrial system. This paper provides a simple, fast yet efficient technique of detection by state-space model-based analysis using System Identification Toolbox of MATLAB. The model is used to determine a transient response for a step input. The variation in response (peak overshoot as well as steady-state value increases as the fault severity increases.) is capable to detect inter-turn stator winding fault of varying severity.

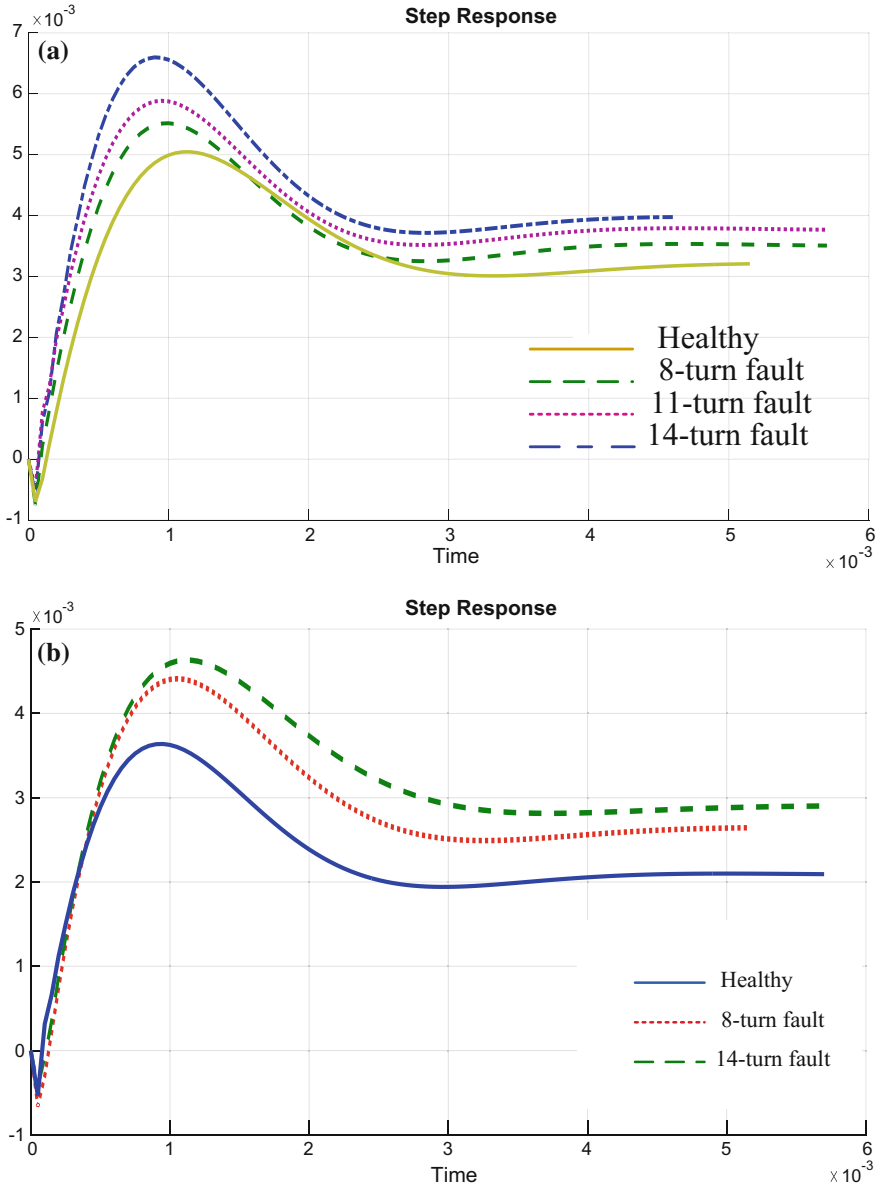

Fig. 10 Step response under **a** full loading conditions. **b** 60% loading condition

Acknowledgements The author would like to acknowledge Arkabrata Dattaroy and Pratim Bhattacharyya, PG Scholar, Jalpaiguri Government Engineering College for their immense help and support.

References

1. Nandi, S., Toliyat, H.A., Member, S., Li, X., Member, S.: Condition monitoring and fault diagnosis of electrical motors—a review. IEEE Trans. Energy Convers. **20**, 719–729 (2005)
2. Vas, P.: Parameter Estimation, Condition Monitoring, and Diagnosis of Electrical Machines. Clarendon, Oxford, U.K. (1993)
3. Zhang, P., Du, Y., Habetler, T.G., Lu, B.: A survey of condition monitoring and protection methods for medium-voltage induction motors. IEEE Trans. Ind. Appl. **47**, 34–46 (2011)
4. Abdallah, H., Benatman, K.: Stator winding inter-turn short-circuit detection in induction motors by parameter identification. IET Electr. Power Appl. **11**, 272–288 (2017)
5. Gandhi, A., Corrigan, T., Parsa, L.: Recent advances in modeling and online detection of stator interturn faults in electrical motors. IEEE Trans. Ind. Electron. **58**, 1564–1575 (2011)
6. Siddique, A., Yadava, G.S., Singh, B.: A review of stator fault monitoring techniques of induction motors. IEEE Trans. Energy Convers. **20**, 106–114 (2005)
7. Karmakar, S., Chattopadhyay, S., Mitra, M., Sengupta, S.: Induction Motor Fault Diagnosis, pp. 7–28 (2016)
8. Tallam, R.M., Lee, S.Bin, Stone, G.C., Kliman, G.B., Yoo, J., Habetler, T.G., Harley, R.G.: A survey of methods for detection of stator-related faults in induction machines. IEEE Trans. Ind. Appl. **43**, 920–933 (2007)
9. Grubic, S., Aller, J.M., Lu, B., Habetler, T.G.: A survey on testing and monitoring methods for stator insulation systems of low-voltage induction machines focusing on turn insulation problems. IEEE Trans. Ind. Electron. **55**, 4127–4136 (2008)
10. Joksimovic, G.M., Penman, J.: The detection of inter-turn short circuits in the stator windings of operating motors. IEEE Trans. Ind. Electron. **47**, 1078–1084 (2000)
11. Takanashi, H., Adachi, S.: Graphical User Interface of System Identification Toolbox for MATLAB (2010)
12. System Identification Toolbox. https://in.mathworks.com/products/sysid.html

Traffic Grooming in Elastic Optical and WiMAX Networks

Deepa Naik, Nikita and Tanmay De

Abstract The integration of elastic optical network with the WiMAX network can provide scalable cost-efficient universal broadband connectivity to end users. Here, we have developed algorithms for traffic grooming in integrated (elastic optical and WiMAX) networks. The simulation is performed on different network topologies. Our algorithm shows better performance in terms of bandwidth blocking ratio and using minimum network resources.

Keywords BVT (Bandwidth variable transponder)
P-ONU (Programmable optical network unit)
WiMAX (World wide interoperability for microwave access networkl)

1 Introduction

Broadband users and their increased demand for high bandwidth have necessitated establishment of hybrid networks. The optical fiber technologies are able to achieve this. But optical cable cannot be deployed anywhere and everywhere [1]. Further, if the users are mobile the uninterrupted seamless connectivity is also required. To support this, wireless technologies are used to complement optical networks. Further, though WiMAX helps in universal broadband connectivity, it suffers from low bandwidth. Hybrid networks achieve both objectives of better data rate and universal broadband connectivity.

D. Naik (✉) · Nikita · T. De
Department of Computer Science and Engineering, National Institute of Technology, Durgapur, Durgapur, India
e-mail: naiksavantdeepa@gmail.com

Nikita
e-mail: nikitaniki027@gmail.com

T. De
e-mail: tanmayd12@gmail.com

U. Biswas et al. (eds.), *Advances in Computer, Communication and Control*, Lecture Notes in Networks and Systems 41, https://doi.org/10.1007/978-981-13-3122-0_23

In the light path, communication is carried out only between the source and destination nodes and intermediate nodes are excluded. Light trail has the advantage of intermediate nodes' participation in data transfer. This maximizes usage of network resources. In [2], traffic grooming for static model using light trail for pure optical nodes is presented. In optical network guard bands minimize interference but at the cost of inefficient bandwidth usage. Hence, traffic grooming is used to aggregate multiple low data rate traffic requests. The channel capacity should be able to accommodate bandwidth requirement of groomed requests. Guard bands are not required in wireless networks. Still signals traveling through wireless route suffer from the interference from neighbors. As guard bands are used to eliminate interference, they reduce spectrum efficiency. The traffic grooming overcomes this drawback by grooming the requests together (which share the common path) without violating the capacity of wireless links. So the guard band required at individual connection requests are avoided.

Here, congestion and delay-aware grooming algorithm using light trail approach is proposed, which minimizes the bandwidth blocking ratio.

The rest of the paper is organized as follows: Sect. 2 presents the previous work. Motivation and Contributions are described in Sects. 3 and 4. In Sect. 5, we have defined the problem in formal notations. The proposed approach is presented in Sect. 6. The experimental result and its analysis are described in Sect. 8. Finally, conclusion and future work is drawn in Sect. 9.

2 Previous Work

Several algorithms and resource allocation models have been developed for hybrid networks. In [1–5], the authors discussed issues related to hybrid optical WiMAX networks to provide broadband connectivity. Routing algorithms and fault tolerance issues in Wireless Optical Broadband Access Network were studied by Sarkar et al. [6].

In traffic grooming, multiple low-speed traffic streams are aggregated into high-speed wavelength channels in order to minimize the network resources [7]. Shortest Path First Traffic grooming (SFT) in static mesh core network proposed by Yoon et al. in [8] minimizes the bandwidth blocking probability and maximizes the network throughput. Light trails established for dynamic traffic requests by Zhang et al. in [9] reduces network resource utilization without disturbing the survival of light trail in case of failure of working links. Traffic grooming based on clique partitioning based multi-hop static traffic grooming was proposed by De et al. in [10]. They used light paths to maximize the network throughput.

Jinno et al. [11] first proposed the EON architecture called SLICE. EON is more flexible than the traditional WDM optical network and results in efficient spectrum usage. Routing and spectrum assignment in EONs was studied by [12, 13]. Some research has been conducted on traffic grooming in the elastic network [9, 14, 15],

spectrum reconfiguration and defragmentation issues to better spectrum utilization are discussed in [16, 17].

3 Motivation

Motivation behind the integration of optical and wireless network is

- **Cost**: Due to economic and geographic limitations, optical cables cannot be deployed in customers premises. In contrast, wireless network can be deployed at lower costs by replacing fiber with free wireless network.
- **Coverage**: By integrating two diversified networks together, the high-speed transmission can be possible for wireless distribution. One of the emerging wireless technologies is WiMAX technology. This technology can provide huge coverage in a cost-efficient way. The network operator could expand connectivity to new service areas without affecting the existing customers, by adding new base stations as per the requirement.
- **Bandwidth**: A huge bandwidth from optical network can be shared by wireless networks. Thus the end users are get connected to broadband network.

4 Contribution

- Traffic grooming light trail approach is used to groom the traffic requests in the hybrid network. A new algorithm with congestion and delay-aware mechanism is proposed with the prime objective to minimize the bandwidth blocking ratio in the hybrid network and reduce the network resource consumption by grooming the requests on already established connection requests.

5 Problem Description

Here congestion and delay-aware traffic grooming is discussed. Given a bidirectional graph $G(V, E)$, where V represents optical/wireless nodes, E represents the links between them. Link capacity is divided into slots of granularity 6.25 GHz (Giga bits/seconds). Further, let the request for 'B' units of bandwidth be requested between a node pair. We assume Bandwidth Variable Transponders (BVT) capable of handling up to T frequency slots. The relay stations are linked with base stations through wireless links. The problem is to set up a set of light trail $Lt = [Lt_1, Lt_2, \ldots, Lt_n]$, so that traffic routed successfully without violating the capacity constraint of optical and wireless networks.

5.1 Notation

We use the following notations in this work.

- Let R = [R_1,…, R_X] represent traffic demands. R_i is the ith traffic demand and represented as $R_i(s_i, d_i, B_i)$, where s_i, d_i, and B_i are source, destination, the required bandwidth between the source and destination node, respectively.
- $p_i = 1$, if bandwidth B_i of the request i is satisfied, otherwise it is 0.
- X: Total number of traffic requests generated in the network.
- s: is the source node.
- d: is the destination node.
- t_{sd}: is the total traffic between s and d node.
- BS: is the set of base stations installed.
- RS: is the set of relay stations installed.
- B_i: bandwidth requested by unicast session request i.

5.2 Objective

The main objective is to minimize the bandwidth blocking ratio of the network and to minimize the usage of network resources.

$$Minimize \quad \left[\frac{\sum_{i=1}^{X} B_i - \sum_{i=1}^{X} (B_i \times p_i)}{\sum_{i=1}^{X} B_i} \right] \tag{1}$$

We assume following constraints and assumptions in this work.

5.3 Constraints

Base station to relay station constraints

- Each RS connects to only one BS. The number of BSs is less than or equal to the number of RSs.
- Number of frequency slots allocated to RSs should not exceed the total frequency slots available with the BS.

Optical network constraints

- **Spectrum contiguity**: Each traffic request is assigned contiguous spectrum slots.
- **Spectrum continuity**: Each traffic request uses the same spectrum slots along all links of its route.
- **Non-overlapping spectrum**: Traffic requests that share common link are assigned non-overlapping parts of the available spectrum.

Assumptions:

- Traffic demands are known ahead.
- Traffic requests are represented in terms of frequency slots. The slots are uniformly distributed between 1 slots, 3 slots, and 12 slots, respectively.
- Traffic requests are bidirectional in nature.
- The relay stations cannot communicate with the neighboring relay stations without the involvement of base station.

6 Proposed Approach

In the proposed congestion and delay-aware grooming algorithm, all possible paths between each node pair is computed and stored in list. For a given traffic matrix T_{sd}, the traffic requests are sorted according to increasing order of traffic demand, i.e., least congested path is selected. The intermediate requests are also groomed along the selected path and they should not violate the number of frequency slots within the transmitter range.

Congestion and delay-aware traffic grooming algorithm takes delay into account along with minimum traffic route. If the delay in the selected route is less than the threshold value only then traffic is routed in that path otherwise alternate route is selected, which satisfies the criteria. The detailed procedure is in Algorithm 1. Mainly, there are four types of delay in routing [5].

Transmission delay—This delay depends on the capacity of each link C_{sd}. If the link capacity is higher, transmission delay will be lower (Where μ is average packet size). It is given by

$$tr_d = \frac{1}{2 * \mu * C_{sd}} \tag{2}$$

Slot Synchronization delay—When a packet travels between two nodes they have to be time synchronized. This also results in a delay which is given by

$$sys_d = \frac{1}{2 * \mu * C_{sd}} \tag{3}$$

Queuing delay—It depends on the rate of arrival of packets and packet service rate at nodes. Higher link capacity and lower arrival rate lead to lower delay. Queuing delay is cumulative hence delays in all links are added for a packet. The delay is given by

$$que_d = \frac{1}{\mu * C_{sd} - \lambda_{sd}} \tag{4}$$

λ_{sd} is load between link sd

Table 1 Traffic grooming based om congestion and delay-aware algorithm

Index	Source destination	Path	Traffic demand	Main/sub trail
0	0–5	0–1–2–5	3	Main trail
s1	0–1	0–1	1	Sub trail
s2	1–5	1–2–5	2	Sub trail
s3	2–5	2–5	3	Sub trail
s4	1–2	1–2	3	Sub trail
s5	0–2	0–1–2	5	Sub trail

Table 2 Delay calculation

Index	Sub trail delay
S1	0.028
S2	0.03
S3	0.0809
S4	0.03255
S5	0.0237
Total delay	0.195

Propagation delay—In network, propagation delay is negligible.
So, total delay can be computed as

$$total_{delay} = tr_d + syn_d + que_d \tag{5}$$

So, the total delay is the summation of transmission, synchronization, and queuing delays.

Example Consider traffic requests as given in Table 1 to explain the working principle of the proposed algorithm. Threshold delay in the path is assumed to be 0.18. Assume 10 slots are allotted to each link. The calculated delay values are as shown in Table 2. The total delay 0.195 is greater than the threshold value of 0.18. Thus, we remove subtrail S5 and then we get a total delay as 0.168. So, the subtrails S1, S2, S3, S4 are satisfied and S5 is blocked.

6.1 Routing in EON

In EON, the bandwidth variable transmitters at each node. After path selection, bandwidth is assigned to a number of requests along the selected path. The spectrum contiguity and continuity frequency slots (FS) along the link on the path are selected for assignment. Present traffic requests are allotted bandwidth along the computed path. When nodes are pure optical in nature as depicted in Fig. 1 intermediate nodes are also allotted spectrum depending on the availability. Traffic demands are allowed till contiguity and continuity constraints satisfied.

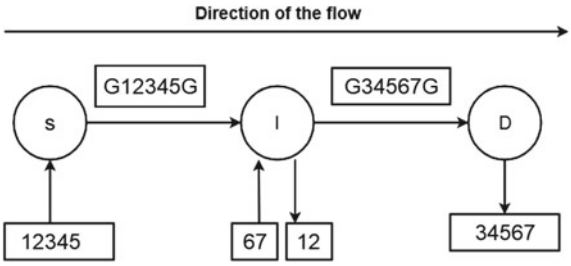

Fig. 1 Trail in elastic optical network

6.2 Routing in the WiMAX Network

In WiMAX combination of s–d pair is as follows:

Situation 1: source-BS, destination-RS

Situation 2: source-RS, destination-BS

Situation 3: source-RS, destination-RS
Present traffic requests are assigned spectrum on the precomputed path (depicted in Fig. 2). To minimize interference between relay nodes, OFDMA is used.

6.3 Hybrid Requests

Here source and destination pairs are in optical/wireless network or wireless/optical network. The traffic from optical to wireless is considered as downstream and from wireless to optical nodes is called upstream traffic.

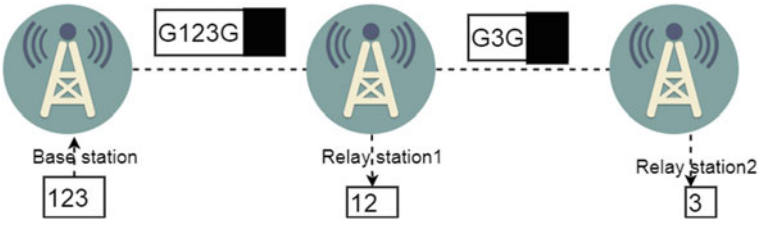

Fig. 2 Traffic grooming using light trail in the wireless network

Algorithm 1: Congestion and Delay-Aware Traffic Grooming (CDAG)

Input: All Unicast requests are represented in a Traffic Matrix elements of which T are $[s, d, B]$ $PATHVECTOR = [s, d, distance]$
Output: Bandwidth blocking of the given network.

step 1: Traffic requests are generated between any pair of nodes. Source, destination, and traffic requests are stored in a list.
step 2: Paths between the source and the destination chosen from list are generated
step 3: Sort the paths between each node pair in increasing order of traffic demand, i.e., least congested path is selected
step 3: Sort the list X in increasing order of hop count
step 4for $j = 1$ *to* $|P|$ **do**
    step 4.a Select path from the top of the list
    step 4.b Check for availability of resources (trans receivers and slot availability
    step 4.cif *(resources are available==TRUE)* **then**
        step 4.c.1 Compute common slot index for entire path
        step 4.c.1.1if *(common slot available==TRUE)* **then**
            step 4.c.1.2if *(there are any traffic requests in intermediate nodes, generate subpaths for those intermediate node)* **then**
                4.c.1.2.1 Compute delay for each subpath
                4.c.1.2.2 Select those subpath whose delay is less than the threshold value.
                4.c.1.2.3 Check for resource availability and common slot index for each subpath.
                4.c.1.2.4 Select only those sub paths which satisfy both the conditions.
                4.c.1.2.5 Assign slots to the main path and sub paths.
                step 4.c.2.6 Update the resources availability
            end
            else
                step 4.c.2 choose alternate path from the path list for the selected node pair
            end
        end
    end
    step 5 This traffic request is blocked,after traversing P alternate paths resources are not available to establish the connection requests.
end
step 6 For loop is executed till all the traffic requests are satisfied or the resources are exhausted.

7 Complexity

Let the total number of requests in hybrid networks are n. The number of slots in each link is c. k is the number of paths between the source node and particular destination(where c and k are constants). In step one, the algorithm needs to compute the k paths between the node pair having the nonzero traffic demands offline, the algorithm takes O(n^2). To generate the traffic matrix of $(n * n)$, the algorithm takes O(n^2). To compute the shortest path between node pair according to links delay will take the time complexity of O(n^2). The slot assignment according to bandwidth

demanded at intermediate steps (checking the slots and network resource availability) will consume $O(Kn^3)$. The total time taken in our algorithm is $O(n^3)$.

8 Analysis of Results

Performance evaluation of our algorithm is done by simulation. Simulation coding is done on IDE Eclipse using Java and results are plotted using MATLAB. Between node pairs, traffic requests are randomly generated. Each transponder capacity is varied between 50 and 100 frequency slots and required bandwidth granularity is randomly chosen among one of the 1, 3, or 12 frequency slots. Simulation is done with NSF network and German network as backend network connected to WiMAX and relay stations as depicted in Figs. 3 and 4. Performance of our algorithm, Congestion and Delay-Aware Grooming (CDAG) is compared with Congestion and Delay-Aware Without Grooming algorithm (CDAWG). The minimization of bandwidth blocking ratio and reducing the consumption of network resources (transponder) are considered as performance parameters. Simulation is an average of 50 iterations.

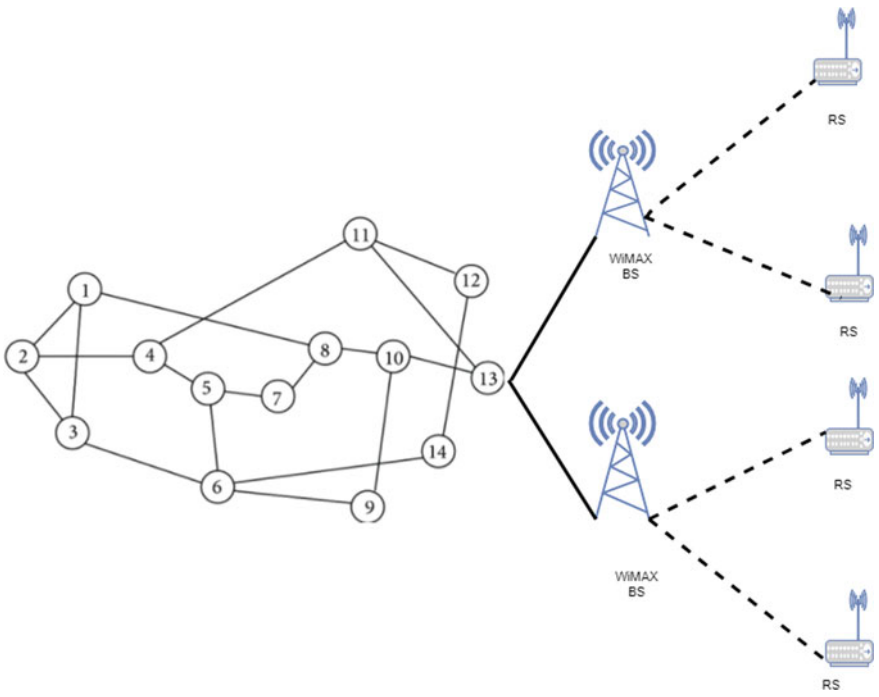

Fig. 3 NSF optical network connected as backend to wireless network

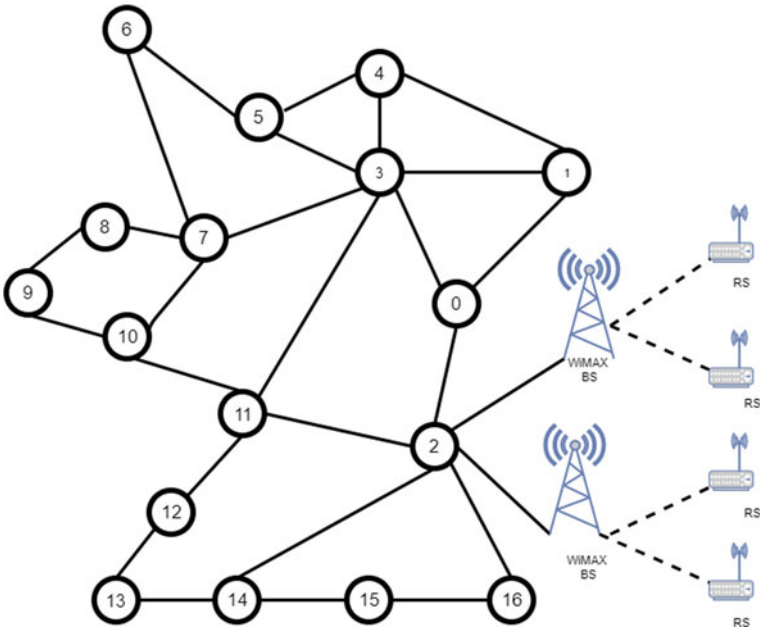

Fig. 4 GERMAN connected as backend network

Fig. 5 Relationship of total number of slots (in each link) and bandwidth blocking ratio when German network is connected as backend to wireless networks

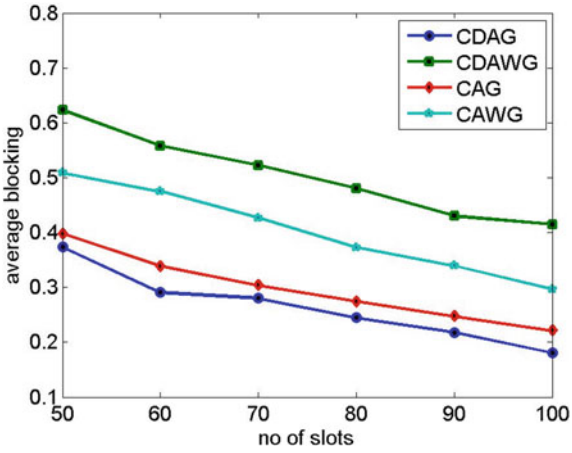

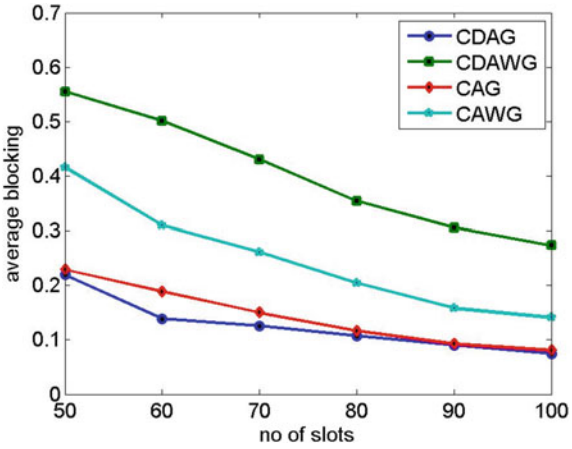

Fig. 6 Relationship of total number of slots (in each link) and bandwidth blocking ratio when NSF network is connected as backend to wireless networks

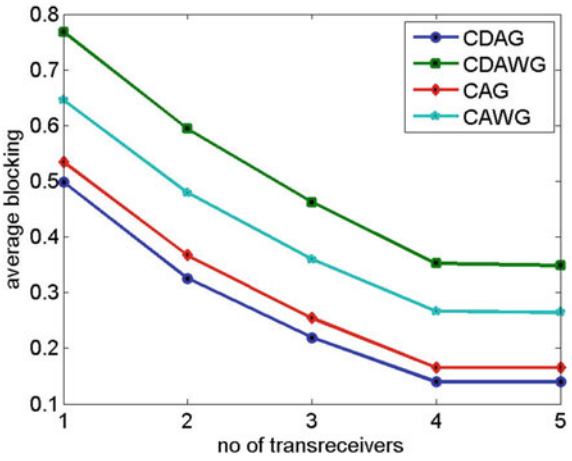

Fig. 7 Relationship of total transponders consumed and bandwidth blocking ratio when German network is connected as backend to wireless networks

Figures 5 and 6 demonstrate the relationship between the number of slots (FS) in each link and the bandwidth blocking ratio results of Congestion and Delay Grooming (CDAG) and Congestion and Delay-Aware Without Grooming(CDAWD). The CDAG performs better in minimizing the bandwidth blocking ratio compared to CDAWG, Congestion-Aware Grooming (CAG) and Congestion-Aware Without Grooming (CAWG) algorithms (with NSF and German network as backend to wireless network).

Figures 7 and 8 demonstrate the relationships between the number of transponders utilized and the bandwidth blocking ratio. The CDAG performs better in minimizing the bandwidth blocking ratio and also minimizes the transponder consumption compared to CDAWG, CAG, and CAWD algorithms (when connected to NSF and German network as backend to wireless network).

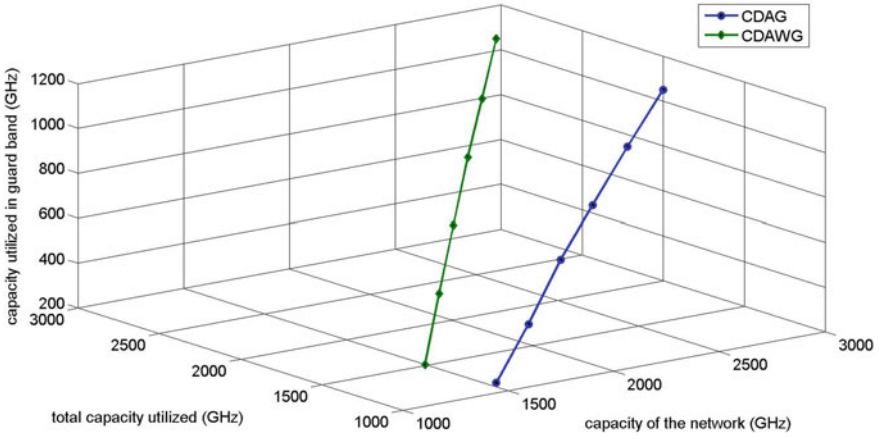

Fig. 8 Relationship of total transponders consumed and bandwidth blocking ratio when NSF network connected as backend to wireless networks

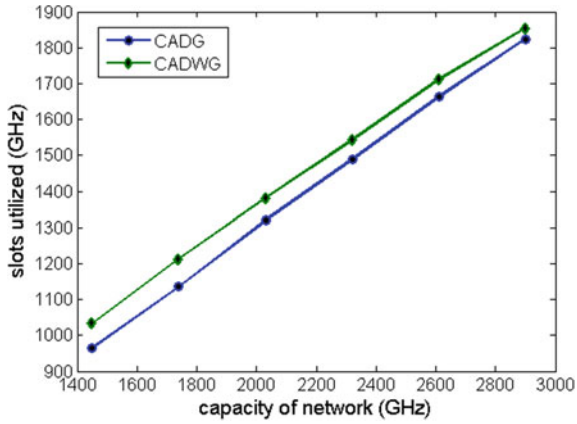

Fig. 9 Relationship of total capacity of the traffic demanded and average slots (FS) utilized when German network is connected to wireless networks

The relation between the number of slots utilized and the total traffic demanded are depicted in Figs. 9 and 10 (with NSF and German network as backbone wireless network). The proposed algorithm CDAG performed better in terms of slots consumed compared to CDAWG algorithm. The CDAG grooms the intermediate requests between the source and destination along the selected path. So the guard band usage is minimized and spectrum resource is efficiently utilized compared to non-grooming approach.

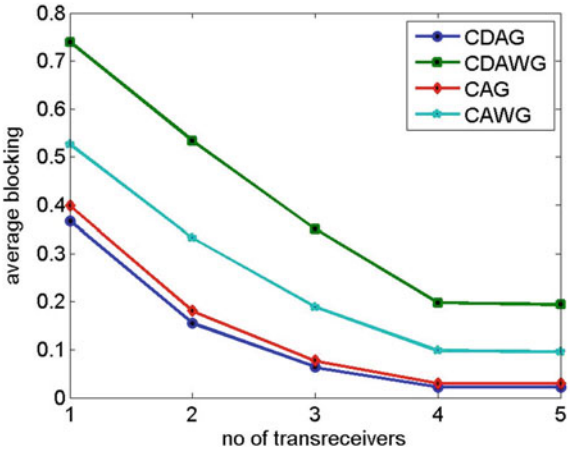

Fig. 10 Relationship of total capacity of the traffic demanded and average slots (FS) utilized when network NSF network is connected to wireless networks

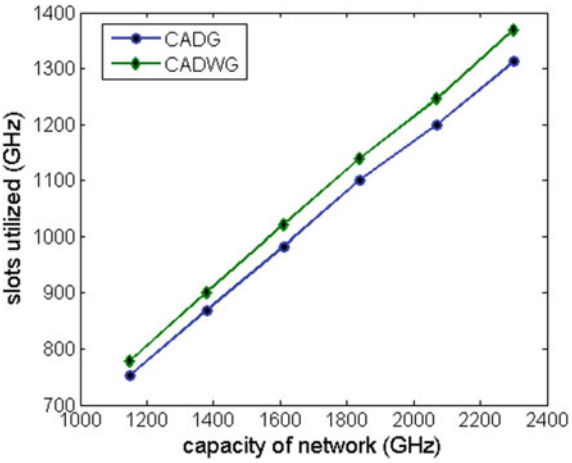

Fig. 11 Relationship of total capacity of traffic demanded and average slots utilized and number of slots consumed by the guard bands when German network connected as backend with wireless network

Similar results are obtained in Figs. 11 and 12. The proposed algorithm (CDAG) consumes less number of resource compared to CDAWG algorithms.

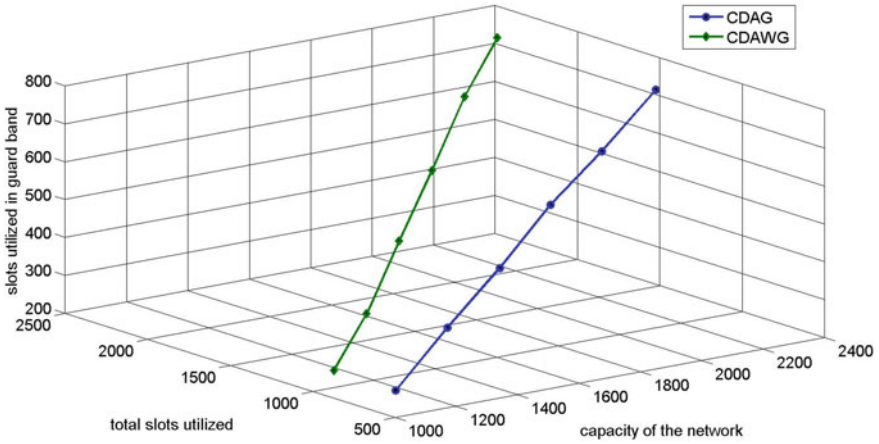

Fig. 12 Relationship of total capacity of traffic demanded and average slots utilized and number of slots consumed by the guard bands when NSF network connected as backend with wireless network

9 Conclusion

We have developed light trail based algorithm, which takes into account delay and congestion. This algorithm performed better compared to non-grooming approach in terms of minimization of bandwidth blocking ratio and reduction in network resources consumption. In future, we will develop light trail based algorithms for minimizing power consumption.

References

1. Ahmed, A., Shami, A.: RPR-EPON-WiMAX hybrid network: a solution for access and metro networks. J. Opt. Commun. Netw. **4**(3), 173–188 (2012)
2. Shi, L., Chowdhury, P., Mukherjee, B.: Saving energy in long-reach broadband access networks: architectural approaches. Commun. Mag. IEEE **51**(2), S16–S21 (2013)
3. Yang, K., Ou, S., Guild, K., Chen, H.H.: Convergence of Ethernet PON and IEEE 802.16 broadband access networks and its QoS-aware dynamic bandwidth allocation scheme. IEEE J. Sel. Areas Commun. **27**(2), 101–116 (2009)
4. Ali, N.A., Dhrona, P., Hassanein, H.: A performance study of uplink scheduling algorithms in point-to-multipoint wimax networks. Comput. Commun. **32**(3), 511–521 (2009)
5. Reaz, A., Ramamurthi, V., Sarkar, S., Ghosal, D., Mukherjee, B.: Hybrid wireless-optical broadband access network (WOBAN): capacity enhancement for wireless access. In: IEEE GLOBECOM 2008, Global Telecommunications Conference, 2008, pp. 1–5. IEEE (2008)
6. Sarkar, S., Yen, H.H., Dixit, S., Mukherjee, B.: Dara: delay-aware routing algorithm in a hybrid wireless-optical broadband access network (WOBAN). In: 2007 IEEE International Conference on Communications, ICC'07, pp. 2480–2484. IEEE (2007)
7. Dutta, R., Rouskas, G.N.: Traffic grooming in WDM networks: past and future. IEEE Netw. **16**(6), 46–56 (2002)

8. Yoon, Y.R., Lee, T.J., Chung, M., Choo, H.: Traffic grooming based on shortest path in optical WDM mesh networks. In: Computational Science–ICCS, pp. 1120–1124 (2005)
9. Zhang, S., Martel, C., Mukherjee, B.: Dynamic traffic grooming in elastic optical networks. IEEE J. Sel. Areas Commun. **31**(1), 4–12 (2013)
10. De, T., Pal, A., Sengupta, I.: Traffic grooming, routing, and wavelength assignment in an optical WDM mesh networks based on clique partitioning. Photonic Netw. Commun. **20**(2), 101–112 (2010)
11. Jinno, M., Takara, H., Kozicki, B., Tsukishima, Y., Sone, Y., Matsuoka, S.: Spectrum-efficient and scalable elastic optical path network: architecture, benefits, and enabling technologies. IEEE Commun. Mag. **47**(11) (2009)
12. Chatterjee, B.C., Sarma, N., Oki, E.: Routing and spectrum allocation in elastic optical networks: a tutorial. IEEE Commun. Surv. Tutorials **17**(3), 1776–1800 (2015)
13. Sahar, T., Alam, F., Katib, I., Khamis, M., Salama, R., Rouskas, G.N.: Spectrum management techniques for elastic optical networks: a survey. Opt. Switch. Network. **13**, 34–48 (2014)
14. Zhang, G., De Leenheer, M., Mukherjee, B.: Optical traffic grooming in OFDM-based elastic optical networks. J. Opt. Commun. Netw. **4**(11), B17–B25 (2012)
15. Kozicki, B., Takara, H., Tsukishima, Y., Yoshimatsu, T., Kobayashi, T., Yonenaga, K., Jinno, M.: Optical path aggregation for 1-Tb/s transmission in spectrum-sliced elastic optical path network. IEEE Photonics Technol. Lett. **22**(17), 1315–1317 (2010)
16. Ba, S., Chatterjee, B.C., Okamoto, S., Yamanaka, N., Fumagalli, A., Oki, E.: Route partitioning scheme for elastic optical networks with hitless defragmentation. J. Opt. Commun. Netw. **8**(6), 356–370 (2016)
17. Chen, X., Li, J., Zhu, P., Tang, R., Chen, Z., He, Y.: Fragmentation-aware routing and spectrum allocation scheme based on distribution of traffic bandwidth in elastic optical networks. J. Opt. Commun. Netw. **7**(11), 1064–1074 (2015)

Real-Time Monitoring of Power Line Data Using Wireless Sensor Network and PowerExcel Software

S. Sau, S. Kumar, Debashis Sarkar, S. Mondal and S. N. Patra

Abstract Real-time monitoring of power line data using Wireless Sensor Network (WSN) is one of the important and challenging tasks in the field of the electrical power system. In this work, a sensor board MDA 300CA is used which is made by Crossbow Technology. This is actually a data acquisition board. A driver software named as MoteView is used for collecting the raw data from different sensor nodes. Separate multiuser 'PowerExcel' software has been developed. This software works as an interface to view the data received from the driver software. Different power line transducers, which are connected with different sensor nodes, are used for measurement of power line data, viz., system phase voltages, load currents, connected active and reactive loads, and its power factor. A user-friendly GUI has been developed for easy and live monitoring of data using MATLAB. These data are also being stored in the .csv format for future reference. A provision for audio and visual safety alert is also available, when any of the data crosses its prespecified limit.

Keywords Wireless sensor network · Power line data monitoring · MoteView PowerExcel

S. Sau (✉) · S. Mondal
Department of Mechanical, Jadavpur University, Kolkata 700032, India
e-mail: susmita.sau@gmail.com

S. Mondal
e-mail: mondalsukanta1000@gmail.com

S. Kumar
Department of Power Engineering, Jadavpur University, Salt Lake III, Kolkata 700098, India
e-mail: sajjan.pradhan48@gmail.com

D. Sarkar
Department of Mechanical Engineering, Asansol Engineering College, Asansol 713305, India
e-mail: aecdeba.me@gmail.com

S. N. Patra
Department of Instrumentation Science, Jadavpur University, Kolkata 700032, India
e-mail: sankar.n.patra@gmail.com

U. Biswas et al. (eds.), *Advances in Computer, Communication and Control*, Lecture Notes in Networks and Systems 41, https://doi.org/10.1007/978-981-13-3122-0_24

1 Introduction

In recent years, wireless communication technology plays a vital role for modernization and advancement of the real world in the field of science. A Wireless Sensor Network (WSN) is the most important thing in wireless communication technology [1]. The Sensor Node is the basic element of WSN, which is composed of sensing, computation, and wireless communication unit. There are many opportunities to develop flexible, reliable, scalable, and cost-effective system, using different technologies and standards of WSN in various industrial applications. Monitoring power demand is one of the important applications of WSN in the field of modern power system measurements [2, 3].

A significant advancement in sensing, computing, and communication technologies, gives rise to the sensor, smaller size semiconductor, microcontrollers, radio transceivers, and other components are integrated on a single board to produce a sensor node. Actually, WSN contains a large number of small, low-cost wireless sensor nodes that are employed to track a wide target [4]. These sensor nodes can do cooperative data acquisition, processing, and wireless communication in sensor network [5]. A WSN is used increasingly in various fields of environmental conditions monitoring and form a bridge between the physical and virtual world [6]. WSN is one kind of mobile network, which is composed of compact sensor nodes, each node built with a sensor board, a processor, a radio antenna, and a battery. These basic components of WSN perform for (1) gathering data from the environment, (2) processing and storing data, (3) transmitting data wirelessly, and (4) supplying energy to the node, respectively [7]. Sensor nodes are programmed to monitor and collect data from the targeted area. The collected data are analyzed and broadcasted toward the base station [8]. However in WSN, sensor nodes have some limitations, sensor nodes have a small memory, processing speed is slow, energy supply is limited, for that reason typical characteristic of sensor nodes affects on sensor network life and the quality. To solve this problem research work is going on power management, in order to reduce the power utilization when the nodes become idle.

The off-line monitoring of power demand for the remote area is very difficult, time consuming and uneconomical. Therefore, in this work, a system has been developed for online monitoring of power line data using transducers, WSN and driver software with GUI for better interaction with the outside world. This driver software, named as **PowerExcel** has been developed for monitoring of the load current, voltage, active power, reactive power, and power factor. These data are gathered online using a wireless sensor network and some transducers from a remote location. This is a multiuser software. The user can see data online from a remote place. Due to some limitations of selected hardware used in this wireless sensor network, the user can monitor data wirelessly within 100 m. Using hopping technology the distance of communication can be enhanced. Still, it comes under per view of WPAN (). Therefore, to communicate these data over a long distance instantly through web and SMS, this software can be linked with the client–server network.

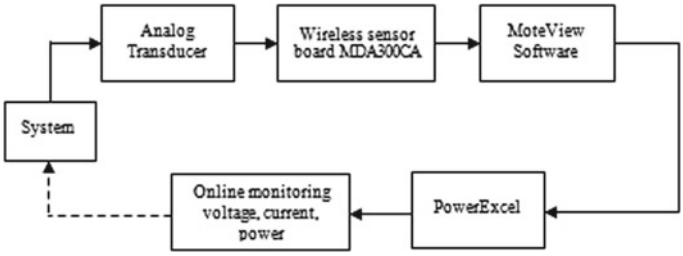

Fig. 1 Block diagram of the work

2 System Design

This work can be categorized into several steps like measurement of system data (system voltage, line current, and load power) by using corresponding analog transducer, transmitting these data by using wireless sensor network, receiving these raw data at another location and fed to the corresponding software (MoteView software), conversion of these raw data into the actual system data for displaying, plotting the graph, and storing the live status of the system using another software (PowerExcel) and MATLAB.

The block diagram of this work is given in Fig. 1. Block diagram contains an analog transducer, wireless sensor board MDA 300CA, MoteView software, PowerExcel software, one block for online monitoring of voltage, current, and power.

2.1 Analog Transducer

In this work, three analog transducers, viz., voltage transducer, current transducer, and power transducer are used for measurement of the phase voltage, line current, and three-phase active power. Voltage, current, and three-phase power transducer actually convert the voltage, current, and power, respectively, into the corresponding DC output voltage ranging from 0 to 5 V. Input range of the voltage, current, and power transducer are 0–500 V AC, 0–5 A AC and 0–4 KW, respectively. Detailed specification is given in the corresponding manual [9]. If the input range exceeded the limit then use the voltage and/or current transformer (CT and PT). Auxiliary power supply (220–230 V) is required for all the transducers. The output terminals of all the transducers are connected to the wireless sensor board for transmitting the data. Prior to connecting these transducers into the circuit, transducers characteristic should be known. Generally, an ideal characteristic of a transducer is linear but practically it is found that its characteristic is not exactly linear. Therefore, for more accurate results, several experiments have been done to find its real characteristics by taking mean of those data (Fig. 2).

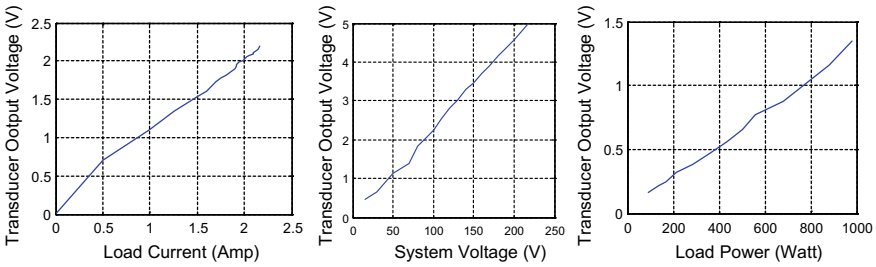

Fig. 2 Characteriztic of current transducer, voltage transducer, power transducer

2.2 Hardware of Wireless Sensor Network (WSN)

To read the transducer output using wireless sensor network, the following hardware components are required:

(1) MDA 300CA sensor board
(2) IRIS mote
(3) Base station

(1) *MDA 300CA sensor board*: The transducer data are directly fed to the data acquisition board of WSN kit named as MDA 300CA. MDA 300CA, made by Crossbow Technology, has 46 pins (Fig. 3). The sensor board is used as a transmitter. MDA 300CA is an environmental data acquisition module, which is connected directly to the Mote. It has the capability to interface with external sensors. It can take both analog and digital inputs from different sensors. Here, three analog channels are used to measure analog inputs. Analog inputs are fed between channels A0, A1, A2, and GND. The signal from 0 to 3 V can be plugged to these channels. The transmitting data from all the channels are in the raw format (not in the voltage form). These raw data are received by the base station, which is connected through the MoteView software. These raw data are also stored in the database through MoteView software.

(2) *IRIS Mote*: IRIS is a 2.4 GHz mote module, which is used for enabling low-power WSN. It follows IEEE 802.15.4 standard for communication purpose. Date rate of this IRIS mote is 250 kbps. This mote supports open-source embedded operating system (TinyOs). Mote is designed for the embedded sensor network. MDA 300CA sensor board is connected with IRIS Mote. Two 1.5 V AA battery is connected with the IRIS mote for enabling the circuit of IRIS mote as well as the circuit of MDA 300CA sensor board.

(3) *Base station*: In this work, MIB 520 base station is used. MIB 520 provides USB connectivity with IRIS mote and MICA mote. In data transfer, MIB 520 also provides a USB programming interface. MIB 520 offers two separate ports—one for system mote programming and other for data communication over USB.

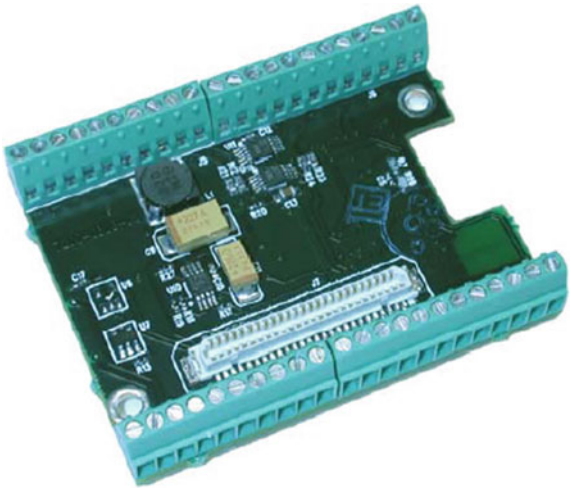

Fig. 3 MDA 300 CA sensor board

It has an on-board processor that programs mote processor. USB bus power eliminates the need for an external power source.

2.3 Software Development

MoteView software, which is supplied by Crossbow Technology, reads and stores the data in the raw format (not in the transducer output voltage form). However, for displaying the actual transducer output voltage (*TOV*) in volt, MoteView software converts these analog–digital channels (ADC) raw data into voltage form according to given equation:

$$TOV = \frac{2.5 * \text{ADC Reading}}{4096} \tag{1}$$

Now, after the conversion, these ADC outputs are actually the transducer dc voltage outputs of the load data. These data do not reflect the actual voltage, current, power, etc., of the load. Actually, it can be analyzed from these transducer output voltages with the help of MATLAB basic fitting tools and corresponding transducer output characteristic. For better user interface and representation of these obtained power line data, the software has been developed, named as '**PowerExcel**', using the C# as front-end logic development language and PostgreSQL as the backend database. A snapshot of this developed software is shown in Fig. 4.

In the background process, the ADC outputs are converted into the actual power line data. This developed software can fetch the data online through the real server and also it is able to analyze the humidity and temperature of the remote area in per the second basis from the remote server. For better reliability and further development,

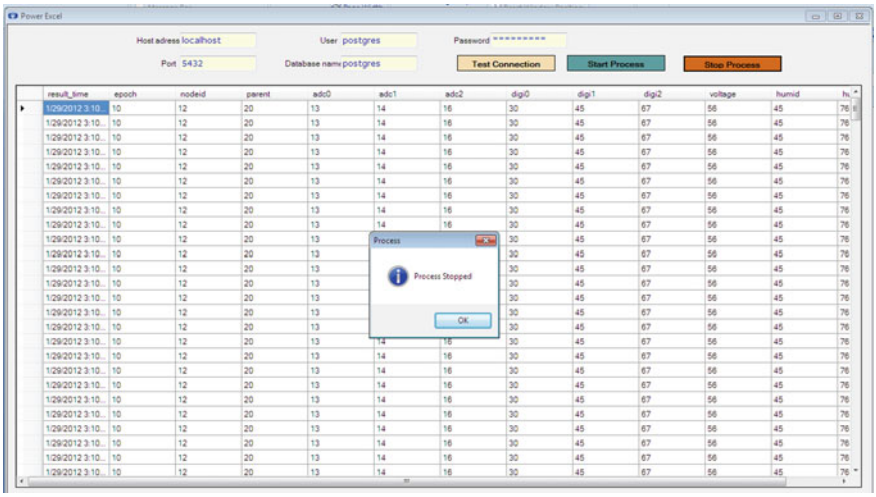

Fig. 4 Snapshot of the PowerExcel software

multiple PowerExcel software can be connected to a single remote server. For the development of this software, it is required to build an application which will connect to the current PostgreSQL database. PostgreSQL runs on all major operating systems including Linux, UNIX, and Windows. It has native programming interfaces with C/C++, Java, .Net, Python, etc. The software pulls out the data from Database, displays these data on a user-friendly interface from a remote machine which is connected to the real server. It also stores the actual data (system voltage, current, and power) into *.csv* file format in every second automatically, which acts as an input to the MATLAB program. After that, these data are interpolated using the basic fitting tool and a lookup table in MATLAB version 7.8.0 (R2009a), and after processing all the results like computed load current, load voltage, load power, reactive power, power factor are stored in a different *.csv* file. All these data are updated every second. All the results are displayed in the software window also. Simultaneously, MATLAB plots the real-time graphs (live) for phase voltage, line current, three-phase power, and the power factor with respect to time. All the graphs are plotted in the same window. There is also a provision for alert. If anyone of the data crosses its prespecified limit, which was already fixed by the user, then an alarm will sound.

2.4 Algorithm for Software Handling

Step 1: Start the PowerExcel Software.
Step 2: Enter the login id and password; this is required for system security.

Step 3: Set the Postgre SQL server settings like database host, user id and password. Some additional settings like the path for two CSV files are also required to set.
Step 4: Click the 'Test Connection' button for testing the connection through MoteView software via server (internet). After that, a new window will appear. If the connection is successful, then 'Connection Succeed' message will appear otherwise error message will appear in that window.
Step 5: Click the 'Start Process' button to see the desired report.
Step 6: Run the MATLAB program or just run the .exe file which is created by MATLAB software, for monitoring the entire system via tabular data form or real-time graph. This is also required for alarm, which is used for notification of violation of safety limit.
Step 7: If the user wants to stop the process, then first click the 'Stop' button which is on the MATLAB GUI window and then click the 'Stop Process' button which is on the PowerExcel software window.
Step 8: If the user wants to see the history of data then go to the location of output directory which is provided in step 3 and then open that *.csv* file.

3 Testing and Result

This work has been tested for normal single floor building. All three transducers are connected to this supply system for online monitoring. A simple circuit diagram for measurement of a balanced load of a building is shown in Fig. 5.

In this setup, only one voltage and current transducer are taken for convenience and it is assumed that loads are balanced. A three-phase power transducer is used for measuring the power consumed by three-phase load. All results are verified by the analog instruments like voltmeter, ammeter and wattmeter. Here three-phase power is measured by using two-wattmeter method. Outputs of these transducers are connected through WSN kit. The base station (receiver) receives the output of WSN kit wirelessly and fed to the MoteView software which is installed on a server connected PC. Now, in another location, PowerExcel software receives that data through real-time server or LAN. Through this PowerExcel and MATLAB software, the user can monitor the status of system voltage, load current, three-phase power, power factor, reactive power, etc. Format of display window of MATLAB and window of its real-time graph are shown in Fig. 6 and in Fig. 7, respectively.

4 Conclusion

A challenging problem of developing software for online monitoring purpose in Wireless Sensor Network is done in this work. Physical quantities such as current, voltage, and power are measured by using proper transducers. The output of the

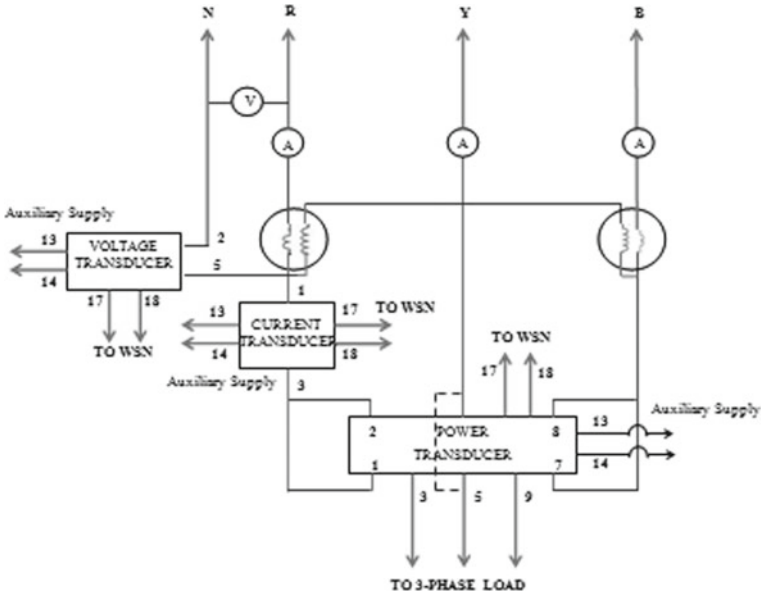

Fig. 5 Circuit diagram for three-phase voltage, current, and power measurement

TRANSDUCER O/P VOLTAGE adc0 (VOLT)	I/P LOAD VOLTAGE (VOLT)	TRANSDUCER O/P VOLTAGE adc1 (VOLT)	I/P LOAD CURRENT (AMP)	TRANSDUCER O/P VOLTAGE adc2 (VOLT)	LOAD POWER (WATT)	REACTIVE POWER (VAR)	POWER FACTOR COS(phi)
2.3956	207.9749	1.2866	1.2866	1.2592	664.7888	149.9893	0.8281
2.3755	206.4305	1.2958	1.2958	1.3251	630.4934	165.4708	0.7857
2.3767	206.5238	1.2634	1.2634	1.2714	625.9068	156.6989	0.7996
2.3877	207.3652	1.2103	1.2103	1.2573	585.7136	157.7118	0.7779
2.3999	208.3039	1.2872	1.2872	1.2445	675.5779	145.5501	0.8398
2.3450	204.1107	1.2549	1.2549	1.2860	596.0900	161.6317	0.7757
2.3773	206.5705	1.2836	1.2836	1.2653	649.5078	153.0681	0.8165
2.3889	207.4589	1.2640	1.2640	1.2469	644.8811	150.1990	0.8197
2.3676	205.8250	1.2665	1.2665	1.2714	624.6854	156.8165	0.7988
2.3846	207.1312	1.2811	1.2811	1.2439	662.0054	147.3844	0.8316
2.3865	207.2716	1.2842	1.2842	1.4404	573.2531	185.2980	0.7179
2.3724	206.1974	1.2683	1.2683	1.2744	627.2202	157.1060	0.7994
2.3834	207.0376	1.2787	1.2787	1.2543	653.3048	150.5398	0.8226
2.3846	207.1312	1.2787	1.2787	1.2195	673.0207	140.7838	0.8470
2.3676	205.8250	1.2817	1.2817	1.2622	644.5827	153.0769	0.8144
2.3810	206.8506	1.3110	1.3110	1.2628	680.7864	148.4807	0.8368
2.3779	206.6171	1.2396	1.2396	1.2494	613.9562	154.0093	0.7990
2.3822	206.9441	1.2738	1.2738	1.2537	648.0625	151.0736	0.8195
2.3853	207.1780	1.1249	1.1249	1.2427	511.1172	159.0142	0.7311
2.3700	206.0112	1.1743	1.1743	1.2909	529.7128	165.3756	0.7299
2.3810	206.8506	1.1578	1.1578	1.2677	528.8838	162.1115	0.7361
2.3920	207.6933	1.2299	1.2299	1.2787	596.3057	160.4284	0.7782
2.3907	207.5995	1.1536	1.1536	1.2494	536.7365	159.1880	0.7471
2.3901	207.5526	1.2103	1.2103	1.1725	630.3459	137.6820	0.8364
2.3975	208.1159	1.2903	1.2903	1.2793	658.6913	154.5938	0.8177
2.3901	207.5526	1.2512	1.2512	1.2561	627.7178	153.8180	0.8057
2.3907	207.5995	1.2592	1.2592	1.2640	631.9023	154.8007	0.8058
2.3907	207.5995	1.2628	1.2628	1.2903	622.3473	160.2900	0.7913
2.3944	207.8810	1.1658	1.1658	1.2762	537.7992	163.0738	0.7397
2.3938	207.8341	1.1664	1.1664	1.2482	550.5220	158.3968	0.7570
2.3944	207.8810	1.1694	1.1694	1.2518	551.9971	158.8818	0.7569
2.3944	207.8810	1.2848	1.2848	1.2317	677.4371	142.6266	0.8455

Fig. 6 Format of the display window

transducer (0–5 V DC) is directly sent to the sensor input side and was monitored by MoteView software display. However, continuous data of load current, load voltage, and load power, reactive power, power factor cannot be monitored from the MoteView display. This problem is overcome using the MoteView's database for development of PowerExcel software. It is multiuser software. The user can log in the software from

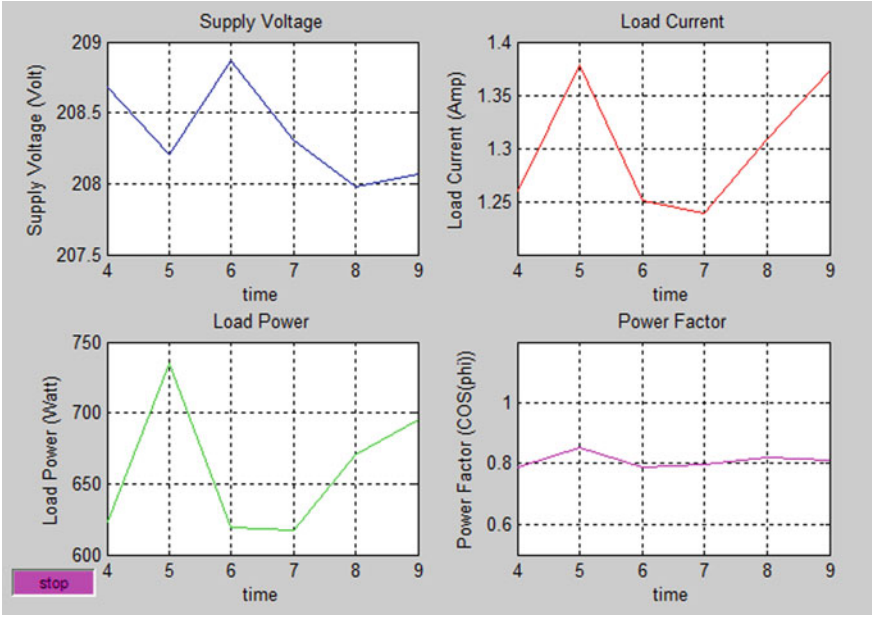

Fig. 7 Real-time graph of supply phase voltage, load current, load power, and power factor with respect to time for a particular instant of time

a remote place to monitor data. The software has been designed in the C# platform. There is a Postgre SQL database, which is directly connected to the server. Database portion is the backend of the software. Data from the server is in the raw format, so it is needed to be converted to the actual format using some formulae derived by the sensor network. The software is updating itself in every 2 s directly from the server. Updated data are also stored in the *csv* extension, from *csv* file data is sent to the MATLAB, interpolation is done using a lookup table from the characterization of transducers. Computed load current, load voltage, load power, reactive power, power factor are displayed in the display window. Thus, the user can monitor data online. The stored data can be monitored off-line also.

References

1. Ohize, O.H.: Emerging issues in wireless sensor networks . J. Softw. Autom. **2**, 11–15 (2011)
2. Yick, J., Mukherjee, B., Ghosal, D.: Wireless sensor network survey. IEEE Sens. J. **8**, 2053–2058 (2008)
3. Ong, J., You, Y.Z., Mills-Beale, J., Tan, E.L., Pereles, B., Ghee, K.: A wireless, passive embedded sensor for real-time monitoring of water content in civil engineering materials. IEEE Sens. J. **8**(12), 2053–2058 (2008)

4. Nasipuri, A., Alasti, H., Puthran, P., Coxand, R., Conrad, J.: Vibration sensing for equipment's health monitoring in power substations using wireless sensors. In: Proceedings of the IEEE SoutheastCon 2010 (SoutheastCon), pp. 268–271, March 2010
5. Chang, C., Nagel, D.J., Muftic, S.: Assessment of energy consumption in wireless sensor networks: a case study for security algorithms. In: Proceedings of the IEEE International Conference on Mobile Adhoc and Sensor Systems, pp. 1–6 (2007)
6. Romer, K., Kasten, O., Mattern, F.: Middleware challenges for wireless sensor networks. Mob. Comput. Commun. Rev. **6**(2)
7. Mahajan, S., Malhotra, S.: Energy efficient path determination in wireless sensor network using BFS approach. Wirel. Sens. Netw. **3**, 351–356 (2011)
8. Martins Fl´avio V.C., Carrano Eduardo, G., Wanner, E.F.: A Dynamic Multi objective Hybrid Approach for Designing Wireless Sensor Networks. In: IEEE Congress on Evolutionary Computation (CEC 2009), pp. 1145–1152 (2009)
9. Power Line Transducers Data Sheet No. PLT 01/04, Automatic Electric Ltd. http://www.aelindia.com/images/Products/Documents/35.pdf

Malignant Melanoma Identification Using Best Visually Imperceptible Features from Dermofit Dataset

Soumen Mukherjee, Arunabha Adhikari and Madhusudan Roy

Abstract In this paper, an analysis of four different feature ranking algorithm is done and a novel approach of hybrid feature selection is proposed for better classification accuracy in malignant melanoma detection. In this work, at first totally 1898 features including geometrical shape, color and texture features are extracted from 1300 melanoma and non-melanoma images archived in Dermofit image library of the University of Edinburgh. Four feature ranking algorithms are used to rank the 1898 features in this work. Three classification algorithms, Support Vector Machine (SVM), K-Nearest Neighbors (KNN) and Ensemble Boosted Tree (EBT) are used as a classifier for the malignant melanoma and nevus lesion. Highest accuracy of 86.1% found with only 700 features selected by minimum correlation based feature ranking algorithm using Support Vector Machine (SVM). In the novel approach, those features are selected which have a higher rank in all the 4 feature ranking algorithms. With only 163 such features, an accuracy of 86.2% is found, which is similar in accuracy level with much less number of features in comparison with the result reported in the related work.

Keywords ABCD rule · GLRLM · GLCM · Minimum correlation Concave minimization · ReliefF

S. Mukherjee
Department of Computer Application, RCC Institute of Information Technology, Kolkata, India
e-mail: soumou601@gmail.com

A. Adhikari (✉)
Department of Physics, West Bengal State University, Barasat, India
e-mail: arunabha.adhikari@gmail.com

M. Roy
Surface Physics and Material Science Division, Saha Institute of Nuclear Physics, Kolkata, India
e-mail: roy.madhusudan57@gmail.com

U. Biswas et al. (eds.), *Advances in Computer, Communication and Control*, Lecture Notes in Networks and Systems 41, https://doi.org/10.1007/978-981-13-3122-0_25

1 Introduction

In recent years, there are several medical reports of increasing death cases due to malignant melanoma [1], a type of skin cancer. Excessive exposures of ultraviolet rays in skin melanocyte cells causes malignant melanoma. Detection and identification of melanoma in an early stage are very important for a complete cure from this lethal disease. Identification of malignant melanoma using visual perception by dermatologist is difficult due to human error [2], as different pathologies present almost visually indistinguishable skin lesion. Dermatologists mainly use different semi-quantitative techniques like Menzies method, 3-point checklist, 7-point checklist, ABCD rule, etc., [3] for detection of malignant melanoma, other than skin biopsy which is a gold standard test for identifying malignant melanoma. Skin biopsy costs around $100, which is difficult to bear by the underprivileged people of developing and underdeveloped countries. Around the past decade, quite a lot of research work has been published in the field of malignant melanoma detection using image processing and machine learning techniques. The growing interest in this field is due to the low cost, accurate, and fast detection and identification of the disease without the direct involvement of Dermatologist. In this work, malignant melanoma is detected and identified with a good accuracy level using best ranked image features common to the lists produced by different supervised and unsupervised feature ranking algorithms using classifiers like Support Vector Machine (SVM), K-Nearest Neighbors (KNN), and Ensemble Boosted Tree (EBT). The paper is organized in the following manner. In the next section, some related work in this field is discussed. In the subsequent section dataset used, detailed information about extracted features, ranking, and classifier algorithms used and classification results are given. Finally, in the conclusion part the importance of this work is discussed.

2 Related Work

Quite a few research works have been carried out using Dermofit dataset of University of Edinburg for its large sample size (1300 images) and good image quality. Tan et al. [4] worked with 1300 images of Dermofit image library and SVM classifier and got 89% Specificity, 83% Sensitivity, and 88% accuracy level. In their work, different preprocessing steps, i.e., contrast enhancement, hair removal, grayscale conversion, and noise filtering are done for each of the 1300 images. A total of 3914 features including geometrical shape, color, and texture features are extracted after lesion image segmentation. Totally 1472 optimized features are selected using Genetic Algorithm (GA) from a total of 3914 features for the final classification task. Laskaris et al. [5] got an accuracy of 80.64% with 31 lesion images of the same

dataset, Ballerini et al. [6] used only 960 images of Dermofit dataset and got 74% classification accuracy and McDonagh et al. [7] archived 83.7% classification accuracy with 234 images. Some works are also done with another popular dataset called Mednode [8] with only 170 melanoma images in this field. Analyses of different feature ranking algorithms are also gaining popularity as an area of research due to the problem called "curse of dimensionality", where increasing feature number may reduce the accuracy. Shardlow [9] in his paper done an analysis of different filter, wrapper, and hybrid feature selection techniques. In this work, Shardlow has used linear support vector machine classifier. He has used different filter method like Pearson's correlation coefficient, mutual information, relief, an ensemble with data permutation and wrapper method like greedy forward search, an exhaustive search for feature selection. He also used two hybrid methods like ranked forward search and refined exhaustive search. He has found that a hybrid method named ranked forward search is the most effective one. Duch et al. [10] has done a comparison between 5 feature ranking methods depending on their information entropy. They have used two artificial datasets "Gauss1" and "Gauss2" and one real dataset "Hypothyroid". It is found that all the 5 ranking algorithm performs in a similar way. It is concluded by their study that there is no best ranking index. Ilangovan et al. [11] have used 10 datasets collected from the UCI repository of machine learning. They have considered 8 feature ranking algorithm ReliefF, gain ratio, InfoGain, one rule, symmetric uncertainty, chi-squared, support vector machine (SVM) and filter. It is found from the work that the ranking methods like InfoGain, filter, symmetric uncertainty and relief perform better than the other feature ranking algorithm. Slavkov et al. [12] used four different feature ranking algorithm like Information Gain (InfoGain), random forests, ReliefF, and SVM. In their work, they have used Neuroblastoma dataset of the brain tumor. It is concluded by Slavkov et al. that no ranking algorithm is superior to the other. Novakovic et al. [13] done one analysis on 6 feature ranking algorithms, namely, information gain (InfoGain), gain ratio, symmetrical uncertainty, ReliefF, one rule and chi-squared. Four classification algorithms are used in the work namely IB1, C4.5 decision tree, naive Bayes, and the Radial Basis Function (RBF). Two real datasets German Credit Data and Australian Credit Approval were taken from the UCI repository of machine learning and used in the work. It is found in their work that no ranking algorithm is better in comparison to the other algorithm.

3 Dataset Used

A total of 1300 melanoma and non-melanoma lesion images archived in Dermofit image library [14], collected by Edinburgh innovations center of the University of Edinburgh is used in this work. All the lesion images of the dataset are examined by

dermatopathologists and dermatologists and marked as gold standard data. There are 10 types of lesion images present in the Dermofit library, which can be categorized into two large groups of malignant melanoma type of total 526 images and nevus type of 774 images. In this work, a two-class classification work between malignant melanoma and nevus has been done with these above mentioned two categories.

4 Feature Extracted

The present work is done in MATLAB (Version R2015b) for writing code for feature extraction, feature ranking, and classification. In the work, the hardware configuration is Intel Core i5-6500 @ 3.20 GHz as a processor with 8 GB RAM. All the 1300 images are at first segmented using Otsu [15] algorithm to find the lesion area. Then a total of 1898 features including geometrical shape [4], color [16, 17] and texture features are extracted from each lesion image. In this work, totally 10 geometrical shape features, 36 color features and 1852 number of texture features (88 gray-level run length matrix (GLRLM) [18] and 1764 gray-level co-occurrence matrix (GLCM) [19–22]) are extracted from each image. In GLRLM and GLCM, texture feature calculation for statistical distributions of pixel intensity relative positions in the image pixel matrix is taken into account. Several second-order statistics are calculated depending on these GLRLM and GLCM matrix. Details of the different types of feature extracted are given in Table 1.

5 Feature Ranking Algorithm

In our work, two unsupervised feature ranking approaches like minimum correlation (MC) [23] and local learning based clustering (LLC) [24] along with two supervised feature ranking algorithm ReliefF [25] and concave minimization (CM) [26] are used to find the rank of each feature. A brief description of each feature ranking algorithm used in this work is given in the following section.

5.1 Minimum Correlation (MC)

In this method [23], at first linear correlation coefficients of each pair of features are calculated and then a score is generated according to minimum correlation and then the ranking of the features are done on these scores then the features are ranked according to their correlation with the other features. The one which is least correlated to other features comes first. As this is unsupervised method, this ranking does not guaranty relevance.

Table 1 Details of features used in the work

Feature type and number of features	Feature details
Geometrical shape (10 features) [4]	(1) Area, (2) solidity, (3) perimeter, (4) circularity index, (5) major axis length, (6) minor axis length, (7, 8, 9, 10) irregularity index (A, B, C, D)
Color ($3 \times 6 \times 2 = 36$ features) [16, 17]	3 channel of each 6 color model ((1) RGB, (2) Lab, (3) XYZ, (4) YCbCr, (5) YIQ, (6) HSV) with 2 features ((1) mean and (2) standard deviation) in each channel
GLRLM texture ($2 \times 4 \times 11 = 88$ features) [18]	11 features ((1) long run emphasis (LRE), (2) short run emphasis (SRE), (3) gray-level non-uniformity (GLN), (4) run percentage (RP), (5) run length non-uniformity (RLN), (6) low gray-level run emphasis (LGRE), (7) short run low gray-level emphasis (SRLGE), (8) high gray-level run emphasis (HGRE), (9) short run high gray-level emphasis (SRHGE), (10) long run high gray-level emphasis (LRHGE), (11) long run low gray-level emphasis (LRLGE)) for 4 angle (135°, 90°, 45°, 0°) and 2 quantization level (64 and 128)
GLCM texture ($21 \times 6 \times 2 \times 7 = 1764$ features) [19–22]	21 features ((1) autocorrelation, (2) contrast, (3) correlation, (4) sum of squares, (5) sum variance, (6) sum average, (7) sum entropy, (8) cluster prominence, (9) cluster shade, (10) dissimilarity, (11) energy, (12) entropy, (13) maximum probability, (14) homogeneity, (15) difference variance, (16) difference entropy, (17) information measure of correlation2, (18) information measure of correlation1, (19) inverse difference normalized, (20) inverse difference, (21) inverse difference moment normalized) for 6 inter-pixel distance (6–1) with 2 quantization level (64 and 128) for 7 format (3 channels of RGB, 3 channels of HSV and gray scale) for 1 angle (0°)

5.2 Local Learning Based Clustering (LLC)

This feature selection method [24] uses two steps, in the first step clustering is done using neighboring data points, i.e., locally learned model and a local cluster label is given to each point and in the second step, those local cluster label are used to select features with large regression coefficient.

5.3 ReliefF

ReliefF [25] provides a relevance weight for any feature depending upon its distinguishing ability among two classes in two class problem. The weight, W of a feature can be calculated as the given Eq. 1:

$$W = \sum_{i=1}^{N} W_i/N = \sum_{i=1}^{N} (-|x_i - NH_i| + |x_i - NM_i|)/N \quad (1)$$

Here N is the number of the samples of the data set; x_i is the feature value of *i*th sample. NM_i is the value of the same type of feature of the nearest sample belonging to the opposite class and NH_i is that of the same class.

5.4 Concave Minimization (CM)

In this feature ranking [26] method, a plane of separation for two sets of point in a feature space is produced by optimizing the sum of distances between the misclassified points.

6 Classifier Used

In this work, three classifiers are used to classify the two categories of lesions. A small description of each classifier is given in the following section.

6.1 Support Vector Machine (SVM)

Support Vector Machine (SVM) [27] is a supervised learning algorithm. Support vector machine constructs set of hyperplanes in multidimensional feature space for classification. The considerable partition can be achieved by that hyper-plane which has the maximum distance from the nearest data point of any class.

6.2 K-Nearest Neighbors (KNN)

KNN [28] stores all available samples in the existing class and classifies new samples based on a similarity measure. It is also known as instance-based learning or case-based reasoning. The algorithm starts with randomly initialized k clusters. The second step is to compute the distance of each sample from the k cluster. In the third step, the distances are sorted and then again K-nearest neighbors is taken into consideration.

6.3 Ensemble Boosted Tree (EBT)

In decision tree classifier the entire feature space is divided into multiple subspaces repetitively by distinguishing line or plane. In ensemble method, several decision trees are combined to generate improved prediction than a single decision tree. In this method, a group of weak learners is combined to form a strong learner. The EBT classifier [29] use supervised learning algorithm. In Ensemble Boosted Tree (EBT), each learner is sequential learner. In each iteration of EBT the aim is to reduce the net error from the previous decision tree. This method supports loss function but it is prone to overfitting.

7 Result Analysis

In this present work, totally 1898 features are extracted from each 1300 images of Dermofit dataset. Out of 1898 features, 10 features are excluded as they are constant throughout the dataset. The rest 1888 features of each 1300 samples are then ranked with different feature ranking algorithms. Two unsupervised feature ranking approaches, i.e., minimum correlation (MC) and local learning based clustering (LLC) along with two supervised feature ranking algorithm, i.e., ReliefF and concave minimization (CM), as described in Sect. 5, are used to find the rank of each feature. The features are then taken in different sizes of sets with ascending order of rank for finding the classification accuracy in each set. Three different classifiers namely Support Vector Machine (SVM), K-Nearest Neighbors (KNN) and Ensemble Boosted Tree (EBT) are used to classify the dataset. In the classification task, 70% of the total images (910 images) are taken for training, 15% (195 images) for validation and 15% (195 images) for testing with fivefold cross-validation. Figure 1 shows the accuracy versus number of features with four different feature ranking algorithms using three different classifiers. It can be easily found that SVM classifier with quadratic kernel performs far better than other two counterparts, KNN and EBT. The accuracy found from KNN is least among the three classifiers. It is found from the graph that the accuracy achieves saturation nearly after 200 features. It is also found that the highest accuracy is 86.1% with only 700 features selected by minimum correlation (MC) feature ranking algorithm using Support Vector Machine (SVM) classifier. It can also be found from Fig. 1 that ranking algorithms perform almost equally on accuracy level.

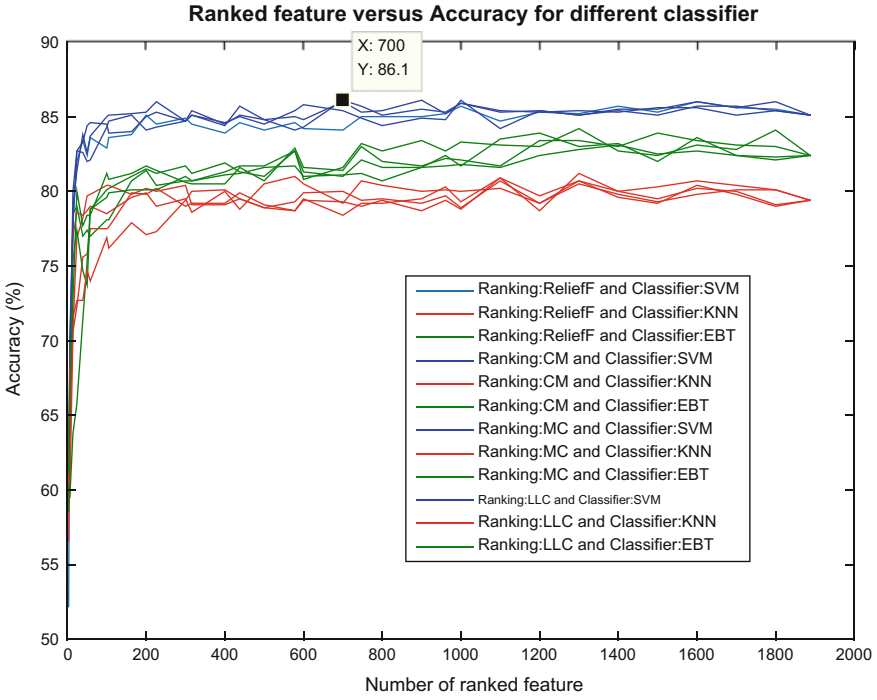

Fig. 1 Accuracy versus number of feature curves with four different feature ranking algorithms using three different classifiers. Different colors indicate different classifiers; individual curves within one color represent features ranked by different algorithms

When N best features were selected according to four different ranking methods obviously the sets were different. N_c represents the cardinality of the intersection of these four sets. All four ranking methods agree upon the selection of these N_c features. In Fig. 2, the relation between number of common features, N_c versus number of features, N is shown. Figure 2 also shows how common feature varies with N when common feature is taken from any two feature ranking algorithms out of the four ranked sets. From the curve, in Fig. 2, it can be noticed that the maximum feature commonality is found between ReliefF and Concave Minimization (CM) feature ranking algorithm in comparison with other combinations of ranking algorithms. When 800 features are taken from 4 different feature ranking algorithms, it is seen that only 383 features are common in ReliefF and Concave Minimization (CM). In Fig. 3, the accuracy with a varying number of common features of 4 different feature ranking algorithms is drawn. It is found that with only 163 common features which have a higher rank in all the feature ranking algorithms the system achieves 86.2% accuracy. It can be seen from Figs. 1 and 3 that higher accuracy can be achieved with less number of features when common best features are taken for classification. This accuracy level is similar to the accuracy level found by Tan et al. [4] while using

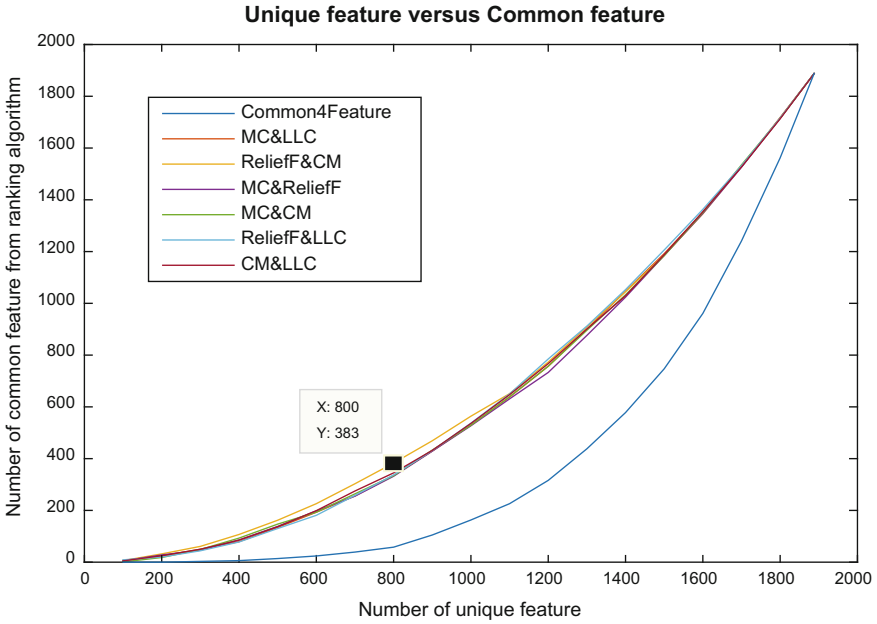

Fig. 2 Number of common features versus number of features

Table 2 Detailed comparison of result with related work

Related work	Feature used	Accuracy (%)	Sensitivity (%)	Specificity (%)
Tan et al. [4]	1472	88	83	89
Present work	163	86.2	84.9	87.2

nearly 1/10th features used by them. It is also found that the sensitivity of the present work is more than the related work Tan et al. [4].

A detailed comparison of result with related work is given in Table 2.

8 Conclusion

There are several findings from this work. First, it can be concluded that no feature ranking algorithm is superior to the other. Second, SVM is a better classification algorithm than KNN and EBT for this dataset. It is also found from the work that there are more similarities in feature if we take ReliefF and concave minimization as a pair in comparison to the other pair from the 4 ranking algorithm discussed in the paper. The most important findings from the work are that a final feature set comprising of only those features which have a higher rank in all the feature ranking algorithms yields higher accuracy with less number of features in comparison with individual

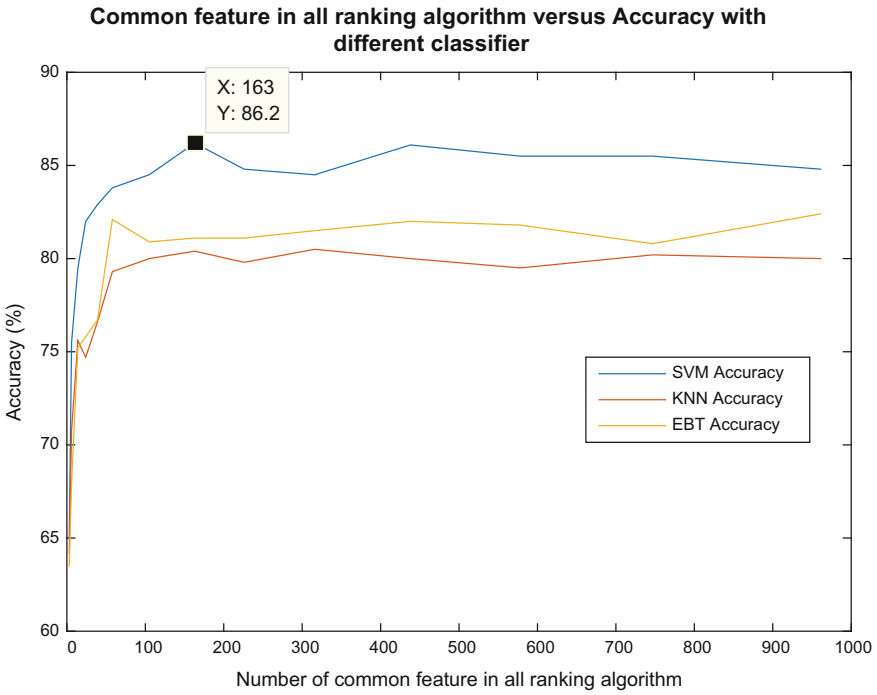

Fig. 3 Accuracy versus varying number of common feature from 4 different feature ranking algorithms

feature ranking algorithm. This multistep feature selection is a novel method and never reported before. It is found from the present work that the system achieved better identification accuracy of malignant melanoma than dermatologist [30]. The authors acknowledge dataset source Dermofit library [14] for their permission.

References

1. Marks, R.: Epidemiology of melanoma. Clin. Exp. Dermatol. **25**, 459–463 (2000). https://doi.org/10.1046/j.1365-2230.2000.00693.x
2. Kopec, D., Kabir, M.H., Reinharth, D., Rothschild, O., Castiglione, J.A.: Human errors in medical practice: systematic classification and reduction with automated information systems. J. Med. Syst. UK **27**(4), 297–313 (2003)
3. Sáez, A., Acha, B., Serrano, C.: Pattern analysis in dermoscopic images. In: Scharcanski, J. (ed.) Computer Vision Techniques for the Diagnosis of Skin Cancer. Series in BioEngineering. Springer, Berlin, Heidelberg (2014). https://doi.org/10.1007/978-3-642-39608-3_2

4. Tan, T.Y., Zhang, L., Jiang, M.: An intelligent decision support system for skin cancer detection from dermoscopic images. In: 12th International Conference on Natural Computation, Fuzzy Systems and Knowledge Discovery (ICNC-FSKD), pp. 2194–2199
5. Laskaris, N., Ballerini, L., Fisher, R.B., Aldridge, B., Rees, J.: Fuzzy Description of Skin Lesions
6. Ballerini, L., Fisher, R.B., Aldridge, B., Rees, J.: A color and texture based hierarchical K-NN approach to the classification of non-melanoma skin lesions
7. McDonagh, S., Fisher, R.B., Rees, J.: Using 3D information for classification of non-melanoma skin lesions
8. Giotis, I., Molders, N., Land, S., Biehl, M., Jonkman, M.F., Petkov, N.: MED-NODE: a computer-assisted melanoma diagnosis system using non-dermoscopic images. Expert Syst. Appl. **42**(6578–6585), 6578–6585 (2015)
9. Shardlow, M.: An Analysis of Feature Selection Techniques
10. Duch, W., Wieczorek, T., Biesiada, J., Blachnik, M.: Comparison of feature ranking methods based on information entropy
11. Ilangovan, S., Antonykumar, V., Appavu Balamurugan, S.: Comparison of feature ranking methods for effective data classification. World Appl. Sci. J. **34**(7), 965–974 (2016)
12. Slavkov, I., Zenko, B., Dzeroski, S.: Evaluation method for feature rankings and their aggregations for biomarker discovery. In: JMLR: Workshop and Conference Proceedings, vol. 8, pp. 122–135
13. Novakovic, J., Strbac, P., Bulatovic, D.: Toward optimal feature selection using ranking methods and classification algorithms. Yugosl. J. Oper. Res. **1**, 119–135 (2011)
14. Ballerini, L., Fisher, R.B., Aldridge, R.B., Rees, J.: A color and texture based hierarchical K-NN approach to the classification of non-melanoma skin lesions, color medical image analysis. In: Celebi, M.E., Schaefer, G. (eds.) Lecture Notes in Computational Vision and Biomechanics, vol. 6 (2013)
15. Otsu, N.: A threshold selection method from gray-level histograms. IEEE Trans. Syst. Man Cybern. **9**(1), 62–66. https://doi.org/10.1109/tsmc.1979.4310076
16. Pereira, S.M., Frade, M.A.C., Rangayyan, R.M., Azevedo-Marques, P.M.: Classification of color images of dermatological ulcers. IEEE J. Biomed. Health Inform. **17**(1) (2013)
17. Emre Celebi, M., Kingravi, H.A., Uddin, B., Hitoshi Iyatomi, Y., Aslandogan, A., Stoecker, W.V., Moss, R.H.: A methodological approach to the classification of dermoscopy images. Comput. Med. Imaging Graph. **31**, 362–373 (2007)
18. Tang, X.: Texture information in run-length matrices. IEEE Trans. Image Process. **7**(11), 1602–1609 (1998)
19. Haralick, R.M., Shanmugam, K., Dinstein, I.: Textural features of image classification. IEEE Trans. Syst. Man Cybern. **SMC-3**(6) (1973)
20. Soh, L., Tsatsoulis, C.: Texture analysis of SAR sea ice imagery using gray level co-occurrence matrices. IEEE Trans. Geosci. Remote Sens. **37**(2) (1999)
21. Clausi, D.A.: An analysis of co-occurrence texture statistics as a function of grey level quantization. Can. J. Remote Sens. **28**(1), 45–62 (2002)
22. Ballerini, L., Li, X., Fisher, R.B., Aldridge, B., Rees, J.: Content-Based Image Retrieval of Skin Lesions by Evolutionary Feature Synthesis
23. Hall, M.A.: Correlation-based feature selection for machine learning. Ph.D. Thesis at The University of Waikato (1999)
24. Zeng, H., Cheung, Y.M.: Feature selection and kernel learning for local learning-based clustering. IEEE Trans. Pattern Anal. Mach. Intell. **33**(8), 1532–1547 (2011). https://doi.org/10.1109/TPAMI.2010.215
25. Kononenko, I., et al.: Overcoming the myopia of inductive learning algorithms with RELIEFF. Appl. Intell. **7**(1), 39–55 (1997)
26. Bradley, P.S., Mangasarian, O.L.: Feature Selection via Concave Minimization and Support Vector Machines

27. Gunn, S.R.: Support vector machines for classification and regression. Technical Report, University of Southampton (1998)
28. Akhil Jabbar, M., Deekshatulua, B.L., Chandra, P.: Classification of heart disease using K-nearest neighbor and genetic algorithm. In: International Conference on Computational Intelligence: Modeling Techniques and Applications (CIMTA) 2013. Procedia Technol. **10**, 85–94 (2013)
29. Buhlmann, P.: Bagging, Boosting and Ensemble Methods
30. Morton, C.A., Mackie, R.M.: Clinical accuracy of the diagnosis of cutaneous malignant melanoma. Br. J. Dermatol. **138**(2), 283–287 (1998). https://doi.org/10.1046/j.13652133.1998.02075.x

Optimal Reactive Power Dispatch Using Modified Differential Evolution Algorithm

Dharmbir Prasad, Abhik Banerjee and Rudra Pratap Singh

Abstract Traditionally, optimal reactive power dispatch (ORPD) is a subset of optimal power flow (OPF) and can be achieved by controlling a number of control variables such as generator voltages, transformers' trappings and compensation of reactive power to optimize specific objectives. ORPD is formulated as a non-linear constrained optimization problem with continuous and discrete variables. This paper presents a recently developed modified differential evolution (MDE) algorithm to solve ORPD problem by minimizing real power loss and total voltage deviation. To accelerate the convergence speed and to improve solution quality, the certain modification is incorporated in original differential evolution (DE) algorithm. The proposed MDE approached is implemented on the modified IEEE 30-bus test system. Results reveal primacy in terms of solution quality of the proposed MDE approach over original DE and other optimization techniques and affirm its potential to solve the ORPD problem.

Keywords Optimal reactive power dispatch · Optimization
Modified differential evolution

1 Introduction

Optimal reactive power dispatch (ORPD) is an important tool for reliable power system operation [1]. The main purpose of ORPD is to find out the settings of control variables for economic operation of a power system in the secure manner.

D. Prasad (✉) · R. P. Singh
Asansol Engineering College, Asansol, West Bengal, India
e-mail: dharmbirprasad9@gmail.com

R. P. Singh
e-mail: rps_crj@yahoo.co.in

A. Banerjee
National Institute of Technology, Yupia, Arunachal Pradesh, India
e-mail: abhik_banerjee@rediffmail.com

U. Biswas et al. (eds.), *Advances in Computer, Communication and Control*, Lecture Notes in Networks and Systems 41, https://doi.org/10.1007/978-981-13-3122-0_26

The active and reactive power generation at power plants, reactive power output from their sources etc. are maneuvered to get the proposed objective (such as minimization of active power losses (P_{Loss}) and total voltage deviation (TVD) objectives) [2].

Hitherto, many optimization methods have been grown to improve system performance. Amongst them few methods are quadratic programming [3], Newton approach [4], interior point methods [5], linear programming [6], nonlinear programming [7], genetic algorithm (GA) [8] and differential evolution (DE) algorithm [9] etc. These techniques have, successfully, demonstrated their effectiveness in finding solution for ORPD problems. DE is one such evolutionary algorithm which has found application in diverse fields. However, it suffers from the problem of slow convergence and various improvements have been suggested in the pats. One such improved version named modified DE (MDE) is adopted for solution of ORPD problem of modified IEEE 30-bus test system.

The remaining portion of this paper is manifested as follows. In Sect. 2, ORPD problems mathematical formulation is presented. Section 3 describes the basic concept of DE and MDE algorithms. Simulation outcomes are discussed in Sect. 4. At the end, conclusions of the current work are derived in Sect. 5.

2 ORPD Problems Mathematical Formulation

The ORPD problem is mathematically given by (1) and (3) [9].

2.1 Undertaken Objective Function

The objectives undertaken during this study are as following:

(i) P_{Loss} *minimization*: The mathematical formulation for objective function of P_{Loss} minimization is given by (1)

$$\text{Min } \mathrm{P}_{Loss} \tag{1}$$

Power losses may be, mathematically, given by (2)

$$P_{Loss} = \sum_{k=1}^{NTL} G_k(V_i^2 + V_j^2 - 2|V_i||V_j|\cos\delta_{ij}) \tag{2}$$

(ii) *TVD minimization*: This objective function may be given by (3)

$$\text{Min } TVD \tag{3}$$

TVD may be formulated as in (4)

$$TVD = \sum_{i=1}^{NL} \left| V_i - V_i^{ref} \right| \tag{4}$$

2.2 Constraints

In the current work, the system is restricted to several equality and inequality constraints. Equations related to power flow are classified as constraints of equality, where as transformer tap setting, reactive power generation and its compensation, and bus voltages of each line are considered as constraints of inequality.

2.2.1 Constraints of Equality

The constraints associated with load flow equations are represented in (5)

$$\left.\begin{aligned} \sum_{i=1}^{NB} (P_{Gi} - P_{Li}) + \sum_{i=1}^{NTCPS} P_{ik} &= \sum_{i=1}^{NB} \sum_{j=1}^{NB} |V_i||V_j||Y_{ij}| \cos(\theta_{ij} + \delta_i - \delta_j) \\ \sum_{i=1}^{NB} (Q_{Gi} - Q_{Li}) + \sum_{i=1}^{NTCPS} Q_{ik} &= -\sum_{i=1}^{NB} \sum_{j=1}^{NB} |V_i||V_j||Y_{ij}| \sin(\theta_{ij} + \delta_i - \delta_j) \end{aligned}\right\} \tag{5}$$

2.2.2 Constraints of Inequality

(i) *Generator voltage constraints*: The permissible limits for generator voltage of the *i*-th bus are given by (6)

$$V_{Gi\,\min} \le V_i \le V_{Gi\,\max} \quad i = 1, 2, \ldots, NG \tag{6}$$

(ii) *Load bus constraints*: Load bus voltage variation should be restricted within the withstand capacity of the system and given by (7)

$$V_{Li\,\min} \le V_i \le V_{Li\,\max}, \quad i = 1, 2, \ldots, NL \tag{7}$$

(iii) *Transmission line constraints*: The line flow capacity for each transmission line represented by (8)

$$S_{l_i} \le S_{l_i\,\max} \quad i = 1, 2, \ldots, NTL \tag{8}$$

(iv) *Transformer tap constraints*: The permissible limits for transformer tap setting may be represented by (9)

$$T_{i\,\min} \leq T_i \leq T_{i\,\max} \quad i = 1, 2, \ldots, NT \tag{9}$$

(v) *Shunt compensator constraints*: Based on the assumption to optimize reactive power yield of shunt VAR compensators, maximum and minimum limits are represented by (10)

$$Q_{ci\,\min} \leq Q_{ci} \leq Q_{ci\,\max} \quad i = 1, 2, \ldots, NC \tag{10}$$

3 Modified Differential Evolution Algorithm

3.1 Overview of DE Algorithm

An innovative numerical optimization approach namely—DE algorithm is simple in execution, comparatively faster and robust than several recent evolutionary algorithms [10]. The major steps for its implementation are given below.

3.1.1 Initialization

Generally, a randomly chosen value of each decision parameter in every vector of the initial population is assigned within its corresponding viable bounds as in (11)

$$X_{j,i}^{(0)} = X_j^{\min} + \mu_j (X_j^{\max} - X_j^{\min}) \quad i = 1, \ldots, NP, \quad j = 1, \ldots, D \tag{11}$$

where, μ_j: random number within the range of [0, 1], generated for each j and $X_j^{\max}$, $X_j^{\min}$: maximum and minimum limits of the j-th decision parameters, respectively.

3.1.2 Mutation

The mutation operator produces mutant vectors X_i' by perturbing a randomly selected vector X_a with the diversity of two other randomly selected vectors X_b and X_c is

$$X_i'^{(G)} = X_a^{(G)} + F(X_a^{(G)} - X_c^{(G)}) \quad i = 1, \ldots, NP \tag{12}$$

where, a, b, c: randomly chosen indices, such that $a, b, c \in i = 1, \ldots NP$ and $a \neq b \neq c \neq i$, F: scaling factor in the range of [0, 2].

3.1.3 Crossover

A variation among the mutant parameter vectors is experienced due to initialization of crossover process. A trial vector X_i'' is created from the components of each mutant vector X_i' and its subsequent target vector X_i, dependence on a series of $D-1$ binomial experiments as given by (13)

$$X_{j,i}^{\prime\prime(G)} = \begin{cases} X_{j,i}^{\prime(G)} \text{ if } \rho_j \leq CR \text{ or } j = q \\ X_{j,i}^{(G)} \text{ otherwise} \end{cases} \quad i = 1, \ldots, NP, \quad j = 1, \ldots, D \tag{13}$$

where, ρ_j: uniformly distributed random number within the range [0, 1], generated for each j; CR: crossover constant chosen within the range [0, 1] which controls diversity of population; q: randomly chosen index $\in [1, \ldots, D]$ to get minimum one parameter from mutant vector.

3.1.4 Selection

The trial vectors and their target vectors together forms a better fitness or are more optimal solution according to (14).

$$X_i^{(G+1)} = \begin{cases} X_i^{\prime\prime(G)} \text{ if } f(X_i^{\prime\prime(G)}) \leq f(X_i^{(G)}) \\ X_i^{(G)} \text{ otherwise} \end{cases} \quad i = 1, \ldots, NP \tag{14}$$

The optimization process is continued for several generations in order to allow individuals to proceed with their fitness in search of optimal values.

3.2 Modified Differential Evolution Algorithm for ORPD

Kaelo and Ali [11] incorporated few modifications in the original DE in order to expedite convergence profile and boosting exploration features. The first modification in DE is to substitute the random base vector $X_a^{(G)}$ in the mutation rule (12) by the tournament best $X_{tb}^{(G)}$ and hence, expedites the convergence [11]. Also, instead of employing a fixed F throughout a run of DE, a random F in $[-1, -0.4] \cup [0.4, 1]$ is used for each mutated point [11]. The flowchart of ORPD solution using MDE is manifested in Fig. 1. The power flow algorithm is implemented for each candidate solution to assess its fitness and find out corresponding state variables. The optimization process terminates while number of generations $G^{\max}$ is reached its specified limits, or in case not improvement over a preset number of generations.

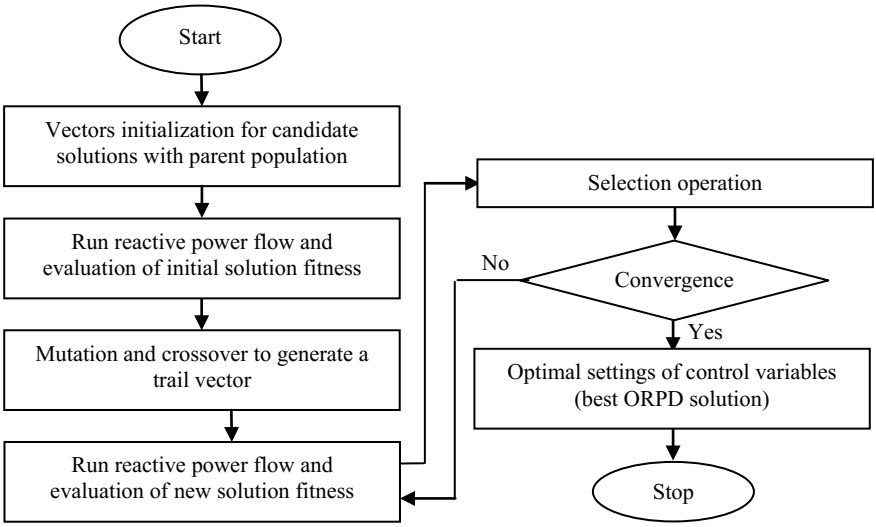

Fig. 1 Flow chart for solution of ORPD problem using MDE algorithm

4 Simulation Results and Discussions

The proposed MDE method is applied on the modified IEEE 30-bus test power system to solve ORPD problem. The generator data, bus data and line data for the studied power network are taken from [9]. The coding of the present work is executed using MATLAB 2008a, on a computer having 2.63 GHz Pentium IV processor and 3 GB RAM. The simulated results are compared to other reported results to affirm usefulness of the proposed MDE method. The needful results are **bold** faced while providing comparative overview in order to check performance of the proposed technique.

Test Case-1 (*Minimization of* P_{Loss}): The control variables for P_{Loss} minimization objective is given in Table 1. A comparative result analysis for DE [9] and MDE algorithm is performed. The recorded P_{Loss} value using the proposed MDE method is **4.5521 MW**. Which is **0.0029 MW** (i.e., saving in power by **19.57%**) less compared to given output of 4.5550 MW by DE method in [9]. The obtained convergence characteristic of P_{Loss} (MW) from the proposed MDE method is shown in Fig. 1. This profile reflects improvement in convergence features for *NFFE* of 500.

Test Case-2 (*Minimization of TVD*): The proposed MDE algorithm is applied on the modified IEEE 30-bus test power system to minimize the voltage deviation. Table 1 consists of optimal control variables along with respective results noted from DE [9] and MDE. The recorded *TVD* value, yielded by MDE method, is **0.0862** p.u., which is lower (i.e., **85.193%** improvement) as compared to that of reported minimal value of 0.0911 p.u. in [9]. A better convergence characteristic of *TVD* minimization objective is presented in Fig. 2.

Table 1 Comparison of simulation results for the modified IEEE 30-bus test power system for *Test Case-1* and *Test Case-2*

Control variable	*For Test Case-1*		*For Test Case-2*	
	DE [9]	MDE	DE [9]	MDE
Generator voltage				
V_1 (p.u.)	1.1000	1.1000	1.0100	1.0845
V_2 (p.u.)	1.0931	1.0918	0.9918	1.0015
V_5 (p.u.)	1.0736	1.0750	1.0179	1.0203
V_8 (p.u.)	1.0756	1.0568	1.0183	0.9991
V_{11} (p.u.)	1.1000	1.1000	1.0114	1.0770
V_{13} (p.u.)	1.1000	1.0765	1.0282	1.0426
Transformer tap ratio				
T_{11} (p.u.)	1.0465	1.0430	1.0265	1.0107
T_{12} (p.u.)	0.9097	0.9050	0.9038	1.1000
T_{15} (p.u.)	0.9867	0.9825	1.0114	1.0545
T_{36} (p.u.)	0.9689	0.9690	0.9635	0.9620
Capacitor banks				
$Q_{\text{C-10}}$ (MVAR)	5.0000	4.9979	4.9420	4.8455
$Q_{\text{C-12}}$ (MVAR)	5.0000	4.9885	1.0885	1.0904
$Q_{\text{C-15}}$ (MVAR)	5.0000	4.9918	4.9985	5.0000
$Q_{\text{C-17}}$ (MVAR)	5.0000	4.9983	0.2393	0.0085
$Q_{\text{C-20}}$ (MVAR)	4.4060	4.4018	4.9958	5.0000
$Q_{\text{C-21}}$ (MVAR)	5.0000	4.9952	4.9075	4.9152
$Q_{\text{C-23}}$ (MVAR)	2.8004	3.8851	4.9863	4.9875
$Q_{\text{C-24}}$ (MVAR)	5.0000	5.0000	4.9663	4.9529
$Q_{\text{C-29}}$ (MVAR)	2.5979	2.9641	2.2325	2.2836
P_{Loss} (MW)	4.5550	**4.5521**	6.4755	6.4718
% P_{Save}	19.523	**19.57%**	–	–
TVD (p.u.)	1.9589	1.9014	0.0911	**0.0862**
% $TVD_{Improve}$	–	–	84.352	**85.193**
CPU time (s)	NR*	116	NR*	199.6421

*NR** means not reported

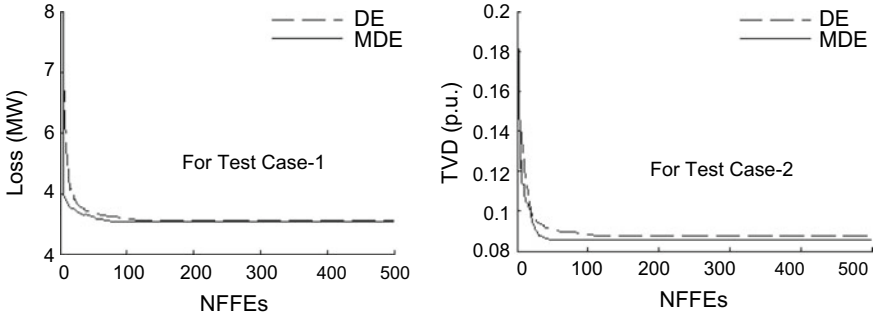

Fig. 2 Comparative convergence profiles of *Test Case-1* and *Test Case-2*

5 Conclusions and Future Research

In this work, MDE algorithm is enacted on the modified IEEE 30-bus test power systems to find solution for most common ORPD problems. During simulation, optimal settings of control variables are achieved for the undertaken test systems. The obtained results of real power losses and total voltage deviation are compared to other reported methods. Comparative study of the results reveals the usefulness of the proposed MDE method, in fulfilling individual objective and offering superior convergence feature. Now, it may be accomplished that the projected method is applied, successfully, to answer complex ORPD issues of power system. Simultaneously, the proposed MDE method may be attributed as an optimistic tool for solving various engineering problems in near future.

References

1. Abido, M.A.: Multi objective optimal VAR dispatch using strength Pareto evolutionary algorithm. In: IEEE Congress on Evolutionary Computation, Vancouver, BC, Canada, pp. 730–736 (2006). https://doi.org/10.1109/cec.2006.1688384
2. Dai, C., Chen, W., Zhu, Y., Zhang, X.: Seeker optimization algorithm for optimal reactive power dispatch. IEEE Trans. Power Syst. **24**(3), 1218–1231 (2009). https://doi.org/10.1109/TPWRS.2009.2021226
3. Nanda, J., Kothari, D.P., Srivastava, S.C.: New optimal power dispatch algorithm using Fletcher's quadratic programming method. IET Gener. Transm. Distrib. **136**(3), 153–161 (1989). https://doi.org/10.1049/ip-c.1989.0022
4. Quintana, V.H., Santos-Nieto, M.: Reactive power-dispatch by successive quadratic programming. IEEE Trans. Energy Convers. **4**(3), 425–435 (1989). https://doi.org/10.1109/60.43245
5. Liu, W.H.E., Papalexopoulos, A.D., Tinney, W.F.: Discrete shunt controls in a Newton optimal power flow. IEEE Trans. Power Syst. **7**(4), 1509–1518 (1992). https://doi.org/10.1109/59.207375
6. Kirschen, D.S., Meeteren, H.P.: MW/voltage control in linear programming based optimal power flow. IEEE Trans. Power Syst. **3**(2), 481–489 (1988). https://doi.org/10.1109/59.192899

7. Lee, K.Y., Park, Y.M., Ortiz, J.L.: A united approach to optimal real and reactive power dispatch. IEEE Trans. Power Appar. Syst. **104**(5), 1147–1153 (1985). https://doi.org/10.1109/TPAS.1985.323466
8. Iba, K.: Reactive power optimization by genetic algorithm. IEEE Trans. Power Syst. **9**(2), 685–692 (1994). https://doi.org/10.1109/59.317674
9. El Ela, A.A., Abido, M.A., Spea, S.R.: Differential evolution algorithm for optimal reactive power dispatch. Electr. Power Syst. Res. **81**(2), 458–464 (2011). https://doi.org/10.1016/j.epsr.20
10. Storn, R., Price, K.: Differential evolution—a simple and efficient heuristic for global optimization over continuous spaces. J. Glob. Optim. **11**(4), 341–359 (1997). https://doi.org/10.1023/A:1008202821328
11. Kaelo, P., Ali, M.M.: A numerical study of some modified differential evolution algorithms. Eur. J. Oper. Res. **169**(3), 1176–1184 (2006). https://doi.org/10.1016/j.ejor.2004.08.047

Analysis of Energy-Efficient Routing Protocols in Mobile Ad Hoc Network

Sumanta Das and Sarit Pal

Abstract Limited energy resource, routing of packets and security are the major challenges in Mobile Ad hoc Networks (MANET) due to their inherent characteristics. This paper focuses on energy consumption in MANET, which is a very serious issue because this affects the network lifetime directly. The authors concentrate on selection of energy-efficient routing protocols to minimize energy consumption by the nodes during message transmission. Attempt has been made to point out the causes of unnecessary consumption in the network. Comparative analysis of different energy-efficient routing techniques has been performed and an attempt has been made to propose a better solution. Quality of service also has been taken into account.

Keywords Mobile Ad Hoc Networks · Routing algorithms · Energy consumption

1 Introduction

The major challenges in Mobile Ad hoc Network (MANET) include routing efficiency, energy and bandwidth consumption, security issues, and electromagnetic interference. Nodes in MANET mainly use portable energy sources and are employed in areas with no centralized infrastructure. So energy consumption requires special attention for the survival of the network. This paper focuses on energy-efficient routing to increase the longevity of MANET. Causes of excess energy consumption in MANET has been studied and techniques to reduce energy consumption have been

S. Das (✉)
Department of Electronics and Telecommunication Engineering, Dr. B. C. Roy Polytechnic, Durgapur, India
e-mail: sumanta.das@bcrec.ac.in

S. Pal
Department of Electronics and Communication Engineering, Dr. B. C. Roy Engineering College, Durgapur, India
e-mail: sarit.pal@bcrec.ac.in

U. Biswas et al. (eds.), *Advances in Computer, Communication and Control*, Lecture Notes in Networks and Systems 41, https://doi.org/10.1007/978-981-13-3122-0_27

discussed. An attempt has been made to incorporate the technique to minimize energy consumption in the existing routing algorithms rather than completely rejecting those protocols.

2 Causes for Excess Energy Consumption

Excess energy consumption in Mobile Ad hoc Network is a vital problem because of limited energy sources in the mobile nodes. The conventional routing protocols used in wireless communication are efficient in managing delay, bandwidth, and network congestion, but they do not consider any energy-related parameter during algorithm formulation for packet transfer. From the literature review, the following causes for excess energy consumption in MANET have been identified:

(a) *Unequal transmission energy due to different path length*
In wireless network, nodes can transmit the packets to the nodes which are in the transmission range of the antenna. In a network with less number of nodes, due to the larger distance among the intermediate nodes more energy is required to transmit packets, which is less in case of the denser network.

(b) *Overhearing by nodes*
In wireless network like MANET, promiscuous nodes refer to those communicating nodes who listen to the incoming packets even though not intended for them. Though promiscuous nodes can play an important role to determine the alternate path in case of sudden route failure, accepting and discarding operation by them consume excess energy unnecessarily.

(c) *Retransmission of data or control messages due to collision or path congestion*
In any network, loss of packets due to collision is a very common phenomena. In case of collision, data is required to be retransmitted. The probability of collision is greater for denser network and hence the number of frequent retransmission is more. Collision not only causes unnecessary energy consumption but also delays the packet transfer.

(d) *Common node/Uneven load distribution*
In any network, there is always a probability to select routes having one or more common nodes between several source–destination pairs. These common nodes lose energy at a higher rate than other nodes and cause the early collapse of the network.

(e) *Route selection through nodes with less residual battery capacity*
Though the above-mentioned causes are most prevailing causes of excess energy consumption, it is also required to consider the residual battery capacity of energy source of nodes. It seems that more number of hops in a network can reduce energy consumption, but the intermediate nodes with less residual energy may cause early collapse of the network.

3 Energy-Efficient Routing Techniques

Energy-aware routing protocols are required to be implemented in Mobile Ad hoc Network to increase the longevity of the network. Proactive routing protocols includes routes for all nodes and not suitable in MANET due to the large routing table. Reactive routing protocols are suitable in this regard because the routing table is created only at the time of transmission. Consumption of energy, bandwidth, and memory is also reduced due to small routing overhead.

3.1 Non-promiscuous Dynamic Source Routing Protocol

Among the existing conventional routing algorithms [1–3], DSR protocol inherently saves energy by dropping the duplicate route request packets which is not in case of other protocols. A non-promiscuous variant of DSR protocol, known as DSR-np [4], reduces energy consumption by adding a header file at the source node which contains the address of all the intermediate nodes once a route has been selected from source to destination. Each of the intermediate nodes of a route maintains the table of address of the immediate neighbor in that route. Therefore, any packet arriving at a node not containing the preselected address of the node is dropped. This technique reduces the energy consumption by reducing the overhearing problem by the nodes. However, in case of route failure, it cannot select an alternate route rapidly due to unavailability of the address of other unused nodes.

3.2 Minimum Total Transmission Power Routing Algorithm

Generally, a route with less number of hops is preferred to send packets from source to destination, which is generally implemented using Dijkstra's Shortest Path Algorithm. However, this does not ensure minimum total power spent. Apparently, less transmission power is required in case of more number of intermediate nodes because of a smaller distance between the neighboring nodes. But an end-to-end delay and route instability due to the random mobility of the nodes are more in this case. To overcome this problem, Minimum Total Transmission Power Routing (MTPR) scheme has been proposed, which considers both receive and transmission power of nodes. The total amount of energy consumed during transmission and reception of packets between these neighboring nodes I and J is given by

$$C_{i,j} = P_{recv}(n_j) + P_{transmit}\left(n_{i,} n_j\right) + cost\left(n_j\right) \tag{1}$$

Here $P_{transmit}\left(n_i, n_j\right)$ is the transmission energy between two neighboring nodes I and J (I is the transmitter and J is the receiver), $P_{recv}(n_j)$ is receiving energy at

the receiving node J and cost(n_j) is the minimum cost of transmission between two consecutive nodes. The cost $C_{i,j}$ is used by the neighbor node n_i to estimate the cost to its own by the following equation:

$$\text{Cost}(n_i) = \min_{j \in NH(i)} C_{i,j} \tag{2}$$

where NH(i) = {j; where n_j is neighbor node of n_i}. Though this MTPR algorithm finds the minimum total energy path from source to destination, it does not consider the residual energy of the individual node. Common node problem also remains unsolved in this algorithm causing an early collapse of the network.

3.3 Minimum Battery Cost Routing (MBCR) Protocol

An effective solution to the residual energy problem is attempted in Minimum Battery Cost Routing (MBCR) protocol, which defines a new metric known as battery cost function to indicate whether the amount of residual energy present in a node is adequate to transfer a packet to a nearest neighbor or not. The proposed battery cost function $f_i(C_i^t)$ of the node n_i is inversely proportional to battery capacity C_i^t at an instant of time t and a larger value of $f_i(C_i^t)$ indicates more unwillingness of the node to forward packet. The battery cost R_j for route j among all possible routes between source and destination having D_j number of nodes is given by

$$R_j = \sum_{i=0}^{D_j - 1} f_i(C_i^t) \tag{3}$$

The battery cost is calculated in this way for all the possible routes between source and destination and the best route R_i is chosen according to the equation:

$$R_i = \min\{R_j | j \in A\} \tag{4}$$

where A denotes the set of all possible routes. From the Eqs. (3) and (4), it is obvious that summation of the battery capacity of a route leads to selection of minimum cost route among all possible routes from source to destination, though it may not avoid selecting the maximum reluctant node in the path. So the selected minimum cost route may cause early network partition.

3.4 Min-Max Battery Cost Routing (MMBCR)

Minimum Battery Cost Routing (MBCR) protocol selects the route to destination considering summation of individual battery cost of the nodes in all possible paths. Among all such routes, the minimum cost route is chosen as the best one for routing.

But summation of battery cost may lead to the selection of nodes with less battery energy which are not capable to transfer the packet to its neighbor and hence causes network partitioning earlier. Min-Max Battery Cost Routing (MMBCR) has been proposed that selects a route, which does not have any node with less battery capacity in the route. In this algorithm, instead of summing up all the battery cost in a route, maximum battery cost function of the *i*th node in the *j*th route is found out. Then the route having the node with a minimum of maximum battery cost function is selected according to the expressions:

$$R_j = \max_{i \in route\_j} \left\{ f_i\left(C_i^t\right) \right\} \tag{5}$$

$$R_i = \min\{R_j \mid j \in A\} \tag{6}$$

where A = set of all possible routes. Equation (5) choose the node having maximum battery cost function or with minimum battery energy in the *j*th route. Equation (6) identifies the route having node with minimum battery cost function among all possible routes. Till it is not assured that MMBCR will select minimum total transmission power path always.

3.5 Conditional Max-Min Battery Capacity Routing (CMMBCR)

Conditional Max-Min Battery Capacity Routing (CMMBCR) [5] algorithm combines the advantageous features of both MBCR and MMBCR protocols. Up to certain threshold value (γ) of battery capacity Minimum Total Transmission Power Route (MTPR) is chosen and as the battery capacity is lower than γ, Min-Max Battery Cost Routing (MMBCR) algorithm is selected. The threshold value of battery capacity (γ) is chosen in the range of 0 and 100% of the maximum battery capacity of node. With this parameter, the best route is chosen according to the following equation:

$$R_j^c = \min_{i \in Route\_j} C_i^t \geq \gamma \tag{7}$$

where 'j' belongs to the set of all routes 'A'. However, this protocol does not consider the battery discharge rate of the node, which also should be taken into account to increase the longevity of the network.

3.6 Lifetime Prediction Routing (LPR)

Researchers have considered battery discharge rate as another parameter for early prediction of lifetime of a route. Battery lifetime is measured as a function of residual energy as well as the energy spent to transmit one bit from the node to its neighbor. Lifetime Prediction Routing (LPR) algorithm [6] uses these parameters to find the

most energy-efficient route in a network. The main goal of LPR is to select a path in which the nodes are lightly loaded. Lifetime $T_i(t)$ of a selected node in a network is predicted from past N number of residual energy values of this node as per the following mathematical relation:

$$T_i(t) = \frac{E_{r,i}(t)}{\frac{1}{N-1}\sum_{k=i-N+1}^{i} R_k(t)} \tag{8}$$

where $T_i(t)$ is the predicted lifetime of *i*th node, $E_{r,i}(t)$ provides the remaining energy of the node at the time *i*th packet being sent or relayed, $R_k(t)$ indicates the rate of energy depletion when *k*th packet is sent and N is the number of intervals for Simple Moving Average (SMA) predictor. This algorithm is implemented with DSR routing protocol and during the route selection process, a minimum lifetime header is included in the control message of route request (RREQ) packet.

If the predicted lifetime of sending node's header is greater than the visiting node's lifetime, then lifetime value in the header is replaced by the lifetime value of visiting node. Upon receiving a route request packet, the intermediate node starts timer T_r and waits for a specified time for the arrival of any duplicate RREQ packet. If any such packet arrives, and minimum lifetime value inside the header is lower than the current node's lifetime, the RREQ packet is dropped. Otherwise, the lifetime in the header is replaced with the current value of node's lifetime and forwarded into the network. To find the best route among all possible routes, the following relation is used:

$$\max_{\pi} T_\pi(t) = \min_{i \in \pi}(T_i(t)) \tag{9}$$

Here, $T_i(t)$ is the predicted lifetime of *i*th node in path π and $T_\pi(t)$ is the lifetime of the path. The path (say π) will be considered as the route with longest survival time which contains the *i*th node with minimum predicted lifetime. Though this protocol saves energy, packet delivery is delayed due to the route selection process and an increase in node mobility. Energy consumption rate increases in a less dense network also.

3.7 Energy-Dependent DSR (EDDSR)

In Energy-Dependent DSR (EDDSR) [7], protocol energy drain rate has been considered as the metric to predict lifetime of the network. Current energy level of a node is periodically computed from the knowledge of the residual battery power. Having sufficient battery power above the threshold value, a node forwards the packet. When the battery power goes below the threshold value, node starts rebroadcasting the route request packets informing its neighbors about its low residual battery power. As soon as the battery power goes down below the critical threshold value, the inter-

mediate node refrains from further packet delivery and informs the source node with a route error message to search an alternate route. The simulation result of EDDSR establishes its superiority over DSR protocol in the higher traffic environment.

3.8 Simple Energy-Aware DSR (SEADSR)

Another variant of DSR protocol known as Simple Energy-Aware Dynamic Source Routing (SEADSR) [8] algorithm introduces a time delay 'τ' which is a function of power consumption by a node. The time delay is implemented by an intermediate node before retransmission of the route request (RREQ) packet. The time delay introduced is given by the following relationship:

$$\tau = (C_{max} - C)\tau_{max}/C_{max} \tag{10}$$

where C_{max} is the battery capacity and C is the current battery level of the present node. The retransmission delay τ is directly proportional to the maximum allowable delay τ_{max} and also directly proportional to the energy consumed by the node. The value of τ can vary between 0 and τ_{max}. The route selected by conventional DSR algorithm may not be the optimal route because always there remains a chance to reselect a route containing power exhausted nodes. The novelty of SEADSR algorithm to increase the lifetime of MANET lies in its capability to choose different paths at the same time for two different source nodes which is found to be difficult for conventional DSR and MMBCR algorithms.

3.9 Power-Aware Routing (PAR) Algorithm

Power-Aware Routing (PAR) algorithm [9] attempts to reduce energy consumption by considering real-time and non-real-time data transfer in non congested and energy-efficient route. This algorithm emphasizes on node id, battery status and traffic level to reduce the energy consumption in the network. Three levels of battery status is suggested based on the percentage of battery energy available. Battery status less than 20% is denoted by level 1, status greater than 20% but less than 60% is level 2 and above 60% is level 3. This algorithm has the ability to estimate the total battery cost along with the number of weak nodes (with less than 20% of battery status) of a route. The level of traffic at each node can also be measured from the number of packets buffered at the interface queue of a given node. The route reply path from destination node to source node is selected by the destination node from the knowledge of different route request packet and their link status ratio R of that path and is given by

$$R = \frac{E_{i,j}}{H_n} \tag{11}$$

In the above equation $E_{i,j}$ denotes the total residual energy of path and H_n denotes the number of intermediate hops. The minimum value of R for a non-real-time type load is considered as 1 and the minimum value for real-time type load as 2. PAR calculates the link status ratio for every different selected route for a given type of load. For multiple link status ratio, a route with a minimum number of weak nodes (having less than 20% of battery energy) is chosen. This algorithm also considers the level of total traffic as a metric to select the best route having a minimum value of this metric, provided, no weak node is present in the possible routes. The simulation result shows that with the increase in node density the remaining average energy of the network increases but the data transfer latency increases as compared to the AODV and DSR routing protocol.

4 Analysis of Energy Efficiency for Different Routing Protocols

In the last few years, several energy-aware routing algorithms have been proposed in the field of ad hoc networks. All of them have their own pros and cons. Comparative analysis of these energy-aware routing algorithms and energy optimization techniques have been performed and is presented in Table 1.

Analysis of aforesaid routing protocols to minimize energy consumption in ad hoc networks reveals the fact that none of these algorithms satisfies all the criteria for the best path to the destination, longer network lifetime and better Quality of Service (QoS). Some algorithms lengthen the network lifetime satisfactorily, but do not offer a guarantee for shortest path and minimum delay to the destination. Since analysis establishes the fact that some variants of DSR protocol reduce energy consumption maintaining Quality of Service, the authors of the present paper attempt to incorporate some energy optimizing techniques in DSR protocols and its variants. In this model, the network is divided into a number of grids or zones in each of which one node will be active, while others will be in sleep mode. Every node in a grid will be active for a predefined amount of time. The nodes in sleep mode will be able to save energy which will in turn increase the longevity of the network. This technique, when incorporated with the energy-aware DSR variants, should produce a satisfactory result with optimized energy consumption and Quality of Service.

5 Conclusion and Future Scope

This paper deals with a very serious issue of excess energy consumption in Mobile Ad hoc Network and an optimum solution to increase the longevity of the network. Probable causes of excess energy consumption in the network have been pointed out.

Table 1 Positive and negative aspects of routing schemes

Routing scheme	Positive aspects	Negative aspects
Non-promiscuous DSR (DSR-np)	(i) Hidden and exposed nodes are set in sleep mode to minimize overhearing problem	(i) Alternate route discovery is delayed during route failure or congestion in the path because nodes other than participating nodes go to sleep mode
Minimum total transmission power routing (MTPR)	(i) Finds minimum total energy route among several routes	(i) Common node problem remains unsolved (ii) Does not consider the residual energy of battery
Minimum battery cost routing (MBCR)	(i) Nodes are not overused up to the verge of network partitioning	(i) The limiting value of energy of a node is not properly defined to make it reluctant in packet transfer (ii) Selection of a route with maximum overall battery cost may contain a node with a less individual cost which may cause early partitioning of the network
Min-max battery cost routing (MMBCR)	(i) Chooses a route with highest individual battery capacity among all possible routes (ii) Ensures that nodes are not overused	(i) Selection of an individual minimum battery cost route does not ensure a minimum transmission path (ii) Common node among different routes cannot be avoided
Conditional Min-Max battery capacity routing (CMMBCR)	(i) Achieves minimum transmission path as well as minimum node cost partially up to some extent (ii) Chooses a threshold battery capacity γ such that $(0 < \gamma < 100)$	(i) The optimum value of γ is not estimated

(continued)

The gradual development of routing techniques to minimize energy consumption by the nodes has been studied. Comparative analysis of the proposed techniques in the last two decades shows that no perfect solution has been achieved. In some cases, minimization of energy consumption causes degradation of Quality of Service (QoS). Literature survey reveals the fact that among the existing routing algorithms some variants of DSR algorithm reduces energy consumption to some extent without compromising Quality of Service a lot. Based on this analysis, the present authors proposed a technique where the network is divided into a number of grids in each of which one node will be fully active and others will remain inactive. Every node in each

Table 1 (continued)

Routing scheme	Positive aspects	Negative aspects
Lifetime prediction routing (LPR)	(i) Uses residual battery life and battery discharge rate as a parameter (ii) Selects less power congested route (iii) Uses route invalidation timer to remove old routes from cache after a predefined time (iv) Variance among node energy is minimized	(i) At high mobility packet delivery ratio decreases (ii) Comparison of minimum lifetime at every visiting node slows down the route discovery process (ii) Flooding through more number of nodes during communication over a long distance causes discharging of the nodes at faster rate
Energy-dependent DSR (EDDSR)	(i) Route error (RERR) message is sent to source when node residual energy goes below threshold level (ii) Energy balance is achieved by discouraging weak nodes from forwarding packets	(i) Intermediate node are not allowed to send a RREP with the information of invalid route back to the source
Simple energy-aware DSR (SEADSR)	(i) Selection of energy-efficient route is dependent upon a delay factor that is proportional to the energy consumption (ii) No need to store route map in cache memory	(i) Increase in signaling overhead due to absence of route cache (ii) Delay is more than DSR, but can be maintained below 40 ms with proper load balancing
Power-aware routing (PAR)	(i) Finds number of weak nodes based on battery status, traffic load type and intensity (ii) Selects route having minimum number of weak nodes	(i) Increases the latency in data transfer

grid will be active for some predefined duration. This technique when incorporated with an energy-efficient variant of DSR algorithm should provide a satisfactory result.

References

1. Gorantala, K.: Routing protocol for mobile ad-hoc network. Master's thesis, Umea University, Department of Computing Science, Sweden (2006)
2. Kanakaris, V., Ndzi, D., Azzi, D.: Ad-hoc networks energy consumption: a review of the ad-hoc routing protocols. J. Eng. Sci. Technol. Rev. (Kavala Institute of Technology) **3**, 162–167 (2010)
3. Larsson, T., Hedman, N.: Routing protocols in wireless ad-hoc networks—a simulation study. Masters thesis, Lulea University of Technology, Computer Science and Engineering, Stockholm (1998)

4. Feeney, L.M.: An energy consumption model for performance analysis of routing protocols for mobile ad-hoc networks. Mob. Netw. Appl. (Springer) **6**, 239–249 (2001)
5. Toh, C.K., Cobb, H., Scott, D.A.: Performance evaluation of battery-life-aware routing schemes for wireless ad hoc networks. In: IEEE International Conference, vol. 9, pp. 2824–2829, Citeseer (2001)
6. Maleki, M., Dantu, K., Pedram, M.: Lifetime prediction routing in mobile ad hoc networks. Wirel. Commun. Netw. (IEEE) **2**, 1185–1190 (2003)
7. Garcia, J.E., Kallel, A., Kyamakya, K., Jobmann, K., Cano, J.C., Manzoni, P.: A novel DSR-based energy-efficient routing algorithm for mobile ad-hoc networks. In: Vehicular Technology Conference, vol. 5, pp. 2849–2854. IEEE (2003)
8. Domingo, M.C., Remondo, D., León, O.: A simple routing scheme for improving ad hoc network survivability. In: Global Telecommunications Conference, GLOBECOM '03, vol. 2, pp. 718–723. IEEE (2003)
9. Rishiwal, V., Yadav, M.,Verma, S., Bajapai, S.K.: Power aware routing in ad hoc wireless networks. J. Comput. Sci. Technol. **09**, ISTEC (2009)

Piezoelectric Transducer and Arduino Based Wirelessly Controlled Energy-Saving Scheme for Street Lights

Somnath Rakshit, Souvik Kar, Tushar Kanti Banerjee and Santanu Das

Abstract Today, a large amount of energy is wasted on continuously lighting street lights. In this paper, a scheme has been proposed to automatically switch on street lights only during the presence of vehicles and pedestrians, using an Arduino-based wireless signal in order to minimize both energy consumption and maintenance need.

Keywords Street light · Piezoelectric · Arduino · Wireless · HC 12 · LDR

1 Introduction

A developing country like India faces acute shortage of electricity during the peak times in the summer season almost every year. Yet, wastage of electricity happens at every step of life in India. One of the well-known wastages of electricity takes place through the usage of street lights. Employing current technologies [1, 2] in the field of automatic street light control, vehicles moving in one direction can be controlled but it cannot be used in roads where vehicles are moving in both the directions like most of the National Highways (NH) in India. Also, since the connection is wire-based between control circuit and street light, the setup and maintenance cost are high [3]. Even when there is absolute absence of vehicle and pedestrian on road, the

Somnath Rakshit and Souvik Kar—These authors contributed equally to this work.

S. Rakshit
Department of Computer Science and Engineering, Jalpaiguri Government Engineering College, Jalpaiguri 735102, West Bengal, India

S. Kar (✉) · T. K. Banerjee · S. Das
Department of Electrical Engineering, Jalpaiguri Government Engineering College, Jalpaiguri 735102, West Bengal, India
e-mail: ersouvikkar@gmail.com

S. Das
e-mail: santanu.das@ee.jgec.ac.in

U. Biswas et al. (eds.), *Advances in Computer, Communication and Control*, Lecture Notes in Networks and Systems 41, https://doi.org/10.1007/978-981-13-3122-0_28

street lights continue to glow, thereby wasting a huge proportion of energy on daily basis, which could otherwise be implemented for suitable purposes.

A huge amount of electricity can be conserved if a low-cost solution to this problem can be achieved. Specifically, the wire-based system has a huge maintenance cost. Also, it is not much fault tolerant. Thus, designing a low-cost solution to this problem can be of immense help to many countries, especially the developing countries that cannot afford to waste electricity.

Previous attempts to solve the problem of automatic switching off of street lights include the works of Wu et al. [4], where the authors used an array of sensors to sense the prevailing conditions on the road to determine if the light is to be switched on or off. Wazed et al. [5] developed a scheme to automatically control the street lights based on the light intensity of the surroundings. This scheme used a light-dependent resistor to determine the presence of light. Amin et al. [6] designed a scheme to control street light based on parameters like surrounding temperature, fog, carbon emissions and noise intensities and suggest corrective measures. Husin et al. [7] proposed a model using microcontroller, light sensor, rain sensor, laser sensor and a set of the light emitting diode (LED) module. Here, it was reported that 77–81% reduction in power consumption was achieved using this. Infrared sensors and LDR were used by Parkash et al. [8] to detect the presence of vehicles and then intelligently control the switching of the light.

In the presented work, an automatically controlled street light system has been proposed. The main objective of the system is to provide wireless control between the Arduino processor-based controller and the nearby street lights. A pair of piezoelectric transducers interfaced with Arduino processor has been used to detect the direction of the motion of vehicles and pedestrians on the road [9, 10]. After sensing the movement, switching operations of the nearby LED-based street lights have been controlled wirelessly by the Arduino processor [11] which concurrently senses signal level coming from the output of an LDR interfaced with same Arduino processor. Therefore, the street lights will be turned on by the Arduino only when the surrounding light is low.

2 Objective

The main objective of this system is to provide wireless control between the Arduino processor and the street lights. Thus, there will be very low maintenance cost in the system. A pair of piezoelectric transducers will detect the direction of the motion of vehicles and pedestrians on the road and send it to the Arduino processor. The switching of the Arduino is controlled by the LDR. So, the LED is turned on by the Arduino only when the surrounding light is low. Thus, the system can be made fully automatic. The reliability of the system will increase, while its cost will decrease from the previously used systems.

Table 1 Legend for Fig. 1

Label	Description
L1 to L9	LED lights (used to show individual street lights)
M1 to M9	Arduino pro mini processors
P1 to P4	Piezoelectric sensors
A1 and A2	Arduino uno processors

3 Scope of the Work

In this system, we switch on the LEDs using wireless signal from the wireless module of the Arduino processor. Here, the processor A1 can control L1 to L9, whereas the processor A2 can control LEDs L7 to L16. LEDs L7 to L9 can be controlled by both the processors. Thus, we use frequencies that adhere to this condition and work within the range of the wireless module.

Let us consider a vehicle moving through this. Whenever we find the pressure value obtained by any one of the piezoelectric sensors crosses a predefined threshold, we switch on three lights in its neighbourhood (both left and right) for 30 s each. When the vehicle goes past the sensor, the lamps are automatically switched off. The same process continues for the next Arduino processors.

In this system, A1 is connected with piezoelectric sensors P1 and P2. Also, it has the ability to communicate with the Arduino Pro Mini modules M1–M6. Each Arduino Pro Mini processor has an LED attached to it, which it controls. P1 and P2 are used to detect the presence and the direction of vehicles/pedestrians. This is then sent to A1, which sends the appropriate signal to the corresponding Mini Pro processor, which in turn controls the LED. Thus, the entire system is wireless. Here, A1 is able to control M1 to M6, which in turn controls L1 to L6. Also, A2 controls M4 to M9, which in turn controls L4 to L9 (Table 1).

4 Development Scheme

4.1 Detection of Objects

The presence of vehicles/pedestrians is detected by means of the piezoelectric sensor, which is connected in parallel with a resistor to increase its sensitivity. Thus, it is said to be in ON mode when the pressure sensed by it crosses a predefined threshold, or else, it is said to be in OFF mode.

4.2 Detection of Direction

Using a pair of piezoelectric sensors, the direction of the vehicle can be detected. The direction is determined by the following rules:

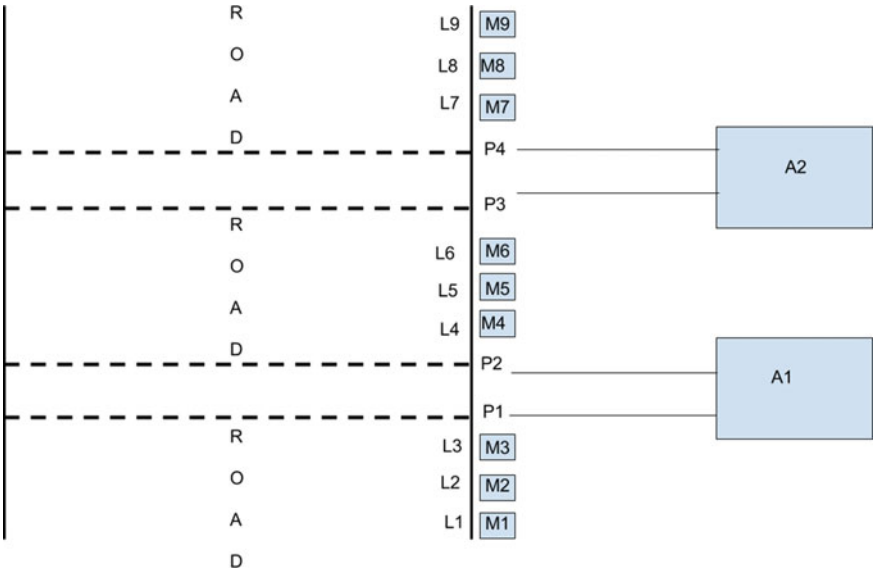

Fig. 1 Development scheme

- **P1 is in ON mode and P2 is in OFF mode**: This means that the vehicle is moving from P1 to P2. Thus, L4, L5 and L6 are switched ON for some predefined amount of time.
- **P2 is in ON mode and P1 is in OFF mode**: This means that the vehicle is moving from P2 to P1. Thus, L3, L2 and L1 are switched ON for some predefined amount of time.
- **P2 is ON within a very small amount of time after P1 is ON**: This means that vehicles from both the directions are approaching. Hence, L1 to L6 are all switched ON.
- **P1 is ON within a very small amount of time after P2 is ON**: This means that vehicles from both the directions are approaching. Hence, L1 to L6 are all switched ON.

Thus, it is evident that the direction of vehicle can be detected and accordingly, lights are turned on.

4.3 Communication Between the Processors

Communication between the A1 or A2 with the Pro Mini processors is made by means of HC 12 modules. HC 12 modules are long-range wireless communication modules that are commonly used for wireless communication. However, it is not possible to select a specific HC 12 module amongst a lot of them. Hence, A1 sends

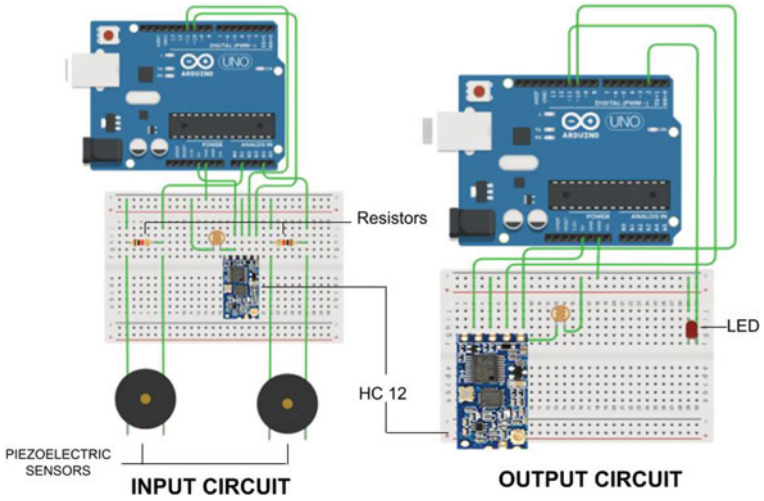

Fig. 2 Circuit diagram

an OPCODE to all Mini Pro processors. This OPCODE contains two information: The target processor and the action to be performed (ON or OFF). The Mini Pro device, after getting the information, decodes it and if it is the target device, then it proceeds to perform the specified action.

4.4 Circuit Diagram

Figure 2 shows the circuit diagram employed to control the lights and the piezoelectric sensors through Arduino processors. Here, although an Arduino Uno has been used to show the output circuit, in reality, an Arduino Mini Pro will be used to reduce the cost as well as the size of the setup.

4.5 Duration of Illumination of Lights

In our proposed model, once a light is switched ON, we keep it in the same state for an arbitrarily long amount of time, which is 30 s in this case. This time duration can be changed according to actual requirement. During this, time if any more object is detected, it extends the time of illumination by the specified amount of time. This is done to avoid frequent switching ON or OFF of the light. Thus, the lights are protected against possible failures.

5 Implementation

This proposed system can be implemented by making an arrangement which automatically supplies power to the Arduino processor when needed. This can be done by using an array of piezoelectric transducers on the road which generates electrical power from the pressure applied by vehicles. Further, this electrical power can be stored in a battery through capacitor. The system can be checked by making a database of the whole smart light system and checking after some small time interval through local IP addresses whether the lights are functioning correctly or not. Further, CCTV cameras can be added on the light pole which also gives a live view of the area for security and monitoring purposes.

Some of the photographs showing the work of a prototype of the final model can be seen in Fig. 3.

Algorithm 1 Algorithm for Sender

```
function SETUP
    Set port number of Piezoelectric sensors
    Start HC 12 module
end function
function LOOP
    p1 ← ReadPiezo()
    p2 ← ReadPiezo()
    Check direction according to section 4.2
    Send information to the HC 12 according to section 4.3
end function
```

Algorithm 2 Algorithm for Receiver

```
function SETUP
    Set port number of LEDs
    Start HC 12 module
end function
function LOOP
    while True do
        Read data from HC 12
        if Data is present in HC 12 then
            Read data
            Decode data to separate the target device and action
            Perform action on the target device
        end if
    end while
end function
```

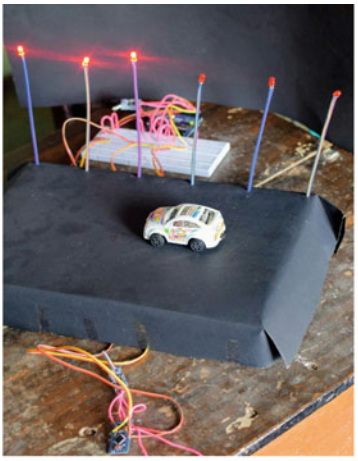

(a) Single car towards left

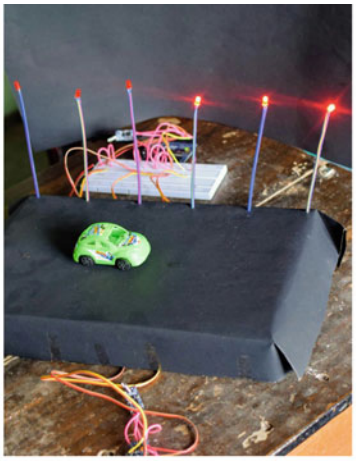

(b) Single car towards right

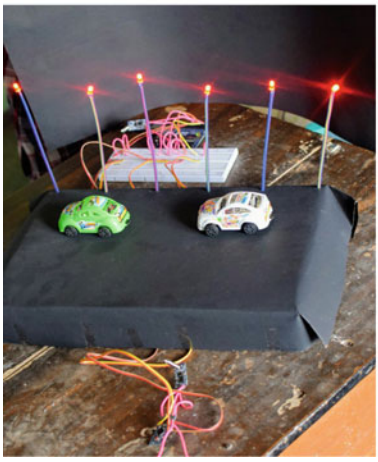

(c) Both cars towards left

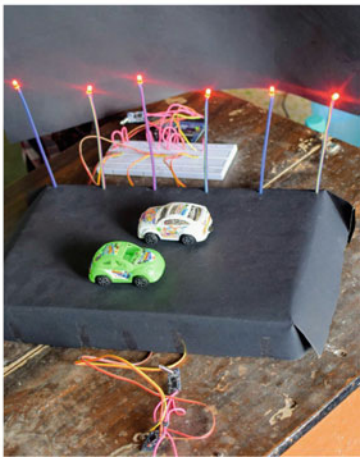

(d) Both cars in opposite directions

Fig. 3 Various states of the model

The algorithm for the sender and receiver has been outlined in Algorithms 1 and 2, respectively. Here, the Arduino Uno has been considered as the sender, while the Arduino Mini Pro has been considered as the receiver device.

6 Conclusion

From the proposed system, the developing countries can be more efficient with their electrical energy as well as the maintenance cost of power lines for street lights. It also reduces the manual work to zero. Automatic smart light system is a very user-friendly approach, and the usage of this smart light system will help in saving large amount of power in the world.

7 Future Scope

This system can be further enhanced using it to count the number of cars travelling through a particular road in real time. This will help the traffic authorities in understanding the current traffic condition and deploying personnel and resources to handle the situation accordingly. Also, the communication between the Arduino processors and the HC 12 modules can be made encrypted for enhanced security.

References

1. Sudhakar, K.S., Anil, A.A., Ashok, K.C., Bhaskar, S.S.: Automatic street light control system. Int. J. Emerging Technol. Adv. Eng. **3**(5), 1–2 (2013)
2. Rosely, E.: Prototype design of remote monitoring software of street lighting system. IJAIT (Int. J. Appl. Inf. Technol.) **1**(02), 37–42 (2017)
3. Abinaya, R., Varsha, V., Hariharan, K.: An intelligent street light system based on piezoelectric sensor networks. In: 2017 4th International Conference on Electronics and Communication Systems (ICECS), pp. 138–142. IEEE (2017)
4. Wu, H., Tang, M., Huang, G.: Design of multi-functional street light control system based on AT89S52 single-chip microcomputer. In: 2010 2nd International Conference on Industrial Mechatronics and Automation (ICIMA), vol. 1, pp. 134–137. IEEE (2010)
5. Wazed, M.A., Nafis, N., Islam, M.T., Sayem, A.S.M.: Design and fabrication of automatic street light control system. Eng. e-Trans. **5**(1), 27–34 (2010)
6. Amin, C., AshutoshNerkar, P.H., Kaul, R.: GSM based autonomous street illumination system for efficient power management. Int. J. Eng. Trends Technol. **4**(1), 54–60 (2013)
7. Husin, R., Al Junid, S.A.M., Majid, Z.A., Othman, Z., Shariff, K.K.M., Hashim, H., Saari, M.F.: Automatic street lighting system for energy efficiency based on low cost microcontroller. Int. J. Simul. Syst. Sci. Technol. **13**(1), 29–34 (2012)
8. Parkash, P.V., Rajendra, D.: Internet of things based intelligent street lighting system for smart city. Int. J. Innov. Res. Sci. Eng. Technol. (An ISO 3297: 2007 Certified Organization) **5** (2016)
9. Kimura, M.: Piezo-electricity generation device. US Patent 5,801,475, 1 Sept. 1998
10. Rivas, J., Wunderlich, R., Heinen, S.J.: Road vibrations as a source to detect the presence and speed of vehicles. IEEE Sens. J. **17**(2), 377–385 (2017)
11. Kospenda, A.: Wireless sensor network for smart street lighting. Ph.D. thesis (2017)

Comparison of Power Penalty Due to Component, SRS, and FWM Crosstalk in a WDM Receiver

P. P. Mukherjee, Santu Sarkar and Nikhil R. Das

Abstract A comparative study on power penalty due to component, SRS, and FWM crosstalk in a WDM receiver is presented in this paper. The relevance of such crosstalk phenomena is analyzed depending upon various parameters and domains of operation. Power penalty is examined as a function of the number of interfering channels to compare the receiver performance in the presence of mentioned crosstalk.

Keywords Wavelength-division multiplexing · Component crosstalk
SRS crosstalk · FWM crosstalk · Power penalty and bit error rate

1 Introduction

The developments of Wavelength-Division Multiplexing (WDM) systems offer efficient use and increment of the global capacity per single fiber. However, the performance of such systems suffers significantly due to a phenomenon called crosstalk, and bit error rate (BER) of the system [1–3] increases. In this paper, we have studied the performance of an optical WDM system in the presence of three crosstalk scenarios, component, Stimulated Raman Scattering (SRS), and Four-Wave Mixing (FWM) crosstalk in terms of power penalty which is a significant parameter. A comparative study on power penalty is carried out to quantify the impact of these three types of crosstalk. Component crosstalk is a linear crosstalk and occurs when a desired signal

P. P. Mukherjee (✉)
Department of Electronics & Communication Engineering, Academy of Technology, Adisaptagram, Hooghly, India
e-mail: ppmukherjee@yahoo.co.in

S. Sarkar · N. R. Das
Institute of Radio Physics and Electronics, University of Calcutta, 92 A.P.C. Road, Kolkata 700009, West Bengal, India
e-mail: santu@ieee.org

N. R. Das
e-mail: nrd@ieee.org

U. Biswas et al. (eds.), *Advances in Computer, Communication and Control*, Lecture Notes in Networks and Systems 41, https://doi.org/10.1007/978-981-13-3122-0_29

and crosstalk have the same nominal frequencies [3]. SRS and FWM crosstalk are nonlinear crosstalk and occur due to the nonlinearity of optical fiber for large power [4–6]. Nonlinearity in the form of nonlinear inelastic scattering processes gives rise to SRS crosstalk, while the nonlinear variations of the refractive index give rise to FWM crosstalk [6].

2 Calculation of Power Penalty

In optical transmitter, electrical current is converted to optical power and in optical receiver (photodetector output) optical power is converted to electrical current. Due to crosstalk, the BER increases because the signal-to-noise ratio (including crosstalk) increases. So to take the BER to the previous value without any crosstalk, the signal power should be increased to increase the signal-to-noise ratio. It means more power is to be sacrificed at the input. This is termed as power penalty. So, the Power Penalty (PP) is found by comparing the photocurrents at the receiver that produces the same BER with and without crosstalk. The responsivity, $\Re$, of the receiver is the constant of proportionality between the received optical power level and the current. If $P_{s|NC}$ and $I_{s|NC}$ are the power and current, respectively, without crosstalk and P_s, I_s are the power and current, respectively, with crosstalk, the responsivity, $\Re$, can then be represented by [1]

$$\Re = \frac{I_{s|NC}}{P_{s|NC}} = \frac{I_s}{P_s} \tag{1}$$

Initially, we assume only thermal noise is present and there is no crosstalk in the system. In this case, the error probability can be written as

$$P_e = \frac{1}{2} erfc\left[\frac{I_{s|NC}}{2\sqrt{2}\sigma_{th}}\right] \tag{2}$$

where σ_{th} is the variance of thermal noise. When a particular crosstalk is present in the system, we calculate the error probability in the presence of that crosstalk which includes the photocurrent I_s. Then, power penalty in dB can be written as [1–3]

$$PP = 10\log_{10}\left(\frac{P_s}{P_{s|NC}}\right) = 10\log_{10}\left(\frac{I_s}{I_{s|NC}}\right) \tag{3}$$

Thus, the ratio of the powers (currents) with and without crosstalk is to be known to calculate the power penalty at a particular BER.

The expressions for power penalties due to these three types of crosstalk are given in [3, 4], and [6] through Eqs. (20), (13), and (21), respectively.

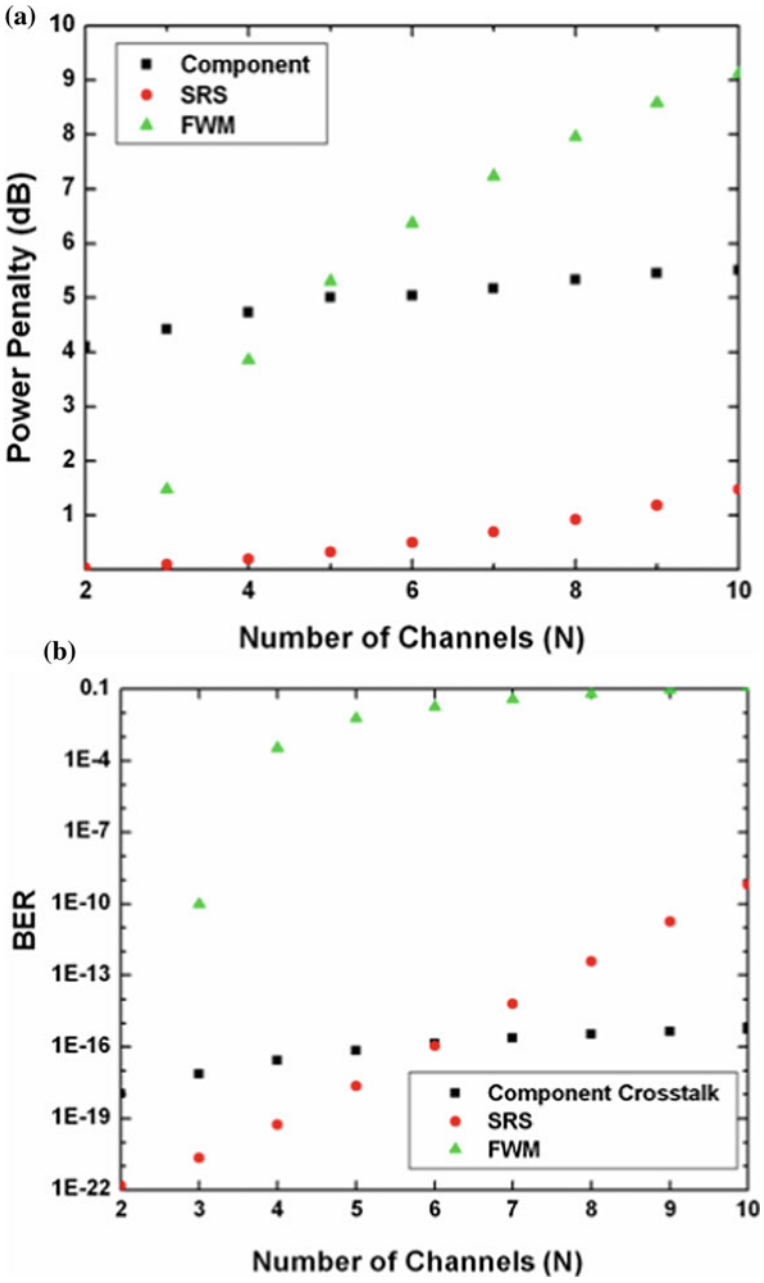

Fig. 1 **a** Power penalty versus number of channels for different crosstalks (component, SRS, and FWM), assuming SNR = 12 dB. **b** BER versus channel number for different crosstalks assuming SNR = 12 dB

3 Results and Discussion

Using the equations given in [3, 4, 6], power penalty is plotted as a function of the number of interfering channels in Fig. 1a to compare the receiver performance in the presence of these crosstalks. The plot is shown for a fixed SNR of 12 dB. The figure shows that, in general, the power penalty increases as the number of channel increases. It results from the increase in BER with the increase in N as in Fig. 1b.

For FWM crosstalk, power penalty is low for small N but increases rapidly to become very high for large N, while for the other two types of crosstalk, the rate of increase is comparatively much slow. If worked with fewer channels, the limiting factor for power penalty is due to component crosstalk. So to reduce the power penalty in a coarse WDM system, component crosstalk should be minimized, i.e., the performance of network element should be improved. The power penalties calculated for different number of channels are summarized in Table 1. The data are shown for two different values of the signal-to-noise ratio. It appears from the table that as the number of channels increases, power penalty increases for all crosstalk. In the case of SRS crosstalk, the rate of increment is low and for FWM crosstalk, it is the maximum.

Table 1 Power penalty in presence of different interfering channels at fixed SNR

SNR (dB)	N	Power penalty (dB)		
		Component	SRS	FWM
10	1	2.138	–	–
	2	2.428	0.0208	–
	3	2.598	0.0624	3.7156
	4	2.628	0.1249	5.6086
	5	2.828	0.2082	6.6992
	6	3.068	0.3123	7.5047
	7	3.208	0.4373	8.1619
	8	3.288	0.5831	8.7254
	9	3.348	0.7496	9.2226
	10	3.408	0.9371	9.6695
12	1	–	–	–
	2	4.108	0.0329	–
	3	4.428	0.0989	1.4755
	4	4.728	0.1978	3.8562
	5	4.998	0.3297	5.3009
	6	5.038	0.4945	6.3713
	7	5.168	0.6924	7.2314
	8	5.328	0.9232	7.9531
	9	5.448	1.1869	8.5757
	10	5.508	1.4837	9.1233

4 Conclusion

From the comparative analysis, it is evident that power penalty increases significantly as a number of interfering channels are increased. This increment is more visible in case of FWM crosstalk, whereas in case of SRS crosstalk power penalty is minimum. As SNR is increased, power penalty due to component and SRS crosstalk is enhanced and FWM crosstalk shows less power penalty with increased SNR. While less number of interferers are present (i.e., coarse WDM system), component crosstalk contributes mostly to power penalty and thus should be monitored.

References

1. Murthy, C.S., Gurusamy, M.: WDM Optical Networks. Pearson Education (2004)
2. Ho, K.P.: Analysis of homodyne crosstalk in optical networks using Gram-Charlier series. J. Lightwave Technol. **17**, 149–154 (1999)
3. Sarkar, S., Das, N.R.: Study of component crosstalk and obtaining optimum detection threshold for minimum bit-error-rate in a WDM receiver. J. Lightwave Technol. **27**, 4366–4373 (2009)
4. Das, N.R., Sarkar, S.: Probability of power depletion due to SRS cross-talk and optimum detection threshold in a WDM receiver. IEEE J. Quantum Electron. **47**, 424–430 (2011)
5. Forghieri, F., Tkach, R.W., Chraplyvy, A.R.: Effect of modulation statistics on Raman crosstalk in WDM system. IEEE Photonic Technol. Lett. **7**, 101–103 (1995)
6. Das, N.R., Sarkar, S.: On the optimum detection threshold for minimum bit error rate due to four-wave mixing in a WDM system. IEEE/OSA J. Opt. Commun. Netw. **5**(4), 370–377 (2013)

Normalized Uplink Bandwidth Scheduling Algorithm for WiMAX Networks

Deepa Naik, Santosh Dora, Nikita and Tanmay De

Abstract WiMAX networks can provide scalable cost-efficient universal broadband connectivity to end users. In WiMAX network, medium access control protocol schedules the bandwidth allocation to different traffic classes. To achieve quality of service requirements while scheduling the bandwidth, well-organized and reliable scheduling algorithms are needed. The existing algorithms are extracted from operating systems job scheduling algorithms, which are not suitable to fulfill the bandwidth requirements of WiMAX network. In this work, we have focused on uplink bandwidth scheduling algorithms. The proposed algorithms and existing algorithms are compared with respect to network throughput. Simulation results show that the proposed algorithms maximize network throughput.

Keywords BE (Best effort), nRTPS (non-real-time polling service)
QoS (Quality of service) · RTPS (Real-time polling service)
SINR (Signal-to-noise ratio), UGS (unsolicited grant service)
WiMAX (Worldwide interoperability for microwave access network)

1 Introduction

WiMAX is the promising candidate for future generation networks providing universal net connectivity. The growth of mobile users and their excessive bandwidth demands with broadband wireless connectivity are the key drivers for the emergence of such technology. Many telecommunication industries deployed WiMAX networks

D. Naik (✉) · S. Dora · Nikita · T. De
Department of Computer Science and Engineering, National Institute of Technology, Durgapur, Durgapur, India
e-mail: naiksavantdeepa@gmail.com

Nikita
e-mail: nikitaniki027@gmail.com

T. De
e-mail: tanmayd12@gmail.com

U. Biswas et al. (eds.), *Advances in Computer, Communication and Control*, Lecture Notes in Networks and Systems 41, https://doi.org/10.1007/978-981-13-3122-0_30

to meet the consumer's demands. WiMAX follows IEEE 802.16 standard. The bandwidth scheduling for different classes of traffic for WiMAX still needs innovative algorithms. The base station can offer 3–5 miles wireless connectivity at the rate of 70 Mbps (assuming line of sight transmission) [1, 2]. Operators manage such networks either by point-to-multi-point (PMP) mode or in mesh mode. Subscriber stations communicate directly with each other and also with base stations in Mesh mode [3], whereas in point-to-multi-point mode, subscriber stations communicate only with base station. The base station is responsible for providing the QoS to each of its subscribing stations. The relay stations enhance coverage area of the network.

In this paper, we have proposed algorithms for centralized uplink bandwidth scheduling using the priority-based normalized bandwidth scheduling (PBNB) and priority-based fixed bandwidth scheduling (PBFB) algorithms.

2 Previous Work

Many scheduling algorithms have been proposed for downlink scheduling. They are traditional and dynamic scheduling. Traditional scheduler in [4] is hired from operating system scheduling technique. Here, subscribers are allotted equal network resources without any priority. However, this method of bandwidth scheduling is not suitable for WiMAX networks, where the traffic demands of varying size arrive in random fashion. The authors Sagar et al. in [5] proposed the Weight Round Robin (WRR) for scheduling the bandwidth to each queue. Queue weight determines bandwidth allocated to it. The main drawback of the WRR is that when the traffic of different classes has different packet sizes, this algorithm will not produce accurate bandwidth allocation. The authors Fathi et al. in [6] proposed joint scheduling and Call Admission Control (CAC) technique or scheduling packets. The proposed algorithm dynamically takes the decision to accept the requests depending on the network load to provide QOS to the users improving network performance. The Earliest Deadline First (EDF) algorithm has also been analytically analyzed which have further proven these performance characteristics [7]. The EDF algorithm has been declared to be suited for connections with guaranteed bandwidth requirements. In this algorithm, each packet is assigned a deadline. The scheduler serves packets in the order of their respective deadlines. The packet with the minimum (i.e., earliest) deadline will be served first. Thus, EDF scheduling tends to give preference to connections with real-time needs. However, it does not provide any form of protection against the dominance of greedy connections, which always set the deadline closer to the arrival time. The server is only able to guarantee that the packet with a smaller deadline will have a higher priority and will be served at the earliest possible time. The authors Yadav et al. in [8] done survey on different scheduling algorithms proposed in recent years. There is no standard algorithm, proposed for WiMAX networks. So it is still open research problem to develop an efficient and robust scheduling algorithm.

3 Problem Formulation

We consider a base station denoted as BS. The M represents the number of relay stations denoted as $ss_1, ss_2, \ldots, ss_M$. Given a network represented by a directed connected graph G (V, E), where V are wireless stations/nodes and E are the bidirectional wireless links (edges) between the base station and subscriber station. The subscriber stations are assumed to be in the range of base station. C is the link capacity between base station and relay station. The base station allocates network resource to relay stations. The connection requests for all class of traffic are represented by notation (S, D, B, PT, $SINR$, GT, DT), where S, D, B, PT, $SINR$, GT, and DT represent the source node, destination node, bandwidth demanded, type of the traffic class, signal-to-noise ratio of the request generated, generated time of the requests, and deadline associated with the request, respectively. The main problem is to assign the bandwidth to different classes of traffic depending on the priority bases without degradation of QoS (in term of deadline) associated with each class of traffic.

We have proposed two algorithms, namely, Priority-Based Normalized Bandwidth scheduling algorithm (PBNB) and Priority-Based Fixed Bandwidth scheduling (PBFB), by considering the varying traffic demand of individual user.

Objective: Maximizing the network throughput at the same time satisfying quality of service to each class of traffic requirement is the objective function which is further defined as follows:

$$R_i = \sum_{K=1}^{M_i^{ss}} B_{k,i} \tag{1}$$

$$Maximize \quad \sum_{i=1}^{N} R_i * p \tag{2}$$

$$p = \begin{cases} 1, & \text{if} R_i \text{is established.} \\ 0, & \text{otherwise.} \end{cases}$$

Subjected to:

BS to RS constraints

$$\sum_{\forall n \varepsilon BS} w_{Mn} = \gamma_M \quad where \quad \forall M \varepsilon ss \tag{3}$$

One RS is connected to only one BS.

$$w_{Mn} \leq \alpha_l \quad where \quad \forall M \varepsilon ss \quad l \varepsilon BS \tag{4}$$

Confirms establishment of the base station to relay station connection.

$$\sum_{i=1}^{n} T_{ss} \times \beta \leq T \tag{5}$$

$$\beta = \begin{cases} 1, & \text{if } ss \text{ used time slot } T_{ss} \text{ and associated with BS.} \\ 0, & \text{otherwise.} \end{cases}$$

T_{ss} is the allotted time slots to each subscriber station/user. Equation 5 ensures that the number of time slots allocated to each subscriber station is less than or equal to the total number of time slot (T) available with base station BS.

Assumptions:

We use the following assumptions in this work.

- Traffic demands are known a priory.
- The total number of traffic is $R_i = N$.
- The R_i, where M_i^{ss} is the number of subscriber station(M)/user, includes the traffic class i in the network. $B_{k,i}$ bandwidth request of kth subscriber/user with traffic class belongs to ith class of traffic.
- $w_{Mn} = 1$ if the relay station M associated with base station n, $M \varepsilon ss$ and $j \varepsilon BS$; 0 otherwise.
- α_l =1 if the BS is installed at site l, $l \varepsilon BS$; 0 otherwise.
- γ_m=1 if the relay station is installed at site m, $m \varepsilon ss$; 0 otherwise.

Constraints:

1. In the network, every relay station will be attached to a fixed base station and routing and resource allocation will be controlled via base stations in WiMAX network in a centralized manner.
2. The base station can generate a fixed size frame after fixed interval of time.
3. No two relay stations can route/allocate bandwidth among them independently.

4 Proposed Approach

In this section, we elaborate on scheduling services suitable for QoS of WiMAX. This network supports five types of the traffic service, namely, Unsolicited Grant Service (UGS), Real-Time Polling Service (RTPS), Extended Real-Time Polling Service (ERTPS), Non- Real-Time Polling Service (NRTPS), and Best Effort (BE). In the centralized bandwidth scheduling, base station assigns the bandwidth to different traffic classes. Priority queues in base stations are of five types: UGS, ERTPS, RTPS, nRTPS, and BE. The arriving requests are stored in their respective priority queues. The scheduler function is called to schedule the requests of base station. This type of scheduling is known as grant per connection (GPC).

The steps involved in our proposed algorithm are given below.

- We have assumed that all the subscribers are under the communication range of base station. The connection requests are uplink from subscriber to base stations.

The function **generateRequest()** is used to generate the request and store in traffic matrix T.

- To estimate the channel condition of the subscriber, we have used the SINR of every request generated and this parameter is updated periodically.
- These connection requests are uplink from subscriber to base stations. Each request is associated with four parameters, namely, bandwidth demanded, priority of each class, deadline, and SINR.
- Depending upon these parameters, a total score is calculated (using the function $updateTotalscore$). On the basis of this total score, the requests are sorted in descending order.
- Initially, the packets are stored in temporary queue for scheduling. The function $updateTotalscore()$ keeps on updating depending on the system time. The packets which are about to expire the deadline are served according to the total score associated with each class of traffic. The deadline of every packet is related to the current system time and time at which the packet arrived into the queue, the waiting time is constantly updated over a period of time.
- The time to expire is computed as the difference between the request generation time and waiting time associated with each request using the function **calculateWaitTime()**.
- The remaining requests are served in the next round (next slot of bandwidth allocation), only if the deadline is not attained and has enough bandwidth to serve the requests of particular class of traffic.
- The function **allocateBandwidth()** is used to allocate the bandwidth to traffic demands.
- The status of the available bandwidth and traffic matrix are updated depending on the request served.
- When higher priority traffic flows are not there, the reserved bandwidth is transferred to the lower class traffic, using the fixed bandwidth sharing approach using the function. The residual bandwidth is returned from each class of traffic **Residual bandwidth()**.
- Finally, this process is repeated until the simulation time is over.

In our algorithm (PBNB), we have normalized the bandwidth allocated to each class of traffic. And in (PBFB) algorithm, bandwidth allocated to each class of traffic is fixed. PBFB works similar to PBNB; only difference is in the bandwidth sharing method. If the base station has 100% of bandwidth, the UGS class reserved 30% of the bandwidth out of total bandwidth and the remaining class is traffic assigned 25, 15, 20, and 10% of the total bandwidth.

For example, PBNB approach divided the base station bandwidth among all classes according to their priority value (5, 4, 3, 2, 1). The normalized priority weight is 15. The weights are assigned to various traffic classes, which has the impact on amount of bandwidth assigned to each traffic class.

$$BWAlloc_{ugs} = 5/15 * B, \quad BWAlloc_{rtps} = 4/15 * B, \quad BWAlloc_{nrtps} = 3/15 * B$$
$$BWAlloc_{ertps} = 2/15 * B, \quad BWAlloc_{BE} = 1/15 * B.$$

For example, PBFB approach divided the base station bandwidth among the UGS, ERTPS, RTPS, and NRTPS and BE traffic classes accordingly in the fixed manner, which has the impact of higher priority traffic getting in place of on more amount of bandwidth assigned to serve the requests.

$$BWAlloc_{ugs} = 30/100 * B, \quad BWAlloc_{rtps} = 25/100 * B, \quad BWAlloc_{nrtps} = 15/100 * B$$
$$BWAlloc_{ertps} = 20/100 * B, \quad BWAlloc_{BE} = 10/100 * B.$$

After every 0.5 s, the base station collects the bandwidth request from each relay station. The requests, which are not served in the previous frame period, are considered in the next frame without violating the deadline associated with each traffic request to ensure the QoS of WiMAX standard.

Function updateTotalScore(SINR,PT,B,GT)

Input : T_{sd}: A Traffic matrix of Unicast requests, where T=[s, d, B, $SINR$, PT, GT, DT] with channel capacity C
Output: Return the score associated with the individual requests

1 It updates the value of totalScore of the request as the wait time or the age of the request is changing with time
2 WT = calculateWaitTime(GT); /*The age of the request */
3 $sum = SINR + WT + PT$;
4 $w1 = SINR/sum$;
5 $w2 = B/sum$;
6 $w3 = WT/sum$;
7 $w4 = 1 - (w1 + w2 + w3)$;
8 $totalScore = w1 * SINR + w2 * B + w3 * WT + w4 * PT$;
$/ * Normalizedtotal Score * /$ return (totalScore);
9 end

Function calculateWaitTime(GT)

Input : T_{sd}: Request generation time GT
Output: Waiting time of the request generated

1 It updates wait Time, to calculate age of the request. Which is updated with time.
2 $CT = calculatecurrentsystemtime(CST)$
3 $WT = GT - CST$/* difference between GT and current system time */
4 return(WT);
5 end

Example 1 We have considered one base station connected to relay station as depicted in Fig. 1. There is just one base station and a number of relay stations

Function Residual bandwidth(RB)

Input : T_{sd}: Request generation time GT
Output: Returns the residual bandwidth, which is not utilized by a particular class of traffic

1 $B = topmost \quad bandwidth \quad request$;
2 if($B \leq reservedbandwidth$)
3 $B = RB - B$/* Assign the request available bandwidth/
4 if(($B >= reservedbandwidth$)
5 Discard the Request.
6 return(RB)
7 end

Algorithm 1: Priority Based Normalized bandwidth scheduling algorithm (PBNB)

Input : T_{sd}: A Traffic matrix of requests, where T_{sd}=[s, d, B, PT, GT, DT] with a channel capacity C
Output: Throughput the of given network

1 At a unit-time, generate requests at each subscriber station.
2 Call to genertateRequest(subscirber station)/*Number of requests generated depends on poisson distribution.*/
3 The request generated contains source,destination, deadline, $priority_{type}$, $bandwidth_required$,$request_{generation_time}$ all these fields information.
4 Separate all the requests R, as per their traffic class in different priority queues like ugs, rtps, nrtps, ertps, be.
5 Reserve the normalized bandwidth according to priority from the available bandwidth to each class of traffic.
6 Call to allocateBandwidth();
7 There are four different priority queues ugs,rtps,nrtps,be for storing requests. This is as per the priority of totalScore of the requests.
8 Select requests from different priority queues (ugs,rtps,nrtps,be) and store them in serving Queue to serve them. Requests will be stored in the order of their totalScore.
9 Now, start serving the request. After a fixed time, again new requests will be generated.
10 Requests which are unserved will be stored in the queue to get served in the next serving time. If a request's deadline gets over,then the request is discarded from the serving queue.
11 Store the requests which has been discarded in unserved queue.
12 Repeat the step 1 until the simulation time is over.
13 Calculate the bandwidth blocking probability, total request served and total request generated in each class.
14 end

are connected to the base station. We have currently four requests for each class with bandwidth demand in kilobytes. The traffic patterns are depicted in Table 1. The working principle of our proposed algorithm is shown in Tables 2, 3, 4, 5, 6, 7, 8, and 9. We use the following example to explain our algorithm. We have set the frame size as 2048 KBps (Kilobytes per second) and frame duration as 0.5 s. Initially, the requests R0, R1, R2, R3, and R4 are generated. The requests are sorted according

Algorithm 2: generateRequest(source)

Input : T_{sd}: A Traffic matrix of requests, where where T_{sd}=[s, d, B, $SINR$, PT, GT, DT]
Output: Generate the requests from all the subscriber stations of given network

1 $s = source$ /*The station where request start */
2 $d = generatearandomdestination$
3 $GT = currentTime$/* Time of request generated to calculate age */
4 $B = allocateBandwidth()$;/required Bandwidth to the request */
5 $SINR = allocateSinr()$;generates random value of SINR */
6 $DT = assignDeadline()$; /* Deadline of the request */
7 $PT = assignType()$ /* Type like UGS,RTPS,BE */
$totalScore = updateTotalScore(SINR, B, T, GT, DT)$; /* total Score by normalization of all the parameters */
8 end

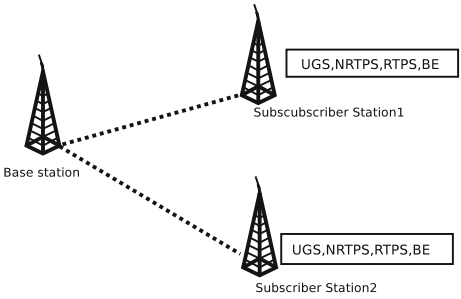

Fig. 1 Scheduler for uplink at base station

Table 1 At 5 unit time, new requests R1, R2, R3, R4 are generated

R	B	Deadline	SINR	PT	Totalscore
R1	1024	8	1.024	UGS	97.2
R2	512	9	5.12	RTPS	248.9
R3	256	3	9.2	BE	373.3
R4	1024	12	1.024	NRTPS	91.5

Table 2 At 5 unit time, requests R1, R2, R3 are in serving queue

R	B	Deadline	SINR	PT	Totalscore
R3	256	3	9.2	BE	373.3
R2	512	9	5.12	RTPS	248.9
R1	1024	8	1.024	UGS	97.2

Table 3 Request R4 is in waiting queue

R	B	Deadline	SINR	PT	Totalscore
R4	1024	12	1.024	NRTPS	91.5

to their total score. The request with the good channel condition, priority, data rate, and deadline are served first. To overcome the starvation of traffic request, we have normalized the bandwidth scheduling to each class of traffic.

Table 4 At next 5 unit, new requests R5, R6, R7, R8 are generated

R	B	Deadline	SINR	PT	Totalscore
R5	1024	8	3.024	UGS	200.9
R6	512	9	1.12	RTPS	122.9
R7	1024	7	9.2	BE	143.3
R8	1024	12	5.024	UGS	65

Table 5 Requests R5, R6, R7 are in serving queue

R	B	Deadline	SINR	PT	Totalscore
R5	1024	8	3.024	UGS	200.9
R6	512	9	5.12	RTPS	122.9
R7	1024	7	9.2	BE	143.3

Table 6 Requests R4, R8 are in waiting queue

R	B	Deadline	SINR	PT	Totalscore
R4	1024	12	1.024	NRTPS	91.5
R8	1024	12	5.024	UGS	65

Table 7 At the next 5 unit time, new requests R9, R10 are generated

R	B	Deadline	SINR	PT	Totalscore
R9	1024	11	5.024	UGS	91
R10	256	6	9.2	BE	1403

Table 8 Requests R8, R10, R9 are in serving queue

R	B	Deadline	SINR	PT	Totalscore
R10	256	6	9.2	BE	1403
R8	1024	12	5.024	UGS	120
R9	1024	11	5.024	UGS	91

Table 9 Request R4 is discarded due to the deadline associated with the request

R	B	Deadline	SINR	PT	Totalscore
R4	1024	12	5.024	UGS	1221

5 Analysis of Result

In this section, we have analysed the performance of our proposed algorithms through simulation. The simulation is performed using c++ coding. Traffic requests for different classes are varied and simulation results observed. In a WiMAX network, the channel capacity is assumed to be 10 MHz and the frame duration is assumed to be 5 ms and we have considered the uplink scheduling. The deadlines for requests are generated randomly. Performance of each class of traffic is evaluated by varying loads.

The proposed algorithms are compared with the existing First Come First Serve (FCFS) scheduling algorithm. To measure the performance of our proposed algorithms, we have considered network throughput and the total number of requests

served for each class and the cost associated to serve the requests as the performance parameters. The cost is associated with the number of requests served for each class of traffic. We have considered the cost in terms of units. The cost computed to serve the request is given in Eq. (6).

$$CF = \sum_{i=1}^{N} BSC/R_i + \sum_{i=1}^{m} TR * R_i \times FR + PT * Noofrequests \tag{6}$$

The notation used to represent the cost function CF is given below. We have considered the cost in terms of units. The BSC is associated with the base station cost. The base station cost is assumed to be 150 units, where TR represents the transceivers cost. The cost is assumed to be 80 units and FR represents the number of frames consumed to serve the requests. The cost associated with the FR depends upon the number of iterations required to complete the request. The PT is the priority associated with the requests and number of request served that belongs to the priority type PT. The cost associated with each priority class is given by 10, 9, 8, 7 and 6 units.

Figure 2 demonstrates the results of both the algorithms compared with the existing algorithm FCFS. They show the relationship between the total number of requests demanded and total number of requests served in UGS class of traffic. The priority-based fixed bandwidth algorithm is showing better performance as compared to FCFS and PBNS algorithms. In UGS traffic class, the requests are generated beyond 30; it is observed that the PBFB showing better performance compared to PBNB algorithm. The UGS class shows better performance for the fixed bandwidth allocation scheme as compared to normalized bandwidth allocation scheme.

Figures 3, 4 and 5 depict the relationship between the total requests demanded and total number requests served in ERTPS, NRTPS, and BE classes. The PBNB performed better than the PBFB and FCFS algorithms in these classes.

Figure 6 demonstrates the relationship between the total bandwidth demanded and total bandwidth served in UGS class of traffic. The priority-based fixed bandwidth algorithm is showing better performance as compared to FCFS and PBNB algorithms.

Figures 7, 8, and 9 show the results of both the algorithms compared with the existing algorithm FCFS. They demonstrate the relationship between the total bandwidth demanded and total bandwidth served in NRTPS, ERTPS, and be class of traffic. The priority-based fixed bandwidth algorithm and priority-based normalized bandwidth algorithm are showing better performance in NRTPS, ERTPS, and BE as compared to FCFS algorithm.

In Figure 10, we have estimated the cost of serving the request in each algorithm. The results demonstrate the relationship between the total bandwidth demanded and total bandwidth served and the total cost of serving the requests. The priority-based normalized bandwidth algorithm costs more than the priority-based fixed bandwidth and FCFS algorithm as it consumes more network resources to serve maximum number of requests (Fig. 11).

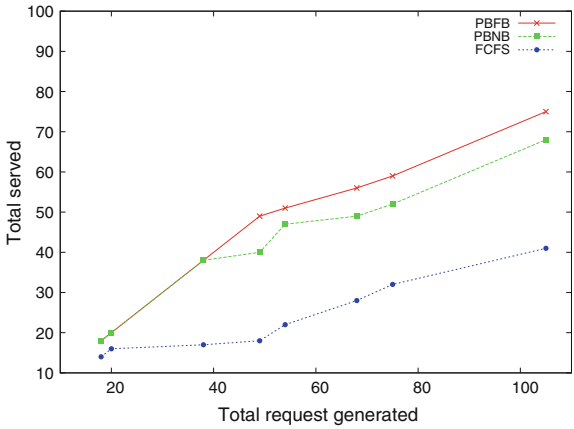

Fig. 2 Relationship of total number of requests demanded and total number of requests served in UGS class

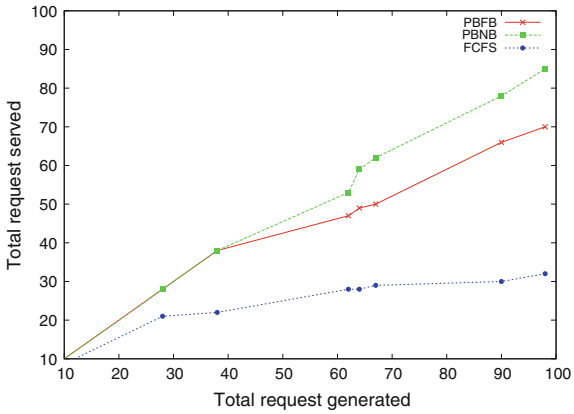

Fig. 3 Relationship of total number of requests demanded and total number of requests served in ERTPS class

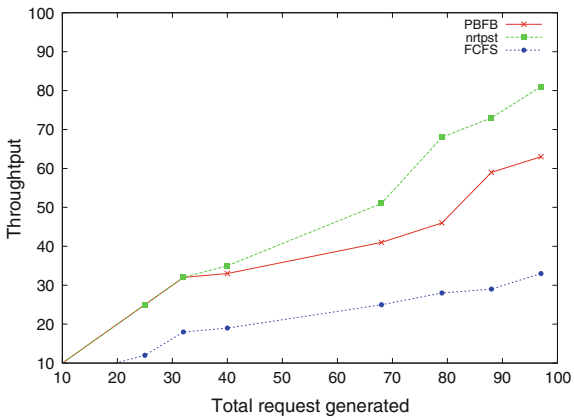

Fig. 4 Relationship of total number of requests demanded and total number of requests served in NRTPS class

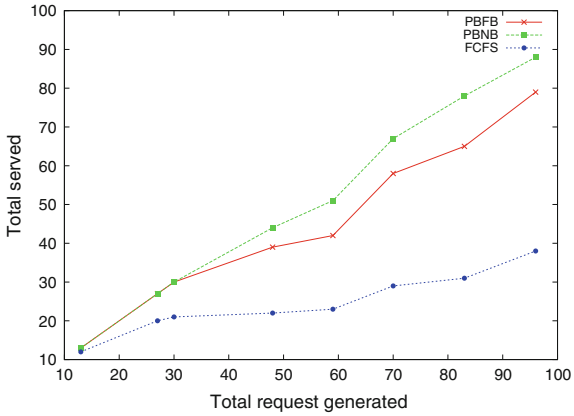

Fig. 5 Relationship of total number of requests demanded and total number of requests served in BE class

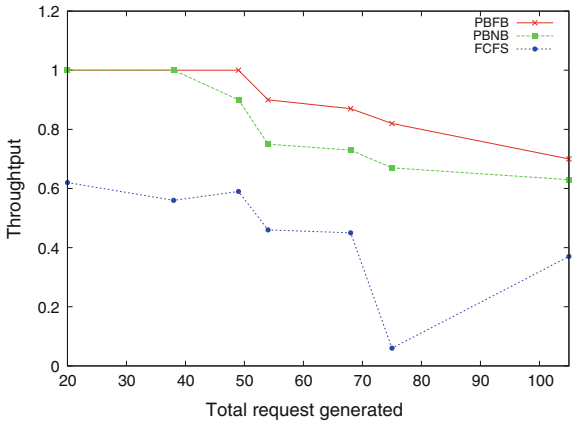

Fig. 6 Relationship of throughput and the total bandwidth request generated in UGS class

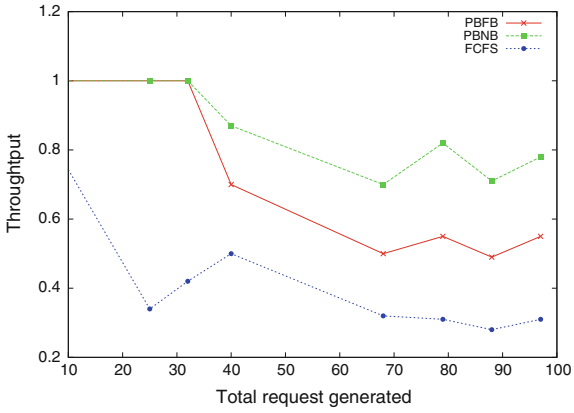

Fig. 7 Relationship of throughput and the total number of requests generated in NRTPS class

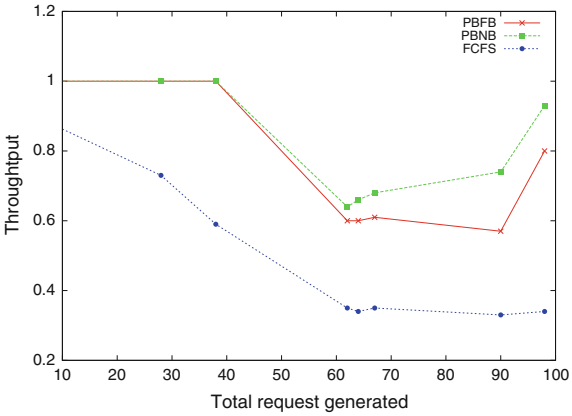

Fig. 8 Relationship of total bandwidth Demanded and the total request generated in ERTPS class

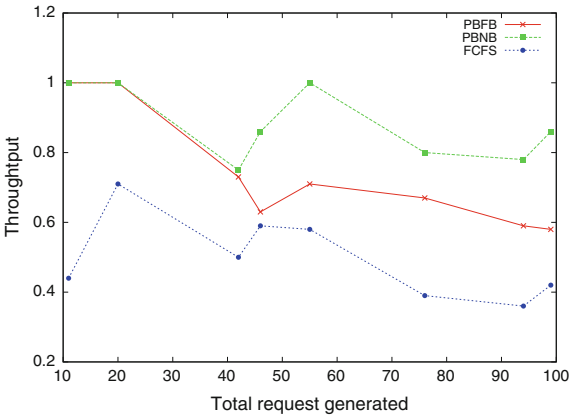

Fig. 9 Relationship of throughput and total requests generated in RTPS class

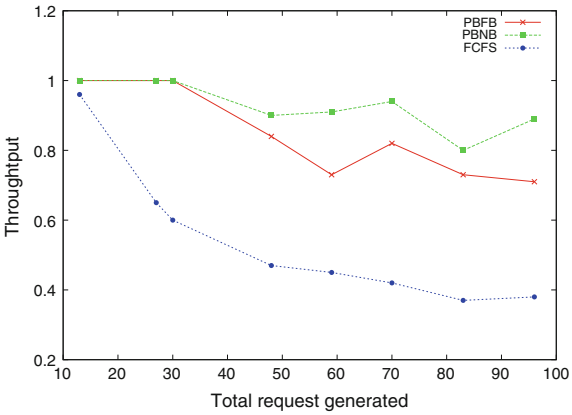

Fig. 10 Relationship of total bandwidth demanded and the total requests generated in BE class

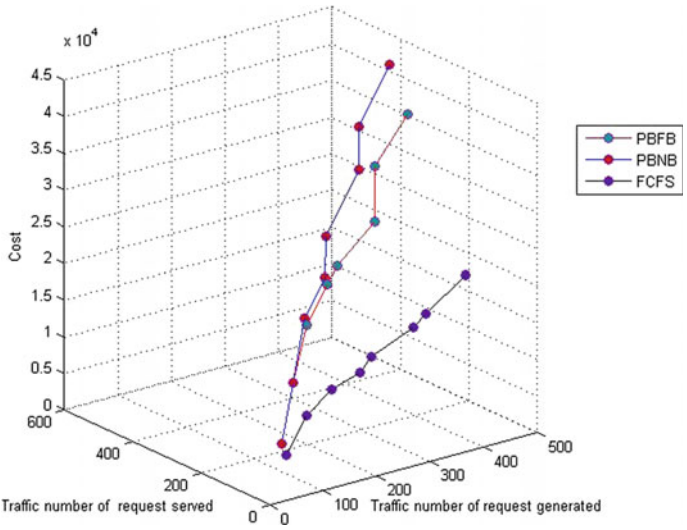

Fig. 11 Relationship of cost, total bandwidth demanded, and the total bandwidth served in all class

6 Conclusion

We have proposed bandwidth scheduler for different traffic class subscribers using grant per connection method. Objective is to increase throughput of all the traffic classes. To resolve the bandwidth sharing problem, we have proposed the two algorithms, namely, Priority-Based Fixed Bandwidth (PBFB) and Priority-Based Normalized Bandwidth (PBNB) algorithms and compared with First Come First Serve (FCFS) algorithm. The proposed algorithms perform better compared to FCFS algorithm. The bandwidth scheduling algorithms for optical to WiMAX communication using traffic grooming technique will be incorporated in future studies.

References

1. Li, B., Qin, Y., Low, C.P., Gwee, C.L.: A survey on mobile wimax [wireless broadband access]. IEEE Commun. Mag. **45**(12), 70–75 (2007)
2. Lawal, I.A., Said, A.M., Muazu, A.A., Shah, P.A.: Performance comparison of centralized and distributed network models to support QoS in fixed WiMAX. Proc. Soc. Behav. Sci. **129**, 441–452 (2014)
3. Eklund, C., Marks, R.B., Stanwood, K.L., Wang, S.: IEEE standard 802.16: a technical overview of the wirelessman/sup tm/air interface for broadband wireless access. IEEE Commun. Mag. **40**(6), 98–107 (2002)
4. Cicconetti, C., Erta, A., Lenzini, L., Mingozzi, E.: Performance evaluation of the IEEE 802.16 MAC for QoS support. IEEE Trans. Mob. Comput. **6**(1) (2007)

5. Sagar, V., Das, D.: Modified EDF algorithm and WiMAX architecture to ensure end-to-end delay in multi-hop networks. In: TENCON IEEE Region 10 Conference, pp. 1–6. IEEE (2008)
6. Fathi, M., Rashidi-Bajgan, S., Khalilzadeh, A., Taheri, H.: A dynamic joint scheduling and call admission control scheme for IEEE 802.16 networks. Telecommun. Syst. 1–8 (2013)
7. Ali, N.A., Dhrona, P., Hassanein, H.: A performance study of uplink scheduling algorithms in point-to-multipoint WiMAX networks. Comput. Commun. **32**(3), 511–521 (2009)
8. Yadav, A., Vyavahare, P., Bansod, P.: Review of WiMAX scheduling algorithms and their classification. J. Inst. Eng. (India): Ser. B **96**(2), 197–208 (2015)

Analysis of Suicides in India—A Study Using the Techniques of Big Data

Shruti Pradhan, Divyansh, Manjusha Pandey and Siddharth S. Rautaray

Abstract The idea behind this study is discovering and presenting the prime factors that affect numbers of suicides in India from the year 2001 to 2012. The features in the study refer primarily to the part of the population which are affected most by suicides. Here, we explore the various profiles of the population and how the profile of an individual is contributing to his/her suicidal behavior. The rate of suicides in India has been increasing since the last decade and only a negligible percentage of decline in the same has been observed. The study reflects suicide as a massive social problem and thus, effective interventions for suicide prevention need to be developed at the earliest. This study employs the use of techniques of data analytics to find and analyze the trends in suicides. Data analytics delivers a rich insight from multiple sources and transactions, to uncover hidden patterns and relationships.

Index terms Suicides in India · Big data · Suicide analysis · Suicide prevention Big data analytics

1 Introduction

It has been observed that suicide is the third leading cause of death amidst the people globally. According to the WHO data, every year, roughly one million people die from suicide and 20 times added people attempt suicide, a global mortality rate of 16 per 100,000, or one death every 40 s, and one attempt every 3 s, on average. India

S. Pradhan (✉) · Divyansh · M. Pandey · S. S. Rautaray
School of Computer Science Engineering, KIIT, Bhubaneswar, India
e-mail: shrutiprad07@gmail.com

Divyansh
e-mail: indiadivyansh@gmail.com

M. Pandey
e-mail: manjushapandey82@gmail.com

S. S. Rautaray
e-mail: sr.rgpv@gmail.com

U. Biswas et al. (eds.), *Advances in Computer, Communication and Control*, Lecture Notes in Networks and Systems 41, https://doi.org/10.1007/978-981-13-3122-0_31

stands 43rd in declining scale of rates of suicide with a rate of 10.9 per 100,000 population recorded in 2009. Most suicide victims are aged between 18 and 45, which is the most productive age group in society. A developing country like India is crippled in its able workforce from a largely preventable problem.

Data on suicide in India is prepared from the National Crime Records Bureau (NCRB; Ministry of Home Affairs). The rate of suicide exhibited a declining course from 1999 to 2002 and a mixed trend during 2003–2006, supported by a growing trend from 2006 to 2010. Throughout 2009, the rate was 10.9 per 100,000 populations. This drew a 1.7% increase in suicides since 2008. In the most up-to-date NCRB report, the rate in 2010 progressed to 11.4 per 100,000 populations, an inflation of 5.9% in numbers of suicides. India has a comparable suicide rate to Australia and USA and with growing rates during recent decades.

Developed countries like The United States of America and Germany have several suicide prevention centers and other necessary bodies to prevent suicides, whereas India, on the other hand, has no national plan for suicide prevention apart from a few NGOs who are currently working on the problem. It is often observed that required attention to those who have tried suicide is dismissed by hospitals and doctors citing legal hassles. This is one of the major issues that the country is facing and is being neglected at the highest level.

In this study, we shall be analyzing suicides under five different categorizations: Causes, Means Adopted, Profession, Social Status (or Marital Status), and Educational Status. Each of these categorizations will be further analyzed under more statistical domains like State, Gender, and Year for a particular suicide. This will enable us to identify the most prominent causes that drive people to commit suicides, including the most common ways of committing suicide, the correlation of the level of education, profession, and marital status with the risk of suicidal thoughts. Using Big Data technologies will allow us to produce and propagate accurate results and visualizations of the data at hand connected to suicides, and more reliable solutions for suicide prevention including planning our course of action when it comes to dealing with suicides in the immediate future.

2 Big Data

2.1 Definition of Big Data

Gartner (2013) illustrates the Big Data theory as “high-volume, high velocity and/or high variety information assets that demand cost-effective innovative forms of information processing for enhanced insight, decision-making, and process optimization.” Big Data provides us with possibilities for exploring new benefits, along with helping us to obtain a widespread perception of the latent patterns and values, and inspires innovative challenges and issues related to efficiently plan and execute various kinds of data collections.

2.2 Applications of Big Data

In BDA: New type of software applications which can leverage data on a large scale to uncover actionable knowledge using parallel-processing infrastructures is called as Big Data Analytics Applications (e.g., Hadoop). **In Clustering**: K-Means clustering algorithm is a simple unsupervised learning algorithm that divides a presented data set according to a specific representation of clusters. **In Data Mining**: It can be applied effectively in fields such as weather forecast, transportation, health care, medicine, insurance, fraud risk, and government. **In Banking**: Recently, a research was conducted which indicated that 62% of banking officials avoid using Big Data techniques due to several privacy issues. Further, security risks are increased when customer data is outsourced or distributed for data analysis activities across departments for the generation of richer insights on the available datasets. **In Stock**: Data analytics plays a huge role in the world of stock markets, by detecting frauds. **In Credit Cards**: Credit card companies make use of the speed and accuracy of analytics included with the database to identify as well as prevent possible fraudulent transactions. **In Consumer Goods**: The aim of a maker of consumer goods is to analyze all the data collected about the product and to understand as to why certain products succeed while others fail. **In Agriculture**: In order to optimize crop efficiency, biotechnology firms use sensor data that is generated with the help of devices set up in the firm. Test crops are planted and simulations are run that measure how plants react to various changes in the surrounding condition(s). **In Health Care**: Big Data supports an extensive variety of pharmaceutical and healthcare purposes, which incorporates disease surveillance, clinical decision aid, and community health administration. **In Smartphones**: Now Android and iPhone users are provided with facial recognition technology for various tasks such as login and sign-in. **In Finance**: Nowadays, it is seen that banking institutions perform their own credit score analysis for existing customers as well as new customers using various data, including savings, checking, credit cards, investment data, and mortgages.

2.3 Role of Big Data in Suicide Analysis

In psychiatry, Big Data describes the tremendous extent of data gathered from patients and by the speed with which data is collected. Big Data gained from the social media can play an important role in preventing suicide in psychiatry. The suicidal phenotype is identified by utmost heterogeneity, and probably suicidal people are often barred from any clinical experiments. Big Data could help by linking complex and comprehensive data samples to discover patterns, indicating suicidal desires.

Thus, we see that Big Data is already being applied in psychiatry for numerous goals. The velocity of data procurement remains to be one of the principal challenges because most data is refreshed on a periodical basis and there are not various real-

time alternatives accessible. However, Big Data can contribute exceptional gains for the treatment of patients in psychiatry and perception of their ailments.

2.4 Need for Proposal

Psychologists say that before committing the final act, a suicidal person must first overcome intense emotional distress and then he/she may be ready to take a decision to terminate their life. Leading suicide researchers contemplated that a feeling of burden is necessary but inadequate to explain as to why people kill themselves. A person must be deeply tolerant of discomfort and conflict to realize as well as understand the distressing beliefs and feelings that develop in his mind when working toward the significant decision of ceasing one's life. This study helps in obtaining a more meaningful insight on which section of the Indian population is most affected by suicides, and thus, it is an invaluable statistic for focusing preventive measures and making major governing decisions for different regions of the country.

3 Literature Survey

In the paper published by Kwon et al. in the year 2015 titled "Big Data Analysis of Counseling Cases for Youth at Risk of Suicide", the author discusses how Big Data Analytics can be used to discover a pattern for common behavior observed in the suicidal youth of Republic of Korea. The paper reviews the contents and characteristics of suicide committed by correlating the data collected from various social networking websites and suicide counseling cases from CYS-Net, and hence proposes a reasonable and competent suicide prevention and early intervention strategies [1].

de Araujo et al. published a paper titled "Suicidology meets Big Data" in 2015 in which they shed light on the topic of how suicide is associated with mental illness, mostly depressive disorders, through substance abuse, and psychotic disorders. The study showcases the potential power of Big Data for research on suicide and its prevention. Methods used in The Durkheim Project have also been discussed [2].

The paper titled "Analysis of Suicide Victim Data for the Prediction of Number of Suicides in India" published by Selva Priyanka et al. in 2016 takes into consideration the suicides committed in certain regions of India in the year 2011. The author has computed the Pearson correlation to determine the strength of the features on numbers of suicides and then linear regression was used to develop a model for the prediction of number of suicides. The results obtained had a prediction accuracy of 99.1% and linear fir close to 99.8%. The objective is to suggest preventive measures focused on these classes of people that will help in bringing down numbers of suicides in the country [3].

In 2015, the paper titled "An ERP study of implicit emotion processing in depressed suicide attempters" by Nengzhi Jiang et al. compares the variations in

the event-related potentials (ERP) of suicide attempters and non-attempters with primary depressive disorder demonstrating significantly different P3 amplitudes during an inherent emotion processing job. The study highlights that using ERP can help doctors in differentiating between patients suffering from depression and those without an inclination toward suicidal behavior [4].

Berrouiguet et al. published a paper titled "Toward E-Health Applications for Suicide Prevention" in 2016 that proposed a mobile application for suicide prevention. A connected tool is developed which allows the patient to report about his/her health status. The author relates the ongoing worldwide initiatives along with requirements toward the development of an efficient intelligent health (i-health) application for suicide prevention [5].

In the paper published by Yaganteeswarudu et al. in the year 2017 titled "Software application to prevent suicides of farmers with asp.net MVC", the author discusses the various challenges that farmers face while growing crops and how these challenges become a major factor in enabling them to commit suicide. The objective of the study was to design a website that would enable the farmers to directly address and discuss their problems with the government [6].

The paper titled "Big Data in Healthcare: A Mobile Based Solution" published by Panda et al. in 2017 addresses healthcare information not being readily accessible in a centralized and informed manner. The study focuses on developing a mobile/web application through which the patients can send their symptomatic queries to doctors via a server. The proposed model serves to be an efficient solution for data collection and healthcare delivery, integrated with analytics [7].

Sikander et al. published a paper titled "Predicting Risk of Suicide Using Resting State Heart Rate" in the year 2016 that explores the potential of using heart rate-related measurements to help clinicians to diagnose and predict suicide risk. The study demonstrates the possibility of developing the prototype of a computational model which uses physiological signals to determine suicide ideation [8].

In the year 2014, paper titled "Suicide Detection System On Twitter" by Varathan et al. detects suicides in a timely manner by analyzing the tweets posted on Twitter. The system is designed to extract the geolocation of the person who posts a suicide-related tweet. The objective behind developing this model is to help and prevent people from committing suicide [9].

The paper published by Vanathi et al. titled "A Robust Architectural Framework for Big Data Stream Computing in Personal Healthcare Real-Time Analytics" in the year 2017 discusses the current developments in the field of Big Data with respect to the healthcare industry. The architecture proposed by the author comprises Hadoop, Apache Storm, Kafka, and NoSQL Cassandra, and aims at presenting provision for healthcare analytics by contributing batch and real-time computing along with expandable storehouse and clustering technology solution and efficient query management [10].

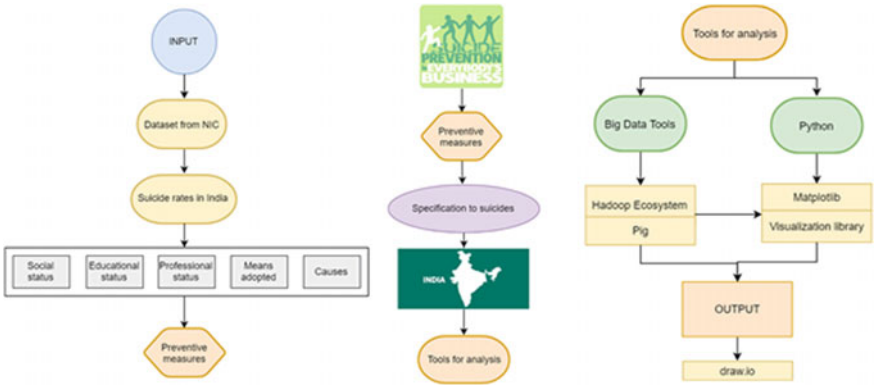

Fig. 1 Data flow of the process

4 Proposal

In the pictorial representation above, the input data passes through various parameters to get the desired output. After obtaining a well-tabulated data from NIC (National Informatics Centre) with various fields, pertaining to suicide rates in the Indian states, the dataset is analyzed for queries using Big Data tools.

The dataset is a multi-field varied collection of information which gives us an account of the suicide rates in Indian states and their causes, means adopted by masses of which professional, educational, social distinction, and age group as well. Output is obtained in graphical format as well. The whole process is shown using draw.io (Fig. 1).

5 Experimental Setup

The hardware configurations of the desktop used are processor speed of 3.20 GHz, RAM of size 8.00 GB, and system type of 64-bit operating system with a x64 based processor to facilitate faster query processing.

The software configurations used for the above research include VMW, Workstation Pro, and Jet Brains PyCharm. VMWare Workstation is a hosted hypervisor that can run multiple operating systems at once on the same Windows or Linux operating systems (x64) enabling the multiple users to use it simultaneously.

The host system must have a 64-bit CPU with 1.3 GHz or faster core speed, along with a 16-bit or 32-bit display adapter. Multiprocessor systems are supported. The minimum memory required on the host system is 1 GB (2 GB and above is recommended). The Workstation will work with any Ethernet controller that is supported by the host operating system.

6 Results and Analysis

It has been observed that among the countries with high suicide rates, India has seen a rapid increase in the number of suicides in the past years, with Indian women having some of the highest frequencies on the planet. Suicide is a self-inflicted death, or can be interpreted as "choosing the mode, time, situation, or occasion for ending one's life." In a more common way of saying, the word "suicide" has a negative implication and is often looked upon with disregard. It is now required to analyze the suicide rates that have been rising at a disturbing rate over the last few years. However, it is difficult to distinguish the right thing from wrong thing, and thus we need to analyze both the viewpoints before arriving at a conclusion.

The analysis revealed how the male gender shows a higher rate of suicide attempts in comparison to the fairer sex besides revealing 15–29 is the prime age group affected by it. Drug abuse, addiction, illness (STD), and prolonged illness are some of the primary causes of suicides among individuals of age 15–29. Consuming insecticide, poison, and drowning are the major activities chosen by males to end their lives whereas in females hanging, poison, and self-immolation are the common means undertaken (Figs. 2, 3 and 4).

The increase in suicide rates chronologically is higher among males than females.

In 2001, the number of males suicides was 66,314 and it became 88,453 by 2012, whereas in females the numbers ranged from 42,192 to 46,992 (Figs. 5, 6 and 7).

In Jharkhand and West Bengal, the rate of housewife attempting suicides is alarming.

Gujarat, Chandigarh, Assam, and Goa are the leading states to have shown the primary social status of population committing suicide consisting of married men and women. Individuals enrolled in primary education were found to be more in number, participating in this drastic state than those enrolled in postgraduation.

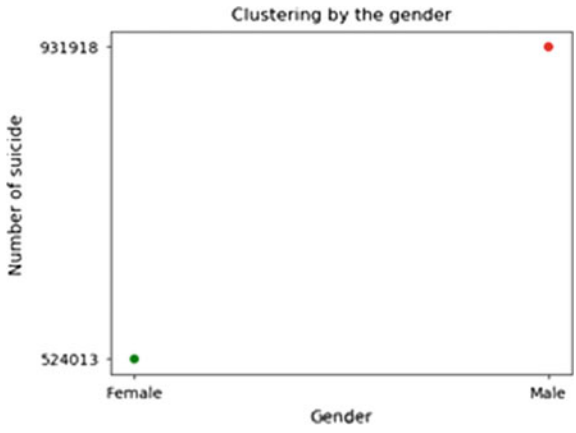

Fig. 2 Clustering by gender

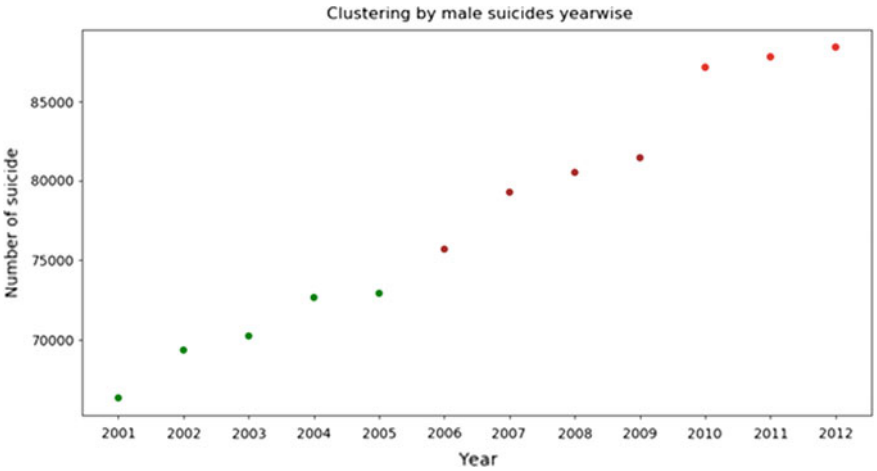

Fig. 3 Range of suicide rates from 2001 to 2012 for men

Fig. 4 Age groups affected by suicide rates

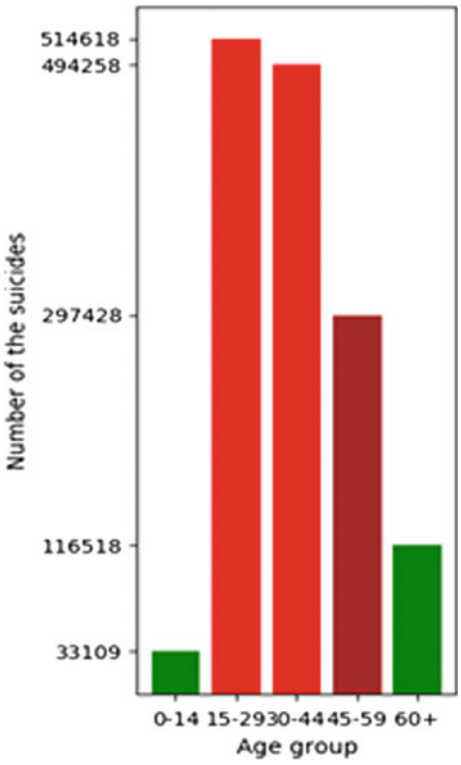

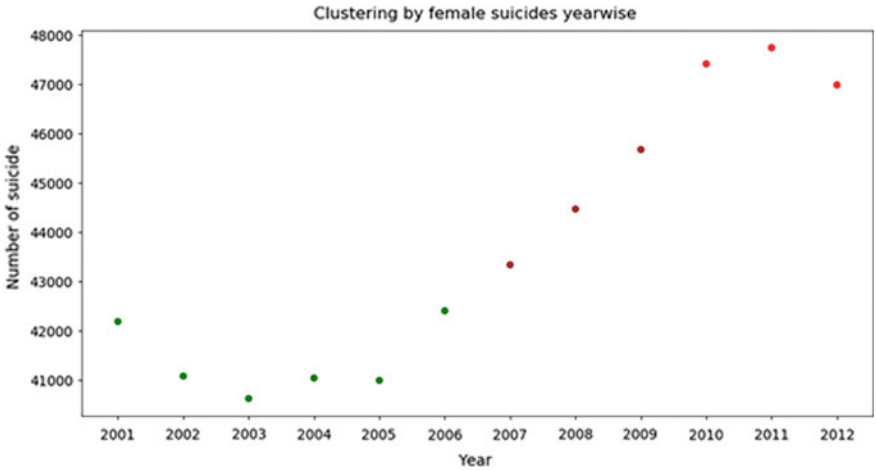

Fig. 5 Range of suicide rates from 2001 to 2012 for women

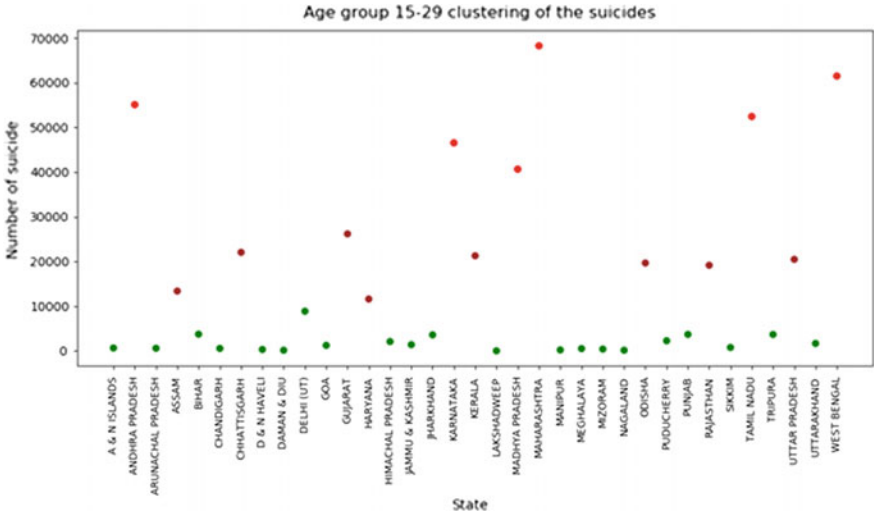

Fig. 6 Statewise number of suicide for the age group 15–29

The two age groups with the maximum hike in the suicide rates in the states like Maharashtra, West Bengal, Andhra Pradesh, and Tamil Nadu, in the decreasing order, were found to be 15–29 and 30–44.

The analysis also revealed that during the span of 12 years, Maharashtra and Andhra Pradesh had witnessed the maximum attempts of suicide in 2012, West Bengal in 2011, and Karnataka and Tamil Nadu in 2012 indicating a consistent increase. The entire realm of demography revealed that married population of all age groups are more inclined to commit this crime with the lowest tendency among

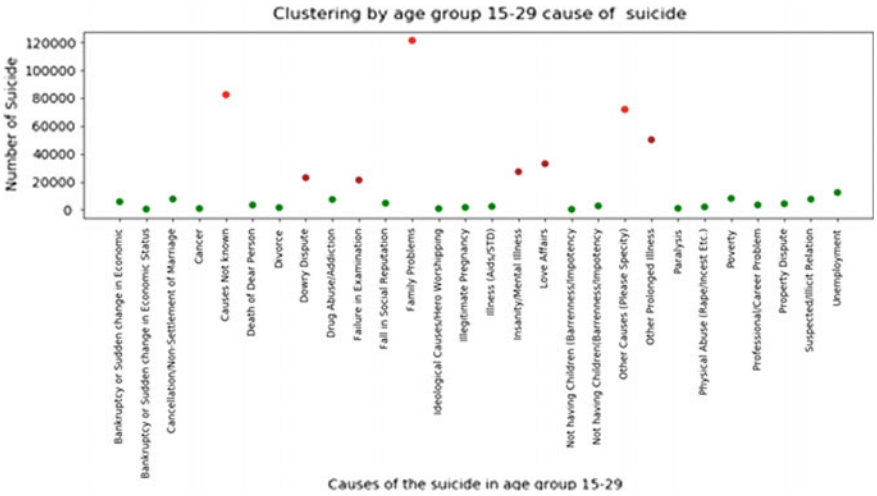

Fig. 7 Causes of suicide for age group 15–29

those who are separated. In the states of Karnataka and Kerala, and union territories of Lakshadweep and Daman Diu, the housewives were seen to have a very high rate of suicides with the lowest rates among retired individuals of the same regions.

When it comes to courses adopted, hanging is a recurrent means among populace of Maharashtra with decreasing trend in those of Andhra Pradesh and Madhya Pradesh followed by lesser in states of Jharkhand, Bihar, Odisha, and the eastern belt. Andhra Pradesh and Maharashtra have high rates of inhabitants committing suicide by consumption of insecticide and poison. Maharashtra tops the chart in suicide attempts by drowning followed by Karnataka and Tamil Nadu with lesser numbers in the union territories of Daman and Diu, Haveli, Andaman and Nicobar, and the other states.

7 Conclusion

With every year, we see that the rate of suicide in India is rising at an alarming rate. Detecting the immediate risk of suicide is a very difficult, yet a potentially lifesaving effort. Standard predictors that are presently in use are not able to address the issue of immediate or acute suicide risk but rather seem to be more related to long-term risk.

Research has shown that more than one hundred thousand lives are lost every year to suicide in our country. In the suicide of Indian women, the issue relating to marriage like dowry, divorce, cancellation or inability to get married, and extra-marital affairs play a critical role.

Alcoholism and drug dependence are the key factors of suicides in India. The Southern States experience higher suicide rates. The possible explanations may consist of high literacy rate, high socioeconomic status, a better reporting system, and higher expectations.

Today, we live in a world of information, where a large volume of high-velocity data are being produced regularly, wherein lies inherent details and patterns of latent knowledge which should be extracted and used efficiently. Hence, Big Data helps in analyzing a large chunk of raw data that is collected and stored through various means, as well as producing efficient results.

Hadoop Ecosystem provides all the necessary tools required for the analysis. Apache Pig a high-level platform scripting language that runs on Apache Hadoop and helps in complex transformation as well as appeals to the developers already familiar with SQL. The high-speed computing abilities of Hadoop have helped in the production, researching, and presentation of the data and facts, obtained from the dataset, accurately. The use of Pig enabled us to create query execution routines for the dataset without having to do the low-level work in MapReduce. Data was convened from the repository of National Informatics Centre (NIC). The graphs were visualized by using Matplotlib, graphing, and data visualization library for Python.

Suicide is a multifaceted problem that needs to be dealt with at the earliest.

In order to save lives of thousands of young Indians, it is essential to know the causes that drive people to commit suicide and to adopt proactive and leadership roles in suicide prevention.

Acknowledgements We would like to express our profound gratitude to the Dean of School Of Computer Engineering, KIIT, Dr. Samaresh Mishra for allowing us to proceed with the report and for giving us full freedom to access the lab facilities. Our heartfelt thanks to Dr. Siddharth Swarup Rautaray and Dr. Manjusha Pandey for taking time and helping us through our work. They have been a constant source of encouragement without which the work might not have been completed on time. Their ideas and thoughts have been of great importance.

References

1. Kwon, S., Yang, M.-J., Yoo, J.-H., Kim, L.-S.: Big data analysis of counseling cases for youth at risk of suicide. In: Proceedings of INTCESS15: 2nd International Conference on Education and Social Sciences, 2–4 Feb 2015
2. Big data analytics: a literature review. https://www.researchgate.net/publication/264555968_Big_Data_Analytics_A_Literature_Review_Paper. Accessed 13 Jan 2018
3. Selva Priyanka, S, Galgali, S., Selva Priya, S., Shashank, B.R., Srinivasa, K.G.: Analysis of suicide victim data for the prediction of number of suicides in India. In: IEEE International Conference on Circuits, Controls, Communications and Computing (I4C), 4–6 Oct 2016, pp. 1–5. Electronic-ISBN: 978-1-5090-5369-8
4. Jiang, N., Wang, Y., Sun, L., Song, Y., Sun, H.: An ERP study of implicit emotion processing in depressed suicide attempters. In: 7th International Conference on Information Technology in Medicine and Education (ITME), pp. 37–40 (2015). Electronic ISBN: 978-1-4673-8302-8

5. Berrouiguet, S., Billot, R., Lenca, P., Tanguy, P., Baca-García, E., Simonnet, M., Gourvennec, B.: Toward E-health applications for suicide prevention. In: IEEE First International Conference on Connected Health: Applications, Systems and Engineering Technologies (CHASE), pp. 346–347 (2016). Electronic ISBN: 978-1-5090-0943-5
6. Yaganteeswarudu, A., Vishnu Vardhan, Y.: Software application to prevent suicides of farmers with asp.net MVC. In: 7th International Conference on Cloud Computing, Data Science and Engineering—Confluence, pp. 543–546 (2017). Electronic ISBN: 978-1-5090-3519-9
7. Panda, M., Ali, S.M., Panda, S.K.: Big data in healthcare: a mobile based solution. In: International Conference on Big Data Analytics and Computational Intelligence (ICBDAC), pp. 149–152 (2017). Electronic ISBN: 978-1-5090-6400-7
8. Sikander, D., Arvaneh, M., Amico, F., Healy, G., Ward, T., Kearney, D., Mohedano, E., Fagan, J., Yek, J., Smeaton, A.F., Brophy, J.: Predicting risk of suicide using resting state heart rate. In: Asia-Pacific Signal and Information Processing Association Annual Summit and Conference (APSIPA), pp. 1–4 (2016). Electronic ISBN: 978-9-8814-7682-1
9. Varathan, K.D., Talib, N.: Suicide detection system based on Twitter. In: Science and Information Conference, pp. 785–788 (2014). Electronic ISBN: 978-0-9893193-1-7
10. Vanathi, R., Shaik Abdul Khadir, A.: A robust architectural framework for big data stream computing in personal healthcare real time analytics. In: World Congress on Computing and Communication-Technologies (WCCCT), pp. 97–104 (2017)

1 × 2 Harmonic Suppression Microstrip Antenna Array for ISM Band Applications at 2.45 GHz

Anushka Tiwari and Sushrut Das

Abstract In this paper, a 1 × 2 microstrip patch antenna array with defected ground structure and stubs for Industrial, Scientific and Medical (ISM) band applications at operating frequency of 2.45 GHz is presented. The antenna array deploys a T-junction power divider as a feeding element and open stubs to suppress harmonics simulated using a Commercial Electromagnetic 3-D Simulator CST Microwave Studio.

Keywords Microstrip antenna array · T-junction power divider
Harmonic suppression · Stubs

1 Introduction

Microstrip patch antennas have made great progress in today's wireless communication due to their small size, low cost, and low profile, and hence compatible with applications such as WLAN, RFID, and WIMAX. Due to harmonic radiations from microstrip patch antenna, Electromagnetic Interference (EMI) comes in picture that degrades the system. In order to avoid it, harmonic suppression antenna is needed.

In recent years, alternate energy sources have become essential as the demand for power increases. The history of communication technology witnessed many fabulous ideas. Wireless power transfer is one among them. Several antenna designs of rectenna have been proposed for use in RF energy harvesting. So to increase the RF to DC efficiency for rectenna applications, harmonic suppression antennas are

A. Tiwari · S. Das (✉)
Department of Electronics Engineering, Indian Institute of Technology (Indian School of Mines) Dhanbad, Dhanbad 826004, Jharkhand, India
e-mail: sushrut_das@yahoo.com

A. Tiwari
e-mail: 1411anushka@gmail.com

U. Biswas et al. (eds.), *Advances in Computer, Communication and Control*, Lecture Notes in Networks and Systems 41, https://doi.org/10.1007/978-981-13-3122-0_32

needed. The major requirement of wireless power transfer is antenna with high gain, and hence several techniques can be used to enhance the gain such as array [1], metamaterials [2], etc.

To suppress the harmonics, different techniques that have been proposed are defected ground structure (DGS) [3–5], right-angle embedded slits [6], slot and stub [7], etc. DGS is a technique used to enhance the bandwidth, shift the resonant frequency, and suppress the higher mode harmonics, mutual coupling between adjacent element and cross-polarization for improving the radiation characteristics of the microstrip antenna, whereas stubs are used to match a load impedance to transmission line characteristic impedance that improves the suppression of higher order harmonics of fundamental frequency.

Microwave circuits employs passive devices like power dividers [8] which couples a power in a transmission line to a port enabling the signal to be used in another circuit such as antenna arrays, power amplifiers, etc. Power divider is frequently used as a feeding network for planar antenna arrays to control the power distribution of each element. The motive of designing antenna array is to overcome the limitations of patch antennas that includes low gain, narrow bandwidth, low efficiency, and surface wave excitation. In this paper, an antenna array is designed with pentagonal-shaped DGS and stubs, using corporate feed network that employs quarter-wave transformer, stepped impedance, and mitered bends, and as a result gain and efficiency are increased.

2 Single-Element Antenna

A 2.45 GHz antenna with defected ground structure (DGS) and stubs has harmonic suppression characteristics is printed on 45 mm × 50 mm size FR4 substrate of thickness (h) 1.6 mm, relative permittivity (ε_r) of 4.4, and loss tangent tan (δ) = 0.02 as dielectric material that makes it suitable antenna element for advanced rectenna systems (Fig. 1).

The geometric parameters of the proposed antenna structure have been modified to tune the return loss frequency as well as gain over a WiFi band using a commercial electromagnetic 3-D simulator CST Microwave studio. The dimensions of the optimized antenna are shown in Table 1.

The return loss of the proposed antenna is shown in Fig. 2. Undesired harmonic radiations are present at high frequencies in addition to require 2.45 GHz band and additional passbands are present at 5.3, 7.1 and 7.9 GHz that will be suppressed using stubs and DGS.

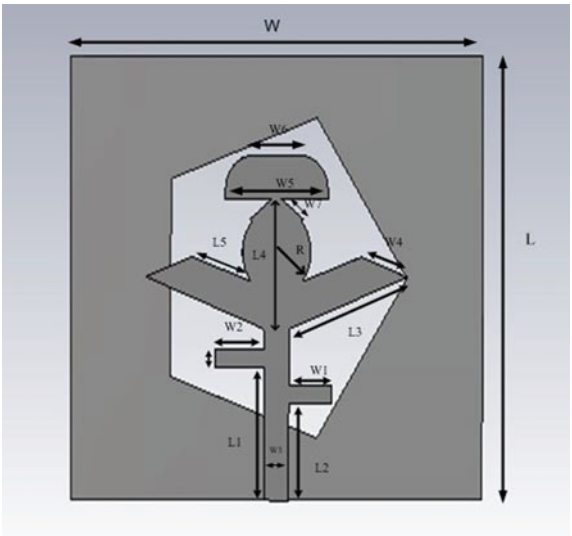

Fig. 1 Geometry of a single-element patch

Table 1 Dimensions of the proposed antenna

W_1	W_2	W_3	W_4	W_5	W_6	W_7
7.5 mm	9 mm	3.2 mm	7.04 mm	14 mm	8.5 mm	3.85 mm
L_1	L_2	L_3	L_4	L_5	R	T
15 mm	11 mm	18.4 mm	14.72 mm	9.02 mm	5 mm	2

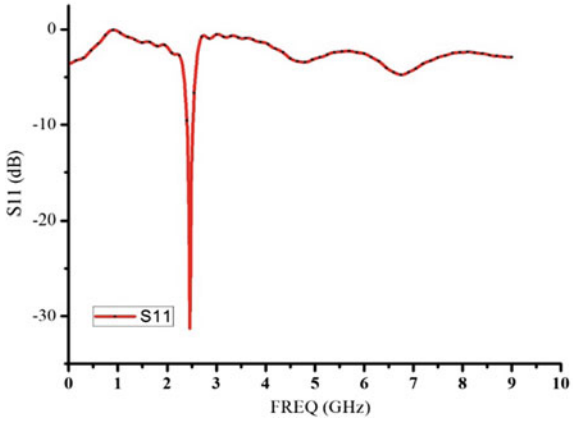

Fig. 2 Simulated frequency response of the proposed antenna

The major characteristics, at the desired frequency of a single element, are shown, respectively, in Figs. 3 and 4.

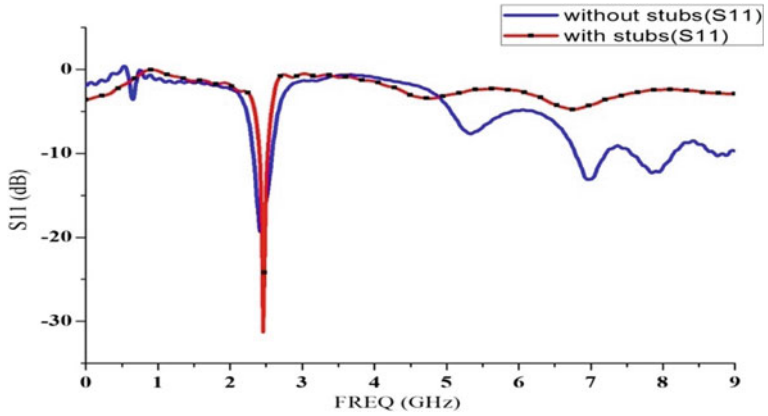

Fig. 3 Simulated return loss of single-element antenna with and without harmonics

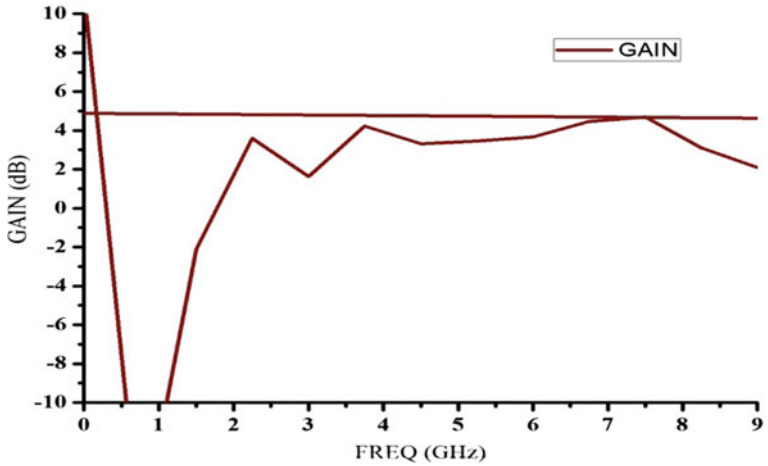

Fig. 4 Gain versus frequency plot

3 Antenna Array Design

The antenna is printed on 100 mm × 88 mm size FR-4 substrate of thickness (h) 1.6 mm, relative permittivity (ε_r) of 4.4, and loss tangent tan (δ) = 0.02 has been considered as dielectric material. Design and optimization of the antenna have been carried out using CST Microwave Studio (Version 14.0) (Fig. 5).

It is designed using power divider specified above with the spacing of 0.35λ.

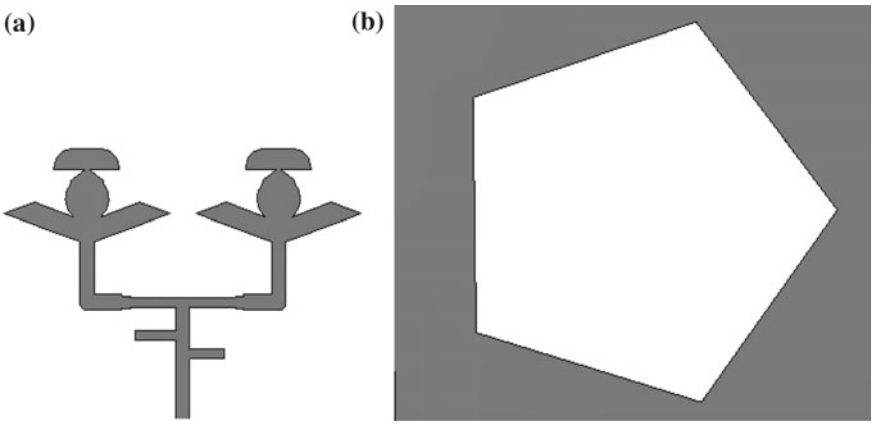

Fig. 5 Planar antenna array **a** top view, **b** bottom view

3.1 Power Divider

The return loss (S_{11}) of the power divider as shown in Fig. 6 is –52 dB that shows that the input terminal is matched and the insertion loss (S_{21}) is −3.35 dB and so the S_{31} that shows equal split of power in both the ports. Hence, the simulated results satisfied all the stipulated constraints specified (Fig. 7).

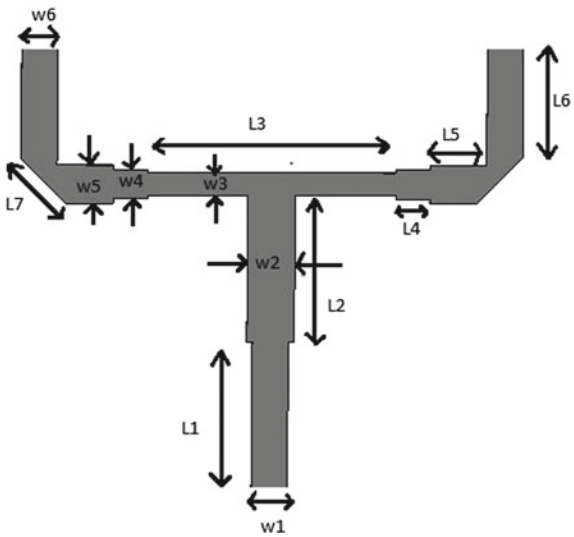

Fig. 6 2:1 T-junction 3-dB power divider

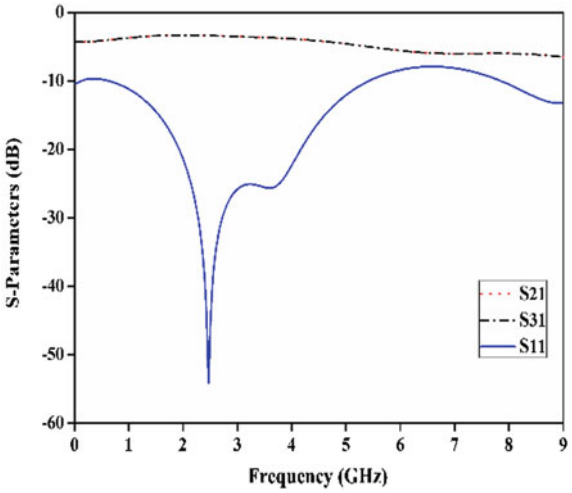

Fig. 7 Simulation results of the 1:2 T-junction power divider for 2.45 GHz

Table 2 Geometry of the power divider

W_1	W_2	W_3	W_4	W_5	W_6	T
3.2 mm	4.4 mm	1.8 mm	2.6 mm	3.4 mm	3.2 mm	0.035 mm
L_1	L_2	L_3	L_4	L_5	L_6	L_7
13 mm	14 mm	22 mm	3 mm	5 mm	23.8 mm	5.6468 mm

This proposed circuit provides better characteristics as well as frequency response S_{11} is stable and does not change on changing the space between its output ports. Hence, the frequency response of the proposed design validates the stipulated concepts. The dimensions of the optimized 1:2 T-junction power divider for 2.45 GHz frequency are shown in Table 2 where W is the width and L is the length of the sections of transmission lines with thickness t, and z is the spacing between two output ports.

3.2 Simulated Results of Antenna Array

The frequency response characteristics of the antenna array are shown in Fig. 8. The harmonics have been suppressed by using stubs and DGS. In order to suppress these additional bands, open stubs are used on the feed line.

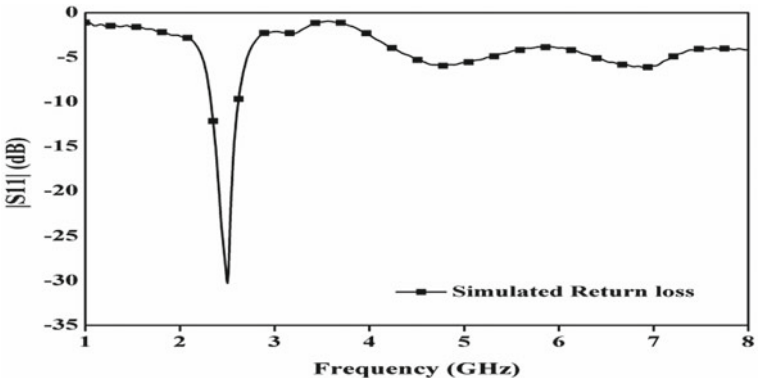

Fig. 8 Simulated return loss of proposed array

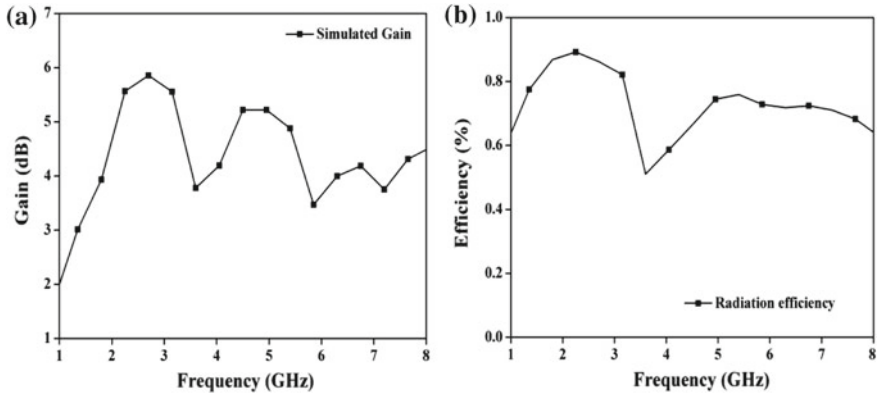

Fig. 9 Simulated results of the antenna **a** gain response of the antenna, **b** radiation efficiency of the antenna

The simulated gain and radiation efficiency of the proposed antenna have been plotted with frequency in Fig. 9. It reveals that in the entire 10 dB return loss bandwidth, gain of the antenna remains almost constant. The proposed antenna array has gain of 5.7 dB and 94% radiation efficiency at the resonating frequency of 2.45 GHz. Simulated results of radiation pattern in XY and XZ plane is shown in Fig. 10.

The use of the harmonic suppression antenna array for rectenna design applications results in high RF to DC conversion efficiency and high gain.

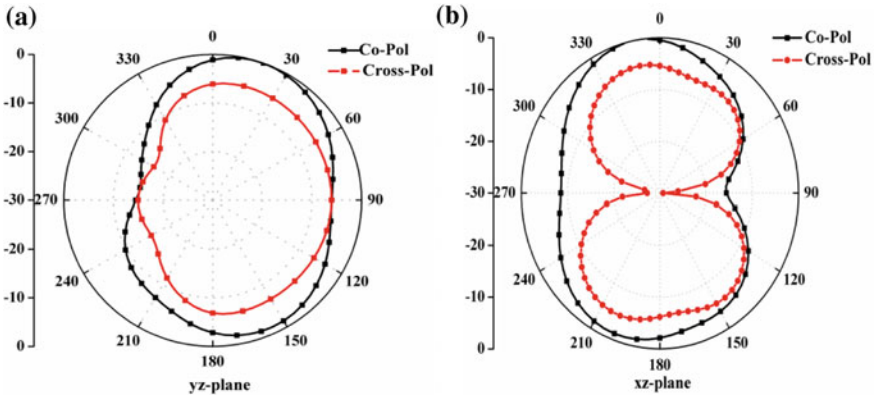

Fig. 10 Simulated normalized Co and cross-polarized radiation pattern on **a** *yz*-plane (Phi = 90° and theta = all), **b** *xz*-plane (Phi = 0° and theta = all)

4 Conclusion

A 2.45 GHz linearly polarized 1×2 harmonic suppression microstrip antenna array with T-junction power divider for ISM band applications has been proposed with return loss of −30 dB and percentage bandwidth of 11.5%. The gain of array has been increased to 5.7 dB from that of 3.2 dB with radiation efficiency of 87%.

References

1. Dharsandiya, N., Parmar, D.I.: Optimization of antenna design for gain enhancement using array 1038–1043 (2014)
2. Wang, S., Feresidis, A.P., Goussetis, G., Vardaxoglou, J.C.: High-gain subwavelength resonant cavity antennas based on metamaterial ground planes. IEE Proc. **153**(1), 1–6 (2006)
3. Udayabhaskar, P., Sonika Priyadarsini, B., Das, S.: A 2.45 GHz DGS based harmonic rejection antenna for rectenna application. In: USNC-URSI Radio Science AP-S Symposium, San Diego, USA, pp. 123–124 (2017)
4. Ramesh, G.: Microstrip Antenna Design Handbook. Artech House (2001). ISBN: 0-89006-513-6
5. Sung, Y., Kim, M., Kim, Y.: Harmonics reduction with defected ground structure for a microstrip patch antenna. IEEE Antennas Wirel. Propag. Lett. **2**, 111–113 (2003)
6. Huang, F.-J., et al.: Design of circular polarization antenna with harmonic suppression for rectenna application. IEEE Antennas Wirel. Propag. Lett. **11**, 592–595 (2012)
7. Kumar, A., Pattapu, U., Chakraborty Das, A., Das, S.: A 2.45 GHz harmonic rejection antenna for wireless power transfer applications. In: IEEE-APS Topical Conference, Verona, Italy, pp. 81–84 (2017)
8. Pozar, D.M., Schaubert, D.H.: Microstrip Antennas: The Analysis and Design of Microstrip Antennas and Arrays. IEEE Press (1995)

Lightweight Session Key Establishment for Android Platform Using ECC

Muneer Ahmad Dar, Ummer Iqbal Khan and Syed Nisar Bukhari

Abstract Being the lightweight cryptographic technique, the elliptic curve cryptography is considered a suitable cryptography for resource-constraint devices like the small handheld devices called the smartphone. As the computational capabilities of these devices are much less, the elliptic curve cryptography is considered as a much better technique to secure the critical data of these devices. As these devices are always connected with Internet for mobile communications like Facebook, WhatsApp, etc., ensuring the security of these devices on a wireless communication channel is an ongoing challenge. A number of protocols have been proposed and implemented to secure the insecure wireless communication channel and check the authenticity of the user and integrity of messages communicated between the mobile devices. In this paper, we implement a robust and secure elliptic curve cryptography-based authentication to secure the communication between two communicating devices. Our research will demonstrate the implementation and analysis of elliptic curve cryptography on world's leading smartphone operating system—Android. Being the open-source mobile operating system, we will explore the cryptographic libraries and enhance those libraries to implement the elliptic curve cryptography. The objective of this paper is to secure our mobile user from the threats which include snooping, alteration, replaying, and interruption of message transmission. Our proof of concept implementation includes two client Android applications, communicating with each other. We will establish a secure communication channel between the two devices by implementing the Elliptic Curve Diffie–Hellman (ECDH)

M. A. Dar (✉) · U. I. Khan · S. N. Bukhari
National Institute of Electronics & Information Technology (NIELIT) Srinagar, Srinagar, J&K, India
e-mail: muneer@nielit.gov.in; muneerdar07@gmail.com

U. I. Khan
e-mail: ummer@nielit.gov.in

S. N. Bukhari
e-mail: nisar@nielit.gov.in

U. Biswas et al. (eds.), *Advances in Computer, Communication and Control*, Lecture Notes in Networks and Systems 41, https://doi.org/10.1007/978-981-13-3122-0_33

algorithm. We also propose an improved ECDH algorithm which can protect our communication from the man-in-the-middle attack. The performance analysis of the improved algorithm is presented in this paper.

Keywords Cryptography · Authentication · ECC · Android · ECDH

1 Introduction

Android-based smartphones have restricted assets in terms of processing, power, and memory. Android takes part in a significant task in the attractiveness of smartphones applications also called apps. As these applications are engaged in communication of information over the network, there is an alarming prerequisite to offer security primitives like validation, trustworthiness, and privacy. However, due to their reserve constrained environment, conventional security protocols cannot be explicitly engaged [1–9]. Symmetric encryption (secret-key cryptography) uses a particular secret key for both encryption and decryption as shown in Fig. 1.

This key has to be reserved undisclosed in the network system, which can be relatively tough in the uncovered surroundings. Symmetric key algorithms are much faster computationally than asymmetric algorithms.

Asymmetric encryption (public-key cryptography) uses two interrelated keys (public and private) for data encryption and decryption, and the security danger of key distribution is eliminated as in Fig. 2. The private key is by no means open to the networks. A communication that is encrypted using the public key can only be decrypted by applying the equivalent algorithm and with the corresponding private key. Similarly, a message that is encrypted by using the private key can only be decrypted with the corresponding public key. Examples are RSA and ECC.

Public-key cryptography alongside with symmetric key cryptography has been realistic in giving security primitive for usual networks. On the other hand, this approach has not been leveraged in the case of Android-based smartphones due to its resource-constraint character. Usual public-key cryptography is not feasible as they take up heavy computational operations. However, elliptical curve cryptography-

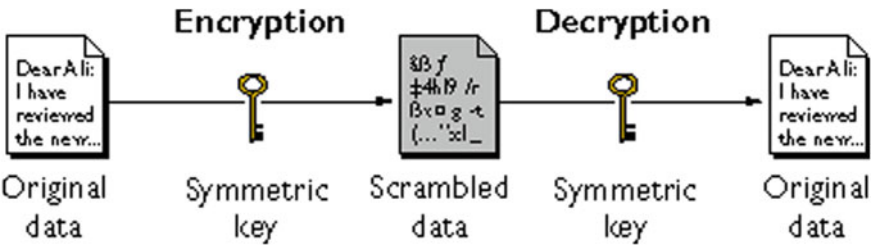

Fig. 1 Symmetric key cryptography

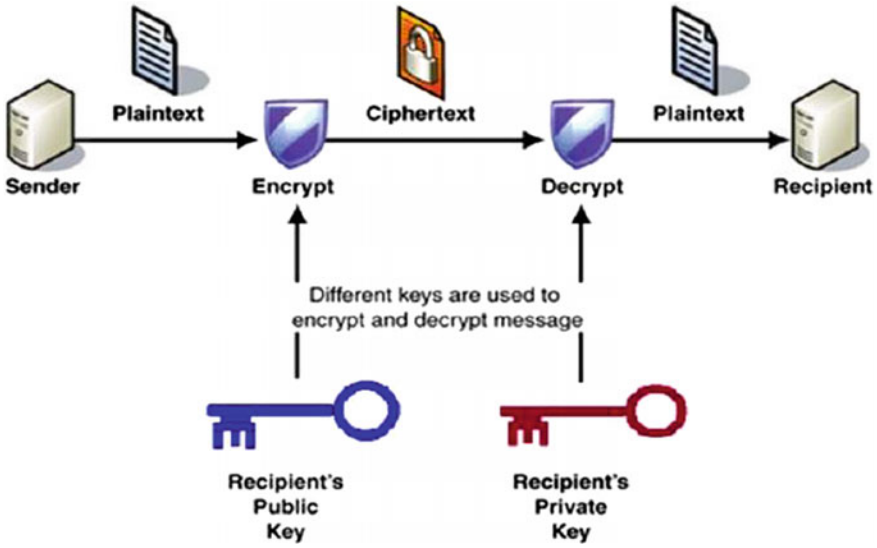

Fig. 2 Asymmetric key cryptography

based substitute of PKC has come out as a realistic substitute for providing PKC platform.

Researchers demonstrated that the elliptic curve cryptography can be competently implemented in the resource-limited devices. The advantage of using ECC as an option of straight RSA is in the truth that 160-bit key in elliptic curve cryptography provides equivalent security to that of 1024 bits of RSA as shown in Table 1.

This paper provides the relevance of ECC on a well-liked Android smartphone operating system. The research in this paper is planned as Sect. 2 provides the background understanding pertaining to Android platform. Section 3 gives the background regarding elliptic curve cryptography. Section 4 provides the proof of concept implementation of lightweight key exchange protocol using ECC in Android and proof of concept implementation is offered. Section 5 proposes an enhancement of ECDH key exchange protocol on Android platform in order to avoid man-in-the-middle attack. Finally, we present our conclusion in Sect. 6.

Table 1 ECC and RSA in terms of security equivalence

Key length of ECC	Key length of RSA	Ratio of ECC/RSA
106	512	1:5
132	768	1:6
160	1024	1:7
210	2048	1:10

2 Android Platform

Andy Rubin, Google's head of PDAs, said "There should be nothing that cell phone customers can access on their PCs that they can't access on their propelled cell phones" [10–19]. With this imaginative capacity and vision, the affirmation of cutting edge cells having Google's Android Working Framework is constantly on the rising in the twenty-first century.

Android is a versatile working framework in view of Linux; it is in like manner a superimposed or layered system [20]. The thorough outline of Android structure is displayed in Fig. 1. Application layer is the UI of all Android applications including an email, SMS, GPS, web program, and others. All applications are made using the Java programming and Java APIs. All Android applications rely upon the application structure. The Android application framework joins the going with sections:

- A well-off arrangement of views that can be actualized to build an application with multi-hued UI, it incorporates set of records, framework sees, content boxes, pictures, catches, and furthermore an engrafted Internet browser.
- A combination of content providers that urges the product architects to manufacture the applications which can get to data from various applications, or to bestow their own specific data to various applications.
- A resource manager that urges to offer access to resources, for instance, strings and outlines.
- A notification manager that offers course of action to all applications to indicate customer portrayed alarms in the status bar of the application.
- An activity manager that urges the application to manage the lifecycle of uses and gives a run of the mill course to the application [19–21] (Fig. 3).
- A portion of the benefits of Android over other cell phone working frameworks are abridged underneath.
- The android is open source with its capacity to run lakhs of applications simply like the iPhone, however, with assortment of telephone models not at all like iPhone whose applications can keep running on iPhone as it were.
- Android permits engineers and software engineers to create (applications) in an "application without outskirts" condition.
- Android is tenderfoot agreeable and especially adjustable. Android has the real offer of the market in light of the fact that the easy to understand involvement and enhancing rapidly according to their necessities.
- Google's Android now explores client area and schedule to logically indicate you correlated data, e.g., activity to work, bistros, and flight data what is more, gives you a chance to investigate with voice orders and answers with regular discourse.
- Android is an open-source platform. This implies we can openly download it and begin assembling our own applications. Anybody can download to change and upgrade the product quality by making it more viable and easy to use. Applications are uninhibitedly created and outlined by various application software engineers worldwide and these created applications are unreservedly accessible

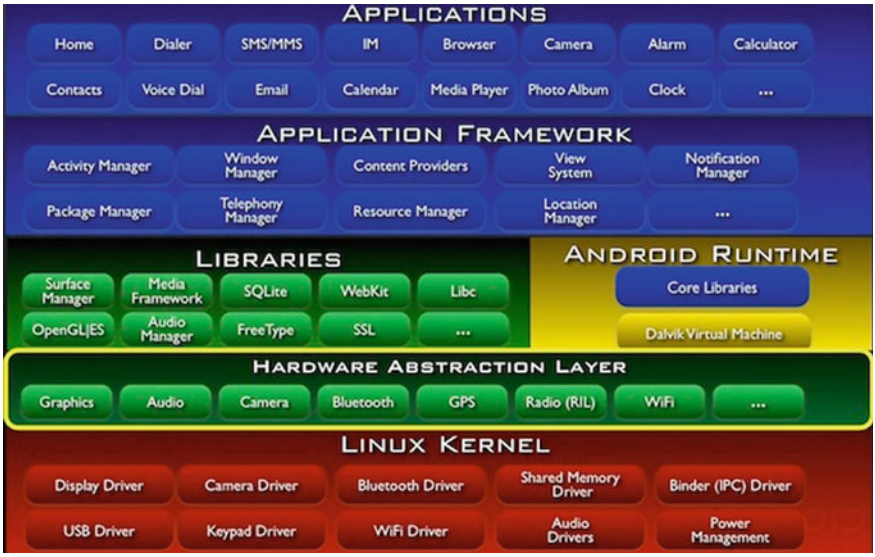

Fig. 3 Android system architecture

on the Android advertise. This appealing element of being open source has additionally pulled in cell phone organizations to fabricate alluring telephones utilizing Android OS.

- Android is not only a working framework intended for people, yet it likewise satisfies genuine business needs in the meantime. Android advertise offers extensive variety of applications that are especially intended to deal with a business. It empowers a more intensive take a gander at different business forms in a hurry with the assistance of these applications.

3 Elliptic Curve Cryptography (ECC)

Elliptic Curve Cryptography (ECC) is a public/open-key cryptography. Out in the open-key cryptography, all customers or the machines amazing part in the message exchange consistently consolidate a couple of keys, an open or public key and a private key, and a game plan of undertakings joined with the keys to do the cryptographic exercises. Just the particular client knows the private key, whereas overall population key is hovered to all customers sharing in the correspondence. Each open-key cryptosystem requires a course of action of predefined constants to be seen by each and every one contraption enchanting part in the correspondence. By virtue of elliptic curve cryptography, "region parameters" are the constants. Open-key cryptography, separating private-key cryptography, does not require any joint puzzle between the

Fig. 4 Elliptic curve

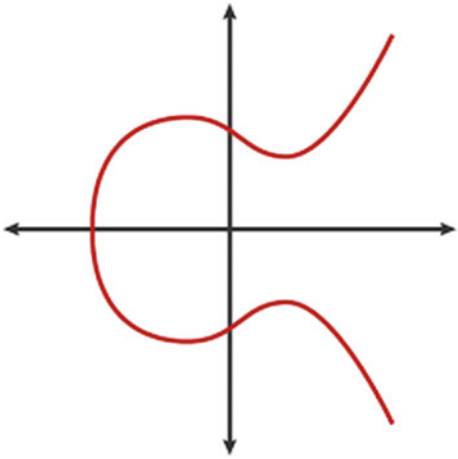

passing on parties yet it is, in a manner of speaking, lower than the private-key cryptography [15–25] (Fig. 4).

The area parameters of elliptic curve are a sextuple:

$$T = (P, a, b, G, n, h)$$

An elliptic curve above a field K is a curve defined by an equation of the form

$$y2 = x3 + ax + b$$

where a, b ∈ K and $4a3 + 27b2 \neq 0$.

3.1 Discrete Logarithm Problem

The security of ECC relies upon the intricacy of elliptic curve discrete logarithm problem. Give P and Q a chance to be two focuses on an elliptic curve with the end goal that kP = Q, where k is a scalar. Given P and Q, it is computationally infeasible to get k, if k is enough substantial. k is the discrete logarithm of Q to the base P (Fig. 5).

3.2 ECC Public-Key Cryptosystem

In general, open/public-key elliptic curve cryptosystems assume that individual A needs to impel a message "m" to singular B safely. Request of a point on the curve

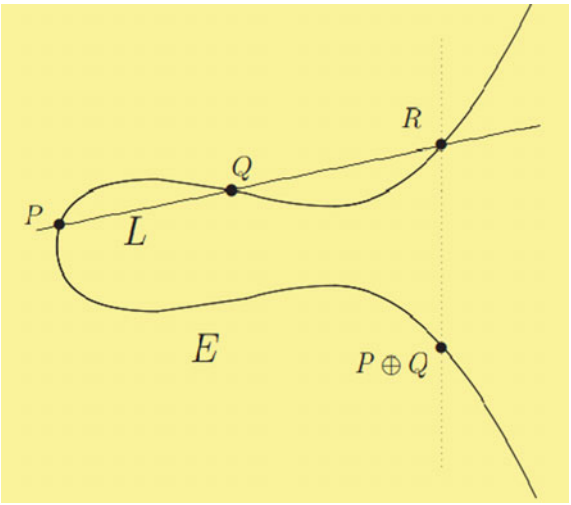

Fig. 5 Point addition in elliptic curve

can be characterized as an esteem n with the end goal that nP = P + P + · · · + P · · · n times = O (endlessness).

3.3 Generation of Public and Private Key

Both the elements in the cryptosystem concur upon the domain parameters (a, b, P, G, n). G is called generator point and n is the request of G. Presently, A creates an arbitrary number nA < n as his private key and figures his open-key set PA = G · nA, B produces an irregular number nB < n as his private key and computes his open-key set PB = G · nB.

3.4 Generation of Common Key

After trade of people in general key between the two gatherings, Entity A figures his Common Key by Computing K = nA · PB. Entity B registers his Common Key by Computing K = nB · PA. The two above keys have same esteem in light of the fact that

$$nA \cdot PB = nA \cdot (nB \cdot G) = nB(nA \cdot G) = nB \cdot PA.$$

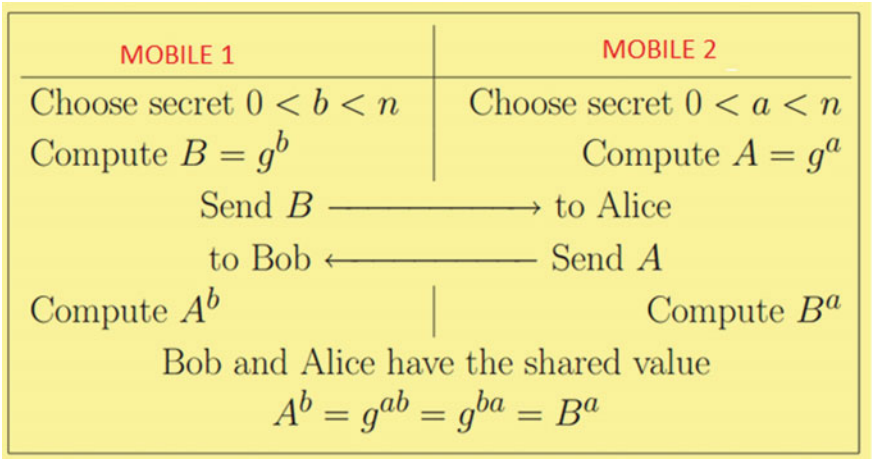

Fig. 6 Diffie–Hellman key exchange

3.5 Encryption

Think about a message "Pm" sent from A to B. "A" picks an irregular positive whole number "k", a private key "nA" and creates a general key PA = nA × G and produces the figure content "Cm" comprising of combine of focuses Cm = {kG, Pm + kPB} where G is the construct point chosen in light of the elliptic curve, and PB = nB · G is the general population key of B with private key "nB".

3.6 Decryption

To unscramble the figure content, B duplicates the first point in the combine by B's mystery and subtracts the outcome from the second point (Fig. 6).

$$\mathrm{Pm} + \mathrm{kPB} - \mathrm{nB}(\mathrm{kG}) = \mathrm{Pm} + \mathrm{k}(\mathrm{nB\,G}) - \mathrm{nB}(\mathrm{kG}) = \mathrm{Pm}.$$

4 Implementation of Lightweight Key Exchange Using ECC

The anticipated technique utilizes the above model of elliptic curve cryptography to scramble the message to impart and dispatch it over a general channel. The dispatcher composes a message and gives the beneficiary's number; when he sends the message, the calculation is propelled on both the advanced cells. The keys are created and

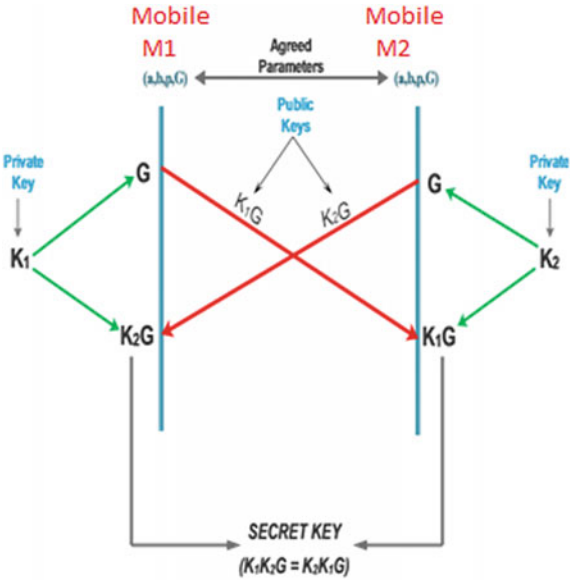

Fig. 7 Elliptic curve Diffie–Hellman message exchange

shared between the gadgets and the encryption happens at the senders stop. Following encryption, the message is sent to the beneficiary and he decodes it by methods for his key to translate it. The encryption and decryption strategies in ECC are planned to encode and translate a point on the curve and not the entire message. Amid encryption, each character in the message must be changed into bytes, then the bytes into purposes of the structure (x, y), and after that the focuses must be encoded by mapping each one of them with all focuses on the elliptic curve and after that the entire encoded indicates have to be changed back to bytes and afterward to strings as SMS can hold just string qualities.

Once the message achieves the recipient, all through the method for unscrambling, the string must be changed to bytes; these bytes must be decoded to focus once more by methods for the mapping strategy, and in this manner, the focuses to bytes and to finish up to characters shape the message and just a while later the unscrambled major content can be seen by the beneficiary. The underneath figure portrays the whole procedure (Fig. 7).

Javax.Crypto is hampered with the classes and interfaces for crypto-graphical tasks. The crypto-graphical activities sketched out inside this bundle comprise the cryptographic classes, key generation and key assertion, and Message Authentication Code (MAC) generation. Support for cryptography incorporates respectively symmetric, deviated, square, and stream figures. This bundle also underpins secure streams and saved articles. A few of the classes gave inside this bundle are supplier based. The classes itself characterize a programming interface to that applications could compose. The class graph of the lightweight ECC execution is as shown in Fig. 8.

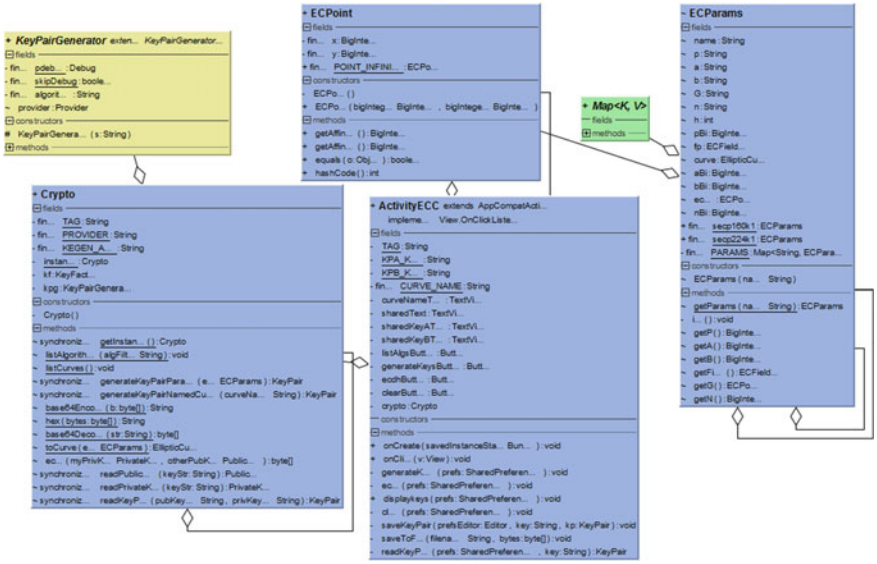

Fig. 8 Class diagram of ECC implementation in Android

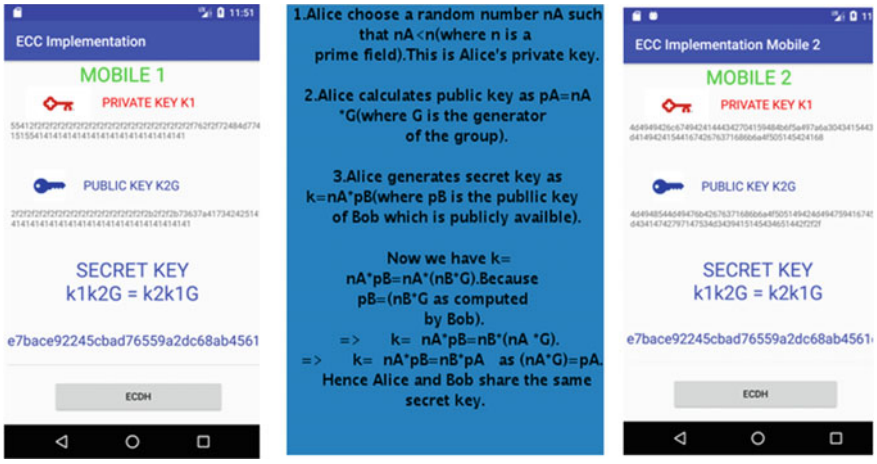

Fig. 9 Implementation of lightweight key exchange using ECC

While implementing the Elliptic Curve Cryptography on Android-based smartphones, we created two applications—Mobile-1 and Mobile-2. In order to communicate, the authentication is done by creating two keys—public and private. After sending the public key over a network, the two devices are able to create a common secret key. With this protocol, the two devices are able to create a session and are able to communicate on an insecure communication channel. The screenshots of two communicating devices and the description are shown in Figs. 8 and 9.

5 Proposed Key Exchange Protocol

Android-based smartphone operating system can be used to devise and execute new security protocols. In the previous section, a lightweight key exchange protocol was established using Elliptic Curve Cryptography. We implemented the ECDH algorithm to securely exchange the shared keys between two smartphone applications. In this section, we propose a new protocol which is better than the ECDH in terms of authentication. ECDH goes through an attack called the man-in-the-middle attack due to lack of authentication [11]. The enhanced protocol has been recommended in Table 3. The algorithm proposed performs a series of steps to set up a shared key (X · G) involving two mobile devices, while in cooperating a method to validate. The symbols used in the proposed protocol are shown in Table 2.

The performance analysis of the proposed protocol in opposition to ECDH is shown in Table 3. It is pertinent to mention that the proposed protocol takes relatively more memory (RAM and ROM) but at the same time, the man-in-the-middle (MIM) attack can be avoided (Table 4).

Table 2 Symbol table

Symbol	Description
X	Number chosen by Mobile 1 randomly
Y	Number chosen by Mobile 2 randomly
G	Point of elliptical curve called generator
X · G	Secret at Mobile 1
Y · G	Secret at Mobile 2
Ka	Private key of Mobile 1
Kb	Private key of Mobile 2
Pua = Ka · G	Public key of Mobile 1
Pub = Kb · G	Public key of Mobile 2

Table 3 Proposed protocol

Step	Mobile 1	Mobile 2
1	Chooses X · G as a secret	
2	Computes $X \cdot PU_b \cdot K_a$ and sends it to the Mobile 2	
3		Computes: $X \cdot PU_b \cdot K_a \cdot K_b^1$ $= X \cdot K_b \cdot G \cdot K_a \cdot K_b^{-1} = X \cdot G \cdot K_a$ Compute $X \cdot G \cdot K_a \cdot Y$ and send it to Mobile 1
4	Compute $X \cdot G \cdot K_a \cdot Y \cdot K_a^{-1} = X \cdot G \cdot Y$ and send it Mobile 2	
5		Compute the secret: $X \cdot G \cdot Y \cdot Y^{-1}$ $= X \cdot G$

Table 4 Performance/resistance of proposed procedure with ECDH

Protocol used	Addition operation	Multiplication operation	Inverse calculation	RAM used	ROM used	Resistance against MIM assault
ECDH	NIL	4	NIL	1250	15,690	No
Protocol proposed	NIL	5	4	1324	16,048	Yes

6 Conclusion

In this paper, an investigation and significance of Elliptical Curve Cryptography for tending to security and protection necessities in Android-based advanced mobile phones have been examined. As Elliptical Curve Cryptography devours a little measure of vitality and power, it turns out to be additional proper for asset limited cell phones. The crude security administrations like confirmation, secrecy, and key dispersion can be sensibly executed in advanced cells utilizing ECC. Protected and sound applications can be created on Android smartphone working framework by utilizing the security modules like ECDH, ECDSA, and ECIES. ECC can likewise be used for creating traditional conventions as confirmed in this paper. An upgraded key trade convention has been prescribed to overcome the downside of ECDH as far as man-in-the-center assault. With an unimportant working expense of RAM and ROM, the created convention gives impressive resistance against man-in-the-middle assault.

References

1. Bos, J.W., Halderman, J.A., Heninger, N., Moore, J., Naehrig, M., Wustrow, E.: Elliptic curve cryptography in practice. In: IACR Cryptologic, pp. 157–175 (2014)
2. Wu, X., Dandash, O., Le, P.D.: The design and implementation of a smartphone payment system based on limited-used key generation scheme. In: Proceedings of the Third International Conference on Information Technology New Generation ITNG 2006, vol. 2006, pp. 458–463 (2006)
3. Ramkumar, S.: Secure communication using elliptic curve cryptography on Android devices **2**(20), 11–13 (2016)
4. Pan, W., Zheng, F., Zhao, Y., Zhu, W.T., Jing, J.: An efficient elliptic curve cryptography signature server with GPU acceleration. IEEE Trans. Inf. Forensics Secur. **12**(1), 111–122 (2017)
5. Li, C.-T.: A new password authentication and user anonymity scheme based on elliptic curve cryptography and smart card. IET Inf. Secur. **7**(1), 3–10 (2013)
6. Sudha, G., Ganesan, R.: Secure transmission medical data for pervasive healthcare system using android. In: 2013 Proceedings of the International Conference on Signal Processing ICCSP, pp. 433–436 (2013)
7. Tawalbeh, L., Mowafi, M., Aljoby, W.: Use of elliptic curve cryptography for multimedia encryption. IET Inf. Secur. **7**(2), 67–74 (2013)

8. Khan, M.M., Bakhtiari, M., Bakhtiari, S.: An HTTPS approach to resist man in the middle attack in secure SMS using ECC and RSA. In: International Conference on Intelligent Systems Design and Applications ISDA, pp. 115–120 (2014)
9. Naik, M., Sindkar, A., Benali, P., Moralwar, C.: Secure and reliable data transfer on Android mobiles using AES and ECC algorithm
10. Moon, A.H., Ummer, K.: Authentication protocols for WSN using ECC and hidden generator. Int. J. Comput. Appl. **133**(13), 42–47 (2016)
11. Druml, N., et al.: A flexible and lightweight ECC-based authentication solution for resource constrained systems. In: 2014 Proceedings of the 17th Euromicro Conference on Digital System Design DSD 2014, pp. 372–378 (2014)
12. Ragunathan, P., Sambath, K., Karthik, V.: Accessing a network using a secure Android application. Int. J. Adv. Netw. Appl. **4**(1), 1503–1508 (2012)
13. Wang, L., Wang, H., Khan, M.K., He, D.: Lightweight anonymous key distribution scheme for smart grid using elliptic curve cryptography. IET Commun. **10**(14), 1795–1802 (2016)
14. Sarhan, H., Hafez, A.A., Safwat, A.: Secure Android-based mobile banking scheme. Int. J. Comput. Appl. **118**(12), 21–26 (2015)
15. Rangarajan, S., Ram, N.S., Krishna, N.V.: Securing SMS using cryptography. **4**(2), 285–288 (2013)
16. Dar, M.A., Parvez, J.: Security enhancement in Android using ellipic curve cryptography. Int. J. Secur. Appl. **11**(6), 27–34 (2017)
17. Simon, L., Anderson, R.: Security analysis of Android factory resets. In: 4th Mobile Security Technologies Workshop, p. 10 (2015)
18. Dar, M.A., Parvez, J.: Novel techniques to enhance the security of smartphone applications 32–36 (2016)
19. Dar, M.A., Parvez, J.: Enhancing security of Android & IOS by implementing need-based security (NBS). In: 2014 International Conference on Control, Instrumentation, Communication and Computational Technologies, ICCICCT 2014, pp. 728–733 (2014)
20. Dar, M.A., Parvez, J.: A live-tracking framework for Smartphones. In: 2015 IEEE International Conference on Innovations in Information, Embedded and Communication Systems, ICIIECS 2015, pp. 3–6 (2015)
21. Dar, M.A., Parvez, J.: Smartphone operating systems: evaluation & enhancements. In: 2014 International Conference on Control, Instrumentation, Communication and Computational Technologies, ICCICCT 2014, pp. 734–738 (2014)
22. Acosta, J.C., Mendoza, H., Medina, B.G.: An efficient common substrings algorithm for on-the-fly behavior-based malware detection and analysis. In: Proceedings of the IEEE Military Communications Conference MILCOM, pp. 1–6 (2012)
23. Alomari, M.A., Samsudin, K.: A framework for GPU-accelerated AES-XTS encryption in mobile devices. In: IEEE Region 10 International Conference Proceedings/TENCON, pp. 144–148 (2011)
24. Sanzziri, A., Nandugudi, A., Upadhyaya, S., Qiao, C.: SESAME: Smartphone enabled secure access to multiple entities. In: 2013 International Conference on Computer Communications and Networks (ICCCN), ICNC 2013, pp. 879–883 (2013)
25. Shukla, H., Singh, V., Choi, Y.H., Kwon, J., Hahm, C.H.: Enhance OS security by restricting privileges of vulnerable application. In: 2013 2nd IEEE Global Conference on Consumer Electronics GCCE 2013, pp. 207–211 (2013)

Isolator-Based Mutual Coupling Reduction of H-Shaped Patches in MIMO Antenna Applications

Ashim Kumar Biswas, Aparna Kundu, Anup K. Bhattacharjee and Ujjal Chakraborty

Abstract This paper presents an approach to reduce the mutual coupling (MC) between two H-shaped patches in a probe fed multi-input multi-output (MIMO) antenna. The antenna covers the frequency spectrum from 3.46 to 3.69 GHz with an impedance bandwidth of 6.5%. The proposed antenna is incorporated with a modified EBG structure as an isolator to increase the port isolation. The isolator reduces mutual coupling of about 30.5 dB between the two ports. The antenna offers very low envelope correlation coefficient (ECC < 0.0023) and provides a good radiation pattern in E- and H-plane.

Keywords Multi-input multi-output (MIMO) · Isolator
Envelope correlation coefficient (ECC) · Mutual coupling (MC)

1 Introduction

In today's world, MIMO antenna gradually becomes very popular in wireless communication systems. The MIMO-based digital communication in wireless link has recently emerged as one of the most important technical revolutions in modern communications [1]. In wireless communication system, high data rate and effective spectrum deployment are highly desirable which can be achieved by using multi-input multi-output (MIMO) antenna [2]. MIMO technology enhances the channel capacity, signal-to-noise ratio and reduces fading effects. However, the mutual cou-

A. K. Biswas (✉) · U. Chakraborty
Department of ECE, National Institute of Technology Silchar, Silchar, Assam, India
e-mail: ashim10@gmail.com

U. Chakraborty
e-mail: ujjal_dgp@yahoo.co.in

A. Kundu · A. K. Bhattacharjee
Department of ECE, National Institute of Technology, Durgapur, Durgapur, WB, India
e-mail: aparna_kundu27@rediffmail.com

A. K. Bhattacharjee
e-mail: akbece12@yahoo.com

U. Biswas et al. (eds.), *Advances in Computer, Communication and Control*, Lecture Notes in Networks and Systems 41, https://doi.org/10.1007/978-981-13-3122-0_34

pling of MIMO antenna reduces the system performances between several patches [3]. Therefore, efforts should be given to reduce the mutual coupling between the ports which is produced from the surface waves and near fields. Different approaches to reduce the mutual coupling between the ports of the MIMO antenna are reported in several literatures [1–6]. Electromagnetic band gap (EBG), complementary split ring resonator (CSRR), different shaped stubs, etc., are used in producing the port isolation in MIMO antennas operating in different frequency bands.

In this article, the mutual coupling reduction of a two-element MIMO antenna has been investigated. In the proposed design, an EBG structure is used as an isolator to reduce the mutual coupling between the two ports. The isolation between the ports is found around 30.5 dB. One EBG cell is connected to image of that to increase the port isolation. The designed patch elements are H-shaped that are employed on an FR4 substrate. The antenna operates in the frequency range from 3.46 to 3.69 GHz. The maximum port isolation is found at the resonant frequency of 3.58 GHz. The detail design procedure, parametric study, results and the conclusion are discussed step by step in proceeding sections.

2 Antenna Design

The unloaded two-element probe fed MIMO antenna is shown in Fig. 1a. The H-shaped patches are etched on a low-cost FR-4 epoxy substrate with a dielectric constant of 4.4 and loss tangent of 0.02. The dimension of the substrate is taken as 55 mm × 28 mm × 1.6 mm. Figure 1b shows the MIMO antenna loaded with an isolator. The isolator is formed by connecting one unit cell of EBG with its image through two connecting stubs as shown in Fig. 2a. The unit cell is formed by connecting some regular rectangular and round shaped blocks. The ground plane of the patch is modified with a round shape DGS as shown in Fig. 2b. Mutual coupling of patches is studied from the antenna shown in Fig. 1 with and without isolator. The design parameters of the antenna are summarized in Table 1. Before obtaining the proposed MIMO antenna a parametric observation is done using ANSYS HFSS [7].

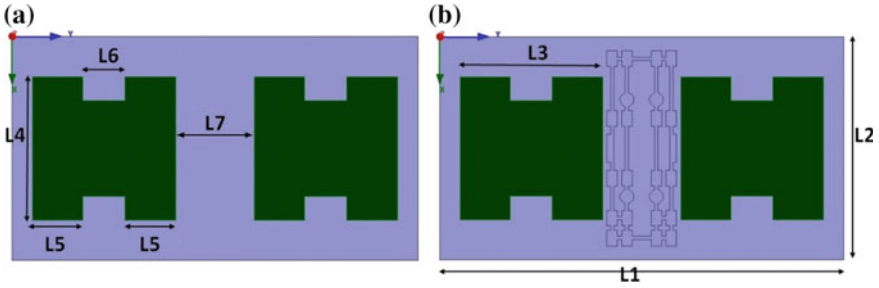

Fig. 1 Designed MIMO antenna **a** without EBG and **b** with EBG

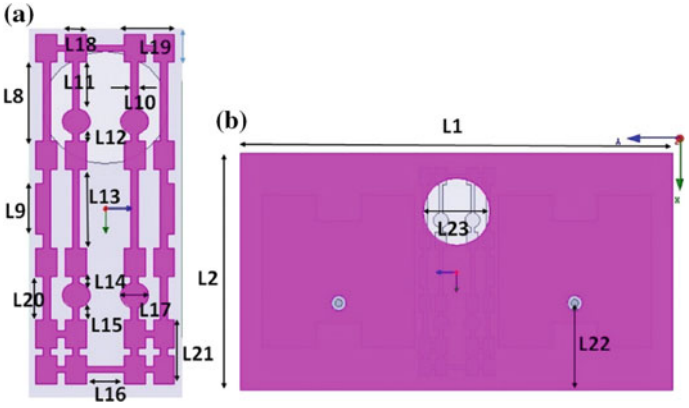

Fig. 2 Simulated **a** structure of the EBG and **b** ground plane of the antenna

Table 1 Antenna parameters

Dimensions	L_1	L_2	L_3	L_4	L_5	L_6	L_7	L_8	L_9
Length (mm)	55	28	20.5	20.5	7.25	6	11.2	6.32	4
Dimensions	L_{10}	L_{11}	L_{12}	L_{13}	L_{14}	L_{15}	L_{16}	L_{17}	L_{18}
Length (mm)	0.5	3.77	0.61	6.32	0.51	1.02	2.72	1.93	1.52
Dimensions	L_{19}	L_{20}	L_{21}	L_{22}	L_{23}				
Length (mm)	3.64	3.46	5.12	7.9	9				

3 Simulated Results and Analysis

As shown in Fig. 1, there are several parameters of the antenna that can affect the antenna performances. A parametric study is done by changing the length L_{11} to observe its effect on the antenna reflection coefficient and port isolation as shown in Fig. 3. A good reflection coefficient and mutual coupling are obtained at $L_{11} =$ 3.77 mm.

The final antenna covers the frequency ranges from 3.46 to 3.69 GHz with S_{11} (dB) minima at 3.58 GHz. The maximum mutual coupling reduction of about 30.5 dB is found at 3.58 GHz. The S_{11} and S_{12} curves of the final MIMO antenna are shown in Fig. 4.

The isolation characteristics of the MIMO antenna can be clearly understood from the electric field distributions shown in Fig. 5a, b. Considering the port 1 as an exciting port, we noticed that high coupling of electric field is observed in Fig. 5a, where no EBG structure is present. On the other hand, due to the insertion of an EBG between the patches, low coupling is produced as shown in Fig. 5b. To validate the performance of the proposed MIMO antenna, it should have very low envelope correlation coefficient (ECC) that can be calculated from the S-parameters by Eq. 1 [8]:

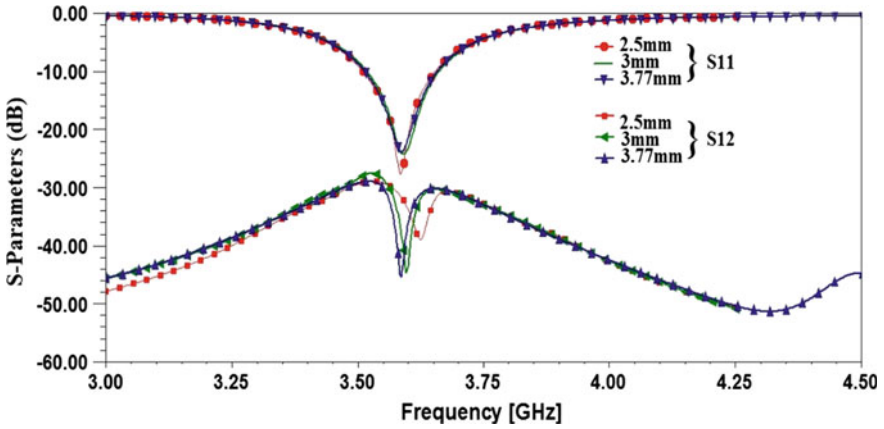

Fig. 3 Simulated S-parameters with the variation of length L_{11}

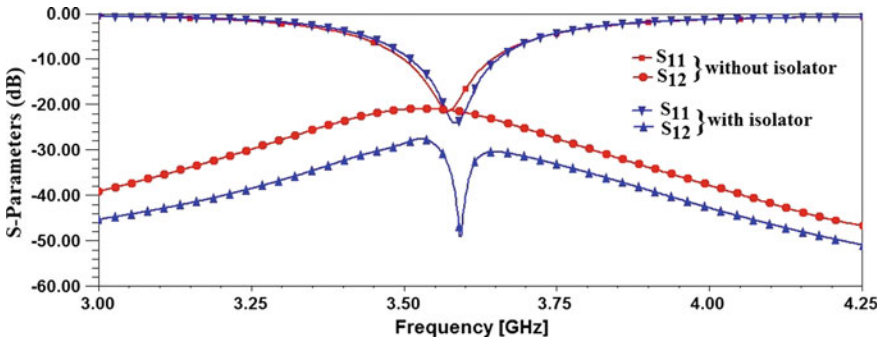

Fig. 4 Simulated S_{11} and S_{12} curve of the MIMO antenna with and without isolator

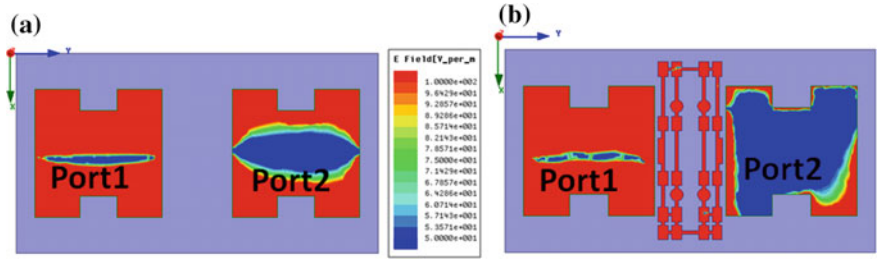

Fig. 5 Electric field distribution at 3.58 GHz **a** without EBG and **b** with EBG

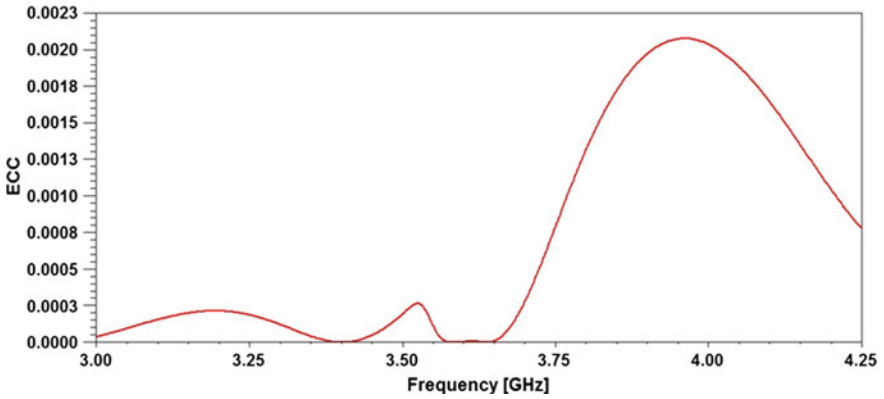

Fig. 6 Envelope correlation coefficient (ECC) curve of the MIMO antenna

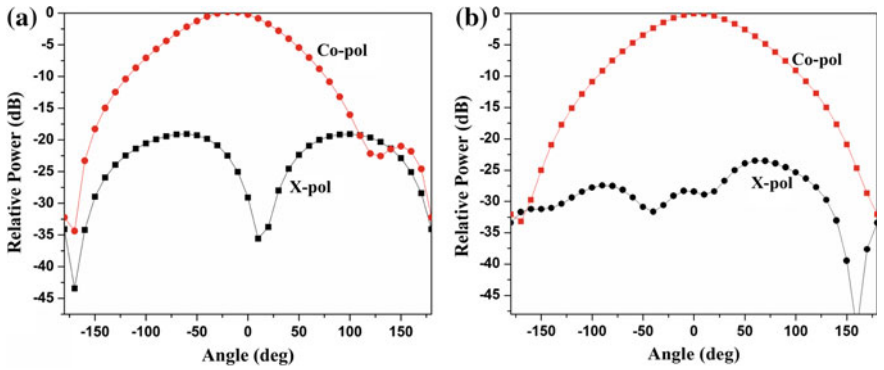

Fig. 7 Simulated Co-pol and X-pol radiation patterns in **a** E-plane and **b** H-plane

$$\mathrm{ECC} = \frac{|s_{11}^{*}s_{12} + s_{21}^{*}s_{22}|^{2}}{(1 - |S_{11}|^{2} - |S_{21}|^{2})(1 - |S_{22}|^{2} - |S_{12}|^{2})} \tag{1}$$

The ECC curve of the antenna is shown in Fig. 6. It shows that the value of ECC is less than 0.0023, which satisfies the ECC condition of MIMO antenna.

The co-polarization and cross polarization radiation pattern (simulated) of the proposed MIMO antenna are depicted in Fig. 7a, b. It is found to be good enough for the MIMO antenna characteristics.

4 Conclusions

The mutual coupling reduction of a compact probe fed MIMO antenna designed with two H-shaped patch elements is presented in this paper. It is found that the EBG structure with two antisymmetric unit cells is more effective to provide higher isolation between two MIMO ports. The simulated −10 dB bandwidth of the antenna is 230 MHz. The result shows that the mutual coupling is reduced by an amount of about 30.5 dB at 3.58 GHz. The envelope correlation coefficient is found to be very low (ECC < 0.0023). Moreover, the antenna provides good stable radiation patterns at 3.58 GHz.

References

1. Gesbert, D., Shafi, M., Shiu, D., Smith, P.J., Naguib, A.: From theory to practice: an overview of MIMO space-time coded wireless systems. IEEE J. Sel. Areas Commun. **61**(3), 281–301 (2003)
2. Hussain, R., Sharawi, M.S., Shamim, A.: An integrated four-element slot-based MIMO and a UWB sensing antenna for CR platforms. IEEE Trans. Antennas Propag. **66**(2), 978–983 (2018)
3. Indumati, S.: Isolation improvement of the MIMO antenna for wideband applications. In: International Conference on Intelligent Computing and Control Systems (ICICCS), India (2017)
4. Sarkar, D., Srivastava, K.V.: Compact four-element SRR-loaded dual band MIMO antenna for WLAN/WiMAX/WiF/4G-LTE/5G applications. Electron. Lett. **53**(25), 1623–1624 (2017)
5. Koga, Y., Yamagajo, T., Kai, M.: A novel multiband MIMO antenna for smartphones with a non-slit metal frame. In: Proceedings of Asia Pacific conferences, Malaysia (2017)
6. Obaid, W., Hamid, A. K.: Mutual Coupling reduction for MIMO CPW bow-tie aperture antennas. In: International Conference of Electrical and Computing Technologies and Applications (ICECTA), UAE, (2017)
7. HFSS ver.17, Ansoft Corporation. Pittsburgh, PA, USA
8. Blanch, S., Romeu, J., Corbella, I.: Exact representation of antenna system diversity performance from input parameter description. Electron. Lett. **39**(9), 705–707 (2003)

Negative Differential Resistance in Random Array of Silicon Nanorods

Sudipta Chakrabarty and Syed Minhaz Hossain

Abstract I-V measurement of electrochemically etched porous Si layer with planner electrode geometry shows negative differential resistance at high bias. This has been explained on the basis of band gap distribution of charge carriers in nanorods of different sizes distributed randomly in the active layer. The carriers follow the low resistive path through the larger rods at smaller applied voltage. But the probability of transport through smaller rods increases at higher voltage due to phonon bottleneck that hinders the relaxation of injected higher energy carriers at the band edges through phonon interaction. The effective charge carrier concentration decreases for smaller rods resulting in the observed negative differential resistance. The flow of charge carrier through nanorods is modelled as random walk in 2D and the simulated I-V characteristics shows a qualitative matching with the experimentally obtained ones.

Keywords Si nanorod · Negative differential resistance · Phonon

1 Introduction

Since the discovery of photoluminescence (PL) from porous silicon (Si) [1], a quantum sponge-like nanostructure [2], the mechanism of light emission has been studied widely [3–6], but the development of an efficient electroluminescent device based on this nanostructure has remained largely elusive till date. This is primarily because charge transport mechanism through the complex structure of porous Si containing nanocrystalline Si-core surrounded by oxide shell and randomly distributed voids [3, 6] is yet to be well understood [7]. In recent studies, tunnelling oscillation through the oxide layer present around individual Si nanocrystal core has been reported [8] by our group. Studies on charge transport through nanostructured porous Si show the possibility of many different transport mechanisms dominating at different voltage

S. Chakrabarty (✉) · S. M. Hossain
Department of Physics, Indian Institute of Engineering Science and Technology, Shibpur, Howrah 711103, India
e-mail: csudipta.rs2016@physics.iiests.ac.in

U. Biswas et al. (eds.), *Advances in Computer, Communication and Control*, Lecture Notes in Networks and Systems 41, https://doi.org/10.1007/978-981-13-3122-0_35

range along with the onset of resistive switching at suitable bias [9, 10]. Negative differential resistance is also observed in transport through porous Si [11] with a different device geometry.

We have obtained negative differential resistance in I-V characteristics of a porous Si prepared by the standard process of electrochemical etching [12] in HF–ethanol electrolyte. Metal contacts are established on the top of the porous Si surface. The porous Si layer contains a random distribution of size of the nanorods that may result in a band-gap variation due to quantum confinement effect [13]. For the smaller particles, the energy band gap is higher leading to less carrier concentration and hence lower conductivity. Moreover, smaller the particle, lesser is the phonon density of states arising from phonon confinement [14, 15]. At smaller applied voltage, the carriers try to find the low resistive path offered by the larger particles. But at higher voltage, the probability of transport through smaller particles having higher band gap increases due to the phonon bottleneck [16] because relaxation of high energy injected carriers becomes slower due to lesser availability of suitable phonon in nano-regime. The carrier mobility as well as the effective number of charge carrier decreases for smaller rods resulting in negative differential resistance. This device has the potential to be used in oscillators and amplifiers at microwave frequency if the negative resistance region may be tuned with the etching time, pore size and porosity of the porous Si layer.

2 Experimental

Porous Si of thickness ~1.5 μm and porosity ~70% is synthesized on boron-doped p-type electro-polished (100) Si wafer of resistivity ~8 Ω cm and thickness ~380 μm by electrochemical etching [12] for 5 min with current density 20 mA/cm^2 in a solution containing 24% HF and Ethanol in equal volume. Structural analysis of the porous Si layer has been done using AFM microscope (Veeco DI CP II). Two Al pads of 2 mm diameter and ~200 nm thickness are deposited by thermal evaporation on porous Si layer to establish metal contact. DC I-V characteristics of the samples have been recorded at room temperature using Keithley 2602B Sourcemeter.

3 Results and Discussion

Figure 1a shows the AFM topographic image for the electrochemically etched porous Si layer. One of the *Z*-height scan profiles is shown in Fig. 1b for a particular region indicated in Fig. 1a. From this Z-height profile, the presence of nanorods of different sizes is observed.

The inset **a** in Fig. 2 shows the schematic cross-sectional view of the device where the metal connection is taken from Al deposited on the top of the porous Si layer. DC I-V characteristics of the samples recorded at room temperature are shown in

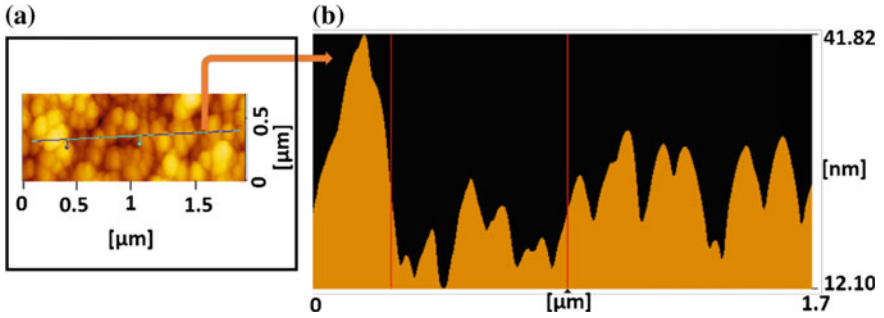

Fig. 1 **a** Two-dimensional topographic AFM image of porous Si layer, **b** Z-height scan profile showing the size of the nanorods and pores

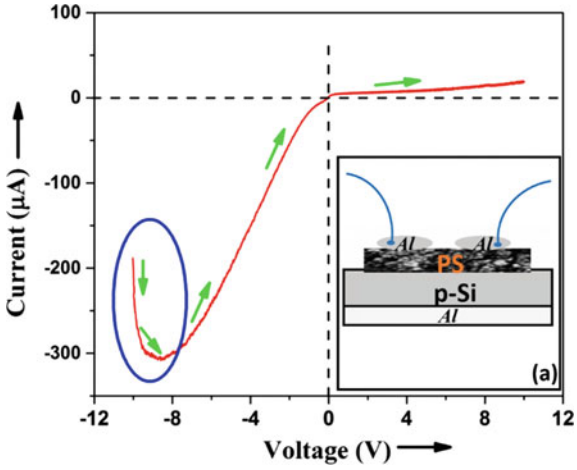

Fig. 2 I-V characteristics with inset **a** showing the schematic cross-sectional view of the device

Fig. 2. The most salient feature of the characteristics is a decrease of current with increasing voltage at around 9 V during reverse scan resulting in negative differential resistance through Si nanorods.

The rods of smaller diameter are much more resistive than the larger ones. This is because of two reasons. First, due to quantum confinement effect, the electronic energy band gap increases in smaller particles leading to less number of free carriers at a given temperature [11, 13]. Second, the carrier mobility decreases with decreasing size of the crystallite [17]. So, charge carriers flow through larger rods at low bias as they offer lower resistance to the carrier. However, at high bias, the carriers can flow through the smaller rods overcoming the band-gap discontinuities present between particles of different sizes. In fact, at high bias, it becomes difficult for a charge carrier injected with higher energy to relax at the band edge of a particle with larger size, hence smaller band gap, through phonon scattering as the availability of phonon

with suitable energy and momentum becomes lesser in nano-dimension [16]. As a result, at higher applied bias the probability of transport through the smaller nanorods becomes comparable to that through larger particles at lower bias. Transport through smaller particles and relaxing slowly at the band edge offers lower effective carrier concentration. This leads to a net decrease in the effective conductivity of the medium at higher bias.

Figure 3a, b show the band diagram of a randomly selected portion of the porous Si layer containing two nanorods of different sizes at low bias. At low bias, charge carriers can flow easily through the larger rods having smaller band gap ($E_{g1} > E_{g2}$). But transport from a larger rod of smaller band gap $\left(E_{g1}\right)$ to a smaller rod having higher band gap ($E_{g1} < E_{g2}$) is less probable (shown in Fig. 3b) as, in this case, the carrier has to overcome a barrier of height $\left(E_{g2} - E_{g1}\right)$. But the scenario becomes different when a high voltage is applied ($V_2 \gg V_1$). The larger particles have lower band gap, and hence during transport, injected carriers at higher voltage need to lose energy through phonon scattering to relax near the band edge of the second particle [17] such that the effective density of states becomes maximum. However, in systems of nano-dimensional crystallites, all the phonon modes are not available [14, 15] as smaller the size, lesser the density of phonon states. In this situation, transport through smaller particles of higher band gap becomes preferable (Fig. 3c). This is because the transport of carriers through a larger rod becomes constrained due to phonon bottleneck as shown in Fig. 3d.

Current density (j) is a linear function of carrier concentration (n) and drift velocity (v) of an injected carrier [18]. An injected carrier collides with impurities, lattice imperfections and phonons, and hence, the movement of an injected carrier is modelled as 2D random walk problem at fixed temperature. The average drift velocity of an injected carrier is simulated considering the displacement along the direction of applied bias as a linear function of the applied voltage. There is a random distribution of size of the nanorods, and the band gap strongly depends on size according to the model proposed by M. V. Wolkin for oxidized Si nanostructure as shown in Eq. (1) [19, 20].

$$E_{g_{eff}} = E_g + \frac{3.42}{a^{1.29}} \tag{1}$$

where the first term is the band gap of bulk Si, the second term is the change in band gap and a is the size of the nanorod.

At higher voltage, the smaller particles having higher band gap will be preferred, and hence, the average band gap ($E^{av}_{g_{eff}}$) of the rods taking part in transport will increase with increasing voltage. So the effective carrier concentration is expected to decrease exponentially as the carrier concentration varies with band gap through the complex network of the nanorods having randomly selected size as shown in Eq. (2)

$$n = n_0 e^{-\frac{E^{av}_{g_{eff}}}{K_B T}} \tag{2}$$

So, the current density can be expressed as

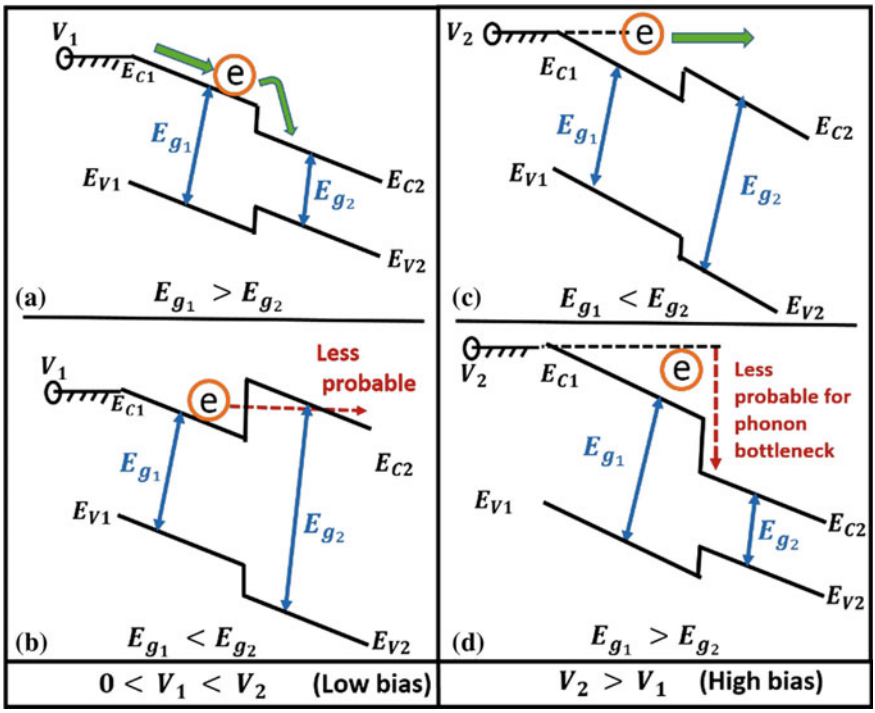

Fig. 3 Schematic band diagram for the randomly selected two adjacent nanorods of different sizes during low and high biasing

$$j = n_0 q v_{av} e^{-\frac{E_{g_{eff}}^{av}}{K_B T}} \tag{3}$$

The effective drift velocity of the injected carrier has been estimated using a routine for 2D random walk through the porous network as a function of applied bias. The drift velocity is expected to increase with increasing voltage for a given particle. For a particular injected carrier the effective drift velocity has been estimated averaging over one million trials. A distribution of particle size has been assumed randomly in a 200×200 square matrix. The weight factor towards forward transition has been estimated on the basis of the difference $\left|E_g - qV\right|$. Here E_g is the band gap of the target particle, and V is the applied voltage. The transition has been assumed to take place towards the particle having a minimum value of $\left|E_g - qV\right|$ among the five available nearest neighbour particles in the forward direction. An average of the band gap of the particles chosen during forward transition of the random walk has been calculated. This has been used to calculate the effective carrier concentration using Eq. (2).

Hence, the effective current density has been obtained by multiplying the average drift velocity with the effective carrier concentration of the system as given in Eq. (3). The result is shown in Fig. 4 with the inset showing the negative differential resistance

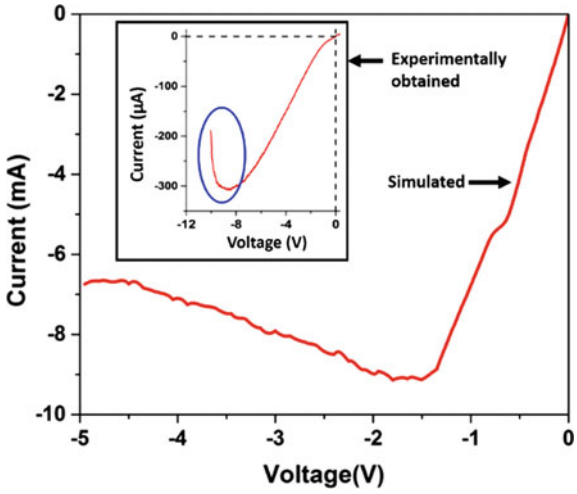

Fig. 4 Simulated I-V graph with the inset showing the negative differential resistance region in experimentally obtained I-V characteristics

in I-V characteristics obtained experimentally. The region of negative differential resistance is obtained near 1.5 V in the simulated graph whereas, experimentally it has been found at nearly 9 V. There is a clear quantitative mismatch in current obtained in the simulated graph with that in the experimentally obtained one. This discrepancy may be due to the fact that we have modelled the transport of charge carriers in 2D and have considered a random orientation of the particles of different sizes on the two-dimensional porous Si matrix. Hence, it would not be wise to expect a quantitative matching between the experimental and simulated results unless we modify the simulation routine for 3D and consider minute details of the transport through the Si nanostructures, which warrants a separate full work.

4 Conclusion

In conclusion, negative differential resistance is obtained in I-V characteristics measured from two Al top contacts on porous Si layer containing randomly distributed thick and thin nanorods. The probability of transport through smaller rods increases at higher voltages due to phonon bottleneck in nano-dimension. Consequently, the number of effective charge carrier decreases resulting in negative differential resistance. We have adopted a simple 2D random walk method to simulate the transport of charge carriers through the randomly interconnected network of particles of different sizes in nano-dimension. This simple model qualitatively explains the basic nature of the observed negative differential resistance. The model needs to be extended to three

dimensions with consideration of microscopic details of the individual nanorods for exact quantitative agreement with the experimental results.

Acknowledgements Sudipta Chakrabarty acknowledges Department of Science and Technology (DST), Government of India for INSPIRE fellowship.

References

1. Canham, L.T.: Silicon quantum wire array fabrication by electrochemical and chemical dissolution of wafers. Appl. Phys. Lett. **57**(10), 1046–1048 (2012). https://doi.org/10.1063/1.103561
2. Bisi, O., Ossicini, S., Pavesi, L.: Porous silicon: a quantum sponge structure for silicon based optoelectronics. Surf. Sci. Rep. **38**, 1–126 (2000)
3. Ray, M., Jana, K., Bandyopadhyay, N.R., Hossain, S.M., Navarro-Urrios, D., Chattyopadhyay, P.P., Green, M.A.: Blue–violet photoluminescence from colloidal suspension of nanocrystalline silicon in silicon oxide matrix. Solid State Commun. **149**, 352–356 (2009). https://doi.org/10.1016/j.ssc.2008.12.023
4. Brown, S.L., Vogel, D.J., Miller, J.B., Inerbaev, T.M., Anthony, R.J., Kortshagen, U.R., Kilin, D.S., Hobbie, E.K.: Enhancing silicon nanocrystal photoluminescence through temperature and microstructure. J. Phys. Chem. C **120**, 18909–18916 (2016). https://doi.org/10.1021/acs.jpcc.6b05837
5. Dasog, M., De los Reyes, G.B., Titova, L.V., Hegmann, F.A., Veinot, J.G.C.: Size vs surface: tuning the photoluminescence of freestanding silicon nanocrystals across the visible spectrum via surface groups. ACS Nano. **8**, 9636–9648 (2014). https://doi.org/10.1021/nn504109a
6. Ray, M., Sarkar, S., Bandyopadhyay, N.R., Hossain, S.M., Pramanick, A.K.: Silicon and silicon oxide core-shell nanoparticles: structural and photoluminescence characteristics. J. Appl. Phys. **105**, (2009). https://doi.org/10.1063/1.3100045
7. Fauchet, M.: Photoluminescence and electroluminescence from porous silicon. J. Lumin. **70**, 294–309 (1996). https://doi.org/10.1016/0022-2313(96)82860-2
8. Ghanta, U., Ray, M., Bandyopadhyay, N.R., Hossain, S.M.: Unipolar resistive switching and tunneling oscillations in isolated Si–SiOx core–shell nanostructure. Nanotechnology **27**, 455702 (2016). https://doi.org/10.1088/0957-4484/27/45/455702
9. Chakrabarty, S., Mandal, S., Ghanta, U., Das, J., Hossain, S.M.: Current controlled switching in Si/PS/a-Si heterostructure. Mater. Today Proc. **5**, 9790–9797 (2018). https://doi.org/10.1016/j.matpr.2017.10.168
10. Ghanta, U., Singh, S., Ray, M., Bandyopadhyay, N.R., Ganapathy, S., Hossain, S.M.: Electrical transport through array of electrochemically etched silicon nanorods. Phys. Status Solidi **214**, 1600879 (2017). https://doi.org/10.1002/pssa.201600879
11. Lee, M., Chu, C., Tseng, Y., Shyr, J., Kao, C.: Negative differential resistance of porous silicon. IEEE Electron Device Lett. **21**, 587–589 (2000). https://doi.org/10.1109/55.887474
12. Hossain, S.M., Das, J., Dutta, S.K., Saha, H.: Mechanism and simulation of uniform nanowires of porous silicon growth on p-si substrate. Int. J. Nanosci. **5**, 69–90 (2006). https://doi.org/10.1142/S0219581X0600419X
13. Sanders, G.D., Chang, Y.: Optical properties of free-standing silicon quantum wires. Appl. Phys. Lett. **60**, 2525–2527 (1992). https://doi.org/10.1063/1.106927
14. Bhattacharyya, S., Samui, S.: Phonon confinement in oxide-coated silicon nanowires. Appl. Phys. Lett. **84**, 1564–1566 (2004). https://doi.org/10.1063/1.1651648
15. Ghosh, R., Pal, A., Giri, P.K.: Quantitative analysis of the phonon confinement effect in arbitrarily shaped Si nanocrystals decorated on Si nanowires and its correlation with the photoluminescence spectrum. J. Raman Spectrosc. **46**, 624–631 (2015). https://doi.org/10.1002/jrs.4704

16. Inoshita, T., Sakaki, H.: Electron-phonon interaction and the so-called phonon bottleneck effect in semiconductor quantum dots. Phys. B Condens. Matter. **227**, 373–377 (1996). https://doi.org/10.1016/0921-4526(96)00445-0
17. Sze, S.M. Ng, K.K.: Physics of Semiconductor Devices. Wiley (2007)
18. Kittel, C.: Introduction to Solid State Physics. Wiley (2015)
19. Hossain, S.M., Chakraborty, S., Dutta, S.K., Das, J., Saha, H.: Stability in photoluminescence of porous silicon. J. Lumin. **91**, 195–202 (2000). https://doi.org/10.1016/S0022-2313(00)00225-8
20. Wolkin, M.V., Jorne, J., Fauchet, P.M., Allan, G., Delerue, C.: Electronic states and luminescence in porous silicon quantum dots: the role of oxygen. Phys. Rev. Lett. **82**, 197–200 (1999). https://doi.org/10.1103/PhysRevLett.82.197

Band Calculation of 2D Square Lattice Using the Method of Successive Over-Relaxation

Shayari Basu and Syed Minhaz Hossain

Abstract Successive over-relaxation method has been adopted to find the wave functions corresponding to the band states and surface states and also to solve energy dispersion relation for 2D finite crystal of desirable shape and size with periodic and non-periodic potentials. This method enables us to study the finite size effect in 2D crystals without costing too much computer time like ab initio methods. The major advantage of over-relaxation method is its simplicity as well as its usefulness in both lower and higher dimensional finite systems.

Keywords Successive over-relaxation · Semiconductor · Surface · 2D system

1 Introduction

Physics of finite systems are of great interest due to their potential applications in electronics, photonics, photovoltaics, and even in medicine [1, 2]. For such systems along with reduction in dimension and size, the surface-to-volume ratio becomes very large, and the electronic property is primarily governed by the surface/interface states which are found only at the atomic layers close to the surface. The termination of a semiconductor crystal with a surface causes deviation from perfect periodicity which leads to a change in the crystal potential leading to the alteration of the electronic band structure along with the onset of surface states at the Brillouin zone boundary [3, 4]. Studies on such states need band calculation for finite systems, which is a good way to visualize the energy dispersion relation, the bandgap, and the possible electronic transitions in nanostructured materials [3–5].

S. Basu (✉) · S. M. Hossain
Department of Physics, Indian Institute of Engineering Science and Technology, Shibpur, Howrah 711103, India
e-mail: shayari.bs@gmail.com

U. Biswas et al. (eds.), *Advances in Computer, Communication and Control*, Lecture Notes in Networks and Systems 41, https://doi.org/10.1007/978-981-13-3122-0_36

To find eigenenergies and wave functions, one should solve the Schrödinger equation in a realistic pseudopotential, which often has to be found in a self-consistent way. For 1D finite crystal, the semi-infinite linear chain model is useful, and the potential along the atomic chain is assumed to vary as a cosine function [6, 7]. In one dimension, the shooting method is used to solve boundary value problem by reducing it to an initial value problem followed by a root-finding routine [8]. For bound-state problems, the energy is not known in advance and the iteration starts from one known boundary condition and is repeated for different energies until the correct boundary condition at the other end is satisfied. But the disadvantage of this method is that it cannot be applicable for non-separable potentials in higher dimensional systems because the boundary conditions must be satisfied on all points at the boundary. Matrix method can also be used to solve time-independent Schrödinger equation [9] by assuming plane wave basis sets and reducing it to an eigenvalue problem. But however, in this case, the finite size effect is not reflected in band calculation. The other rigorous method for band calculation in such systems is ab initio DFT methods that take tremendous computer hour for a 2D finite system even of size of the order of 10 nm [10].

Successive over-relaxation method is a variant of Gauss–Seidel method resulting in faster convergence and can be used to solve time-independent Schrödinger equation [11]. In this paper, we have adopted this method for obtaining ground state along with other low lying excited states and surface state in a 2D finite square lattice of desirable dimension. Energy dispersion relation has been solved numerically which is in good agreement with the theoretical result for empty lattice model, and hence, the algorithm has been extended to a square lattice with 2D periodic potential. The algorithm does not require any sophisticated background in numerical analysis. It is reasonably intuitive and easy to code for lower as well as higher dimensional systems.

2 Numerical Method

Surface state arises as the solution of time-independent Schrödinger equation in the framework of nearly free electron approximation [3, 6]. Time-independent Schrödinger equation can be written as

$$(-\nabla^2 + V(\vec{r}) - E)\psi(\vec{r}) = 0. \tag{1}$$

Our aim is to solve this equation numerically for obtaining ground states and other excited states for periodic potential of the form $v(\vec{r}) = v_0 \cos\left(\vec{G} \cdot \vec{r}\right)$ where v_0 is the potential form factor, E is the energy eigenvalue, and $\vec{G} = \hat{\mathbf{I}}(2\Pi/a) + \hat{\mathbf{J}}(2\Pi/b)$ is the reciprocal lattice vector. Here, we are using natural units where $\frac{\hbar 2}{2m} = 1$.

Now, any second-order elliptic equation, e.g., Laplace Equation, while solving by finite difference method [11] always reduces to an equation containing the values of

ψ at any grid point along with the corresponding values at the nearest neighboring points. Hence, this equation for all grid points (i, j) may be converted to a system of linear equations. Rewriting Eq. (1), we obtain

$$\psi_{i-1,j} + \psi_{i+1,j} + \psi_{i,j+1} + \psi_{i,j-1} - [4 - h^2(E - V(\vec{r}))]\psi_{i,j} = 0. \tag{2}$$

The uniqueness of the above equation lies in the fact that each interior point is directly linked with the neighboring points of the two-dimensional grid of constant mesh width h. Running two nested loops over i and j between 1 and N for solving the set of linear equations, we obtain a system of $(N \times N)$ equations which can be solved by any convenient method to get $\psi_{i,j}$ at all nodes. There are a number of implicit methods for solving the elliptic partial differential equation but it becomes unmanageable and involves more computational complexity for higher dimensional systems. The way for increasing the simplicity and accuracy is to modify the scheme for solving Eq. (2), and one of the simplest techniques used for this purpose is the successive over-relaxation (SOR) method [11, 12].

The algorithm we have used is based on successive over-relaxation method for solving time-independent Schrödinger equation which is easily extendible over an $(N \times N)$ grid of the 2D square lattice.

The algorithm is as follows:

(1) At first, initialize the trial wave function as the free particle wave function $\psi_{in}(x, y) = \sin\left(\frac{m\pi x}{L}\right)\sin\left(\frac{n\pi y}{L}\right)$ corresponding to the empty lattice approximation, where L is the size of the square system.

(2) Calculate the expectation value of the Hamiltonian operator, $\hat{\mathrm{H}}\left(= -\nabla^2 + \mathrm{v}(\vec{\mathrm{r}})\right)$ as

$$\langle E\rangle = \frac{\langle\psi_{in}(\vec{r})|H|\psi_{in}(\vec{r})\rangle}{\langle\psi_{in}(\vec{r})|\,\psi_{in}(\vec{r})\rangle}, \tag{3}$$

which has been taken as the initial guess for the energy.

(3) Run the loop over all interior grid points to calculate intermediate values of $\psi_{i,j}$ given as

$$U = \frac{\psi_{i-1,j} + \psi_{i+1,j} + \psi_{i,j+1} + \psi_{i,j-1}}{[4 - h^2(\langle E\rangle - V(\vec{r}))]}. \tag{4}$$

(4) Update the values of $\psi_{i,j}$ calculated with the weight factor ω using the following formula:

$$\psi_{i,j}^{new} = \psi_{i,j}^{old} + \omega(U - \psi_{i,j}^{old}). \tag{5}$$

Here, ω is called relaxation parameter. It must be chosen properly for speeding up the algorithm. We have taken $\omega = 1.2$ for fastest convergence.

(5) Update the modified wave functions, i.e., repeat the steps from (2) to (4) until $\langle E \rangle$ and $\psi(\vec{r})$ no longer changes within the desired accuracy at all points on the grid.
(6) Normalize the wave function.

Finally, we obtain $\psi_{i,j}$ for which the eigenenergy converges to the correct value within the desired accuracy. After finding ground state, other higher order states and surface states have been calculated with a minor modification to the algorithm. As the surface states are expected to vanish inside the bulk, the initial guess, in this case, has been assumed as the corresponding empty lattice wave function multiplied by an exponential pre-factor.

3 Results

To verify the algorithm, we have solved the problem of 1D finite crystal and compared the results with those as obtained from the well-known shooting method commonly used in similar system [11]. Figure 1 shows the normalized wave functions corresponding to (a) ground state, (b) first excited state, (c) ninth state, and (d) surface state as obtained from (i) shooting method and (ii) successive over-relaxation for a 1D finite crystal with potential, $\mathrm{v(x)} = \mathrm{v_0} \cos \frac{2\pi \mathrm{x}}{\mathrm{a}}$, where $\mathrm{a} = 1.0$ and $\mathrm{v_0} = 5.0$. The system size has been chosen as $\mathrm{L} = 10$ atomic unit.

From this figure, it is evident that the band states within the Brillouin zone and surface state at the Brillouin zone boundary as calculated from successive over-relaxation are in good agreement with those of the results obtained using shooting method.

Figure 2 depicts the band diagrams as obtained from shooting method and successive over-relaxation for a 1D finite crystal with the same dimension and potential. On confirmation of this agreement in 1D system, we have extended the algorithm to 2D square lattice with finite boundary and periodic potential. Figure 3 shows the plots of four typical wave functions corresponding to (a) ground state (for $\mathrm{m} = \mathrm{n} = 1$), (b) band state ($\mathrm{m} = 1, \mathrm{n} = 9$), and surface states in (c) (01) direction ($\mathrm{m} = 1, \mathrm{n} = 10$) and (d) (11) direction ($\mathrm{m} = \mathrm{n} = 10$) for a 2D square lattice (1000×1000) with non-separable potential of the form $\mathrm{v(x, y)} = \mathrm{v_0} \cos\left(\frac{2\pi \mathrm{x}}{\mathrm{a}} + \frac{2\pi \mathrm{y}}{\mathrm{b}}\right)$ with $a = \mathrm{b} = 1.0$ and $\mathrm{v_0} = 5.0$. The ground state shown in Fig. 3a is a truncated 2D plane wave modulated by the crystal potential as expected from Bloch's theorem. The wave function depicted in Fig. 3b corresponds to the edge of the first band along (01) direction, which is also a two-dimensional truncated Bloch wave as expected. Figure 3c, d correspond to the two lowest lying surface states at the edge of the zone boundary along (01) and (11) directions, respectively. The energy corresponding to these states lie with energies in the forbidden gap $\left(E_g\right)$ and the wave functions decay exponentially toward the crystal boundary as expected. Thus Surface states are of aperiodic nature [3] which results due to the change in electron potential associated solely with the crystal termination.

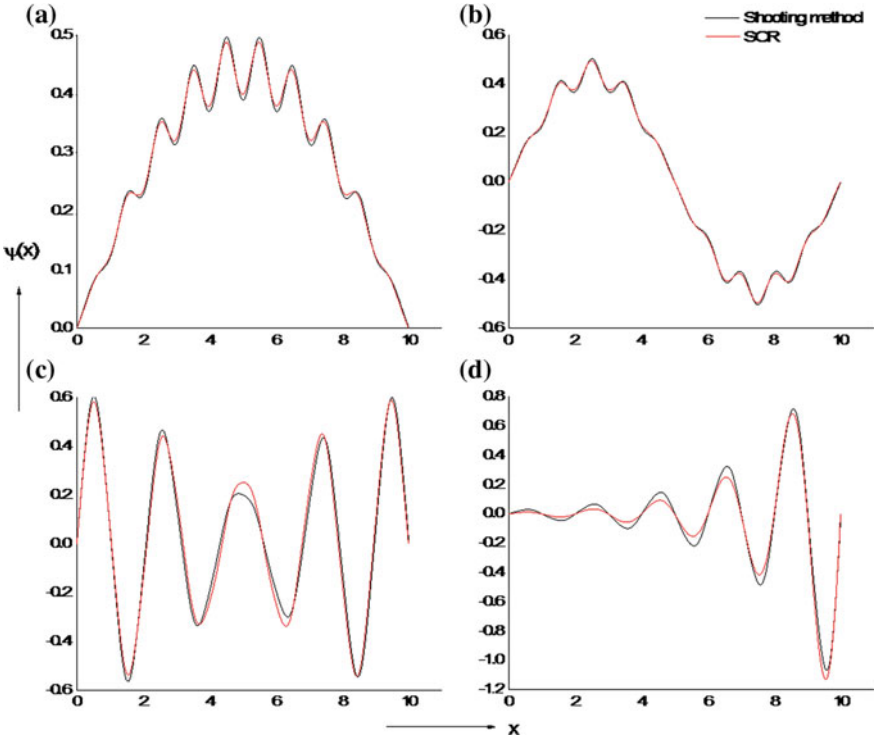

Fig. 1 Normalized wave functions corresponding to **a** ground state, **b** first excited state, **c** ninth state, and **d** surface state as obtained from (i) shooting method and (ii) successive over-relaxation for a 1D finite crystal with $L = 10,\ a = 1.0,$ and $v_0 = 5.0$

We have checked the validation of the obtained results for the same system with separable potential of the form $v(x, y) = v_0\left[\cos\frac{2\pi x}{a} + \cos\frac{2\pi y}{b}\right]$ which is shown in Fig. 4, and it represents the corresponding plots of four typical wave functions corresponding to (a) ground state (for $m = n = 1$), (b) band state ($m = 1, n = 9$), and surface states in (c) (01) direction ($m = 1, n = 10$) and (d) (11) direction ($m = n = 10$) with $a = b = 1.0$ and $v_0 = 5.0$.

From Table 1, it has been observed that for 2D square system with separable potential, the eigenenergy corresponding to any state matches with the combination of the respective values of eigenenergies in 1D system which is also theoretically expected. Eigenenergies obtained with non-separable potential slightly differ from those obtained with separable potential for the same system.

Calculated E-K diagram for 2D square lattice with closed circles at the zone boundaries is shown in Fig. 5. This figure shows the first five lower lying bands of the system in both (01) and (11) directions, respectively. The figure indicates finite size effects like discretization of energy bands along with the emergence of

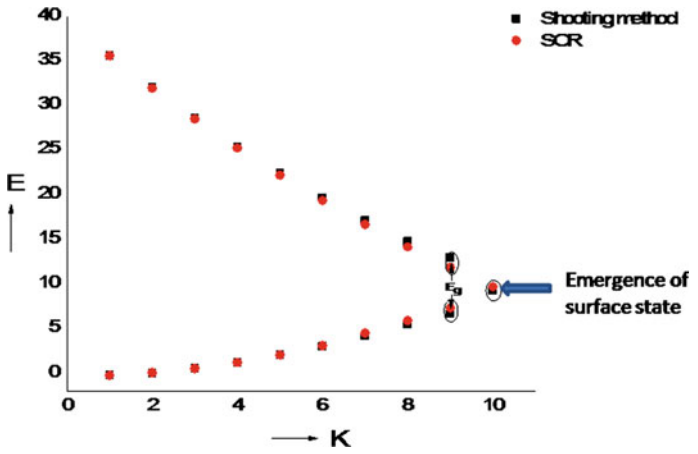

Fig. 2 E-K diagram as obtained using **a** shooting method and **b** successive over-relaxation for a 1D finite crystal with L = 10, a = 1.0, and $v_0 = 5.0$

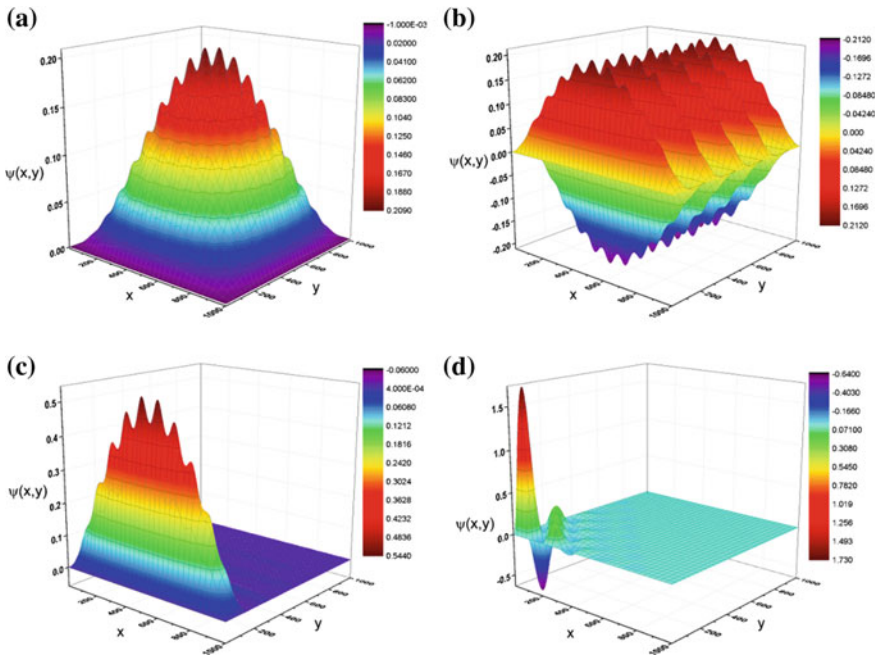

Fig. 3 Wave functions corresponding to **a** ground state (m = n = 1), **b** band edge state (m = 1, n = 9), and surface states in **c** (01) direction (m = 1, n = 10) and **d** (11) direction (m = n = 10) for a 2D square lattice (1000 × 1000) with non-separable potential (a = b = 1.0 and $v_0 = 5.0$)

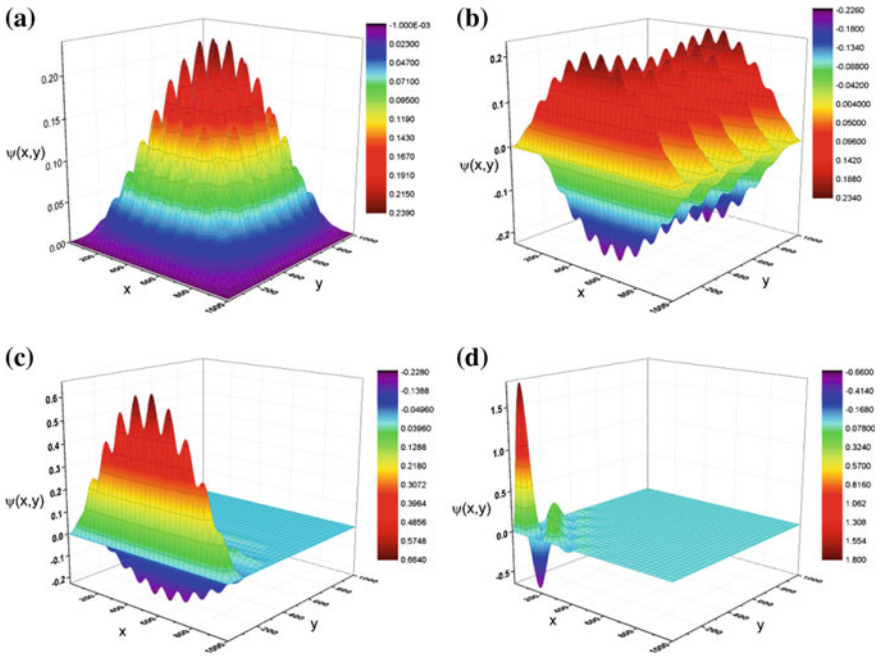

Fig. 4 Wave functions corresponding to **a** ground state (m = n = 1), **b** band state (m = 1, n = 9), and surface states in **c** (01) direction (m = 1, n = 10) and **d** (11) direction (m = n = 10) for a 2D square lattice (1000 × 1000) with separable potential (a = b = 1.0 and $v_0 = 5.0$)

Table 1 Eigenenergies as obtained using SOR method in 1D and 2D systems for separable and non-separable potential, respectively, with L = 10.0, a = b = 1.0 and $v_0 = 5.0$

Energies in case of 1D system with potential of the form: $v(x) = v_0 \cos \frac{2\pi x}{a}$	Energies for 2D system (1000 × 1000) with	
	Separable potential of the form: $v(x, y) = v_0\left[\cos \frac{2\pi x}{a} + \cos \frac{2\pi y}{b}\right]$	Non-separable potential of the form $v(x, y) = v_0 \cos\left(\frac{2\pi x}{a} + \frac{2\pi y}{b}\right)$
$E_1 = -0.219$	$E_{1,1} = -0.421$	$E_{1,1} = 0.047$
$E_9 = 6.667$	$E_{1,9} = 8.089$	$E_{1,9} = 7.910$
$E_{10} = 9.475$	$E_{1,10} = 8.490$	$E_{1,10} = 10.959$
	$E_{10,10} = 18.149$	$E_{10,10} = 19.877$

surface states at the Brillouin zone boundaries. The marked points labeled as Γ, X, M correspond to high symmetry points in the Brillouin zone.

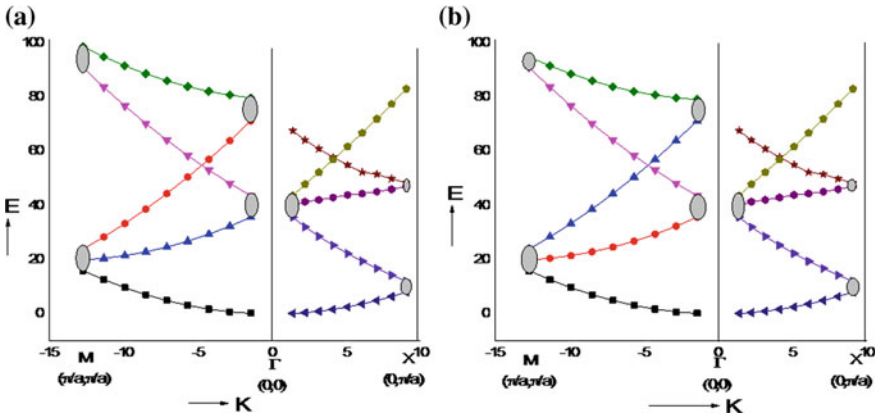

Fig. 5 E-K diagram for 2D square lattice (1000 × 1000) for **a** non-separable and **b** separable potentials, with a = b = 1.0 and $v_0 = 5.0$

4 Conclusion

In this paper, successive over-relaxation method has been adopted to solve 2D Schrödinger equation for an (1000 × 1000) grid size of the 2D square lattice for separable as well as non-separable periodic potentials that leads to discretization of bands including the emergence of the surface states. The algorithm needs to be modified for calculating higher bands with better accuracy. The algorithm has the potential to be applied in real-world systems such as quantum dots and other nanostructures.

Acknowledgements Shayari Basu is grateful to DST, Govt. of India for INSPIRE Fellowship.

References

1. Bhattacharya, P.: Semiconductor Optoelectronic Devices, 2nd ed. Pearson Education (1997)
2. Streetman, B.G., Banerjee, S.K.: Solid State Electronic Devices, 6th ed. Pearson Education (2006)
3. McLachlan, N.W.: Theory and Application of Mathieu Functions, 1st ed. Oxford (1947)
4. Inglesfield, J.E.: Surface electronic structure. IOP Sci. Rep. Prog. Phys. **45** (1982)
5. Callaway, J.: Energy Band Theory. Academic Press, New York and London (1964)
6. Kittel, C.: Introduction to Solid State Physics, 8th ed. Wiley (2005)
7. Chow, P.C.: Computer solutions to the Schrödinger equation. Am. J. Phys. **40**, 730734 (1972)
8. Press, W.H., Teukolsky, S.A., Vetterling, W.T., Flannery, B.P.: Numerical Recipes in Fortran 77, The Art of Scientific Computing. 2nd ed. Cambridge University Press (1992)
9. Pillai, M., Goglio, J., Walker, Thad G.: Matrix numerov method for solving Schrödinger's equation. Am. J. Phys. **80**, 1017 (2012)
10. Parr, R.G.: Density functional theory. Ann. Rev. Phys. Chem. **34**, 631–656 (1983)

11. Schmid, E.W., Spitz, G., Lösch, W.: Theoretical Physics on the personal Computer. Springer (1987)
12. Daniel, V.: Schroeder: the variational-relaxation algorithm for finding quantum bound states. Am. J. Phys. **85**, 698 (2017)

Trap-Assisted Transport in Silicon Nanorods

Ujjwal Ghanta and Syed Minhaz Hossain

Abstract In this work, we have studied the charge transport and photoluminescence (PL) properties of silicon nanorods (SiNRs) on substrate synthesized by the electrochemical etching of p-type Si wafer. The DC current–voltage (I-V) characteristics of SiNR within temperature 100–350 K show nonlinear and asymmetric behavior. From the temperature-dependent DC conductivity measurement, activation energy of 0.78 eV has been found. The room temperature emission spectrum is characterized by the appearance of single PL band in the visible region which can be de-convoluted into two Gaussian bands. The observed phenomena are interpreted in terms of defect states in the random SiNR network.

Keywords Silicon · Nanorods · Activation energy · Carrier transport

1 Introduction

The nanostructures of Si are of great significance and technological interest due to their attractive new applications in the area of microelectronics, photonics, and photovoltaics [1–3]. Si nanostructures in the form of porous Si are reported to have a typical resistivity of five orders of magnitude higher than that of crystalline bulk silicon [4, 5]. For any kinds of device applications of Si nanostructure, it is indeed essential to understand the transport property. In the present work, we have studied the effect of temperature on the lateral DC I-V characteristics and conductivity of the SiNR. Our observation suggests the dominant role of defect states in conduction through random SiNR network which is supported by the PL study.

U. Ghanta (✉)
School of Materials Science and Engineering, Indian Institute of Engineering Science and Technology, Shibpur, Howrah-3, India
e-mail: ujjwal.besu@gmail.com

S. M. Hossain
Department of Physics, Indian Institute of Engineering Science and Technology, Shibpur, Howrah-3, India

U. Biswas et al. (eds.), *Advances in Computer, Communication and Control*, Lecture Notes in Networks and Systems 41, https://doi.org/10.1007/978-981-13-3122-0_37

2 Experimental

2.1 Sample Preparation

SiNR on Si substrate was synthesized by electrochemical etching of p-type, 2–5 Ω-cm resistivity, and (100) crystalline Si wafer. We have used mixture of (24%) HF and ethanol solution with volume ratio 1:1 as the electrolyte. The electrochemical etching was carried out in a Teflon bath. The details of the sample preparation techniques are reported elsewhere [6, 7]. The etching current density and etching time were 20 mA/cm^2 and 10 min, respectively.

2.2 Metal Contact

Two micro-point contacts were made up on top of the SiNR layer with a separation of 1 mm. The metal contact has been done at 120 °C. We have used aluminum (Al) as contact material. The cross-sectional configuration of the device is schematically shown in Fig. 1.

2.3 Electrical Characterization

For the electrical characterization of SiNR, we have used Keithley 2400 Source Meter. The temperature was controlled by a liquid nitrogen cooled cryogenic system with LakeShore, 330 temperature controller. The DC I-V characteristics were

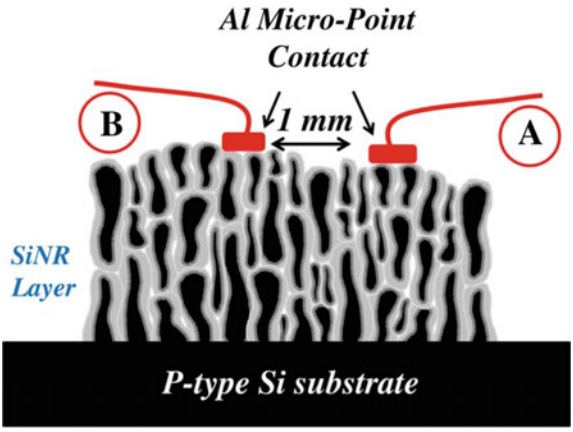

Fig. 1 Schematic cross-sectional view of the SiNR layer along with metal contacts on top

recorded at constant temperature using two-probe method with ± 5 V. The temperature dependence of the DC conductivity was measured at constant voltage mode.

2.4 Optoelectronic Characterization

For the optoelectronic characterization, we have used Horiba–Jobin Yvon, Nanolog (Fluorolog-3) single grating spectrofluorometer with water-cooled photomultiplier tube (PMT). The sample was excited by 325 nm wavelength of 10 mW HeCd laser. The PL spectrum of SiNR was recorded at room temperature within 500–750 nm emission wavelengths.

3 Results and Discussions

Figure 2 represents the I-V characteristics of the device within the applied bias ± 5 V for different temperatures in the range of 100–350 K. It is clearly evident from Fig. 2 that the I-V characteristics are nonlinear. The magnitude of current is in μA range which increases with temperature. The magnitude of current in positive bias is large in comparison with negative bias for a fixed temperature showing an asymmetric behavior. This asymmetric I-V characteristic is attributed to the modified potential barrier due to the accumulation of carriers at interface defect states that depend on the sweep direction [8].

The DC conductivity of the device as a function of temperature is shown in Fig. 3. The logarithmic of the conductivity increases sharply with inverse temperature and follows linear treads at high temperature showing an activation nature. The temperature-dependent conductivity of the device can be represented as [9]

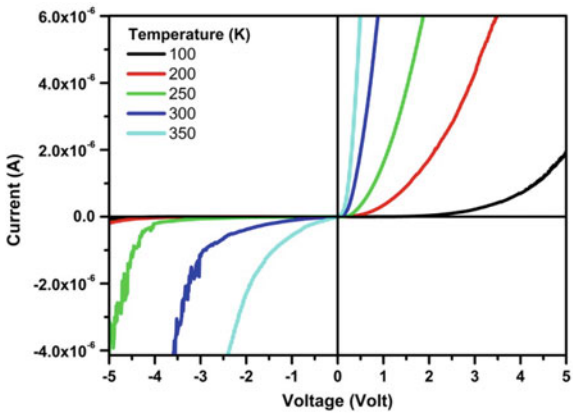

Fig. 2 I-V characteristics of the device for different temperatures within ± 5 V

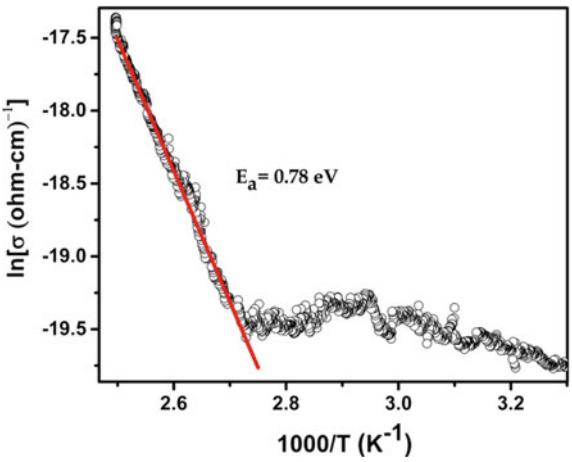

Fig. 3 The scattered data represents the temperature dependence of the DC conductivity. The solid line corresponds to the liner fit with estimated activation energy 0.78 eV

$$\sigma = \sigma_0 \exp(-\frac{E_a}{K_B T}) \tag{1}$$

where σ_0 is the conductivity prefactor, E_a is the activation energy, K_B is Boltzmann constant, and T is temperature in absolute scale. From the linear fit of the data, the estimated value of σ_0 and E_a has been found to be $3.46 \times 10^2\,(ohm - cm)^{-1}$ and 0.78 eV, respectively. The estimated values are well in agreement with the previous works [9–11].

Figure 4 shows the room temperature photoluminescence (PL) emission spectrum of SiNR under 325 nm laser excitation. The PL spectrum is broad; apparently, single band is centered around 617 nm but cannot be represented by a single Gaussian function. The Gaussian de-convolution of the spectrum clearly indicates that the luminescence from SiNR consists of two distinct bands as shown in Fig. 4. We found that the high energy first PL band and low energy second PL band centered at around 584 nm and 628 nm, respectively. The appearance of PL bands can be interpreted by the electronic states of SiNRs as suggested by Wolkin [12]. Oxygen passivation will result in oxide defect states within the widen bandgap of SiNRs as shown schematically in Fig. 5. Optoelectronic transitions from the conduction band (CB) to valance band (VB) of SiNRs cause high energy first PL band [13], whereas transitions from oxide defect state to VB result in low energy second PL band [13]. The PL study clearly reveals the existence of shallow defects in the SiNR system.

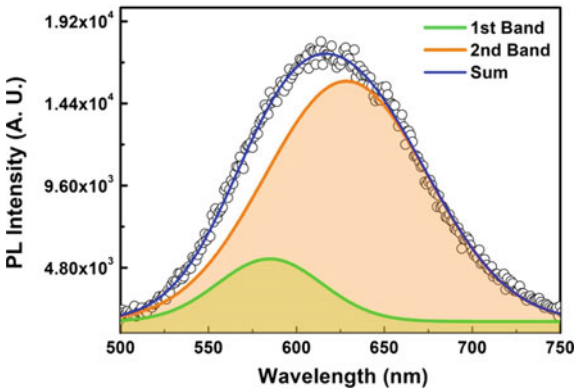

Fig. 4 Room temperature PL spectrum of SiNR under 325 nm laser illumination. The scattered plot represents the raw data. The solid line (green and orange) corresponds to the Gaussian de-convolution and sum of the Gaussians (blue)

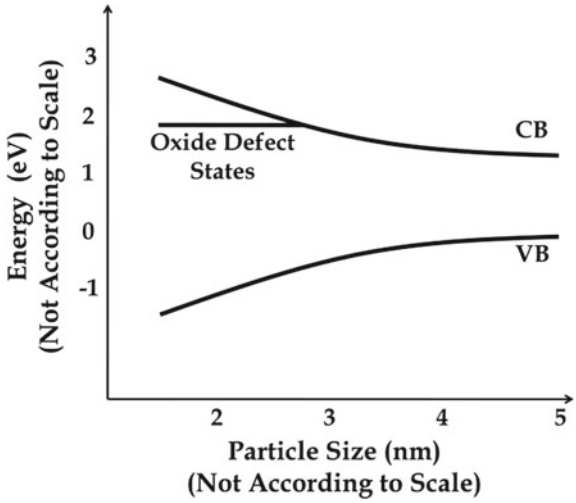

Fig. 5 Schematic representation of electronic states of Si nanocrystals as a function of their size as suggested by Wolkin [12]

4 Conclusions

In conclusion, we have studied the temperature-dependent transport properties of the electrochemically etched SiNR random network. The I-V characteristics are asymmetric and nonlinear. The temperature-dependent conductivity measurement shows activation type of behavior. Also, PL study reveals the existence of shallow defects in the system. The presence of defect states plays a crucial role in the carrier transport through random SiNR network.

References

1. Cheng, K.-Y., Anthony, R., Kortshagen, U.R., Holmes, R.J.: Nano Lett. **11**, 1952 (2011)
2. Priolo, F., Gregorkiewicz, T., Galli, M., Krauss, T.F.: Nat. Nanotechnology **9**, 19 (2014)
3. Maier-Flaig, F., Rinck, J., Stephan, M., Bocksrocker, T., Bruns, M., Kü bel, C., Powell, A.K., Ozin, G.A., Lemmer, U.: Nano Lett. **13**, 475 (2013)
4. Anderson, R.C., Muller, R.S., Tobias, C.W.: J. Electrochem. Soc. **138**, 3406 (1991)
5. Lehman, V., Hofmann, F., Möller, F., Gruning, U.: Thin Solid Films **255**, 20–22 (1995)
6. Hossain, S.M., Das, J., Chakraborty, S., Dutta, S.K., Saha, H.: Semicond. Sci. Technol. **17**, 55 (2002)
7. Ray, M., Ganguly, S., Das, M., Datta, S., Bandyopadhyay, N.R., Hossain, S.M.: Mater. Manuf. Processes **24**, 83 (2009)
8. Ghanta, U., Singh, S., Ray, M., Bandyopadhyay, N.R., Ganapathy, S., Hossain, S.M.: Phys. Status Solidi A **214**, 1600879 (2017)
9. Lubianiker, Y., Balberg, I.: Phy. Rev. Lett. **78**, 2433 (1997)
10. Lubianiker, Y., Balberg, I., Partee, J., Shinar, J., Non-Cryst, J.: Sol. **198–200**, 949–952 (1996)
11. Kocka, J., Pelant, I., Fejfar, A., Non-Cryst, J.: Sol. **198–200**, 857–862 (1996)
12. Wolkin, M.V., Jorne, J., Fauchet, P.M., Allan, G., Delerue, C.: Phy. Rev. Lett. **82**, 197 (1999)
13. Ray, M., Bandyopadhyay, N.R., Ghanta, U., Klie, R.F., Pramanick, A.K., et al.: J. Appl. Phys. **110**, 094309 (2011)

Comparison of Different SRAM Cell Topologies Using 180 nm Technology

D. Chaudhuri, Kousik Roy and A. Nag

Abstract With an overview and the limitations of the conventional SRAM cell, different SRAM cell topologies (4T–11T) are discussed. The cells are designed using Tanner EDA tool with 180 nm technology. The variation of power and read delay of different cell topologies compared to conventional SRAM cell are considered. The behaviour of power against supply voltage V_{dd} for different cell topologies reveals that the higher cell topologies offer better stability by maintaining the power as low as possible.

Keywords SRAM cell · Low power · Read stability

1 Introduction

Modern system-on-chip (SOC) designs increases the usage of static random access memory (SRAM) cell in order to utilize the minimum sized transistor to realize a higher density. The area of an SRAM cell is vital because the cell area contributes extensively to the Si area. The lowest operational V_{dd} for SRAM is restricted either by the cell stability or write-ability [1]. There are three modes, viz., (i) standby mode, (ii) read mode and (iii) write mode in which the SRAM operates [2]. In standby mode, word line (WL) is not affirmed. Consequently, the pass transistor is deactivated, and

D. Chaudhuri (✉)
Department of Electronics & Communication Engineering, Modern Institute of Engineering & Technology, Hooghly 712123, West Bengal, India
e-mail: debika.chaudhuri@gmail.com

K. Roy
Department of Electronics & Communication Engineering, Asansol Engineering College, Asansol 713305, West Bengal, India
e-mail: kousikroy002@gmail.com

A. Nag
Department of Physics, Modern Institute of Engineering & Technology, Hooghly 712123, West Bengal, India
e-mail: tnnag79@gmail.com

U. Biswas et al. (eds.), *Advances in Computer, Communication and Control*, Lecture Notes in Networks and Systems 41, https://doi.org/10.1007/978-981-13-3122-0_38

no read and write operation is performed, and thus, the RAM holds the stored data in this mode. The power required for holding the data is more. In read mode, read operation is performed by first activating the WL and the pass transistors are then activated. The voltage at bit line (BL) is kept high and the bit bar line (BLB) is pulled to low. When the difference between two voltages is high, '1' is read. When the difference between them is low, '0' is read from the cell. In write mode, when '1' has to write into the cell, first BL is kept high and BLB is kept at low voltage. Similarly, when '0' has to write into the cell, then BL is kept at low and BLB is at high voltage. New techniques are being comprehended to get better energy efficiency in the design of the SRAM cells. In this paper, 4T–11T SRAM cells are designed using Tanner EDA tool with 180 nm technology and power and read delay of the cells reveals that the higher cell topologies offer better stability margin by making the power as low as possible.

2 Different SRAM Cell Topologies Implemented

4T–11T SRAM cell topologies under consideration are, respectively, shown in Figs. 1, 2, 3, 4, 5, 6, 7 and 8 and are discussed in brief along with their individual merits and demerits.

4T-SRAM cell: Figure 1 shows the basic block of a 4T SRAM cell. Though have dominated the marketplace of low power logic circuits initially due to its less cell area, for the reduced stability at lower voltages, the 4T SRAMs have not been used nowadays for on-chip storage in different logic circuits [3].

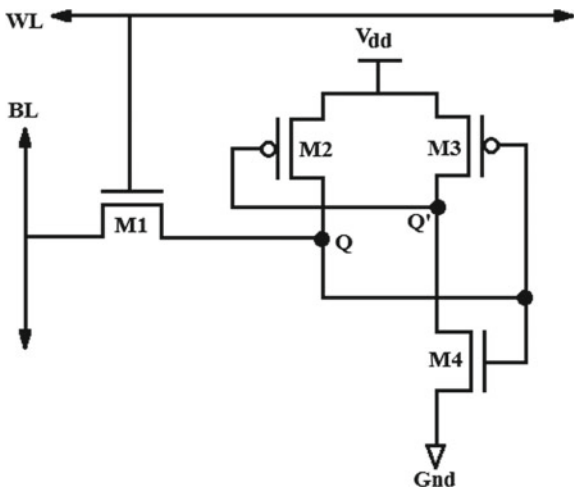

Fig. 1 4T SRAM cell diagram [3]

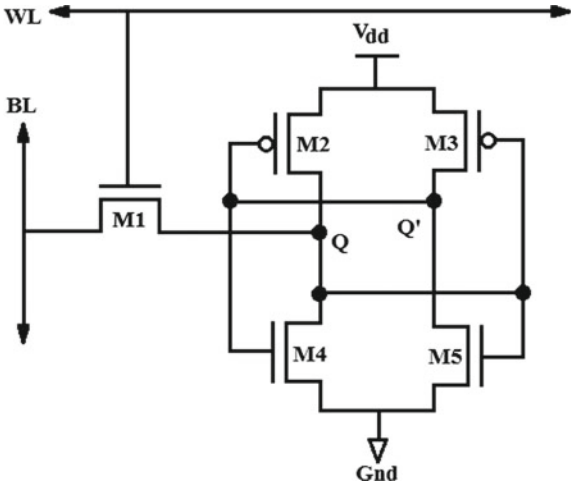

Fig. 2 5T SRAM cell diagram [3]

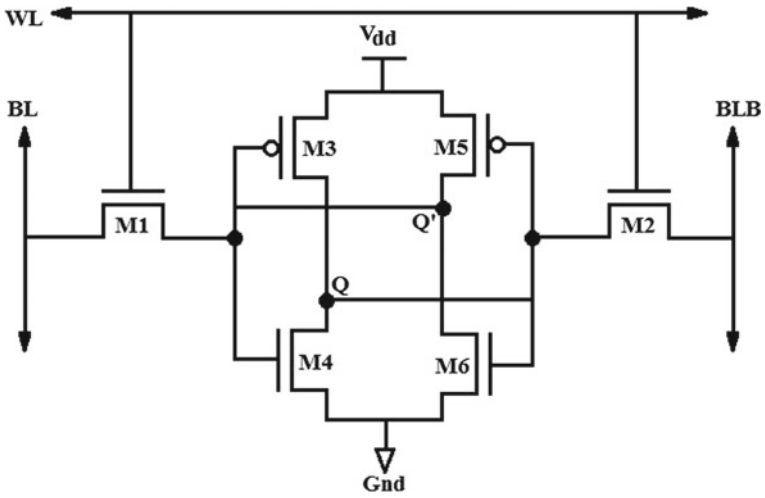

Fig. 3 6T SRAM cell diagram [4]

5T-SRAM cell: The basic block of a 5T SRAM cell as shown in Fig. 2 appears similar to a conventional 6T SRAM cell of Fig. 3, but the only distinction is missing of one access transistor [3].

Writing a '0' to the 5T cell [4] is not a concern as the access transistor M1 can pass a strong '0'. However, writing a '1' is practically unfeasible without a writing support since M1 cannot pass a strong '1'.

6T-SRAM cell: The basic block of this cell as depicted in Fig. 3 is designed by using 2 PMOS and 4 NMOS transistors in the form of two cross-coupled inverters

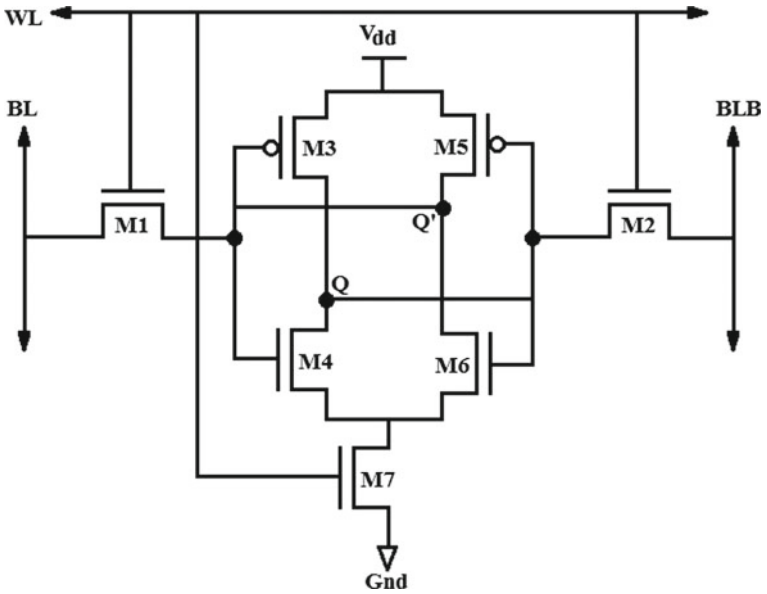

Fig. 4 7T SRAM cell diagram [5, 6]

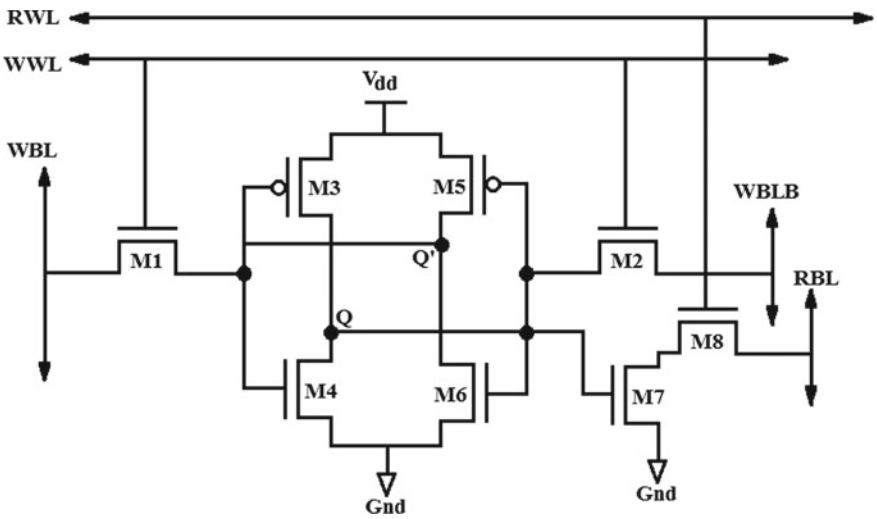

Fig. 5 8T SRAM cell diagram [5]

connected side by side and two access transistors M1 and M2. With the help of M1 and M2, data can be either accessed or written into the cell [4]. The inverters are used for accumulating bit information at an instance.

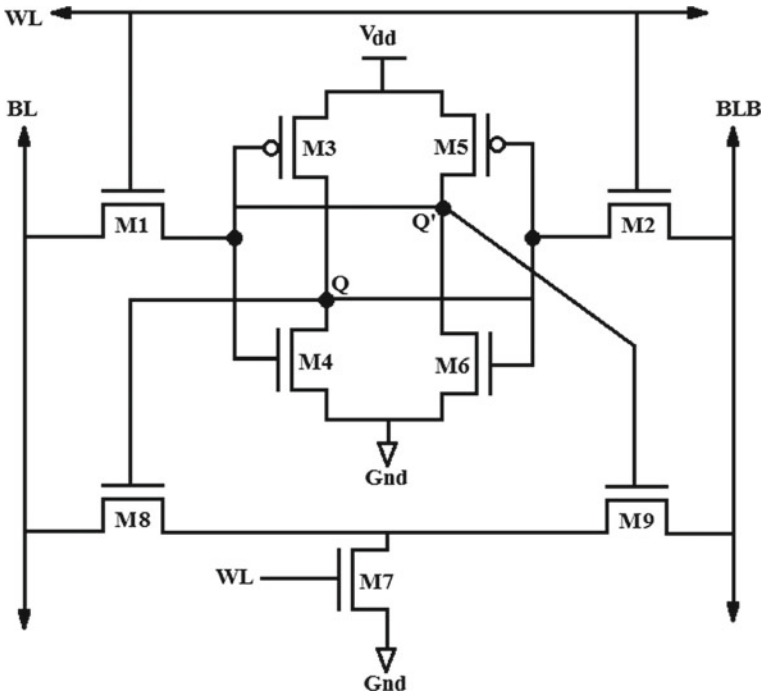

Fig. 6 9T SRAM cell diagram [5]

7T-SRAM cell: The basic block of this cell, which is shown in Fig. 4, consists of an additional transistor M7 placed in the ground path of a 6T cell to minimize leakage while the cell is in standby mode [5]. In standby mode, the transistor M7 is anticipated to cut-off the ground path and to get rid of the leakage paths through the inverter transistor sources but this cell cannot increase the read stability [6].

8T-SRAM cell: In order to retain the read stability, data stability and utility of a 6T and 7T SRAM cells; 8T SRAM cell is used [5]. The basic block this cell is shown in Fig. 5 by incorporating an additional read word line (RWL) and read bit line (RBL) for read operation and write word line (WWL) and write bit line (WBL) for write operation other than the conventional cells.

9T-SRAM cell: Better data stability can be achieved in this cell [5], the basic block of which is shown in Fig. 6. Here data is completely isolated from the BL to perform a read operation. Betterment in read static-noise-margin can be obtained using this cell in comparison to conventional one.

10T-SRAM cell: The basic block of 10T cell is depicted in Fig. 7 with a single-end RBL, employing an inverter as transmission gate (TG) [7] connected to Q′. The additional signal read enable bar (REB) is an inversion signal of a read WL, control the additional PMOS transistor M9 at the TG. While the REB and read enable (RE) are asserted and the TG is on, a stored node is connected to Q through the inverter.

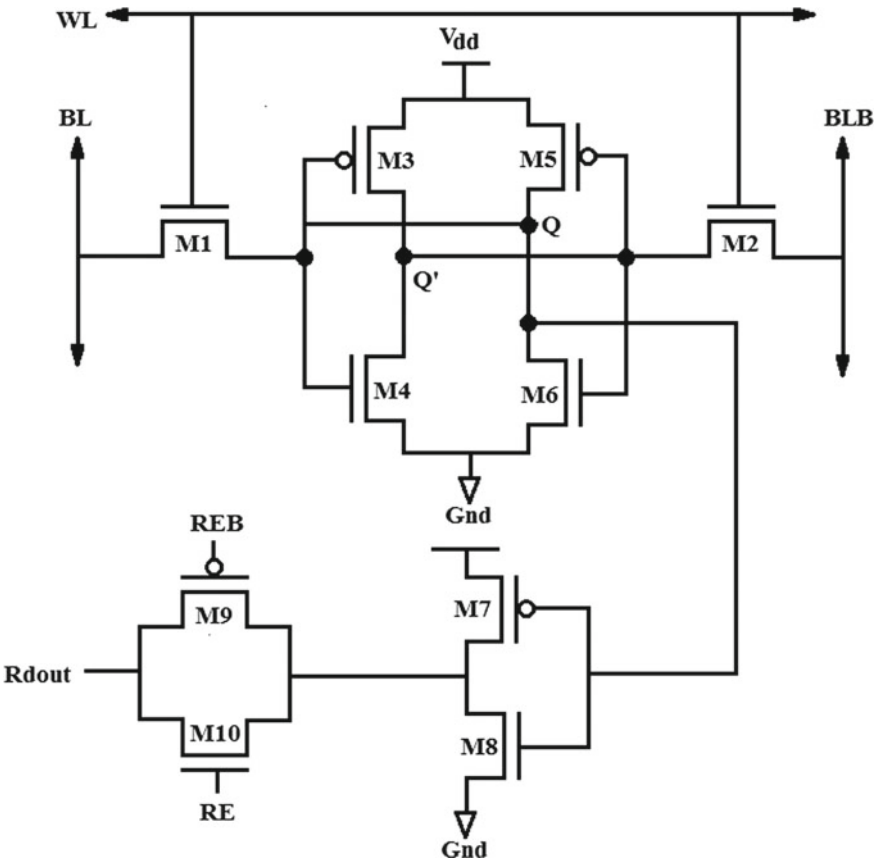

Fig. 7 10T SRAM cell diagram [7, 8]

Here pre-charge circuit is not essential because the inverter fully charges or discharges the RBL [8].

11T-SRAM cell: This cell, shown in Fig. 8, is having two cross-coupled inverters along with a transistor which is accessed by the RWL for read operation and other two transistors which are controlled by the WWL for write operation [9].

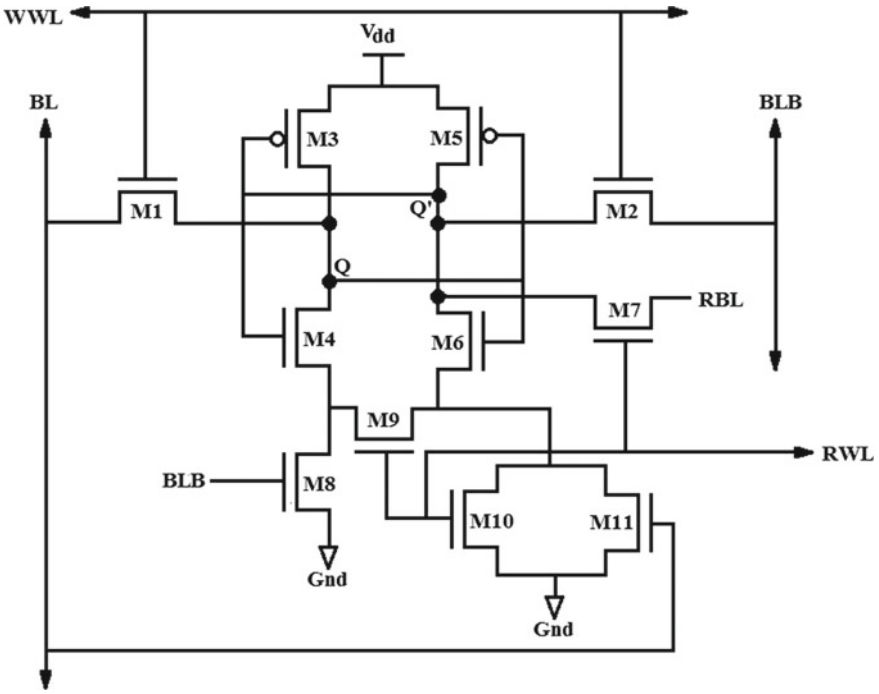

Fig. 8 11T SRAM cell diagram [9]

3 Simulation Results

We have obtained the simulation results for the different considered 4T–11T SRAM cell topologies using 180 nm technology in terms of power and read delay.

Tables 1 and 2 show, respectively, the variation of power and read delay obtained at different supply voltages for different SRAM cell topologies. Figure 9 shows the variation of power in different SRAM cell topologies for chosen values of V_{dd}, and Fig. 10 shows the variation of read delay in different SRAM cell topologies for the same chosen values of V_{dd}.

The behaviour of power against supply voltage V_{dd} for different cell topologies has been shown in Fig. 11. From the power and read delay behaviour of all considered SRAM cells, it reveals that the higher cell topologies offer better stability by maintaining the power as low as possible.

Table 1 Power obtained at different supply voltages for different SRAM cell topologies

Supp. vol./Cell	0.8 V	0.9 V	1.0 V	1.1 V	1.2 V
Sram 4t	1.12E−07	1.42E−07	1.73E−07	2.03E−07	2.32E−07
Sram 5t	4.80E−07	6.15E−07	7.64E−07	9.40E−07	1.13E−06
Sram 6t	4.97E−07	6.37E−07	8.00E−07	9.83E−07	1.18E−06
Sram 7t	4.85E−07	6.17E−07	7.70E−07	9.43E−07	1.14E−06
Sram 8t	2.37E−07	3.06E−07	3.85E−07	4.73E−07	5.70E−07
Sram 9t	6.15E−07	8.12E−07	1.03E−06	1.27E−06	1.54E−06
Sram 10t	6.02E−08	8.31E−08	1.08E−07	1.39E−07	1.73E−07
Sram 11t	6.65E−08	8.95E−08	1.13E−07	1.46E−07	1.62E−07

Table 2 Read delay obtained at different supply voltage for different SRAM cell topologies

Supp. vol./Cell	0.8 V	0.9 V	1.0 V	1.1 V	1.2 V
Sram 4t	3.01E−11	2.89E−11	2.75E−11	2.58E−11	2.37E−11
Sram 5t	5.00E−11	5.50E−11	5.84E−11	6.09E−11	6.11E−11
Sram 6t	5.50E−11	6.03E−11	6.48E−11	6.80E−11	7.06E−11
Sram 7t	5.06E−11	5.54E−11	5.87E−11	6.12E−11	6.16E−11
Sram 8t	3.00E−11	2.82E−11	2.65E−11	2.51E−11	2.37E−11
Sram 9t	7.14E−11	7.52E−11	7.75E−11	8.05E−11	8.24E−11
Sram 10t	2.75E−11	2.53E−11	2.29E−11	2.04E−11	1.85E−11
Sram 11t	2.63E−11	2.41E−11	2.20E−11	2.01E−11	1.89E−11

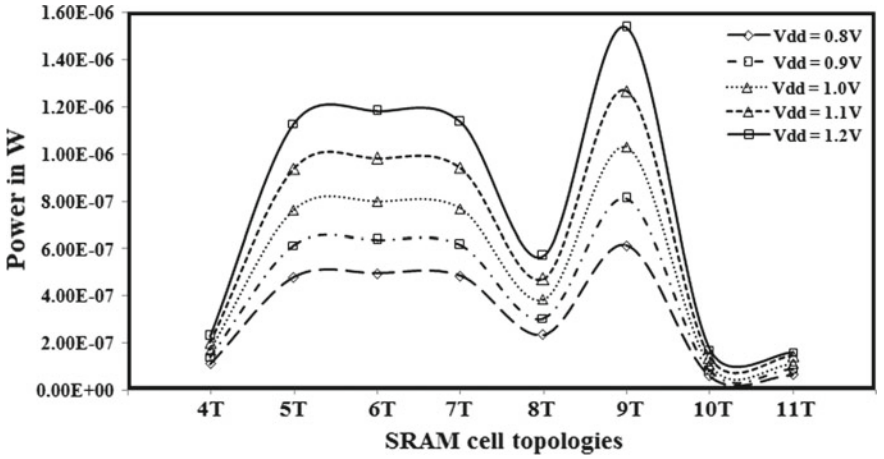

Fig. 9 Variation of power in different SRAM cell topologies for chosen values of V_{dd}

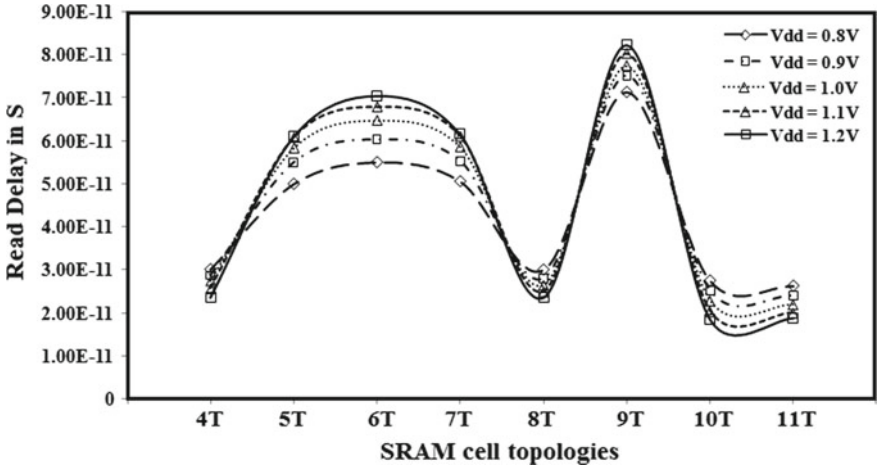

Fig. 10 Variation of read delay in different SRAM cell topologies for chosen values of V_{dd}

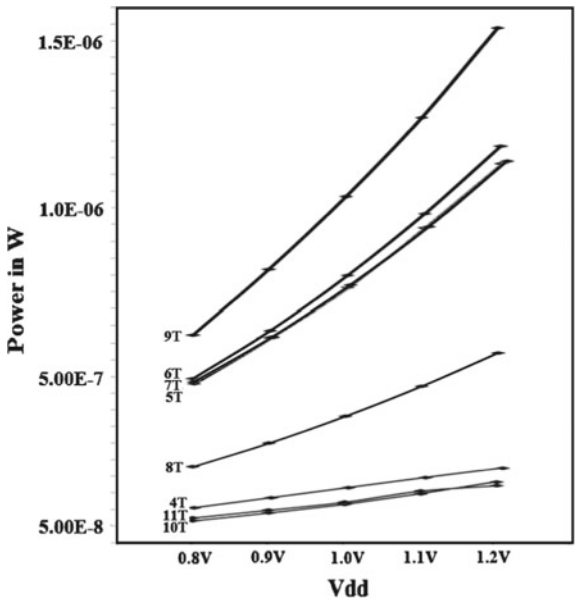

Fig. 11 Power versus V_{dd} curves for different SRAM cells

4 Conclusion

In recent past due to the rising requirement of embedded systems, laptops, communication devices and memory cards, rapid advancement of low power, low voltage SRAM cells has been experienced [10]. As a result of these, new techniques are being comprehended to get better energy efficiency in the design of the SRAM cells. In

this paper, the power and read delay behaviour of all considered SRAM cells reveal that the higher cell topologies offer better stability margin by maintaining the power as low as possible.

References

1. Takeda, K., et al.: A read-static-noise-margin-free SRAM cell for low-V_{dd} and high-speed applications. IEEE J. Solid-State Circuits **41**(1) (2006)
2. Thakare, P.V., Tembhurne, S.: A power analysis of SRAM cell using 12T topology for faster data transmission. Int. J. Sci. Technol. Eng. **2**, 441–446 (2016)
3. Singh, W., Kumar, A.G.: Design of 6T, 5T and 4T SRAM cell on various performance metrics. In: 2nd International Conference on Computing for Sustainable Global Development (INDIACom), pp. 899–904 (2015)
4. Rabaey, J., Chandrakasan, A., Nikolic, B.: Digital Integrated Circuits: A Design Perspective, 2nd ed. Prentice-Hall, Englewood Cliffs, NJ (2003)
5. Kiran, P.N.V., Saxena, N.: Design and analysis of different types SRAM cell topologies. In: IEEE Sponsored 2nd International Conference on Electronics and Communication System (ICECS 2015), pp. 167–173 (2015)
6. Kulkarni, J.P., Goel, A., Ndai, P., Roy, K.: A read-disturb-free, differential sensing 1R/1W Port, 8T bitcell array. IEEE Trans. Very Large Scale Integr. Syst. **19** (2011)
7. Hamzaoglu, F., Zhang, K., Wang, Y., Ahn, H.J., Bhattacharya, U., Chen, Z., Ng, Y.G., Pavlov, A., Smits, K., Bohr, M.: A 3.8 GHz 153 Mb SRAM design with dynamic stability enhancement and leakage reduction in 45 nm high-k metal gate CMOS technology. IEEE J. Solid-State Circuits **44** (2009)
8. Shamanna, G., Kshatri, B., Gaurav, R., Tew, Y.S., Marfatia, P., Raghavendra, Y., Naik, V.: Process technology and design parameter impact on SRAM Bit-cell sleep effectiveness. IEEE (2010)
9. Kumar, S.V., Noor, A.: Characterization and comparison of low power SRAM cells. J. Electron. Devices **11** (2011)
10. Majumdar, B., Basu, S.: Low power single bitline 6T SRAM cell with high read stability. In: International Conference on Recent Trends in Information Systems, pp. 169–174 (2011)

Ferroelectric-Cladded Tunable Silicon Photonic Coupler

M. Mishra, F. Morichetti and Nikhil R. Das

Abstract A silicon photonic directional coupler with ferroelectric cladding has been studied. It is shown that the domain switching in ferroelectric material can be utilized to reduce continuous power consumption and thermal noise in dense photonic integrated circuits when compared to conventional thermo-optic actuators.

Keywords Actuator · Directional coupler · Tunable · Ferroelectric · Nonvolatile

1 Introduction

Thermo-optic actuator has a significant role in the field of silicon photonics for tuning the refractive index of the waveguide cladding for realizing tunable couplers and other silicon photonic devices [1, 2]. But they suffer from limitations such as the need for continuous power supply and the presence of severe thermal cross talk. To avoid these issues, ferroelectric tunable couplers have been proposed. Ferroelectric material such as barium titanate ($BaTiO_3$) shows varying refractive index values (n_{cl} = 2.36–2.41) depending on the orientation of their domains. This domain switching may be done by applying an electric field with appropriate intensity and orientation, thus changing the refractive index of the material [3–6]. Here, ferroelectric $BaTiO_3$

M. Mishra (✉) · N. R. Das
Institute of Radio Physics and Electronics, University of Calcutta, 92,
A.P.C. Road, Kolkata 700009, West Bengal, India
e-mail: madhusudandbt@gmail.com

N. R. Das
e-mail: nrd@ieee.org

F. Morichetti
Department of Electronics Information and Bioengineering, Politecnico di Milano,
20133 Milan, Italy
e-mail: francesco.morichetti@polimi.it

U. Biswas et al. (eds.), *Advances in Computer, Communication and Control*, Lecture Notes in Networks and Systems 41, https://doi.org/10.1007/978-981-13-3122-0_39

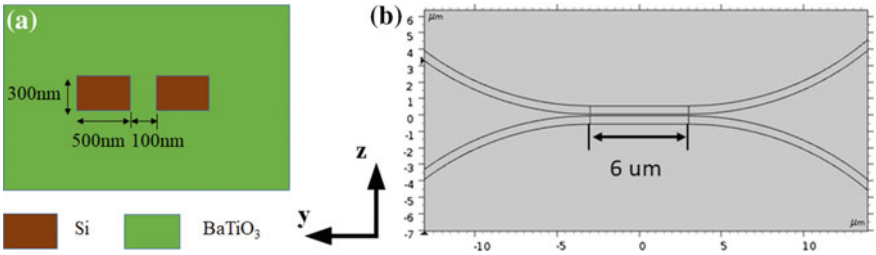

Fig. 1 **a** The coupler structure and **b** the simulated structure

material has been used as a cladding material for silicon photonic directional coupler. Different propagation modes and coupled powers for a fixed coupling length have been studied for different values of effective refractive index (n_{cl}).

2 Device Structure

The directional coupler considered in the present study has two waveguide cores (500×300 nm), separated by 100 nm, having $BaTiO_3$ as its cladding as shown in Fig. 1. The length of the parallel coupling portion is 6 μm, and the bending radius of the cores at both the ends is 8 μm.

3 Results and Discussion

Results from simulations are given below. In Fig. 2, the coupling TE, TM modes for different values of refractive index (n_{cl}) of the cladding are shown. It can be seen that, as n_{cl} of cladding increases, the coupling becomes stronger.

The cross-sectional view of light coupling between the two waveguides in the coupler is shown in Fig. 3 for different values of n_{cl}. It can be seen from these results that use of $BaTiO_3$ as a cladding material for Si core couplers instead of traditional SiO_2 not only enables us to tune the coupling power but also increases the power coupling rapidly within a shorter coupling length.

Figure 4 shows the coupled power for different changing n_{cl} for the given structure. As the n_{cl} value changes from 1.45 (Si) to 2.36 (the extraordinary axis refractive index value of $BaTiO_3$), a coupling power increases significantly. Again, it further

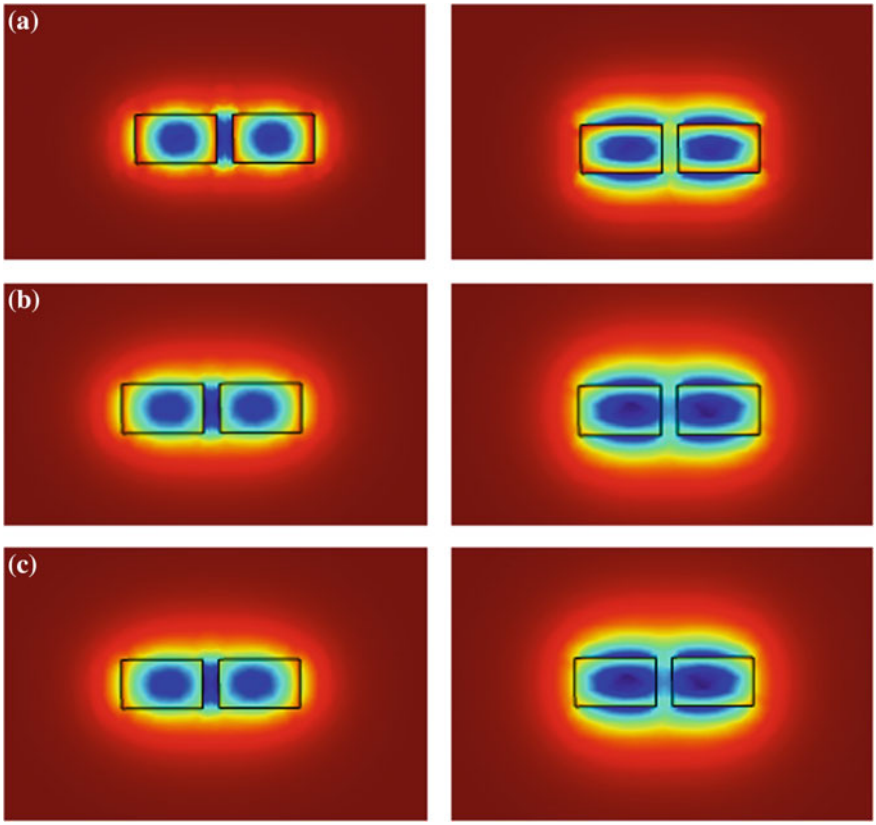

Fig. 2 TE_{00} and TM_{00} modes: **a** SiO_2 [$n_{cl} = 1.45$], **b** $BaTiO_3$ [$n_{cl} = 2.36$], and **c** $BaTiO_3$ [$n_{cl} = 2.41$]

increases rapidly, as the n_{cl} values changes from 2.36 to 2.41, i.e., the ordinary axis refractive index of $BaTiO_3$. This change in refractive index value for n_{cl} can be tuned by applying the appropriate amount of electric field to $BaTiO_3$ cladding of the respective coupler; hence, the coupling power can be tuned by applying electric field.

From the above discussion, it can be noted that the ferroelectric $BaTiO_3$-cladded silicon photonic couplers can achieve more coupling in effectively shorter coupling length, and the coupling can be tuned using the applied electric field. This is very important for photonic integrated circuits.

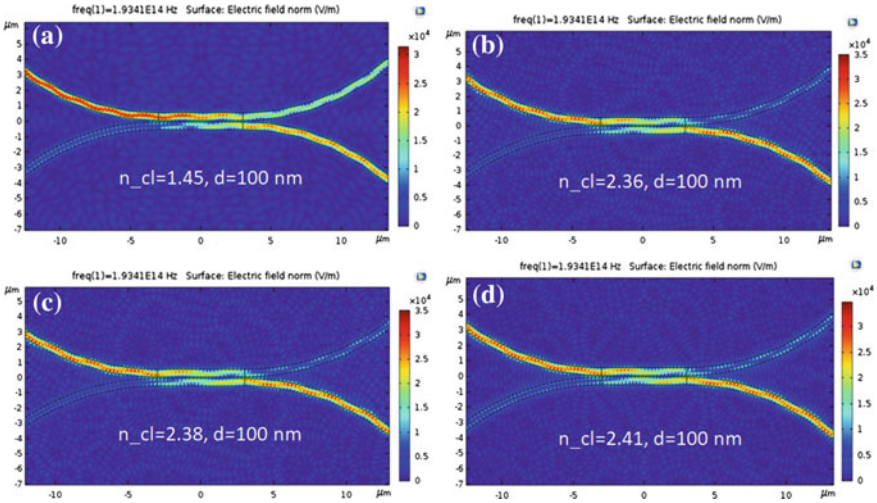

Fig. 3 Light coupling for n_{cl} = **a** 1.45, **b** 2.36, **c** 2.38, and **d** 2.41

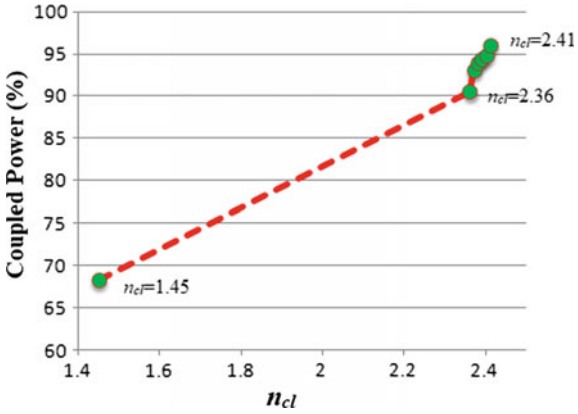

Fig. 4 Variation of coupled power with refractive index (n_{cl}). As no data have been used between n_{cl} = 1.45 and 2.36, the exact trace (nonlinear) cannot be shown in the plot and, so, the two points are joined by dashed line

4 Conclusion

The study shows that the coupling can be significantly modified by changing the refractive index of the cladding. The refractive index of $BaTiO_3$ cladding is modified due to the switching of ferroelectric domains by electric field. Thus, power coupling in ferroelectric-cladded silicon photonic coupler can be efficiently tuned by electric field.

Acknowledgements This work is financially supported by INSPIRE Fellowship program of Department of Science and Technology (DST), India (IF 150280). The authors also acknowledge the research support under Erasmus LEADERS program and the Italian Fondazione Cariplo Project ACTIO (Rif. 2016-0881).

References

1. Kim, J.-H., et al.: Tunable grating couplers for broadband operation using thermo-optic effect in silicon. IEEE Photon. Technol. Lett. **27**, 2304–2307 (2015). https://doi.org/10.1109/lpt.2015.2462081
2. Chu, T.: Compact 1 × N thermo-optic switches based on silicon photonic wire waveguides. Opt. Express **13**, 10109–10114 (2005). https://doi.org/10.1364/OPEX.13.010109
3. Merz, W.J.: Domain formation and domain wall motions in ferroelectric batio$_3$ single crystals. Phys. Rev. **95**, 690 (1954)
4. Abel, S., et al.: A strong electro-optically active lead-free ferroelectric integrated on silicon. Nature Comm. **4** (2013). Article no. 1671. https://doi.org/10.1038/ncomms2695
5. Lopez, A.: Finite element model of a ferroelectric. In: COMSOL Conference Proceeding, Paris (2010)
6. Dicken, M.J., et al.: Electrooptic modulation in thin film barium titanate plasmonic interferometers. Nano Lett. **8**, 4048–4052 (2008). https://doi.org/10.1021/nl802981q

Circular Antenna Array Optimization Using Flower Pollination Algorithm

Krishanu Kundu and Narendra Nath Pathak

Abstract Flower pollination is a fascinating process in the innate world. Its evolutionary features can be utilized to design innovative optimization algorithms for antenna arrays. In this paper, we use flower pollination algorithm, stimulated by pollination practice of flowers for optimizing circular antenna arrays. FPA is utilized to circular array for obtaining optimized positions of antennas to attain array pattern comprising lowest side lobe alongside positioning of deep nulls in needed directions.

Keywords Circular antenna array · Flower pollination algorithm

1 Introduction

Antenna array is a combination of several antennas in order to obtain a given radiation pattern [1]. Array antennas are divided into two modules based on how the element antennas axis is correlated to the path of radiation. A broadside array is array of one or two dimensions where the direction of radiation is at a 90° angle to the plane of the antennas, whereas end-fire array is basically termed as linear array where the direction of radiation is exactly all along the line of antennas. By proper arrangement of number of elements in an array, by modifying inter-element spacing between array elements, by changing elemental amplitude as well as phase and most obviously with proper scheming of antenna array geometry the problems like low directivity, high side lobe level and wide beam width faced in single antenna can be eliminated. Recent trends focus on array synthesis with null placement. To compensate delays of received signals commencing from a particular source at individual

K. Kundu (✉)
Department of Electronics and Communication Engineering,
Dronacharya College of Engineering, Gurgaon, India
e-mail: krishanukundu08@gmail.com

N. N. Pathak
Department of Electronics and Communication Engineering,
Dr. B. C Roy Engineering College, Durgapur, India

U. Biswas et al. (eds.), *Advances in Computer, Communication and Control*, Lecture Notes in Networks and Systems 41, https://doi.org/10.1007/978-981-13-3122-0_40

elements of antenna array null steering or null placement is best used policy. Null placement helps in obtaining justified signal-to-noise ratio by avoiding unauthorized interference. Moreover, minimization of side lobes in addition to null placement contributes in effective array designing. In circular array, minimization of side lobes and placement of null could be obtained by optimizing amplitude as well as phase keeping inter-element spacing constant or by changing inter-element spacing keeping amplitude, phase unchanged. Various nature-based algorithms like genetic algorithm, simulated annealing, particle swarm optimization and ant colony optimization have been utilized so far for optimization of circular arrays. In this paper, flower pollination algorithm (FPA) [2, 3] has been utilized for optimization of circular array. FPA is a nature-based algorithm based on pollination of flowers, i.e. pollen transfer with the help of pollinators for the purpose called reproduction.

2 Circular Antenna Array

Figure 1 describes a circular array geometry of N isotropic elements equally placed over x-y plane along a circular ring of radius a [4]. Array factor of circular array with N-element whose centre is at the x-y plane's origin is described by Eqs. 1a and 1b.

$$\mathrm{AF}(\theta, \phi) = \sum_{n=1}^{N} \mathrm{I_n} e^{\mathrm{jka}(\cos\phi - \cos\phi_0)} \tag{1a}$$

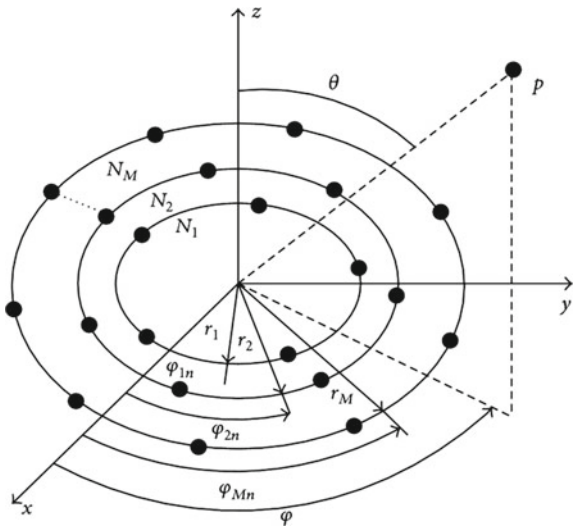

Fig. 1 Structure of circular array

$$AF(\theta, \phi) = \sum_{n=1}^{N} I_n e^{jkp_0 \cos(\phi_n - \varepsilon)} \tag{1b}$$

where

$$\varepsilon = \tan^{-1}[(\sin\theta \sin\varphi - \sin\theta \sin\varphi_0)/(\sin\theta \cos\varphi - \sin\theta_0 \cos\varphi_0)]$$
$$p_0 = a[(\sin\theta \cos\varphi - \sin\theta_0 \cos\varphi_0)^2 + (\sin\theta \sin\varphi - \sin\theta \sin\varphi_0)^2]^{1/2}$$

$$a_n = I_n e^{j}\alpha_n$$
$$\alpha_n = -k\, a \sin\theta_0 \cos(\varphi_0 - \varphi_n)$$

where I_n = amplitude excitation of nth element, $\varphi_n = 2\Pi_n/N$, angular position of *n*th element on x-y plane, a_n = excitation coefficients (amplitude and phase) of *n*th element.

3 Flower Pollination Algorithm

Flower pollination algorithm is based on pollination property of plants and depends on the following four rules:

I. Biotic and cross-pollination are treated as global pollination process.
II. Abiotic and self-pollination are classified as local pollination.
III. Flower constancy is being developed by insects and termed as the reproduction probability.
IV. A switching probability (p) facilitates the switching between local and global pollination.

The basic parameters are as follows: population size (n), switching probability (p), step size L(β), scaling factor (γ) and local pollination constancy factor (Ɛ). Switching probability (p) is biased to local pollination process as nearby flowers are more obvious to be pollinated than far away flowers. During FPA execution, a random number in the range 0–1 is produced and done comparison with switching probability (p). For number value less than p, global pollination takes place or else local pollination. Step size L(β) is dedicated to global pollination process and dictates the pollinators such as insects ability to fly over long distance. Scaling factor (γ) controls the step size in global pollination process.

$$\text{Global pollination} : x_i^{t+1} = x_i^t + L\left(x_i^t - g^*\right) \tag{2}$$
$$\text{Local Pollination} : x_i^{t+1} = x_i^t + \varepsilon\left(x_i^t - x_k^t\right) \tag{3}$$

Solution vector (x_i^t) at iteration t and $g*$ denotes the present best found till throughout iteration. The switching probability between two equations throughout iterations is denoted by p. ε represents random number opted from a uniform distribution where L represents step size opted from a Lévy distribution.

Lévy flights by means of Lévy steps are an effective random walk as global and local search capabilities could be carried out at a similar time. In comparison with standard random walks, Lévy flights encompass occasional long jumps, which facilitate the algorithm to jump out any local valleys. Lévy steps obey the following approximation:

$$L \sim (s + \beta)^{-1}$$

where β states Lévy exponent. It could be challenging to draw Lévy steps properly and a simple way of generating Lévy flights is to use two normal distributions u and v by a transform $s = u/(|v|^{1+\beta})$, x_j^t and x_k^t are pollen as of different flowers of same plant.

4 Results of Optimization

Here the FPA has been utilized for optimizing circular antenna array so that it can decide the optimized array element positions for minimizing peak SLL as well as for placement of nulls in preferred directions. In Example 1, the optimized array element positions are determined for minimizing peak SLL in the particular spatial region. Example 2 elaborates the relevance of FPA to conclude the optimized array element positions for minimizing peak SLL in addition to situate deep nulls in the preferred directions. The FPA has been programmed on MATLAB and runs for 15 times. In each run, the total number of iterations is put equivalent to 1000. All experimental results are observed using n = 25, ß = 1.5, p = 0.8, and $\gamma = 0.1$.

Fitness function utilized for minimizing peak SLL

$$Fitness = \min(\max(20 \log|AF(\theta)| \tag{4}$$

4.1 Example 1

Example 1 elaborates circular antenna array (2 N = 10 element) synthesis for obtaining SLL minimization for regions, $\theta = [0°, 74°]$ and $\theta = [106°, 180°]$. It is assumed that phase and amplitude excitations are uniform. Table 1 depicts the optimized element positions where Fig. 2 explains array pattern. The projected method (FPA) provides peak side lobe level equal to −26.36 dB (Table 2).

Table 1 Optimized locations in positive half of 10-element circular antenna array of Example 1

Method	Optimized antenna positions				
FPA	0.111λ	0.325λ	0.6522λ	0.895λ	1.4239λ

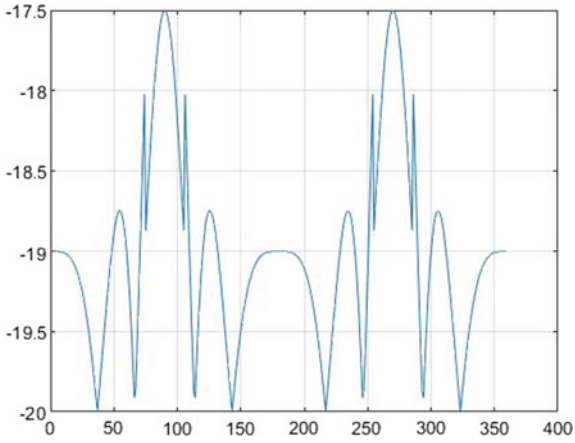

Fig. 2 Array pattern for design Example 1 {Y axis: array factor (in DB) X axis: azimuth angle (in degree)}

Table 2 Optimized peak side lobe level in case of 10-element circular antenna array

Sr. no.	Algorithm used	Peak SLL (in DB)
1	Flower pollination algorithm	−26.36

4.1.1 Minimization SLL Along with Null Placement

Fitness function taken into consideration for minimizing SLL as well as for placing of nulls in preferred directions is represented as in (5).

$$\text{Fitness} = \sum_{i} 1/\Delta\theta_i \int_{\theta li}^{\theta vi} |\text{AF}(\theta)|^2 \text{d}\theta + \sum_{k} |\text{AF}(\theta_k)|^2 \tag{5}$$

4.2 Example 2

Example 2 elaborates circular antenna array (28 element) synthesis for obtaining SLL minimization for regions $\theta = [0°, 84°]$ as well as $\theta = [96°, 180°]$ along null placement at $\theta = 55°, 57.5°, 60°, 120°, 122.5°$, and 125°. Array pattern has been shown in Fig. 3, where the null depths attained by using FPA at every specified directions are compiled in Table 3. It can be observed from Fig. 3 that the recommended method using FPA capacitates the deep null placements (deep as −92.56 dB) at particular directions (Table 4).

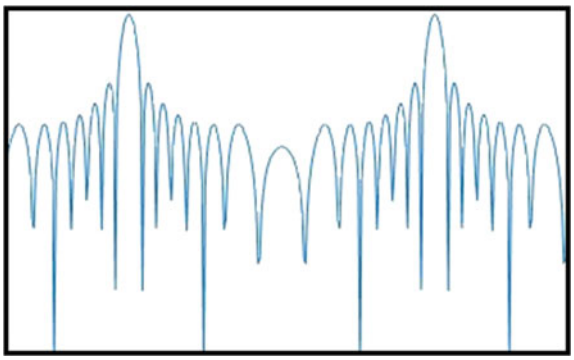

Fig. 3 Array pattern depicting Example 2 {Y axis: array factor (in DB) X axis: azimuth angle (in degree)}

Table 3 Null depths post-optimization upon applying FPA

Circular array type	Null depths in DB					
θ	55	57.5	60	120	122.5	125
28-element array	−92.56	−98.37	−93.62	−93.62	−98.37	−92.56

Table 4 Null depth and peak SLL in Example 2

	FPA method
Minimum null depth	−92.56
Peak SLL	−23.69

4.3 Convergence Based on FPA

Graph between convergence due to fitness function and total iteration numbers (Example 1 and Example 2) is being represented by Figs. 4 and 5. Table 5 describes the comparative analysis of number of total iterations needed for convergence in case of Example 1 and Example 2.

Table 5 Comparative analysis of number of total iterations needed for convergence in case of Example 1 and Example 2

	Design Example 1	Design Example 2
FPA	468	156

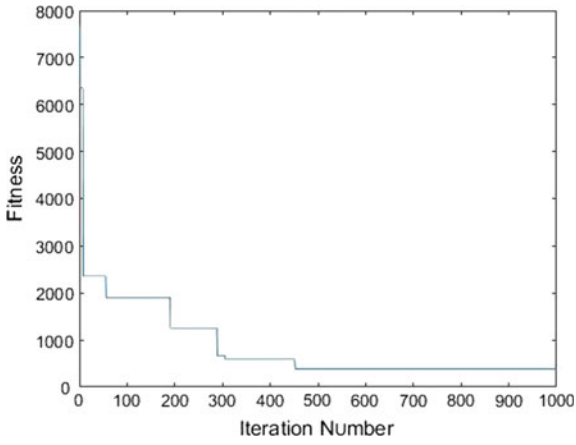

Fig. 4 Graph between convergence due to fitness function and total iteration numbers (Example 1)

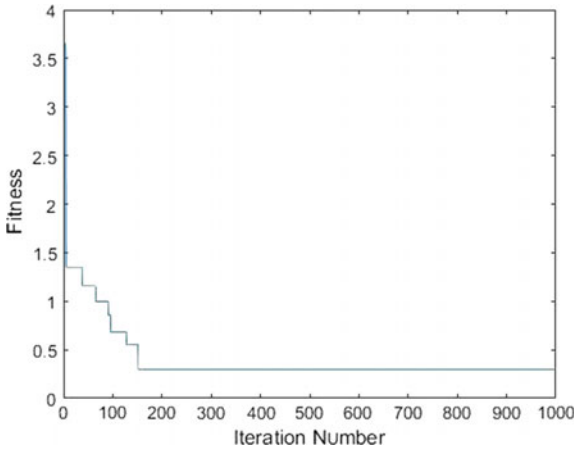

Fig. 5 Graph between convergence due to fitness function and total iteration numbers (Example 2)

5 Conclusion

This paper suggested flower pollination algorithm for optimizing circular antenna arrays. FPA was utilized for obtaining enhanced antenna positions for achieving desired pattern having minimum SLL as well as null placement in stipulated directions. Design examples elaborately focused on below mentioned conditions.

Suppression of peak SLL is described through Example 1, and Example 2 elaborates minimization of SLL with proper placement of several nulls near to one another in spatial region. Consequences of variation in control parameters over solution quality can be focused on further research.

References

1. Balanis, C.: Antenna theory-analysis and design, 2nd edn. Wiley, New York (1997)
2. Yang, X.S.: Flower pollination algorithm for global optimization. In: Durand-Lose, J., Jonoska, N. (eds.) International Conference on Unconventional Computing and Natural Computation, pp. 240–249. Springer, Berlin (2012)
3. Yang, X.-S., Karamanoglu, M., He, X.: Flower pollination algorithm: a novel approach for multiobjective optimization. Eng. Optim. **46**(9), 1222–1237 (2014)
4. Khodier, M.M., Christodoulou, C.G.: Linear array geometry synthesis with minimum side lobe level and null control using particle swarm optimization. IEEE Trans. Antennas Propag. **53**(8), 2674–2679 (2005)

Solving ($2 \times n$) Fuzzy Matrix Games

Laxminarayan Sahoo and Pintu Pal

Abstract In this article, ($2 \times n$) fuzzy matrix game is introduced, and its solution procedure has been suggested. Here, payoffs elements are supposed to be fuzzy-valued numbers, and these numbers are represented by triangular fuzzy numbers (TFNs). The solution methodology is employed by the process of defuzzification of fuzzy payoffs and usage of graphical method. Here, a new defuzzification technique based on beta distribution has been used for defuzzification of fuzzy payoffs. Finally, numerical examples are given for illustration purpose.

Keywords Fuzzy matrix game · Payoffs · Fuzzy number · Beta distribution Defuzzification

1 Introduction

In every real-life decision-making problem in a competitive economical situation, it is very much important to take the decision where there are two or more opposite parties in contradictory situations, and the action of one may rely on the action taken by the contesting party. Such types of conflicting situations are seen in every day, viz., in politics, elections, advertisements, marketing, etc. The history of game theory was established in the early twentieth century but a new direction has been taken about its only in 1944, when Von Neumann and Morgenstern [1] described game theory in their most pioneering work "Theory of Games and Economic Behavior". Since then several types of mathematical game problems have been framed and different solution procedures have been proposed. In the past, several researchers constructed

L. Sahoo (✉)
Department of Mathematics, Raniganj Girls' College, Raniganj 713358, India
e-mail: lxsahoo@gmail.com

P. Pal
Department of Computer Application, Asansol Engineering College, Asansol 713305, West Bengal, India
e-mail: p5_pal@yahoo.co.in

U. Biswas et al. (eds.), *Advances in Computer, Communication and Control*, Lecture Notes in Networks and Systems 41, https://doi.org/10.1007/978-981-13-3122-0_41

and solved the matrix game considering crisp/precise payoff. This means that the information's about the game are entirely known by the players. But in reality, the exact information about payoffs is clearly not known by the players, and it is observed that the players of games may not be able to calculate the outcomes of the games precisely due to lack of genuine information and hence, payoffs of some games cannot be measured exactly. To tackle such types of condition, the game problem can be reformulated using the theme of fuzzy set theory [2]. Fuzzy set is defined with the help of grades of membership function. Among several types of fuzzy sets, there are some special characteristics for the fuzzy sets that are defined on the set of real valued numbers. Membership functions of these sets can be viewed as fuzzy numbers. Fuzzy numbers plays an important role in fuzzy game theory. The use of fuzziness in game problem has been well studied by Campos [3]. Research direction about fuzziness in game problems one may mention the works of Bector et al. [4–6], Vijay et al. [7], Nayak and Pal [8, 9] and Sahoo [10–12]. In fuzzy game problems, all payoffs are fuzzy-valued numbers. In this article, we have to think about $2 \times n$ matrix game without saddle point whose payoffs are TFNs. Here, the fuzzy game problem has been transformed to crisp game by making use of defuzzification of fuzzy payoffs. For this purpose, a new defuzzification technique based on beta distribution has been exerted for defuzzification of fuzzy payoffs. The strategy for each player as well as the value of the game is obtained by solving the corresponding crisp game by use of graphical method. Finally, to adorn the solution procedure, a numerical example has been carried out and the computational results have been shown.

2 Some Basic Concepts and Definitions

In this section, some basic ideas and definitions used in this article are discussed.

2.1 Fuzzy Set Theory

A fuzzy set $\tilde{A}$ is defined by a membership function $\mu_{\tilde{A}}(x)$, which assigns each element x in X to a real number between 0 and 1. Here, $\mu_{\tilde{A}}(x)$ gives the grade of membership of x in $\tilde{A}$.

2.2 Normal Fuzzy Set

A fuzzy set $\tilde{A}$ is called a normal if there exists at least one $x \in X$ for which $\mu_{\tilde{A}}(x) = 1$.

2.3 Convex Fuzzy Set

A fuzzy set $\tilde{A}$ is called convex iff for $x_1, x_2 \in X$, the membership function of $\tilde{A}$ provides the inequality $\mu_{\tilde{A}}(\lambda x_1 + (1-\lambda)x_2) \geq \min\{\mu_{\tilde{A}}(x_1), \mu_{\tilde{A}}(x_2)\}$, where $\lambda \in [0, 1]$.

2.4 Fuzzy Number

A fuzzy number $\tilde{A}$ is a fuzzy set, which is both convex and normal.

2.5 Triangular Fuzzy Number (TFN)

The TFN is a normal fuzzy set denoted by $\tilde{A} = (a_1, a_2, a_3)$ and its membership function $\mu_{\tilde{A}}(x) : X \to [0, 1]$ is defined as follows:

$$\mu_{\tilde{A}}(x) = \begin{cases} \frac{x-a_1}{a_2-a_1} & \text{if } a_1 \leq x \leq a_2 \\ 1 & \text{if } x = a_2 \\ \frac{a_3-x}{a_3-a_2} & \text{if } a_2 \leq x \leq a_3 \\ 0 & \text{otherwise} \end{cases}$$

2.6 Beta Distribution

The random variable X is said to follow beta distribution if its probability density function is given by

$$f(x) = \begin{cases} \frac{x^{s-1}(1-x)^{t-1}}{\beta(s,t)} & 0 < x < 1 \\ 0 & \text{otherwise} \end{cases}$$

where $s > 0$ and $t > 0$ are parameters of beta distribution.

2.7 Defuzzification of Triangular Fuzzy Number Based on Beta Distribution

Let $\tilde{A} = (a_1, a_2, a_3)$ is a TFN. The projection of $\tilde{A} = (a_1, a_2, a_3)$ on the interval $(0, 1)$ is $\tilde{A} = (0, \frac{a_2-a_1}{a_3-a_1}, 1)$. If we define the parameter s corresponding to the beta

distribution as $s = \frac{a_2-a_1}{a_3-a_1} + 1$ we get $t = \frac{a_3-a_2}{a_3-a_1} + 1$. And the mean value ($\xi$) of beta distribution corresponding to the TFN $\tilde{A} = (a_1, a_2, a_3)$ is $\xi = \frac{s}{s+t} = \frac{a_3+a_2-2a_1}{3(a_3-a_1)}$.

Now, $\xi_{\tilde{A}}$ is the real number by transforming ξ from the interval $(0, 1)$ to the interval (a_1, a_3) is considered as the real number corresponding to the fuzzy number $\tilde{A} = (a_1, a_2, a_3)$ and $\xi_{\tilde{A}}$ is given by

$$\xi_{\tilde{A}} = \xi(a_3 - a_1) + a_1 = \frac{a_3 + a_2 + a_1}{3}$$

Lemma 2.1 *The crisp real number (defuzzified value) $\xi_{\tilde{A}}$ corresponding to the triangular fuzzy number $\tilde{A} = (a_1, a_2, a_3)$ is $\xi_{(a_1,a_2,a_3)} = \frac{a_1+a_2+a_3}{3}$.*

2.8 Fuzzy Payoff Matrix

Let $\tilde{a}_{ij}$ be the fuzzy payoff which is the gain of player A from player B if player A chooses strategy x_i whenever player B chooses y_j. Then the fuzzy payoff matrix is $\left(\tilde{a}_{ij}\right)_{m\times n}$.

Definition 2.2 (($2 \times n$) *fuzzy matrix Game*) The $(2 \times n)$ matrix Game can be defined as $\left(\tilde{a}_{ij}\right)_{2\times n}$ and represented by

$$\left(\tilde{a}_{ij}\right)_{2\times n} = \begin{matrix} \\ A_1 \\ A_2 \end{matrix} \begin{matrix} \begin{matrix} B_1 & B_2 & \cdots & B_n \end{matrix} \\ \begin{pmatrix} \tilde{a}_{11} & \tilde{a}_{12} & \cdots & \tilde{a}_{1n} \\ \tilde{a}_{21} & \tilde{a}_{22} & \ldots & \tilde{a}_{2n} \end{pmatrix} \end{matrix}.$$

where $A_i \in \{x_1, x_2\}$ be a strategy for player A and $B_j \in \{y_1, y_2, \ldots, y_n\}$ be a strategy for player B.

2.9 Mixed Strategy

The mixed strategy for the player A is denoted by $x = (x_1, x_2, \cdots, x_m)$, where $\sum_{i=1}^{m} x_i = 1$, and $x_i \geq 0$. Similarly, a mixed strategy for the player B is denoted by $y = (y_1, y_2, \cdots, y_n)$ where $\sum_{j=1}^{n} y_j = 1$ and $y_j \geq 0$.

2.10 Expected Payoff

Fuzzy expected payoff is denoted by $E(x, y)$ and is given by

$$E(x, y) = \sum_{i=1}^{m} \sum_{j=1}^{n} \tilde{a}_{ij}\, x_i y_j.$$

Lemma 2.2 *Defuzzified expected payoff is denoted by* $E_{df}(x, y)$ *and is given by*

$$E_{df}(x, y) = \sum_{i=1}^{m} \sum_{j=1}^{n} \xi_{\tilde{a}_{ij}}\, x_i y_j.$$

2.11 Saddle Point

The point (x_0, y_0) is said to be the saddle point if $E_{df}(x, y_0) \leq E_{df}(x_0, y_0) \leq E_{df}(x_0, y)$.

3 Graphical Method for $(2 \times n)$ Fuzzy Matrix Game

Let us consider a $(2 \times n)$ fuzzy matrix game without saddle point. Since the player A has two strategies $x = (x_1, x_2)$, it follows that $x_1 + x_2 = 1,\ x_1 \geq 0,\ x_2 \geq 0$. Thus, for each of the pure strategies available to the player B, the expected payoff for the player A is given by

$$E_j(x_1, x_2) = \xi_{\tilde{a}_{1j}} x_1 + \xi_{a_{2j}} x_2,\ j = 1, 2, \ldots, n$$

Therefore,

$$E_j(x_1) = \xi_{\tilde{a}_{1j}} x_1 + \xi_{\tilde{a}_{2j}}(1 - x_1) = (\xi_{\tilde{a}_{1j}} - \xi_{\tilde{a}_{2j}})x_1 + \xi_{\tilde{a}_{2j}},\ j = 1, 2, \ldots, n.$$

Now

$$E_j(x_1) = \begin{cases} \xi_{\tilde{a}_{2j}} \text{ if } x_1 = 0 \\ \xi_{\tilde{a}_{1j}} \text{ if } x_1 = 1 \end{cases}.$$

Hence, $E_j(x_1)$ represents a line segment joining the point $(0, \tilde{a}_{2j})$ and $(1, \tilde{a}_{1j})$. According to the maximin criterion for mixed strategy, the player A should select the value of x_1 so as to maximize his minimum expected payoff. Now, we have plotted the following n line segment $E_j(x_1) = (\xi_{\tilde{a}_{1j}} - \xi_{\tilde{a}_{2j}})x_1 + \xi_{\tilde{a}_{2j}},\ j = 1, 2, \ldots, n$. Here, the lowest boundary of these line segment will give the maximin expected payoff and optimum value of $x_1 (= x_1^*)$. Hence, our task is to determine only two strategies for player B corresponding to those lines which pass through the maximin point. Let these line segments are $E_k(x_1)$ and $E_l(x_1)$. Thus (2×2) payoff matrix corresponding

to A's moves A_1, A_2 and B's moves B_k, $B_l (k, l \in \{1, 2, \ldots, n\})$ will give the required result. Finally, solving (2×2) game algebraically, one may get the value of the game.

4 Numerical Example

In this section, for illustration purpose, we have considered an example of a (2×3) matrix game with fuzzy payoffs which is as follows:

		B		
		B_1	B_2	B_3
A	A_1	$(-1, 1, 2)$	$(2, 3, 4)$	$(9, 11, 12)$
	A_2	$(7, 8, 10)$	$(4, 5, 6)$	$(1, 2, 3)$

In this example, we have represented fuzzy payoff as a triangular fuzzy number. Suppose A chooses A_1 and A_2 with strategies x_1 and x_2, respectively, such that $x_1 + x_2 = 1$. Thus, the player A's expected payoff corresponding to the player B's pure strategies are given in Table 1.

Now, we have drawn two vertical lines $x_1 = 0$ and $x_1 = 1$ at unit distance apart and we have also drawn the line segments between two vertical lines which shown in Fig. 1.

From Fig. 1, it is seen that A, P, B, C on the lowest envelope represented the lowest possible gain for the player A for any values of x_1 between 0 and 1. The highest point of intersection point P of two line segments $E_2(x_1)$ and $E_3(x_1)$ represents the maximin expected value of the game for the player A. Hence, the solution to the original game is obtained from (2×2) matrix game, and the corresponding game is as follows:

		B	
		B_2	B_3
A	A_1	$(2, 3, 4)$	$(9, 11, 12)$
	A_2	$(4, 5, 6)$	$(1, 2, 3)$

Let $x = (x_1, x_2)$ and $y = (y_2, y_3)$ be the optimal strategies for the players A and B.

Now, equating $E_1(x_1) = E_2(x_1)$ we get, $x_1^* = \frac{9}{32}$ and hence $x_2^* = 1 - x_1^* = \frac{23}{32}$.

Table 1 Player A's expected payoff corresponding to the player B's pure strategies

B's pure strategies	A's expected payoff
B_1	$E_1(x_1) = (\xi_{(-1,1,2)} - \xi_{(7,8,10)})x_1 + \xi_{(7,8,10)}$
B_2	$E_2(x_1) = (\xi_{(2,3,4)} - \xi_{(4,5,6)})x_1 + \xi_{(4,5,6)}$
B_3	$E_3(x_1) = (\xi_{(9,11,12)} - \xi_{(1,2,3)})x_1 + \xi_{(1,2,3)}$

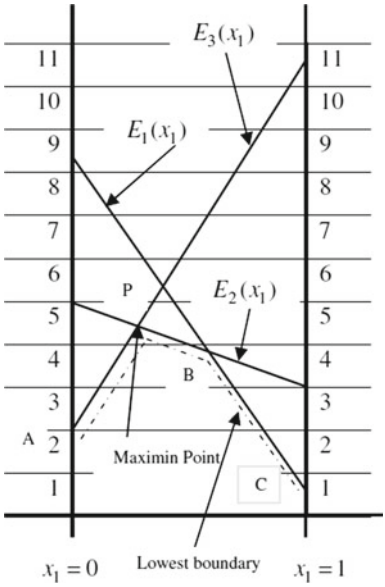

Fig. 1 Graphical representation for solving (2×3) game

Similarly, equating $E_2(y_2) = E_3(y_2)$ we get $y_2^* = \frac{13}{16}$ and hence $y_3^* = 1 - y_2^* = \frac{3}{16}$.

Therefore, the optimal strategy for the player A is $x = (\frac{9}{32}, \frac{23}{32})$, and the optimal strategy for player B is $y = (0, \frac{13}{16}, \frac{3}{16})$. The value of the game is $E_2(x_1^*) = \frac{71}{16}$.

5 Concluding Remarks

Game problem is one of the most important problems for the action or process of making important decision. In many everyday situations, payoffs of a game are not precise. So, $(2 \times n)$ matrix game problem with fuzzy payoff is presented, and its solution methodology has been discussed. Here fuzzy payoffs are represented by triangular fuzzy number, and using defuzzification process based on statistical beta distribution, the corresponding game problem is transformed to crisp game problem. Finally, the game problem with fuzzy payoffs has been solved, and computed results have been displayed and compared. It may be asserted that the proposed method discussed in this work can be applied to solve $(m \times 2)$ fuzzy game problems in the near future.

References

1. Neumann, J.V., Morgenstern, O.: Theory of Games and Economic Behavior. Princeton University Press, New York (1944)
2. Zadeh, L.A.: Fuzzy sets. Inf. Control. **8**(3), 338–352 (1965)
3. Campos, L.: Fuzzy linear programming models to solve fuzzy matrix games. Fuzzy Sets Syst. **32**, 275–289 (1989)
4. Bector, C.R., Chandra, S.: On duality in linear programming under fuzzy environment. Fuzzy Sets Syst. **125**, 317–325 (2002)
5. Bector, C.R., Chandra, S., Vijay, V.: Duality in linear programming with fuzzy parameters and matrix games with fuzzy payoffs. Fuzzy Sets Syst. **146**, 253–269 (2004)
6. Bector, C.R., Chandra, S., Vijay, V.: Matrix games with fuzzy goals and fuzzy linear programming duality. Fuzzy Optim. Decis. Mak. **3**, 255–269 (2004)
7. Vijay, V., Chandra, S., Bector, C.R.: Matrix games with fuzzy goals and fuzzy payoffs. Omega **33**, 425–429 (2005)
8. Nayak, P.K., Pal, M.: Solution of interval games using graphical method. Tamsui Oxf. J. Math. Sci. **22**(1), 95–115 (2006)
9. Nayak, P.K., Pal, M.: Linear programming technique to solve two-person matrix games with interval pay-offs. Asia Pac. J. Oper. Res. **26**(2), 285–305 (2009)
10. Sahoo, L.: Effect of defuzzification methods in solving fuzzy matrix games. J. New Theory. **8**, 51–64 (2015)
11. Sahoo, L.: An interval parametric technique for solving fuzzy matrix games. Elixir Appl. Math. **93**, 39392–39397 (2016)
12. Sahoo, L.: An approach for solving fuzzy matrix games using signed distance method. J. Inf. Comput. Sci. **12**(1), 073–080 (2017)

Study of Inset Fed Rectangular Patch Antenna Using Partial Ground Plane

Pratik Ghosh, Kousik Roy, Chiranjib Goswami, Naimul Hasan, Saswata Chakraborty and Arup Kumar Chandra

Abstract In this paper, we have designed a microstrip patch with inset feed mechanism. The fundamental benefit of utilizing inset cut feed is not only increasing the antenna bandwidth but return loss are satisfactorily improved. The antenna has been simulated using rectangular patch on partial and non partial ground plane. It has been examined that the antenna performance acquires improvement over conventional design by partial ground plane according to the size of the patch. Here we have generated a third-order mode to get a broad bandwidth.

Keywords Inset feed · Return loss · Bandwidth · Partial ground plane

P. Ghosh (✉)
Department of Electronics & Communication Engineering, Murshidabad College of Engineering and Technology, Murshidabad 742102, West Bengal, India
e-mail: prakanika2014@gmail.com

K. Roy (✉) · S. Chakraborty
Department of Electronics & Communication Engineering, Asansol Engineering College, Asansol 713305, West Bengal, India
e-mail: kousikroy002@gmail.com

S. Chakraborty
e-mail: saswata.cmeri@gmail.com

C. Goswami · A. K. Chandra
Department of Electronics & Instrumentation Engineering, Asansol Engineering College, Asansol 713305, West Bengal, India
e-mail: avi.chiranjib@gmail.com

N. Hasan
Department of Electronics & Communication Engineering, Sanaka Educational Trust's Group of Institution, Durgapur 71321, West Bengal, India
e-mail: naimul_hasan@yahoo.in

U. Biswas et al. (eds.), *Advances in Computer, Communication and Control*, Lecture Notes in Networks and Systems 41, https://doi.org/10.1007/978-981-13-3122-0_42

1 Introduction

Microstrip antenna is one of the most popular antennas that have various advantages such as miniature size, low profile, not much weight, simple and reasonably price, simple fabrication and installation etc. [1, 2, 3]. The most significant disadvantage of microstrip antenna is narrow bandwidth. The antenna bandwidth can be increased by various techniques. One of the techniques is partial Ground Plane [4, 5]. The imperfection formed in a ground plane is one of the distinctive techniques for diminishing the antenna size. Antenna designed with partial ground plane decreases the antenna size. By applying partial ground plane we can improve impedance bandwidth, VSWR, and gain also.

2 Antenna Design and Geometry

Figures 1 and 2 signifies the geometry of proposed microstrip antenna with and without partial ground plane. As shown in the figure, inset feed is utilized to feed the microstrip patch antenna of definite feed line width so that the antenna impedance equals with port impedance of 50 Ω [6, 7]. The antenna is designed on substrate having relative permittivity of 4.7. Here we have considered the substrate thickness that equals to 1.57 mm. The feed line width as well as spacing is amended to make sure that the impedance of antenna is 50 Ω. Here we have utilized a third-order mode to obtain a wide bandwidth which is the significance of surface current distribution. We will get a clear picture of impedance bandwidth (VSWR < 2) to get a VSWR as well as reflection bandwidth to analyze smith chart representation of input impedance. There are two reasons to see the VSWR (i) to measure the input impedance bandwidth (ii) It is to see how well matching is achieved.

3 Simulation Results of the Proposed Microstrip Patch Antenna Without Partial Ground Plane

The proposed antenna has been simulated with the help of ANSYS HFSS 2017 and the mechanism of the antenna has been examined in terms of bandwidth, return loss, VSWR, radiation pattern and gain, input impedance, current distribution, 3D polar plot [8, 9, 10]. Without partial ground plane we have got the return loss, bandwidth, VSWR, gain and input impedance −24.3240 dB, 3.07 GHz, 1.1294, 4.0209 dB, and 46.22 Ω, respectively.

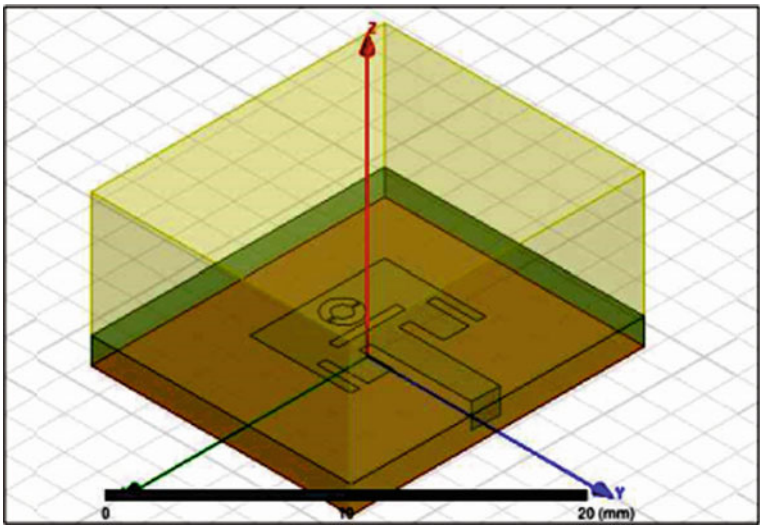

Fig. 1 3D geometry of the proposed microstrip patch antenna without partial ground plane

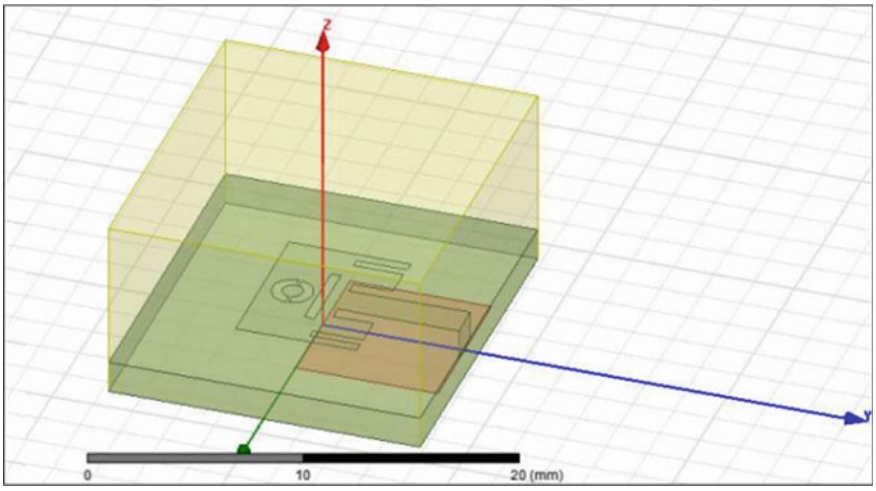

Fig. 2 3D Geometry of the proposed geometry of microstrip patch antenna with partial ground plane

3.1 Return Loss and Bandwidth of Proposed Antenna Without Partial Ground Plane

Figure 3 illustrates the simulated return loss plot and bandwidth of inset fed slot loaded rectangular microstrip patch antenna which has a resonance frequency of

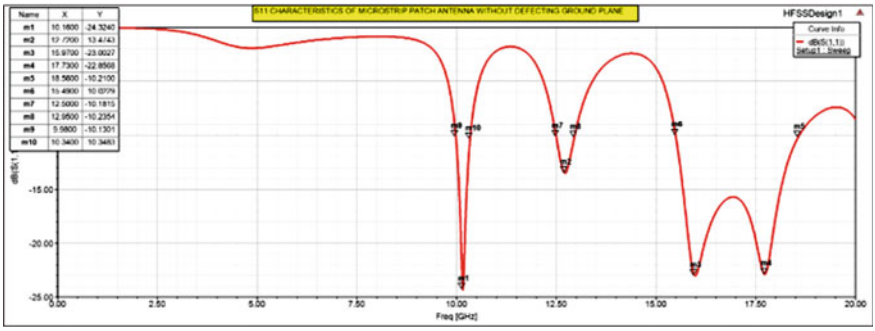

Fig. 3 Return loss plot and bandwidth of slot loaded MSA without partial ground plane

10 GHz. It has been examined that the return loss of proposed design is −24 dB and the meliorated bandwidth of microstrip patch antenna with shrinked ground and inset fed loaded ground is 530 MHz.

3.2 Gain of Proposed Antenna Without Partial Ground Plane

Figure 4 shows the 3D radiation pattern that demonstrates the gain of microstrip patch antenna. The examined gain at resonant frequency of proposed antenna is 4.0209 dB.

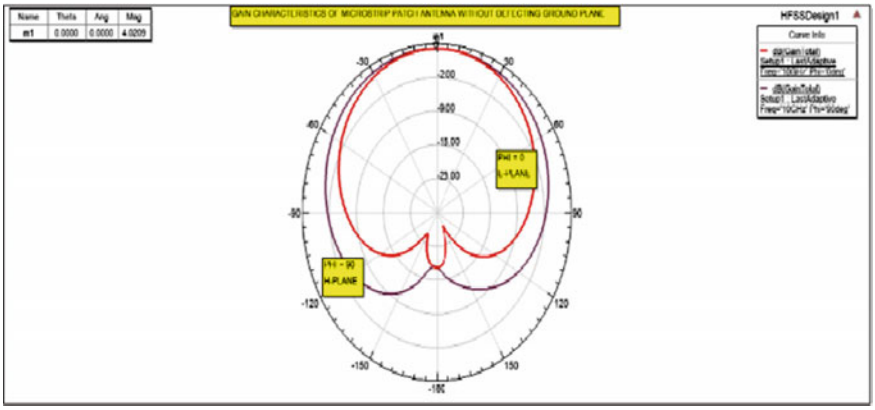

Fig. 4 Gain for proposed inset fed slot loaded MPA antenna without partial ground plane

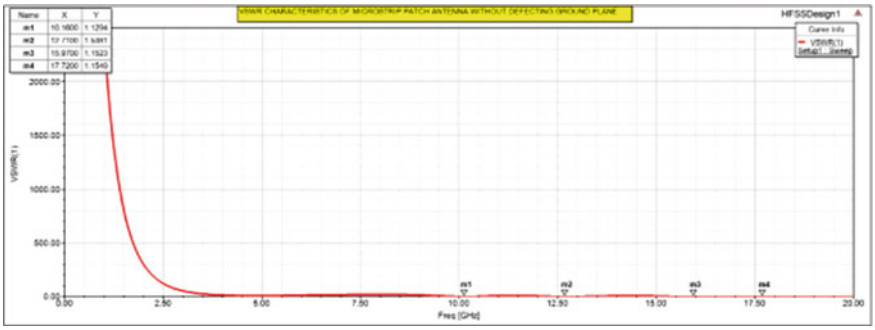

Fig. 5 VSWR plot for proposed inset fed slot loaded MPA antenna without partial ground plane

3.3 VSWR Plot for Proposed Antenna

Figure 5 shows the VSWR plot for proposed inset fed slot loaded microstrip patch antenna without partial ground plane.

For effective functioning of antenna, VSWR should be less than equal to 2. The observed value of VSWR is below up to standard value.

3.4 Surface Current Distribution of Proposed Antenna

Figure 6 shows the current distribution on the patch.

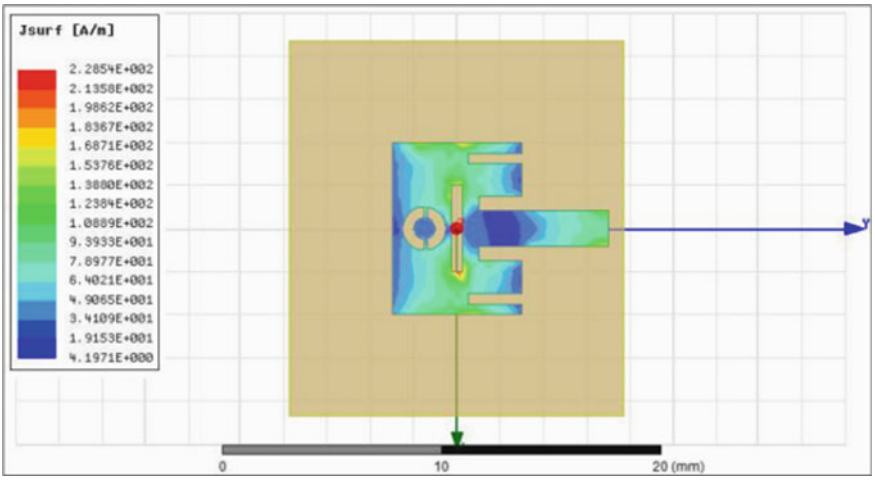

Fig. 6 Surface current distribution of proposed MPA without partial ground plane

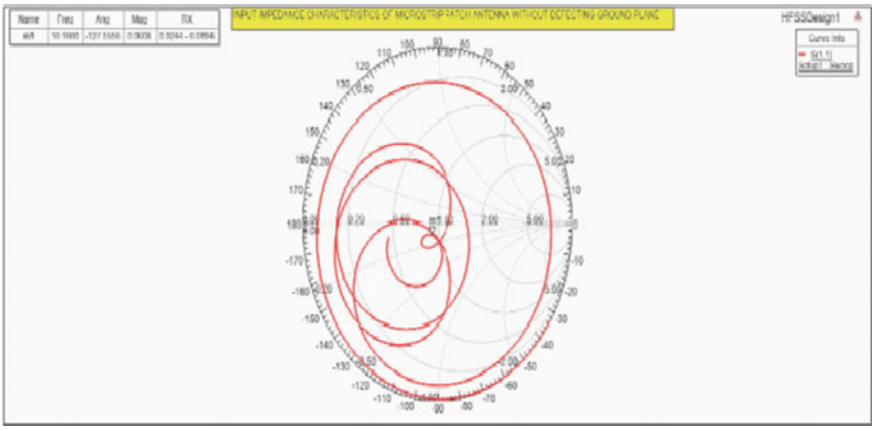

Fig. 7 Input impedance of proposed MPA without having partial ground plane

3.5 Input Impedance of Proposed Antenna

Figure 7 depicts the input impedance of the proposed antenna without having partial ground plane. The analyzed input impedance at resonant frequency of proposed antenna is 46.22.

3.6 3D Polar Plot Radiation Pattern of Proposed Antenna

Figure 8 shows the 3D polar plot radiation pattern of proposed antenna.

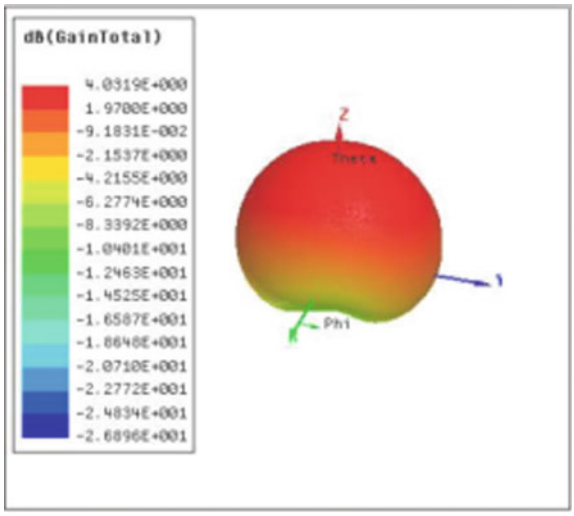

Fig. 8 3D polar plot of the proposed MPA without partial ground plane

4 Results of the Proposed Microstrip Patch Antenna with Partial Ground Plane

The proposed slot loaded inset fed microstrip patch antenna having partial ground plane along with rectangular type of slot cut has been simulated using ANSYS HFSS 2017 and the operation of the antenna has been examined in terms of bandwidth, return loss, VSWR, radiation pattern and gain, input impedance, current distribution, 3D polar plot [8, 9, 10]. With partial ground plane having rectangular slot we have got the return loss, bandwidth, VSWR, gain and input impedance −21.6275 dB, 3.39 GHz, 1.1808, 4.0033 dB, and 45.165 Ω, respectively.

4.1 Return Loss and Bandwidth of Proposed Antenna with Partial Ground Plane

Figures 9, 10, 11, 12, 13 and 14 depict the simulated return loss as well as bandwidth of inset fed slot loaded microstrip patch antenna having partial ground plane.

4.2 Gain, Input Impedance, and VSWR of Proposed Antenna with Partial Ground Plane

See Figs. 10, 11 and 12.

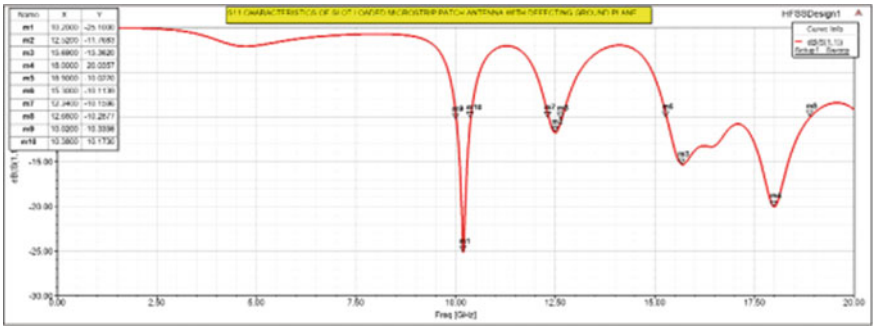

Fig. 9 Return loss and bandwidth of proposed MPA with partial ground plane

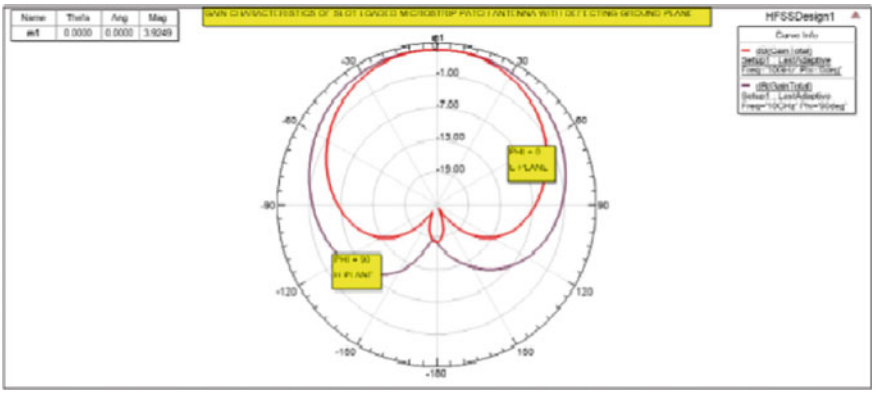

Fig. 10 Gain of proposed MPA with partial ground plane

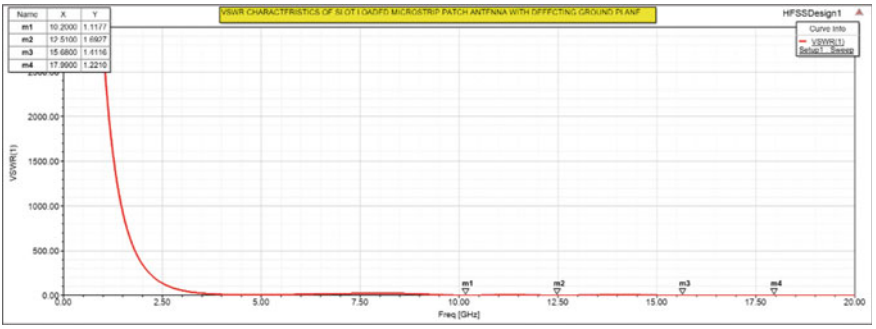

Fig. 11 VSWR result of slot loaded MPA with partial ground plane

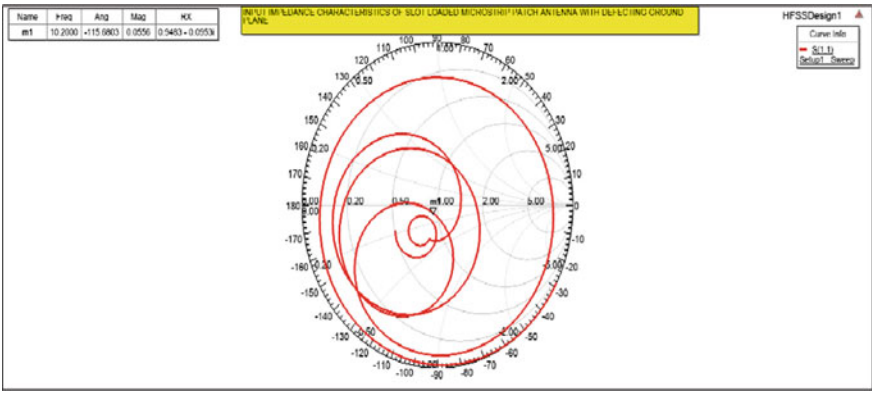

Fig. 12 Input impedance of slot loaded MPA having partial ground plane

4.3 Surface Current Distribution and 3D Polar Plot of the Gain of the Proposed Microstrip Antenna with Partial Ground Plane

See Figs 13 and 14.

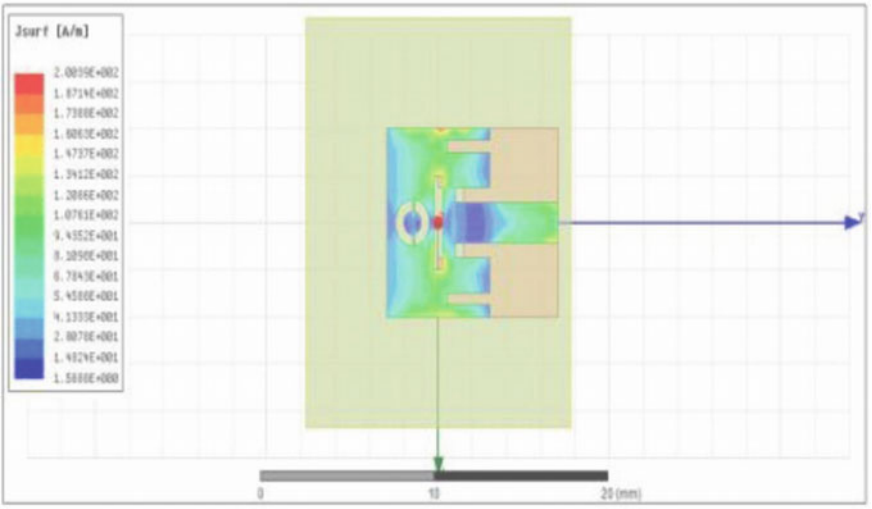

Fig. 13 Current distribution of slot loaded MPA having partial ground plane

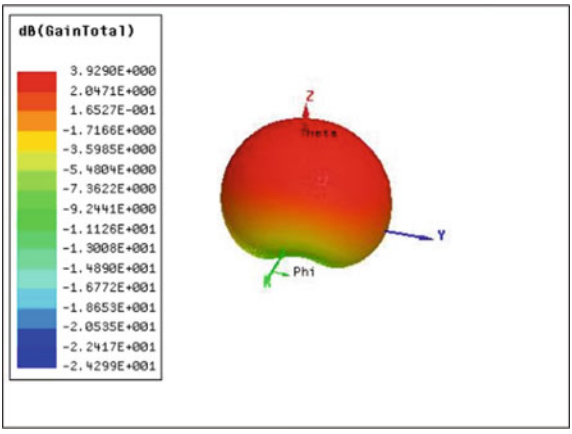

Fig. 14 3D polar plot of gain of slot loaded MPA having partial ground plane

5 Comparison of Results Between Partial Ground Plane and Non Partial Ground Plane Proposed Microstrip Patch Antenna

Proposed MPA	Return loss (dB)	Bandwidth (GHz)	VSWR	Input impedance
Without partial ground plane	24.3240	3.07	1.1294	46.22
With partial ground plane	25.1000	3.6	1.1177	47.415

From the above comparison, it is noticed that after applying partial ground plane we can improved impedance bandwidth, VSWR and gain also. Here, comparatively lower return loss is achieved after adding partial ground plane.

6 Conclusions

The designed microstrip patch antenna with loaded inset fed on partial ground plane and non partial ground has been simulated in ANSYS HFSS 2017. The analyzed outcomes such as bandwidth, gain, directivity, return loss, VSWR, the surface current has been examined. It is noticed that bandwidth and return loss has been amended by utilizing partial ground plane procedure. Simulated outcomes propose that the dependence of the input impedance on feed location is unlike for the non partial and partial ground plane in company with diverse slot cut. By concerning partial ground plane on the proposed inset fed rectangular microstrip patch antenna the bandwidth, return loss and input impedance of the proposed design acquired satisfaction.

References

1. Kraus, J.D.: Antennas for All Applications, 3rd edn. McGraw Hill Inc, New York
2. Balanis, C.A.: Antenna Theory, Analysis and Design, 2nd edn. Wiley, New York (2005)
3. Kumar, G., Roy, K.P.: Broadband Microstrip Antennas. Artech house, London (2003)
4. Milligan, T.A.: Modern Antenna Design, 2nd edn. Wiley, New York (2005)
5. Deb Kumar, P., Moyra, T., Bhowmik, P.: Return loss and bandwidth enhancement of microstrip antenna using defected ground structure (DGS). In: 2nd International Conference on Signal Processing and Integrated Networks, 19–20 Feb 2015. https://doi.org/10.1109/spin.2015.7095318
6. Yang, F., Zhang, X.X., Ye, X., Rahmat-Samii, Y.: Wide-band E shaped patch antennas for wireless communications. IEEE Trans. Antennas Propag. **49** (2001)
7. Rajgopal, K.S., Sharma, K.S.: Investigations on ultrawideband pentagon shape microstrip slot antenna for wireless communications. IEEE Trans. Antennas Propag. **57**(5) (2009)

8. Roy, K., Nag, A. Chaudhuri, D., Bose, S.: A novel dual band antenna for C and X band satellite communication. In: International Conference on Electrical, Electronics, Signals, Communication and Optimization, IEEE, pp. 953–955. ISBN: 978-1-4799-7676-8; 978-1-4799-7678-2/15/$31.00 ©2015 (2015)
9. Roy, K., Chaudhuri, D., Bose, S., Nag, A: A novel dual band antenna for radar application. In: Proceedings of 3rd International Conference on Advanced Computing Networking and Informatics, vol. 2, pp. 643–650. ISBN: 978-81-322-2528-7. https://doi.org/10.1007/978-81-322-2529-4, vol. 44, Springer, India (2015)
10. Nag, A., Roy, K., Chaudhuri, D: A crown-shaped microstrip patch antenna for wireless communication systems. In: Kalam, A., Das, S., Sharma, K. (eds.) Advances in Electronics Communication and Computing. Lecture Notes in Electrical Engineering, vol. 443, pp. 399–405 (2018)

UWB Bandpass Filter Using Stepped Impedance Resonator with Rectangular- and Dumbbell-Shaped DGS

Intekhab Hussain, Sushrut Das and M. G. Tiary

Abstract In this paper, an ultra-wideband (UWB) bandpass filter (BPF) using stepped impedance resonators and defected ground structure (DGS) with fractional bandwidth 119% is proposed. The design is based on stepped impedance resonators (SIR) with DGS. The frequency response shows three transmission poles in the passband and the frequency range of the passband is 2.76–10.97 GHz. The return loss of the proposed filter is more than 15 dB and the insertion loss is less than 1.1 dB. The filter is simple and small in size.

Keywords Ultra-wideband · Bandpass filter · Stepped impedance resonator (SIR) Defected ground structure (DGS)

1 Introduction

A bandpass filter (BPF) passes the desired frequencies and attenuates the unwanted signals. With a bandwidth of 7.5 GHz (3.1–10.6 GHz), UWB systems have a number of advantages, such as very high transmission data rates (up to 500 Mb/s), low energy density over a wideband spectrum and extremely low transmission energy (less than 0.1 mW), etc. In this paper, we have presented a bandpass filter for ultra-wideband applications using stepped impedance resonators with DGS. The filter is small in size (21 mm × 5 mm) and hence this simple planar geometry makes it compatible with existing microwave-integrated circuits.

I. Hussain (✉)
AEIE Department, Asansol Engineering College, Asansol, West Bengal, India
e-mail: hussain.intekhab@gmail.com

S. Das
Department of Electronics Engineering, Indian Institute of Technology (Indian School of Mines) Dhanbad, Dhanbad 826004 , Jharkhand, India

M. G. Tiary
ECE Department, Asansol Engineering College, Asansol, West Bengal, India

U. Biswas et al. (eds.), *Advances in Computer, Communication and Control*, Lecture Notes in Networks and Systems 41, https://doi.org/10.1007/978-981-13-3122-0_43

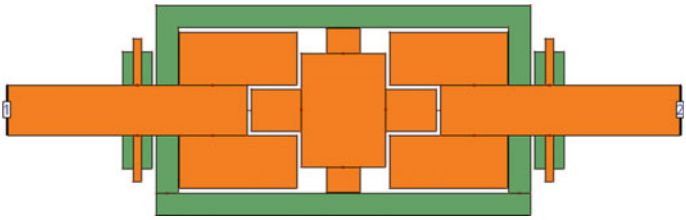

Fig. 1 Geometry of the proposed UWB BPF

2 Filter Design

The proposed UWB bandpass filter is designed using substrate RT/Duroid 5880 with dielectric constant 2.2 and thickness 0.787 mm (Fig. 1). The loss tangent of the dielectric material is 0.009. Initially, we started with the simple geometry having stepped impedance structures and a rectangular DGS as shown in the Fig. 2. The frequency response of the corresponding geometry is shown in Fig. 3. Here we obtained three transmission poles but the return loss is not so good. Also, the stop band response is not acceptable.

To improve upon this we inserted another stepped impedance resonator in the middle of the filter structure as shown in Fig. 4. The frequency response of the corresponding filter is shown in Fig. 5. We observe that still the stop band response is not improved. So, now we used two dumbbell-shaped DGSs in the ground plane on both sides of the rectangular DGS, as shown in Fig. 6.

In Fig. 7 we see a remarkable improvement in the stop band response of the filter. We further insert two stubs on both sides of the filter geometry to achieve a better result as shown in Fig. 8. The corresponding frequency response is shown in Fig. 9.

Now we performed the parametric analysis of various parameters of the filter geometry to obtain the final frequency response. Thus, the final geometry of the proposed UWB bandpass filter is obtained and shown in Fig. 10. The corresponding final frequency response of the filter is shown in Fig. 11.

Table 1 gives a list of the values of various parameters of the proposed filter.

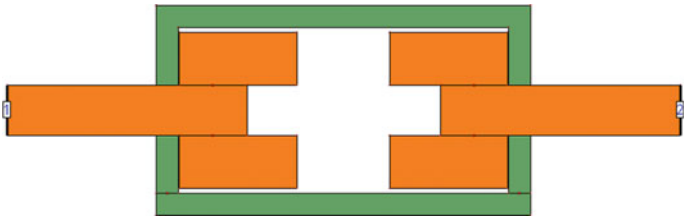

Fig. 2 Initial geometry-1

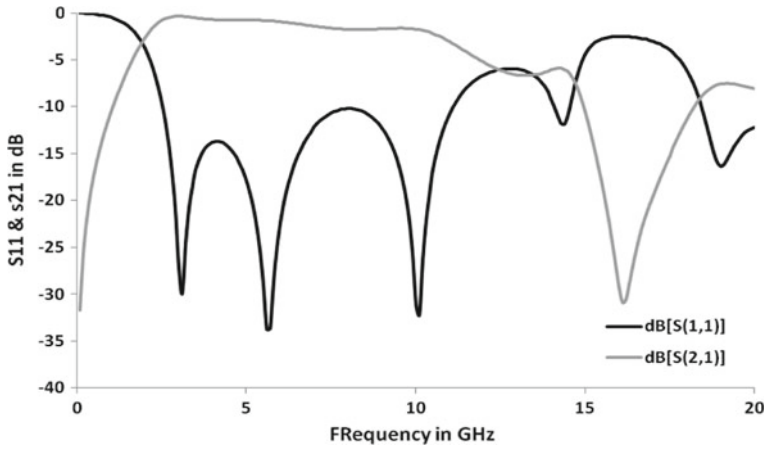

Fig. 3 Frequency response-1

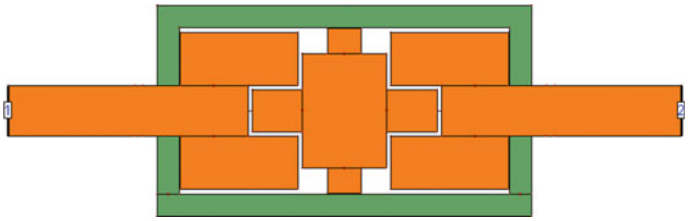

Fig. 4 Geometry-2

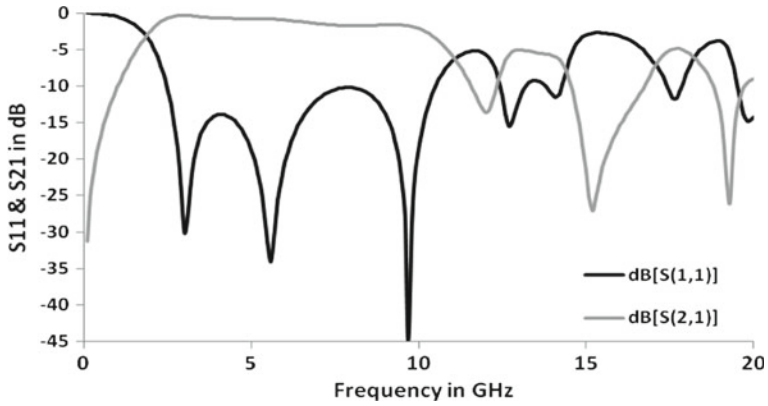

Fig. 5 Response-2

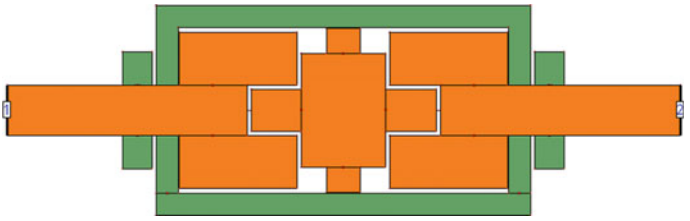

Fig. 6 Geometry-3

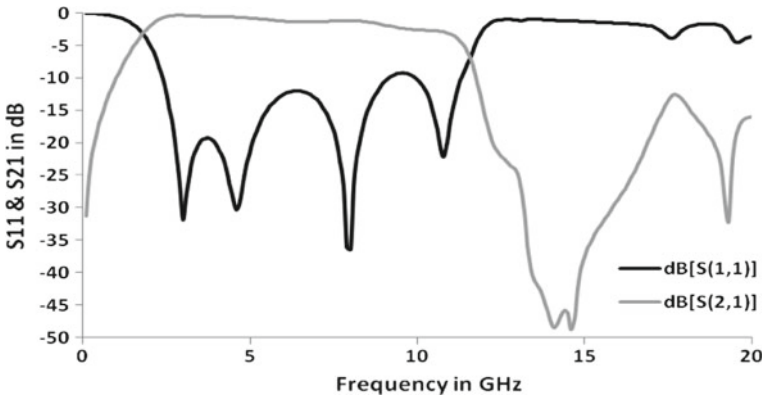

Fig. 7 Response-3

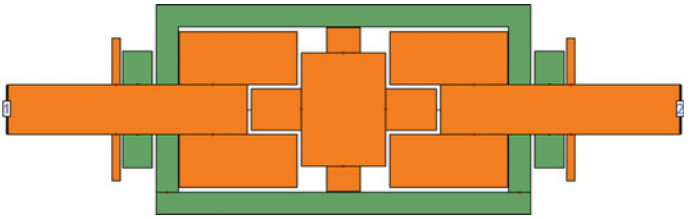

Fig. 8 Geometry

3 Results

The filter has been designed using the substrate RT/Duroid 5880 with dielectric constant of 2.2 and a thickness of 0.787 mm. The filter is compact and small in size. Three transmission poles are obtained within the wide passband ranging from 2.76 to 10.97 GHz covering a bandwidth of 8.21 GHz. The filter has low insertion loss as well as high return loss. The center frequency of the filter is 6.865 GHz and the fractional bandwidth is 119%. The filter has a wide stopband and it extends beyond 20 GHz. The simulation software IE3D v.14 was used for designing and simulation of the filter.

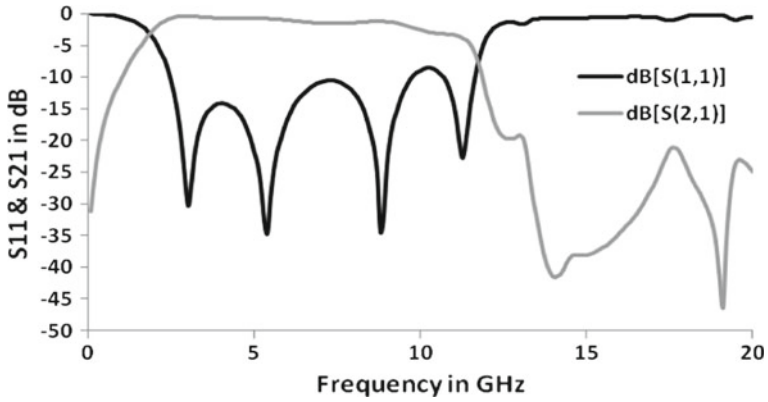

Fig. 9 Frequency response to the geometry shown in Fig. 8

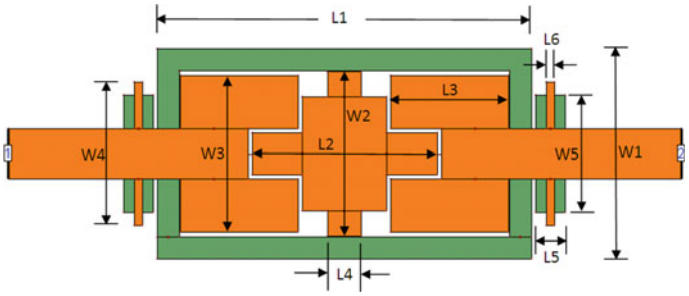

Fig. 10 Final geometry

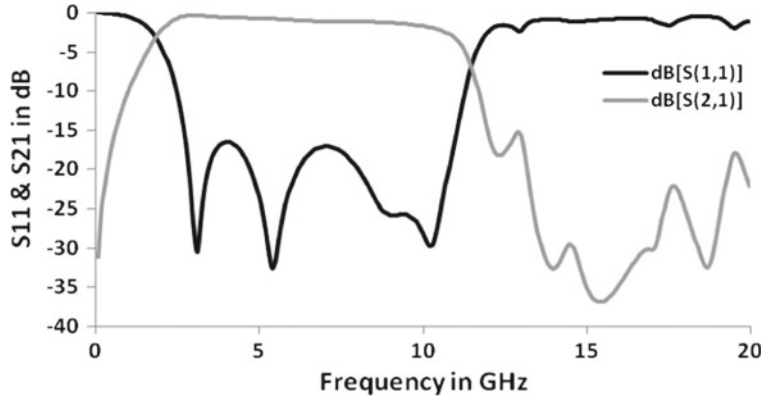

Fig. 11 Final Frequency response

Table 1 Dimensions of final geometry

Parameter	Value (mm)
L1	17.8
L2	8.8
L3	5.6
L4	1.6
L5	1.4
L6	0.4
W1	10
W2	7.8
W3	7.4
W4	6.8
W5	5.6

4 Conclusions

In this paper, we have designed and simulated a bandpass filter covering the entire ultra-wide band of frequency. The filter has a wide stopband exceeding 20 GHz. The geometry of the filter is simple and the size is compact. This BPF may be used in ultra wideband systems such as short-range high data rate communication systems and wireless personal area networks (WPANs) for personal computers and electronic devices.

Process Enhancement of Sparks Erosion Machining System Using FPGA Algorithm

Koushik Shit, Dharmbir Prasad and Rudra Pratap Singh

Abstract Today, use of the electrodes is not limited to making contacts only; rather, it has found a vast application as a machining tool (due to the erosive effect of electrical discharge or sparks of electrodes). Spark erosion machining (SEM) is an extensively used thermal type advanced machining process, capable of machining most electrically conductive materials irrespective of their hardness and toughness producing complex geometries, shapes, and features. It is a controlled spark erosion process in which material removal is felicitated through melting and vaporization by a series of repeated electrical discharges occurring between the tool electrode and the workpiece in the presence of a suitable dielectric fluid. This paper presents an improved monitoring process and the peripheral control system for SEM. The SEM process, under study, runs based on the field programmable gate arrays (FPGA) algorithm. The proposed system implemented in software and hardware both. The software implementation has been done using MATLAB Simulink. The results presented in this paper demonstrate the potential of the proposed approach.

Keywords Materials · Process · Spark · Erosion

1 Introduction

Spark erosion machining (SEM) is working on the erosive effect of electrical discharges or sparks. This effect is discovered by chemist Joseph Priestly in 1770, after a long period, in 1943, Lazarenko explored the destructive properties of

K. Shit (✉)
National Power Training Institute, Faridabad, India
e-mail: koushik.shit@gmail.com

D. Prasad · R. P. Singh (✉)
Asansol Engineering College, Asansol, India
e-mail: rpsingh.aec@gmail.com

D. Prasad
e-mail: dharmbirprasad9@gmail.com

U. Biswas et al. (eds.), *Advances in Computer, Communication and Control*, Lecture Notes in Networks and Systems 41, https://doi.org/10.1007/978-981-13-3122-0_44

electrical discharges for constructive use. It is the non-conventional material removal processes [1]. The machine needs electrical power for material erosion purpose. Materials cutting in various shapes are also dependent on the electrodes. Today, an electrode as small as 0.1 mm can be used to "drill" holes into curved surfaces at steep angles without drill "wander". This paper is describing monitoring and control system for efficient SEM. The FPGA provides controlling of all electrical data and related mechanical parameters.

1.1 Spark Erosion Machining Process

In this system, electrical spark energy turns into thermal energy and produces plasma between the electrodes and workpiece by immersing into dielectric fluid. The plasma temperature is in the range of 8000–12,000 °C. And it initializes a substantial amount of heating and melting of the material at the surface of each pole. A high frequency directs current supply to the system approximately in kHz range. On the turned-off time, the plasma channel is broken down. This causes sudden reduction in the temperature and dielectric fluid to implore the plasma circulating channel and flush the molten material from both pole surfaces in the form of microscopic debris. This process causes melting and evaporation of the material from the workpiece surface from both the pole. The volume of material removed per discharge in the range of 10^{-6}–10^{-4} mm^3 and the material removal rate (MRR) is normally 2–400 mm^3/min it depends upon material specification. In the manufacture of aeronautical, aerospace parts and difficult 3D design can be easily designed by the system. SEM is a cutting process; depending on liquid flow and sparking frequency and material property [2]. This FPGA control system can adjust his speed according to time. Controllable fluid flow and electrical discharge can overcome 300 Ω/cm. SEM has a very fist data emulating and corresponding responses generated by the system. The proposed study help us to stabilize the system of the present frequency-depended process. This system is controlled by FPGA system; it can control MRR, tool wear rate (TWR) and surface quality (SR) of the system [3].

In this prototype system, all components are connected as per FPGA system. It has three peripheral systems, e.g., dielectric flow system, axis condoling system, and HMI system. Dielectric flow is attributing an impotent roll in the erosion of the material. The proper fluid flow is done by 12 V DC motor and for filtration of dielectric a filter is installed. The fluid sensor indicates the quality of the produced fluid. Axis controlling system has four elements viz., permanent magnate synchronous motor, generator, stepper motor, LDR, and LED system. Two synchronous motors are used for drive SEM to move on the surface. The generators are connected with the synchronous motor and it calculates the distance data and send to the control unit. LDR and LED are used for sentience the position axis. Stepper motor is only response bale for Z-axis moment. Human–machine interface (HMI) system is a combination

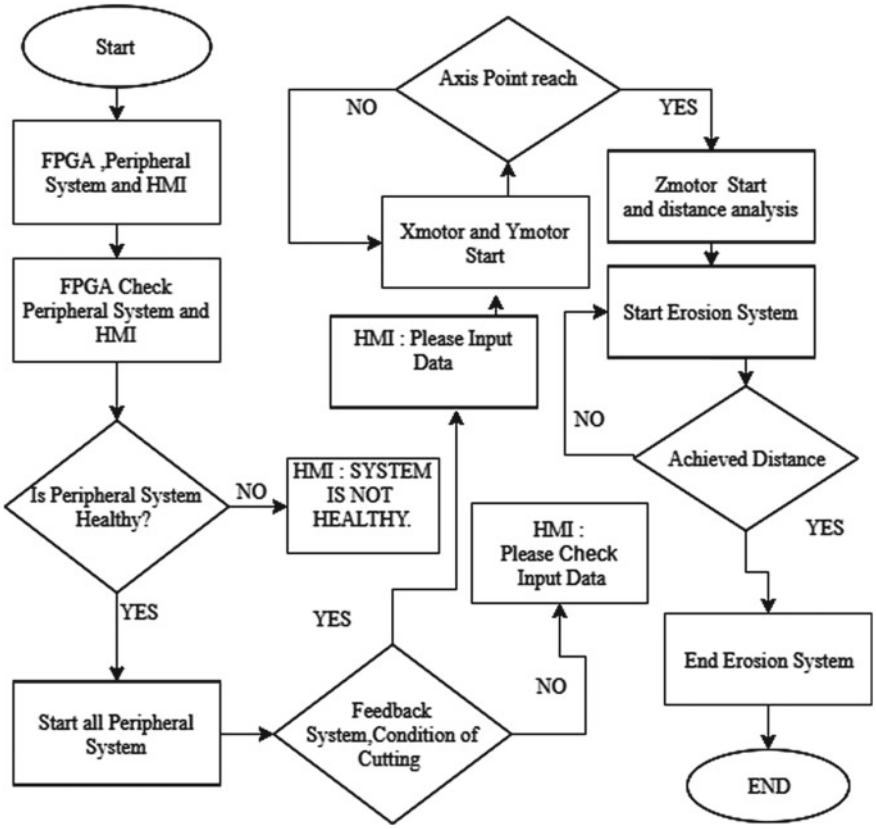

Fig. 1 Programming block diagram of the SEM system

of one STN-LCD, keyboard with function keys, numeric keys, and direction keys are assembled and a USB port for programming of SEM. The logical wave form and signal output are shown in Fig. 1.

2 Mathematical Formulations of SEM

Mathematical formulation of the SEM process is presented in the succeeding subsection.

2.1 Gap State

Machining efficiency will depend on the gap of between electrode and workpiece. For better stability, if gap state is small, then machining efficiency will decrease. Because the small gap will generate lot many pulses sufficient abut of plasma will not generated. A gap state can be mathematically given by (1) [2, 3].

$$Y(t) = \frac{\tau_{stab} + \tau_{shor}}{\tau_{spark} + \tau_{travsarc} + \tau_{stabarc} + \tau_{short} + \tau_{open}}, \tag{1}$$

where $Y(t)$: gap state at time t, τ_{spark}: accumulated number of discriminated spark states, $\tau_{travsarc}$: accumulated number of discriminated transient arc states, $\tau_{stabarc}$: accumulated number of discriminated stable arc states, τ_{short}: accumulated number of discriminated short states, τ_{open}: accumulated number of discriminated open states.

In order to establish,

$$A(q)y(t) = B(q)u(t) + C(q)e(t), \tag{2}$$

where q is a forward shift operator, $A(q) = 1 + a_1 q^{-1} + \cdots + a_n q^{-n}$, $B(q) = b_1 q^{-1} + b_2 q^{-2} + \cdots + b_n q^{-n}$ and $C(q) = 1 + c_1 q^{-1} + \cdots + c_n q^{-n}$.

$$\theta_t = \arg\min \sum \sum_{k=1}^{t} \beta(t,k)\left[y(k) - \Phi^t(k)\right]^2, \tag{3}$$

where $\beta(t,k) = \lambda(t)^{t-k}, 0 \le k \le t-1$, $\lambda(t)$: forgetting factor and $\beta(t,k) = 1$, $\phi(t)$ contains lagged input and output variables.

Other factors can be given as in (4), (5) [4, 5].

$$R(t) = \sum_{k=1}^{t} \beta(t,k)\varphi(k)\varphi^t(k) \tag{4}$$

$$F(t) = \sum_{k=1}^{t} \beta(t,k)\varphi(k)y^t(k) \tag{5}$$

Then,

$$\theta_t = R^{-1}(t)f(t) \tag{6}$$

And to avoid inverting $R(t)$ introduces (7) [6].

$$P(t) = R^{-1}(t), \tag{7}$$

where θ: a vector containing estimated parameters of EDM process model, $\lambda(t)$: forgetting factor, $\lambda(t)$: forgetting factor, u_c: reference input, $u(t)$: control variable.

3 Application of SEM Process

The SEM is the better machining processes than traditional machining processes for some specific cases. It isolates all hardness-related process because the process is not induced mechanical stresses during machining. F. T. Weng has carried out an experiment with 50 μm a diameter of electrodes. This process is found to be suitable for micro-size industrial work, as like micro-pins, micro-nozzles, and micro-cavities. Material boron carbide and silicon infiltrated silicon carbide is successful use in the cutting industries with help of mechanical arrangement SEM will adapt all as electrode. SEM can work on the Sialon ceramics or silicon nitride. With proper arrangement of SEM as milling purpose [7, 8].

4 Simulation Results and Discussions

ModelSim Intel-FPGA (version 10.5b) software tool is used for the FPGA simulation. This simulation shows only the input/output logic of the random process of electrical discharge (as provided in Fig. 2). Gap manning, electrical discharge, and location conformation system control is described in the simulation. In this system, clock pulse shows the system speed. X and Y inputs are providing the conformation of the exact location. As par information output motor X and motor Y is working. Z-axis movement system is controlled by ZF and ZR signal. SEM-carried voltage in kV range for batter safety spark system will start after conformation of all peripheral process's and random processes, in simulation it starts after 300 unit time.

The Simulink help to understand the peripheral argent mint control. SEM movement permanent magnet synchronous motor for the X-axis and Y-axis movement and for the Z-axis movement sapper motor is used. Every motor has connected to analyze the motor position and motor movement. Three motors are parallelly connected

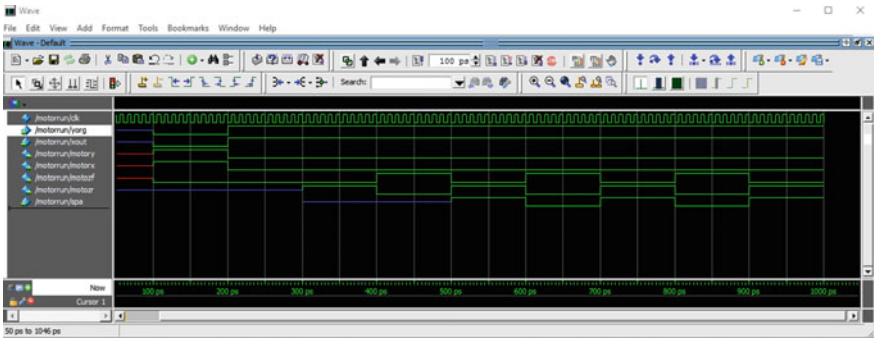

Fig. 2 Process output of the FPGA

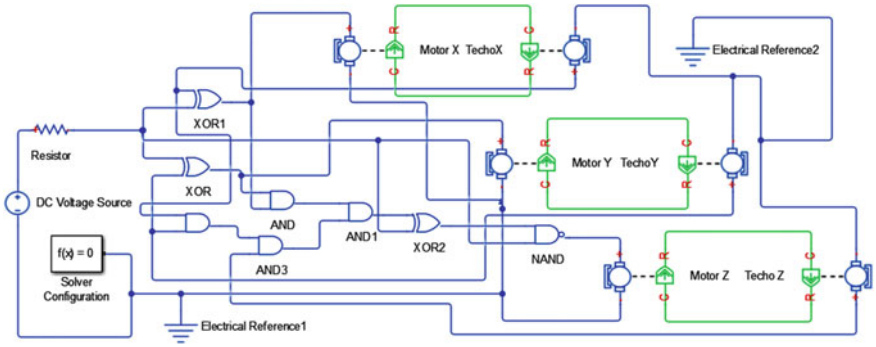

Fig. 3 MATLAB simulink model of feedback logical circuit

Fig. 4 Result output spark signal data of the prototype model

with the mechanical arrangement. Electronic logical element shows the replica of feedback logical circuit in FPGA (as shown in Fig. 3).

In the prototype model electrical spark is working in 38.46 Hz with a controlling signal of 1.7 kHz. A current sensing unit will be connected with the discharge path of workpiece and reflected signal presented in Fig. 4 using a digital oscilloscope.

5 Conclusions and Future Research

This system will provide two-way communication, self-monitoring and self-healing control system. For this optimal operation, efferent power consuming is attended by the FPGA system. It shows that single discharges can produce more metal erosion than one crater. The contact area between workpiece and plasma is also systematically managed by this technology. It will help to minimize the time consumption, enhance production quality, and safety aspects.

References

1. Ho, K.H., Newman, S.T.: State of the art electrical discharge machining (EDM). Int. J. Mach. Tools Manuf. **43**(13), 1287–1300 (2003)
2. Furutani, K., Mohri, N., Saito, N., Takezawa, H., Shin, T., Higashi, M.: Simultaneous finishing a pair of dies by electrical discharge grinding. Rapid Prod. Dev. 263–272 (1997)
3. Mondal, K., Das, S., Mandal, B., Sarkar, D.: An investigation on turning hardened steel using different tool inserts. Mat. Mfg. Process. **31**(13), 1770–1781 (2016)
4. Kaneko, T., Tsuchiya, M.: Three-dimensionally controlled EDM using cylindrical electrode (4th report). J. Japan Soc. Elect Mach. Eng. **18**(35), 1–14 (1984)
5. Wan, Y., Xu, L., Liu, Z., Yu, H.: Fabrication of a super-amphiphobic aluminium alloy surface via wire electrical discharge machining and chemical etching technology. Micro Nano Lett. **12**(3), 175–178 (2017)
6. Bhattacharyya, S.K., Kettle, M.: Some observations on spark-erosion machining. Prod. Eng. **51**(9), 305–311 (1972)
7. Mysinski, W.: Linear current source as a power generator for the spark erosion process. In: 2014 IEEE 23rd International Symposium Industrial Electronics, pp. 537–542 (2014)
8. Datta, S., Mahapatra, S.: Modeling, simulation and parametric optimization of wire EDM process using response surface methodology coupled with grey-Taguchi technique. Int. J. Eng. Sci. Tech. **2**(5), 162–183 (2010)

Path-Planning of Snake-Like Robot in Presence of Static Obstacles Using Critical-SnakeBug Algorithm

Ajoy Kumar Dutta, Subir Kumar Debnath and Subir Kumar Das

Abstract A wheeled snake robot presents a remarkable opening in many areas such as observation and support, exploration and rescue process. A snake can navigate through cluttered and uneven surroundings using its body as push points to support the forward motion. This typical quality of natural snake locomotion, known as obstacle-aided locomotion, is studied for snake robot locomotion. In this paper, path-planning method of snake-like robot avoiding static obstacles is given. The interaction among the snake-like robot and surroundings generates serpentine act to push the body ahead. The robot can successfully find a way to arrive at its target while avoiding collisions with multiple static obstacles using this algorithm.

Keywords Path-planning · Mobile robot navigation · Bug algorithm
Snake-like robot

1 Introduction

Snake-like robots are classic examples of robots with many degrees of freedom. They are planned to be biologically motivated, smart mobile robots. These robots can change their figures to accomplish definite tasks using a number of links and joints on their lengthy and slim bodies. Lots of issues on snake-like robots have been considered by learning normal living beings with the expectation that configuration and morphology of natural snakes may be functional to them. Snake frames are made

A. K. Dutta · S. K. Debnath · S. K. Das (✉)
Department of Production Engineering, Jadavpur University, Kolkata, West Bengal, India
e-mail: subirkrdas@gmail.com

A. K. Dutta
e-mail: ajoydutta@yahoo.co.in

S. K. Debnath
e-mail: skrdebnath@yahoo.com

S. K. Das
Department of Computer Application, Asansol Engineering College, Asansol, West Bengal, India

U. Biswas et al. (eds.), *Advances in Computer, Communication and Control*, Lecture Notes in Networks and Systems 41, https://doi.org/10.1007/978-981-13-3122-0_45

up of repetitive little segments whose activities are fairly limited with respect to each other. This repeated small piece helps snake to move through avoiding irregularly shaped obstacles. Sometimes it is termed as obstacle exploitation [1]. Regardless of its expediency, the snake as a biological mechanism, achieves higher performance by changing its very much redundant body to adapt to the environment [2]. Path-planning and controlling robot is one of the most important issues in current research on the robot. An approach is given combining insect eyes and the body structure and movement of the snake for autonomous robot navigation [3]. Forward dynamics algorithm (RGL05) is an efficient collision detection and obstacle avoidance [4] algorithm. This paper takes inspiration from Snake Robot with Active Wheels [5] and how to plan a path in a cluttered environment using Voronoi graph [6]. Another approach of path-planning is using Artificial Potential Field [7, 8]. Other Planning Algorithm is based on virtual holonomic constraints [9], configuration spaces and compliant motion [10], Serpenoid Curve and Genetic Algorithms [11], Changing Support Polygon [12], Sidewinding and Slithering with Virtual Chassis and Virtual Wheels [13]. Most of the algorithm suffers from some slippage in case of snake-like robot. Adding passive wheels can give little effect on the wrench applied to the object and therefore, little change in its acceleration or we can say that under certain conditions the slippage of the robot can be reduced while pushing the object [14]. This paper gives an algorithm using Critical-PointBug [15] algorithm to reach a snake-like robot from a source to destination avoiding the static obstacles.

2 Local Path-Planning and Critical-PointBug

In local Path-Planning, the region nearby the robot is unfamiliar or little familiar. The robot uses sensors to sense the obstruction and a collision escaping scheme must be built-in into the robot to stay away from the obstacles. The algorithms from bug family are depending on the fact that the smallest distance between two points is a straight line. Thus, the main object is to find out a path for the mobile robot so that it goes as close as possible to the straight line that passes through the start and the finish point. In this study, the obstacle escaping policy handles both stationary and moving obstacles in a 2D workspace. The algorithm is based on Critical-PointBug Algorithm [15]. Figure 1 shows the trajectory generated by a point robot using Critical-PointBug Algorithm.

The stationary obstacles can be of two types: known and unknown. Known static obstacles are known in advance to the planner during offline planning, while unknown stationary obstacles are unidentified to the planner and can only be identified by the sensor at some stage in navigation. In global path-planning the position and shape of the obstacles are known. For the known and identified static obstacles, the planner will judge them in the preliminary phase during producing the trajectory. Thus the generated trajectory should be away from the potentially colliding obstacles. In the case of local path-planning, the obstacles information is unknown. The data about the obstacles will only be considered when the mobile robot starts to navigate through the

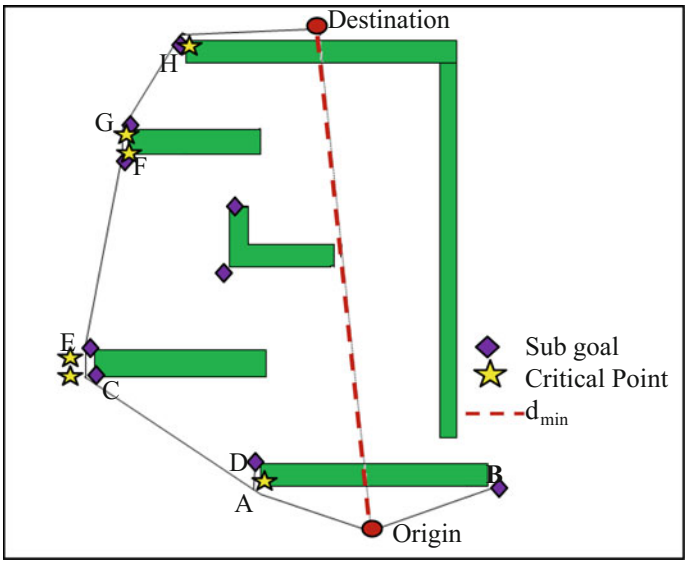

Fig. 1 Trajectory of a robot using Critical-PointBug algorithm

environment. We called the current Algorithm Critical-SnakeBug algorithm which is a small modification of existing Critical-PointBug algorithm for snake-like robot with some necessary assumptions.

3 Critical-SnakeBug Algorithm

This algorithm helps to find the way for a snake-like robot in a flat surface filled with stationary obstacles of unknown regular shape, size, and position. The robot applies range sensor to identify a sudden change in distance to sense obstacle locations. Depending on the positions of the obstacles it analyzes and decides the next point to move. We suppose a possibly unbounded space $Q \subset R^2$ which is occupied by a set of bounded stationary obstacles $O = \{O_1, O_2, \ldots, O_K\}$. We consider a snake robot which is structured by a series of wheeled point robot. The first wheeled robot is furnished with sensors to sense obstacles. While moving through the surface each part or link of the robot should follow the same path of coordinate. With respect to a global frame of reference, the robot has its preliminary coordinates. The definition of sub-goal point and the critical point is as per literature [15]. The algorithm maintains three sets SG, D, and T where

$T_n = \{(x_1, y_1), (x_2, y_2), \ldots, (x_i, y_i)\}$ is a set of points traversed by the robot's nth link where (x_i, y_i) represents the coordinate values and n represents the total number of links of the snake.

$SG = \{(\alpha_a, d_a), (\alpha_b, d_b), \ldots, (\alpha_k, d_k)\}$ is a set of next subgoal points detected by the sensor where α and d represents the angles and distances of subgoals from the robot respectively.

$D = \{((x_i, y_i), \delta_i), \ldots, ((x_j, y_j), \delta_j)\}$ is a set of subgoal points and distance from destination of that point.

We make some necessary, helpful assumptions and definitions for this algorithm prior to proceeding to the explanation of the algorithms.

3.1 Assumptions

A1. The robot is deemed as physically and systematically connected few point robot
A2. World coordinate system is used
A3. Every point (including beginning and goal) are in the first quadrant
A4. The velocity and angular velocity of all links of the robot is constant in every movement and rotation respectively
A5. Plane is smooth and in same altitude
A6. All the obstacles are motionless and of any regular shape and size
A7. The snake travels in a two-dimensional space.

3.2 Algorithm

Main Procedure

1. Robot Start
2. Obtain input of the location co-ordinates of origin and goal
3. Compute the distance and direction angle from origin to goal d_{min} and ϕ respectively
4. WHILE not goal
5. IF obstacle in direction angle ϕ
6. Find out the sub goal points and save it in SG and D
7. FOR each point in D
8. Select the point having the minimum distance from goal
9. IF the point exists in Traverse point set T_1
10. Discard the point
11. Select the point having next lowest distance from D
12. Follow step 7

13. ELSE Save the coordinate in traverse point set T_1
14. END FOR
15. CALL Move Procedure
16. Calculate angle of rotation
17. Get new direction ϕ
18. ELSE
19. Calculate the coordinate at radius towards the direction ϕ
20. Save the coordinate in T_1
21. END IF
22. END WHILE
23. Robot Stop

Move Procedure

1. For i=n to 2
2. Save the last coordinate of T_{i-1} in traverse point set T_i
3. END FOR
4. FOR i=1 to n
5. Move the ith link toward the last point of T_i
6. END FOR

3.3 Propagation Procedure of Snake

The relationship between robot links is managed by way of a transmission method carried out through links. Assume that the snake's first part is taken as link n. It is shifted ahead constantly until its tip arrives at the path. When the link accomplishes the path, the link is said to be complete. Then, link (n − 1) is moved and link n is settled again. As soon as (n − 1) is settled, link (n − 2) is moved and both link (n − 1) and link n are resettled. This method carries on until the base link which is the furthest link in the reverse side of the snake's head arrives. Therefore, the robot accomplishes the first part of the snake-like motion.

The robot initiates to progress and gradually takes the figure of the path (Fig. 2). When the robot completely updates all the T_i sets, i.e., mapped on the path, the algorithm starts to move the robot's base from its current position to the next position on the path. Whenever the robot's base is moved to the next point on the path, all the links of the robot are adjusted in the way that the tip of each link is kept on the path points.

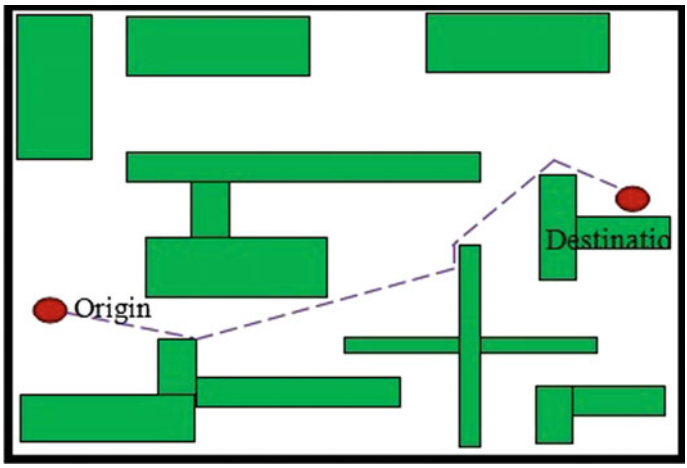

Fig. 2 Trajectory generated by Critical-SnakeBug algorithm in office like environment

Fig. 3 Current (x_i, y_i) and next (x_{i+1}, y_{i+1}) position of the robot

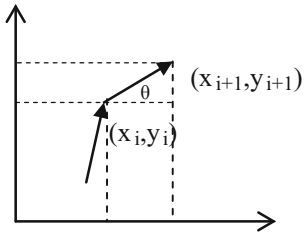

3.4 Algorithm Analysis

Let us consider a mobile robot as shown in Fig. 2, with its initial position (x_0, y_0). The formulation takes into account the evaluation of the next obstacle free location of the robot. The robot is aware of its goal position.

During its movement at any instance of time

Let,

(x_i, y_i)	The current position of the nth link of the robot
(x_{i+1}, y_{i+1})	The next possible position to move by nth link of the robot
α	Angle where subgoal point is detected by the sensor
β	Link rotation angle with respect to the line parallel to the x-axis and passing through (x_i, y_i) before movement
θ	Angle generated by β with respect to the line parallel to x-axis for subgoal point coordinates calculation
d_k	Distance of a subgoal point from current location
v	Velocity of the robot
ω	Angular velocity of the robot (Fig. 3).

Next Point Coordinate Calculation by 1st link
$\beta_i = (\alpha + \beta_{i-1})\ \%\ 360$ where '%' is a modulo operator

$$\left.\begin{aligned} x_{i+1} &= x_i + d_k \cos\theta(x_s) \\ y_{i+1} &= y_i + d_k \sin\theta(y_s) \end{aligned}\right\},$$

where x_s and y_s are the decision parameters referenced as in literature [15].

Total Time and Path Length Calculation of Each Individual Links
If the nth link of the robot takes m intervals to reach its 1st link to the destination then the total path, P covered in m intervals is

$$P = \sum_{i=0}^{m} d_i,$$

where d_i is the Euclidian distance traversed at each interval.

Time Taken by Link n in Moving
If d_i and v_i are the distance covered and velocity at ith interval then the time taken during ith movement is d_i/v_i. Total time taken in moving is

$$T_M = \sum_{i=0}^{m} d_i/v_i$$

Time Taken in Rotating the Robot at Each Interval
If α_i is the detection angle of the critical point and ω_i is the angular velocity, then time taken for rotation at ith interval is α_i/ω_i. Total time taken in rotation is

$$T_R = \sum_{i=0}^{m} \alpha_i/\omega_i$$

Therefore the cost function will be the sum of the time taken in both cases, i.e., moving time and rotation time

$$C = \sum_{i=0}^{m} (d_i/v_i) + \sum_{i=0}^{m} (\alpha_i/\omega_i)$$

Therefore the total cost for all the n links or the full robot to reach at goal:

$$TC = \sum_{i=0}^{n} C_i$$

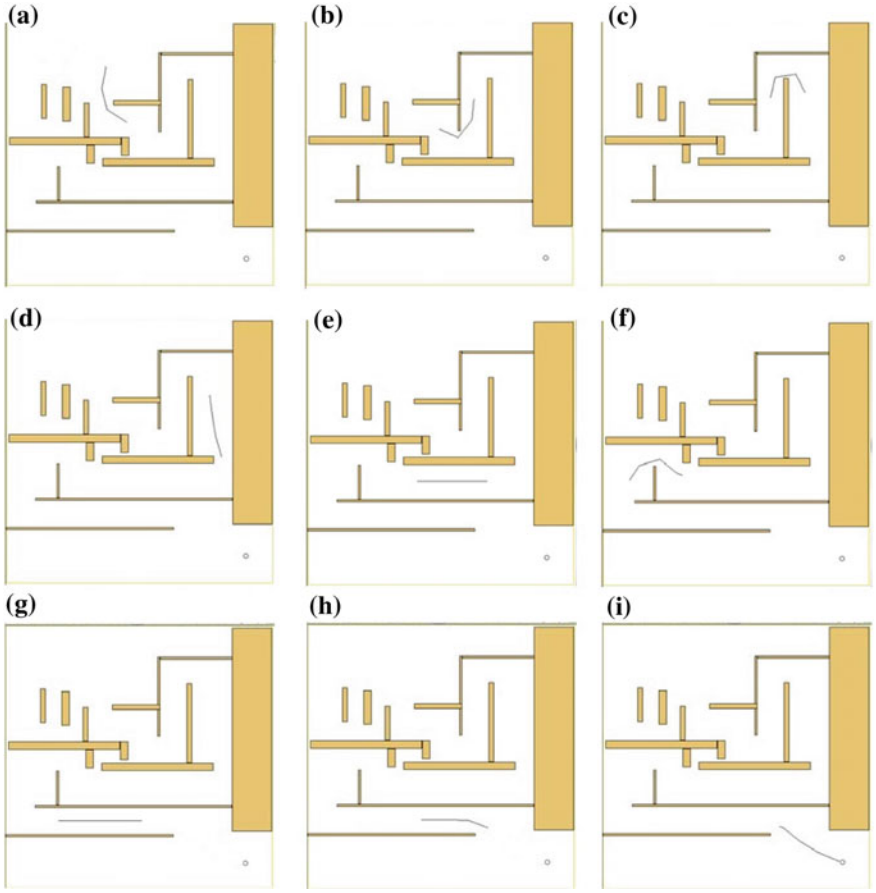

Fig. 4 Snapshots of trajectories generated by the snake-like robot

4 Computer Simulation and Results

There is an example of snake-like robots given in this section. A snake-like robot in a W-space cluttered with many arbitrarily shaped obstacles is shown in Fig. 4.

Simulations are performed on a i3-2350 M CPU @2.30 Ghz Laptop with 2 GB RAM. Figure 4a–i shows the snapshots of the snake-like robot accomplishing the goal avoiding collision with obstacles.

5 Conclusions

In this paper, the problem of pathplanning for snake-like robots is taken into account. The algorithm offered here can help a snake robot to reach goal bypassing obstacles. This robot is constructed as a series of point robot linked with others. Though a smoothly curved path cannot be generated using the algorithm, it is simple. The snake robot executes a kind of discrete serpent-tine motion on this path consisting of a number of points. As we can see from the example given, the robots with many degrees of freedom pursue the path to arrive at the goal.

Acknowledgements Thanks to Prof. Dr. Subhasis Bhoumik of IIEST, Shibpur for giving the idea to develop a snake-like robot. Thank you to the Production Engineering Department, Jadavpur University and Asansol Engineering College for giving us the opportunity to use their resources.

References

1. Liljebäck, P., Pettersen, K.Y., Stavdahl, Ø., Gravdahl, J.T.: A hybrid model of obstacle-aided snake robot locomotions, pp. 675–682. IEEE (2010). 978-1-4244-5040-4/10
2. Shugen, M.: Analysis of creeping locomotion of a snake-like robot. Adv. Robot. **15**(2), 205–224 (2001)
3. Cheng, Y., Jiang, P., Hu, Y.F.: A-snake-integration of path planning with control for mobile robots with dynamic constraints, vol. 2, pp. 127–134. IEEE (2010). 978-1-4244-5586-7/10
4. Gayle, R., Redon, S., Sud, A., Lin, M., Manocha, D.: Efficient path planning for highly articulated robots using adaptive forward dynamics. In: IEEE International Conference on Robotics and Automation, ICRA 2007, pp. 1–16
5. Murugendran, B., Transeth, A.A., Fjerdingen, S.A.: Modeling and path-following for a snake robot with active wheels, pp. 3643–3650. IEEE (2009). 978-1-4244-3804-4/09
6. Singh, A., Gong, C., Choset, H.: Modelling and path planning of snake robot in cluttered environment. SciRate, cs.RO, vol. 1. arXiv:1710.02610v1
7. Yagnik, D., Ren, L., Liscano, R.: Motion planning for multi-link robots using artificial potential fields and modified simulated annealing, pp. 421–427. IEEE (2010). 978-1-4244-7101-0110
8. Ye, C., Hu, D., Ma, S., Li, H.: Motion planning of a snake-like robot based on artificial potential method, pp. 1496–1501. IEEE (2010). 978-1-4244-9318-0/10
9. Rezapour, E., Pettersen, K.Y., Liljebäck, P., Gravdahl, J.T., Kelasidi, E.: Path following control of planar snake robots using virtual holonomic constraints-theory and experiments. Robot. Biomimet. **1**(3), 1–15 (2014)
10. Sacks, E.: Path planning for planar articulated robots using configuration spaces and compliant motion. IEEE Trans. Robot. Autom. **19**(3), 381–390 (2003)
11. Liu, J., Wang, Y., Ii, B., Ma, S.: Path planning of a snake-like robot based on serpenoid curve and genetic algorithms. In: Fifth World Congress on Intelligent Control and Automation, vol. 6, pp. 4860–4864. IEEE (2004)
12. Cappo, E.A., Choset, H.: Planning end effector trajectories for a serially linked, floating-base robot with changing support polygon. In: American Control Conference (ACC), pp. 4038–4043. IEEE (2014)

13. Hatton, R.L., Knepper, R.A., Choset, H., Rollinson, D., Gong, C., Galceran, E.: Snakes on a plan-toward combining planning and control. In: IEEE International Conference on Robotics and Automation (ICRA), IEEE (2013)
14. Reyes, F., Ma, S.: Studying slippage on pushing applications with snake robots. Robot. Biomimet. Springer **4**(9), 1–12 (2017)
15. Dutta, A.K., Debnath, S.K., Das, S.K.: Local path planning of mobile robot using critical-pointbug algorithm avoiding static obstacles. Int. J. Robot. Autom. (IJRA) **5**(3), 182–189 (2016)

Photonic Crystal for Gas Sensing Application

Shreerupa Biswas, Shampa Guin and Nikhil R. Das

Abstract In this paper, 1D Photonic Crystal structure, consisting of alternate layers of silicon and air, is theoretically studied for gas sensing application. With one of the air layers replaced by a different gas layer, the resulting defect mode can be utilized for sensing a particular gas, from the transmittance curve, calculated by Transfer matrix method. Very small refractive index variation, $\Delta n = 1.5 \times 10^{-5}$ and a sensitivity = 979 nm/RIU is found by this sensor.

Keywords 1D photonic crystal · Photonic bandgap · Gas sensor

1 Introduction

Photonic crystals [1] are periodic dielectric structures which are designed to control the propagation of electromagnetic waves. A semiconductor cannot support electrons of energy lying in the electronic bandgap. Similarly, a photonic crystal cannot support photons lying in the photonic bandgap. Those wavelengths that are not able to pass through the structure is called Photonic bandgap. Three types of photonic crystals structures are studied according to their periodicity, those are one-dimensional-, two-dimensional-, and three-dimensional photonic crystal structures [2].

S. Biswas (✉) · S. Guin · N. R. Das (✉)
Institute of Radio Physics & Electronics, University of Calcutta,
92, A.P.C. Road, Kolkata 700009, West Bengal, India
e-mail: shreerupabiswas@gmail.com

N. R. Das
e-mail: nrd@ieee.org

S. Guin
e-mail: shampaphysics@gmail.com

U. Biswas et al. (eds.), *Advances in Computer, Communication and Control*, Lecture Notes in Networks and Systems 41, https://doi.org/10.1007/978-981-13-3122-0_46

In 1887, the English physicist Lord Rayleigh [3] investigates a periodic system, he found out that there are special frequency ranges, depending on designed structures, that are forbidden in transmission spectra. In 1987, Yablonovitch [4] and John [5] researched on periodic optical structures with more than one dimension, after that this periodic structure is called photonic crystals.

Gas detection [6] is a major part in many areas such as industry, coal mines, environmental studies or medical application for monitoring or controlling respiratory gases. There are various methods for detection of gases, such as, metal oxide semiconductor for gas sensing, where gases are detected by a redox reaction [7], calorimetric methods, in which catalytic oxidation is mainly used to detect the gases [8]. Here we give some recent work on photonic crystal gas sensors. T. Sünner et al. studied a gas sensor that can detect up to 10^{-4} RIU refractive index change [9]. An optical-based NO_2 gas monitoring system has been studied by Rshmatet et al. [10]. To sense a gas accurately a very small refractive index change of 1.4×10^{-5} is achieved by T. Chen et al. using 1D photonic crystal [11]. A 1D photonic crystal with two defects has been designed to sense novel ozone gas [12]. Two alternating layers of MgF_2 and Si with an empty layer in the middle are used to make a sensor which is studied by Bouzidiet et al. [13]. A gas sensor which is studied by S. M. Hamidia et al. where peak frequency measurement is used to sense a gas [14].

In this paper, multilayer stacks of high and low refractive index materials such as Air and Si are chosen to construct 1D photonic crystal gas sensor which is able to sense the presence of a gas, a defect layer, from the change in transmission spectrum, with reference to that of air. Section 2 explains the transfer matrix method [15, 16]. In Sect. 3, the results are discussed and Sect. 4 concludes the result.

2 Theory

2.1 Transmission in the One-Dimensional Photonic Crystal Structure

Figure 1 shows the schematic of 1D photonic crystal. In this structure, alternating periodic layers of silicon and air are used.

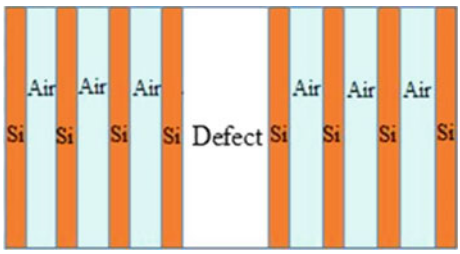

Fig. 1 Schematic structure of one-dimensional (1D) photonic crystal structure with defect layer

Consider that first layer is Si (silicon) which has permittivity ε_1, permeability μ_1, thickness d_1, and refractive index n_1 and second layer is air layer which has permittivity ε_2 permeability μ_2, thickness d_2, and refractive index n_2.

The transverse component of E and H field inside the Structure from the Maxwell's equation, for TE polarization is given by

$$E = A \cdot e^{i(\omega t - kd)} + B \cdot e^{i(\omega t + kd)} \tag{1}$$

$$H = \frac{1}{\eta}\left(A \cdot e^{i(\omega t - kd)} - B \cdot e^{i(\omega t + kd)}\right), \tag{2}$$

where k = wave number and η = intrinsic impedance are

$$k_L = \omega\sqrt{(\varepsilon_0 \mu_0 \varepsilon_L \mu_L)} \tag{3}$$

$$\eta_L = \sqrt{(\varepsilon_0 \mu_0 / \varepsilon_L \mu_L)} \tag{4}$$

L is the total number of periodic layers inside the photonic crystal structure.

We can found a relation between the electromagnetic field components E_L and H_L inside the structure and the electromagnetic field components E_1 and H_1 in the air in matrix form using the transfer matrix method.

$$\begin{vmatrix} E_1 \\ H_1 \end{vmatrix} = M_1 M_2 \ldots M_{L-1} M_L \begin{vmatrix} E_L \\ H_L \end{vmatrix} \tag{5}$$

M_L is the characteristic matrix of Lth layer

$$M_L = \begin{vmatrix} \cos(k_L d_L) & j\eta_1 \sin(k_L d_L) \\ \frac{j}{\eta_L} \sin(k_L d_L) & \cos(k_L d_L) \end{vmatrix} \tag{6}$$

If we consider the angle of incident light (θ_L) then the characteristic matrix of Lth layer can be written as

$$M_L = \begin{vmatrix} \cos(\delta_L) & j\gamma_L \sin(\delta_L) \\ \frac{j}{\gamma_L} \sin(\delta_L) & \cos(\delta_L) \end{vmatrix} \tag{7}$$

δ_L and γ_L being the matrix parameters and depending on the incident angle θ_L of light, the optical constants and the layer thickness are expressed as,

$$\delta_L = k_L\, d_L\, \cos(\theta_L) \tag{8}$$

$$\gamma_L = \eta_L / \cos\theta_L (\text{TE mode}) \tag{9}$$

By considering the characteristic matrix of each layer, we can obtain the transmission matrix of the whole structure, where p is the number of periods,

$$\prod_{1}^{p}(M_p) = \begin{bmatrix} m_{11} & m_{12} \\ m_{21} & m_{22} \end{bmatrix} \tag{10}$$

$$Mp = M_1 \times M_2 \tag{11}$$

The transmittance t is defined as the ratio of the fluxes of the transmitted wave to the flux of the incident wave.

$$t = \frac{2\eta_i^{-1}}{(m_{11} + m_{12}\eta_s^{-1})\eta_i^{-1} + (m_{21} + \eta_s^{-1} m_{22})} \tag{12}$$

Here η_i and η_s are the intrinsic impedance of the first and last medium of the structure which is given as,

$$\eta_s = \begin{cases} \frac{\eta_s \cos\theta_s}{Z_0}\,\text{TE mode} \\ \frac{\cos\theta_s}{\eta_s Z_0}\,\text{TM mode} \end{cases} \tag{13}$$

where

$$Z_0 = \sqrt{\frac{\mu_0}{\varepsilon_0}} \tag{14}$$

Hence the transmittance T spectrums can be obtained by using the expressions

$$T = |t|^2 \tag{15}$$

The sensitivity of this sensor is given by the following expression:

$$S = \Delta\lambda / \Delta n\ (\text{nm/RIU}) \tag{16}$$

3 Results and Discussion

The analysis using the transfer matrix approach uses four periodic layers of silicon and air on each side of the defect layer.

Different lengths of defect layer are studied to get defect mode within 1.55 μm range, assuming a thickness of Si layer of $d_{Si} = 540$ nm and thickness of Air layer of $d_{Air} = 440$ nm, as shown in Fig. 2. For a normal incident of light, defect mode appears within the photonic bandgap, depending on the length of the defect layer. The wavelength of defect mode shifts when cavity length increases from 700 to 900 nm.

The wavelength shifting is linear with the length of the defect layer as shown in Fig. 3. This shift of the wavelength within the photonic bandgap also depends on the thickness of the Si layer (d_{Si}).

When light incident on the structure at an angle other than normal incidence, defect mode shifts in lower wavelength value as shown in Fig. 4. It may also be noted from Fig. 4 that the photonic bandgap increases with increase in incident angle of light which is clear from Fig. 5.

Figure 6a, b shows the transmission characteristics of 1D photonic crystal in the presence of different gases such as Helium (He), Hydrogen (H_2), Carbon dioxide (CO_2), Methane (CH_4), Argon (Ar), Neon (Ne), and Sulfur dioxide (SO_2) in the defect layer. The shift in wavelength peak-position is measured taking air as reference. It may be seen from the figure that the peak-position shifts to lower wavelengths for

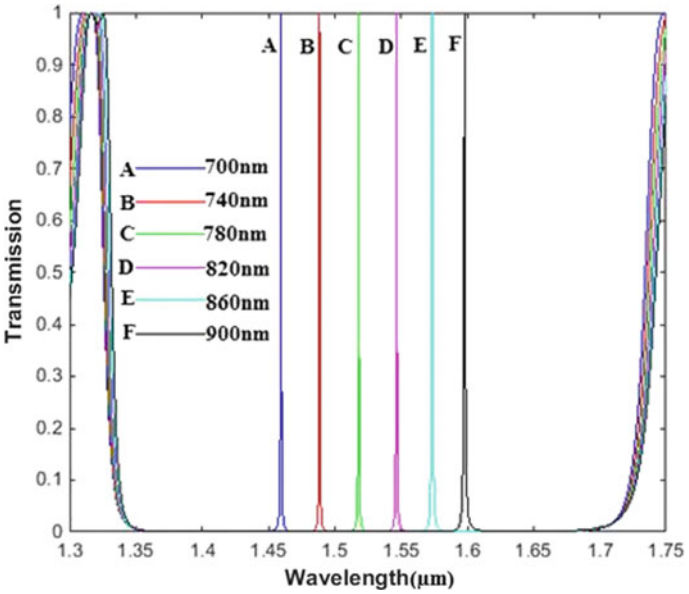

Fig. 2 Transmission spectrum of 1D photonic crystal for different defect layers thickness. Si layer thickness $d_{Si} = 540$ nm and air layer thickness $d_{Air} = 440$ nm

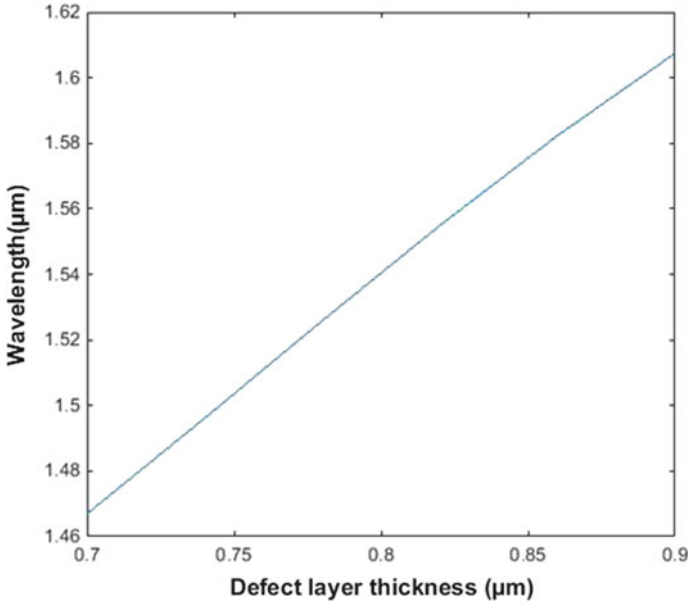

Fig. 3 Wavelength of defect layer as a function of defect layers thickness for $d_{Si} = 540$ nm, $d_{Air} = 440$ nm where cavity length changes from 700 to 900 nm

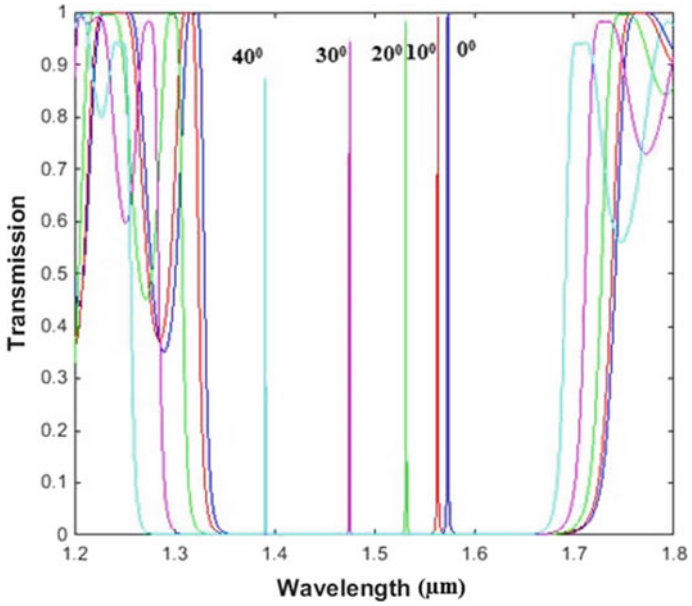

Fig. 4 Transmission spectrum for different incident angle of light for Si layer thickness $d_{Si} = 540$ nm and air layer thickness $d_{Air} = 440$ nm

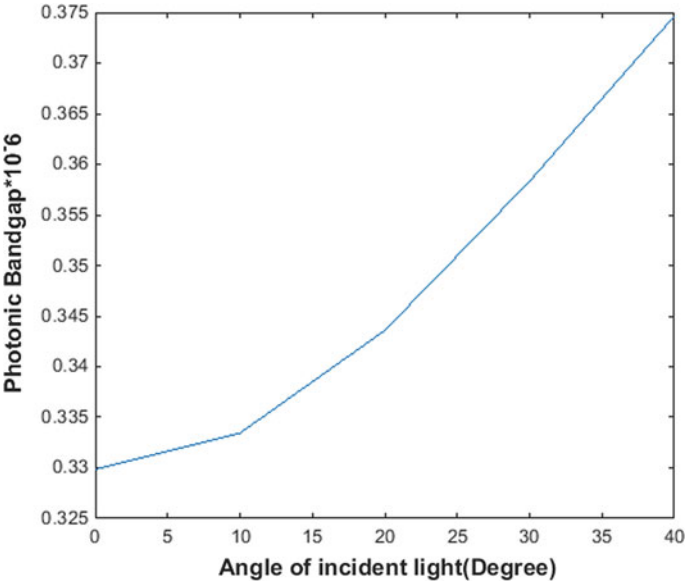

Fig. 5 Photonic bandgap for different incident angle of light for Si layer thickness = 540 nm and air layer thickness = 440 nm

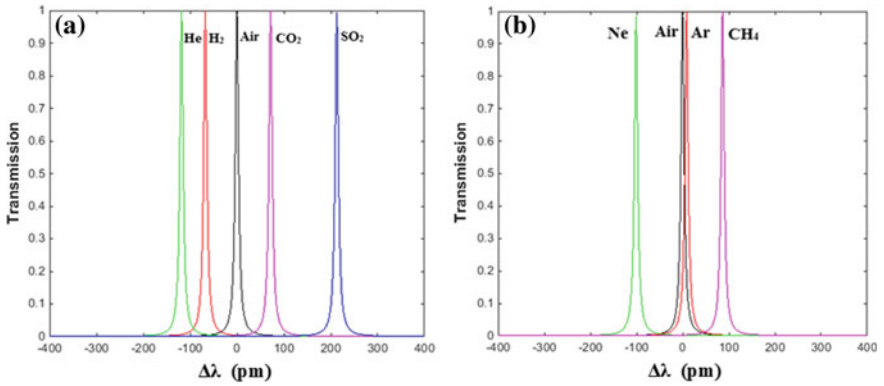

Fig. 6 Transmission spectrum for different gases with air as the reference medium $d_{defect} = 860$ nm

gases having refractive indices less than air, while it shifts to higher wavelengths for gases having higher refractive indices. Thus, the result can be utilized for sensing of different gases.

To study the sensitivity of the device, different thicknesses of silicon and air layer are studied. Curve A, B, C, and D in Fig. 7 denote the corresponding results. Sensitivity, calculated from (16), for those designed structures are 440 nm/RIU, 550 nm/RIU, 654 nm/RIU, and 979 nm/RIU respectively.

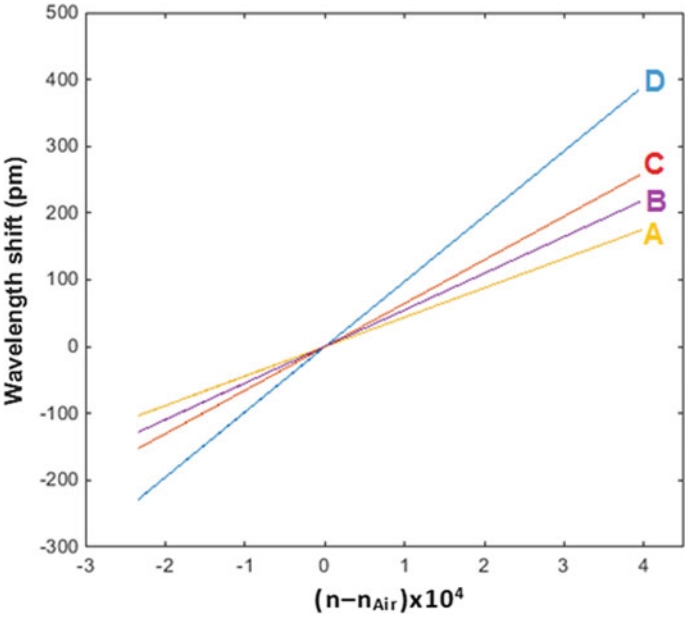

Fig. 7 Wavelength shift as a function of the refractive index change. A (d_{Si} = 540 nm, d_{Air} = 440 nm, d_{defect} = 800 nm), B (d_{Si} = 380 nm, d_{Air} = 280 nm, d_{defect} = 700 nm), C (d_{Si} = 340 nm, d_{Air} = 620 nm, d_{defect} = 700 nm), D (d_{Si} = 160 nm, d_{Air} = 240 nm, d_{defect} = 700 nm)

4 Conclusion

In this paper, a 1D photonic crystal structure as a gas sensor is studied. The sensor can sense the shift in wavelength of transmission spectra, using Transfer matrix method. The study shows that the defect mode inside the bandgap can shift in between the gap of the photonic bandgap if the length of the Si layer or the length of the defect layer or the angle of incidence of the light on the structure is changed. As a result, this structure is very sensitive to the refractive index change of gases which are present in the dry air. The sensitivity of this sensor will increase if we consider different designs of the device structure.

References

1. Joannopulos, J.D., Steven, G., Johnson, C.: Photonic Crystals: Molding the Flow of Light. Princeton University Press, Princeton and Oxford (2008)
2. Steven, G., Johnson, Joannopoulos J.D.: Introduction to Photonic Crystals: Bloch's Theorem, Band Diagrams, and Gaps (But No Defects). MIT (2003)
3. Rayleigh, J.W.S.: On waves propagating along the plane surface of an elastic solid. J. Mol. Biol. **7**(1), 4–11 (1885)

4. Yablonovitch, E.: Photonic band-gap structure: the face centered-cubic case employing non-spherical atoms. Phys. Rev. Lett. **67**(20), 2295–2298 (1991)
5. John, S.: Strong localization of photons in certain disordered dielectric superlattices. Phys. Rev. Lett. **58**(20), 2486–2489 (1987)
6. Chraim, F., Erol, Y.B., Pister, K.: Wireless gas leak detection and localization. IEEE Trans. Industr. Inf. **12**(2), 768–779 (2016)
7. Liu, X., Cheng, S., Liu, H.: C: a survey on gas sensing technology. Sensors **12**, 9635–9665 (2012)
8. Nam-Hee Park, T., Akamatsu, T., Itoh, C.: Calorimetric thermoelectric gas sensor for the detection of hydrogen, methane and mixed gases. Sensors **14**, 8350–8362 (2014)
9. Sünner, T., Stichel, T., Kwon, S.-H.: C: photonic crystal cavity based gas sensor. App. Phys. Lett. **92**, 261112–261113 (2008)
10. Rshmat, M., Maulina, W., Rustami, E.: C: performance in real condition of photonic crystal sensor based NO_2 gas monitoring system. Atmos. Environ. **79**, 480–485 (2013)
11. Chen, T., Han, Z., Liu, J., Hong, Z.: Terahertz gas sensing based on a simple one-dimensional photonic crystal cavity with high-quality factors. App. Optics. **53**, 3454–3458 (2014)
12. Rahmata, M., Maulinaa, W., Isnaeni, C.: Development of a novel ozone gas sensor based on sol–gel fabricated photonic crystal. Sensors Actuators A Phys. **220**, 53–61 (2014)
13. Bouzidi, A., Bria, D., Akjouj, A., Pennec, Y.: C: A tiny gas-sensor system based on 1D photonic crystal. App. Phys. **48**(495102), 1–7 (2015)
14. Hamidia, S.M., Ramezania, R.: C: hydrogen gas sensor based on long-range surface plasmons in lossy palladium film placed on photonic crystal stack. Opt. Mater. **53**, 201–208 (2016)
15. Barkat, O.: theoretical investigation of transmission and dispersion properties of one dimension photonic crystal. J. Electr. Electron. Eng. **3**(2), 12–18 (2015)
16. Mohamed, M.S., EL-Okr, M.M., Mostafa, M.T.: Transmission and Dispersion Relation of One Dimensional Photonic Crystal Quantum Matter, vol. 5, pp. 1–6 (2016)

Automatic Classification of Mango Using Statistical Feature and SVM

Santi Kumari Behera, Shrabani Sangita, Amiya Kumar Rath and Prabira Kumar Sethy

Abstract Natural fruit like mango contributes a major part of national growth. Due to flavor, nutrition, and taste, mango is one of the popular fruits. There are around 283 types of mangoes present in India only, from that 30 types of mangoes are well known. Human vision sometimes leads to mismatch between the varieties of mango fruit. Using machine vision technique, it helps to reduce human effort and achieve a better result. The aim of this paper is to extract the features of mango fruit with GLCM (Gray-Level Co-Occurrence Matrix) and classify the variety of mango fruits by multiclass Support Vector Machine (SVM) with K-means clustering.

Keywords Image processing · SVM · GLCM · K-means

1 Introduction

The king of fruit, mango, is a tropical fruit which is consumed worldwide. As mango is a seasonal fruit, it is collected from the tree on that season and transported to different locations. According to 2010, FAO India is the world's largest producer in many fresh fruits. India produces 50% of the total world's mango producing countries. Among the 30 well-known mangoes of India, we take top 10 mangoes for our project. The top 10 varieties of mangoes are Suvernarekha, Alphonsos (Happus), Dasheri, Kesar, Neelam, Langra, Raspuri, Himsagar, Banganapalli, Amrapali.

S. K. Behera (✉) · S. Sangita · A. K. Rath
Department of Computer Science and Engineering, VSSUT, Burla, Odisha, India
e-mail: b.santibehera@gmail.com

S. Sangita
e-mail: sangitashrabani@gmail.com

A. K. Rath
e-mail: amiyaamiya@rediffmail.com

P. K. Sethy (✉)
Department of Electronics, Sambalpur University, Sambalpur, Odisha, India
e-mail: prabirasethy@suniv.ac.in

U. Biswas et al. (eds.), *Advances in Computer, Communication and Control*, Lecture Notes in Networks and Systems 41, https://doi.org/10.1007/978-981-13-3122-0_47

As there are many varieties of mangoes present and some mangoes have nearly same gesture, sometimes it is difficult to identify the particular kind of mango. Due to this problem, many people face problem at the time of identification. For solving this problem, we introduce an approach to classify a different kind of mango fruit.

Here we use the single view of mango image, i.e., one side of the mango image is captured. First, we use the K-Mean clustering for separate the background of the image. Here we use GLCM (Gray-Level Co-occurrence Matrix) method, which helps to evaluate 13 parameters based on which we classify the kind of mango fruit. These 13 features are extracted and trained to SVM (Support Vector Machine). So that the SVM matches the feature of the trained feature and the feature of the test sample and classify accordingly.

2 Literature and Review

In the past, many research works have been carried for detecting, classify, and quantify the quality of fruits. Most of the research work is done for grading of fruits. In this paper [1], the author presents the MADM technique and SVM technique for classifying the fruit as its shape, size, and color. Here, the main purpose of the classification is for packaging of fruit for transportation [2]. Here, the author presents K-means clustering for disease detection. It is helpful for grading purpose [3]. Here, the author classifies the mango fruit as disease and disease-free. Here he uses the feature extraction method, and classifies the mango fruit by the neural network [4], and classifies the citrus fruit using image processing and GLCM. This process helps to identify the citrus fruit. In image processing technique, the color analysis is very important and is helpful for segmentation [5–7]. Many types of color models like RGB, L*a*b*, CMYK, HSV, YCbCr are present. Many research works have been carried for detecting, localizing, and countingtree fruit [8–10] by implementing KNN, SVM, ANN, and texture analysis. It is easily detected fruit but sometimes the problem occurs due to overlapping, shape, or color [11]. Here the author describes how to estimate the sweetness of mango using HSB color space.

3 Materials and Method

In this work, we classify a different kind of mango fruit images using image processing and SVM. First, we use the k-mean clustering to remove the background of the image and detect the fruit, from the segmented image we extracted the features using GLCM, and then by the help of SVM, we classify a different kind of mango fruit.

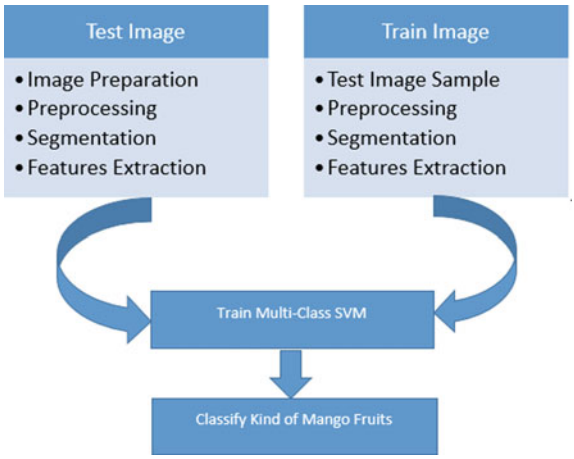

Fig. 1 Frame work of different kind of mango fruit classification

3.1 Classification of Kind of Fruits

Proposed Algorithm for the above framework (Fig. 1).

Step 1: Input an Image.
Step 2: Contrast Enhancement of image.
Step 3: Transfer the image from RGB color space to L*a*b* color space.
Step 4: Use the k-mean to detect the fruit.
Step 5: Extract the feature from the segmented image.
Step 6: Classify a different kind of mango fruit with the help of multiclass SVM.

3.1.1 Kind of Mango Fruits

In this project, we mainly focused on 10 kinds of mango fruits. We collected these pictures from Internet. The sample images are shown in Fig. 2.

3.1.2 Preprocessing

Image preprocessing may be a prophase relative to feature extraction and image reorganization. The image that has input is often not satisfactory in spite of what image aquation devices are adapted. Here preprocessing part consist of two-steps: image improvement and color transformation, i.e., L*a*b. Image improvement is one among the foremost fascinating and vital problems in image processing field. The main purpose of image improvement is to extract the details that are within a picture. Image improvement process returns an image, i.e., subjectively better appearance than the input image by changing the pixel intensity. We use L*a*b*

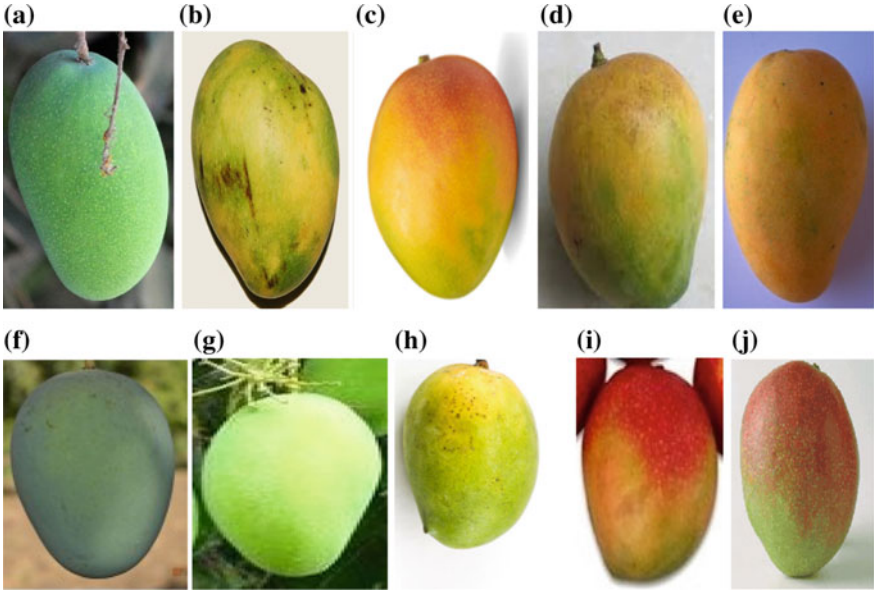

Fig. 2 Different types of mango **a** Amrapali, **b** Baganapalli, **c** Kesar, **d** Neelum, **e** Happus, **f** Langra **g** Dusheri, **h** Himsagar, **i** Suvernarekha, **j** Raspuri

color space because the color information in the L*a*b* color space is stored in only two channels (i.e., a* and b* component),

3.1.3 Segmentation

Image segmentation is the classification of an image into different groups. K-means clustering algorithm is an unsupervised algorithm and it is used to segment the interest area from the background. Here we have taken the number of clusters, $K = 3$ to separate background, foreground, and the affected area (Fig. 3).

3.1.4 Feature Extraction

It involves simplifying the quantity of resources needed to explain a large set of data accurately. When performing analysis of complex data, the main drawback is the requirement of a large amount of memory and computational power for classification. The classification algorithm is over fits trained sample but generalizes poor to a new sample. Thirteen number of textures are extracted from GLCM, i.e., contrast, correlation, energy, homogeneity, mean, standard deviation, entropy, RMS, variance, smoothness, kurtosis, skewness, IDM.

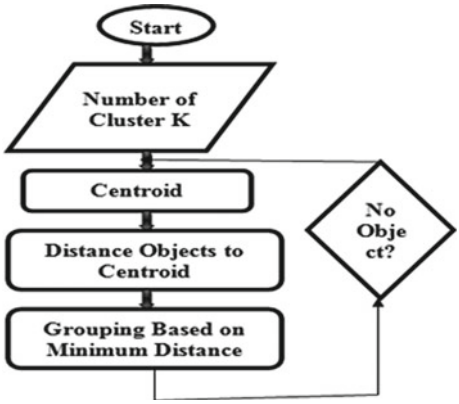

Fig. 3 Flow chart for k-means clustering

3.1.5 Classification

Support vector machines are supervised learning models with an associated learning algorithm that analyzes data used for classification. Given a set of training example, each marked as belonging to one or the other of two categories, module an SVM training algorithm builds a model that assigns new example to one category or the other, making it a non-probabilistic binary linear classifier. Multiclass SVM classifies different types of mangoes by considering the features of the trained image and test sample image.

4 Result and Discussion

In the proposed algorithm, first of all, the feature extraction process has occurred. During this process, 13 number of features have been extracted. By considering those features we can classify the kind of mangoes. We have experimented 30 number of mango fruits and out of 30 number, only three of them are misidentified by the proposed algorithm. Here we take "T" for the correct value and "F" for the wrong value. The observation is shown in Table 1.

5 Conclusion and Future Scope

In this paper, we successfully classify the different kinds of mangoes with 90% accuracy. This research can be extended to increase the accuracy using soft computing technique and validate with more number of sample.

Table 1 Classification of mango fruit

Sl. no.	Detect fruit name	Detect fruit name by algorithm	Identification
1	Langra mango	Langra mango	T
2	Langra mango	Langra mango	T
3	Langra mango	Langra mango	T
4	Baganapalli mango	Baiganpalii mango	T
5	Baiganpalli mango	Neelum mango	F
6	Baganapalli mango	Baganapalli mango	T
7	Happus mango	Happus mango	T
8	Happus mango	Happus mango	T
9	Happus mango	Happus mango	T
10	Raspuri mango	Raspuri mango	T
11	Raspuri mango	Raspuri mango	T
12	Raspuri mango	Suvernarekha mango	F
13	Suvernarekha mango	Suvernarekha mango	T
14	Suvernarekha mango	Suvernarekha mango	T
15	Suvernarekha mango	Suvernarekha mango	T
16	Himsagar mango	Himsagar mango	T
17	Himsagar mango	Neelum mango	F
18	Himsagar mango	Himsagar mango	T
19	Kesar mango	Kesar mango	T
20	Kesar mango	Kesar mango	T
21	Kesar mango	Kesar mango	T
22	Dusheri mango	Dusheri mango	T
23	Dusheri mango	Dusheri mango	T
24	Dusheri mango	Dusheri mango	T
25	Neelum mango	Neelum mango	T
26	Neelum mango	Neelum mango	T
27	Neelum mango	Neelum mango	T
28	Amrapali mango	Amrapali mango	T
29	Amrapali mango	Amrapali mango	T
30	Amrapali mango	Amrapali mango	T

References

1. Nandi, C.S., Tudu, B., Koley, C.: A machine vision technique for grading of harvested mangoes based on maturity and quality. IEEE Sensors J. **16**(16), 6387–6396 (2016)
2. Pham, V.H., Lee, B.R.: An image segmentation approach for fruit defect detection using k-means clustering and graph-based algorithm. Vietnam J. Comput. Sci. **2**(1), 25–33 (2015)
3. Ashok, V., Vinod, D.S.: A comparative study of feature extraction methods in defect classification of mangoes using neural network. In: 2016 Second International Conference on Cognitive Computing and Information Processing (CCIP), IEEE (2016)
4. Kumar, C., Chauhan, S., Narmadha Alla, R.: Classifications of citrus fruit using image processing-GLCM parameters. In: 2015 International Conference on Communications and Signal Processing (ICCSP), IEEE (2015)
5. Mustafa, N.B.A. et al.: Classification of fruits using probabilistic neural networks-improvement using color features. In: TENCON 2011–2011 IEEE Region 10 Conference. IEEE (2011)
6. Mendoza, F., Dejmek, P., Aguilera, J.M.: Calibrated color measurements of agricultural foods using image analysis. Postharvest Biol. Technol. **41**(3), 285–295 (2006)
7. Yam, K.L., Papadakis, S.E.: A simple digital imaging method for measuring and analyzing color of food surfaces. J. Food Eng. **61**(1), 137–142 (2004)
8. Gongal, A., et al.: Sensors and systems for fruit detection and localization: a review. Comput. Electron. Agric. **116**, 8–19 (2015)
9. Payne, A.B., et al.: Estimation of mango crop yield using image analysis–segmentation method. Comput. Electron. Agric. **91**, 57–64 (2013)
10. Qureshi, W.S., et al.: Machine vision for counting fruit on mango tree canopies. Precis. Agric. **18**(2), 224–244 (2017)
11. Khairunniza-Bejo, S., Kamarudin, S.: Chokanan mango sweetness determination using hsb color space. In: 2011 Third International Conference on Computational Intelligence, Modelling and Simulation (CIMSiM), IEEE (2011)

Tailoring the Parameters to Increase the Efficiency of a Micro-Ring Resonator Sensor for Biosensing

Piyali Mukherjee and Nikhil R. Das

Abstract Photonic micro-ring resonators can be used as sensor which finds promising bio-analytical applications. The light propagating through the micro-ring and the resultant evanescent field beyond the structure are sensitive to the refractive index of the environment. This sensing capability can be used for detection of biological targets. In this paper, a vertically coupled micro-ring resonator for biosensing is studied. Silicon-on-insulator (SOI) based resonator is preferred for its high index contrast, low cost, and compatibility. Analytical derivations and computations are done to study the effects of structural parameters of the resonator to increase the efficiency of the sensor.

Keywords Micro-ring resonator · Biosensing · Vertically coupled Silicon-on-insulator

1 Introduction

Micro-ring resonators (MRRs) are versatile structures that can be implemented for diverse applications such as amplifiers, sensors, wavelength filters, switches, logic gates, and frequency converters [1, 2]. These resonators have recently been retasked for biosensing due to their scalability, sensitivity, and versatility. The small-scale size of the micro-resonators currently achievable allows integration of many devices.

The development of biosensors has increased significantly, especially in diagnostics [3, 4], since early diagnosis can change dramatically the development of a disease. In micro-resonator, the light propagating through the micro-ring cavity gets confined within the structure by total internal reflection, forming resonant modes.

P. Mukherjee (✉) · N. R. Das
Institute of Radio Physics & Electronics, University of Calcutta,
92, A.P.C. Road, Kolkata 700009, West Bengal, India
e-mail: mukherjee.piyali92@gmail.com

N. R. Das
e-mail: nrd@ieee.org

U. Biswas et al. (eds.), *Advances in Computer, Communication and Control*, Lecture Notes in Networks and Systems 41, https://doi.org/10.1007/978-981-13-3122-0_48

The evanescent field extending beyond the structure is sensitive to the refractive index of the local environment, which modulates the resonant wavelength and thus helps in the sensing mechanism. Continued improvements in the resonator parameters towards the development of new biosensors are vital aims in this field of research.

Silicon, a leading material in micro-optoelectronics makes SOI photonic devices potentially low cost and compatible with existing technology. Silicon and its oxide layer provide a large refractive index difference, allowing the creation of single-mode waveguide and compact devices enabling large-scale integration thus making SOI a suitable choice for device design.

This paper deals with the designing of vertically coupled [5], high refractive index contrast silicon-on-insulator (SOI) micro-ring resonator sensor [6] for biosensing. It provides analytical derivations and simulation results to study the effect of structural parameters of the micro-resonator on the efficiency of biosensing.

2 Theory

2.1 Resonator Structure

A micro-ring resonator in its basic form consists of a ring waveguide that channels light and serves as a resonant cavity that supports the light in both longitudinal and transverse modes. A coupling mechanism exists such that the ring waveguide closely couples with the straight bus waveguides which serves as input and output ports (Fig. 1).

The relation between the electric field components can be obtained by solving the electric field interactions by transfer matrix as

$$\begin{bmatrix} E_4 \\ E_2 \end{bmatrix} = \begin{bmatrix} r_1 r_2 & it_1 \\ it_1 & r_1 \end{bmatrix} \begin{bmatrix} E_3 \\ E_1 \end{bmatrix} \tag{1}$$

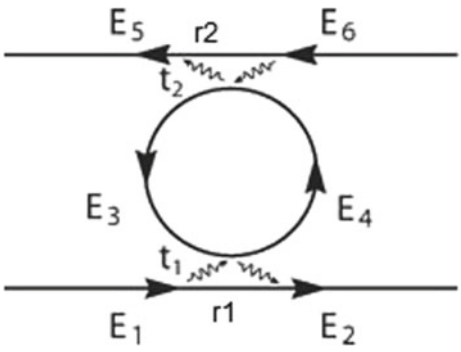

Fig. 1 Fields associated with add-drop resonator

$$\begin{bmatrix} E_5 \\ E_4 \end{bmatrix} = \begin{bmatrix} r_2 & it_2 \\ it_2 & r_1 r_2 \end{bmatrix} \begin{bmatrix} E_6 \\ E_3 \end{bmatrix}, \tag{2}$$

where r_1, r_2 are the self-coupling coefficients, t_1, t_2 are the cross-coupling coefficients.

Within the ring waveguide, the fields are related as

$$E_3 = ae^{i\phi} E_4, \tag{3}$$

where a is the transmission amplitude that takes into account the propagation loss within the waveguide, $\phi = \beta L$ is the phase shift with β as the propagation constant of the circulating mode, and L is the round trip length.

When the ring resonator is coupled to two bus waveguides, the incident field is partly transmitted to the through the port and the rest through drop port. These waveguide structures can be analyzed to relate the intensities and obtain the transmission coefficient of the two ports with respect to the input port as

$$T_{pass} = \frac{I_2}{I_1} = \frac{r_2^2 a^2 - 2r_1 r_2 a \cos\phi + r_1^2}{1 - 2r_1 r_2 a \cos\phi + (r_1 r_2 a)^2} \tag{4}$$

$$T_{drop} = \frac{I_5}{I_1} = \frac{(1 - r_1^2)(1 - r_2^2)a}{1 - 2r_1 r_2 a \cos\phi + (r_1 r_2 a)^2} \tag{5}$$

The ring will be in resonance if the light wavelength becomes an integer multiple of the optical length of the ring. From the transmission spectrum, the resonance condition is obtained as

$$\lambda_r = \frac{n_{eff} L}{m}, \mathrm{m} = 1,\ 2,\ 3, \ldots \tag{6}$$

with

$$n_{eff} = \frac{\beta}{k}, \tag{7}$$

k being the wave number.

2.2 Structural Parameters

The characteristic parameters can be obtained from the transmission spectrum of the resonator as well as they can be obtained analytically. All the device performance parameters are governed by the structural parameter of the ring resonator. So, defining the ring dimensions are essential for device design.

A. ***Free Spectral Range (FSR)***

FSR is the distance between two consecutive resonant peaks at the drop port. This determines the selectivity of the sensor. Mathematically, it is given by

$$FSR = \frac{\lambda_{res}^2}{n_g L} \tag{7}$$

n_g is the group index. The group index takes into account the dispersion in the waveguide and is given as [7]

$$n_g = n_{eff} - \lambda_0 \frac{dn_{eff}}{d\lambda} \tag{8}$$

B. ***Quality Factor***

The quality factor of a resonator is a measure of the sharpness of the resonance relative to its center frequency.

$$Q - factor = \frac{\lambda_{res}}{FWHM} = \frac{\pi n_g L \sqrt{r_1 r_2 a}}{\lambda_{res}(1 - r_1 r_2 a)} \tag{9}$$

FWHM (Full Width at Half Maxima) can be obtained from the transmission spectrum and is given by the wavelength range for which the intensity is half the maximum intensity.

2.3 Design Considerations

A. ***Silicon/Silicon Dioxide (SOI) Based Resonator***

Silicon, a leading material in micro-optoelectronics makes SOI photonic devices potentially low cost and compatible with existing technology. Passive silicon waveguide structures have shown an unprecedented reduction in the footprint of waveguides and especially in wavelength-selective devices [8, 9]. Silicon and its oxide layer provide a large refractive index difference that allows the creation of single-mode waveguide and compact devices enabling large-scale integration thus making SOI a suitable choice for device design.

B. ***Vertically Coupled Resonator***

Micro-ring resonator structures have been fabricated using several materials so far. Coupling between the micro-ring and the waveguides is a critical consideration for fabrication issues which can be achieved either vertically or laterally. Laterally coupled resonators are being used widely by researchers. Vertically coupled resonators were first designed and presented in [10] which were fabricated by the method of Chemical Vapor Deposition (CVD).

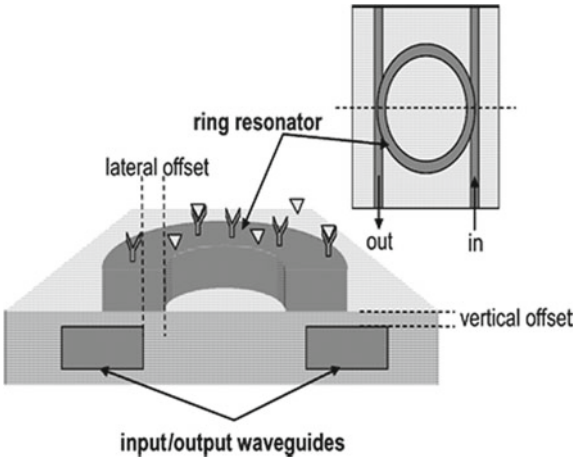

Fig. 2 Vertically coupled ring resonator structure [5]

In laterally coupled structures, the input/output waveguides and the rings are all coplanar. Narrow coupling gaps are required in the lateral geometry, which taxes photolithography and results in large variations in the device performance. Also, in the lateral geometry, all the waveguides would be exposed to the surface treatments. In vertical coupling (Fig. 2), the straight waveguides are buried below the ring waveguide and hence remain isolated from the effects of surface treatment. The resonator-waveguide separation is done by cladding material deposition, which makes the process better controlled than lithography and etching.

3 Results and Discussion

The transmission spectrums of the field intensity at the drop port and through port respectively are shown in Fig. 3 for a 10-μm ring radius.

The difference in wavelengths between the two peaks at the drop port transmission gives the free spectral range (FSR) of the sensor. FWHM can also be determined from the same spectrum and is the range of wavelengths for which the intensity reaches half the maximum intensity.

With the variation in the structural parameters of the ring, the obtained spectrum also varies. As the ring radius increases, the round-trip length of the ring resonator increases (Fig. 4).

FSR 1 is the wavelength difference between two peaks for 5-μm ring size, FSR 2 for 10-μm- and FSR 3 for 25-μm ring size. FSR is thus seen to have an inverse relation with the ring radius.

Figure 5 shows that as the length of resonator increases, FSR decreases which matches the mathematical relation obtained earlier in (7). The effective index and in turn the group index is calculated considering the height of the resonator as 220 nm.

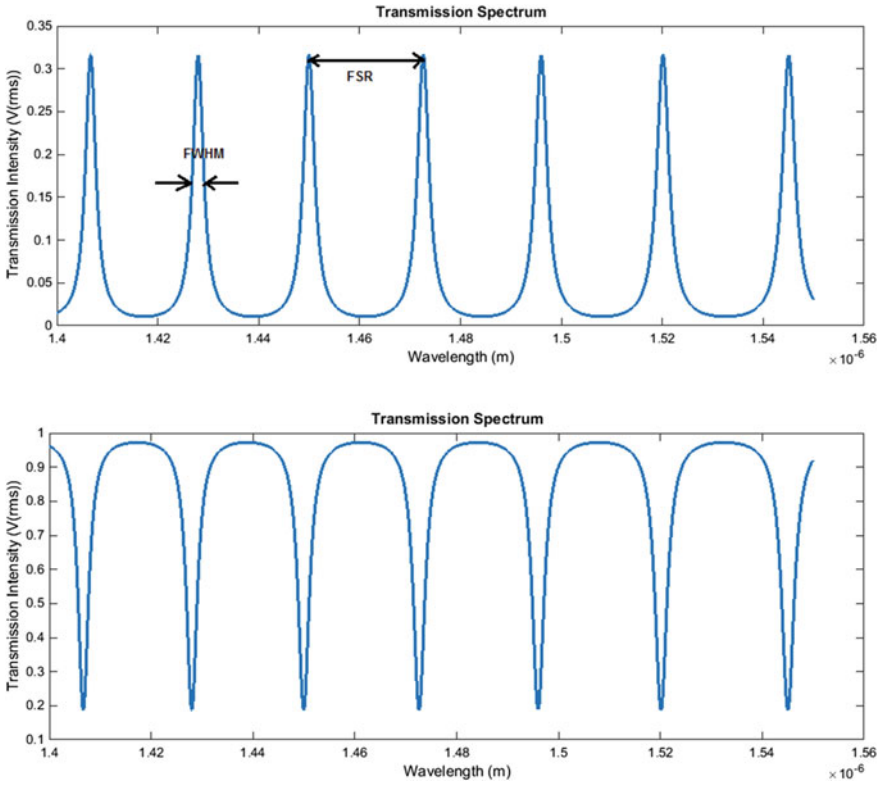

Fig. 3 Transmission spectrum at drop port (left) and at through port (right)

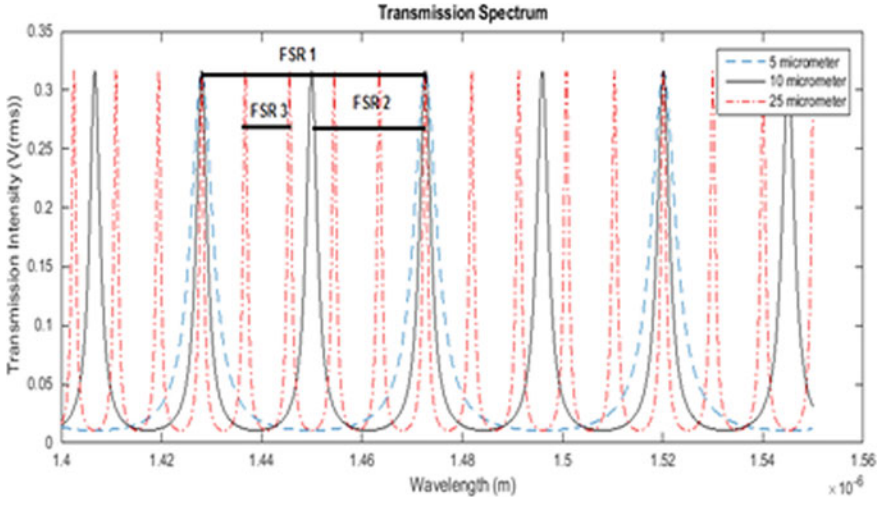

Fig. 4 Variation of FSR with ring radius

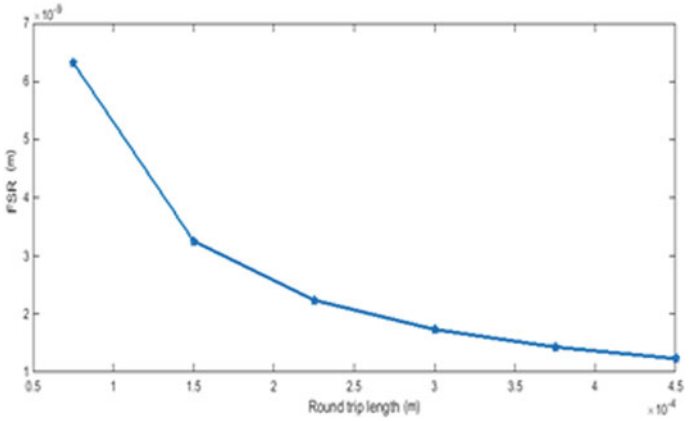

Fig. 5 Variation of FSR with round trip length

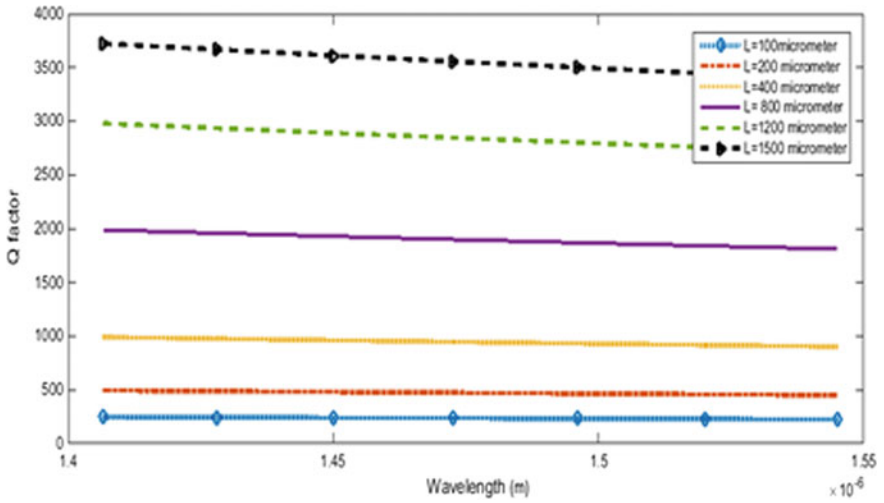

Fig. 6 Change of quality factor with change in ring length

The increase in the ring height above 250 nm limits the single-mode operation of the waveguide [11, 12].

The ring dimensions also affect another parameter, namely Quality factor. A plot of Q-factor for different lengths of the ring is shown in Fig. 6.

We can see that as ring length increases, there is an increase in the quality factor which is almost constant for a particular length. But the ring length cannot be increased indefinitely as that will result in a large dimension of the sensor. So, loss minimization within the cavity is required. Propagation loss and bend loss [13, 14] can be minimized and accordingly the group index has been considered.

4 Conclusion

The efficiency of the sensor depends on both selectivities as well as specificity. Variations in the resonator dimensions lead to change in the sensor's response in terms of Quality factor and FSR. As revealed from the mathematical expressions, FSR and Q-factor varies differently with the resonator length and the ring radius. So, a tailoring between the parameters is required.

There is a restriction of the resonator height so as to enable single-mode operation. From the computational results obtained, we see that ring radius above 30–50 μm lowers the FSR leading to ambiguous results. So, ring radius below it is desired. At the same time, Q-factor obtained is very low for lower values of resonator length. Length greater than 1.2 mm is desired. Also, a lower waveguide loss (propagation loss and bend loss) is required which further depends on design procedure.

References

1. Heebner, J., Grover, R., Ibrahim, T.A.: Optical microresonators: theory, fabrication and applications. In: Springer Series in Optical Sciences (2008)
2. Rabus, D.G.: Integrated ring resonators, the compendium. In: Springer Series in Optical Sciences (2007)
3. Kindt, J.T., Bailey, R.C.: Biomolecular analysis with microring resonators: application in multiplexed diagnostics and interaction screening. Curr. Opin. Chem. Biol. **17**(5) (2013)
4. Chao, C.Y., Guo, L.J.: Design and optimization of microring resonators in biochemical sensing applications. J. Lightwave Technol. **24**(3), 1395–1402 (2006)
5. Yalcin, A., Popat, K.C., Alridge, J.C., Desai, T.A., et al.: Optical sensing of biomolecules using microring resonators. IEEE J. Select. Topics Quant. Mech. **12**, 148–155 (2006)
6. Niehusmann, J., Vorckel, A., Bolivar, P.H., Wahlbrink, T., Henschel, W., Kurz, H.: Ultrahigh-quality-factor silicon-on-insulator microring resonator. In: Optics Letters, vol. 29, pp. 2861–2863. Optical Society of America (2004)
7. Bogaerts, W., et al.: Silicon microring resonators. In: Laser Photonics Reviews, no. 1, pp. 47–73 (2012)
8. Bogaerts, W., Dumon, P., Thourhout, D.V., Taillaert, D., Jaenen, P., Wouters, J., Beckx, S., Wiaux, V., Baets, R.G.: Compact wavelength-selective functions in silicon-on-insulator photonic wires. IEEE J. Select. Topics Quant. Electron. **12** (2006)
9. Bogaerts, W., selvaraja, s.k., dumon, p., brouckaert, j., vos, k.d., thourhout, d.v., baets, r.: silicon-on-insulator spectral filters fabricated with CMOS technology. IEEE J. Select. Topics Quant. Electron. **16** (2010)
10. Little, B.E., Chu, S.T., Pan, W., Ripin, D., Kaneko, T., Kokubun, Y., Ippen, E.P.: Vertically coupled glass microring resonator channel dropping filters. IEEE Photon. Technol. Lett. **11**, 215–217 (1999)
11. Dulkeith, E., Xia, F., Schares, L., Green, W., Vlasov, Y.: Group index and group velocity dispersion in silicon-on-insulator photonic wires. Opt. Express **14**(9), 3853–3863 (2006)

12. Turner, A.C., Manolatou, C., Schmidt, B.S., Lipson, M., Foster, M.A., Sharping, J.E., Gaeta, A.L.: Tailored anomalous group-velocity dispersion in silicon channel waveguides. Opt. Express **14**(10), 4357–4362 (2006)
13. Selvaraja, S., Jaenen, P., Bogaerts, W., Thourhout, D.V., Dumon, P., Baets, R.: Fabrication of photonic wire and crystal circuits in silicon-on-insulator using 193-nm optical lithography. J. Lightwave Technol. **27**(18), 4076–4083 (2009)
14. Bogaerts, W., Selvaraja, S.: Compact single-mode silicon hybrid rib/strip waveguide with adiabatic bends. IEEE Photon. J. **3**(3), 422–432 (2011)

9T and 8T Full Subtractor Design Using Modified GDI and 3T XOR Technique

Shubham Sarkar, Sujan Sarkar, Arun Atta, Tuhin Pahari, Nishanta Majumdar and Sourav Mondal

Abstract Circuit designing is an emerging field and as per the recent trend it evolves digital devices in use—portable as well as smaller in size. This paper proposes two designs of full subtractor circuit based upon eight and nine transistors demonstrating low power consumption and high-speed switching. The combination of 3T XOR and modified gate diffusion input (M-GDI) technique has been implied to realize the circuits. The circuit realization and simulations have been performed using DSCH 3.5. The design has been further verified and simulated in Xilinx ISE 14.7 environment, coded using Verilog HDL.

Keywords Circuit · Low power · High speed · Subtractor
Gate diffusion input (GDI) · Modified gate diffusion input (M-GDI) · 3T XOR
DSCH 3.5 · Verilog HDL

S. Sarkar (✉) · S. Sarkar · A. Atta · T. Pahari · N. Majumdar · S. Mondal
Department of Electronics and Communication Engineering, Jalpaiguri Government Engineering College, Jalpaiguri, India
e-mail: shubhams.jgec@ieee.org

S. Sarkar
e-mail: sujansa1997@gmail.com

A. Atta
e-mail: arunatta6@gmail.com

T. Pahari
e-mail: tuhinpahari@gmail.com

N. Majumdar
e-mail: nishantamajumdar09@gmail.com

S. Mondal
e-mail: sm1855@ece.jgec.ac.in

U. Biswas et al. (eds.), *Advances in Computer, Communication and Control*, Lecture Notes in Networks and Systems 41, https://doi.org/10.1007/978-981-13-3122-0_49

1 Introduction

With the development of digital technology, it has become essential to design circuits which consume less power, operate at high speed, and occupy minimum area on a chip. To increase the performance of any circuit, we should design it incorporating scaling. The number of transistors used to implement logic gates largely affects the design parameters of a digital circuit. In last few decades, designers have mainly emphasized on VLSI technology for design purpose which involves packing more than a million transistors on a chip.

To improve various circuits, designers use different logic design techniques such as complementary MOS (CMOS), pseudo-NMOS, transmission gate, dynamic CMOS logic, and pass transistor logic. All these techniques have different design mechanisms, with some advantages as well as disadvantages. Almost 90% of the total semiconductor devices are fabricated using CMOS. CMOS is a combination of NMOS and PMOS which are functionally and structurally complement to each other. The advantages of pseudo-NMOS logic are its high speed and low transistor count, on the other hand, static power consumption of the pull-up transistor as well as the reduced output voltage swing and gain, which makes the gates more susceptible. Transmission gate is a bidirectional switch made up of an NMOS and PMOS connected in parallel. It avoids the problem of reduced noise margin, increased static power dissipation, but requires that the control and its complement are available. Disadvantages of this technology are lower speed, due to charge sharing problem we cannot connect more than three transmission gates in cascade. Pass transistor logic reduces the count of transistor used to make different logic gates, by eliminating redundant transistors. In PTL, designers use transistors as switches to pass logic levels between nodes of a circuit, instead of switches which are connected directly to voltage supply. Main disadvantage of PTL is the voltage difference between high and low logic levels decrease at each stage.

In digital technology, arithmetic operations (like addition, subtraction, multiplication, division, etc.) are extensively used in various applications. In microprocessor operations, image processing, digital signal processing subtractor plays a significant role. One-bit subtractor is the fundamental unit used for subtraction operation of two binary digits. It consists of one NOT gate, one XOR gate, and one AND gate. A full subtractor is a combinational circuit that performs subtraction involving three bits, namely, minuend bit, subtrahend bit, and the borrow from the previous stage and it produces two outputs named difference (D) and borrow out (B). To design a full subtractor, we require more number of logic gates which increases the number of transistor, and hence takes up more area on a chip. Therefore, delay, power consumption, and area required are more. We can reduce the number of transistors using modified gate diffusion input technique (M-GDI).

The main contribution of this paper is to present an optimal solution to address the design of full subtractor using eight and nine transistors, using M-GDI technique and three-transistor-based XOR gate design technique.

2 Literature Survey

We have already discussed the main problem to design any digital circuit. The main aim is to decrease the number of transistors, that is why, we have designed full subtractor using GDI technique (using only eight and nine transistors) which requires lesser chip area, consumes less power, results in lower propagation delay, and hence faster and efficient. In modern times, with the advancement of portable devices, low power consumption amounts to longer battery life. Also, low power consumption will reduce heat generation resulting in reduction in cost of packaging and cooling [1]. There are various works and researches in this field to reduce these types of problems and to design efficient models [1, 2–5]. In [2], we found significant improvement in speed, power dissipation, and area of a half-subtractor circuit using GDI technique compared to standard CMOS, transmission gate, and complementary pass transistor logic. In [3], we saw that a 2-bit magnitude comparator using GDI technique saved on-chip area and decreased power dissipation compared to CMOS design. In [4], a full subtractor circuit has been designed using 10 transistors. In [5], full adder circuits were designed using GDI technique and analysis shows that it was more efficient than the conventional CMOS techniques. In [1], a full subtractor circuit is designed using 14 transistors. We know that for the first time subtractor is invented for single bit operation [2]. In our everyday life, we use various types of digital media and devices like smartphone, computer, TV, and gaming devices. These devices use processors, which consists of ALU, which in turn is majorly responsible for carrying out arithmetic and logical operations. In computer, ALU does all the arithmetic operation such as addition, subtraction, multiplication, division, and logical operation such as NOT, AND, OR, XOR, NAND, NOR, etc. In order to fulfill the requirement of faster computation along with lesser power consumption, it is required that all the individual circuits consume less power and are efficient. Here, we use full subtractor for arithmetic operation, i.e., subtraction of 3 bits (two input bits, one borrow bit from previous stage). In the past, subtractor circuit has been designed using CMOS technology, standard transmission gates, complementary pass transistor logic, and gate diffusion input technology using 50, 38, 34, and 14 transistors, respectively [1]. In our paper, we have designed full subtractor circuits using nine and eight transistors, reducing further the on-chip area, power dissipation, and propagation delay thereby improving the power-delay product (figure of merit) of the circuit.

2.1 GDI Cell

The basic GDI unit is comparable to that of a CMOS inverter, but the function varies according to the inputs given at P, N, and G. The individual inputs are assigned to the ports such as—"G" is used as an input to the common gate terminal of NMOS and PMOS. "P" is used as an input to the source terminal of the PMOS, whereas "N" is used as an input to the source terminal of the NMOS. The output is collected

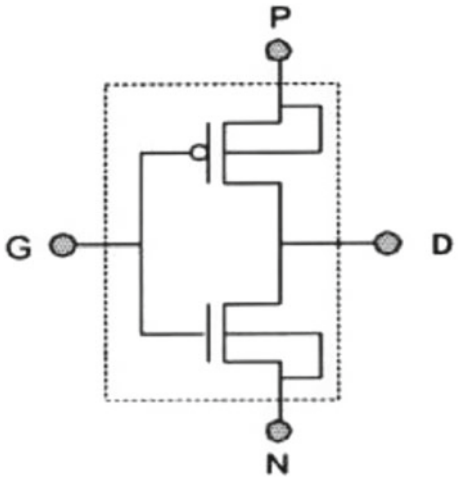

Fig. 1 A basic GDI cell

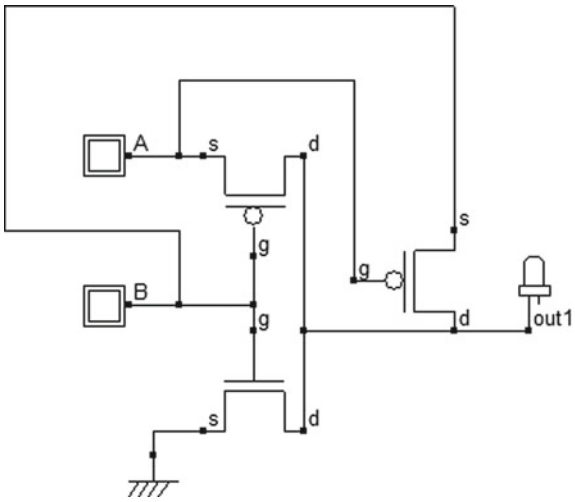

Fig. 2 3T XOR design using M-GDI

from the common drain terminals of NMOS and PMOS. GDI technique is based upon Shannon's theorem of small-scale library. Figure 1 depicts the basic GDI unit. Figure 2, depicts 3T XOR Design based on M-GDI technique.

The functions that can be implemented using the basic GDI cell have been summarized in Table 1.

Table 1 GDI cell summarization

P	G	N	Output	Function
B	A	'0'	$A' \cdot B$	$F1$
'1'	A	B	$A' + B$	$F2$
B	A	'1'	$A + B$	OR
'0'	A	B	$A \cdot B$	AND
A	Sel	B	$A \cdot Sel + B \cdot (Sel')$	..
'1'	A	0	A'	NOT

2.2 M-GDI Technique

Modified gate diffusion input (M-GDI) is an alternate technique to design digital circuits resulting in better performance compared to CMOS and pass transistor logic (PTL). It reduces the required number of transistors, and hence reduces the area of digital circuits, power dissipation, and delay. Mod-GDI is very similar to GDI except that the bulk of NMOS(S_n) and PMOS(S_p) is connected to ground and V_{DD}, respectively. Figure 3 presents a basic 2:1 Mux design based on GDI Technique. Figure 4, depicts basic M-GDI cell.

By connecting the bulk of NMOS and PMOS to GND and V_{DD}, respectively, Mod-GDI overcomes the practical difficulties of fabricating in standard CMOS process. Mod-GDI is completely compatible for implementation using standard CMOS fabrication process. Mod-GDI can also be implemented by twin-well CMOS technique and silicon on insulator (SoI) technique.

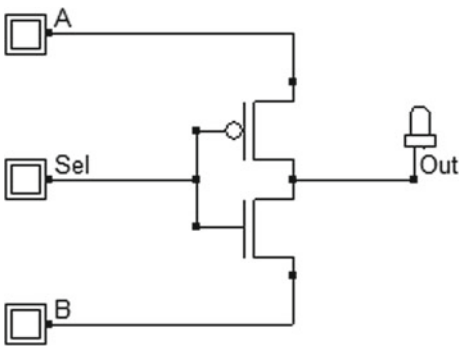

Fig. 3 2:1 MUX design using GDI

3 Basic Full Subtractor (CMOS Logic)

The full subtractor can be thought of as one-bit subtractor which performs subtraction of two binary bits, namely, minuend and subtrahend and the borrow generated from the previous stage called borrow in. Hence, the Bin is subtracted from the input Y as well as input X. To represent, this is an equation as given below:

$$Diff = X - Y - Bin \tag{1}$$

A borrow out signal is generated when it needs to borrow from the next digit, as the subtraction is taking place in order—X by Y and Bin, the Borrow out signal must be generated when

$X < Y + Bin$, i.e., $Bout$ would be 1 if the equation follows otherwise it would be 0.

The equations for difference and carry using the logical gates can be implemented by following the equations (Fig. 5, Table 2):

$$Diff = X \oplus Y \oplus Bin \tag{2}$$

$$Borrow = Bin\,(A \oplus B)' + A' \cdot B \tag{3}$$

Fig. 4 A basic M-GDI cell

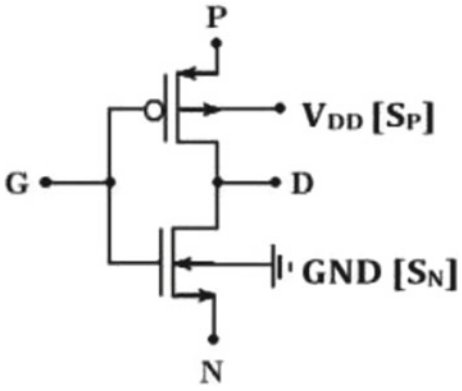

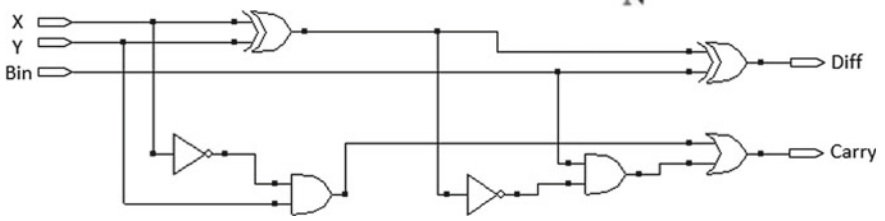

Fig. 5 The figure demonstrates the circuit of conventional full subtractor

Table 2 Full subtractor truth table

A	B	Bin	Diff	Borr
0	0	0	0	0
0	0	1	1	1
0	1	0	1	1
0	1	1	0	1
1	0	0	1	0
1	0	1	0	0
1	1	0	0	0
1	1	1	1	1

3.1 XOR-Gate-Based Full Subtractor Design

From Eqs. (3) and (4), it could be well understood that the full subtractor circuit can be realized with the help of XOR gate and 2:1 multiplexer circuit. The design on both the possible scenarios has been depicted in Fig. 6.

In MUX 1, *Bin* is the select line, $S1 = A \oplus B$, and $S2 = A \odot B$. When $Bin = 0$, the line $S1$ is selected and when $Bin = 1$ then $S2$ is selected.

So, the output of

$$\begin{aligned} \text{MUX 1} &= Bin'\,(A \oplus B) + Bin\,(A \oplus B)' \\ &= A \oplus B \oplus Bin \end{aligned} \tag{4}$$

For MUX2, (A $\odot$ B) is the select line and $S1 = B$ and $S2 = Bin$. When $(A \odot B)$, it results in 0, B is selected and when $(A \odot B) = 1$, *Bin* is selected (Fig. 7).

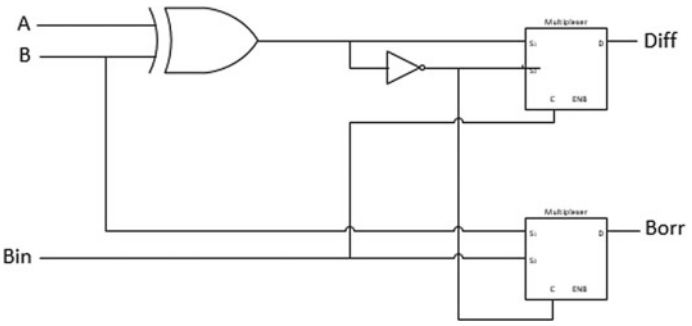

Fig. 6 9T subtractor design using GDI and 3T XOR design

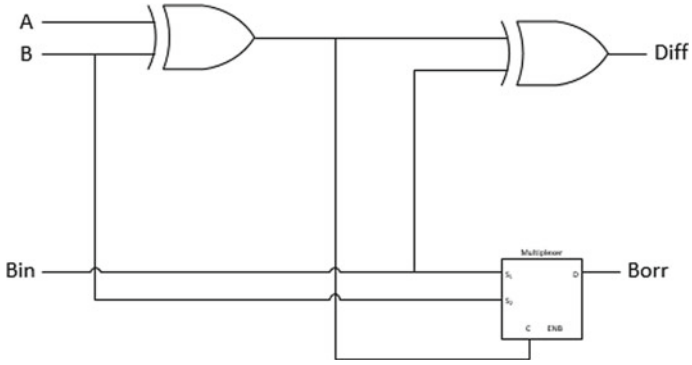

Fig. 7 8T subtractor design using GDI and 3T XOR design

So, the output of

$$\begin{aligned} \text{MUX}\,2 &= (A \odot B)'B + (A \odot B)Bin \\ &= \left(AB' + A'B\right) \cdot B + (A \oplus B)'Bin \\ &= A'B + Bin\,(A \oplus B)' \qquad (5) \\ Difference &= A \oplus B \oplus Bin \qquad (6) \end{aligned}$$

In MUX, we use $(A \oplus B)$ as select line. Here, $S1 = Bin$ and $S2 = B$. When select line is 0, then $S1$ is selected and when the select line is 1, then $S2$ is selected.

So, the output of the

$$\begin{aligned} MUX &= (A \oplus B)'Bin + (A \oplus B) \cdot B \\ &= Bin\,(A \oplus B) + A'B \qquad (7) \end{aligned}$$

3.2 GDI Realization of Full Subtractor (XOR and MUX Logic)—Transistor-Level Design

Input A is connected to the source of Q1 and gate of Q3. Input B is connected to the common gate terminal of Q1 and Q2. Source of Q2 is grounded. The drain of Q1 and Q2 is connected with the drain of Q3, gate of Q4 and Q5, and to the source of Q6. Input B is also connected with the source of Q3 and Q8. Common drain of Q4 and Q5 is connected with the source of Q7 and to the common gate terminal of Q8 and Q9. Input Bin is connected to the source of Q9 and to the common gate terminal of Q6 and Q7. Difference output is taken from the common drain terminal of Q6 and Q7. Borrow output is taken from the common drain terminal of Q8 and Q9 (Figs. 8 and 9).

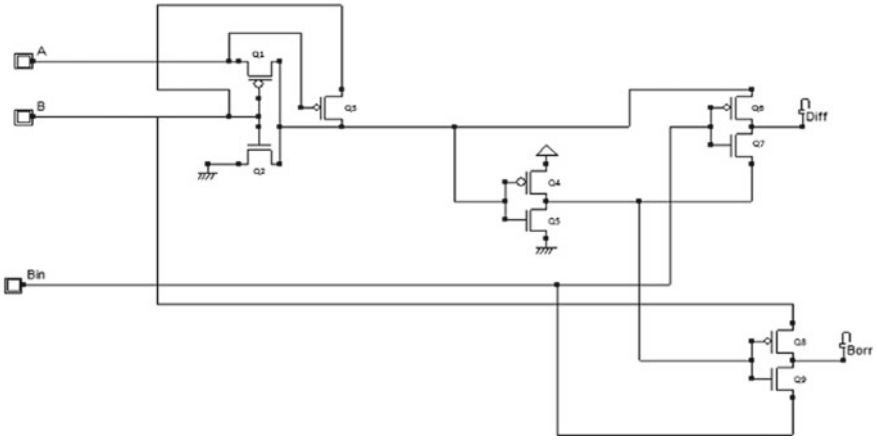

Fig. 8 9T-based full subtractor

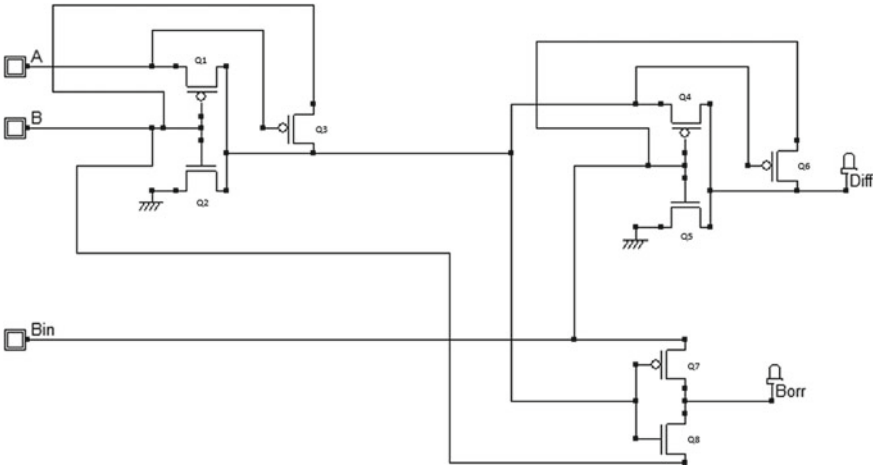

Fig. 9 8T-based full subtractor

Input A is connected to the source of Q1 and to the gate of Q3. Input B is connected to the common gate terminal of Q1 and Q2 and the source of Q3 and Q8. Input Bin is connected to the source of Q6 and Q7 and to the common gate terminal of Q4 and Q5. Common drain terminal of Q1 and Q2 is connected with the drain of Q3 and source of Q4 and gate of Q6, Q7, and Q8. Common drain terminal of Q4 and Q5 is connected to the drain of Q6. Difference output is taken from common drain terminal of Q4, Q5, and Q6. Borrow output is taken from the common drain terminal of Q7 and Q8.

4 Result Section

The simulation has been carried out using DSCH 3.5, starting from transistor-level design and further verified using Xilinx ISE 14.7 environment (Figs. 10 and 11).

Table 3 shows the comparison of various parameters of different techniques used for full subtractor design. We have made our comparison on basis of power consumption, propagation delay, and area occupied on a chip. Some graphical analysis has been carried with the help of this table that is shown in Fig. 12.

From Comparison Table 3 and Fig. 12, it is clearly depicted that the propagation delay has been reduced with respect to transistor number. As we have implemented the full subtractor using 9T and 8T transistors, these have the lowest propagation delay when compared to the subtractors designed using other techniques. For 9T transistor, the delay has improved by 89.32%, 89.01%, and 30% in comparison with normal CMOS, CPL, and GDI techniques, respectively. While, in the other hand, if we calculate the percentage of improvement in transistor count in order to realize full subtractor circuit using different techniques, then it can be observed that our 9T subtractor is 82% and 36% more efficient than CMOS and GDI techniques, respectively. While for the 8T-transistor-based full subtractor model, the propagation delay has improved by 90.45%, 90.17%, and 37% with respect to CMOS, CPL, and normal GDI techniques, respectively.

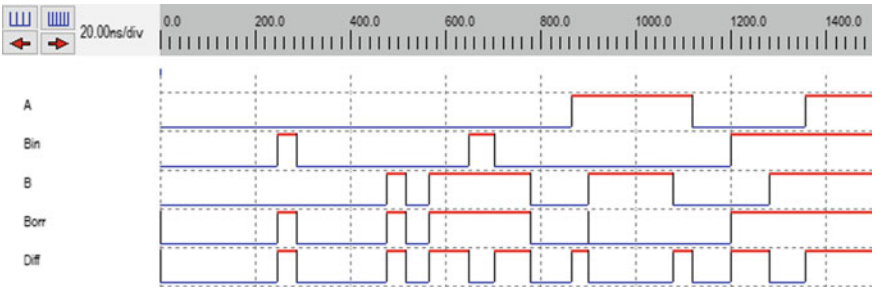

Fig. 10 8T simulation waveform

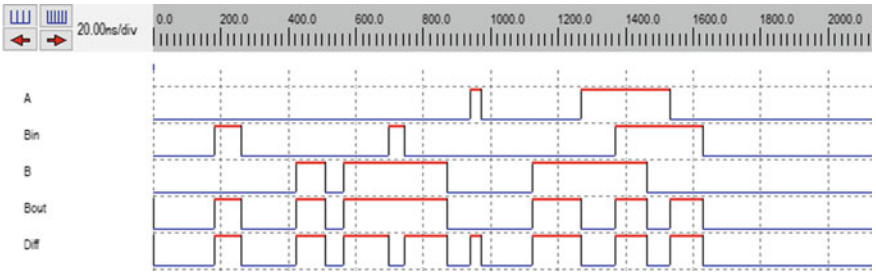

Fig. 11 9T simulation waveform

Table 3 Result summary based on transistor count, area on chip, and delay and average power consumption

Parameters	Full subtractor using CMOS technique	Full subtractor using complementary pass transistor logic (CPL)	Full subtractor using gate diffusion input (GDI)	Full subtractor using modified GDI (9T)	Full subtractor using modified GDI (8T)
Number of transistors used	50	34	14	9	8
Average power consumed (W)	4.395×10^{-6}	1.006×10^{-4}	1.396×10^{-8}	1.21×10^{-8}	1.25×10^{-8}
Delay time (ps)	118.92	115.47	18.02	12.69	11.35
Surface area (cm^2)	3.24×10^{-5}	1.82×10^{-5}	8.92×10^{-7}	5.83×10^{-7}	5.1×10^{-7}

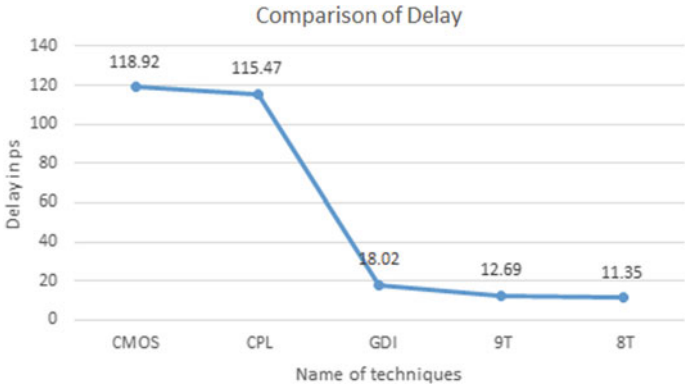

Fig. 12 Comparison of delay

In the Fig. 13, we have compared the surface area (cm^2) consumed by the full subtractor circuit of our proposed techniques 9T and 8T with respect to normal GDI method. It is clearly shown that both the proposed circuits are more efficient with respect to surface area consumption. 9T full subtractor consumes 34.64% less surface area on a chip and 8T design consumes 42.82% less surface area on a chip as compared to GDI method. If the M-GDI-based designs are compared with CMOS method of designing subtractors then our 8T-based subtractor designs result to have 98.42% reduction in surface area consumed on a chip.

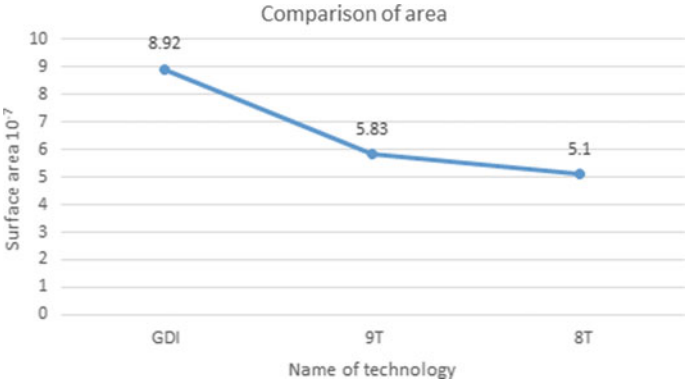

Fig. 13 Comparison of surface area

So, in this result section, it has been demonstrated that both the proposed circuits—8T-based full subtractor and 9T-based full subtractor are more efficient than the previously realized.

5 Conclusion

With the increasing demand for low-power portable device, our main focus of the work was to minimize the power consumption and the area of the full subtractor logic. The modification of the GDI technique has been used to realize the XOR gate using three transistors, the multiplexers were modeled using GDI technique. These gates as primitives have been used to come up with full subtractor circuit design. Two designs have been proposed using eight transistors and nine transistors, respectively. The primary layout design has been done using DSCH schematic editor and further verified in Xilinx ISE 14.7 environment using Verilog HDL. Results clearly show that our proposed design is more efficient than normal GDI technique, CMOS technique, and CPL technique with respect to propagation delay, average power consumed, number of transistors required to realize the circuit, and the surface area occupied by the designed circuit.

References

1. Dhar, K., Chatterjee, A., Chatterjee, S.: Design of an energy efficient, high speed, low power full subtractor using GDI technique. In: Proceeding of the 2014 IEEE Students' Technology Symposium TS14P01 041 978-1-4799-2608-4/14/$31.00 ©2014 IEEE 199
2. Prince, R.M.: Design of an energy efficient, low power dissipation half subtractor using GDI technique. Int. J. Eng. Trends Technol. **36**(2) (2016)

3. Shekhawat, V., Sharma, T., Sharma, K.G.: 2-bit magnitude comparator using GDI technique. In: IEEE International Conference on Recent Advances and Innovations in Engineering (ICRAIE-2014), 09–11 May 2014, Jaipur, India
4. Singh, H., Kumar, R.: 10-T full subtraction logic using GDI technique. In: 2014 Sixth International Conference on Computational Intelligence and Communication Networks
5. Uma, R., Dhavachelvan, P.: Modified gate diffusion input technique: a new technique for enhancing performance in full adder circuits. In: 2nd International Conference on Communication, Computing & Security (ICCCS-2012)

CdS/ZnSe-Based Multicolor Quantum Well Infrared Photodetector for Infrared Application

Md. Aref Billaha, Sourav Rakshit, Bhaskar Roy, Bikas Mondal, Santosh Kumar Choudhary and Kumari Arti Yadav

Abstract In this paper, the performance of CdS/ZnSe-based quantum well infrared photodetector is studied considering physics-based theoretical modeling. In this model, finite difference method is used to determine eigenenergy states in the quantum well structure. Results show that the absorption coefficient concerning bound-to-bound intersubband transitions using CdS/ZnSe-based QWIP is much larger than III–V-based QWIP like GaAs/AlGaAs. Moreover, multispectral region of infrared operation such as the mid- and long wavelengths of operation is obtained.

Keywords CdS/ZnSe · Eigenstates · Absorption coefficient · QWIPs

1 Introduction

Quantum well infrared photodetectors (QWIPs) has numerous applications like medical science, military, night vision camera, environment monitoring, etc. [1–3]. These applications required intersubband transitions (ISBTs) based photodetectors with high sensitivity and the multispectral ability for the detection of infrared light [4–6]. Infrared (IR) photodetectors based on ISBTs in single, multiple quantum wells, and superlattices have been studied extensively [7–9]. However, most of the ISBT-based quantum well (QW) structures have been demonstrated mainly on III–V-based compound semiconductor materials [10, 11]. Band structure engineering has made it possible to obtain ISBT-based devices operating over a wide range of spectrum

Md. A. Billaha (✉) · S. Rakshit · B. Roy · B. Mondal · K. A. Yadav
Department of Applied Electronics & Instrumentation Engineering,
Asansol Engineering College, Asansol 713305, India
e-mail: rf.billaha@gmail.com

B. Mondal
e-mail: bikas.mondal143@gmail.com

S. K. Choudhary
Department of Electronics and Communication Engineering,
VNR Vignana Jyothi Institute of Engineering and Technology, Hyderabad, India

U. Biswas et al. (eds.), *Advances in Computer, Communication and Control*, Lecture Notes in Networks and Systems 41, https://doi.org/10.1007/978-981-13-3122-0_50

region without the need to change the material system. In recent times, QW structures based on II–VI semiconductors like CdS/ZnSe-based photodetector has emerged out a promising technology to meet such requirements. Moreover, multispectral response in QWIP requires a large conduction band discontinuity (CBD). In CdS/ZnSe-material-based QWIP, conduction band discontinuity is 0.8 eV without considering strain, whereas the conduction band discontinuity of $GaAs/Al_xGa_{1-x}As$ is very low. Hence, multicolor QWIP cannot be obtained using simple $GaAs/Al_xGa_{1-x}As$-based QWIP. Few works have already been carried out in this area. For example, type-II and (CdS/ZnSe)/BeTe-based device investigated by Akimoto et al. [12]. Intersubband transitions in type-I band alignment based on $Zn_{0.46}Cd_{0.54}Se/Zn_{0.24}Cd_{0.25}Mg_{0.51}Se$ MQWs with 3.99 and 5.35 μm wavelengths observed by Lu et al. [13].

In this paper, theoretical model of QWIP is developed based on CdS/ZnSe material for the purpose of the multicolor-based system. Finite difference method is used to solve the Schrödinger equation for the determination of quantized states and their corresponding wave functions. Possible transition energy and absorption coefficient are also reported in this paper. Rest of the paper is organized as follows. In Sect. 2, device structure and theoretical calculation of finding eigenenergy states are described. In Sect. 3, the confined electron states and probable transition energies are evaluated. Finally, a summary of conclusions is given in Sect. 4.

2 Device Structure and Theoretical Calculations

The device structure consists of 10 periods of N-type CdS well and undoped ZnSe barrier layer. Each period contains 5.4 nm CdS well and 30 nm ZnSe barrier layer. The whole structure is again sandwiched between ZnSe contacts layers (N-type doped with 2×10^{18} cm^{-3}). The active well layer doping concentration is taken as 5×10^{17} cm^{-3}. The growth axis is assumed to be along z-direction.

Now, the eigenenergy states and corresponding wave functions are an important requirement to observe the multispectral capability of our proposed device structure. This requires the solution of one-dimensional (1D) time-independent Schrödinger equation (SE). The mathematical expression for 1D time-independent SE can be written as

$$-\frac{\hbar^2}{2m_e^*}\frac{\partial^2\psi(z)}{\partial z^2} + V(z)\psi(z) = E\psi(z) \tag{1}$$

where $\hbar$ is the reduced Planck constant, m_e^* is the effective mass of electron, $\psi(z)$ is the wave function of electrons with energy E, and $V(z) = (V_c(z) + V_H(z) + \delta E_c)$, where $V_c(z)$ is the band offset potential, $V_H(z)$ is the Hartree potential, and δE_c is the change in conduction band energy due to strain. The strain plays an important role in the calculation of band structure due to the mismatch of lattice constant of CdS and ZnSe. In this context, model solid theory suggested by Van de Walle [14]

is used for the calculation of strain. The $V_H(z)$ can be obtained from the solution of the Poisson equation [15].

From Eq. (1), the Hamiltonian matrix can be expressed as

$$H = -\frac{\hbar^2}{2m_e^*}\frac{\partial^2}{\partial z^2} + V(z) \tag{2}$$

Finite difference method (FDM) is used to solve the Schrödinger equation. It is important to mention here that the total region of interest is divided into m number of small pieces of elements of equal width (a) and the equation is solved for each of the elements. Then, the Hamiltonian matrix, H in terms of m is obtained. Equation (2) is used to convert into a difference equation by standard finite difference technique and is given by

$$\left(\frac{\partial^2\psi(z)}{\partial z^2}\right)_{z=z_m} = \frac{1}{a^2}[\psi(z_{m+1}) - 2\psi(z_m) + \psi(z_{m-1})] \tag{3}$$

Using Eqs. (1), (2), and (3), the final expression of Hamiltonian in terms of the matrix form can be represented as

$$H = \begin{pmatrix} 2T_0 + V_1 & -T_0 & 0 & 0 & 0 \ldots 0 & 0 \\ -T_0 & 2T_0 + V_2 & -T_0 & 0 & 0 \ldots 0 & 0 \\ 0 & -T_0 & 2T_0 + V_3 & -T_0 & 0 \ldots 0 & 0 \\ \vdots & & & & & \\ 0 & 0 & 0 & 0 & 0 \ldots 2T_0 + V_{m-1} & -T_0 \\ 0 & 0 & 0 & 0 & 0 \ldots -T_0 & 2T_0 + V_m \end{pmatrix} \tag{4}$$

where $T_0 = \hbar^2 / 2m_e^* a^2$

3 Results and Discussion

The conduction band energy profile of CdS/ZnSe-based quantum well structure is shown in Fig. 1. The position of eigenstates and their corresponding electron wave functions are obtained from Eq. (4). It is seen that four possible bound eigenstates are confined with the quantum well structure. Transition from ground state to excited states occurs on the incident of the suitable wavelength of infrared light. Odd-to-odd or even-to-even transition is forbidden since symmetric QW structure is considered in this analysis. The reason behind the fact is explained as follows. The transition rate from one eigenenergy state to another eigenenergy state can be obtained from Fermi's golden rule [16] and it strongly depends on the dipole matrix element. The value of the dipole matrix element is zero in the case of odd-to-odd or even-to-even

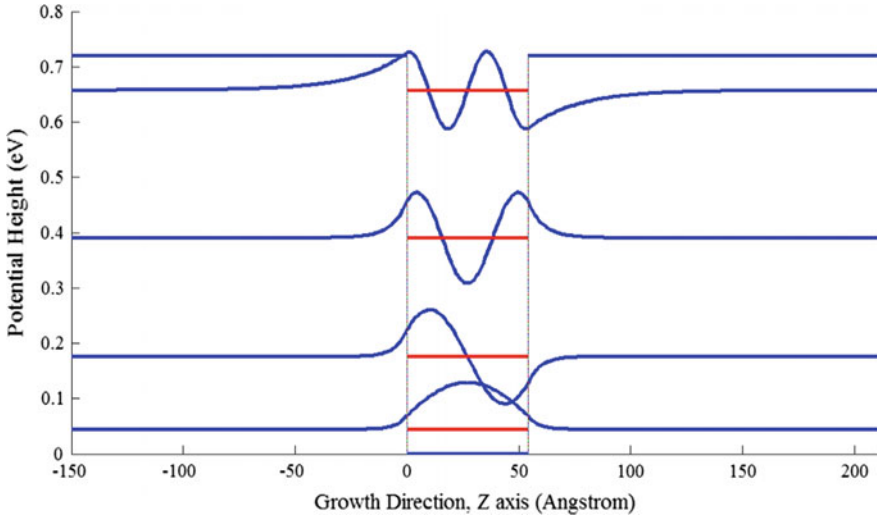

Fig. 1 Formation of the conduction band profile, where subband energies and corresponding wave functions are shown

transition due to the symmetric QW structure, and hence the transition between odd-to-odd or even-to-even energy states is not possible in symmetric QW structure. This is one of the drawbacks of the symmetric structure. So, other possible transition has taken place within the confined structure and is discussed in the next section.

The variation of eigenenergy states as a function of well width is shown in Fig. 2. It is observed that all possible values of bound eigenstates (four numbers) decrease with the increasing CdS width of the well layer. However, the decrease of the ground state (E_1) is less significant, whereas excited bound states, i.e., E_2, E_3, and E_4 decrease significantly with an increase in well width. Moreover, it is noted that three numbers of confined or bound states are observed for 4 nm CdS well width. It is due to the formation of low effective band offset that results in the disappearance of E_4 excited state in the case of lower values of well layers. Figure 3 shows the variation of transition wavelength and transition subband energy as a function of CdS width of the well layer at 300 K. Results show that transition energy varies from long wavelength to near infrared through the mid-wavelength infrared region, i.e., 9.47–2.03 μm through 5.84 μm for a particular well width of 5.4 nm. Moreover, this variation of wavelength increases rapidly with the increasing well width. For example, wavelength varies from 18.12 to 3.67 μm for 8 nm CdS well width. This result indicates multicolor wavelength of operation is obtained with CdS/ZnSe-based QWIP by suitable selection of width of well layer. All these selective wavelengths of operation should have high absorption in order to achieve considerable amount of carrier generation which can contribute significant photocurrent, and hence responsivity of the detector. This requires the calculation of bound-to-bound transition based absorption coefficient. The standard mathematical expression of

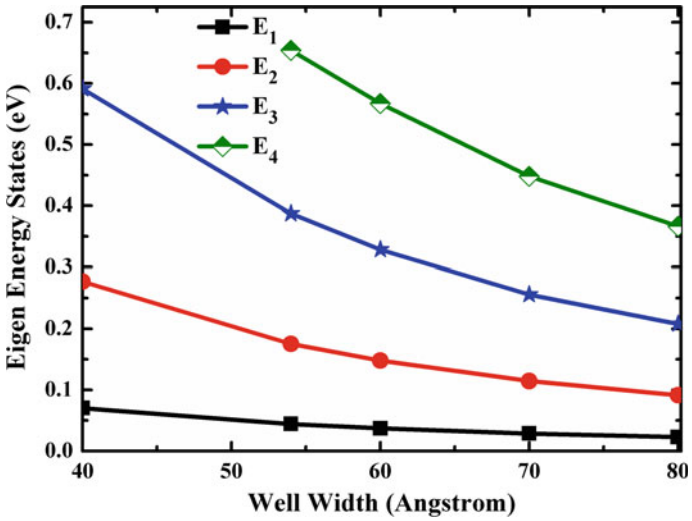

Fig. 2 Variation of eigenenergy states with CdS width of the well layer at 300 K

absorption coefficient has already been reported by various literature [17, 18]. Mathematically, absorption coefficient for bound-to-bound (BB) transition can be written as $\alpha_{C_{B-B}}(\hbar\omega) = \left(\left(q^2\hbar^3 N\right)\Big/\left(\left(m_{we}^*\right)^2\varepsilon_0 n_r c(\hbar\omega)\right)\right)\left[\left|\langle\psi_f(z)\left|\frac{\partial}{\partial z}\right|\psi_i(z)\rangle\right|^2\cos^2\phi\right]\mathrm{x}$ $\left(\left(\Gamma/2\right)\Big/\left(\left(E_f - E_i - \hbar\omega\right)^2 + \left(\Gamma/2\right)^2\right)\right)$ and using the expression, absorption of our proposed model is calculated. Absorption of 2514 cm^{-1} at $\lambda = 5.84$ μm and 1208 cm^{-1} at $\lambda = 9.47$ μm is obtained in this model. However, negligible absorption around 42 cm^{-1} at $\lambda = 2.03$ μm is observed. The absorption primarily depends on the overlap integral of wave functions between two possible eigenstates, spectral broadening, the effective mass of electrons, refractive index of the material, doping in the active layer, and incident photon angle with the suitable wavelength of light. In case of the mid-operational wavelength, strong overlap integral of wave functions is observed in comparison with the long wavelength of operation. As a result, a high value of absorption coefficient is observed in mid-wavelength as compared to long wavelength of operation. Moreover, absorption in mid-infrared region is quite large as compared to GaAs/AlGaAs-based QWIP as reported in literature [17]. It is due to the combined effect of all the above mentioned parameters which enhances the absorption coefficient in CdS/ZnSe-based QWIP. So, mid- and long wavelengths of absorption can be used to obtain significant photocurrent and it is expected that the device may be operable at mid- and long wavelengths of infrared region.

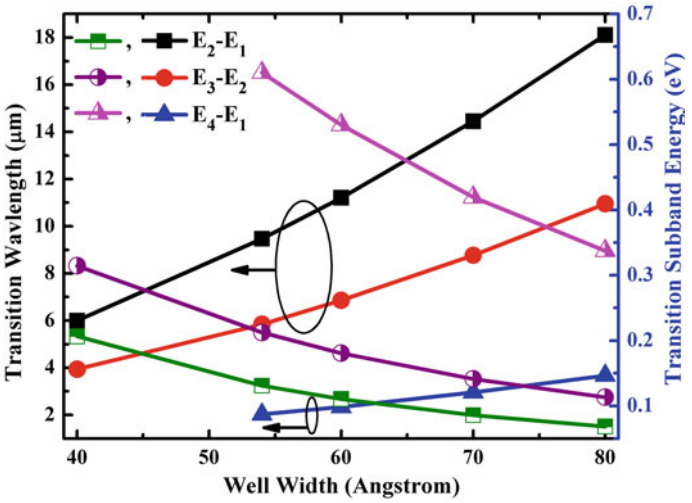

Fig. 3 Plot of transition wavelength and transition subband energy as a function of CdS width of the well layer at 300 K

4 Conclusions

Performance of CdS/ZnSe-based multicolor QWIP is studied based on the theoretical modeling. It is observed that the mid- and long wavelengths of infrared detection are obtained. However, the strength of absorption in mid-operational wavelength region is much higher than the long wavelength of operation. Moreover, results show that the calculated absorption in this model is improved as compared to GaAs/AlGaAs-based QWIPs.

References

1. Szweda, R.: QWIPs-multi-spectral mine clearance and medical. III–Vs Rev. **18**, 44 (2005)
2. Gunapala, S.D., Bandara, S.V., Liu, J.K., Luong, E.M., Stetson, N., Shott, C.A., Bock, J.J., Rafol, S.B., Mumolo, J.M., McKelvey, J.: Long-wavelength 256 x256 GaAs/AlGaAs quantum well infrared photodetector (QWIP) palm-size camera. IEEE Trans. Electron Dev. **47**(2), 326–332 (2000)
3. Liu, H.C.: Liu, H.C., Capasso, F., (eds.) Intersubband Transition in Quantum Wells: Physics and Device Applications, pp. 126–196 (Chap. 3). Academic, San Diego (2000)
4. Cohen, N., Zussman, A., Sarusi, G.: A monolithic LWIR/NIR multi spectral QWIP for night vision and see spot. Infrared Phys. Technol. **42**, 391–396 (2001)
5. Li, J., Choi, K.K., Klem, J.F., Reno, J.L., Tsui, D.C.: High gain, broadband InGaAs/InGaAsP quantum well infrared photodetector. Appl. Phys. Lett. **89**, p. 081128-(3p) (2006)
6. Zeiri, N., Abdi-Ben Nasrallah, S., Sfina, N., Said, M.: Intersubband transitions in quantum well mid-infrared photodetectors. Infrared Phys. Technol. **64**, 33–39 (2014)

7. Mehdi, I., Haddad, G.I., Mains, R.K.: Novel use of resonant tunneling structures for optical and IR modulators. Superlattices Microstruct. **5**, 443–449 (1989)
8. Loehr, J.P., Singh, J., Mains, R.K., Haddad, G.I.: Theoretical studies of the applications of resonant tunneling diodes as intersubband laser and interband excitonic modulators. Appl. Phys. Lett. **59**, 2070–2072 (1991)
9. Ershov, M., Hamaguchi, C., Ryzhii, V.: Device physics and modelling of multiple quantum well infrared photodetectors. Jpn. J. Appl. Phys. **35**, 1395–1400 (1996)
10. Guériaux, V., Nedelcu, A., Bois, P.: Double barrier strained quantum well infrared photodetectors for the 3-5 μm atmospheric window. J. Appl. Phys. **105**, 114515 (2009)
11. Moon, J., Li, S.S., Lee, J.H.: A high performance quantum well infrared photodetector using superlative-coupled quantum wells for long wavelength infrared detection. Infrared Phys. Tech. **44**, 229–234 (2003)
12. Akimoto, R., Li, B.S., Akita, K., Hasama, T.: Subpicosecond saturation of intersubband absorption in (CdS/ZnSe)/BeTe(CdS/ZnSe) /BeTe quantum-well waveguides at telecommunication wavelength. Appl. Phys. Lett. **87**, 181104 (2005)
13. Lu, H., Shen, A., Tamargo, M.C., Song, C.Y., Liu, H.C., Zhang, S.K., Alfano, R.R. Muñoz, M.: Midinfrared intersubband absorption in $Zn_xCd_{1-x}Se/Zn_xCd_yMg_{1-x-y}Se$ multiple quantum well structures. Appl. Phys. Lett. **89**, 131903-1–131903-3 (2006)
14. Van de Walle, C.G.: Band lineups and deformation potentials in the model-solid theory. Phys. Rev. B **39**(3), 1871–1883 (1989)
15. Cuesta, J.A., Sànchez, A., Adame, F.D.: Self-consistent analysis of electric field effects on Si-doped GaAs. Semicon. Sci. Technol. **10**, 1303–1309 (1995)
16. Davies, J.: The Physics of Low-Dimensional Semiconductors An Introduction. Cambridge University Press, Cambridge (1998)
17. Billaha, A., Das, M.K.: Influence of doping on the performance of GaAs/AlGaAs QWIP for long wavelength applications. Opto-Electron. Rev. **24**(1), 25–33 (2016)
18. Alves, F.D.P., Amorim, J., Byloos, M., Liu, H.C., Bezinger, A., Buchanan, M., Hanson, N., Karunasiri, G.: Three band quantum well infrared photodetector using interband and intersubband transitions. J. Appl. Phys. **103**, 114515 (2008)

Low-Cost Wireless Data Transmission System for Industrial Applications

Bikas Mondal, Sourav Rakshit, Md. Aref Billaha, Bhaskar Roy and Rajan Sarkar

Abstract This paper demonstrated an economic, reconfigurable, portable, and precise radio frequency (RF) based wireless data transmission system in process industries in the domain of public frequency band. This paper highlights the new way of a wireless communication system using commercially available RF transmitter and receiver. In this proposed system, we may connect five sensors simultaneously for transmission purpose. Sensor output data in the range of 0–5 V are taken in this work and this time-varying analog data is converted to 8-bit parallel data. This 8-bit parallel data is then transferred through two transmitter modules. At the receiver end, two receiver modules receive this 8-bit parallel data. After obtaining 8-bit parallel output data, we use some suitable equation to get equivalent decimal value ranging from 0 to 255, where 0 represents 0000 0000 and 255 represents 1111 1111 and based on this, we can easily calculate the equivalent analog output data.

Keywords Industrial sensors · Radio frequency · Data transmission Microcontroller

1 Introduction

In modern process industries, the interest of the wireless data transmission system is increasing day by day in the field of digital data communications system with respect to the wired counterpart to minimize the huge expensive cabled and excess

B. Mondal (✉) · S. Rakshit · Md. Aref Billaha · B. Roy
Department of Applied Electronics & Instrumentation Engineering,
Asansol Engineering College, Asansol 713305, India
e-mail: bikas.mondal143@gmail.com

Md. Aref Billaha
e-mail: rf.billaha@gmail.com

R. Sarkar
Department of Electrical Engineering,
Asansol Engineering College, Asansol 713305, India

U. Biswas et al. (eds.), *Advances in Computer, Communication and Control*, Lecture Notes in Networks and Systems 41, https://doi.org/10.1007/978-981-13-3122-0_51

infrastructural cost. The wireless data communication system improves the network scalability, reconfigurability, and allows the multi-tapping for different purposes or it may be used for mobile terminals, etc. Industrial environments are unique and different from the environments of office and home. Very high temperature, long distances separating equipment and machines, excessive air particles, multiple obstacles, and creating very special challenges make it difficult to suitably place and reach sensors, transmitters, and other data communication devices. High-speed data transmission is done by RF-based wireless communication system [1, 2]. Traditional data acquisition scheme which is wired could not be able to fulfill the necessities, as there is a rapid growth in the field of embedded system as well as wireless communication techniques which depend on RF as wireless data transmission will be soon widely used in industry [3, 4].

Recently, many researchers focused on the wireless data transmission system in various fields. Akyildiz et al. [5] have done a survey where lots of research works have analyzed commercially available wireless sensor networks (WSNs) node evaluation with the system design, networking, security factor, and distributed algorithm. Liang et al. [6] have developed an implantable microcontroller-based simulation system with external wireless controller for data and power transmission. Dai et al. [7] have introduced the architecture of the wireless sensor features of networks and also studied recent routing protocols for wireless sensor networks. Angrisani et al. [8] have highlighted the problems of coexistence between IEEE 802.11b and IEEE 802.15.4 wireless data communication networks and optimized these problems in their setup over 2.4 GHz frequency domain in some real-life applications. An algorithmic framework is proposed by Chowdhury and Akyildiz [9], which allows the sensor nodes to identify the type of the interference to reduce packet losses in the network. Srinivasan et al. [10] have empirically studied WSNs focusing on the designing portion of common assumptions protocol to make while designing sensornet protocols and network layer protocols. Cao et al. [11] have explored the problem of flexible and efficient data dissemination and retrieval in wireless sensor networks. Gungor et al. [12] have focused on the statistical characterization of different empirical measurements. They also provided experimental results to understand IEEE 802.15.4-compliant sensor network platforms to design WSN-based smart grid applications. Huerta et al. [13] have presented the theoretical and experimental result analysis to evaluate the effects on electromagnetic fields which is produced by high-voltage lines in the field of wireless data transmission at the 900 MHz frequency band. Sivathasan and Brien [14] have described the comparative analysis of hybrid radio frequency transmission through free-space optical and radio frequency transmissions through wireless sensor networks. Yang et al. [15] have done a survey for low-power data transmission purpose between IEEE 802.11- and IEEE 802.15.4-based networks. Basagni et al. [16] have investigated the impact of separation in radio frequency between data and the multiple concurrent energy transmissions. Jain and Franz [17] have highlighted merits and demerits of optical wireless networks over the RF networks. Dohare et al. [18] have reported the data monitoring system in underground coal mines. Meng et al. [19] have proposed architecture for

RF-based low-power subsampling technique in the application of wireless communication system. Tan Lam et al. [20] have designed a wireless sensing module using wireless sensor network in the field of rural monitoring and precision agriculture applications in the range of 0–150 m. Rusia et al. [21] have developed a reconfigurable, economic, low-power consumption, and high processing speed wireless communication system between field programmable gate array (FPGA) using RF 433 MHz transmitter module. Edemirukaye et al. [22] have aimed to design an accurate automatic energy meter system by RF transmitter, digital voltage, and current sensor in low cost.

This paper focused on a data from the sensor which is transmitted through wireless in public frequency band with very low budget commercial RF transmitter and receiver model which could be used in different process industries. In this proposed system, we mainly focused on how data was accurately transmitted and received without any bit error. The rest of the paper is described as follows. Section 2 contains the description of the proposed model. Results are described in Sect. 3, a snapshot of the proposed model is shown in Sect. 2, and the conclusion is given in Sect. 4.

2 Description of the Proposed Model

The proposed data transmission system is based on the concept of RF communication. Figure 1 depicts the block diagram being used in the transmitting section to transmit the data so that it can be received at the receiving end. In the proposed system, first data is taken from field sensors which is analog in nature. Since five (05) sensors are used and at once only one can be selected. The output voltage signal of the sensor is fed to the analog-to-digital converter (ADC) through an amplifier with suitable gain if needed. The conversion is done by successive approximation technique. After the ADC module, the signal has been configured as per desired. For that reason, the required channel to which the sensors are connected must be obtained before the data conversion has begun. The analog input channels through which sensor data are to be transmitted must have their corresponding TRIS bits selected as an input as shown in Fig. 2. This analog data of sensor is converted into its corresponding 8-bit digital signal by PIC16F72 IC, which has five input channels.

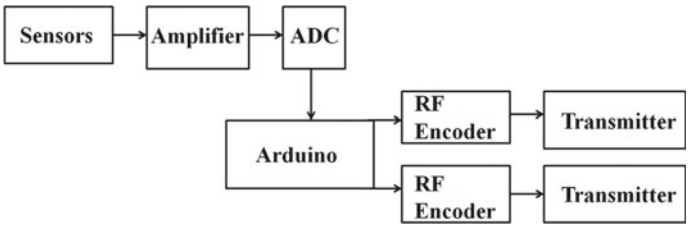

Fig. 1 Block diagram of transmission section

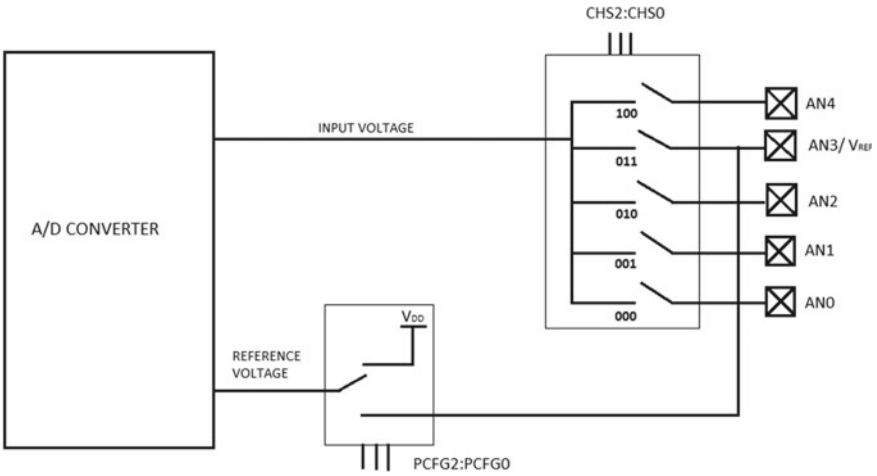

Fig. 2 Collection of sensor data for ADC

The input–output relationship of analog-to-digital conversion is given by

$$D_{ADC} = \frac{2^N * V_i}{V_r} \tag{1}$$

where D_{ADC} is the digital output of ADC, V_i is analog input voltage, V_r is reference voltage, and N is the number of bits in ADC.

By this, the required digital data is obtained which is then converted into an equivalent binary signal of 8 bit, which is then broken into a set of two 4-bit parallel data, and this data is sent to two separate encoder ICs encoded by MC145026.

The encoding mechanism can be well understood from Figs. 3 and 4. The encoder encodes and transmits serial data which depends on the state of the pins A_1–A_5 and pins A_6/D_6 –A_9/D_9. The sequence of the transmitted data is initiated by a low level of the transmission enable (TE) input pin. From Fig. 3, it can be observed that no signal is sent for three data periods between the two data words, and each transmitted ternary digit is encoded into pulses as shown in Fig. 4. Logic-0 is low after two consecutive short pulses are passed. Logic-1 is high after two consecutive long pulses. An open or high impedance state appears when there is a long pulse followed by a short pulse. While TE is high, the transmission of second word has been timed out and the encoder is completely disabled. And, when TE is in a low state, the oscillator is being started and the transmit sequence starts. The inputs are then sequentially selected, and determinations are made as to the input logic states. This information is transmitted through D_{out} pin serially.

The modulation scheme used here is amplitude shift keying that is referred to as ASK. In this modulation technique, the amplitude of the RF carrier signal is changed in accordance with the baseband digital input signal. The operation of ASK modulation is shown in Fig. 5. As shown in Fig. 5, binary-1 will be represented by

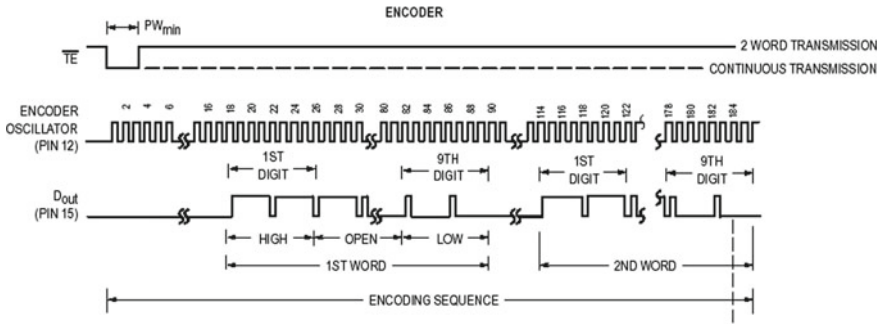

Fig. 3 Timing diagram of encoder

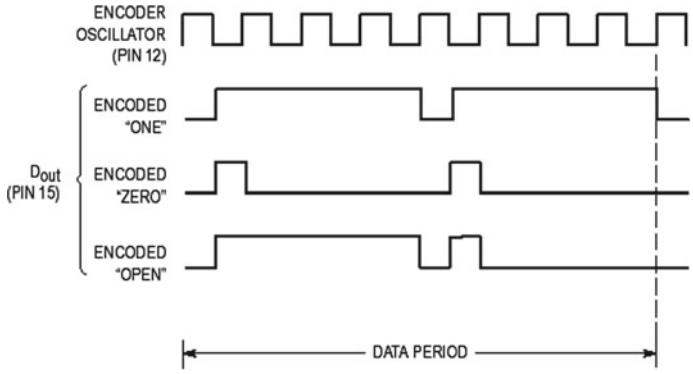

Fig. 4 Encoder data waveforms

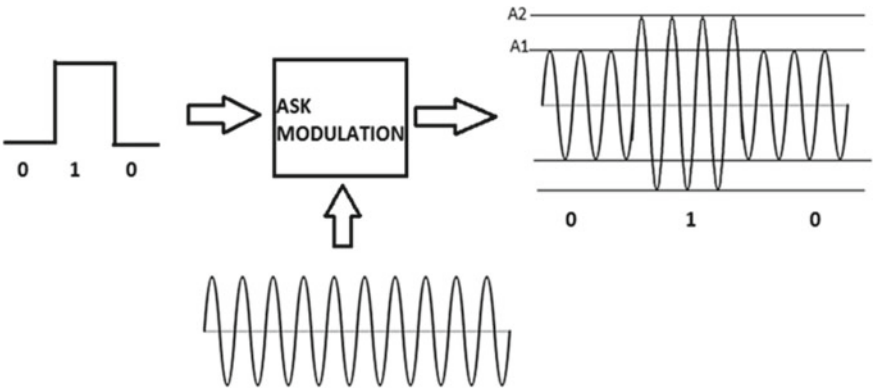

Fig. 5 ASK modulation

the carrier signal with amplitude signal of A_2, while binary-0 will be represented by the carrier signal with the amplitude of A_1.

ASK modulation can be expressed as shown in the following equation:

$$s(t) = A_2 \cos(2\pi f_C t) \text{ for Binary logic} - 1 \quad (2)$$

$$s(t) = A_1 \cos(2\pi f_C t) \text{ for Binary logic} - 0 \quad (3)$$

where s(t) is the modulated signal, A_2 is the amplitude representing the binary logic 1, A_1 is the amplitude representing the binary logic 0, f_C is the carrier frequency, and t is the bit duration.

It is worth to mention that two RF transmitters of same frequency cannot work simultaneously as they get interfered with each other and the receiver receives no signal from either. Figure 6 shows the operational algorithm required for the transmitter section. It shows that to work reliably, each transmitter needs to send bursts at different time slots. Occasionally, they will collide and then the corrupted signal will be rejected by the decoders. Since they will send the signal at different time slots, their signals can be transmitted successfully without collision.

The transmitted data is received at the receiving end and to achieve it accurately, several steps are followed. Figure 7 shows the block diagram of receiving section and Fig. 8 shows the flowchart of receiving end where two RF receivers are present.

The compatible decoder M145027 is used according to the encoder. The decoders receive the serial data from the RF receiver and give the output data if it is valid. In the receiving module, the transmitted data containing the two identical words are examined by bit during reception and the first five ternary digits are assumed to be the address. If the received address is fully matched with the local address, then the next four (data) bits are internally stored. The stored data is not transferred to the output data latch, as the second encoded word is received, the address must again match. If a match is found, then the new data bits are verified against the previously stored data bits. If the two nibbles of data (four bits each) matched, the data is then transferred to the output data latch by valid transmission (VT). The data then remains until new data replaces it. At the same time, the VT output pin is brought high and remains high until an error is received. After the decoder IC decodes the encoded data, the decoded data is then available in pin $<D_6:D_9>$ which is used to turn on the indicating LED.

Figure 9 shows the circuit simulation of transmitting section and receiving end, which is designed in Proteus. Some assumptions are made in order to simulate the hardware circuit in the software Proteus. It does not contain the library functions of IC PIC16F72 being used in designing hardware, whereas ADC 0804 is used in case of simulation. Hardware model of our proposed transmitter and receiver section are illustrated in Figs. 10 and 11.

3 Results and Discussions

In this section, the proposed RF data transmission system is experimentally tested in order to demonstrate its effectiveness, accuracy, sensitivity, and versatility. All

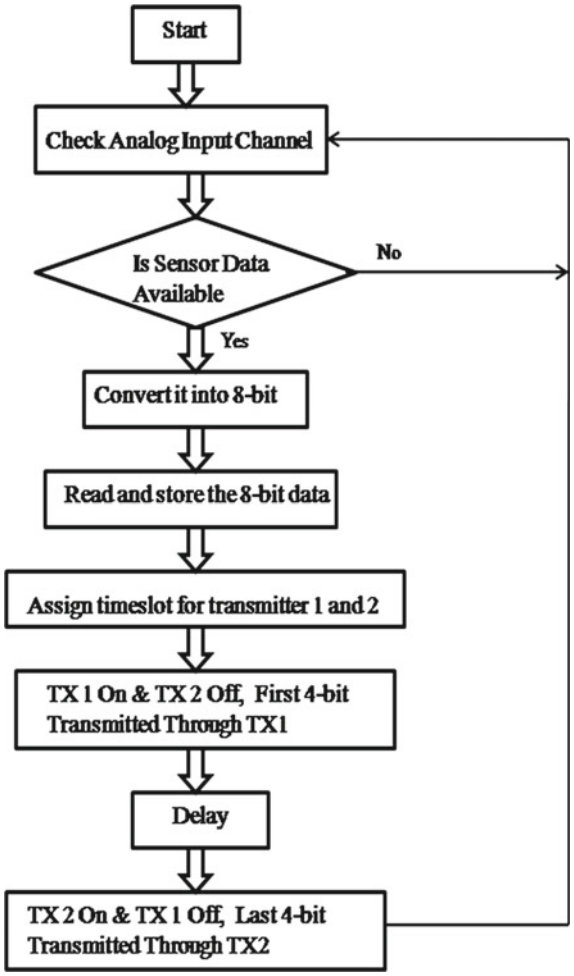

Fig. 6 Algorithm of transmitting section

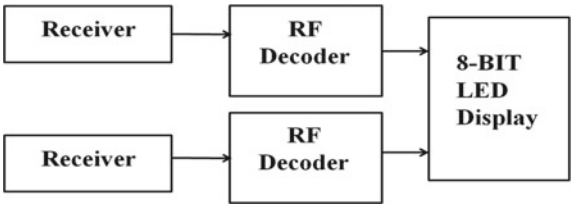

Fig. 7 Block diagram of receiving end

the results are obtained and reported by this proposed RF sensor data transmission system. While taking the result, we mainly concern about how the sensor output

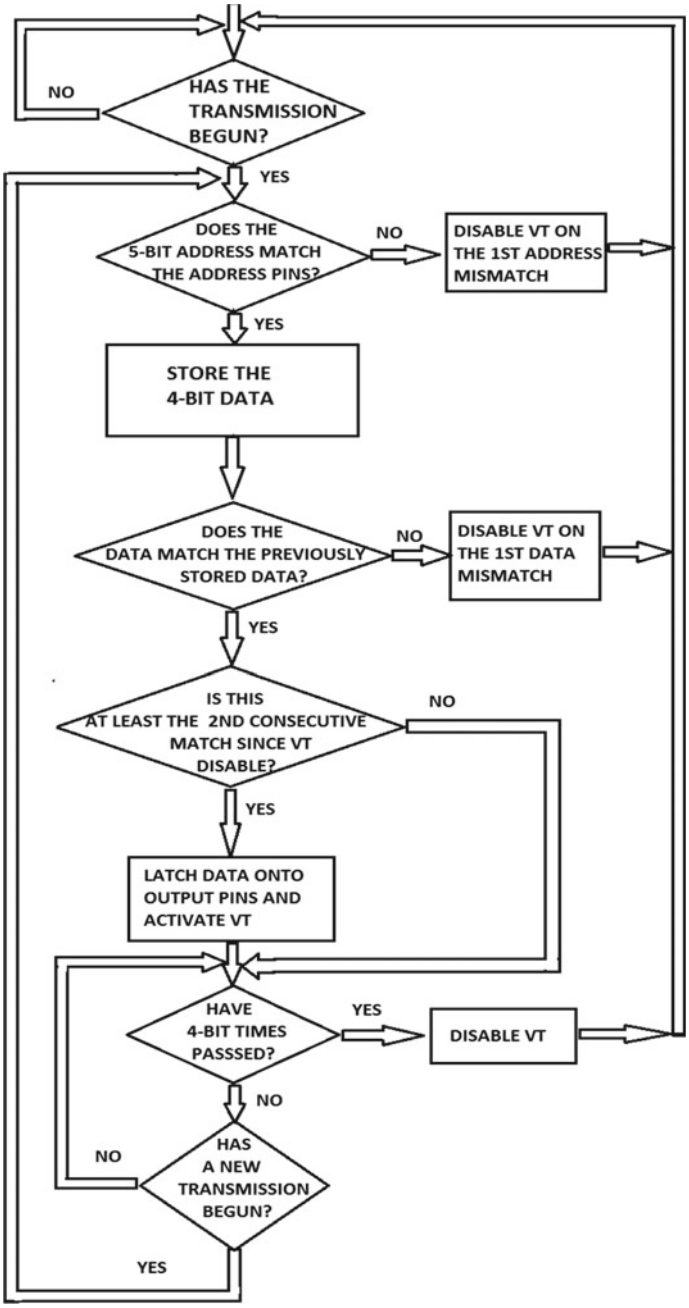

Fig. 8 Algorithm of receiving section

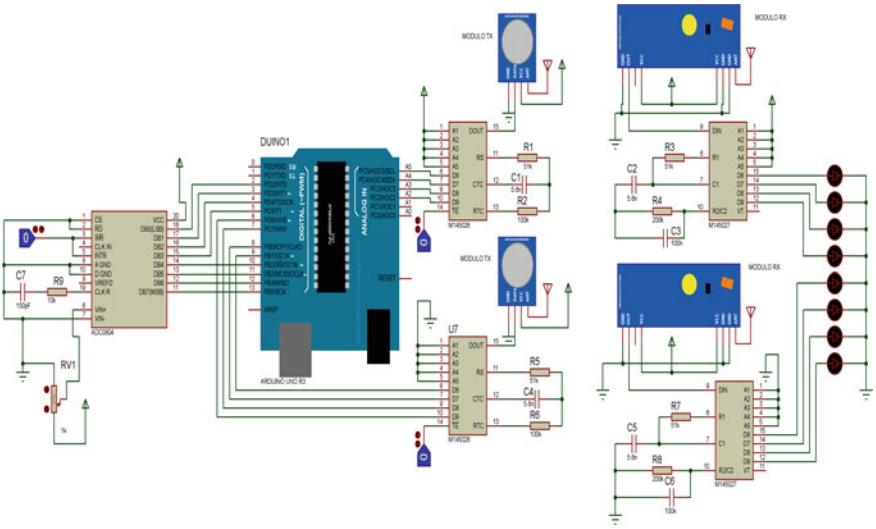

Fig. 9 Circuit simulation in Proteus

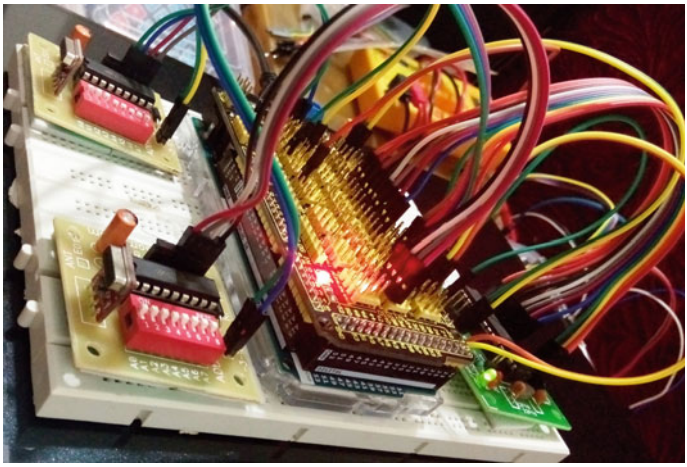

Fig. 10 Transmitter section

data is converted into 8-bit binary data and how precisely the transmitted 8-bit data is received at receiver without any bit error. For each individual input voltage, the 8-bit parallel data of the transmitter and 8-bit parallel output data of the receiver are shown in Table 1. We can see from Table 1 that the receiver correctly received all transmitted data. It is important to mention here that the RF module has been placed in different distances within the working range for finding the consistency of our proposed module.

Table 1 Conversion of analog to digital signal in transmitter and received digital signal at the receiver section

O/P	Transmitted 8-BIT								Received 8-BIT							
Voltage	D_0	D_1	D_2	D_3	D_4	D_5	D_6	D_7	D_O	D_1	D_2	D_3	D_4	D_5	D_6	D_7
0	0	0	0	0	0	0	0	0	0	0	0	0	0	0	0	0
0.1	0	0	0	0	0	0	0	0	0	0	0	0	0	0	0	0
0.21	1	1	0	1	0	0	0	0	1	1	0	1	0	0	0	0
0.3	1	1	1	1	0	0	0	0	1	1	1	1	0	0	0	0
0.4	0	0	1	0	1	0	0	0	0	0	1	0	1	0	0	0
0.5	1	0	0	1	1	0	0	0	1	0	0	1	1	0	0	0
0.6	0	1	1	1	1	0	0	0	0	1	1	1	1	0	0	0
0.7	1	1	0	0	0	1	0	0	1	1	0	0	0	1	0	0
0.8	1	0	0	1	0	1	0	0	1	0	0	1	0	1	0	0
0.91	1	0	1	1	0	1	0	0	1	0	1	1	0	1	0	0
1.00	1	1	0	0	1	1	0	0	1	1	0	0	1	1	0	0
1.19	0	0	1	1	1	1	0	0	0	0	1	1	1	1	0	0
1.29	1	0	0	0	0	0	1	0	1	0	0	0	0	0	1	0
1.39	0	1	1	0	0	0	1	0	0	1	1	0	0	0	1	0
1.5	0	0	1	1	0	0	1	0	0	0	1	1	0	0	1	0
1.59	1	0	0	0	1	0	1	0	1	0	0	0	1	0	1	0
1.71	0	1	1	0	1	0	1	0	0	1	1	0	1	0	1	0

(continued)

Table 1 (continued)

O/P	Transmitted 8-BIT								Received 8-BIT							
Voltage	D_0	D_1	D_2	D_3	D_4	D_5	D_6	D_7	D_O	D_1	D_2	D_3	D_4	D_5	D_6	D_7
1.81	0	0	1	1	1	0	1	0	0	0	1	1	1	0	1	0
1.91	1	0	0	0	0	1	1	0	1	0	0	0	0	1	1	0
2.00	0	1	1	0	0	1	1	0	0	1	1	0	0	1	1	0
2.11	1	1	0	1	0	1	1	0	1	1	0	1	0	1	1	0
2.21	1	0	1	1	0	1	1	0	1	0	1	1	0	1	1	0
2.3	1	0	1	0	1	1	1	0	1	0	1	0	1	1	1	0
2.41	0	0	0	1	1	1	1	0	0	0	0	1	1	1	1	0
2.5	1	1	1	1	1	1	1	0	1	1	1	1	1	1	1	0
2.6	0	0	1	0	0	0	0	1	0	0	1	0	0	0	0	1
2.7	1	0	0	1	0	0	0	1	1	0	0	1	0	0	0	1
2.8	0	1	1	1	0	0	0	1	0	1	1	1	0	0	0	1
2.9	1	1	0	0	1	0	0	1	1	1	0	0	1	0	0	1
2.9	1	1	0	0	1	0	0	1	1	1	0	0	1	0	0	1
3.00	1	1	1	0	1	0	0	1	1	1	1	0	1	0	0	1
3.1	1	0	1	1	1	0	0	1	1	0	1	1	1	0	0	1
3.2	1	1	0	0	0	1	0	1	1	1	0	0	0	1	0	1
3.3	0	0	0	1	0	1	0	1	0	0	0	1	0	1	0	1
3.4	1	0	1	1	0	1	0	1	1	0	1	1	0	1	0	1
3.51	0	1	0	0	1	1	0	1	0	1	0	0	1	1	0	1
3.6	1	1	1	0	1	1	0	1	1	1	1	0	1	1	0	1

(continued)

Table 1 (continued)

O/P	Transmitted 8-BIT								Received 8-BIT							
Voltage	D_0	D_1	D_2	D_3	D_4	D_5	D_6	D_7	D_O	D_1	D_2	D_3	D_4	D_5	D_6	D_7
3.8	1	0	0	0	0	0	1	1	1	0	0	0	0	0	1	1
3.7	0	0	1	1	1	1	0	1	0	0	1	1	1	1	0	1
3.91	1	1	1	0	0	0	1	1	1	1	1	0	0	0	1	1
4.00	0	0	1	1	0	0	1	1	0	0	1	1	0	0	1	1
4.11	1	0	0	0	1	0	1	1	1	0	0	0	1	0	1	1
4.2	0	1	1	0	1	0	1	1	0	1	1	0	1	0	1	1
4.3	1	1	0	1	1	0	1	1	1	1	0	1	1	0	1	1
4.4	1	0	0	0	0	1	1	1	1	0	0	0	0	1	1	1
4.5	1	0	1	0	0	1	1	1	1	0	1	0	0	1	1	1
4.6	1	1	0	1	0	1	1	1	1	1	0	1	0	1	1	1
4.72	1	1	1	1	0	1	1	1	1	1	1	1	0	1	1	1
4.81	1	0	1	0	1	1	1	1	1	0	1	0	1	1	1	1
4.9	0	1	0	1	1	1	1	1	0	1	0	1	1	1	1	1
4.99	1	1	1	1	1	1	1	1	1	1	1	1	1	1	1	1

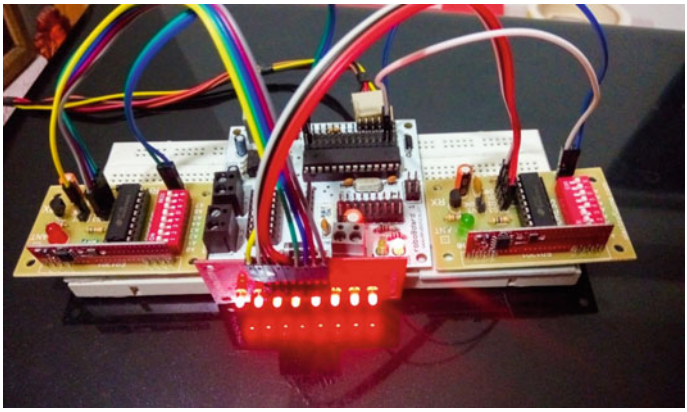

Fig. 11 Receiver section

In this proposed system, we mainly focused on how data is accurately transmitted and received, and hence we did not bother about rest of the calculation. Once the transmitted 8 bit is accurately received, we can easily calculate the analog voltage. First, we need to store the 8-bit received data and after storing the 8-bit data assigned to some integer named D_0–D_7 and obtained equivalent decimal output by Eq. (4),

$$A = D_0 2^0 + D_1 2^1 + D_2 2^2 + D_3 2^3 + D_4 2^4 + D_5 2^5 + D_6 2^6 + D_7 2^7 \tag{4}$$

where A is the equivalent decimal output for 8-bit binary input and then using Eq. (5), we can achieve the analog voltage which is same as the sensor output voltage in transmitting section.

$$V_{Out} = \frac{V_r * A}{2^N} \tag{5}$$

where V_{Out} is analog output, V_r is reference voltage, and N is the number of bits in ADC.

This paper provides the implementation of RF-based transmitter and receiver systems to get a trade-off between power consumption, gain, noise, and sensitivity. It can achieve −110 dBm sensitivity with the range of 20 m for an amplitude shift keying (ASK) modulation with the clock sampling frequency of 433 MHz. Finally, the theoretical analysis and practical results show that the performance of this wireless transmitter has fairly agreed with the others [12, 19–21] and has several advantages over other techniques of wireless data transmission. The effective communication range of the wireless between transmitter and receiver may be increased up to 130 m in the open-field environment.

4 Conclusions

The current research work illustrates the design and performance of a real-time monitoring system for measuring physical parameters. The developed system mainly highlights the functional characteristics with wireless network capacity, sensor hardware compatibility, low-cost production, and efficient capture. This system also has low-power consumption and has negligible impact on the environment. The result after testing and performing this experiment is a positive one. Better response has been obtained which saves energy, has strong communication ability, and presents a real-time accurate measurement. The wireless data acquisition system can be further improved by the following aspects: combining more sensors for measuring in larger areas, can be further improved by utilizing the new generation of microcontrollers, and to establish an intelligent power management system. The proposed system is being designed by us and has given a lot of options to the users. The system is cost effective yet allows controlling five different sensors simultaneously. This system uses parallel communication and since parallel communication is faster than serial communication, this system gives optimal performance.

References

1. Gonzalez, G.: Microwave Transistor Amplifiers: Analysis and Design, 2nd edn. Prentice-Hall (1997)
2. Pozar, D.M.: Microwave and RF Design of Wireless Systems. Wiley (2001)
3. Ludwig, R., Bogdanov, G.: RF Circuit Design, Theory and Applications. Pearson Asia Education Edition (2001)
4. Radmanesh, M.M.: Radio Frequency and Microwave Electronics. Pearson Education Asia Edition (2001)
5. Akyildiz, F., Su, W., Sankarasubramaniam, Y., Cayirci, E.: Wireless Sensor Networks: A Survey. Comput. Netw. **38**(4), 393–422 (2002)
6. Liang, C.K., Young, G.S., Chen, J.J.J., Chen, C.K.: A microcontroller-based implantable neuromuscular stimulation system with wireless power and data transmission for animal experiments. IETE Tech. Rev. **26**(4), 493–501 (2003)
7. Dai, S., Jing, X., Li, L.: Research and analysis on routing protocols for wireless sensor networks. In: IEEE Proceedings of International Conference on Communications, Circuits and Systems, vol. 1, pp. 407–411 (2005)
8. Angrisani, L., Bertocco, M., Fortin, D., Sona, A.: Experimental study of coexistence issues between IEEE 802.11b and IEEE 802.15.4 wireless networks. IEEE Trans. Instrum. Measur. **57**(8), 1514–1523 (2008)
9. Chowdhury, K.R., Akyildiz, I.F.: Interferer classification, channel selection and transmission adaptation for wireless sensor networks. Proc. of IEEE ICC **2009**, 1–5 (2009)
10. Srinivasan, K., Dutta, P., Tavakoli, A., Levis, P.: An empirical study of low-power wireless. ACM Trans. Sens. Netw. **6**(2), Article 16, 16:1–16:49 (2010)
11. Cao, N., Wang, Q., Ren, K., Lou, W.: Distributed storage coding for flexible and efficient data dissemination and retrieval in wireless sensor networks. In: IEEE International Conference on Communications 2010, pp. 1–5 (2010)
12. Gungor, V., Lu, B., Hancke, G.: Opportunities and challenges of wireless sensor networks in smart grid. IEEE Trans. Industr. Electron. **57**(10), 3557–3564 (2010)

13. Huertas, J.I., Barraza, R., Echeverry, J.M.: Wireless data transmission from inside electromagnetic fields. IETE Tech. Rev. **44**(2), 88–97 (2010)
14. Sivathasan, S., Brien, D.O.: Radio frequency/free space optical and radio frequency-only wireless sensor networks: a comparative study of performance. IETE Tech. Rev. **36**(1), 52–61 (2010)
15. Yang, D., Xu, Y., Gidlund, M.: Wireless coexistence between IEEE 802.11- and IEEE 802.15.4-based networks: a survey. Int. J. Distrib. Sens. Netw. **2011**, 1–17 (2011)
16. Naderi, M.Y., Chowdhury, K.R., Basagni, S., Heinzelman, W., De, S., Jana, S.: Experimental study of concurrent data and wireless energy transfer for sensor networks. In: Proceedings of IEEE Global Communication Conference, pp. 2543–2549 (2014)
17. Jain, V.K., Franz, J.H.: Some design issues in infrared wireless networks. IETE Tech. Rev. **21**(5), 335–343 (2015)
18. Dohare, Y.S., Maity, T., Das, P.S., Paul, P.S.: Wireless communication and environment monitoring in underground coal mines – review. IETE Techn. Rev. **32**(2), 140–150 (2015)
19. Meng, F., Liu, H., Wang, M., Zhang, X., Tong, T.: RF low power sub sampling architecture for wireless communication applications. EURASIP J. Wirel. Commun. Netw (2016)
20. Tan Lam, P., Quang Le, T., Nguyen Le, N., Dat Nguyen, S.: Wireless sensing modules for rural monitoring and precision agriculture applications. IETE Tech. Rev. 107–123 (2017)
21. Rusia, J., Naugarhiya, A., Majumer, S., Majumdar, S., Acharya, B., Verma, S.: RF based wireless data transmission between two FPGAs. In: IEEE International Conference on ICT in Business, Industry & Government (ICTBIG), April 2017
22. Edemirukaye, U.O., Amaize, A.P., Uzairue, S., Meng, W.: Implementation of an RF based wireless automated energy metering and billing system. J. Cogent Eng. **5**(1), 1–15 (2018)

Kinematics Application: As a New Mechanical Cycle

Braj Kishore Singh, Kundan Kumar, Achyut Raj, Aakash Kumar Roy and Dharmbir Prasad

Abstract The objective of the study is to make the cycle into an efficient vehicle and as comfortable like a car. The demerits of today's era cycle are that it cannot move in the reverse direction by simply paddling and it also does not protect us from rain and sunlight during the extreme condition. So the objective is to make such type of vehicle that is similar to the car but its working principle will be solely based on the gear system without using any heat engine. The proposed model is named as "mechanical cycle". It consists of a set of gear of different diameters connected to each other in a parallel way. During forward motion, one freewheel works and the other is free with respect to the first one, whereas during the backward motion the later one will work and the former one is free with respect to the later one. In this way, we can control both forward and backward motions in this "mechanical cycle" which is not possible in the simple cycle. Also, the shed protects us from rain and sunlight and it also gives comfort. The cost-effectiveness of this cycle makes it affordable to common people, and its speed is much more than that of simple cycle.

1 Introduction

Kinematics is a branch of classical mechanics that describes the motion of points, bodies (objects), and systems of bodies (groups of objects) without considering the mass of each or the forces that caused the motion. Kinematics, as a field of study, is often referred to as the "geometry of motion" and is occasionally seen as a branch of mathematics [1]. A Kinematics problem begins with the geometry of the system with any one of the known parameters and by analyzing the problem keenly and solving it to find out the unknown parameters such as velocity, acceleration, and many more. Basic differences between "kinetics" and "kinematics" is that the former basically deals with the motion of the body by taking the forces into consideration, and hence these forces cause the motion in the body, whereas later one only deals in the motion

B. K. Singh · K. Kumar · A. Raj · A. K. Roy · D. Prasad (✉)
Asansol Engineering College, Asansol, West Bengal, India
e-mail: dharmbirprasad9@gmail.com

U. Biswas et al. (eds.), *Advances in Computer, Communication and Control*, Lecture Notes in Networks and Systems 41, https://doi.org/10.1007/978-981-13-3122-0_52

Table 1 Comparative study of various cycles

Parameters	Normal bicycle	Mechanical cycle
Sense of motion	It can move in only one direction	It can move in both forward and backward directions
Weather protection	It cannot protect us from the sunlight and rain	It can protect us from the sunlight and rain
Efficiency	Its efficiency is low	Its efficiency is relatively higher than the normal bicycle

of the body without considering the forces causing the motion in the system. There is a wide application of kinematics; it is also used in astrophysics. In mechanical engineering, robotics, and biomechanics, it is used to describe the motion of the system of the joint parts [2].

Basically, the part of kinematics used in this article is that it consists of a set of gear of different diameters connected to each other in a parallel way [3]. This set of gear is placed in front half of the car chassis [4]. A paddle is fixed on the upper gear. A crankshaft connects the front gear to the back wheel. Back wheel consists of a differential along with a two freewheel [5]. The crankshaft which connects the front gear to the back wheel is fixed between these freewheels. During forward motion, one freewheel works and the other is free with respect to the first one, whereas during the backward motion the other freewheel will work and the first one is free with respect to the second one. In this way, we can control both forward and backward motions in this "mechanical cycle" which is not possible in the simple cycle. Also, the shed protects us from rain and sunlight and it also proves comfortable. Our "mechanical cycle" is cost-efficient so that the lower and middle-class families can easily buy it and its speed is much more than that of simple cycle. Table 1 provides the differences between normal cycle (forward moving cycle) and mechanical cycle (forward as well as backward). The material used by us is light in weight and strong having high ultimate stress with factor of safety up to 2.5 and it must be tough [6]. The proposed mechanical cycle is an evolutionary concept of the bicycle industry.

2 Mathematical Modeling of the Proposed Cycle

Let R_1 be the radius of the smaller gear and R_2 be the radius of the larger gear as shown in Figs. 1, 2, the parallel gear connection gives the relation between arc length (L) and radius (R) at the constant twist angle (θ) [7].

For two gear connected in series, we have,

$$\theta = \frac{L}{R} \tag{1}$$

where θ is twist angle, L is arc length, and R is radius.

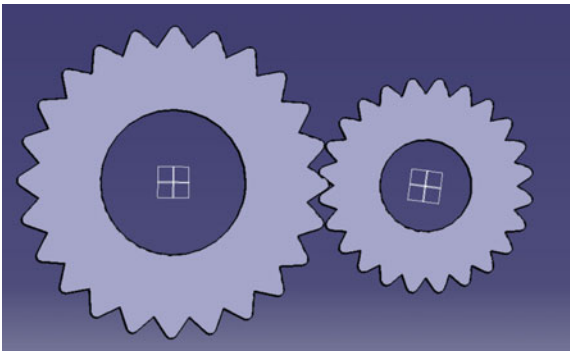

Fig. 1 Series-connected gear system

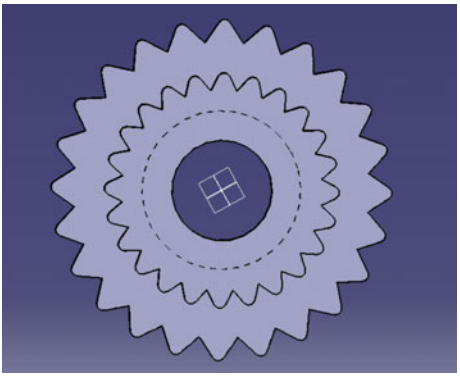

Fig. 2 Parallel-connected gear system

For series connected gear, arc length is constant.

$$\theta_1 = \frac{\theta_2 R_2}{R_1} \tag{2}$$

$$S_1 = \frac{L}{R} \tag{3}$$

where S_1 is revolution per minute and N is number of tooth.

$$S_1 = \frac{S_2 \times N_2}{N_1} \tag{4}$$

$$N \propto R \tag{5}$$

From Eqs. (2) and (4), we have concluded that the output power is more than the input power. Table 2 shows the type of materials which are used for the specific parts (carbon steel, mild steel) [2].

Table 2 Major components and material types

Sl No.	Part name	Material
1	Frame	Carbon steel
2	Back wheel support	Carbon steel
3	Front wheel support	Carbon steel
4	Gear	Mild steel
5	Gearbox	Mild steel
6	Nutt and bolt	Mild steel
7	Paddle	Mild steel
8	Steering	Mild steel

3 Finite Element Analysis of the Mechanical Cycle Model

In order to establish the proposed concept, the model has been checked after several analyses during FEA study. Figure 3 shows the proposed model of mechanical cycle.

Let R_1 be the radius of the smaller gear and R_2 be the radius of the bigger gear. Since for parallel connected gear system, the angle of twist remains the same as in (6),

$$L_1 = \frac{L_2 R_1}{R_2} \tag{6}$$

$$L_2 = \frac{L_1 N_2}{N_1} \tag{7}$$

From Eqs. (6) and (7), we have concluded that the output power is more than the input power. So, using Eqs. (2)–(5), we have higher angular velocity. Table 3 shows

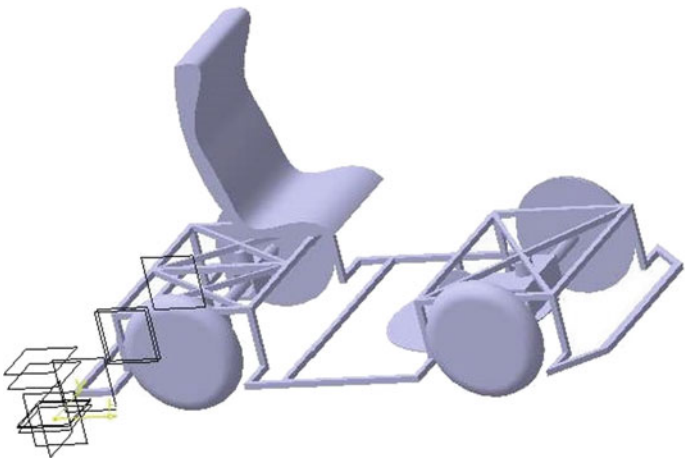

Fig. 3 General sketch of mechanical cycle

Table 3 Property of the base

Particulars	Outputs
Material	Carbon steel
Young's modulus	1.2e+011 Nm^2
Poisson's ratio	0.291
Density	7870 kgm^3
Coefficient of thermal expansion	1.21e-005 Kdeg
Yield strength	3.1e+008 Nm^2

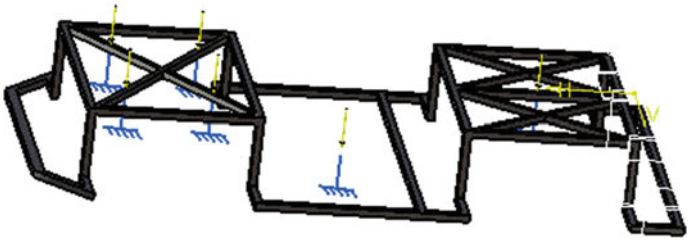

Fig. 4 Frame support analysis

Table 4 Force and moment of inertia acting on the base

Particular	Output
F_X	$5.167e^{-004}$ N
F_Y	$-7.589e^{-004}$ N
F_Z	$-9.621e^{-002}$ N
M_X	$-5.746e^{-003}$ N_X m
M_Y	$8.299e^{-003}$ N_Y m
M_Z	$-6.586e^{-005}$ N_Z m

the good, poor, bad, and worst qualities of the material used for the base [2]. Figure 4 shows the frame support analysis that provides the base support to the mechanical cycle. Table 4 shows the properties parameter (Young's modulus, Poisson ratio, and density) of the base.

Figure 5 shows the stress analysis developed inside the frame when applied load in the mechanical cycle. Table 5 shows the force and moment of inertia acting on X-, Y-, and Z-directions, respectively, on the base.

Figure 6 shows the bending analysis developed inside the frame when applied load on the base in the mechanical cycle. Table 6 shows the different parameters or dimensions of the spear parts name that are used. Figure 7 shows the base of

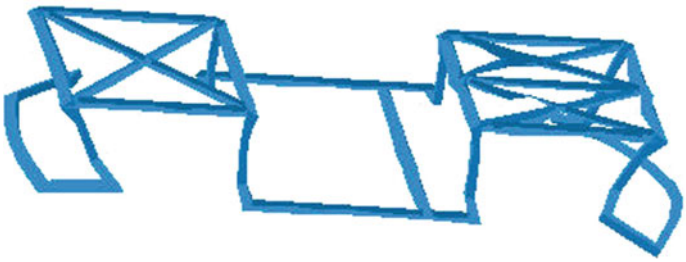

Fig. 5 Frame bending analysis

Table 5 Dimensions of the base

Method	Sparse
Number of factorized degrees	1131
Number of supernodes	221
Number of overhead indices	2790
Number of coefficients	17052
Maximum front width	36
Maximum front size	666
Size of factorized matrix (M_b)	0.130096
Number of blocks	1
Number of M flops for factorization	$3.552e^{-001}$
Number of M flops for solve	$7.386e^{-002}$
Minimum relative pivot	$6.302e^{-004}$

chassis that provides the structure and outlook of mechanical cycle. Table 6 shows the degree of freedom and displacement of center of mass along X-, Y-, and Z-directions, respectively.

4 Conclusion

This paper provides the solution of enhancing the efficiency, modifying the working principles and the comfort level of traditional bicycle. From the above equations and analysis results, we can conclude that by giving less input power we can extract high output power through the intervening gear system as shown in the above figures and results. It can be concluded that the maximum loading capacity of our structure is up to 300 N and the factor of safety lies between 2 and 3, from the above structure analysis.

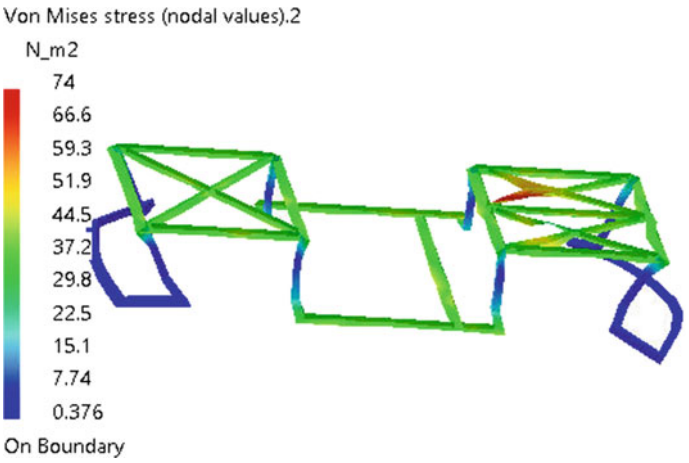

Fig. 6 Frame stress analysis

Table 6 Property analysis of the base

Value	Dof	Node	Displacement along various axes		
			X (mm)	*Y* (mm)	*Z* (mm)
8.65E+05	T_z	110	1.67E+02	2.80E+01	2.20E+01
2.00E+06	T_x	110	1.67E+02	2.80E+01	2.20E+01
2.13E+06	T_x	437	1.31E+02	4.32E+01	2.20E+01
2.52E+06	T_y	437	1.31E+02	4.32E+01	2.20E+01
3.23E+06	T_y	110	1.67E+02	2.80E+01	2.20E+01
3.77E+06	T_z	436	1.38E+02	5.23E+01	2.20E+01
8.18E+06	T_z	411	1.38E+02	9.20E+01	2.20E+01
1.00E+06	T_z	408	1.20E+02	9.20E+01	1.26E+01
1.01E+07	T_x	411	1.38E+02	9.20E+01	2.20E+01

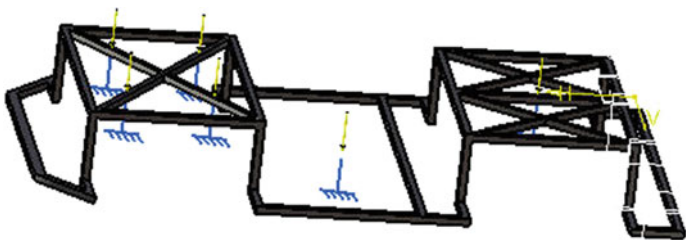

Fig. 7 Base of the chassis

References

1. Wampfler, G., Salecker, M., Wittenburg, J.: Kinematics, dynamics, and control of omnidirectional vehicles with mecanum wheels. Mech. Based Des. Struct. Mach. **17**(2), 165–77 (1989)
2. Chaari, F., Kantchev, G., Haddar, M.: Modelling the mechanical efficiency of a spur gear system. Proc. Inst. Civil Eng-Eng. Comput. Mech. **163**(2), 83–90 (2010)
3. Liande, Z., Xiaoduan, S., Yongsheng, C., Jie, Z.: Exploring the relationships between crash rates and average speed difference between cars and large vehicles on a suburban freeway. In: Intel Transportation Systems Conference, 2006, ITSC'06. 1638–1641 (2006)
4. Whitney Jr., W.J., Schwab, B.E.: Crankshaft surfaces: finishing methods, surface characterization and their influence on wear. Wear **108**(4), 345–356 (1986)
5. Beltrán, M.A., González, J.L., Rivas, D., Hernández, F., Dorantes, H.: On the role of microstructural properties on mechanical behavior of API-X46 steel. Procedia Struc. Integrity. **1**(3), 57–67 (2017)
6. Marques, P.M., Martins, R.C., Seabra, J.H.: Gear dynamics and power loss. Tribol. Int. **1**(97), 400–411 (2016)
7. Ahangarnejad, A.H., Azar, S.A.: A dynamic analysis of automobile bumpers with smart connections: a front crash simulation using Ls-Dyna. Int. J. Acad. Res. **6**(1) (2014)

Analysis of ZnO/Si Heterojunction Solar Cell with Interface Defect

Lipika Mandal, S. Sadique Anwer Askari, Manoj Kumar and Muzaffar Imam

Abstract The ZnO/Si heterojunction solar cell has attracted a great deal of interest among researchers in recent days due to its lower process steps, and hence lower cost than Si solar cell. However, the experimentally fabricated ZnO/Si solar cell shows efficiency for below the theoretically predicted values (Hussain et al Sol Energy Mater Sol Cell 139:95–100, 2015 [1], Chabane et al Thin Solid Films 636:419–424, 2017 [2]). Researchers predicted that the difference may be due to the interface defects between ZnO and Si. Mainly, the open-circuit voltage (Voc) is below the theoretical value. But there is no such detail on interface effect which has been studied in detail. A 1D solar cell simulator SCAPS is used for this purpose. Result shows that the efficiency 15.42% with open-circuit voltage of 541 mV for a very low interface defect density, in the order of 10^{10} cm^{-2}. With increasing interface defect density, efficiency decreases significantly, the Voc is as low as 211 mV for interface defect density of 5×10^{14} cm^{-2}.

Keywords ZnO/Si heterojunction · Interface defect density · SCAPS 1D

1 Introduction

A serious drawback for the high-efficiency Si homojunction solar cell is its high fabrication cost. As heterojunction solar cells (HJSCs) prepared by depositing wide bandgap transparent conductive oxide (TCO) on Si wafer has gained significant attention. During last decade, zinc oxide (ZnO) has drawn attention of the semiconductor industry. ZnO has immense potential in short wavelength optoelectronic

L. Mandal (✉)
Department of Applied Electronics & Instrumentation Engineering, Asansol Engineering College, Asansol, India
e-mail: lipikamandal81@gmail.com

S. Sadique Anwer Askari · M. Kumar · M. Imam
SAP Research Laboratory, Department of Electronics Engineering, IIT (ISM), Dhanbad, India

U. Biswas et al. (eds.), *Advances in Computer, Communication and Control*, Lecture Notes in Networks and Systems 41, https://doi.org/10.1007/978-981-13-3122-0_53

devices application [3–5]. It has capability to be operated at elevated temperature and in strident conditions. High transparency in visible spectrum range and wide bandgap makes it a suitable candidate to be used as window layer in heterojunction solar cell [6–9]. Due to direct bandgap nature, the absorption coefficient is very high which makes it a suitable material for thin film solar cell. Because of low processing temperature, nontoxic, abundance, and excellent responsivity in UV region are some additional features of ZnO which can be effectively implemented to scale the growth of various optoelectronic devices [10]. Thin film ZnO on silicon wafer can be used as a window layer and surface passivation layer for reduction of interface defects. Reduction of interface and grain boundary defects can decrease the dark current [7] and that will increase in the V_{OC}. ZnO films, among the materials for TCO available, show promising optical and electrical properties in combination with cost-effective alternatives. Here, ZnO/Si heterojunction solar cells have very high efficiency for solar light collection because of its double band structure. The photons having low energy in visible region will be absorbed near the depletion region as they will easily transmit through ZnO layer. Photons having high energy in UV region will be trapped by ZnO layer. Recently, few attempts based on ZnO/n-Si [7, 8] solar cells have been presented with very low efficiency. The bulk defect in ZnO film and defect/traps at interface of ZnO/Si layers. Mostly, the bulk defects within the ZnO film and defects/traps at the interface of ZnO/Si layers are main culprits for poor photovoltaic performance [11–15]. This paper is all about deep investigation of low efficiency of ZnO/p-Si heterojunction solar cells by simulation of interface defect using 1D solar simulator SCAPS.

2 Device Structure and Simulation

Device structures of ZnO/p-Si-based heterojunction solar cells used in the simulation are shown in Fig. 1. A thin layer of ZnO acts as an emitter layer on top of main absorber p-Silicon substrate. Aluminum is used as a back contact layer. Thickness of the ZnO and p-Si layers has been taken as 100 nm and 200 μm, respectively. A SiO_2 layer has been introduced as an interface between ZnO and silicon.

In this work, we have used solar cell capacitance simulator (SCAPS-1D) to simulate and analyze the performance parameter of the ZnO/p-Si heterojunction solar cell. We have included surface recombination and interface recombination in our simulation.

In simulator, the steady-state recombination is given in [16]. The interface recombination rate can be calculated from Eq. 1.

$$R^{S+1} = (\mathrm{N}_S + N_{S+1}) \frac{npc_n^{s+1/2} c_p^{s+1/2} - e_n^{s+1/2} e_p^{s+1/2}}{nc_n^{s+1/2} + pc_p^{s+1/2} + e_n^{s+1/2} + e_p^{s+1/2}} \tag{1}$$

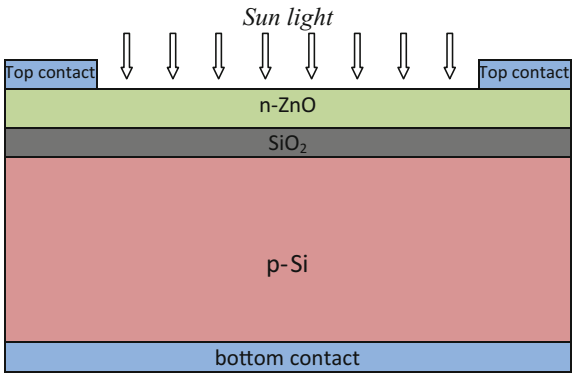

Fig. 1 n-ZnO/p-Si heterojunction structures used in device simulation

Table 1 Material parameters used in the SCAP-1D simulation

Parameter	n-ZnO	p-Si
Eg (eV)	3.3	1.120
χ (eV)	4.350	4.050
ε (relative)	9.000	11.900
N_C (cm^{-3})	4.4×10^{18}	2.8×10^{19}
N_V (cm^{-3})	7.1×10^{19}	1.0×10^{19}
V_{thn} (cm/s)	1.0×10^{7}	2.3×10^{7}
V_{thp} (cm/s)	1.0×10^{7}	1.65×10^{7}
μ_n ($cm^2V^{-1}\ s^{-1}$)	60	1400
μ_p ($cm^2V^{-1}\ s^{-1}$)	10	450
N_D (cm^{-3})	1.0×10^{18}	1.0×10^{13}
N_A (cm^{-3})	1.0×10^{13}	1.0×10^{15}

where R^{S+1} is the recombination rate associated with transitions between the states s and s + 1; N_S, N_{S+1} are the densities of a defect in states s and s + 1, respectively. C_n and C_p are the electron and hole capture constants, respectively. e_n, e_p are the emission coefficients for electron and holes. Detail of the simulation parameters for ZnO/p-Si structures is given in Table 1.

3 Results and Discussion

Using parameters shown in Table 1, J–V characteristics by SCAPS simulation for different interface defect densities under AM1.5 illumination condition (100 mW/cm^2) is shown in Fig. 2. Figures 3, 4 show the photovoltaic performance parameters (V_{OC}, J_{SC}, η) of the ZnO/p-Si heterojunction solar cell with different interface defect den-

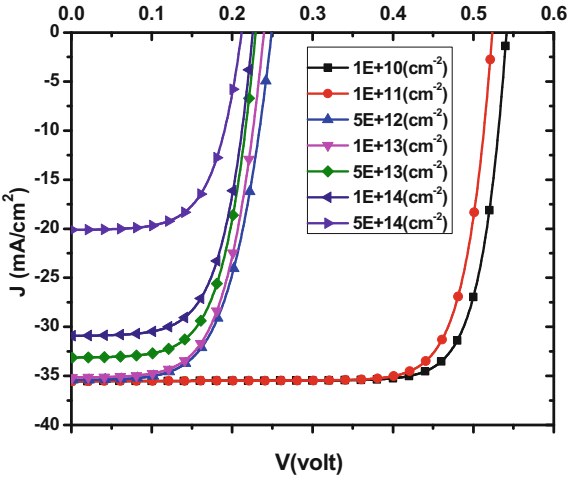

Fig. 2 J–V characteristics of ZnO/p-Si heterojunction solar cell for different interface defect densities

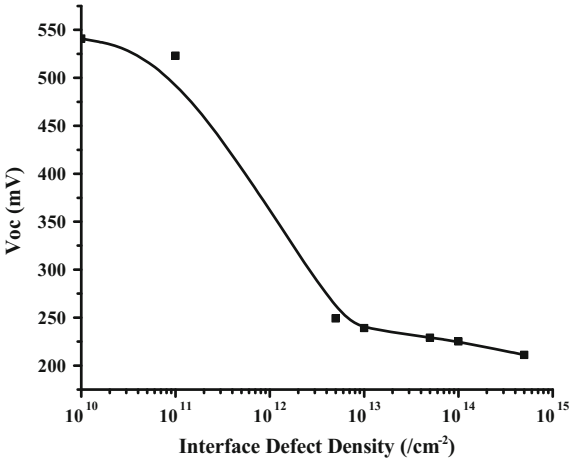

Fig. 3 Interface defect density versus open-circuit voltage plot of ZnO/p-Si heterojunction solar cell

sities. From Fig. 4, it is clear that as we are increasing the interface defect densities, only slide variation in J_{SC}, but the power conversion efficiency reduces mainly due to reduction on V_{OC}. By observation from the simulated result, best photovoltaic performance is obtained at low interface defect density in form of 1.0×10^{10} cm^{-2}. It can be seen that V_{OC} and J_{SC} are ruined by increasing the interface defect density. It is because of the interface recombination with the localized energy levels. These energy levels are created by interface defects and it degrades the V_{OC} as well as the power conversion efficiency (PCE) of the ZnO/p-Si heterojunction solar cell.

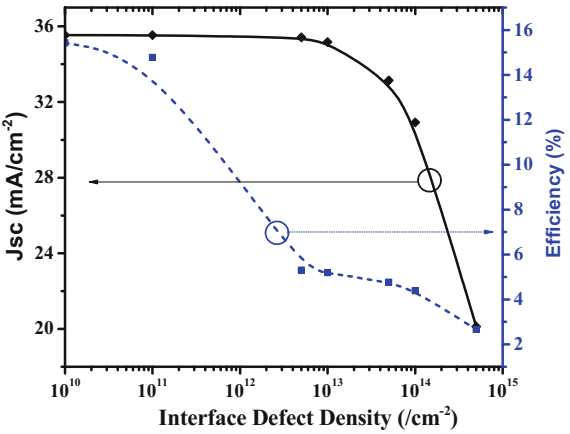

Fig. 4 Interface defect density versus short-circuit current density and efficiency plot of ZnO/p-Si heterojunction solar cell

4 Conclusion

We have observed the performance of ZnO/p-Si heterojunction solar cell with different interface defect densities. The V_{OC} of the solar cell is far from the theoretical value. It is mainly due to the interface defect density at ZnO/p-Si heterointerface. It is observed, in this paper, that by increasing interface defect density from 10^{10} to 5 $\times$ 10^{14} cm^{-2}, the open-circuit voltage (V_{OC}) reduces from 541 to 211 mV and the efficiency reduces from 15.42 to 2.66%.

Acknowledgements This work is supported by MHRD, Govt. of India through the project, Establishment of Centre of Excellence in Renewable Energy, Project under FAST (Sanc. No. F. No. 5-6/2013-TS-VII dated 4th August, 2014) at Indian Institute of Technology (Indian School of Mines), Dhanbad.

References

1. Hussain, B., Ebong, A., Ferguson, I.: Zinc oxide as an active n-layer and antireflection coating for silicon based heterojunction solar cell. Sol. Energy Mater. Sol. Cells **139**, 95–100 (2015)
2. Chabane, L., Zebbar, N., Trari, M., Kechouane, M.: Opto-capacitive study of n-ZnO/p-Si heterojunctions elaborated byreactive sputtering method: Solar cell applications. Thin Solid Films **636**, 419–424 (2017)
3. Purica, M., Budianu, E., Rusu, E.: Heterojunction with ZnO polycrystalline thin films for optoelectronic devices applications. Microelectron. Reliab. **51**–**52**, 425–431 (2000)
4. Mandalapu, L.J., Xiu, F.X., Yang, Z., Zhao, D.T., Liua, J.L.: p_type behavior from Sb-doped ZnO heterojunction photodiodes. Appl. Phys. Lett. **88**, 112108-1–112108-3 (2006)
5. He, J.H., Ho, C.H.: The study of electrical characteristics of heterojunction based on ZnO nanowires using ultrahigh-vacuum conducting atomic force microscopy. Appl. Phys. Lett. **91**, 233105-1–233105-3 (2007)

6. Afify, H.H., El-Hefnawi, S.H., Eliwa, A., Elnaby, M.M.A., Ahmed, N.M.: Realization and characterization of ZnO/n-Si Solar cells by spray pyrolysis. Egypt. J. Solids **28**(2), 243–254 (2005)
7. Yen, T., Li, M., Chokshi, N., DeLeon, R.L., Kim, J., Tompa, G., Anderson, W.A.: Current transport in ZnO/Si heterojunctions for low-cost solar cells. In: 4th Photovo/Taic Energy Conversion Conference, pp. 1653–1656 (2006)
8. Baik, D.G., Cho, S.M.: Application of sol-gel derived films for ZnOln-Si junction solar cells. Thin Solid Films **354**, 227–231 (1999)
9. Wei-Ying, Z., Sheng, Z., Li-Jie, S., Zhu-Xi, F.: Dependence of photovoltaic property of ZnO/Si heterojunction solar cell on thickness of ZnO films. Chin. Phys. Lett. **25**(5), 1829–1831 (2008)
10. Hussain, B.: Improvement in open circuit voltage of n-ZnO/p-Si solar cell by using amorphous-ZnO at the interface. Prog Photovolt Res Appl. **25**(11), 919–927 (2017)
11. Auret, F.D., Goodman, S.A., Legodi, M.J., Meyer, W.E.: Electrical characterization of vapor phase-grown single crystal ZnO. Appl. Phys. Letts. **80**(8), 1340–1342 (2002)
12. Lee, J.Y., Choi, Y.S., Choi, W.H., Yeom, H.W., Yoon, Y.K., Kim, J.H., Im, S.: Characterization of films and interfaces in n-ZnO/p-Si photodiodes. Thin Solid Films **420**, 112–116 (2002)
13. Bingce, L., Cihui, L., Bo, Y.: Grain boundary layer behavior in ZnO/Si heterostructure. J. Semicond. **31**(3), 032003 (2010)
14. Bingce, L., Cihui, L., Bo, Y.: Effect of grain boundary barrier in ZnO/Si heterostructure. Chin. Phys. Lett. **26**(11), 117101 (2009)
15. Cihui, L., Bingce, L., Xi, F.Z.: Electrical and deep levels characteristics of ZnO/Si heterostructure by MOCVD deposition. Chin. Phys. B **17**(6), 172292 (2008)
16. Lee, C., Shin, M., Lim, M., Seo, J.Y., Lee, J.E., Lee, H.Y., Kim, B.J., Choi, D.: Material properties of microcrystalline silicon for solar cell application. Sol. Energy Mater. Sol. Cells **95**(1), 207–210 (2011)

Design of 4-Bit Reversible Johnson Counter with Optimized Quantum Cost, Delay, and Number of Gate

Aman Agarwal, Heranmoy Maity, Arindam Biswas, Sambit S. Mandal and Amit Rai

Abstract In this paper, we have proposed the design quantum cost, delay, and number of reversible logic gate optimized 4-bit Johnson counter using existing reversible logic gate. The proposed work is designed using HNF gate and Feynman gate. The proposed work is derived with quantum cost (QC), delay (D), constant inputs (CI), garbage output (GO), and number of gates (GC). The QC, D, and GC of the proposed Johnson counter are 21, 5, and 5, respectively. The percentage (%) of improvement is 12.5, 37.5, and 37.5% w.r.t. latest reported result.

Keywords Quantum computing · Reversible logic gate · Flip-flop · Quantum cost Delay

1 Introduction

The 4-bit Johnson counter can be designed using four D flip-flops. In this paper, we have proposed the design quantum cost, delay, and number of reversible logic gate optimized 4-bit Johnson counter using existing reversible logic gate. In this paper, two types of D flip-flops are used, first is D flip-flop with only Q output terminal and second is D flip-flop with Q and Q′ output terminals. The many researcher have designed Johnson counter but the proposed work is most suitable for quantum computation due to optimized of QC, D and GC. This paper is organized as follows: Section-2 describes the basic concepts of reversible logic, Sect. 3 describes the proposed work, Sect. 4 describes the analysis and discussion of the proposed work, and Sect. 5 conclusion.

A. Agarwal · A. Biswas (✉) · S. S. Mandal · A. Rai
Asansol Engineering College, Asansol 713305, India
e-mail: mailarindambiswas@yhaoo.co.in

H. Maity
NSHM Knowledge Campus Durgapur, Durgapur 713212, India
e-mail: heranmoy@gmail.com

U. Biswas et al. (eds.), *Advances in Computer, Communication and Control*, Lecture Notes in Networks and Systems 41, https://doi.org/10.1007/978-981-13-3122-0_54

2 Basic Concepts

2.1 Reversible Logic Gate

The reversible logic gate is a R × R logic function in which R is the number of input and number of output. The input and output are one-to-one correspondence, i.e., output can be uniquely determined from the input and also the input can be recovered from the output [1–5]. The garbage output (GO) refers to the number of unused outputs present in the reversible logic circuits. Quantum cost (QC) of a reversible gate is the number of 1 × 1 and 2 × 2 quantum gate required to design.

The quantum cost of all reversible 1 × 1 and 2 × 2 gates are taken as unity [3]. The delay of a logic circuit is the maximum number of gates in a path from any input line to any output line. There are several reversible logic gates, but in this paper, we use only 2 × 2 Feynman gate (FG) with QC 1 [3], 4 × 4 HNF gate (HNFG) [4] with QC 5. Figures 1, 2 show the block diagram and quantum representation of FG. Figures 3, 4 show the block diagram and quantum representation of HNFG.

2.2 D Flip-Flop

We know that the characteristics equation of D flip-flop is $Q_{n+1} = D.C + Q_nC'$, where C is clock pulse. The D flip-flop may be designed using different ways; in this paper, D flip-flop is designed in two ways. First, it can be designed using only one HNF

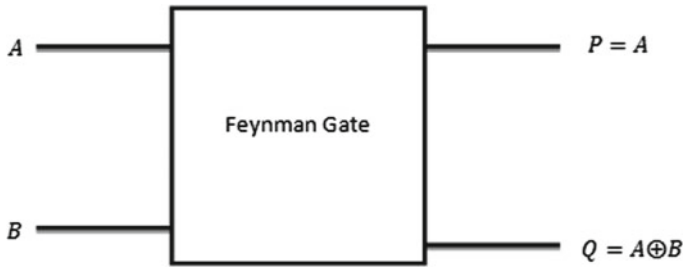

Fig. 1 Block diagram of FG

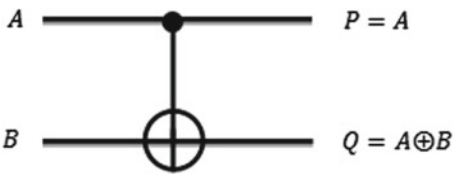

Fig. 2 Quantum representation of FG

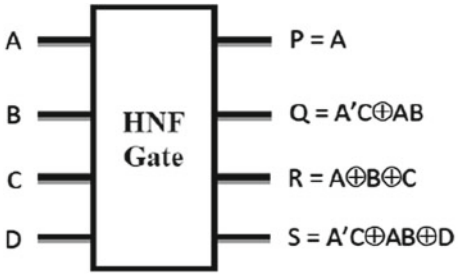

Fig. 3 Basic block diagram of HNF gate (HNFG)

gate with Q output terminal, and second, it can be designed using one HNF gate and one FG with Q and Q′ output terminals.

The quantum cost of D flip-flop with Q terminal is five and D flip-flop with Q and Q′ terminals is 6. Figure 5 shows the D flip-flop using HNF gate with Q terminal only. Figure 6 shows the D flip-flop using one HNF gate and one FG with Q and Q′ terminals.

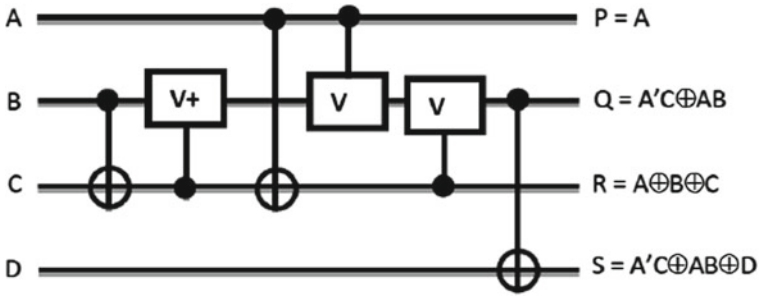

Fig. 4 Quantum representation of HNFG

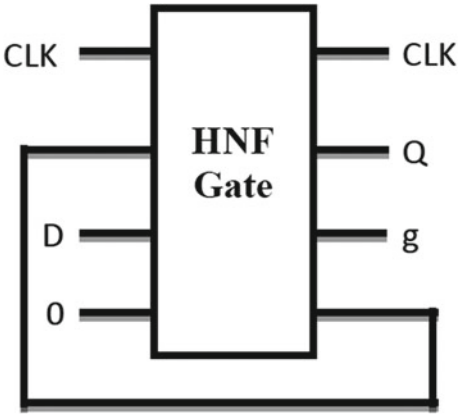

Fig. 5 The D flip-flop using HNFG with Q terminal

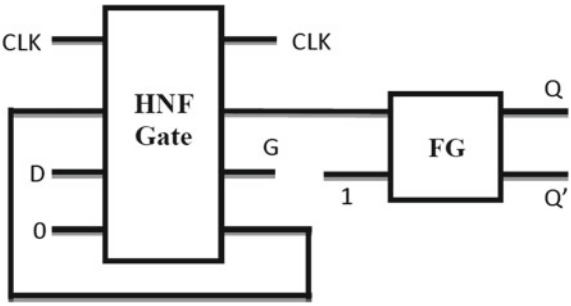

Fig. 6 The D flip-flop using HNFG and FG with Q and Q′ terminals

3 Proposed Johnson Counter

The basic block diagram of Johnson counter is shown in Fig. 7. The inverted output of DFF4 flip-flop is connected to the input of DFF1 flip-flop to construct Johnson counter. The truth table of Johnson counter is given in Table 1. For a 4-bit Johnson counter, there are eight states. The first state is $Q_1Q_2Q_3Q_4 = 0000$ and last state is $Q_1Q_2Q_3Q_4 = 0001$.

Figure 8 shows the proposed design of Johnson counter using HNF gate and Feynman gate. CLK is the clock input terminal and Q1, Q2, Q3, and Q4 are the

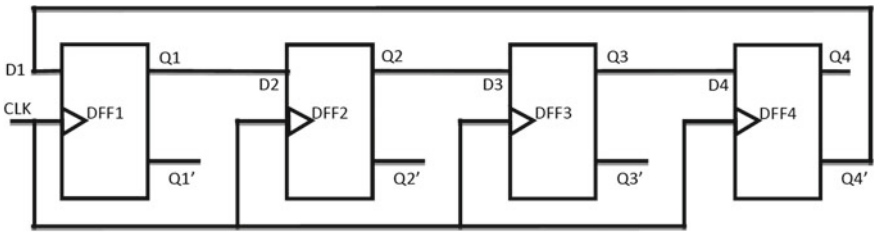

Fig. 7 The basic block diagram of Johnson counter

Table 1 Functional table of proposed 4-bit Johnson counter

CLK	Q_1	Q_2	Q_3	Q_4
0	0	0	0	0
1	1	0	0	0
1	1	1	0	0
1	1	1	1	0
1	1	1	1	1
1	0	1	1	1
1	0	0	1	1
1	0	0	0	1
1	0	0	0	0

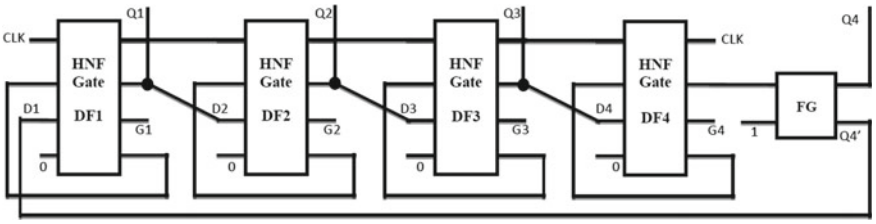

Fig. 8 The proposed 4-bit Johnson counter with optimized quantum cost, delay, and number of reversible logic gate

Table 2 Comparison result of proposed 4-bit Johnson counter

	No. of gates	Quantum cost	No. of constant input	Delay
Proposed	5	21	5	5
Existing [6]	8	24	8	8
Improvement % w.r.t [6]	37.5	12.5	37.5	37.5

outputs terminals of Johnson counter. G1, G2, G3, and G4 are the garbage output terminals. The clock is applied to all flip-flops.

4 Analysis of the Proposed Work

The proposed design of 4-bit Johnson counter is designed using four HNF gates having quantum cost (QC) of 4×5=20 and one Feynman gate (FG) having quantum cost $= 1 \times 1 = 1$. Total quantum cost required to design proposed 4-bit Johnson counter is 21. The number of gates required to design proposed circuit is five. The constant input, garbage output, and delay are 5, 4, and 5. The comparison result is shown in Table 2.

5 Conclusions

The authors have presented the basic concepts of reversible logic gates. Such gates can be used in regular circuits realizing Boolean functions. This paper proposes designs of quantum cost efficient Johnson counter using existing reversible logic gate. Here, in this paper, the proposed designs are better in terms of quantum cost, number of constant inputs, and garbage outputs. The proposed design can have greater impact in quantum computing. The proposed design has the applications in nanotechnology, low power circuit design, cryptography, optical computing, etc.

References

1. Bennett, C.H.: Logical reversibility of computation. IBM J. Res. Dev. **17**, 525–532 (1973)
2. Kiran, P.K., Rao, P.P., Kishore, K.H.: Optimal design of reversible parity preserving new full adder/full subtractor. In: Proceedings of 11th IEEE International Conference on Intelligent System and Control (ISCO), Coimbatore, India, pp. 368–373, 5–6 Jan 2017
3. Feynman, R.: Quantum mechanical computers. Opt. News **11**, 11–20 (1985)
4. Majumder, A., Singh, P.L., Chowdhury, B., Mondal, A.J., Anand, V.: Efficient design and analysis of N-bit reversible shift registers. In: Proceeding of 3rd IEEE International Conference on Recent Trends in Computing (ICRTC-2015), Ghaziabad, India, vol. 57, pp. 199–208, 12–13 Mar 2015
5. Maity, H., Biswas, A., Bhattacharjee, A.K., Pal, A.: Design of quantum cost efficient 4-bit reversible universal shift register. In: Proceedings of 2nd IEEE International Conference on Device for Integrated Circuits (DevIC 2017), Kalyani, India, 44–47 (2017)
6. Maity, H., Dey, A., Singh, S.K.: A novel design of 4-bit johnson counter using reversible logic gate. Int. J. Sci. Res. Dev. **2**, 119–121 (2014)

Simultaneous Clustering and Feature Selection Using Nature-Inspired Algorithm

Sabyasachi Mukherjee and Lumbini Bhaumik

Abstract Clustering means partitioning of data set into individual clusters where the similarity among the data exists and the procedure requires more substantial methodology when the dimension of the input data set is very high as well as we have to select more relevant dimensions or features which are necessary enough for clustering. Nature-inspired algorithm like firefly gives a promising result in function optimization and clustering. The proposed work will represent a new feature selection cum clustering algorithm called iterative firefly k-means features selection (FKM_FS) algorithm by minimizing the inter-cluster distance as well as maximizing the intra-cluster distance and maximizing the average relevance of the particular feature to the clustering. We define a methodology based on variance of observation in a cluster with respect to global variance to identify relevant feature subset. Finally, the algorithm will run both on real and data set.

1 Introduction

Data clustering is the procedure where data set can be partitioned into an unknown number of clusters (or groups) while minimizing the within intra-cluster distance and maximizing the inter-cluster variability. Clustering is one of the key features and even more challenging task in unsupervised machine learning. Several clustering algorithms have been proposed in the literature, including hierarchical, partitional, density based, and grid based [1, 2]. Partitional clustering has been the most popular, because it is dynamic, has good performance, and it considers the global shape and size of clusters. In partitional clustering like k-means procedure, each data object is represented by a vector of features. In successive iteration, the algorithm organizes

S. Mukherjee (✉) · L. Bhaumik
Department of Computer Science and Engineering,
Asansol Engineering College, Asansol, West Bengal, India
e-mail: sabyasachi.mukherjee24@gmail.com

L. Bhaumik
e-mail: lumbinibhaumik@gmail.com

U. Biswas et al. (eds.), *Advances in Computer, Communication and Control*, Lecture Notes in Networks and Systems 41, https://doi.org/10.1007/978-981-13-3122-0_55

the data set into number of clusters in such a way that the distance of each data point to the respective centroids of each cluster is minimized. The distance between two data points, i.e., the distance between the data points and the centroids can be computed separately using similarity or distance functions This is also called Euclidean distance. Most partitional algorithms (e.g., k-means, k-medoids), generally assume all features to be essential for clustering, but in reality we do not require all set of features and subsequently most relevant features need to be extracted for dimensionality reduction as well as good clustering result. Feature selection (FS) is the task of selecting the relevant features in a high-dimensional data set [3]. Feature selection simultaneously with clustering can improve the performance of the clustering algorithm very efficiently [4]. Feature selection when performed before the clustering process in algorithms referred to as filters procedure; on the other side (called wrappers), which combine feature selection procedures simultaneously with the clustering process [4]. In this paper, a new algorithm for clustering with feature selection called **FKM_FS** has been developed which is mainly based on wrapper method. In this methodology, firefly search algorithm [5] has been used as a global search procedure and k-means clustering method has been called for local search of location.

2 Methodology

Our algorithm called **iterative firefly k-means feature selection algorithm** (**FKM_FS**) uses the firefly search algorithm as a global metaheuristic search strategy across as well as integrating k-means for improving the solutions called centroids. In the basic procedure, we have three different steps. First, we are going to initialize the various parameters, in the next step, we are calling firefly k-means algorithm and return three different values which are centroids, list_of_dimention selected, and value of the fitness function which correspond to each row of best memory result (BMR) data structure (matrix). We have selected the initial location of centroids with forgy strategy and fitness for this solution. We are allowing the centroids to move toward the best global position using firefly search algorithm and finding out the current best solution. Then, we are calculating the new fitness value based on new centroids. The new vector will replace the previous if the fitness function value of the new vector gives better result than the previous. The iteration will continue until some condition is being satisfied, otherwise, the previous steps will be again performed. Then, we will sort the rows of the data matrix based on the value of fitness and find out the greatest one and perform the local search k-means operation to refine the centroids and again we are calculating the fitness value. At last, we are returning this best fitness value associated with centroids and list of dimension selected to the main program or routine. From the main program, we are again performing the sorting operation based on fitness value and the row corresponding to the best fitness would be the desired result, i.e., location of centroids, list of dimensions selected, and fitness value. In the above procedure, the objective function encodes two parameters

from where we are getting good compactness of clustering solution and relevant feature selection. These two parameters are trace (i.e., the criteria of compactness of the cluster) and penalty function (which is a function of maximum score values) which depend on the relevant feature selection and in this fitness function, we are maximizing the product of trace and penalty. Similar to Zeng and Cheung in [6], we will determine variance of any features w.r.t. global variance, i.e., **the value of $\mathbf{Variance_{F,J}}$ and $\mathbf{Variance_F}$ becomes closer to each other leaving $\mathbf{Score_F}$ values almost zero**, and hence this feature will not be selected and where $Variance_{F,J}$ signifies the relevance of F-th feature into J-th cluster and $Variance_F$ signifies the global variance of F-th dimension in D dimensionality feature space.

$$\mathbf{Score_F} = \mathbf{1/k} \sum_{\mathbf{j=1}}^{\mathbf{n}} \left(\mathbf{1 - Variance_{F,J}/Variance_F}\right)$$

where $Score_F$ defines the average relevance of the F-th feature to the clustering structure. **If the value of $\mathbf{Score_F}$ is maximum, then the final clusters would be far apart from each other and we will get good quality solution.**

Algorithmic description of iterative firefly k–means feature selection algorithm for simultaneous clustering and relevant feature selection (FKM_FS).

In this algorithm, there exist mainly three basic steps. These steps are as follows:

2.1 The Detailed Descriptions of These Steps are Given Below

1. **Initialize the algorithm parameters**: In this proposed methodology, the optimization problem is a function of the product of trace($S_W^{-1}S_b$) and a heuristic function which is dependent on selecting the relevant features. Initializing the number of rows in the data matrix (which needs to be formed) of firefly memory data structure which is equal to the number of firefly k-means method call iteratively, number of clusters desired(k) and percentage of dimensions(PI) and maximum number of call to firefly k-means method = BMRS and BMR = Best firefly memory result.

$$\begin{aligned}\textbf{BFMR (DataMatrix)}; = \; & [\text{centroids}_1 \quad \text{List of dimension selected}_1 \quad \text{Fitness value}_1] \\ & [\text{centroids}_2 \quad \text{List of dimension selected}_2 \quad \text{Fitness value}_2] \\ & [\quad \cdots \qquad\qquad \cdots \qquad\qquad \cdots] \\ & [\text{centroids}_{BMRS} \quad \text{Listofdimensionselected}_{BMRS} \quad \text{Fitness value}_{BMRS}]\end{aligned}$$

2. **Initialize the best memory result and calling the firefly k-means routines**: Best memory result is a row corresponding to best fitness function value. Each row will be created by one time calling **firefly _k-means** routine. In each row, there exists three parts and they are centroids, list of dimension selected, and

fitness value. Initially, we are going to calculate range of each dimension and perform min–max normalization on the data set.

3. **Return the best result**: Selection of the best row corresponding to the best-optimized fitness value and the result will contain the best solution (centroids, list of dimension selected, and fitness).

2.2 Firefly k-means Routine

1. **Intialize the firefly memory data structure**: The firefly memory is a data structure where all the finally calculated vectors will be stored. Each solution is created with a random number of dimensions (d), centroids which represents each and every firefly in the search space and fitness function value for these solutions. In this step, we generate the firefly memory solution vector and then calculate the fitness value for each vector.
2. **Generating a new firefly** (**centroids**): Newly generated centroids evolved from firefly move operation in basic firefly algorithm by traversing all firefly toward brighter one.
3. **Updating the firefly memory**: The new value of vector solution replaces the previous one if its new value is better than the previous.
4. **Checking the stopping criterion**: If the given conditions are satisfied then the iteration is terminated otherwise steps go to again 2 and 3.
5. **Select the best firefly memory vector**: The best firefly memory corresponds to the best fitness value. In every iteration, the further search k-means is applied and created a new value of fitness and final location of centroids.
6. Extracting the best firefly memory vector (centroids, list of dimension selected, and fitness) to best memory result (BMR).

2.3 Objective Function Evaluation Routine

1. Calculate **Trace** ($\mathbf{S_W^{-1}S_b}$) **based on covariance matrix** which represents the distance of each data element with respect to the centroids in the desired cluster.
2. Calculate the $\mathbf{Score_F}$ for each dimension in the current solution and accumulating its value to obtain sum of score (SS). Then, sorting the results in descending order.
3. Selecting the value of PI percentage from the number of dimensions in the current solution as the number of relevant dimension.

Total = 0
RD = 0/* Number of relevant dimensions
For each i∈[1, d] do

$$\text{Total} = \text{Total} + \text{Score}_i$$

$$RD = RD + 1$$

If Total > SS * FI then Exit-For
Next For
Heuristic function H(f) = SS/(d-RD) when NRD < d
Or = SS when RD = d
Calculate Fitness = Trace($S_W^{-1} S_b$) * H(f) and return the value.

Note **The value of PI varies from 0 to 1. The higher value of PI gives better result.**

3 Result

Several data set like three real (iris, WDBC, and image segmentation) has been tested in the proposed algorithm for determining set of relevant features of the data. We shall also calculate the error classification percentage and number of feature selected to compare our result with iterative harmony search k-means (IHSK) and k-means algorithm for fixed features.

Description of Dataset **IRIS-Total features = 4 and clusters = 3.**
WDBC-Total features = 30 and clusters = 2.
Image Segmentation Total features = 19 clusters = 7.

Error classification percentage (ECP) calculation.
Number of features selected (NFS).
Number of relevant dimensions (NRD).
In our case, NFS = NRD (Tables 1, 2, and 3).

4 Future Work

There are several tasks we are going to suggest for future work like applying the iterative firefly k-means feature selection algorithm on more synthetic data set to find

Table 1 ECP, NFS by the algorithm for Iris dataset

Data set	Algorithms	ECP	NFS
Iris	k-means	17.8 + 6.9 7.8 − 6.9	Fixed at 4
	IHSM	4.00 + 0.00 4.00 − 0.00	2.0 + 0.00
	FKM_FS	4.00 + 0.00 4.00 − 0.00	3.00 + 0.00

Table 2 ECP, NFS by the algorithm for WDBC dataset

Data set	Algorithms	ECP	NFS
WDBC	k-means	15.6	Fixed at 30
	IHSK	9.07 + 0.02 9.07 − 0.02	14.0 + 6.72 14.0 − 6.72
	FKM_FS	8.07 + 0.00 8.07 − 0.00	29

Table 3 ECP, NFS by the Algorithm for Image segmentation dataset

Data set	Algorithms	ECP	NFS
Image segmentation	k-means	38.6 + 3.8 38.6 − 3.8	Fixed at 19
	IHSK	37.15 + 0.4 37.15 − 0.4	6.5 + 0.2 6.5 − 0.2
	FKM_FS	36.25 + 0.2 36.25 − 0.2	17

out not only irrelevant features but also redundant features. We can also formulate the clustering criteria, i.e., trace value as described here to normalize using cross-projection method [3] to find out suitable feature sets. We will also have a plan to apply the multi-objective variant of firefly with k-means as local search to get better result.

References

1. Jain, A.K., Murty, M.N., Flynn, P.J.: Data clustering: a review. ACM Comput. Surv. **31**, 264–323 (1999)
2. Jacob, K., Charles, N., Marc, T.: Grouping Multidimensional Data Recent Advances in Clustering, pp. 25–72. Springer-Verlag, New York (2006)
3. Dy, J.G., Brodley, C.E.: Feature selection for unsupervised learning. J. Mach. Learn. Res. **5**, 845–889 (2004)
4. Geem, Z., Kim, J., Loganathan, G.V.: A new heuristic optimization algorithm. Harmon. Search Simul. **76**, 60–68 (2001)
5. Yang, X.S.: Firefly algorithm, stochastic test functions and design optimization. Int. J. Bio-Inspired Comput. **2**, 78–84 (2010)
6. Zeng, H., Cheung, Y.M.: A new feature selection method for Gaussian mixture clustering. Pattern Recogn. **42**, 243–250 (2009)

Short-Term Load Forecasting for Peak Load Reduction Using Artificial Neural Network Technique

Ayandeep Ganguly, Kuheli Goswami, Arpita Mukherjee and Arindam Kumar Sil

Abstract Load forecasting is a process for electrical load prediction. In today's deregulated market, it is imperative for the generating company to know about the load demand in advance to provide accurate power. A problem of irregular supply arises if the generation is not sufficient, and the company may have to incur losses in case of excess generation as the energy cannot be stored. In this end, short-term load forecasting plays an important part. There are several methods of load forecasting among which artificial neural network is one of the processes gaining popularity. This work intends to study the applicability of artificial neural network model to short-term load forecasting.

Keywords Load forecasting · Artificial neural network · MLP · MLPE

1 Introduction

The most important commodity of today's world is energy. Energy is used in various forms by each and every one of us in our everyday life. Energy in the form of electricity, LPG, wind energy, solar energy, and chemical energies in the form of batteries is in wide circulation. Energy utilization depends upon several factors such as variation in temperature, seasons, humidity, day of the week, special holidays,

A. Ganguly (✉)
Electrical Engineering Department, HIT, Haldia 721657, India
e-mail: gangulyayandeep@gmail.com

K. Goswami
Electrical Engineering Department, BGI, Kolkata 700124, India
e-mail: kuheli.ee.prfsnl@gmail.com

A. Mukherjee
Electrical Engineering Department, Camellia Group of Institutions, Kolkata, India

A. K. Sil
Electrical Engineering Department, Jadavpur University, Kolkata, India
e-mail: ak_sil@yahoo.co.in

U. Biswas et al. (eds.), *Advances in Computer, Communication and Control*, Lecture Notes in Networks and Systems 41, https://doi.org/10.1007/978-981-13-3122-0_56

etc. and as such varies widely day to day, making it a complex series exhibiting several levels of seasonality. This complexity of the energy use makes it a difficult task to forecast the load demand in advance. But load forecasting is important to ensure the efficient supply of energy to the consumers and minimize losses of the service provider. It can be used as a useful tool to know about the scenario of present and future load demands. So, load forecasting has become a major area of research in electrical engineering in recent years. There are many applications of load forecasting in energy purchasing and generation, load switching, contract evaluation, and infrastructure development. A model of high accuracy is very important to the planning and operation of a company. It is also important for participants in electric energy generation, transmission, distribution, and markets. Load forecasting can be divided into three categories as follows:

1. Short-term load forecast, usually ranging from 1 h to 1 week.
2. Medium forecasts, ranging from a week to a year.
3. Long-term load forecast, longer than a year.

The importance of the quality of the short-term load forecasts arises from the fact that it has a significant impact on the economic operations of the electric utility as decisions regarding economic scheduling of generation capacity, available transmission capacity transactions, and they can have economic consequences of high significance.

This work involves the design of a short-term load forecasting (STLF)/artificial neural network (ANN) model to forecast the load data of West Bengal for a 24-hour span, a week in advance. The neural network model is trained using historical load data and the daily maximum, minimum, and average temperature. The training function used was the batch gradient function with momentum. The network was trained with the load data of the year 2017 obtained from the website of eastern region load dispatch center. The advantage of using an ANN-based STLF tool lies in the fact that a single structure having the same input and output configurations can be used for obtaining the hourly or daily load forecast of different utilities and regions of varying sizes and consumers. The only modification that needs to be done is for a few parameters of the ANN model.

This paper begins with a short introduction to STLF and ANN followed by the description of the architecture of the neural network used and ends with a discussion of the results obtained and a comparison of the forecasted loads with the actual loads for the target day to determine the error present if any.

2 Review of Load Forecasting Methods

The rapid increase in the load demand of our cities and the goal of decreasing the response time of the service providers have led to the increased importance of load forecasting. A comparative study of four popularly used load forecasting techniques was done by Cheepati and Prasad [1]. A review of load forecasting methods using

artificial intelligence techniques, hybrid techniques, and knowledge-based expert systems was given by Srivastava et al. [2]. A technique using curve fitting combined with genetic algorithm for load forecasting and selecting training vectors was proposed by Talaat [3]. A hybrid model by combining separate forecasting of the seasonal item and the trend item by seasonal exponential adjustment method and regression methods for improving forecasting accuracy was proposed by Wu et al. [4]. Another model combining artificial neural network and multiple linear regression was proposed by Kumar et al. [5]. A random forest model for load forecasting is proposed by Lahouar and Slama [6]. The proposed model was tested with a real load data set from the Tunisian power company, where the load profile is specific to countries with higher temperatures resulting in excessive demand during the summer season. A neural-network-based 1-hour-ahead load forecasting has been proposed by Pindoriya et al. [7]. The hourly load data of the Californian electricity market was used for training and testing purposes. Another method for short-term load forecasting with increased accuracy for proposing the daily peak load was proposed by Amjadi [8]. A day-ahead forecasting model using neural network was proposed by Sahay and Tripathi [9] using the PJM and New England Electricity Market. A 1-day-ahead load forecasting model using artificial neural network for the electricity market of Iran was proposed by Azadeh et al. [10]. Thus, we can see that day-ahead forecasts with different load forecasting methods have yielded satisfactory results. But the efficiency of the load forecasting models for week-ahead load forecasting is yet to be explored. So, an attempt has been made to use neural network for a week-ahead forecast using the West Bengal electricity market.

3 Design

Backpropagation neural network is selected as the tool for load forecasting in this work. Backpropagation simply consists of the repeated application of the chain rule through all the possible paths of the network. The ultimate goal in training the neural network is to update the gradient of each weight with respect to the output as given below:

$$w_{ij} = w_{ij} - \rho \frac{\partial E}{\partial w_{ij}} \tag{1}$$

Let us consider the following network:

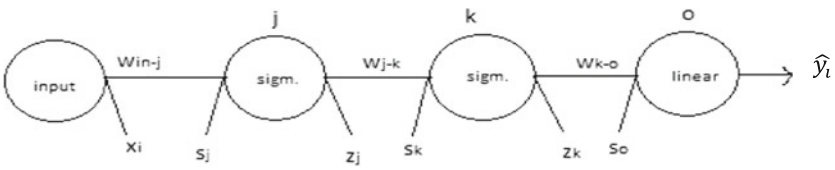

The values of each variable of this network can be written as

$$s_j = w_1 \cdot x_i \tag{2}$$

$$z_j = \sigma\left(in_j\right) = \sigma(w_1.x_i) \tag{3}$$

$$s_k = w_2 \cdot z_2 \tag{4}$$

$$z_k = \sigma(in_k) = \sigma(w_2 \cdot \sigma(w_1 \cdot x_i)) \tag{5}$$

$$s_o = w_3 \cdot z_k \tag{6}$$

$$\widehat{y_i} = in_0 = w_3 \cdot \sigma(w_2 \cdot \sigma(w_2 \cdot x_i)) \tag{7}$$

$$E = \frac{1}{2}\left(\widehat{y_i} - y_i\right) = \frac{1}{2}(w_3 \cdot \sigma(w_2 \cdot \sigma(w_i \cdot x_i)) - y_i)^2 \tag{8}$$

The weight updates for the different layers can be found as follows:

$$\frac{\partial E}{\partial w_{ko}} = \frac{\partial}{\partial w_{ko}} \frac{1}{2}\left(\widehat{y_i} - y_i\right)^2 = \frac{\partial}{\partial w_{ko}} \frac{1}{2}(w_{ko} \cdot z_k - y_i)^2 = \left(\widehat{y_i} - y_i\right)(z_k) \tag{9}$$

Similarly, we can get the updates of the other layers as

$$\frac{\partial E}{\partial w_{jk}} = \left(\widehat{y_i} - y_i\right)(w_{ko})(\sigma(s_k)(1 - \sigma(s_k)))(z_i) \tag{10}$$

$$\frac{\partial E}{\partial w_{ij}} = \left(\widehat{y_i} - y_i\right)(w_{ko})(\sigma(s_k)(1 - \sigma(s_k)))\left(w_{jk}\right)\left(\sigma\left(s_j\right)\left(1 - \sigma\left(s_j\right)\right)\right)(x_i) \tag{11}$$

So, in summary, we have,

$$\Delta w_{ij} = -\rho\left[\left(\widehat{y_i} - y_i\right)(w_{ko})(\sigma(s_k)(1 - \sigma(s_k)))\left(w_{jk}\right)\left(\sigma\left(s_j\right)\left(1 - \sigma\left(s_j\right)\right)\right)(x_i)\right] \tag{12}$$

$$\Delta w_{jk} = -\rho\left[\left(\widehat{y_i} - y_i\right)(w_{ko})(\sigma(s_k)(1 - \sigma(s_k)))(z_i)\right] \tag{13}$$

$$\Delta w_{ko} = -\rho\left[\left(\widehat{y_i} - y_i\right)(z_k)\right] \tag{14}$$

The neural network is made to learn from the historical data of 2017 hourly load data and average temperatures of West Bengal. To fulfill the objective of forecasting the week-ahead load demand of a day, a program was written in MATLAB utilizing the ANN toolbox in MATLAB. The multilayer feedforward network architecture has three layers consisting of two hidden layers and one output layer (Fig. 1).

The number of neurons in the hidden layer was varied from 5 to 21 to find the best fit model with the highest efficiency. It was seen that 12 neurons in the first hidden layer and 21 neurons in the second hidden layer gave the best output. The forecasted load of each hour for the target day is obtained from the 24 neurons, respectively, in the output layer of the ANN architecture. The input neurons are used to provide information of the historical load, temperature, and target day, specifically the temperature of the target day and the type of the day. The details of the input and output of the ANN is given in the Table 1.

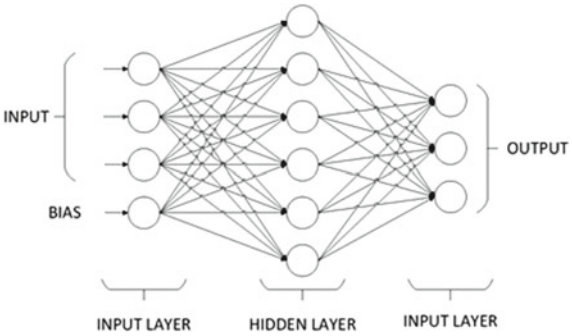

Fig. 1 Artificial neural network architecture

Table 1 ANN inputs and outputs

Inputs	Description
1–24	L (d-7, h); h = 1–24
25–27	Tmax (d-7); Tmin (d-7); Tavg (d-7)
28–30	Tmax (d); Tmin (d); Tavg (d)
31	Day type
Outputs	Description
1–24	L (d, h); h = 1–24

The inputs are scaled using the MATLAB function "prestd" to prevent the saturation of the input neurons. To get the proper output, the process is reversed for the output neurons using the MATLAB function "poststd" and the outputs are scaled back to the original range. The network was trained by backpropagation algorithm using the log-sigmoid activation function for the hidden layer and linear activation function for the output layers. The load and temperature data of West Bengal for a span of 1 year, i.e., 2017 obtained from eastern region load dispatch center was used for training the proposed neural network. After the training of the network is completed, a separate set of input and target data was used to test the performance of the neural network, keeping the weights and biases of the network obtained after training as constant. One neural network is trained for each day of the week to make a week-ahead forecasting system. The importance of week-ahead forecasting lies in the fact that it gives us enough time to prepare for the upcoming load demand and decide how the load can be optimally dispatched using conventional and renewable sources and decide upon the proper coordination of the available power generation sources.

4 Results and Discussion

The training of the network was done using the historical data of West Bengal for 365 days. The total available data was divided into a training (75% of the data) and testing set (25% of the data). The network was trained using the training set and then it was tested with the test set. The error tolerance was set to 1e-5 and the maximum number of iterations was set to 5000. The error of the network output was calculated using the mean absolute error (MAE) with the formula shown below:

$$\text{MAE} = \sqrt{\left(\frac{\text{Actual Value} - \text{Forecasted Value}}{\text{Actual Value}}\right)^2}$$

The network was trained using the gradient descent training function with a momentum component. One neural network was trained for each day of the week. The testing and training of the networks were done using only the weekday data. The holidays and the weekends were not involved in this forecasting. The output of the forecast for each day is shown in the figures below. The blue line shows the target value, that is, the original load of the target day while the blue line represents the output of the neural network (Figs. 2, 3, 4, 5, and 6).

The error values are given in Table 2.

The accuracy of the neural network could have been increased further if it was possible to train the network with more data. But as the data available at the source was inconsistent and only for 1 year the training accuracy of the neural network was

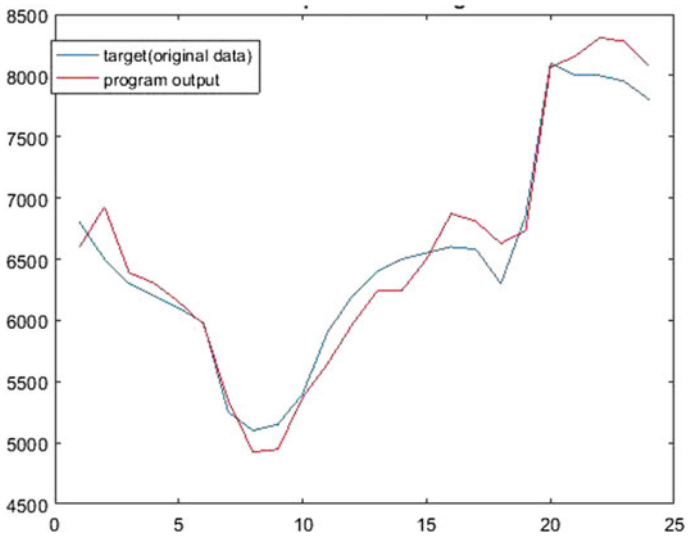

Fig. 2 Monday load forecasting

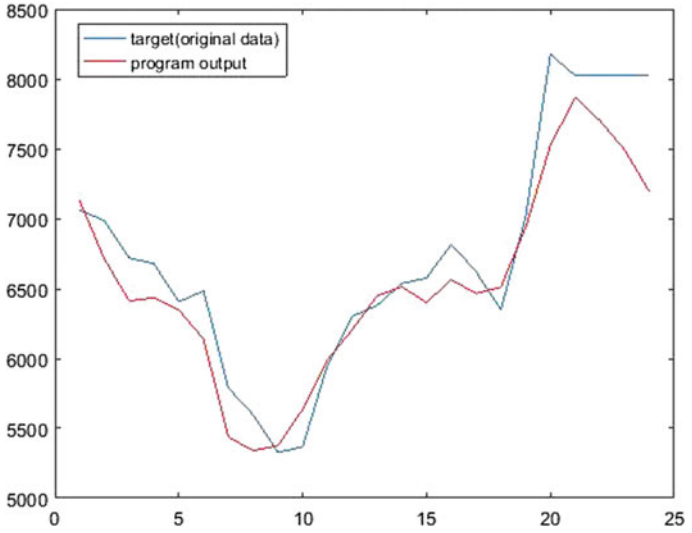

Fig. 3 Tuesday load forecasting

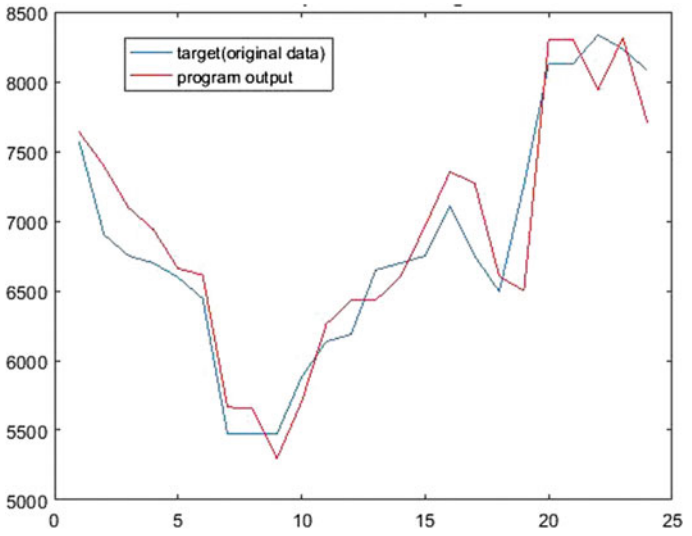

Fig. 4 Wednesday load forecasting

affected. It was also seen that using a log-sigmoid activation function in the second hidden layer provided better results compared to a tan-sigmoid function.

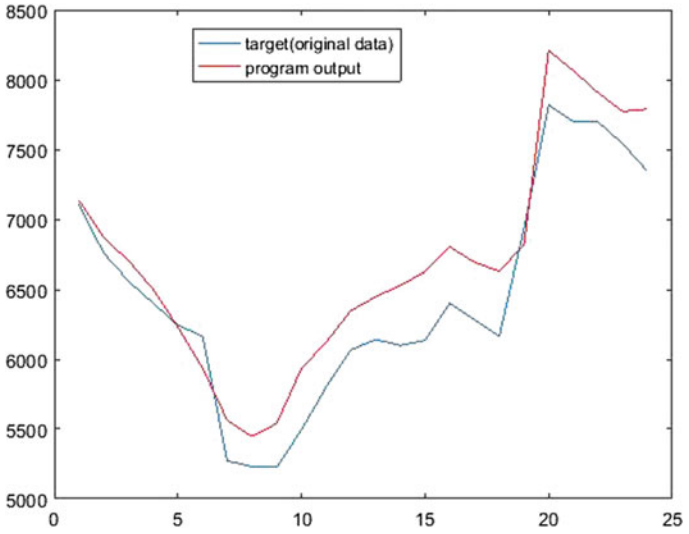

Fig. 5 Thursday load forecasting

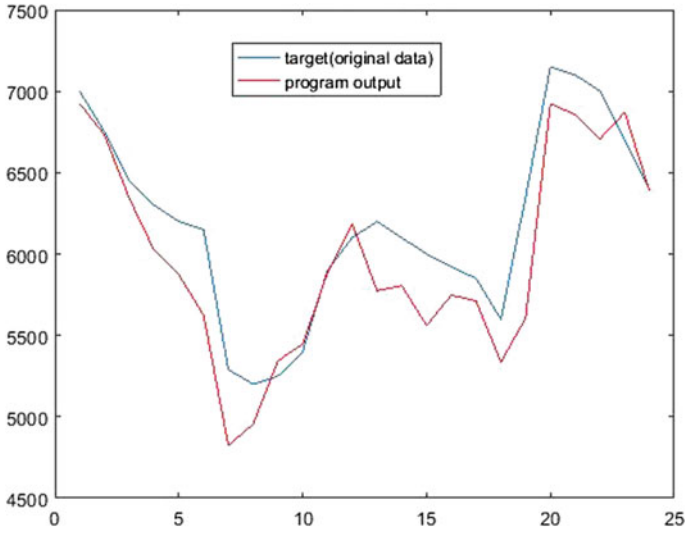

Fig. 6 Friday load forecasting

5 Conclusion

It was seen that neural network as a tool for load forecasting performs fairly in terms of accuracy. The main advantage of using a neural network is that the architecture is not needed to be modified with change of inputs or span of forecasting. So, this

Table 2 Error percentage for each day

Target day	Error (in %)
Monday	2.7736
Tuesday	3.6189
Wednesday	3.5414
Thursday	4.2377
Friday	4.1397

can be considered a suitable tool for a wide range of applications. Using the forecast obtained from this too a better load dispatch strategy can be formulated and the system response can be automated thus reducing the time of response and margin of error. Any number of factors can be used as the input of the artificial neural network and the training of the network can be done with the help of other artificial intelligence with a goal of increasing the accuracy of the tool.

References

1. Cheepati, K.R., Prasad, T.N.: Performance comparison of short term load forecasting techniques. Int. J. Grid Distrib. Comput. **9**(4), 267–302 (2016)
2. Srivastava, K., Pandey, A.S., Singh, D.: Short-term load forecasting methods: a review. In: 2016 International Conference on Emerging Trends in Electrical Electronics & Sustainable Energy Systems (ICETEESES), Sultanpur, pp. 130–138 (2016)
3. Talaat, M.: The using of curve fitting prediction optimized by genetic algorithms for short-term load forecasting. Int. Rev. Electr. Eng. **7**(2012), 6209–6215 (2012)
4. Wu, J., Wang, J., Lu, H., Dong, Y., Lu, X.: Short term load forecasting technique based on the seasonal exponential adjustment method and the regression model. Energy Convers. Manag. **70**, 1–9 (2013). ISSN 0196-8904
5. Kumar, S., Mishra, S., Gupta, S.: Short term load forecasting using ANN and multiple linear regression. In: 2016 Second International Conference on Computational Intelligence & Communication Technology (CICT), Ghaziabad, pp. 184–186 (2016)
6. Lahouar, A., Slama, J.B.H.: Random forests model for one day ahead load forecasting. In: IREC2015 The Sixth International Renewable Energy Congress, Sousse, pp. 1–6 (2015)
7. Pindoriya, N.M., Singh, S.N., Singh, S.K.: One-step-ahead hourly load forecasting using artificial neural network. In: 2009 International Conference on Power Systems, Kharagpur, pp. 1–6 (2009)
8. Amjady, N.: Short-term hourly load forecasting using time-series modeling with peak load estimation capability. IEEE Trans. Power Syst. **16**(3), 498–505 (2001)
9. Sahay, K.B., Tripathi, M.M.: Day ahead hourly load forecast of PJM electricity market and iso new England market by using artificial neural network. In: ISGT, Washington, DC, pp. 1–5 (2014)
10. Azadeh, A., Ghadrei, S.F., Nokhandan, B.P.: One day ahead load forecasting for electricity market of Iran by ANN. In: 2009 International Conference on Power Engineering, Energy and Electrical Drives, Lisbon, pp. 670–674 (2009)

Author Index

U. Biswas et al. (eds.), *Advances in Computer, Communication and Control*, Lecture Notes in Networks and Systems 41, https://doi.org/10.1007/978-981-13-3122-0